QUANTUM STATES OF LIGHT IN HYBRID 2D MATERIAL-NANOPHOTONIC SYSTEMS

by

Joseph Chad Stage

A dissertation submitted in partial fulfillment
of the requirements for the degree

of

Doctor of Philosophy

in

Physics

MONTANA STATE UNIVERSITY
Bozeman, Montana

May 2026

©COPYRIGHT

by

Joseph Chad Stage

2026

All Rights Reserved

ACKNOWLEDGEMENTS

This dissertation would not have been possible without the support, guidance, and encouragement of many people. Nicholas Borys, your radiant passion for science and personal development have motivated me to become a more thoughtful, well-rounded, and precise individual. You are a true mentor. I am extremely grateful for the time and effort you have invested in my development as a scientist. Thank you for always supporting my ideas and pushing me to do my best in every manner.

To my committee members, John Neumeier, Jiong Qiu, Wataru Nakagawa, and Anton Vorontsov, thank you for your time, consideration, and participation in the evaluation of this dissertation.

I cannot understate the importance of MMF and ICAL staff, especially Andrew Lingley and Sara Zacher. Thank you for maintaining a state-of-the-art facility that made possible the high-quality nanofabrication and metrology of the structures I made over the course of my Ph.D., and for our discussions on nanoscale physics that shaped how I think about these systems.

The work in this dissertation could not have been accomplished without my collaborators and lab mates. Thank you all for your contributions, presentation feedback, and the enjoyable times we shared in the lab.

Finally, I would like to thank my parents, David Stage and Laurie Lundstrom, for their constant support and sacrifice throughout my life and this journey. I also want to thank my best friend, Brenan Hammer, for his friendship and unwavering encouragement. I am equally grateful to Jud and Licette Hammer, who have been like a second family to me, for their kindness and support over the years.

TABLE OF CONTENTS

1. INTRODUCTION 1

1.1 Van der Waals Materials 1
1.2 Light Matter Interactions and Strain Effects in 1L-WSe_2 9
1.3 Quantum Emitters 14
1.4 Strain Centers for Deterministic Generation of SPEs in 1L-WSe_2 24
1.5 Conclusion 32
Chapter 1 References 37

2. METHODS 67

2.1 Exfoliation Techniques 67
2.1.1 Scotch Tape Exfoliation 67
2.1.2 Gel-Assisted Exfoliation 70
2.1.3 Gold-Assisted Exfoliation 72
2.2 Lithography Techniques for Nanophotonic Stressor Fabrication 76
2.2.1 Optical Lithography 77
2.2.2 Thermal Scanning Probe Lithography 78
2.2.3 Fabrication of Embedded Plasmonic Nanoantennas Using TSPL 79
2.2.4 Imprint Lithography 85
2.3 Finite Element Modeling in COMSOL 87
2.4 2D Material Transferring 92
2.4.1 Dry Transfer Using PDMS 94
2.4.2 Dry Transfer Using Polymer Layers (PPC, PCL, PC) 97
2.4.3 Wet Transfer Using PDMS 102
2.5 Photoluminescence (PL) and Raman Spectroscopy 104
2.5.1 Measuring the Laser Spot Size 105
2.5.2 Laser Power-Induced Damage on 2D Materials 108
2.6 Optimization of an HBT Interferometer for Low Fluence SPE Measurements 109
2.6.1 Spectral Filters to Isolate SPE States 110
2.6.2 Elimination of Reflections Using Rotated Optics and a Plate Beam Splitter 113
2.6.3 Enhanced Collection Efficiency Using a Beam Reducer 114
2.6.4 Time Correlated Single-Photon Counting (TCSPC) 114
2.7 Photoluminescence Excitation Spectroscopy (PLE) 116
2.7.1 PLE Data on Nanophotonic Systems with Quantum Light Sources 120
2.8 Near-Field Optical Spectroscopy 121
2.8.1 Near-Field Contrast 122
Chapter 2 References 125

TABLE OF CONTENTS CONTINUED

3. DETERMINATION OF THE ROLES OF STRAIN AND TEARING IN SINGLE PHOTON EMISSION FROM NANOINDENTED WSe_2 145

Contributions of Authors and Co-Authors 145
Manuscript Information 147
Abstract 148
Introduction 149
Results and Discussion 151
Conclusion 164
Methods 165
Sample Fabrication 165
Exfoliating WSe_2 onto PMMA 165
Generation of Nanoindents 166
Inversion of Nanoindents 166
Wet Transfer of Thin Graphite 167
Optical Measurements 167
Room Temperature Photoluminescence (PL) 167
Cryogenic PL 168
Supplementary Information 169
Details on Nanoindentation and Indentation Force Calculation 169
Development of Inversions with Non-normal Incidence Au Evaporation 170
Sliding of the AFM Tip from a Misaligned Contact Angle 172
Yaw Tilt of the AFM Cantilever Generating an Asymmetric Buildup Region 173
Tearing in Indented Materials from Dulled AFM Tips with Different Y-Displacements 174
Properties of the Emitter Ensemble at Each Site in Batch 3 175
Chapter 3 References 181

4. A PLATFORM FOR NANO-OPTICAL ENGINEERING OF LIGHT-MATTER INTERACTIONS IN 2D MATERIALS WITH INDEPENDENTLY TAILORED STRAIN 194

Contributions of Authors and Co-Authors 194
Preamble to the Status of This Work 196
Manuscript Information 197
Abstract 198
Introduction 199
Results and Discussion 201
Conclusion 212
Methods 213

TABLE OF CONTENTS CONTINUED

Sample Fabrication 213
Fabrication of Embedded Plasmonic Nanoantennas 213
Dry Transfer of 1L-WSe_2 214
Optical Measurements 214
Cryogenic optical spectroscopy 214
Near-Field Optical Spectroscopy 215
Photoluminescence excitation spectroscopy (PLE) 215
Supplementary Information 216
Tuning the Convergence of Embedded Nanoantennas 217
Modeling Expected Reliefs Using Electron Beam Evaporation Rates 218
Modeling the Optical Field Intensities from Reflections 220
Calibrating for Drift During a PL Intensity Localization Measurement 221
Chapter 4 References 229

5. GRAPHITE-INDUCED PHOTOLUMINESCENT BRIGHTENING OF QUANTUM LIGHT IN MONOLAYER WSe_2 NANOINDENTS 244

Contributions of Authors and Co-Authors 244
Manuscript Information 245
Abstract 246
Introduction 247
Results and Discussion 250
Conclusion 260
Methods 261
Sample Fabrication 261
Gel-Assisted Exfoliation onto PMMA Substrates 261
Nanoindentation of 1L-WSe_2 262
Hybrid Wet and Dry Transfer of Graphite 262
Optical Measurements 263
Room Temperature Photoluminescence 263
Cryogenic Photoluminescence 263
Spectral and Time Resolved Photoluminescence 264
Chapter 5 References 265

6. CONCLUSION 276

6.1 Summary and Outlook 276
6.2 Ongoing Studies and Future Directions 277
Embedded Micropillar Arrays 277
Selective Excitation of SPEs Using Narrow Beams 279

TABLE OF CONTENTS CONTINUED

Enhancing the Outcoupling of SPEs in Graphite Covered 1L-WSe_2 Nanoindents Using Polymer Microlenses 280
Using Dielectric Layers for the Nanoinversion Process 281
The Role of Au Nanostructures on SPE Emission in 1L-WSe_2 Nanoribbons 283
6.3 Future Directions 284
Chapter 6 References 287

CUMULATIVE REFERENCES CITED 289

LIST OF TABLES

Table Page

1. Table 1.1.1: Table of common vdW materials. A table of the most common vdW materials, their material classification, crystal structure, optical bandgaps, and applications. *h-BN is not an insulator in the traditional sense, but the bandgap is large in comparison to TMDs and black phosphorus..... 3

LIST OF FIGURES

Figure Page

1. Figure 1.1.1: Tight-binding model of the electronic states of graphene. (a-b) Electronic dispersion of graphene for the first BZ obtained using a tight-binding model (t = 2.8 eV, a = 1.42 Å). (c) Plot of the electronic dispersion taken along the first BZ path shown in the inset. At the K and K' high symmetry points, the dispersion is near linear for both the conduction and valence bands, forming Dirac cones. 4

2. Figure 1.1.2: Formation of a morié superlattice. (a-b) A schematic representation of a h-BN and graphene lattice, respectively, with coaligned crystal axes. (c) A schematic showing a new morié lattice that appears by stacking the materials with ~7.5° of relative crystal axis rotation. Stacking of atomic sites smoothly changes from direct atom over atom (AA stacking) to atom over hollow site (AB or BA stacking), forming the larger morié potential spacing. 5

3. Figure 1.1.3: Layer-dependent electronic band structure of MoS_2 calculated using DFT. (a) Calculated band structure for Bulk MoS_2 (b), 4L-MoS_2 (c), 2L-MoS_2 (d), and 1L-MoS_2. Bulk MoS_2 is characterized by an indirect optical bandgap. The direct optical transitions occur at the K/K' points. With reduced layer thickness, the indirect gap becomes larger while the direct gap barely changes. Here, the solid arrows indicate the lowest energy transitions for each layer configuration. Adapted from "Emerging Photoluminescence in Monolayer MoS_2", Nano Lett. Splendiani, A et al., 2010, 10(4), 1271-1275. 7

4. Figure 1.1.4: Consequences of vdW heterostructures. (a) Band diagram for graphene and 1L-WSe_2 before contacting one another. The Fermi energies shown here are only for this example. In a realistic setting, absorbates, doping, substrate material, and gating could shift these values significantly. (b) Band diagram for a graphene and 1L-WSe_2 after being brought into contact. Now, for this example, electrons move from the graphene into the 1L-WSe_2 to maintain a uniform electrochemical potential. (c) A diagram of plane polarized excitons in 1L-WSe_2 on a SiO_2 substrate and their field lines to indicate the uniformity of the dielectric environment. Here, two factors contribute to a nonuniform dielectric environment: the surface roughness of the SiO_2 and absorbents on the 1L-WSe_2 surface. (d) A similar diagram to (c), but now with h-BN encapsulation. This vdW heterostructure adds uniformity to the dielectric environment by mitigating substrate and absorbent charge influence. 8

LIST OF FIGURES CONTINUED

5. Figure 1.2.1: Absorption signatures of 1L-WSe_2. (a) Absorption spectrum of 1L-WSe_2 with labeled A, B, and C exciton resonances. Inset is the labeled high symmetry points in the BZ of 1L-WSe_2 and the path taken to plot the electronic band structure in (b). (b) Density functional theory (DFT) calculations of the electronic band structure of 1L-WSe_2. Highlighted in this plot are the direct transitions that make up the A, B, and C exciton resonances. The A and B exciton resonances share the same set of conduction bands, and the C exciton resonance originates from band nesting near the Q point in the BZ. The absorption spectrum is adapted from "Self-consistent dielectric constant determination for monolayer WSe_2", Optics Express. Lee, S et al., 2018, 26(18), 23061-23068. DFT calculations are adapted from "Beyond the K-valley: exploring unique trion states in indirect band gap monolayer WSe_2", npj 2D Materials and Applications. Nielsen, M et al., 2025, 9(1). 10

6. Figure 1.2.2: Lowest energy bright and dark excitons in unstrained 1L-WSe_2. (a) The lowest energy dark excitons. Arrows at the upper left of each band indicate the spin state of each specific band, and the dashed ovals indicate the excited electron and hole that would form the excitons. All excitons shown have either spin or momentum-forbidden optical transitions. (b) The lowest energy bright excitons. Note how, in comparison to (a), now the electron and hole that compose the excitons have matching momentum and spin configurations, permitting radiative recombination. $E_{K'Q} < E_{K\uparrow K\downarrow} = E_{K\uparrow K'\uparrow} < E_{K\uparrow K.\uparrow}$. *The spin state of the different Q-point conduction bands is a mixed spin state from heavy orbital mixing. The indicated spin states are the largest contributors to optical transitions. 11

7. Figure 1.2.3: Exciton funneling and strain in 1L-WSe_2. (a) Schematic showing the exciton funneling mechanism. Top: Real-space schematic of 1L-WSe_2 strained in the form of a nanobubble. After photoexcitation of an exciton near the base of the nanobubble, the exciton funnels towards the apex of the nanobubble before recombination. Bottom: Position-dependent band diagram showing that the energy separation between the CBM and VBM shifts as a function of position along the nanobubble. In the areas of highest strain (apex of the nanobubble), the exciton energy is the lowest, making it favorable for excitons to funnel and localize in high-strain regions. (b) Example PL spectra taken from strained and unstrained regions of 1L-WSe_2 at RT. The strained PL spectra are notably redshifted in comparison to the unstrained spectra, matching the expected behavior represented in (a). 13

LIST OF FIGURES CONTINUED

8. Figure 1.2.4: Strain-dependent shifts of excitons in 1L-WSe_2. (a) Tensile strain-induced shifts of the electronic bands in 1L-WSe_2. With increasing tensile strain, the direct bandgap at the K/K' points redshifts, lowering the exciton energy, and the Q point conduction bands increase in energy. Shifting directions with applied strain in (a) and (b) are indicated by dashed black arrows. (b) Compressive strain-induced shifts of the electronic bands in 1L-WSe_2. As opposed to the tensile case, with added compressive strain, the direct bandgap at the K/K' points is blueshifted, and the Q point conduction bands decrease in energy. *The spin state of the different Q-point conduction bands is a mixed spin state from heavy orbital mixing. The indicated spin states are the largest contributors to optical transitions. 14

9. Figure 1.3.1: Linhart schematic for SPE formation in 1L-WSe_2. (a) Real space representation: A free exciton is created (dark red arrow), strain efficiently funnels the exciton with its electron in the bright (solid black line) or dark (dashed black line) conduction band towards the energetic minimum at the strain maximum due to the strain-dependent bandgap. Mixing of the strain-localized dark exciton with a defect state leads to the formation of a strongly localized defect exciton. (b) Reciprocal space: While dark strain-localized exciton states (dashed) remain dark, hybridization with a point defect (horizontal cyan line) breaks the valley selectivity and leads to efficient photoemission (dark blue and yellow arrows). Adapted from "Localized Intervalley Defect Excitons as Single-Photon Emitters in WSe_2", Phys Rev Lett. Linhart, L et al., 2019, 123(14), 146401. 16

10. Figure 1.3.2: 4 K PL spectra of strained and unstrained 1L-WSe_2. (a) 4K PL spectra of strained 1L-WSe_2. Black arrows point to possible SPE states. (b) 4K PL spectra of unstrained 1L-WSe_2. Instead of the narrow lines present in (a), now the PL spectrum only shows broad defect emission, indicating that the formation of SPEs has not occurred. 18

11. Figure 1.3.3: HBT interferometer block diagram and expected $g^{(2)}(\tau)$ curves. (a) A block diagram of an HBT interferometer. (b) Example $g^{(2)}(\tau)$ curves for different types of light sources. 19

12. Figure 1.3.4: Spatial/temporal photon distributions for different light sources. Schematic showing different photon distributions from idealized light sources. In descending order, the rows represent super-Poissonian, Poissonian, and sub-Poissonian distributions. The mean photon number is consistently 1 across each row. 21

LIST OF FIGURES CONTINUED

13. Figure 1.4.1:Overview of strain generation techniques. (a) PL map of a 1L-WSe_2 flake with nanobubbles outlined with white boxes. Adapted from "Nanobubble induced formation of quantum emitters in monolayer semiconductors", 2D Materials. Shepard, G et al., 2017, 4(2), 021019. (b) AFM image of wrinkles in 1L-WSe_2 formed after dry transfer onto a square array of Au nanocones. Adapted from "Programmable nanowrinkle-induced room-temperature exciton localization in monolayer WSe_2", Nat Commun. Yanev, E et al., 2024, 15, 1543. (c) AFM image after a grid of nanoindents is made for a range of different indentation forces (cantilever displacements). Adapted from "Quantum Calligraphy: Writing Single-Photon Emitters in a Two-Dimensional Materials Platform", ACS Nano. Rosenberger, M et al., 2019, 13(1), 904-912. (d) Large-scale molecular dynamics simulation of the strain field in a WSe_2 monolayer induced by a gold nanostar. Top panel: the atomistic model consisting of a 100 nm x 100 nm WSe_2 monolayer on a 3 nm thick silicon substrate and the Au nanostar on top. The insets show the contact areas between the WSe_2 monolayer and the long and short arms of the Au nanostar. Atoms in the WSe_2 monolayer are colored based on their volumetric strain values. Bottom panel: cross-section views of the areas shown in the top panel insets, showing the penetration depths of the deformation field created by the Au nanostar. Adapted from "Creation of Single-Photon Emitters in WSe_2 Monolayers Using Nanometer-sized Gold Tips", Nano Lett. Peng, L et al., 2020, 20(8), 5866-5872. (e) Schematic of the fabricated structure and the optical dark-field image of the sample. A stack of h-BN/WSe_2/h-BN is transferred on a SiO_2 nanopillar array. Bright emission is observed from the top of the pillars due to exciton funneling. Next, the tops of the pillars are irradiated e- arrows) to induce structural defects. Adapted from "Defect and strain engineering of monolayer WSe_2 enables site-controlled single-photon emission up to 150 K", Nat Commun. Parto, K et al., 2021, 12, 3585. 26

LIST OF FIGURES CONTINUED

14. Figure 1.4.2: Field enhancement from various Au resonators. (a) Near-field intensity distribution for an in-plane rounded triangular prism. A strong localized hotspot is present near the apex, while weaker hotspots are present at the base. Adapted from "Quantum Light Funneling in Tailored Triangular Plasmonic Nanocavities", ACS Nano. Xiao, L et al., 2026, 20(4), 3610-3617. (b) Simulated intensity enhancement distribution profile illustrating confinement of the plasmon across the gap between the Au cube and Au mirror. Scale bar is 50 nm. Adapted from "Deterministic coupling of site-controlled quantum emitters in monolayer WSe_2 to plasmonic nanocavities", Nat Commun. Luo, Y et al., 2018, 13, 1137-1142. (c) Local electric field enhancement factor in the vicinity of a Au nanostar at the energy of 1.72 eV. Incident light is polarized along the long axis of the nanostar. Adapted from "Creation of Single-Photon Emitters in WSe_2 Monolayers Using Nanometer-Sized Au Tips", Nano Lett. Peng, L et al., 2020, 20(8), 5866-5872. 29

15. Figure 1.4.3. Proposed model for improving BB84 quantum key distribution using a hybrid WSe_2/nanophotonic device. (a) PL spectrum of SPEs on a pillar pair showing three single-photon emitters at a pillar pair oriented at a 30° angle, as highlighted by the yellow circle in the schematic inside the inset. The inset shows a schematic of the pillar pair sample fabricated and measured with a monolayer of WSe_2 transferred onto the sample. (b) Polarization measurement of the ~730 nm emitter shown in (a). (a-b) Are adapted from "Purcell enhancement and polarization control of single-photon emitters in monolayer WSe_2 using dielectric nanoantennas", Nanophotonics. Azzam, S et al., 2023, 12(3), 477-484. (c) Schematic proposing a device for high bit rate BB84 quantum key distribution using 1L-WSe_2 and dielectric pillar pairs. V, H, A, and D represent four different linear polarization states coinciding with different pillar pair orientations. The green arrows moving from V to H, A, or D represent fast motion of the excitation laser between polarization channels using a galvo scan mirror. Outlined in blue is the 1L-WSe_2 flake that would produce single-photon emission from between pillar pairs. 31

LIST OF FIGURES CONTINUED

16. Figure 2.1.1: Generation of a master tape for exfoliation. (a) A long piece of Scotch tape is attached to a flat surface, adhesive side up, and a thin line of bulk 2D material is pressed onto the tape. (b) The other side of the Scotch tape is pressed onto the bulk 2D material. (c) The two sides of the tape are separated, and the line of 2D material is thinned and propagated to the other side. (d) The line of 2D material is spread across the tape, effectively doubling the covered area. (e) The tape is separated, and the 2D material is further thinned. (f) Steps (b) - (e) are repeated to create a large area of exposed and thinned 2D material for exfoliation. 68

17. Figure 2.1.2: Scotch tape exfoliation. (a) A copy tape is attached to a pre-made master tape while cleaned Si/SiO_2 substrates are in an O_2 plasma for ~10 mins. (b) Once the Si/SiO_2 substrates have been treated in O_2 plasma, the copy tape is removed from the master tape and adhered to the O_2 plasma-treated SiO_2 surface. (c) The substrate and copy tape were placed onto a 100 °C hotplate for ~ 90 s to increase the contact area. (d) After cooling for another ~ 90 s, the copy tape is slowly removed, leaving behind exfoliated 2D material on the SiO_2 surface. 69

18. Figure 2.1.3: Optical micrograph of exfoliated WSe_2 on a SiO_2 surface. Optical micrograph of WSe_2 exfoliated on a SiO_2 surface with labels highlighting relative flake thickness (bulk, intermediate, and monolayer) and tape residues (scale bar = 100 μm). The inset is a higher resolution image of the indicated region containing a monolayer WSe_2 crystallite (scale bar = 20 μm)..... 70

19. Figure 2.1.4: Gel-assisted exfoliation. (a) A Nitto copy tape is attached to a pre-made master tape while a PDMS substrate is in UV ozone for ~2 mins. (b) The Nitto copy tape is attached to the UV ozone-treated PDMS, while a PMMA substrate is in UV ozone for ~ 2 mins. (c) The PDMS copy tape is attached to the UV ozone-treated PMMA and slowly removed to exfoliate 2D flakes..... 71

LIST OF FIGURES CONTINUED

20. Figure 2.1.5: Gold-assisted exfoliation. (a) A Si/SiO_2 substrate is thoroughly cleaned. (b) A ~50 nm thick Au layer is deposited using electron beam evaporation at 2A/s. (c) 7 wt% PVP is spun onto the Au surface at 2000 rpm for 7 mins to evaporate most of the DIW in solution. (d) TRT is attached to the PVP surface. (e) A Nitto copy tape is prepared. (f) Moving quickly to avoid Carbon contamination of the Au surface, the TRT/PVP/Au membrane is removed, and the copy tape is adhered. (g) The copy tape is removed from the TRT/PVP/Au/WSe_2 membrane and adhered to a clean Si/SiO_2 substrate. (h) The sample is heated to 140 °C to delaminate the TRT, soaked in DIW for ~ 5 minutes to remove the PVP, and etched in KI/I_2 for ~ 60 s to remove excess Au. Afterwards, the sample is rinsed in DIW and dried with a N_2 gun, leaving behind mostly 1L-WSe_2..... 73

21. Figure 2.1.6: PL intensity degradation with extended KI/I_2 etch times. Plot showing the integrated PL intensity of gold-assisted monolayers, generated using the same master tape, as a function of KI/I_2 etch time. Data points represent an average intensity acquired from hyperspectral imaging of monolayer flakes. 74

22. Figure 2.1.7: Optical micrograph of 1L-WSe_2 obtained using gold-assisted exfoliation. Optical micrograph showing the large-area exfoliation of 1L-WSe_2 generated using gold-assisted exfoliation (scale bar = 100 μm). 75

23. Figure 2.2.1: Optical lithography (lift-off). (a) A Si/SiO_2 substrate is cleaned. (b) Positive photoresist is spun onto the Si/SiO_2 substrate. (c) A mask is brought near the resist surface and is illuminated by UV light. Transparent regions of the mask permit exposure in regions of the resist. (d) Development removes regions of the resist that were exposed in (c). (e) Cr or Ti/Au is evaporated onto the sample surface using an electron beam evaporator. (f) The resist layer and excess Cr or Ti/Au are removed by dissolving the resist in Acetone. 77

24. Figure 2.2.2: Fabrication of embedded nanoantennas using TSPL. (a) A Si/SiO_2 substrate is cleaned. (b) A Bilayer polymer resist is spun onto the surface of the SiO_2. (c) TSPL is done on the PPA to generate a mask. (d) The underlying PMMA/MA and SiO_2 are etched in sonicated IPA/DIW and 6:1 BOE, respectively. (e) Cr/Au is deposited onto the PPA surface with a normal angle of incidence. Normal deposition begins to form a leading edge of convergence. (f) Once the nanoantenna is fully formed from the converging leading edge, the resists and excess Cr/Au are removed in Acetone..... 79

LIST OF FIGURES CONTINUED

25. Figure 2.2.3: Polymer uniformity after spin coating. (a) Image showing a mostly uniform bilayer spin coat. Uniformity is visually validated as a consistent color gradient from the center to the edge of the sample. At the edge of the sample, polymer that was not ejected during spin coating accumulates, forming a thicker edge, hence the larger color gradient. The defect in the bottom left of the chip is a tweezer mark. (b) Image of a non-uniform spin coat. Here, the substrate surface was not properly cleaned and dehydrated. This resulted in a low surface energy that repelled much of the polymer during spin coating, leaving only a small area of the chip with polymer coverage of an unknown thickness. (c) Microscope image of a uniform polymer spin coat highlighting microscopic defects. Despite the uniform appearance of (a), since this spin coating is not done in a cleanroom, dust particles still accumulate on the surface between cleaning and spin coating, leaving behind defects (comets) in the polymer surface. Scale bars in (a-b) are 500 mm, and in (c) are 200 μm. 80

26. Figure 2.2.4: Polymer development after TSPL. (a) Microscope image showing two TSPL patterns after 105 s of development. The color of the patterns at this time is inconsistent, reflecting that development has not fully etched down to the substrate. (b) Microscope image of the same patterns in (a), but now after 135 s. The color is now closer to fully uniform in the border regions. However, the effective etch rate of the border regions is higher than that of the nanoscale holes in the center of the patterns because the developing solution can circulate and eject polymer-rich solution more easily. (c) Microscope image of the same patterns now after 165 s. Now the border region is uniform in color, but also wider than in (a-b), indicating that those regions are over etched. Slight over etching of the border region signifies that the nanoscale holes are likely perfectly etched due to the slower effective etch rate. Scale bars in (a-c) are 10 μm. 82

27. Figure 2.2.5: Effect of sonication during BOE etching. (a) Microscope image of a fully etched TSPL pattern conducted in sonicated 6:1 buffered oxide. (b) Microscope image of a non-uniform etch. Here, sonication was not used, resulting in air bubbles that caused inconsistent etching of the nanoscale holes. In comparison, the buffer region is fully etched in both (a) and (b) because air bubbles are easily circulated/popped in these large channels. Scale bars in (a-b) are 3 μm. 83

LIST OF FIGURES CONTINUED

28. Figure 2.2.6: SEM imaging of embedded nanoantennas. (a) SEM image of embedded nanoantennas made in a 90 nm thick SiO_2 layer. (b) SEM image of embedded nanoantennas made in a 285 nm thick SiO_2 layer. (c) High-resolution SEM image of an embedded nanoantenna (scale bars = 1 μm for (a-b), and 200 nm for (c)). 84

29. Figure 2.2.7: Nanoindentation and nanoinversion. (a) Schematic illustration of nanoindentation. An AFM tip is brought into near contact with 1L-WSe_2 on a PMMA surface. By raising the substrate into the AFM tip, the PMMA is plastically deformed, forming a nanoindent. (b) Schematic illustration of nanoinversion. Depositing Au with a normal angle of incidence uniformly fills the nanoindents made in (a). Then, by attaching a second Si/SiO_2 substrate using epoxy, the Au inversion and 1L-WSe_2 are separated from the PMMA. (c) AFM image of nanoindents in 1L-WSe_2. (d) AFM image of the inverted indents seen in (c). The inset represents the structural asymmetry of the buildup region, with the dashed and solid arrows in (c-e) highlighting the asymmetry in the data. (e) SEM image of the inverted indents in (c) (scale bars = 1 μm). 87

30. Figure 2.3.1: COMSOL Geometries. (a) COMSOL geometry of a nanopyramid. (b) COMSOL geometry of a nanocone. 88

31. Figure 2.3.2: Boundaries and domains for wave optics COMSOL models. (a) Locations of the PMC boundary conditions. When the geometry is split to simplify the model, a PMC boundary is set on the split geometry to mimic a method of images problem. (b) Location of the PEC boundary on the exterior of the PML domain. (c) Location of the PML domain. By defining the PML as a concentric layer on the exterior of the modeling region with a PEC boundary, reflected waves from the nanostructure are efficiently terminated. 89

32. Figure 2.3.3: Mesh example in COMSOL. (a) Mesh for a nanocone model. The non-highlighted regions in (a) and (b) are the nanocone. (b) Zoomed-in mesh of a nanocone showing the smaller domains near the apex of the nanocone. (c) Radial mesh of the PML domain. 90

33. Figure 2.3.4: Model results for a nanocone. (a) COMSOL model results for a gold nanocone showing local field enhancement at the apex from a localized surface plasmon mode. (b) Plasmonic enhancement spectra of the nanocone seen in (a) by running a parametric sweep over excitation wavelength and extracting the max field enhancement above the apex. Scale bar = 5 nm 91

LIST OF FIGURES CONTINUED

34. Figure 2.4.1: Transfer microscope components. An image highlighting the core components of the transfer microscope used for 2D material transferring. 93

35. Figure 2.4.2: PDMS-based dry transfer. (a) A PDMS-based stamp with 1L-TMDC. (b) The stamp is brought into contact with a Si/SiO_2 substrate heated to ~70 °C to increase the substrate adhesion. (c) The stamp is retracted from the substrate, leaving behind the 1L-TMDC. 95

36. Figure 2.4.3: Contact front drift. (a) A schematic showing a 1L-WSe_2 flake on a PDMS stamp positioned in near contact above an area of interest. The contact front between the PDMS stamp and substrate is in the bottom left and moving towards the top right. (b) As the stamp is brought into full contact, the flake is moved away from the area of interest in the direction of the contact front's motion. (c) Left: Ideal positioning of 1L-WSe_2 to accommodate flake drift from the contact front. Right: After contact is made, the 1L-WSe_2 is positioned over the area of interest. 96

37. Figure 2.4.4: AFM of 1L-WSe_2 after PDMS transfer. An AFM image of a 1L-WSe_2 flake on SiO_2 after PDMS-based transfer. Arrows drawn towards wrinkles and nanobubbles that emerge because of using PDMS solely. 97

38. Figure 2.4.5: Fabrication of thin polymer films. (a) A glass coverslip is cleaned. (b) PC polymer is spun onto the glass coverslip at 4000 rpm for 120 s. (c) A tape frame is made of Scotch tape, and the polymer side is adhered. (d) The coverslip is flipped over, and the glass is intentionally fractured. (e) The broken glass is removed from the PC surface. (f) The thin polymer film is attached to a PDMS stamp. (g) Excess PC / tape is removed, and the PC polymer is reflowed over the PDMS at 190 °C. 98

39. Figure 2.4.6: Different stamp types. (a) PDMS-based stamp. (b) Polymer layer stamp on flat PDMS. (c) Double dome PDMS, polymer layer stamp. 99

40. Figure 2.4.7: Double dome stamp fabrication. (a) A piece of double-sided tape is attached to a bare glass slide. (b) A PDMS dome is made on double-sided tape by drop casting liquid Sylgard 184 PDMS. The PDMS dome is then cured in a 100 °C oven. (c) A second dome is made on top of the first in the same manner as (b). (d) The double dome PDMS is treated in an O_2 plasma for ~ 60 s, and the thin polymer film is quickly adhered and reflowed. 100

LIST OF FIGURES CONTINUED

41. Figure 2.4.8: Circular contact front. Optical image of the circular contact front made by a double dome PDMS stamp. Melted polymer, “fingers”, indicate that the thin polymer layer has melted. 101

42. Figure 2.4.9: Wet transfer. (a) An ~8 nm graphite flake is identified on a Si/SiO_2 substrate using AFM. (b) PDMS is spun onto the substrate to act as the stamp media. The PDMS is then cured at 100 °C. (c) The sample is placed into a 1M NaOH in DIW solution heated to 90 °C. (d) After ~10 minutes, the PDMS and graphite detach from the Si/SiO_2 substrate. (e) The PDMS layer is transferred to a DIW bath to rinse excess NaOH off the graphite flakes. (f) The PDMS layer is flipped so the flakes are facing out. (g) The PDMS layer is scooped out of the DIW using a PDMS stamp. (h) The resulting PDMS stamp with graphite flakes. 103

43. Figure 2.4.10: Flake condition during wet transfer. (a) Optical image of a ~8 nm graphite flake on a SiO_2 substrate. (b) Optical image of the same graphite flake in (a) on PDMS. (c) Optical image of the 1L-WSe_2 indents of interest. (d) Optical image of the graphite flake transferred over 1L-WSe_2 indents. 104

44. Figure 2.5.1: Measuring the laser spot FWHM. (a) Simulated data showing a line cut across the center of the laser spot as seen by the QOM camera fit by a Gaussian function to approximate the FWHM. (b) PL intensity linecut taken along the red line seen in the inset scan. By measuring the distance between no emission (off the flake) and the steady state emission of the 1L-WSe_2, and dividing by 2.4, the FWHM is approximated. Inset scale bar = 10 μm 107

45. Figure 2.5.2: Laser-induced damage of 1L-WSe_2 (a) PL intensity scan of a 1L-WSe_2 flake on SiO_2 showing a nominally homogenous intensity across the flake. (b) PL intensity scan of the same 1L-WSe_2 flake as in (a), but after Raman spectra were taken. The high-intensity laser caused reductions in the PL intensity in the locations where Raman spectroscopy was taken. Scale bars = 5 μm 109

46. Figure 2.6.1: Isolating a SPE in 1L-WSe_2. (a) 4 K PL time series of SPE states in 1L-WSe_2 showing spectral blinking and wandering occurring on second time scales. (b) 4 K PL spectra of SPE states. A single SPE state is isolated using two 10 nm FWHM spectral band pass filters rotated to clip the low and high wavelength tails of the SPE. 110

LIST OF FIGURES CONTINUED

47. Figure 2.6.2: Optimized HBT setup and consequential $g^2(\tau)$ baseline. (a) HBT optical setup. In the bottom right is the original HBT setup, where reflected light off a 50/50 cube beam splitter causes reflection peaks in a $g^2(\tau)$ baseline measurement. In the upper center is the optimized HBT setup. Here, a beam reducer is implemented to increase photon counts on each APD channel. To resolve the problem of reflection peaks, the objectives are rotated by ~11°. Due to the rotation, reflected PL is collimated off-axis from the incident optical path, causing it to decouple from the HBT interferometer. (b) Antibunching calibration showing a series of peaks emerging due to reflections in the HBT interferometer. (c) Antibunching calibration with no reflections leads to a featureless noise floor. 112

48. Figure 2.6.3: Histogram of SPE wavelengths in literature. Histogram of SPE wavelengths reported in studies of single photon emission in 1L-WSe_2. 113

49. Figure 2.5.4: Extracting the excited state lifetime. (a) Lifetime curve of a 1L-WSe_2 SPE state. This state exhibits time-dependent emission that fits well with a monoexponential function, indicating a pure two-level system. (b) Lifetime curve of a 1L-WSe_2 SPE state. This state is not well fit by a monoexponential function, indicating multiple states/recombination pathways. To extract the lifetime of this curve, the $1/e$ time is used rather than the τ value from the monoexponential fit. 115

50. Figure 2.7.1: PLE spectra maps absorption. Example PLE and absorption spectra taken on 1L-WSe_2 showing the A, B, and C exciton resonances. The absorption spectra are adapted from Lee, Jeong, et al., Optics Express, 2018, 26, 18, 23061 – 23068[99]. 116

51. Figure 2.7.2: PLE spectroscopy calibration measurements. (a) Measured excitation powers, converted to power on sample, at each wavelength during a PLE measurement. (b) Interpolated curve showing the FWHM of the excitation laser spot. (c) Calculated correction factors at each excitation wavelength. 117

52. Figure 2.7.3: Effect of correction factors on a PLE spectrum. PLE curves with and without correction factors applied. Without the correction factors, the spectral position, linewidth, and noise floor are not accurately shown. 118

LIST OF FIGURES CONTINUED

53. Figure 2.7.4: Optical setup for PLE spectroscopy. Schematic showing the optical setup used to collect PLE data. Due to the need for various excitation wavelengths, a white light laser coupled to an AOTF is used to isolate narrow excitation bands. Instead of a dichroic mirror, a 730 nm spectral LP filter is used to reflect the excitation laser while transmitting the PL signal. 118

54. Figure 2.7.5: Averaging multiple PLE spectra eliminates noise. Average and single measurement PLE spectra showing how anomalous quantum behavior is reduced. The spike seen in the single PLE spectra, shown in the black dashed circle, is resolved using the average of 7 independent PLE measurements. 120

55. Figure 2.7.6: Emitter integrated PLE spectra. (a) PLE data before integration. The red dashed line represents different intensity scaling for the short and long wavelength regions. Labeled in red solid lines are the integration regions for the emitters in (b). (b) Emitter integrated PLE spectra. The enhanced emitter at 803 nm lies within the plasmonic hotspot of the underlying Au nanoantenna, represented by the enhancement spectra matching the PLE data. 121

56. Figure 2.8.1: Tip up vs Tip down in SNOM. (a) Simplified schematic showing that the evanescent field, generated from an LSPR in the Au tip, is not interacting with the underlying Au surface because the tip is retracted from the surface. (b) A similar schematic to (a), but now with the tip near the Au surface. This proximity permits the evanescent field to enhance electron excitations in the Au film. (c) Example Au luminescence spectra taken with the Au tip up and down. By subtracting the tip-up spectra from the tip-down spectra, the enhanced luminescence and Raman lines from material within the gap are shown. 122

57. Figure 2.8.2: Polarization-dependent gap plasmons between two Au tips. (a) An example excitation scheme and COMSOL model for a p-polarized gap plasmon between the Au-coated AFM tip and an underlying Au nanoantenna with the same dimensions. (b) An example excitation scheme and COMSOL model for an s-polarized gap plasmon between the Au-coated AFM tip and an underlying Au nanoantenna. Scale bars = 5 nm 123

LIST OF FIGURES CONTINUED

58. Figure 2.8.3: Polarization-dependent near-field maps. (a) Near-field map of Au luminescence from an underlying Au nanoantenna taken with p-polarization. Highlighted with a red dashed circle in both (a) and (b) is the estimated base diameter of the Au nanoantenna. (b) A similar map to (b), but now taken with a s-polarized incident laser. Now, instead of a circular spatial dependence, two lobes appear, representing the gap plasmon between the two tips when they are side by side. 124

59. Figure 1 – The nanoindentation process and room temperature PL characterization: (a) A schematic of the indentation process. An AFM tip is positioned over a 1L-WSe_2 flake on a PMMA/SiO_2 substrate. The substrate is moved into the tip, where the WSe_2 and PMMA are deformed into the shape of the tip. When the substrate is retracted, an indent in the shape of the tip is left. AFM scale bars are 400 nm. (b) High-resolution AFM scans of nine indents made with indentation forces ranging from 22 to 71 μN. (c, d) The average PL spectra of before and after indenting from Batch 1 and Batch 2, respectively. (e) The difference in the full-width half maximum (FWHM) of the PL spectra between after and before indentation. A positive difference corresponds to an increase in FWHM after indentation. (f) The difference in PL emission energy is calculated by taking the difference between before and after indenting. Negative values correspond to a redshift or decrease in emission energy after indenting. Scale bars in (c) are 400 nm. 152

60. Figure 2 – Inverting the nanoindents: (a) A schematic demonstrating the inversion process. Starting with an indented 1L-WSe_2/ PMMA/SiO_2/Si sample, a ~550 nm thick layer of gold is deposited on the sample, filling the indent with gold, and leaving a gold surface on which a second SiO_2/Si substrate is epoxied. The PMMA holding the initial SiO_2/Si substrate is dissolved, leaving an inverted indent (b, c). AFM topography maps of Batch 1 indents and the corresponding inverted structure, respectively. The inset in (c) is a schematic demonstrating that the asymmetric PMMA buildup in the indents becomes valleys when inverted. The black (white) dashed and solid lines mark how the larger and smaller buildup regions around the indent correspond to the larger and smaller valleys when inverted. (d) SEM of the inverted indents in panel c. The scale bars are 1 μm. 154

LIST OF FIGURES CONTINUED

61. Figure 3 – SEM of Batch 1 and 2 inverted indents: (a) SEM images of inverted indents from Batch 1. The red dash ovals mark tears in the 1L-WSe_2. This tearing is in sharp contrast to Batch 2, where no tearing is observed in (b). The insets are of the same inverted indents but rotated 180° to show the other side. The blue values in each panel are the indentation forces used to make the indent. Main figure scale bars are 200 nm (insets are 400 nm). 156

62. Figure 4 – Confirmation of single-photon emitters in Batch 1 and 2: (a, b) Average PL spectra at 4 K of an indent from Batch 1 and Batch 2, respectively. The inset in (a) is the integrated intensity map of Batch 1 integrated over the range 1.52 – 1.84 eV. The inset in (b) is the integrated intensity map of Batch 2 integrated over the range 1.51 – 1.83 eV. The scale bars of the insets are 5 μm. (c, d) Second-order correlation function ($g^2(\tau)$) of the emitters marked by red dashed lines in (a) and (b), respectively. Both emitters measured show antibunching behavior with $g^2(0)$ below or near 0.5. 158

63. Figure 5 – Emitter density and emitter count dependence on indentation force: (a) Average 4 K PL spectra from an intact indent without graphite (top) and an intact indent with graphite (bottom). N is the number of emitters counted from the average spectra. The schematics in (a) represent the indents with or without graphite. The inset in (a, bottom) is the time series of the emitters circled in black and marked E1 and E2. The corresponding emitters in the time series are marked with white dashed lines. (b) Emitter number and emitter density with respect to indent area as a function of indentation force. In (b), the red circles correspond to Batch 1 (torn), and the yellow triangles correspond to Batch 2 (intact). The Batch 3 indents without graphite are marked by the black triangles, and the indents with graphite are represented by the purple triangles. (c) The tear length of each indent in Batch 1 as a function of indentation force. The tear lengths were measured from SEM images. The dashed black line is a guide to the eye. An example of how the tear was measured is shown in the SEM inset. The SEM image scale bar is 200 nm. 161

64. Supplementary Figure 1: Comparing new and dulled AFM tips via SEM. (a) SEM images of a new Tap300Al-G AFM, k= 40 N/m probe before dulling. (b) SEM of the same AFM probe after dulling. 169

65. Supplementary Figure 2: Indentation force calibration. Calculating an equation to convert z-displacement into indentation force in μN. The y-axis is the raw signal of the indentation force. 170

LIST OF FIGURES CONTINUED

66. Supplementary Figure 3: Effect of non-normal incidence during inversion. (a) Schematic showing perfect filling of an indent when a normal angle of incidence is used. (b) Schematic of a non-normal incidence evaporation leading to shadow masking at the apex of the indent/inversion. (c) SEM image of an inversion generated with non-normal incidence evaporation (scale bar = 200 nm). 171

67. Supplementary Figure 4: Inversions are near replications of nanoindents. (a, b) High-resolution AFM images of a 34 μN indent and inversion, respectively. (c) The depth of indents made using indentation forces ranging from 22 – 71 μN, and the heights of the corresponding inversions (scale bars = 500 nm). 171

68. Supplementary Figure 5: Sliding of the AFM tip from a misaligned contact angle. (a) Schematic representing an indent made with a contact angle of 0° (no y-translation of the AFM stage). (b) Schematic representing an indent made with a perfectly aligned contact angle. 173

69. Supplementary Figure 6: Yaw tilt generating an asymmetric buildup region. (a) Schematic of an AFM tip with yaw tilt (θ) positioned above the PMMA surface before indentation. (b) Schematic of indentation where the AFM cantilever has a yaw tilt leading to an asymmetric buildup region. 174

70. Supplementary Figure 7: Two inverted 1L-WSe_2 indent arrays made with the same AFM probe before and after dulling. The same indentation force was used, and the angle was changed from 0 to 60° in steps of 2° for both arrays of indents. (a) SEM image of an array of inverted indents made with a dulled Tap300Al-G, k = 40 N/m AFM probe. The angles set the y-displacement of the sample stage. The Indentation force for all the indents in panels (a – e) was 53 μN. (b, c) SEM of two indents outlined by red squares in (a), made with angles of 36° and 50°, respectively. The red ovals mark tears in the 1L-WSe_2. (d, e) SEM of inverted indents made with a fresh AFM probe, meaning the probe was not dulled. The indents were made with 16° (d) and 8° (e) and do not show signs of tearing as seen in (b) and (c). 175

LIST OF FIGURES CONTINUED

71. Supplementary Figure 8: Locating indentation sites in Batch 1. (a) Hyperspectral image integrated from ~1.59 – 1.61 eV used to identify the 34 and 41 μN indents in white and red, respectively. (b) Hyperspectral image integrated from ~1.61 – 1.62 eV used to identify the 47 μN indent. (c) Hyperspectral image integrated from ~1.65 – 1.66 eV used to identify the 53 μN indent. (d) Hyperspectral image integrated from ~1.71 – 1.72 eV used to identify the 68 and 84 μN indents in red and white, respectively (scale bars = 5 μm). (e) AFM image of the indents in Batch 1, ranging in indentation force from 22 – 84 μN (scale bars = 1 μm). 176

72. Supplementary Figure 9: Locating indentation sites in Batch 2. (a) Hyperspectral image integrated from 1.51 – 1.82 eV. (b) Hyperspectral image integrated from 1.69 – 1.70 eV used to identify the 28 and 65 μN indents in white and red, respectively (scale bars = 10 μm). 176

73. Supplementary Figure 10: Emitter ensemble properties of each site in Batch 3. (a) Average energy of the emitter ensemble at each indentation site. (b, c) The lowest and highest energy emitter of the ensemble at each site, respectively. (d) Integrated PL intensity (1.575 – 1.725 eV) at each indentation site. 177

74. Supplementary Figure 11: PL spectra of each site in Batch 1. PL spectra of indentation sites made with indentation forces ranging from 34 to 84 μN. 177

75. Supplementary Figure 12: PL spectra of each site in Batch 2. PL spectra of indentation sites made with indentation forces ranging from 22 – 71 μN. 178

76. Supplementary Figure 13: Average PL spectra of each site in Batch 3. Average PL spectra of indentation sites made with indentation forces ranging from 28 – 71 μN. (a) Average PL spectra from a 120 s PL time-series without graphite. (b) Average PL spectra from a 120 s PL time-series with graphite. 179

77. Supplementary Figure 14: Total indent area of each site. Indent areas, including the indent and buildup region of each site, were acquired from high-resolution AFM imaging. 180

78. Supplementary Figure 15: Tear length of Batch 1 indents using SEM imaging. (a-h) SEM images of Batch 1 inversions. Torn regions are highlighted using a red line, and the indentation force used to generate each indent is listed in blue (scale bars = 200 nm). 180

LIST OF FIGURES CONTINUED

79. Figure 1 – Fabrication and characterization of relief tunable embedded gold nanoantennas: (a) Schematic representation of the fabrication procedure. TSPL is used to create openings in the PPA layer, permitting development and BOE etching down to the Si surface. Afterwards, Au deposition normal to the surface creates a leading edge that converges towards the center, forming the embedded antennas. (b-c) SEM images of a single and an array of embedded nanoantennas, respectively. (d) Plot comparing the measured relief of nanoantennas made in two different oxide thicknesses for a variety of hole diameters, d. Scale bars in the SEM images are 200 nm (b) and 1 μm (c). 201

80. Figure 2 – Near-field enhancement from gold nanoantennas: (a) Finite element model of a gold nanocone with base diameter of 130 nm, height of 135 nm, and radius of curvature of 7.5 nm under 625 nm excitation polarized along the long axis of the nanocone. (b) Plasmonic enhancement spectra (PES) of a typical nanocone made in 90 nm oxide, (a), and 285 nm oxide. The PES is generated by extracting the maximum field intensity 1 nm above the surface of the nanocone at a variety of excitation wavelengths. (c) Finite element model of a gap plasmon between a gold nanocone and a similar near-field probe under polarized excitation along the long axis of the resonators. (d) Finite element model of the offset gap plasmon between a gold nanocone and a similar near-field probe under polarized excitation perpendicular to (c). (e) Near-field spectra of Au luminescence under the excitation condition shown in (c). Near-field intensity is clearly enhanced when the two tips are above one another. The inset shows a near-field map where the yellow circle is the approximate diameter of the cavity, and the white and red bounding boxes are the integration regions for the black and red spectra, respectively. (f) Near-field spectra of Au luminescence under the excitation condition shown in (d). As opposed to (e), near-field enhancement is maximized when the offset gap plasmon is excited. The inset shows a near-field map where the yellow circle is the approximate diameter of the cavity, and the red, magenta, and white bounding boxes represent the integration regions for the red, magenta, and black spectra, respectively. Scale bars for the insets in (e-f) are 100 nm. 203

LIST OF FIGURES CONTINUED

81. Figure 3 – Strain and photonic effects on room temperature PL: (a) AFM image of an embedded nanocone with 103 nm of positive relief covered by 1L-WSe_2. (b) SEM image of an embedded nanocone with 139 nm of positive relief covered by 1L-WSe_2. In both the AFM and SEM, hyperfine nanowrinkles radiating outward from the apex are observed. The radius of curvature seen in (b) is increased from nano-optical probing of the antenna. (c) Room temperature PL of nanoantennas with reliefs ranging from -182 to 150 nm made in 285 nm thick oxide. Inset is the spectral median and B exciton resonance of this range of nanoantennas. Scale bars are 200 nm. 205

82. Figure 4 – Single photon emission and spectral dependence on the excitation process: (a) Cryogenic (4 K) PL spectra of 5 single photon emitters present from a 65 nm positive relief nanoantenna made in 90 nm oxide. Inset is the result of a single photon antibunching for the bound emitter. (b) Cryogenic PL of the same nanoantenna sites seen in Figure 3c. Now, a more notable blueshift of the spectral median and B exciton resonance is present (inset). The colored dots on each PL spectra are the respective calculated spectral medians. (c) Emitter resolved PLE spectra of a ~724 nm emitter from a -182 nm relief nanoantenna site. Note the reduced intensity of the B exciton resonance. (d) Emitte resolved PLE spectra of a ~724 nm emitter from a +150 nm relief nanoantenna site. Now the intensity ratio between the A and B excitons is closer to 1. PLE spectra are normalized to the C exciton. (e) Summary of the A/B exciton ratios for various emitters at nanoantenna sites with reliefs ranging from -182 to 150 nm. The A/B exciton ratio for low wavelength emitters in negative relief sites is substantially increased. 207

83. Figure 5 – Localization and plasmonic enhancement of SPEs: (a) Localization spectroscopy of the 5 emitters shown in Figure 4a to a ~500 x 500 nm^2 region about the center of a 65 nm positive relief nanoantenna site made in 90 nm oxide (black circle). (b) Emitter resolved PLE for a ~790 and ~725 nm emitter from the site shown in (a). The ~790 nm emitter shows anomalous enhancement in between the B and A excitons that directly correlates with the plasmonic enhancement spectra (PES) calculated for this nanoantenna site. (c) 180 K PL of a localized emitter. (d) 180 K Single photon antibunching of the emitter shown in (c). Scale bar is 800 nm. 209

LIST OF FIGURES CONTINUED

84. Figure 6 – Near-field optical spectroscopy of a nanoantenna site with 1L-WSe_2: (a) AFM image of a 38 nm positive relief nanoantenna site. The inset shows a near-field map of the bounded region adjacent to the apex of the nanoantenna. Increased enhancement is present from the wrinkle of the 1L-WSe_2. (b) Near-field spectra integrated from the bounding boxes seen in the inset of (a). On the wrinkle, there is an added low-energy shoulder, indicating defect emission in the 1L-WSe_2. Scale bars are 400 nm and 125 nm for the AFM and near-field map, respectively. 211

85. Supplementary Figure 1: Cavity diameter to SiO_2 thickness ratio determines convergence location. (a) An SEM image of a plateau structure formed within a wide SiO_2 cavity, such that convergence did not occur after 550 nm of Au deposition. (b) An SEM image of a deeply embedded nanoantenna within a narrow SiO_2 cavity. Here, the leading edge converged early during the deposition, setting the relief of this site to be negative. Inset in (a-b) are diagrams indicating how these structures emerge during Au evaporation. Scale bars = 200 nm..... 216

86. Supplementary Figure 2: High-resolution AFM of nanoantenna sites. (a) AFM taken of nanoantenna sites made in a 285 nm thick SiO_2. (b) AFM collage of nanoantenna sites made in a 90 nm thick SiO_2. Vertical black lines indicate the stitch locations of the collage. Scale bars are 2 μm and 400 nm for (a) and (b), respectively. 216

87. Supplementary Figure 3: Mask hole diameter and nanoantenna height relationship. Plot showing the hole diameter at write depth (mask diameter) against the overall height of each nanoantenna. This plot differs from the plot in Figure 1 of the main manuscript as relief is swapped for overall height. The near-linear relationship here, even across different SiO_2 thicknesses, indicates that the convergence mechanism is consistent across the same electron beam evaporator. 217

88. Supplementary Figure 4: Relief model. Model showing the expected relief of a nanoantenna site considering the site's hole diameter and the sample's SiO_2 thickness. Contours represent lines of equal relief, labeled in the model. The overall deposition thickness in this model is 600 nm, limiting the region of convergence. Sites with diameters above ~545 nm will not converge and instead form plateaus. 218

LIST OF FIGURES CONTINUED

89. Supplementary Figure 5: Reflectance model. (a) Simulated reflectance model of optical field intensities generated by assuming reflections off a Si surface at various wavelengths and distances from the Si. (b) Simulated effect of photonic reflections on the spectral position of a Gaussian peak. These results came from applying the optical field intensities seen in (a) to a Gaussian centered at 748 nm. (c) Simulated effect of photonic reflections on the intensity of a Gaussian peak. 220

90. Supplementary Figure 6: Drift calibration measurement. (a) PL intensity scan of the ensemble of long wavelength emitters seen in the main manuscript Figure 4. Overlaid are the contours of a 2D Gaussian fit, with the center position listed in the figure. (b) PL intensity scan of the same ensemble of emitter, but 40 s later. 40 s represents the average time between scans for the localization measurement conducted in the main manuscript, Figure 5. Scale bars are 1 μm. 221

91. Supplementary Figure 7: Emitter PLE curves. (a) Cryogenic PL spectra of the long wavelength ensemble of emitters labeled E1-E5, and the control emitter. (b-f) Emitter PLE spectra compared against the control emitter. Certain emitters, such as E3, E4, and E5, show strong enhancement with respect to the PES, while E1 and E2 show weaker enhancement. We believe this to be caused by the proximity of the emitter to the apex of the nanoantenna. 223

92. Supplementary Figure 8: Single photon antibunching of plasmonically enhanced emitters. (a-e) Antibunching curves of emitters E1 – E5 with their respective $g^2(0)$ values. (f) Antibunching curve of what we suspect is E5, now at 180 K. 224

93. Supplementary Figure 9: Temperature-dependent PL spectroscopy. (a) Temperature-dependent PL spectroscopy of a 65 nm positive relief nanoantenna in 90 nm oxide. The long-wavelength emitters present are E1 – E5. Notably, the spectral fluctuations of these emitters make tracking a specific emitter throughout the temperature series difficult, especially considering the expected Varshni shift behavior. 225

94. Supplementary Figure 10: Rupture of the 1L-WSe_2. (a-b) AFM images of a nanoantenna site before and after near-field optical spectroscopy. During near-field measurements, rupture was a common outcome caused by excessive forces on the delicate 1L-WSe_2 by the near-field probe. Scale bars are 200 nm. 226

LIST OF FIGURES CONTINUED

95. Supplementary Figure 11: Localization spectroscopy. (a-b) PL intensity maps for E2 and the ensemble of long-wavelength emitters, respectively. Overlaid are 2D Gaussian fits to the intensity spatial distributions. (c-g) Normalized PL difference maps to visualize the localization of each emitter with respect to the emitter ensemble. Overlaid are the respective 2D Gaussian fits for each emitter scan and long wavelength emitter scan. For example, (f) shows (a)-(b) and the fits from both (a) and (b). The difference in center positions of these fits is what is used for the localization of the emitters with respect to the apex of the nanoantenna. Scale bars are 1 μm. 227

96. Supplementary Figure 12: Long wavelength emitter PLE dataset. The raw PLE data before integration for the long wavelength emitters that show plasmonic enhancement. The red dashed line in the center represents a change in the color scale from a maximum of 1 kcts/s to 1.5 kcts/s 228

97. Figure 1 – Generation of graphite-covered indents and room temperature PL: (a) Schematic representation of nanoindentation and the hybrid dry/wet transfer of graphite. (b) Room temperature PL map of a graphite/1L-WSe_2 heterostructure. The red and white X's relate to the locations where the point spectra in (c) were taken. (c) Point spectra PL comparison showing a redshift, slight linewidth broadening, and reduction in intensity in regions of interlayer coupling between graphite and 1L-WSe_2. Scale bar is 10 μm. 250

98. Figure 2 – 4 K PL spectra of nanoindents before and after graphite transfer: (a-h) A range of 4 K PL spectra taken at nanoindent sites made with indentation forces from 28.81 – 71.35 μN. 251

99. Figure 3 – Spectrally and time resolved PL of A-exciton-like emission: (a-b) Maps of the spectrally and time resolved PL of a 40.53 μN nanoindent before and after graphite transfer, respectively, limited to A-excitonic-like emission. (c) Example PL transience from A-exciton-like emission with and without graphite. (d) Histograms of the lifetimes of A-exciton-like emission with and without graphite..... 253

100. Figure 4 - Spectrally and time resolved PL of quantum emission: (a-b) Maps of the spectrally and time resolved PL of a 40.53 μN nanoindent before and after graphite transfer, respectively, limited to quantum emission. (c) Example PL transience from quantum emission with and without graphite. (d) Histograms of the lifetimes of quantum emission with and without graphite. 255

LIST OF FIGURES CONTINUED

101. Figure 5 – Energy and strain dependence on PL lifetimes: (a-b) Energy-dependent scatter plots of PL lifetimes vs band integrated intensities for 1L-WSe_2 nanoindents without and with a graphite adlayer, respectively. (c-d) Scatter plots of indentation force-dependent PL lifetimes vs band integrated intensities for 1L-WSe_2 nanoindents without and with graphite, respectively. 257

102. Figure 6.2.1: Embedded aluminum micropillars. (a) An SEM image of a h-BN/1L-WSe_2 heterostructure transferred onto an embedded micropillar site. (b) 4 K hyperspectral PL intensity map of an array of embedded micropillar sites covered by a h-BN/1L-WSe_2 heterostructure. (c) 4 K PL spectra of 4L-WSe_2 on top of an embedded micropillar. Scale bars are 1 μm and 10 μm for (a) and (b), respectively. 278

103. Figure 6.2.2: Selective near-field excitation. (a) Finite element model showing the near-field hotspot of a gold nanocone offset by ~45° due to a rotated angle of incidence of the excitation beam. Here, Φ is the angle away from the nanocone long axis that shows maximum field intensity. (b) A summary of finite element models similar to (a), where the maximum field intensity is extracted for a variety of different angles of incidence. At an angle of incidence of 0°, the maximum intensity is directly above the long axis of the nanocone, but as the angle of incidence is rotated, this maximum also rotates, indicated by the maximum intensity in (b) going to the left. 279

104. Figure 6.2.3: SEM images of polymer microlenses. (a-b) SEM images of Au-coated polymer microlenses fabricated on a SiO_2 surface taken at 45° and 0° angle of incidence, respectively. Scale bars are 4μm. 281

105. Figure 6.2.4: Plasmonic enhancement in 1L-WSe_2 nanoribbons on Au nanostressors. (a-b) SEM images of 1L-WSe_2 nanoribbons transferred onto Au nanocones. (c) PLE spectra of an enhanced emitter state, and the full 4 K PLE spectrum. 283

ABSTRACT

Layered van der Waals materials are held together with strong in-plane bonds and weak out-of-plane van der Waals forces, permitting facile exfoliation into monolayers. One particularly interesting class of van der Waals materials is transition metal dichalcogenides, mainly monolayer WSe_2, which has been shown to host quantum states of light that emit single photons at cryogenic temperatures in regions of tensile strain. These single-photon emitters have a broad range of applications in emergent quantum technologies, but understanding the formation, placement, and control of these states has proven difficult and attracted a large amount of research attention. Here, the work in this dissertation investigates single photon emission in monolayer WSe_2 via integration with nanophotonic structures. One such platform is nanoindentation, where WSe_2 placed on a polymer substrate is deformed using a sharp atomic force microscopy tip to induce single photon emitters. An open question is whether the delicate WSe_2 tears or remains intact after nanoindentation. This work presents a nanoinversion technique that converts nanoindents into protruding Au pillars that permit metrological analysis of the WSe_2 to identify tears and conclude that, regardless of tearing, single photon emitters persist. It is also reported in this dissertation that single photon emitters at nanoindentation sites can be selectively brightened through the addition of a capping graphite layer, quenching broadband defect emission. However, localized defects have been theorized to play a major role in WSe_2-based single photon emission. Because of high defect densities, to conclusively validate this theory, one must correlate room temperature defect emission with cryogenic single photon emission using near-field optical spectroscopy. Cryogenic near-field spectroscopy is exceedingly difficult and only exists in a small number of laboratories around the world. To address this limitation, this dissertation reports the fabrication of integrated near-field antennas into the substrate of a WSe_2 flake that selectively enhances single photon emitters above its apex. By then identifying the localization of emitters to spatial regions around the apex of the probe using localization spectroscopy and photoluminescent excitation spectroscopy, this platform can enable correlation between cryogenic single photon emission and room temperature defect emission for the first time.

CHAPTER 1

INTRODUCTION

In this dissertation, quantum states of light in the monolayer transition metal dichalcogenide (TMD), tungsten diselenide (WSe_2), are studied and tailored using nanophotonic structures. The different nanostructures used all serve the purpose of generating tensile strain in the monolayer to permit single photon emitter (SPE) formation. Going over the brief description of each research chapter, Chapter 3 looks at the role of tearing in SPE formation within nanoindented single-layer (1L)-WSe_2 by inverting the indentations into protruding pillars for metrological studies. Chapter 4 reports the development of embedded plasmonic nanoantennas for Purcell enhancement and SPE localization in 1L-WSe_2, and Chapter 5 investigates the role of a graphite adlayer on SPEs in 1L-WSe_2 nanoindents using cryogenic photoluminescence (PL) and PL lifetime measurements.

1.1 Van der Waals Materials

Atomically thin van der Waals (vdW) materials permit studies of new quantum phenomena in reduced-dimensional systems. Since the beginning of the field in 2004 by Novoselov *et al.*[1] with monolayer graphite, the study of different vdW materials has gained traction. One of the most studied classes of vdW materials is TMDs. WSe_2, one TMD used in every Chapter of this dissertation, was found in 2015 to host electronic states responsible for quantum light emission, generally called SPEs that are well positioned for use in quantum information and computing platforms[2-7]. Later in 2019, the addition of a hexagonal boron nitride (h-BN) crystallite to WSe_2 was found to narrow the linewidth of the SPEs by providing a more uniform dielectric

environment, atomically flat surface, reduction of random strain, and protection for the WSe_2 from adsorbates[8, 9]. Consequently, combining h-BN with WSe_2 into a vdW heterostructure improved the properties of SPEs with a sub-10 nm addition in sample thickness. Today, the integration of WSe_2 with nanophotonic structures provides a powerful platform for engineering light-matter interactions[10, 11]. In this dissertation, WSe_2 is coupled with nanophotonic structures, deterministic strain generators, and graphene to study SPEs.

VdW materials are layered materials held together in plane by strong covalent/ionic bonds, while weaker van der-Waals forces hold individual layers together out of plane[12]. Depending on their chemical composition and atomic ordering, the ~3,000 vdW[13] materials are classified into different groups. VdW materials have a broad range of electronic, optical, and mechanical properties. Table 1.1.1 highlights some of the most notable vdW materials, their crystal structure, optical bandgap, and applications. Photoexcited emission from vdW materials spans from THz to ultraviolet, permitting a wide variety of optical use cases. Also, by combining multiple different layers of vdW materials into one composite system, these heterostructures have properties not held individually by any of the constituent materials. One common version of vdW heterostructes are morié heterostructures where two materials are stacked with a relative rotation between their crystal axis, forming a morié superlattice[14, 15]. VdW materials/heterostructures, when coupled with nanophotonic stressors, are used to form or study quantum states of light for future applications in integrated quantum light sources[12, 16-20], quantum key distribution[21-24], and quantum computing[25-33].

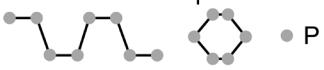
Material	Crystal structure	Optical bandgap (eV) at 300 K	Applications
Common TMDs (Semiconductor)	Side view Top view 	MoS_2 : 1.88 WS_2 : 2.02 $MoSe_2$: 1.65 WSe_2 : 1.65	Quantum photonics Light emitting diodes Photodetectors Field-effect transistors
h-BN (Insulator*)	Top view 	6.00	Substrate in vdW devices Quantum key distribution
Graphene (Semimetal)	Top view 	0 (Dirac cones)	Ultrafast photonics Conductive electrodes
Black phosphorus (Semiconductor)	Side view Top view 	Bulk 0.3 → Monolayer 1.7	Mid-IR photodetectors Field-effect transistors

Table 1.1.1: Table of common vdW materials. A table of the most common vdW materials, their material classification, crystal structure, optical band gaps, and applications. *h-BN is not an insulator in the traditional sense, but the bandgap is large in comparison to TMDs and black phosphorus.

One widely studied vdW material is graphene. Consisting of carbon atoms organized into a hexagonal lattice, graphene hosts a semi-metallic electronic band structure on a truly 2D scale. Shown in Figure 1.1.1a-c, graphene's Brillouin zone (BZ) consists of Dirac cones at the K/K' symmetry points. This linear dispersion has many benefits for two-dimensional (2D) device design in future technologies, such as RF electronics[34, 35], tunable metamaterials[36, 37], p-n junctions[38], and high-sensitivity sensors[39]. Even in the multilayer case, graphite (multilayer graphene) has been used as the anode in Li ion batteries[40], as a part of 2D material-based devices[41-43]. In Chapters 3 and 5 of this dissertation, graphite is used to dope another vdW material, WSe_2, to purify quantum light emission. With a large variety of applications, research efforts into the large-scale growth of graphene sheets have shown promise that graphite/graphene-based scalable devices are possible in emergent systems[44-47].

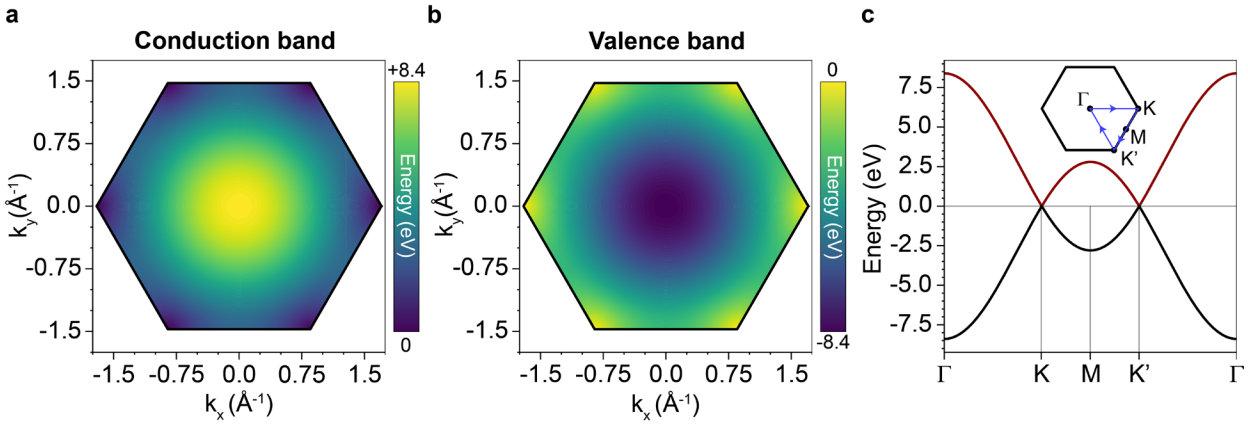


Figure 1.1.1: Tight-binding model of the electronic states of graphene. (a-b) Electronic dispersion of graphene for the first BZ obtained using a tight-binding model (t = 2.8 eV, a = 1.42 Å). (c) Plot of the electronic dispersion taken along the first BZ path shown in the inset. At the K and K' high symmetry points, the dispersion is near linear for both the conduction and valence bands, forming Dirac cones.

Commonly used in the encapsulation of 2D vdW devices, h-BN is a wide bandgap semiconductor due to its ~6 eV bandgap. H-BN is comprised of boron and nitrogen covalently bonded into a hexagonal lattice that is relatively free of dangling bonds on the surface. This mostly inert and atomically flat nature makes h-BN an ideal candidate for encapsulation of other 2D vdW materials by hindering bubbles and wrinkles, generating a uniform strain landscape[48, 49]. H-BN has a primary use case as a generator of room-temperature quantum states of light in the visible to near infrared (~550 – 800 nm). Defects within the h-BN lattice create deep in-gap defect levels in the electronic band structure that act as a two-level system under laser excitation[50]. In comparison to other optical vdW materials, the quantum emitters found in h-BN have low spectral uniformity, few avenues for deterministic generation, and reduced brightness[51]. Another class of 2D vdW materials that addresses many of these problems and is the optically active material class of focus for this dissertation is TMDs.

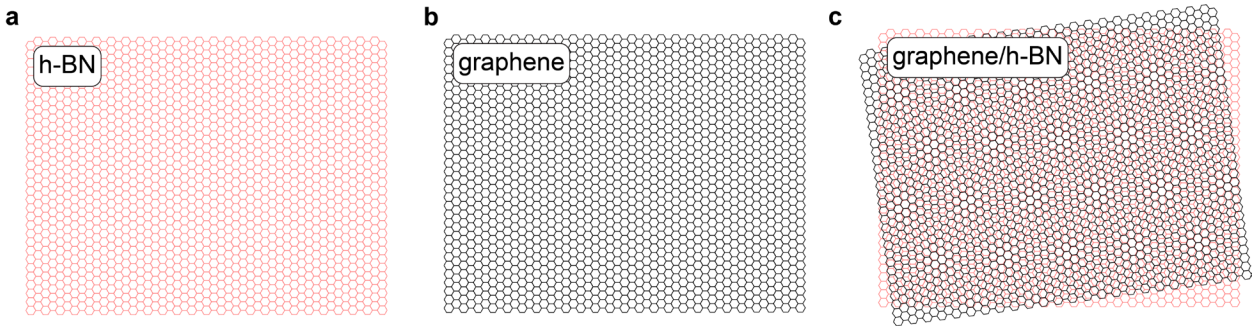


Figure 1.1.2: Formation of a morié superlattice. (a-b) A schematic representation of a h-BN and graphene lattice, respectively, with coaligned crystal axes. (c) A schematic showing a new morié lattice that appears by stacking the materials with ~7.5° of relative crystal axis rotation. Stacking of atomic sites smoothly changes from direct atom over atom (AA stacking) to atom over hollow site (AB or BA stacking), forming the larger morié potential spacing.

Naturally, since h-BN was used as an encapsulation layer, morié superlattices were found to form between the hexagonal lattices of graphene and h-BN. Seen in Figure 1.1.2a-c, by changing the relative rotation angle between the crystal lattice vectors of the respective materials, an additional periodic morié potential is formed that can modulate the optoelectronic properties of the 2D heterostructure[52, 53]. Homobilayer (two-layers of the same material) morié superlattices have also been shown in graphene at the magic twist angle to create emergent superconductivity[54], and produce ultra-flat electronic bands[55]. Also, in another vdW material class, TMDs, morié heterostructures between WS_2 and WSe_2 have been shown to host morié excitons, where photoexcited electron-hole pairs are confined to the morié potential[56].

TMDs are a subclass of vdW materials consisting of three atomic layers of atoms, two layers of chalcogen atoms (commonly: S, Se, Te) in the top and bottom, and a layer of transition metal atoms (commonly: W, Mo) in the middle. The individual triangular lattices, when viewed from above, form an overall hexagonal lattice. The four most popular TMD materials are MoS_2,

$MoSe_2$, WS_2, and WSe_2. These semiconducting materials in bulk form host indirect band gaps, limiting their applications. However, when isolated into 1L-flakes, the indirect bandgap transitions to a direct bandgap at the energy degenerate K/K' points in the BZ due to non-symmetric layer-dependent shifts of the gamma and K/K' point energy levels in the band structure[57-60]. This non-symmetric shifting can be seen in Figure 1.1.3 and occurs because the electronic states at the K/K' points are blueshifted at the conduction band minimum (CBM) and are nearly constant at the valence band maximum (VBM). In comparison, at the gamma point, both the VBM and the CBM are shifted away from one another. These shifts with reducing layer thickness occur because the electronic states at the K/K' point CBM and gamma point VBM and CBM are comprised of mostly z orbitals, so their energy levels are strongly affected by the added confinement. In comparison, the K/K' point VBM is mostly comprised of in-plane x and y transition metal orbitals, so the energy levels here are less sensitive to reduced layer thickness[58]. The indirect-to-direct bandgap transition that occurs in TMDs concentrates research efforts towards monolayer samples, which are typically obtained using mechanical exfoliation or directly grown using chemical vapor deposition.

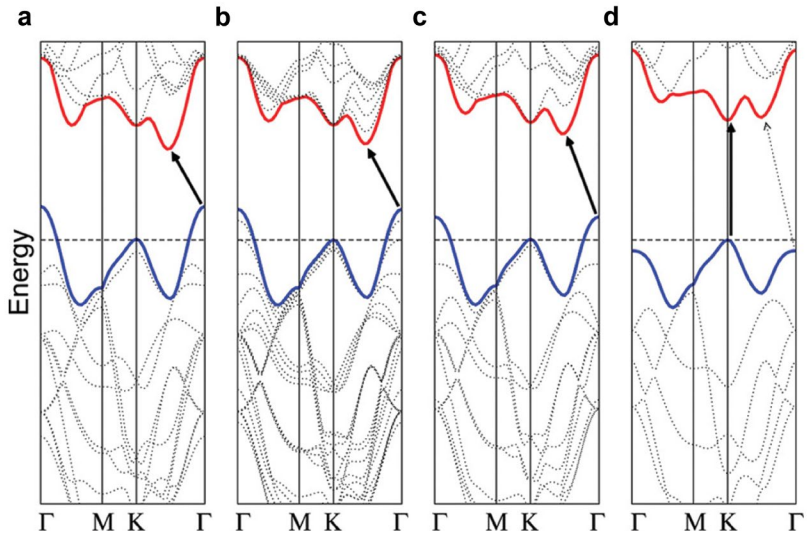


Figure 1.1.3: Layer-dependent electronic band structure of MoS_2 calculated using DFT. (a) Calculated band structure for Bulk MoS_2 (b), 4L-MoS_2 (c), 2L-MoS_2 (d), and 1L-MoS_2. Bulk MoS_2 is characterized by an indirect optical bandgap. The direct optical transitions occur at the K/K' points. With reduced layer thickness, the indirect gap becomes larger while the direct gap barely changes. Here, the solid arrows indicate the lowest energy transitions for each layer configuration. Adapted from "Emerging Photoluminescence in Monolayer MoS_2", Nano Lett. Splendiani, A et al., 2010, 10(4), 1271-1275.

In Chapters 3, 4, and 5 of this dissertation, monolayer WSe_2 is used as the photoactive material for the generation of SPE states. These monolayer flakes were obtained using the Scotch tape exfoliation method popularized by the initial discovery of graphene in 2004[1]. By simply adhering a bulk crystal to a piece of Scotch tape and thinning the crystal through repeated stamping of the material against the tape, thin sections of the crystal are generated. The exfoliation process, which is discussed in depth in Chapter 2, revolutionized the study of vdW materials. Instead of requiring direct growth of monolayer material using chemical vapor deposition[61-64], the barrier to entry to monolayer vdW material studies is commercially available tape and a bulk crystal. Large-area exfoliation of monolayer flakes can also be accomplished using gold-assisted exfoliation[65, 66], but these flakes have been found to have inferior optical properties due to charge doping and

intrinsic inhomogeneous strain profiles[67, 68]. Because of the drawbacks of gold-assisted exfoliation, it was only used for prototyping in this dissertation, and Scotch tape exfoliation was used for all the final applications/samples reported here.

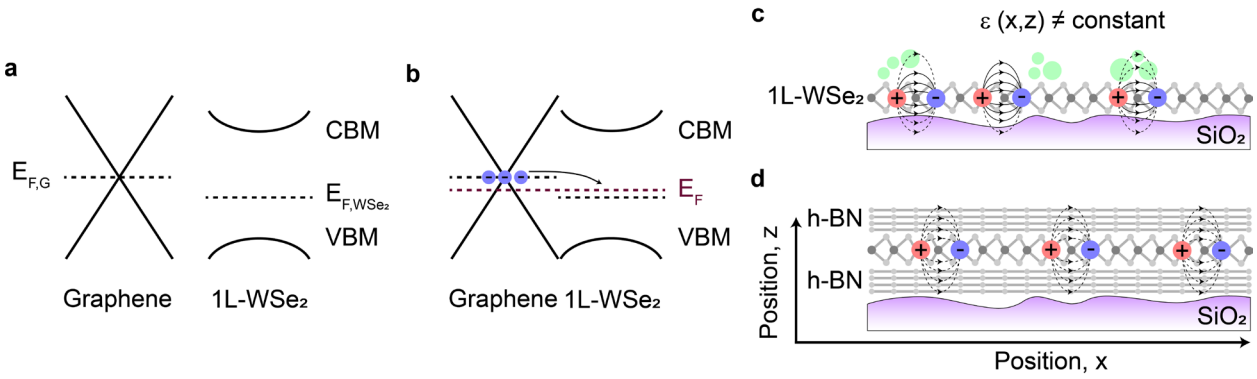


Figure 1.1.4: Consequences of vdW heterostructures. (a) Band diagram for graphene and 1L-WSe_2 before contacting one another. The Fermi energies shown here are only for this example. In a realistic setting, absorbates, doping, substrate material, and gating could shift these values significantly. (b) Band diagram for a graphene and 1L-WSe_2 after being brought into contact. Now, for this example, electrons move from the graphene into the 1L-WSe_2 to maintain a uniform electrochemical potential. (c) A diagram of plane polarized excitons in 1L-WSe_2 on a SiO_2 substrate and their field lines to indicate the uniformity of the dielectric environment. Here, two factors contribute to a nonuniform dielectric environment: the surface roughness of the SiO_2 and absorbents on the 1L-WSe_2 surface. (d) A similar diagram to (c), but now with h-BN encapsulation. This vdW heterostructure adds uniformity to the dielectric environment by mitigating substrate and absorbent charge influence.

VdW material heterostructures, like the graphene/WSe_2 heterostructure studied in Chapters 3 and 5, host rich interface physics governed by the relative band alignment, charge transfer, and energy transfer between the constituent materials. Highlighted in Figure 1.1.4a-b, when two materials are brought into contact with one another, charge carriers will flow between layers until a single equilibrium electrochemical potential forms. The direction of charge transfer is sensitive to the initial doping of both materials, surface absorbates, substrate material, and gating, but for nominally intrinsic graphene and WSe_2, the small work-function difference leads electrons to flow

into the WSe_2[69]. Excited states in the WSe_2 are also affected by the graphene. Quickly after photo excitation of an electron in the WSe_2, charged particles can transfer to the graphene, resulting in dissociation of the excited state[70]. In comparison, interfaces formed between WSe_2 and h-BN do not see much charge transfer because the Fermi levels are already very close to equilibrium. However, the addition of h-BN encapsulation adds uniformity to the dielectric environment surrounding the WSe_2 because of an atomically flat substrate, separation/protection from surface absorbates, and additional dielectric screening, as shown in Figure 1.1.4c-d when h-BN is used as the substrate for WSe_2 rather than traditional SiO_2[8, 9]. This change in the dielectric environment stabilizes excited state energies and narrows the optical linewidths of excitons, making these heterostructures more appealing to quantum technologies.

1.2 Light Matter Interactions and Strain Effects in 1L-WSe_2

Light matter interactions in monolayer WSe_2 (1L-WSe_2) are dominated by the absorption of photons into the formation of excitons. Excitons are charge-neutral quasiparticles composed of a valence band hole and a conduction band electron that are Coulombically bound to one another. Different exciton manifolds (A, B, and C excitons) are present in the absorption spectra of 1L-WSe_2 (Figure 1.2.1a), coinciding with optical transitions [71-74]. The orbitals that contribute to each group of excitons are shown in the 1L-WSe_2 electronic band structure shown in Figure 1.2.1b. After some time, the electron of the exciton will recombine with the hole. This recombination can be radiative and emit a photon through the process of PL, or non-radiative and contribute to Auger recombination, intervalley scattering, or phonon emission, to name a few. For the work in this dissertation, higher energy excitons (B and C excitons) rapidly thermalize into the lowest energy A excitons, making A excitons the dominant excited states that are probed.

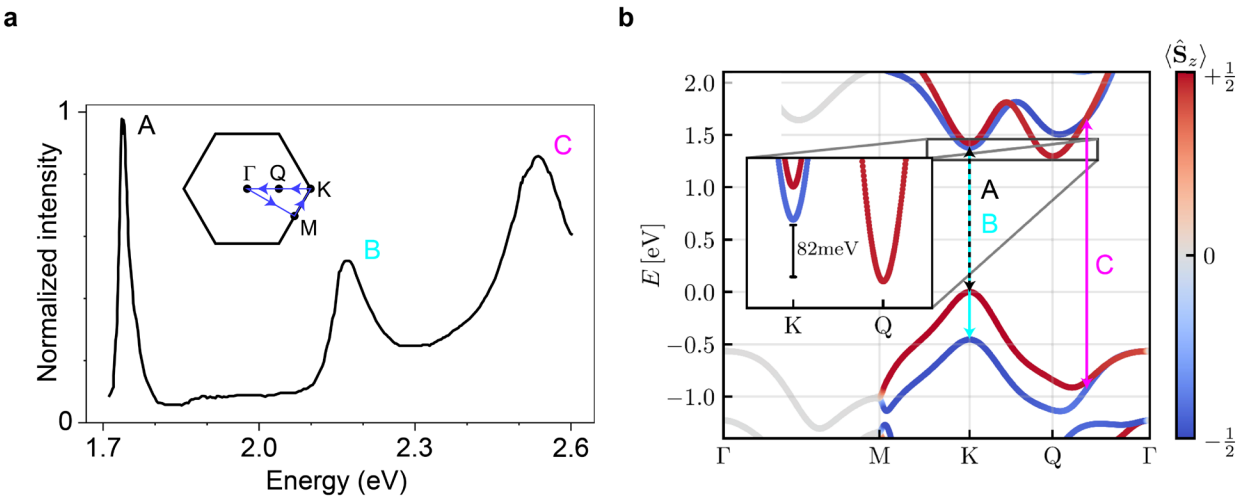


Figure 1.2.1: Absorption signatures of 1L-WSe_2. (a) Absorption spectrum of 1L-WSe_2 with labeled A, B, and C exciton resonances. Inset is the labeled high symmetry points in the BZ of 1L-WSe_2 and the path taken to plot the electronic band structure in (b). (b) Density functional theory (DFT) calculations of the electronic band structure of 1L-WSe_2. Highlighted in this plot are the direct transitions that make up the A, B, and C exciton resonances. The A and B exciton resonances share the same set of conduction bands, and the C exciton resonance originates from band nesting near the Q point in the BZ. The absorption spectrum is adapted from "Self-consistent dielectric constant determination for monolayer WSe_2", Optics Express. Lee, S et al., 2018, 26(18), 23061-23068. DFT calculations are adapted from "Beyond the K-valley: exploring unique trion states in indirect band gap monolayer WSe_2", npj 2D Materials and Applications. Nielsen, M et al., 2025, 9(1).

The lowest energy excitons in 1L-WSe_2 are K valley excitons. The K valley in 1L-WSe_2 is energy degenerate with the K' valley, only with different spin orientations and crystal momenta, so these valleys are commonly grouped in discussion. Figures 1.2.2a-b show the lowest energy bright and dark excitons in unstrained 1L-WSe_2, where bright and dark refer to the dominant recombination pathways of the excitons. In general, bright excitons have direct recombination pathways that favor radiative recombination, while dark excitons have spin or momentum-forbidden recombination pathways that strongly suppress radiative recombination[59, 75-77]. Dark excitons in 1L-WSe_2 are a result of spin-split conduction bands at the K/K' points that arise due to strong spin-orbit coupling. Despite their spin/momentum forbidden transitions, PL emission from

dark excitons is possible through phonon-assisted recombination[78, 79], magnetic-field-assisted spin flipping[75, 80], or coupling to out-of-plane plasmonic fields[81-85]. At room temperature (RT), the PL of 1L-WSe_2 is dominated by bright excitons, with dark excitons playing a reduced role through population dynamics. However, at cryogenic temperatures, dark excitons alongside local tensile strain serve as the feeding channel for defect-based quantum light emission.

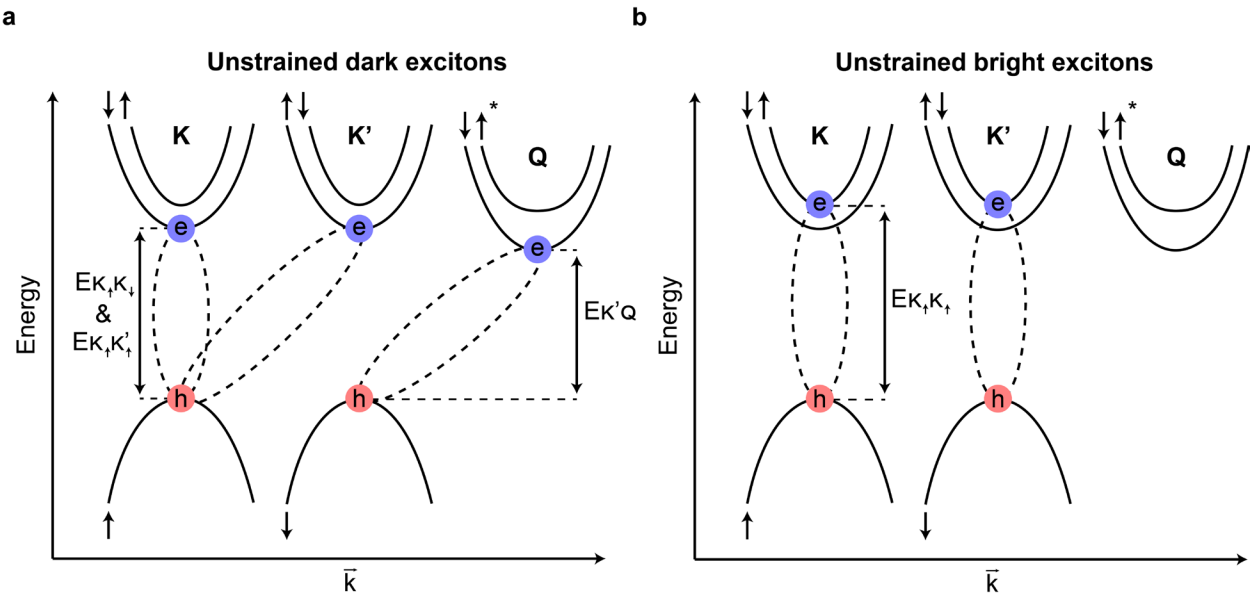


Figure 1.2.2: Lowest energy bright and dark excitons in unstrained 1L-WSe_2. (a) The lowest energy dark excitons. Arrows at the upper left of each band indicate the spin state of each specific band, and the dashed ovals indicate the excited electron and hole that would form the excitons. All excitons shown have either spin or momentum-forbidden optical transitions. (b) The lowest energy bright excitons. Note how, in comparison to (a), now the electron and hole that compose the excitons have matching momentum and spin configurations, permitting radiative recombination. $E_{K'Q} < E_{K\uparrow K\downarrow} = E_{K\uparrow K'\uparrow} < E_{K\uparrow K\uparrow}$. *The spin state of the different Q-point conduction bands is a mixed spin state from heavy orbital mixing. The indicated spin states are the largest contributors to optical transitions.

The electronic bands that contribute to A exciton formation are highly sensitive to strain within the 2D sheet[74, 86, 87]. Schematically shown in Figure 1.2.3a, when 1L-WSe_2 is under tensile strain, the bandgap is spatially modulated, so exciton funneling toward regions of high tensile

strain is energetically favorable[43, 88-90]. Exciton funneling fundamentally differs from omnidirectional exciton diffusion. Funneling guides excitons specifically toward highly strained regions, making it a powerful mechanism for guiding radiative recombination to occur in the proximity of waveguides, photonic cavities, or other nanophotonic devices[17, 19, 20, 91-93]. PL spectroscopy is one way to observe spatial shifts of exciton energies. In Figure 1.2.3b, a PL spectrum of 1L-WSe_2 taken from a strained and unstrained region of 1L-WSe_2 is shown. The spectrum taken from strained 1L-WSe_2 is notably redshifted and broadened in comparison to the unstrained spectrum. Strain-dependent bandgap modulation originates from changes in the inter-atomic orbital overlap, and inhomogeneous linewidth broadening emerges from the spatial averaging across multiple strain values/potentials[94, 95].

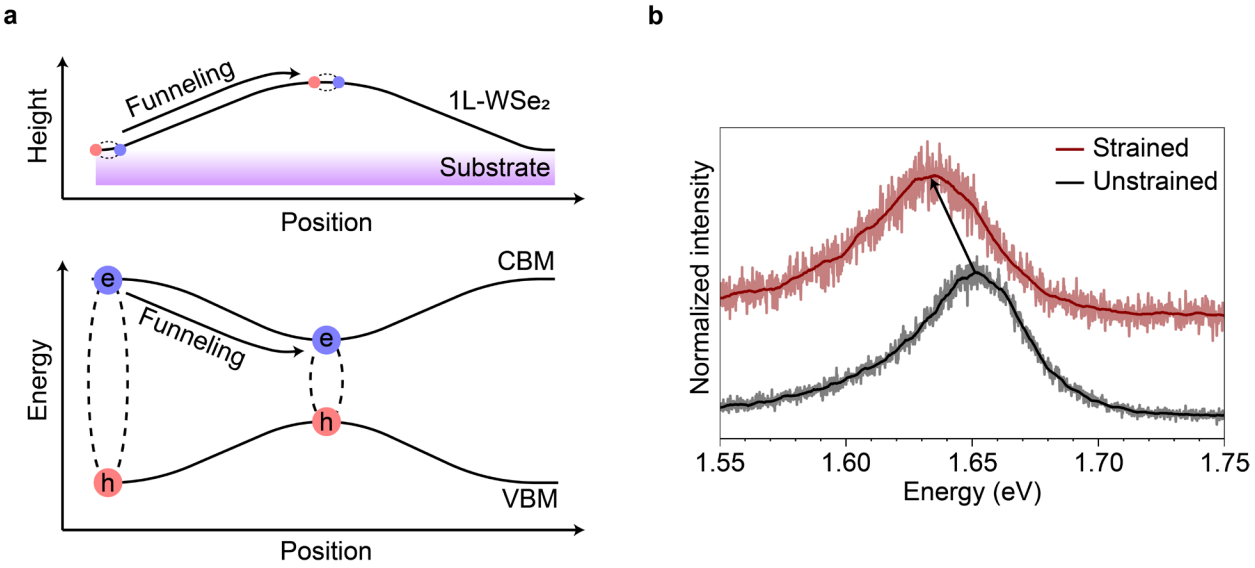


Figure 1.2.3: Exciton funneling and strain in 1L-WSe_2. (a) Schematic showing the exciton funneling mechanism. Top: Real-space schematic of 1L-WSe_2 strained in the form of a nanobubble. After photoexcitation of an exciton near the base of the nanobubble, the exciton funnels towards the apex of the nanobubble before recombination. Bottom: Position-dependent band diagram showing that the energy separation between the CBM and VBM shifts as a function of position along the nanobubble. In the areas of highest strain (apex of the nanobubble), the exciton energy is the lowest, making it favorable for excitons to funnel and localize in high-strain regions. (b) Example PL spectra taken from strained and unstrained regions of 1L-WSe_2 at RT. The strained PL spectra are notably redshifted in comparison to the unstrained spectra, matching the expected behavior represented in (a).

Exciton funneling has recently been shown to change direction for dark excitons because of how the K/K' and Q point conduction bands shift opposite to one another depending on the type of strain on the lattice. This difference in band shifting under tensile/compressive strain makes dark excitons favor funneling towards high compressive strain rather than tensile strain. Shown in Figure 1.2.4 is a band diagram representing how the K/K' and Q point bands shift under tensile/compressive strain. Black dashed arrows with $\pm\Delta\varepsilon$ indicate the shifting direction of each set of bands. As compressive strain is imparted, the energy of dark KQ excitons is reduced while the energy of bright K/K' excitons is increased. This distinction in how bright and dark excitons

funnel was an important consideration in Chapter 4 of this dissertation, where compressive and tensile strain was generated within different locations of the same sample.

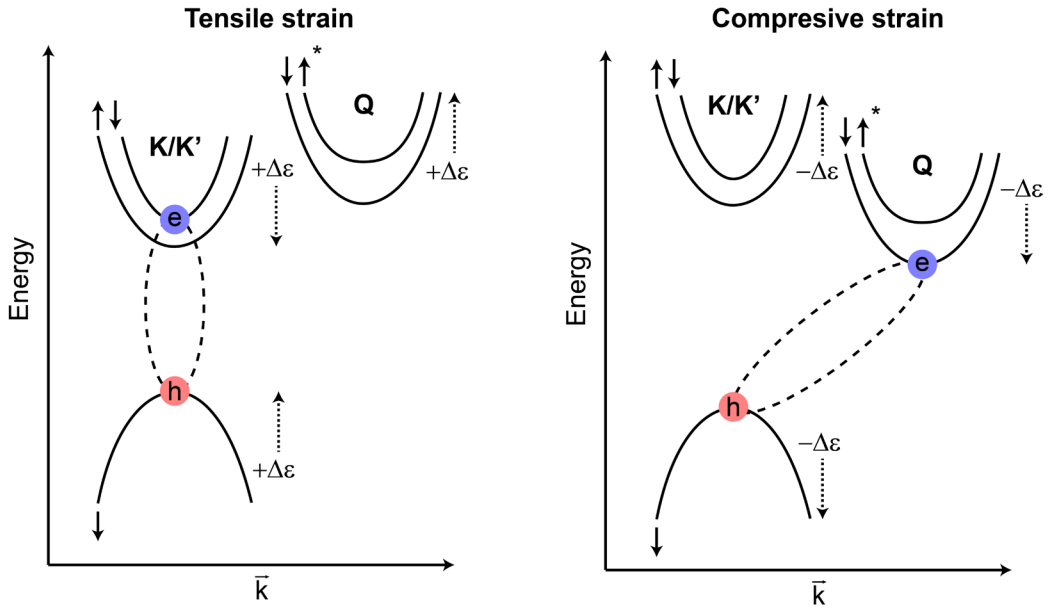


Figure 1.2.4: Strain-dependent shifts of excitons in 1L-WSe_2. (a) Tensile strain-induced shifts of the electronic bands in 1L-WSe_2. With increasing tensile strain, the direct bandgap at the K/K' points redshifts, lowering the exciton energy, and the Q point conduction bands increase in energy. Shifting directions with applied strain in (a) and (b) are indicated by dashed black arrows. (b) Compressive strain-induced shifts of the electronic bands in 1L-WSe_2. As opposed to the tensile case, with added compressive strain, the direct bandgap at the K/K' points is blueshifted, and the Q point conduction bands decrease in energy. *The spin state of the different Q-point conduction bands is a mixed spin state from heavy orbital mixing. The indicated spin states are the largest contributors to optical transitions.

1.3 Quantum Emitters

Quantum emitters are isolated states with discrete energy levels that emit photons through quantum transitions. Quantum emitters that produce a sub-Poissonian stream of light are called single photon emitters (SPEs). The ideal quantum emitter hosts a narrow spectral bandwidth and long coherence time, suiting most applications in next-generation quantum technologies, where

indistinguishability and precise control are desired. Early SPEs came from quantum dots[96-98], quantum wells[99, 100], single molecules[101-103], and NV centers[104-106], but have recently emerged in vdW materials such as h-BN[16, 50, 51], and TMDs[2-7]. The most widely studied of these materials is 1L-WSe_2. SPEs in 1L-WSe_2 struggle to find applications in devices due to various constraints (scalability, difficulty in integrating into devices, limited fabrication protocols), one of which is the spatial inhomogeneity of emission. To better advance the understanding and control the emission, the origin of SPEs in 1L-WSe_2 needs to be understood.

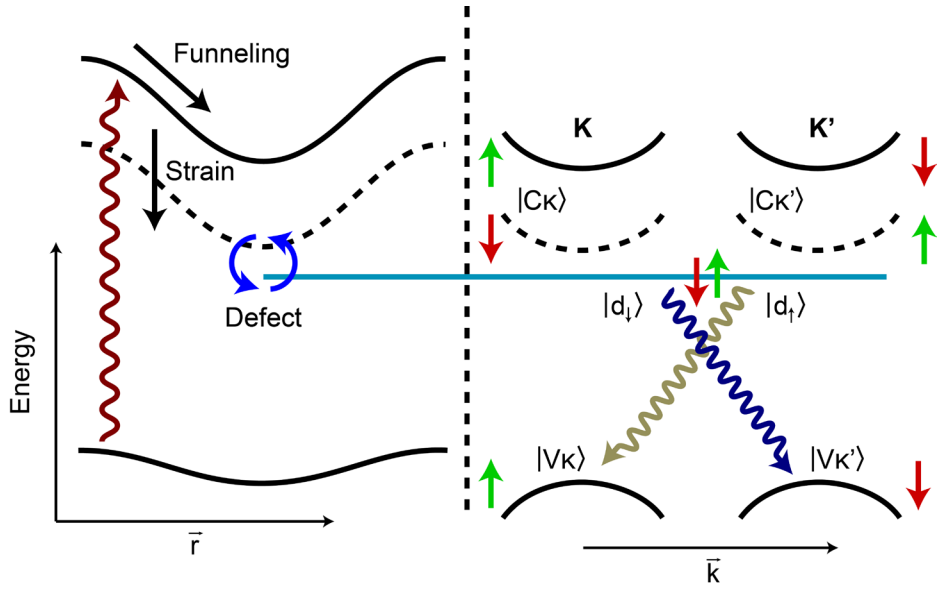


Figure 1.3.1: Linhart schematic for SPE formation in 1L-WSe_2. (a) Real space representation: A free exciton is created (dark red arrow), strain efficiently funnels the exciton with its electron in the bright (solid black line) or dark (dashed black line) conduction band towards the energetic minimum at the strain maximum due to the strain-dependent bandgap. Mixing of the strain-localized dark exciton with a defect state leads to the formation of a strongly localized defect exciton. (b) Reciprocal space: While dark strain-localized exciton states (dashed) remain dark, hybridization with a point defect (horizontal cyan line) breaks the valley selectivity and leads to efficient photoemission (dark blue and yellow arrows). Adapted from "Localized Intervalley Defect Excitons as Single-Photon Emitters in WSe_2", Phys Rev Lett. Linhart, L et al., 2019, 123(14), 146401.

When the first experimental evidence of SPEs in 1L-WSe_2 was published in 2015, two[3, 4] of the five[3-7] seminal papers proposed a general hypothesis that defects mediate the radiative emission of the isolated electronic state. In 2019, Linhart *et al.*[107] published a more detailed theory of the combined roles of excitons and defects that describes quantum light emission in 1L-WSe_2. They theoretically established that due to tensile strain and the large spin-orbit band splitting in 1L-WSe_2, the lowest energy momentum-forbidden dark exciton state can radiatively recombine through a hybrid state formed with a momentum-broad defect level in the electronic band structure.

Figure 1.3.1 highlights the energy levels, spin orientations, and hybridization that they predicted to occur to generate quantum light in 1L-WSe_2.

The Linhart hypothesis requires tensile strain, defects, and dark excitons. Tensile strain is the most studied contributor, as nearly all 1L-WSe_2 SPE literature uses tensile strain, and one specific study showed the emergence of SPEs with in-situ tunable strain[108]. Defects have also been shown to correlate with higher density SPE formation[109], but the type of defect is still in question. Currently, selenium vacancies or oxygen substitutions seem to be the relevant defect types for SPEs[110, 111]. However, magneto-optical studies into the g-factor of SPE states show up to three different species of SPEs with g-factors ranging from 9.4 to no observable Zeeman shift, arguing that multiple different defect-mediated recombination channels exist[112]. The theoretical expected g-factors for localized excitons in 1L-WSe_2 lie between 6-12[2-6, 113], making the SPE state with no observable Zeeman shift notably mysterious, possibly reflecting a different subclass of SPE state. Another impactful study into the validity of the Linhart hypothesis looked into the effect of an in-plane magnetic field on SPE emission and observed strain-dependent redshifting with an increasing field magnitude alongside no commensurate PL brightening[114]. This result supports the hybridization model because a purely dark exciton state would be expected to brighten with an in-plane field due to a mixing of spin states. Also supporting the hybridization picture, one study used chiral plasmons to break valley degeneracy at the K/K' points and measured some SPEs to have no valley polarization despite selective pumping with circularly polarized light[115]. This result also supports the dark exciton/point defect hybridization picture, but some gaps in the Linhart theory still exist. The main unresolved questions are whether one or more emitter classes exist, how much valley polarization exists after hybridization, and what the exact defects are that contribute to

single photon emission. In Chapter 4, we aim to shed light on the role of defects in the SPE formation of 1L-WSe_2 by using low-defect-density material and embedded plasmonic nanoantennas to enhance a quantifiable amount of SPEs to study their relative positions local to the nanoantenna apex.

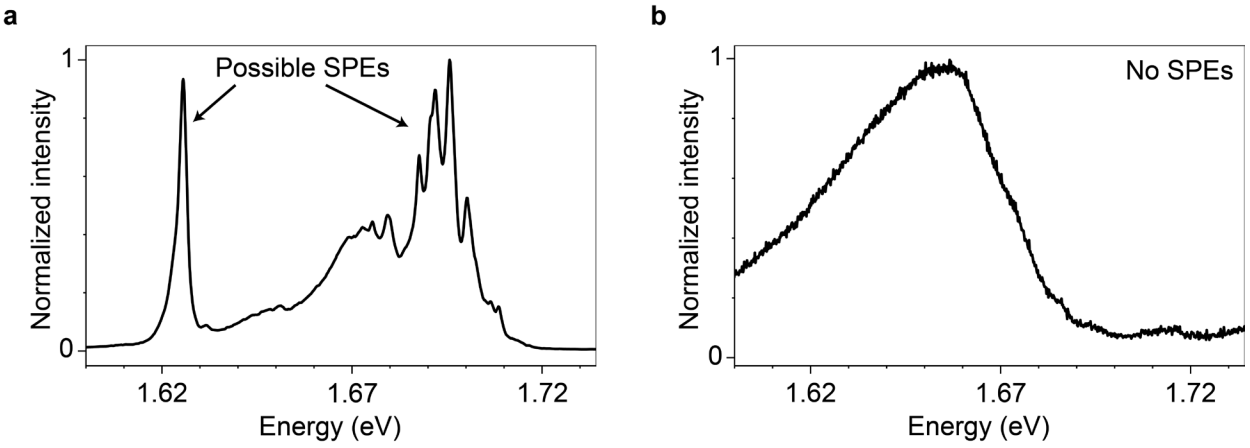


Figure 1.3.2: 4 K PL spectra of strained and unstrained 1L-WSe_2. (a) 4K PL spectra of strained 1L-WSe_2. Black arrows point to possible SPE states. (b) 4K PL spectra of unstrained 1L-WSe_2. Instead of the narrow lines present in (a), now the PL spectrum only shows broad defect emission, indicating that the formation of SPEs has not occurred.

SPEs in 1L-WSe_2 are activated at cryogenic temperatures. Figure 1.3.2a-b shows an example of 4K PL spectra from strained and unstrained 1L-WSe_2, respectively, where the narrow lines present are possible SPE states. Notably, these states are lower in energy than the lowest energy bright exciton (A-exciton), and the measured linewidths of these emitters are low, on the order of 100 μeV[5, 116]. Significant challenges for the adoption of 1L-WSe_2 SPEs into quantum applications are local electric field and phonon interactions that can broaden the emission linewidth and spectrally shift the emission wavelength, diminishing the indistinguishability of the emitted photons. Another limiting factor is the broad emission background surrounding 1L-WSe_2 SPEs. Background emission lowers the purity of SPE states, which is measured using Hanbury Brown-

Twiss (HBT) interferometry, since other non-SPE photons are included in the same emission wavelength band for any device application.

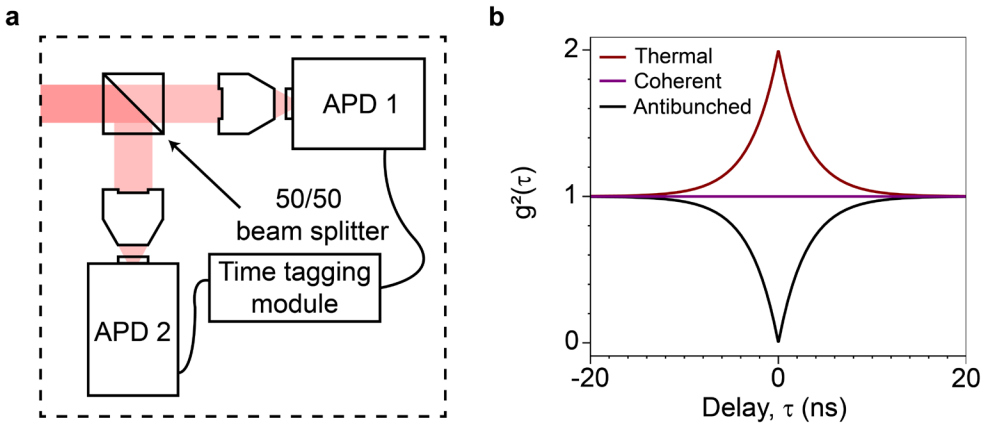


Figure 1.3.3: HBT interferometer block diagram and expected $g^{(2)}(\tau)$ curves. (a) A block diagram of an HBT interferometer. (b) Example $g^{(2)}(\tau)$ curves for different types of light sources.

Used in Chapters 3 and 4 of this dissertation, HBT interferometry is the primary experimental technique for validating the sub-Poissonian stream of photons expected from an SPE state. HBT interferometry is conducted by isolating a narrow band of emission, generally the bandwidth of an SPE, and directing it incident onto a 50/50 beamsplitter with single-photon avalanche photodiodes (APDs) on either path that are both connected to a time-correlated single-photon counting (TCSPC) module. A block diagram of an HBT interferometer can be seen in Figure 1.3.3a. The TCSPC module acts as a global clock to track photon detection events on the APD channels as a function of time. Once the measurement is completed, a normalized histogram is generated with coincidence counts on the y-axis and delay time on the x-axis. Coincidence counts refer to the simultaneous detection of photons on both APDs within the same timing window, and delay time (τ) is the timing separation between each APD's photon detection record. This histogram of coincidence counts against delay time is the measured second-order

autocorrelation function, $g^{(2)}(\tau)$. The expression of the second-order autocorrelation function relating to an HBT interferometry experiment is:

$$g^{(2)}(\tau) = \frac{\langle I_1(t) I_2(t+\tau)\rangle}{\langle I_1(t)\rangle\langle I_2(t)\rangle} \tag{1.3.1}$$

where $I_{1,2} \propto \left|E_{1,2}(t)\right|^2$ and $I_{1,2}(t)$ is the time-averaged intensity at a given time. This expression then represents the correlation between two temporally separated intensity signals with a time delay, τ, from a single light source. When the time delay is brought toward zero, the second-order autocorrelation function represents how likely it is to detect a second photon at the same time that one photon was also detected. If two photons are detected at the same time, $\tau = 0$, on both APDs, this is considered a coincidence count.

In the expression of Equation 1.3.1, the detection of a photon at time t, does not reduce the number of photons at time $t + \tau$. This distinction becomes exceedingly important when working with individual photons coming from an SPE state. To apply a quantum mechanical description to Equation 1.3.1, rather than I_1 and I_2, we will now consider the source field itself and represent it as a time-variant electric field within the second-quantization formalism with mode k as $\hat{E}_k = \hat{E}_k^{(+)}(t) + \hat{E}_k^{(-)}(t)$ giving[117]:

$$g^{(2)}(\tau) = \frac{\langle I(t) I(t+\tau)\rangle}{\langle I(t)\rangle^2} = \frac{\langle \hat{E}_k^{(-)}(t)\hat{E}_k^{(-)}(t+\tau)\hat{E}_k^{(+)}(t+\tau)\hat{E}_k^{(+)}(t)\rangle}{\langle \hat{E}_k^{(-)}(t)\hat{E}_k^{(+)}(t)\rangle^2} \tag{1.3.2}$$

Then, with $\tau = 0$ and in terms of the ladder and number operators[117]:

$$g^{(2)}(0) = \frac{\langle (\hat{a}_k)^\dagger (\hat{a}_k)^\dagger \hat{a}_k \hat{a}_k\rangle}{\langle (\hat{a}_k)^\dagger \hat{a}_k\rangle^2} = \frac{\langle n(n-1)\rangle}{\langle n\rangle^2} = 1 + \frac{(\Delta n)^2 - \langle n\rangle}{\langle n\rangle^2} \tag{1.3.3}$$

Here, the photon number of a single mode, n, has variance, $(\Delta n)^2 = \langle n^2\rangle - \langle n\rangle^2$ [117].

0	0	3	0	2	0	4	0	1	0	3	0	1	1	0
1	0	2	1	1	0	1	2	0	1	1	2	1	1	1
1	1	1	1	1	1	1	1	1	1	1	1	1	1	1

Figure 1.3.4: Spatial/temporal photon distributions for different light sources. Schematic showing different photon distributions from idealized light sources. In descending order, the rows represent super-Poissonian, Poissonian, and sub-Poissonian distributions. The mean photon number is consistently 1 across each row.

Depending on the type of light source, $(\Delta n)^2$ is expressed differently. For example, take an unknown light source that emits photons such that, on average, there are 15 photons per nanosecond. The distribution of photons can manifest in three main categories, shown in Figure 1.3.4, where each subgroup is equivalent to ~ 2 cm spatially or ~ 67 ps temporally. These different categories are traditionally defined as thermal, coherent, and single-photon (SP) light sources. Each different type of light source then gives $(\Delta n)^2$ as[117-120]:

$$(\Delta n)^2_{thermal} = \langle n^2 \rangle + \langle n \rangle \rightarrow g^{(2)}(0) = 2 \quad 1.3.4$$

$$(\Delta n)^2_{coherent} = \langle n \rangle \rightarrow g^{(2)}(0) = 1 \quad 1.3.5$$

$$(\Delta n)^2_{SP} = 0 \rightarrow g^{(2)}(0) = 1 - \frac{1}{n} \; (n \geq 1) \quad 1.3.6$$

Within the context of the work in this dissertation, Equation 1.3.6 is most important. A perfect SPE emits a $n = 1$ Fock state per emission event, so the expected result of a second-order autocorrelation measurement of a perfect SPE is $g^{(2)}(0) = 0$.

Now, assume there are two nearly energy-degenerate but independent SPE sources contributing to the intensity signal. For a timing window T, the probability of detecting either zero, one photon, or more than one photon is, $P_i(0) = 1 - p$, $P_i(1) = p$, or $P_i(\geq 2) = 0$, respectively, from an individual emitter i. Since the emitters are independent, the joint probability for a total of

0, 1, or 2 photon emissions within T is the product of the individual emitter probabilities. So, the joint probabilities $P(x)$ for x, total photons go as:

$$P(0) = (1-p)(1-p) = (1-p)^2 \quad 1.3.7a$$

$$P(1) = p(1-p) + (1-p)p = 2p(1-p) \quad 1.3.7b$$

$$P(2) = p^2 \quad 1.3.7c$$

Now using Equation 1.3.3 to calculate $g^{(2)}(0)$ for two degenerate but independent SPE sources:

$$\langle n \rangle = 0 \cdot P(0) + 1 \cdot P(1) + 2 \cdot P(2) = 2p(1-p) + 2p^2 = 2p \quad 1.3.8a$$

$$\langle n(n-1) \rangle = 0 \cdot P(0) + 0 \cdot P(1) + 2 \cdot P(2) = 2p^2 \quad 1.3.8b$$

Substituting Equations 1.3.8a-b into Equation 1.3.3 then gives:

$$g^{(2)}(0) = \frac{2p^2}{\langle 2p \rangle^2} = \frac{1}{2} \quad 1.3.9$$

This result means that a measured value of $g^{(2)}(0)$ between 0 and 0.5 cannot be obtained by more than a single SPE state. As mentioned previously, a perfect SPE state should result in $g^{(2)}(0) = 0$. Values of $g^{(2)}(0)$ between 0 and 0.5 are then caused by the addition of Poissonian background emission or noise.

Considering the importance of defects to the formation of SPEs in 1L-WSe_2, a variety of studies into the different defect types have been done to elucidate their different roles[42, 110, 111, 121]. The relevant defect populations are single tungsten vacancies (V_W), oxygen interstitials (O_{ins}), and selenium vacancies (V_{Se}). DFT calculations show that emission mediated by the various defect populations should place SPE emission 40-100 meV, ~350 meV, and ~150 meV lower in energy than the A-exciton for V_W, O_{ins}, and V_{Se} defects, respectively[110]. By observing the distribution of SPE wavelengths in 1L-WSe_2, the V_{Se} defect seems most likely to be the mediator[122]. This result

is supported by other studies tracking the variety of SPE energies under controlled defect engineering of V_{Se} defects using electron beam irradiation[109, 123]. Controlling the defect density of 1L-WSe_2 then comes with tradeoffs. A high defect density material (10^{13} cm^{-2}) can support a large number of SPE states, but has a high intensity, broad emission background that ruins the SPE purity of any given state. On the other hand, a low defect density material (10^{10} cm^{-2}) has reduced background emission and higher purity SPEs but a more sparse spatial distribution.

The most straightforward way to control the defect density in bulk material/flakes is by using different growth techniques and measuring the defect density using scanning tunneling microscopy. Growth techniques in the order of highest to lowest expected defect density go as: CVD-grown flakes (~2×10^{13} cm^{-2})[124, 125], chemical vapor transport (CVT) grown bulk crystal (~5×10^{12} cm^{-2})[126], and flux-synthesized bulk crystal (~$10^{11}\times cm^{-2}$)[126-128]. The CVD, CVT, and flux-grown materials are commercially available via online retailers such as HQ Graphene and 2D Semiconductors, but the lowest defect density two-step flux-synthesized bulk crystal is currently only available through collaboration with the Hone/Barmak groups at Columbia University or by following their published method. In their 2023 paper[127], they emphasize the importance of a high chalcogen-metal ratio within the flux and a modified post-processing step using lower thermal loads than in other similar growth techniques to avoid excessive contamination. SPE emission from flux-grown material has been shown to persist to record-breaking temperatures (160 K)[129] and have exceptional SPE purity, temporal stability, and polarization control[83, 89]. For these reasons, flux-synthesized 1L-WSe_2 was used in the study of plasmonically coupled defect-localized emission in Chapter 4 of this dissertation.

For WSe_2 with a higher defect density than the two-step flux-synthesized material, background emission can be controlled through other avenues. One method, used in Chapter 5 of this dissertation, is graphite passivation[41]. In this technique, an ~8 nm graphite flake is placed onto an array of 1L-WSe_2 indents. The graphite both dopes the 1L-WSe_2 and creates a fast non-radiative decay channel for defect exciton emission while permitting defect-bound SPE emission to still occur. Background suppression is also done using chemical functionalization[130-132], h-BN encapsulation[116], and electrostatic gating[133, 134]. Enhancing the purity of SPEs positions the use of these states for real-world applications outside of the laboratory, but to gain full control, deterministic arrays of SPEs are desired. By patterning strain centers using nanophotonic structures, SPEs can be locally activated, leading to a more robust platform.

1.4 Strain Centers for Deterministic Generation of SPEs in 1L-WSe_2

Early SPE sources were composed of nanobubbles (Figure 1.4.1a), wrinkles, and tears that naturally occur during tape/polymer-based exfoliation/manipulation of monolayer flakes[3-7, 135]. These randomly occurring sites lack deterministic placement and render the majority of samples optically dim or disordered at cryogenic temperatures due to inhomogeneous strain profiles and a lack of photonic enhancement. Figure 1.4.1a-e shows a variety of different SPE generation techniques in 1L-WSe_2. One method used for addressing the deterministic placement of emissions is nanoindentation[41, 122, 134, 136-141] (Figure 1.4.1c). Similar to the work conducted in Chapters 3 and 5 of this dissertation, nanoindentations are made by driving a sharp atomic force microscopy (AFM) tip into a 1L-WSe_2 flake positioned on a polymer substrate, leaving behind a plastic deformation in the polymer with the 1L-WSe_2 tightly adhered, imparting tensile strain. SPEs are

then localized to nanoindent sites. Other approaches to SPE patterning without manipulation of the 1L-WSe_2 are nanopositioning of sub-wavelength particles[83, 89, 129, 142] (Figure 1.4.1d) and defect engineering[109, 123, 130, 143, 144]. These techniques benefit from the 1L-WSe_2 remaining positioned on the substrate it was exfoliated onto. By not having to transfer the 1L-WSe_2 from the exfoliation substrate to another patterned substrate, the quantity of stochastically generated wrinkles/bubbles and polymer residues is reduced. When it comes to using patterned strain centers such as nanopillars, nanocones, or other metallic/dielectric stressors, the reduction of disordered strain does not occur; however, patterned strain centers can enhance and control SPE emission, making the photonic engineering of nanostressors a popular research avenue.

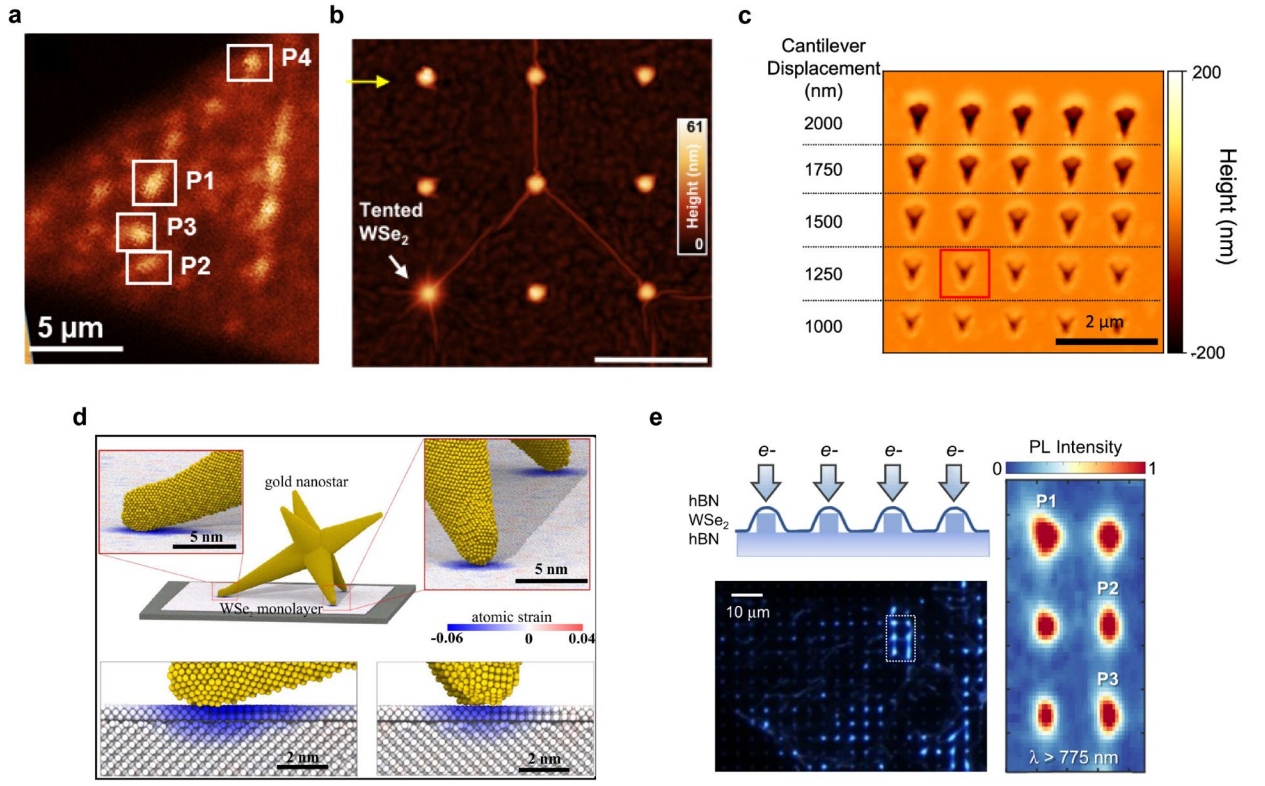


Figure 1.4.1:Overview of strain generation techniques. (a) PL map of a 1L-WSe_2 flake with nanobubbles outlined with white boxes. Adapted from "Nanobubble induced formation of quantum emitters in monolayer semiconductors", 2D Materials. Shepard, G et al., 2017, 4(2), 021019. (b) AFM image of wrinkles in 1L-WSe_2 formed after dry transfer onto a square array of Au nanocones. Adapted from "Programmable nanowrinkle-induced room-temperature exciton localization in monolayer WSe_2", Nat Commun. Yanev, E et al., 2024, 15, 1543. (c) AFM image after a grid of nanoindents is made for a range of different indentation forces (cantilever displacements). Adapted from "Quantum Calligraphy: Writing Single-Photon Emitters in a Two-Dimensional Materials Platform", ACS Nano. Rosenberger, M et al., 2019, 13(1), 904-912. (d) Large-scale molecular dynamics simulation of the strain field in a WSe_2 monolayer induced by a gold nanostar. Top panel: the atomistic model consisting of a 100 nm x 100 nm WSe_2 monolayer on a 3 nm thick silicon substrate and the Au nanostar on top. The insets show the contact areas between the WSe_2 monolayer and the long and short arms of the Au nanostar. Atoms in the WSe_2 monolayer are colored based on their volumetric strain values. Bottom panel: cross-section views of the areas shown in the top panel insets, showing the penetration depths of the deformation field created by the Au nanostar. Adapted from "Creation of Single-Photon Emitters in WSe_2 Monolayers Using Nanometer-sized Gold Tips", Nano Lett. Peng, L et al., 2020, 20(8), 5866-5872. (e) Schematic of the fabricated structure and the optical dark-field image of the sample. A stack of h-BN/WSe_2/h-BN is transferred on a SiO_2 nanopillar array. Bright emission is observed from the top of the pillars due to exciton funneling. Next, the tops of the pillars are irradiated e- arrows) to induce structural defects. Adapted from "Defect and strain engineering of monolayer WSe_2 enables site-controlled single-photon emission up to 150 K", Nat Commun. Parto, K et al., 2021, 12, 3585.

Enhancing emission from SPEs using nanophotonic structures is traditionally achieved through increasing the local optical density of states (LDOS) by enhancing the excitation field intensity in sub-wavelength regions using either plasmonics or cavities excited on resonance. Positioning SPE states within the sub-wavelength region enhances the emitters via the Purcell effect. Enhanced emission via the Purcell effect manifests as a reduction of the lifetime of an emitter from an increase in the LDOS. When it comes to SPEs within a cavity, the Purcell enhancement factor, F_P, comes from integrating the partial LDOS (PLDOS) in the proximity of the resonator, $\rho_{\hat{e}}(\boldsymbol{r}, \omega)$, coaligned with the emitter dipole orientation, over the free space PLDOS, $\rho_0(\omega)$, across the bandwidth of the emitter ($\omega_1$to ω_2)[145].

$$F_P = \int_{\omega_1}^{\omega_2} \frac{\rho_{\hat{e}}(\boldsymbol{r}, \omega)}{\rho_0(\omega)} d\omega \qquad 1.4.1$$

In Equation 1.4.1, $\rho_{\hat{e}}(\boldsymbol{r}, \omega)$ depends on the position of the emitter, $\boldsymbol{r}$, and the specific dipole orientation of the emitter, $\hat{e}$, because the resonator in question generally does not isotropically enhance the PLDOS. To calculate the Purcell enhancement factor, one must obtain an expression for the PLDOS[145].

Experimentally, F_P, can be measured by comparing the lifetime of an emitter in free space (or as close to free space as possible) to that of the same emitter in the proximity of the resonator in question.

$$F_P = \frac{\tau_0}{\tau} = \frac{\Gamma_{tot}}{\Gamma_0} \qquad 1.4.2$$

Here, τ_0 and Γ_0, and τ and Γ_{tot}, are the emitter lifetimes and decay rates in free space and near the resonator, respectively. Reductions of τ are not purely in radiative channels. In general, emitters have radiative, Γ_{rad}, and non-radiative, Γ_{nr}, decay rates that can both be enhanced.

$$\Gamma_{tot} = \Gamma_{rad} + \Gamma_{nr} = \frac{1}{\tau} \qquad 1.4.3a$$

$$\Gamma_0 = \Gamma_{0,rad} + \Gamma_{0,nr} = \frac{1}{\tau_0} \qquad 1.4.3b$$

This interpretation means that a measured F_P of 4 does not necessarily mean a 4 times increase in the photon flux of the emitter because non-radiative decay rates may increase as well. In plasmonic systems, such as the Au nanoantennas in Chapter 4 of this dissertation, Ohmic losses, non-radiative energy transfer, and surface-induced quenching commonly increase non-radiative decay.

Dielectric pillars placed near each other are a common structure used to enhance emission[146, 147]. Depending on the pillar materials' index of refraction, geometry, and separation with respect to the nearest other pillar, the resonance can be tuned to be degenerate with excitons in 1L-WSe_2. As an example, GaP pillars oriented in a dimmer configuration showed a 1L-WSe_2 SPE intensity enhancement of four orders of magnitude in comparison to SiO_2 pillars of the same shape and separation under the same excitation power[147]. Similar results have also been seen using photonic[20, 91, 148, 149] and Bragg cavities[93, 150-152], highlighting a direct path to higher SPE fluences coming from deterministic locations. Dielectric cavities generally have lower Purcell factors than their metallic plasmonic counterparts, caused by a lower Q-factor to mode volume ratio, but this does not mean they are inherently worse. Dielectric systems have minimal Ohmic heating, linewidth broadening, quenching, and non-radiative losses, making them ideal for quantum applications with established physics, but metallic plasmonic structures excel for use in studying highly localized dim states due to their exceptionally small mode volumes.

The small mode volumes in metallic plasmonic nanostructures permit selective brightening/coupling of states positioned within the enhancement region. This effect was utilized

in Chapter 4 to study defect localized emission in 1L-WSe_2 using plasmonic embedded nanoantennas. Nano-cones[11, 153], stars[142], cubes[83, 129], and prisms[89], have all been used to observe enhanced emission. As previously mentioned, quenching is a concern with metallic nanostructures. To address quenching, most sample architectures use thin dielectric spacers like Al_2O_3 or h-BN to isolate the 1L-WSe_2 from the metal directly while maintaining the position of the flake within the plasmonic enhancement region.

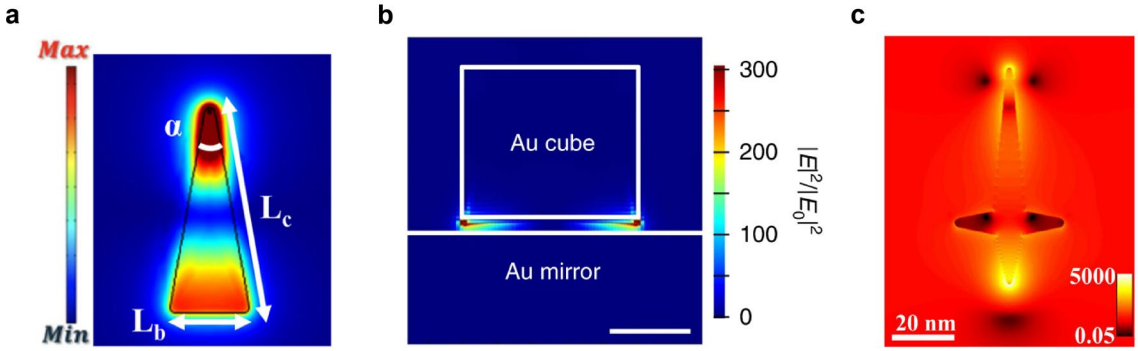


Figure 1.4.2: Field enhancement from various Au resonators. (a) Near-field intensity distribution for an in-plane rounded triangular prism. A strong localized hotspot is present near the apex, while weaker hotspots are present at the base. Adapted from "Quantum Light Funneling in Tailored Triangular Plasmonic Nanocavities", ACS Nano. Xiao, L et al., 2026, 20(4), 3610-3617. (b) Simulated intensity enhancement distribution profile illustrating confinement of the plasmon across the gap between the Au cube and Au mirror. Scale bar is 50 nm. Adapted from "Deterministic coupling of site-controlled quantum emitters in monolayer WSe_2 to plasmonic nanocavities", Nat Commun. Luo, Y et al., 2018, 13, 1137-1142. (c) Local electric field enhancement factor in the vicinity of a Au nanostar at the energy of 1.72 eV. Incident light is polarized along the long axis of the nanostar. Adapted from "Creation of Single-Photon Emitters in WSe_2 Monolayers Using Nanometer-Sized Au Tips", Nano Lett. Peng, L et al., 2020, 20(8), 5866-5872.

Field enhancement in metallic plasmonic nanostructures comes from the localized surface plasmon resonance (LSPR) of the structure. By exciting a structured plasmonic material with features beneath the excitation wavelength, electrons oscillate and form standing wave patterns that are dependent on the geometry. These collective excitations have resonance conditions and

focus evanescent fields at the vertices of the nanostructure. Examples of the field localization can be seen in Figures 1.4.2 a-c for a few different geometries. LSPRs are polarization dependent, meaning that certain points can be selectively enhanced by tuning the excitation polarization. An example of the polarization dependence is shown in Figure 1.4.2c. Here, the plasmonic resonance of a gold nanostar is modeled under continuous wave (CW) excitation polarized vertically with respect to the image. The largest field enhancement then occurs at the vertices along the CW polarization axis, while the vertices perpendicular to the CW polarization show nominally no enhancement. Similarly, the polarization state of the SPE emission can be modulated using the specific tensile strain field generated by placing these metallic nanostructures on top of a 1L-WSe_2 flake[83, 89].

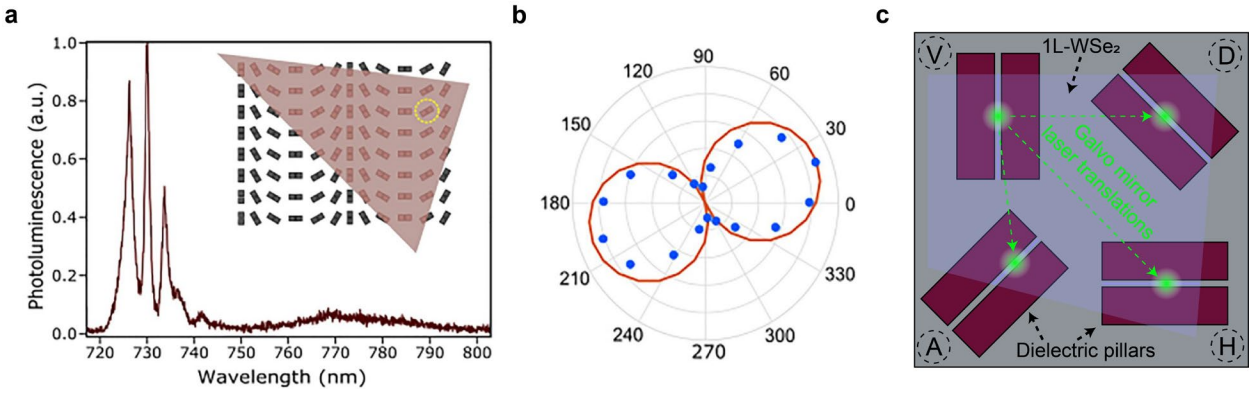


Figure 1.4.3. Proposed model for improving BB84 quantum key distribution using a hybrid WSe_2/nanophotonic device. (a) PL spectrum of SPEs on a pillar pair showing three single-photon emitters at a pillar pair oriented at a 30° angle, as highlighted by the yellow circle in the schematic inside the inset. The inset shows a schematic of the pillar pair sample fabricated and measured with a monolayer of WSe_2 transferred onto the sample. (b) Polarization measurement of the ~730 nm emitter shown in (a). (a-b) Are adapted from "Purcell enhancement and polarization control of single-photon emitters in monolayer WSe_2 using dielectric nanoantennas", Nanophotonics. Azzam, S et al., 2023, 12(3), 477-484. (c) Schematic proposing a device for high bit rate BB84 quantum key distribution using 1L-WSe_2 and dielectric pillar pairs. V, H, A, and D represent four different linear polarization states coinciding with different pillar pair orientations. The green arrows moving from V to H, A, or D represent fast motion of the excitation laser between polarization channels using a galvo scan mirror. Outlined in blue is the 1L-WSe_2 flake that would produce single-photon emission from between pillar pairs.

Polarization control, deterministic placement, fluence enhancement, and high SPE purity position hybrid 1L-WSe_2/nanophotonic structures for use in future quantum technologies. As an example, the features of these hybrid devices could greatly improve BB84 quantum key distribution. Polarization control is crucial for use in the BB84 quantum cryptography protocol. The BB84 protocol uses SPE states with a high degree of linear polarization to develop a quantum key that can be used for further classical communication. The quantum keys made under the BB84 protocol are sensitive to eavesdropping because the eavesdropper can never know the polarization bases that are used to emit/detect the single photons, so they will always observe a superposition state rather than an eigenstate. This results in the eavesdropper transmitting photons that are in a

different basis than the original emission/detection, which nullifies the quantum key distribution attempt[24, 154]. Preparation of linearly polarized SPE states correlated to nanophotonic structure orientations in 1L-WSe_2 has been shown previously using pairs of dielectric pillars. Figure 1.4.3a-b shows this result from Azzam *et al.*. Here, the three SPE states shown in Figure 1.4.3a originate from the gap between an angled pair of dielectric nanopillars circled in yellow. In Figure 1.4.3b, these emitters are shown to be linearly polarized perpendicular to the gap. Normally, the polarization state preparation is done using rotating polarization optics, but since nanophotonic structures can deterministically place high fluence SPEs with prescribed linear polarization states, nanostructures oriented along different axes could allow for selective polarized emission using a galvo scan mirror to quickly move the excitation laser between pairs of nanostructures. The change to a galvo scan mirror as opposed to rotating optics could increase the quantum key bit rate by approximately two orders of magnitude. Lastly, the improved SPE purity of coupled devices could lower the bit error rate. Since purity can be seen as a proxy of the ratio of photons emitted from the SPE to photons emitted through other radiative channels, by increasing the purity, the number of simultaneous SPE and defect emissions is lowered.

1.5 Conclusion

VdW materials open the door to new quantum technologies on a truly 2D scale. Since weak out-of-plane van-der-Waals forces hold their layers together, exfoliating vdW materials into monolayers is easily done using Scotch tape. WSe_2, the optically relevant vdW material used in the work for this dissertation, has a bandgap that changes from indirect to direct when the material is reduced to a monolayer from bulk. In 2015, single photon emitters were observed in 1L-WSe_2, and later in 2019, SPEs were theorized to originate from dark exciton/defect state hybridization

under tensile strain. Then, to control SPEs, reliable techniques for deterministic strain patterning, defect density, and polarization control were desired and studied. Integration of high-quality 1L-WSe_2 with plasmonic nanostructures quickly emerged as a source of high-purity and high operating temperature SPEs for direct integration into quantum technologies.

In Chapter 2, the methods and techniques used to develop and study SPE platforms are described. The chapter is laid out following the natural progression of device conception to fabrication to final characterization. First, the process of monolayer exfoliation is discussed alongside the fabrication of various nanophotonic structures, such as the nanoindents seen in Chapters 3 and 5, and the embedded plasmonic nanoantennas of Chapter 4. Next, these nanostructures are modeled using finite element modeling in COMSOL Multiphysics to understand the collective excitation of localized surface plasmons that play the role of locally enhancing SPEs in Chapter 4. With the nanostructures theoretically motivated and geometrically optimized, the process of integrating 1L-WSe_2 with the nanostructures using transfer techniques is discussed. Characterization of the final devices is done using a multitude of different optical techniques. In Chapters 3-5, SPE states were validated using HBT interferometry, and their excited state lifetimes were measured using time-correlated single-photon counting (Chapter 5). Lastly, for the embedded antenna system in Chapter 4, plasmonic enhancement of SPEs was observed using photoluminescence excitation spectroscopy (PLE), and the plasmonic nature of the antennas was probed using scanning near-field optical spectroscopy.

Chapter 3 is a study into the role of strain, mainly tearing, in the formation of SPEs in 1L-WSe_2 nanoindents. Previously published research describes deterministic SPE generation using indentation, but lacks a way to access strain generation and the possibility of fracture or tearing

that may occur during the indentation process. Here, we report a technique to confirm tensile strain in 1L-WSe_2 nanoindents using the spectral median and full width at half maximum of the PL spectra at RT. We then demonstrate that SPEs are present in nanoindented samples that have both been confirmed to host tensile strain and those that do not host tensile strain. It has been shown previously that SPEs can form in disordered areas like tears, leading to the hypothesis that strain is released via tearing in indents that do not show signs of room temperature tensile strain. Confirmation of this hypothesis is done by directly observing tears in SEM images of nanoindents that are inverted into protruding pyramids using an inversion technique we developed. With the ability to confirm tearing using RT PL and SEM imaging, we then quantify the areal density of SPEs using an emitter counting protocol and high-resolution AFM imaging. We found that emitter densities between torn and untorn nanoindents scale differently. The difference in scaling indicates that SPEs form in different regions of the nanoindents, depending on the intact or torn state of the 1L-WSe_2.

Chapter 4 presents a nano-optical platform to enable selective near-field excitation of SPEs in 1L-WSe_2 to later build on the Linhart theory by correlating SPE emission to V_{Se} defect sites using low-defect-density WSe_2. Embedded plasmonic nanoantennas are first fabricated using thermal scanning probe lithography, wet etching, and lift-off within SiO_2 cavities. The apex of a given nanoantenna site rises either above or beneath the SiO_2 surface by a prescribable amount, depending on the thickness of the SiO_2 and diameter of the cavity. Naturally, this sets the apex, and in turn, the 1L-WSe_2 that is draped over the apex, to different heights above the reflective Si surface. Photonic modulation of the RT and cryogenic PL spectra is observed and modeled as interference between reflections off the Si surface and excitonic emission. Then, long-wavelength

SPE states were identified to originate from within the plasmonic hotspot of the Au nanoantennas by using PLE and HBT interferometry. Since we use the two-step flux-synthesized 1L-WSe_2 discussed earlier in this chapter, there is a countable amount of defects expected to be within the plasmonic hotspot, in this case, 1-10. With 5 SPE states observed to show plasmonic enhancement, we conduct a spectrally resolved emitter localization measurement to estimate the position of each emitter with respect to the centroid of long-wavelength emission. We found that each emitter was localized to a different region around the apex of the Au nanoantenna, indicating that each emitter may correspond to a different V_{Se} site in the 1L-WSe_2, adding this work to a small collection of studies working to directly validate the Linhart theory. In the aim of correlating cryogenic SPE emission to localized RT defect emission, we took scanning near-field optical spectroscopy of these samples, but irreversibly damaged them in the process. However, we were able to confirm that gap mode plasmons between the underlying Au nanoantenna and Au-coated AFM probe exist using polarization-dependent Au luminescence, leading the way to finally correlate cryogenic SPE emission to localized RT defect emission in 1L-WSe_2.

Chapter 5 expands on the work done in Chapter 3. At the end of Chapter 3, the areal density of emitters is made more accurate by suppressing the quadratic defect emission in 1L-WSe_2 by the introduction of a thin graphite layer. During this experiment, we noticed that the emission intensity and excited state lifetimes of the SPE states before and after the introduction of the graphite layer have changed significantly. Previous studies on similar systems gave no reason to suspect these changes, and in some cases, suggest the contrary (reduction in emission intensity). To gather the full picture, spectrally resolved excited state lifetimes were measured using a 532 nm pulsed laser and TCSPC module alongside a tunable monochrometer exit slit. These data sets show that the

average lifetime of SPE states in the vicinity of graphite is increased by approximately a factor of two, and the emission intensity of similar SPE states before and after graphite can be enhanced by up to two orders of magnitude. We hypothesize these effects to be caused by graphite-induced electron doping of the 1L-WSe_2, degradation/suppression of surrounding SPE states with the addition of graphite, and exciton population redistribution into a smaller quantity of available SPEs.

Finally, in Chapter 6, the work in this dissertation is summarized, and the impact of each is given in the context of its contribution to a deeper understanding within the field. Also, a short introduction and outlook into projects that require further investigation/formatting before publication is provided. These projects include:

- The fabrication of scalable micropillar arrays to study 2D SPEs in h-BN, 1L-WSe_2, and 4L-WSe_2
- Selective excitation of SPE states above embedded plasmonic nanoantennas using pencil beams
- The role of Au nanostructures on SPE emission in 1L-WSe_2 nanoribbons
- Enhancing the outcoupling of nanoindent-based SPE states using microlenses
- Using dielectric layers during nanoinversion as cost-effective nanophotonic stressors

Chapter 1 References

(1) Novoselov, K. S.; Geim, A. K.; Morozov, S. V.; et al. Electric field effect in atomically thin carbon films. *Science* **2004**, *306* (5696), 666-669. DOI: 10.1126/science.1102896

(2) Kumar, S.; Kaczmarczyk, A.; Gerardot, B. D. Strain-Induced Spatial and Spectral Isolation of Quantum Emitters in Mono- and Bilayer WSe_2. *Nano Lett* **2015**, *15* (11), 7567-7573. DOI: 10.1021/acs.nanolett.5b03312

(3) Chakraborty, C.; Kinnischtzke, L.; Goodfellow, K. M.; et al. Voltage-controlled quantum light from an atomically thin semiconductor. *Nat Nanotechnol* **2015**, *10* (6), 507-511. DOI: 10.1038/nnano.2015.79

(4) He, Y. M.; Clark, G.; Schaibley, J. R.; et al. Single quantum emitters in monolayer semiconductors. *Nat Nanotechnol* **2015**, *10* (6), 497-502. DOI: 10.1038/nnano.2015.75

(5) Koperski, M.; Nogajewski, K.; Arora, A.; et al. Single photon emitters in exfoliated WSe_2 structures. *Nat Nanotechnol* **2015**, *10* (6), 503-506. DOI: 10.1038/nnano.2015.67

(6) Srivastava, A.; Sidler, M.; Allain, A. V.; et al. Optically active quantum dots in monolayer WSe_2. *Nat Nanotechnol* **2015**, *10* (6), 491-496. DOI: 10.1038/nnano.2015.60

(7) Tonndorf, P.; Schmidt, R.; Schneider, R.; et al. Single-photon emission from localized excitons in an atomically thin semiconductor. *Optica* **2015**, *2* (4). DOI: 10.1364/optica.2.000347

(8) Raja, A.; Waldecker, L.; Zipfel, J.; et al. Dielectric disorder in two-dimensional materials. *Nat Nanotechnol* **2019**, *14* (9), 832-837. DOI: 10.1038/s41565-019-0520-0

(9) Dass, C. K.; Khan, M. A.; Clark, G.; et al. Ultra-Long Lifetimes of Single Quantum Emitters in Monolayer WSe_2/hBN Heterostructures. *Advanced Quantum Technologies* **2019**, *2* (5-6). DOI: 10.1002/qute.201900022

(10) Chhaperwal, M.; Tongale, H. M.; Hays, P.; et al. Simultaneously Enhancing Brightness and Purity of WSe_2 Single Photon Emitter Using High-Aspect-Ratio Nanopillar Array on Metal. *Nano Lett* **2024**, *24* (40), 12461-12468. DOI: 10.1021/acs.nanolett.4c03168

(11) Yanev, E. S.; Darlington, T. P.; Ladyzhets, S. A.; et al. Programmable nanowrinkle-induced room-temperature exciton localization in monolayer WSe_2. *Nat Commun* **2024**, *15* (1), 1543. DOI: 10.1038/s41467-024-45936-2

(12) Novoselov, K. S.; Mishchenko, A.; Carvalho, A.; et al. 2D materials and van der Waals heterostructures. *Science* **2016**, *353* (6298), aac9439. DOI: 10.1126/science.aac9439

(13) Campi, D.; Mounet, N.; Gibertini, M.; et al. Expansion of the Materials Cloud 2D Database. *ACS Nano* **2023**, *17* (12), 11268-11278. DOI: 10.1021/acsnano.2c11510

(14) Xiao, Y.; Liu, J.; Fu, L. Moiré is More: Access to New Properties of Two-Dimensional Layered Materials. *Matter* **2020**, *3* (4), 1142-1161. DOI: 10.1016/j.matt.2020.07.001

(15) Carr, S.; Massatt, D.; Fang, S.; et al. Twistronics: Manipulating the electronic properties of two-dimensional layered structures through their twist angle. *Physical Review B* **2017**, *95* (7). DOI: 10.1103/PhysRevB.95.075420

(16) Li, C.; Fröch, J. E.; Nonahal, M.; et al. Integration of hBN Quantum Emitters in Monolithically Fabricated Waveguides. *ACS Photonics* **2021**, *8* (10), 2966-2972. DOI: 10.1021/acsphotonics.1c00890

(17) Dutta, S.; Cai, T.; Buyukkaya, M. A.; et al. Coupling quantum emitters in WSe_2 monolayers to a metal-insulator-metal waveguide. *Applied Physics Letters* **2018**, *113* (19). DOI: 10.1063/1.5045727

(18) Ling, H.; Li, R.; Davoyan, A. R. All van der Waals Integrated Nanophotonics with Bulk Transition Metal Dichalcogenides. *ACS Photonics* **2021**, *8* (3), 721-730. DOI: 10.1021/acsphotonics.0c01964

(19) Parto, K.; Azzam, S. I.; Lewis, N.; et al. Cavity-Enhanced 2D Material Quantum Emitters Deterministically Integrated with Silicon Nitride Microresonators. *Nano Lett* **2022**, *22* (23), 9748-9756. DOI: 10.1021/acs.nanolett.2c03151

(20) Ren, T.; Granados Del Aguila, A.; Chen, Z.; et al. Van der Waals photonic integrated circuit with coherent light generation. *Nat Commun* **2025**, *16* (1), 5931. DOI: 10.1038/s41467-025-60778-2

(21) Al-Juboori, A.; Zeng, H. Z. J.; Nguyen, M. A. P.; et al. Quantum Key Distribution Using a Quantum Emitter in Hexagonal Boron Nitride. *Advanced Quantum Technologies* **2023**, *6* (9). DOI: 10.1002/qute.202300038

(22) Samaner, Ç.; Paçal, S.; Mutlu, G.; et al. Free-Space Quantum Key Distribution with Single Photons from Defects in Hexagonal Boron Nitride. *Advanced Quantum Technologies* **2022**, *5* (9). DOI: 10.1002/qute.202200059

(23) Zeng, H. Z. J.; Ngyuen, M. A. P.; Ai, X.; et al. Integrated room temperature single-photon source for quantum key distribution. *Opt Lett* **2022**, *47* (7), 1673-1676. DOI: 10.1364/OL.454450

(24) Gao, T.; von Helversen, M.; Antón-Solanas, C.; et al. Atomically-thin single-photon sources for quantum communication. *npj 2D Materials and Applications* **2023**, *7* (1). DOI: 10.1038/s41699-023-00366-4

(25) Rizzato, R.; Schalk, M.; Mohr, S.; et al. Extending the coherence of spin defects in hBN enables advanced qubit control and quantum sensing. *Nat Commun* **2023**, *14* (1), 5089. DOI: 10.1038/s41467-023-40473-w

(26) Ramsay, A. J.; Hekmati, R.; Patrickson, C. J.; et al. Coherence protection of spin qubits in hexagonal boron nitride. *Nat Commun* **2023**, *14* (1), 461. DOI: 10.1038/s41467-023-36196-7

(27) Haykal, A.; Tanos, R.; Minotto, N.; et al. Decoherence of VB- spin defects in monoisotopic hexagonal boron nitride. *Nat Commun* **2022**, *13* (1), 4347. DOI: 10.1038/s41467-022-31743-0

(28) Eich, M.; Herman, F.; Pisoni, R.; et al. Spin and Valley States in Gate-Defined Bilayer Graphene Quantum Dots. *Physical Review X* **2018**, *8* (3). DOI: 10.1103/PhysRevX.8.031023

(29) Banszerus, L.; Hecker, K.; Moller, S.; et al. Spin relaxation in a single-electron graphene quantum dot. *Nat Commun* **2022**, *13* (1), 3637. DOI: 10.1038/s41467-022-31231-5

(30) Garreis, R.; Tong, C.; Terle, J.; et al. Long-lived valley states in bilayer graphene quantum dots. *Nature Physics* **2024**, *20* (3), 428-434. DOI: 10.1038/s41567-023-02334-7

(31) Kormányos, A.; Zólyomi, V.; Drummond, N. D.; et al. Spin-Orbit Coupling, Quantum Dots, and Qubits in Monolayer Transition Metal Dichalcogenides. *Physical Review X* **2014**, *4* (1). DOI: 10.1103/PhysRevX.4.011034

(32) Zhang, Z. Z.; Song, X. X.; Luo, G.; et al. Electrotunable artificial molecules based on van der Waals heterostructures. *Sci Adv* **2017**, *3* (10), e1701699. DOI: 10.1126/sciadv.1701699

(33) Lu, X.; Chen, X.; Dubey, S.; et al. Optical initialization of a single spin-valley in charged WSe_2 quantum dots. *Nat Nanotechnol* **2019**, *14* (5), 426-431. DOI: 10.1038/s41565-019-0394-1

(34) Colmiais, I.; Silva, V.; Borme, J.; et al. Towards RF graphene devices: A review. *FlatChem* **2022**, *35*. DOI: 10.1016/j.flatc.2022.100409

(35) Han, S. J.; Garcia, A. V.; Oida, S.; et al. Graphene radio frequency receiver integrated circuit. *Nat Commun* **2014**, *5*, 3086. DOI: 10.1038/ncomms4086

(36) Ju, L.; Geng, B.; Horng, J.; et al. Graphene plasmonics for tunable terahertz metamaterials. *Nat Nanotechnol* **2011**, *6* (10), 630-634. DOI: 10.1038/nnano.2011.146

(37) Li, J.; Chen, J.; Yan, D.; et al. A Review: Active Tunable Terahertz Metamaterials. *Advanced Photonics Research* **2024**, *5* (7). DOI: 10.1002/adpr.202300351

(38) Zhang, X.; Ren, W.; Bell, E.; et al. Gate-tunable Veselago interference in a bipolar graphene microcavity. *Nat Commun* **2022**, *13* (1), 6711. DOI: 10.1038/s41467-022-34347-w

(39) Levesque, P. L.; Sabri, S. S.; Aguirre, C. M.; et al. Probing charge transfer at surfaces using graphene transistors. *Nano Lett* **2011**, *11* (1), 132-137. DOI: 10.1021/nl103015w

(40) Asenbauer, J.; Eisenmann, T.; Kuenzel, M.; et al. The success story of graphite as a lithium-ion anode material – fundamentals, remaining challenges, and recent developments including silicon (oxide) composites. *Sustainable Energy & Fuels* **2020**, *4* (11), 5387-5416. DOI: 10.1039/d0se00175a

(41) Chuang, H. J.; Stevens, C. E.; Rosenberger, M. R.; et al. Enhancing Single Photon Emission Purity via Design of van der Waals Heterostructures. *Nano Lett* **2024**, *24* (18), 5529-5535. DOI: 10.1021/acs.nanolett.4c00683

(42) Yu, Y.; Seo, I. C.; Luo, M.; et al. Tunable single-photon emitters in 2D materials. *Nanophotonics* **2024**, *13* (19), 3615-3629. DOI: 10.1515/nanoph-2024-0050

(43) Ai, R.; Cui, X.; Li, Y.; et al. Local Strain Engineering of Two-Dimensional Transition Metal Dichalcogenides Towards Quantum Emitters. *Nanomicro Lett* **2025**, *17* (1), 104. DOI: 10.1007/s40820-024-01611-1

(44) Reina, A.; Jia, X.; Ho, J.; et al. Large area, few-layer graphene films on arbitrary substrates by chemical vapor deposition. *Nano Lett* **2009**, *9* (1), 30-35. DOI: 10.1021/nl801827v

(45) Bae, S.; Kim, H.; Lee, Y.; et al. Roll-to-roll production of 30-inch graphene films for transparent electrodes. *Nat Nanotechnol* **2010**, *5* (8), 574-578. DOI: 10.1038/nnano.2010.132

(46) Kim, K. S.; Zhao, Y.; Jang, H.; et al. Large-scale pattern growth of graphene films for stretchable transparent electrodes. *Nature* **2009**, *457* (7230), 706-710. DOI: 10.1038/nature07719

(47) Li, X.; Cai, W.; An, J.; et al. Large-area synthesis of high-quality and uniform graphene films on copper foils. *Science* **2009**, *324* (5932), 1312-1314. DOI: 10.1126/science.1171245

(48) Dean, C. R.; Young, A. F.; Meric, I.; et al. Boron nitride substrates for high-quality graphene electronics. *Nat Nanotechnol* **2010**, *5* (10), 722-726. DOI: 10.1038/nnano.2010.172

(49) Wang, L.; Meric, I.; Huang, P. Y.; et al. One-dimensional electrical contact to a two-dimensional material. *Science* **2013**, *342* (6158), 614-617. DOI: 10.1126/science.1244358

(50) Tran, T. T.; Bray, K.; Ford, M. J.; et al. Quantum emission from hexagonal boron nitride monolayers. *Nat Nanotechnol* **2016**, *11* (1), 37-41. DOI: 10.1038/nnano.2015.242

(51) Sajid, A.; Ford, M. J.; Reimers, J. R. Single-photon emitters in hexagonal boron nitride: a review of progress. *Rep Prog Phys* **2020**, *83* (4), 044501. DOI: 10.1088/1361-6633/ab6310

(52) Dean, C. R.; Wang, L.; Maher, P.; et al. Hofstadter's butterfly and the fractal quantum Hall effect in moire superlattices. *Nature* **2013**, *497* (7451), 598-602. DOI: 10.1038/nature12186

(53) Ponomarenko, L. A.; Gorbachev, R. V.; Yu, G. L.; et al. Cloning of Dirac fermions in graphene superlattices. *Nature* **2013**, *497* (7451), 594-597. DOI: 10.1038/nature12187

(54) Cao, Y.; Fatemi, V.; Fang, S.; et al. Unconventional superconductivity in magic-angle graphene superlattices. *Nature* **2018**, *556* (7699), 43-50. DOI: 10.1038/nature26160

(55) Cao, Y.; Fatemi, V.; Demir, A.; et al. Correlated insulator behaviour at half-filling in magic-angle graphene superlattices. *Nature* **2018**, *556* (7699), 80-84. DOI: 10.1038/nature26154

(56) Tran, K.; Moody, G.; Wu, F.; et al. Evidence for moire excitons in van der Waals heterostructures. *Nature* **2019**, *567* (7746), 71-75. DOI: 10.1038/s41586-019-0975-z

(57) Mak, K. F.; Lee, C.; Hone, J.; et al. Atomically thin MoS_2: a new direct-gap semiconductor. *Phys Rev Lett* **2010**, *105* (13), 136805. DOI: 10.1103/PhysRevLett.105.136805

(58) Splendiani, A.; Sun, L.; Zhang, Y.; et al. Emerging photoluminescence in monolayer MoS_2. *Nano Lett* **2010**, *10* (4), 1271-1275. DOI: 10.1021/nl903868w

(59) He, K.; Kumar, N.; Zhao, L.; et al. Tightly bound excitons in monolayer WSe_2. *Phys Rev Lett* **2014**, *113* (2), 026803. DOI: 10.1103/PhysRevLett.113.026803

(60) Arora, A.; Koperski, M.; Nogajewski, K.; et al. Excitonic resonances in thin films of WSe_2: from monolayer to bulk material. *Nanoscale* **2015**, *7* (23), 10421-10429. DOI: 10.1039/c5nr01536g

(61) Yu, H.; Liao, M.; Zhao, W.; et al. Wafer-Scale Growth and Transfer of Highly-Oriented Monolayer MoS_2 Continuous Films. *ACS Nano* **2017**, *11* (12), 12001-12007. DOI: 10.1021/acsnano.7b03819

(62) Lan, C.; Zhou, Z.; Zhou, Z.; et al. Wafer-scale synthesis of monolayer WS_2 for high-performance flexible photodetectors by enhanced chemical vapor deposition. *Nano Research* **2018**, *11* (6), 3371-3384. DOI: 10.1007/s12274-017-1941-4

(63) Hu, J.; Zhou, F.; Wang, J.; et al. Chemical Vapor Deposition Syntheses of Wafer-Scale 2D Transition Metal Dichalcogenide Films toward Next-Generation Integrated Circuits Related Applications. *Advanced Functional Materials* **2023**, *33* (40). DOI: 10.1002/adfm.202303520

(64) Chou, S. A.; Chang, C.; Wu, B. H.; et al. Large-scale alkali-assisted growth of monolayer and bilayer WSe_2 with a low defect density. *Nat Commun* **2025**, *16* (1), 2777. DOI: 10.1038/s41467-025-57986-1

(65) Velicky, M.; Donnelly, G. E.; Hendren, W. R.; et al. Mechanism of Gold-Assisted Exfoliation of Centimeter-Sized Transition-Metal Dichalcogenide Monolayers. *ACS Nano* **2018**, *12* (10), 10463-10472. DOI: 10.1021/acsnano.8b06101

(66) Chen, S.; Li, B.; Dai, C.; et al. Controlling Gold-Assisted Exfoliation of Large-Area MoS_2 Monolayers with External Pressure. *Nanomaterials (Basel)* **2024**, *14* (17). DOI: 10.3390/nano14171418

(67) Panasci, S. E.; Schiliro, E.; Greco, G.; et al. Strain, Doping, and Electronic Transport of Large Area Monolayer MoS_2 Exfoliated on Gold and Transferred to an Insulating Substrate. *ACS Appl Mater Interfaces* **2021**, *13* (26), 31248-31259. DOI: 10.1021/acsami.1c05185

(68) Panasci, S. E.; Schilirò, E.; Migliore, F.; et al. Substrate impact on the thickness dependence of vibrational and optical properties of large area MoS_2 produced by gold-assisted exfoliation. *Applied Physics Letters* **2021**, *119* (9). DOI: 10.1063/5.0062106

(69) Zhang, L.; Chen, Z.; Zhang, R.; et al. Direct Observation of Charge Injection of Graphene in the Graphene/WSe_2 Heterostructure by Optical-Pump Terahertz-Probe Spectroscopy. *ACS Appl Mater Interfaces* **2019**, *11* (50), 47501-47506. DOI: 10.1021/acsami.9b13996

(70) Pan, Y.; Rahaman, M.; He, L.; et al. Exciton tuning in monolayer WSe_2 via substrate induced electron doping. *Nanoscale Adv* **2022**, *4* (23), 5102-5108. DOI: 10.1039/d2na00495j

(71) Carvalho, A.; Ribeiro, R. M.; Castro Neto, A. H. Band nesting and the optical response of two-dimensional semiconducting transition metal dichalcogenides. *Physical Review B* **2013**, *88* (11). DOI: 10.1103/PhysRevB.88.115205

(72) Mørch Nielsen, C. E.; Fischer, F.; Bester, G. Beyond the K-valley: exploring unique trion states in indirect band gap monolayer WSe_2. *npj 2D Materials and Applications* **2025**, *9* (1). DOI: 10.1038/s41699-025-00532-w

(73) Shih, Y.-C.; Nilsson, F. A.; Guo, G.-Y. Electron energy loss spectra and exciton band structure of WSe_2 monolayers studied by ab initio Bethe-Salpeter equation calculations. *Physical Review B* **2024**, *110* (20). DOI: 10.1103/PhysRevB.110.205417

(74) Fang, S.; Carr, S.; Cazalilla, M. A.; et al. Electronic structure theory of strained two-dimensional materials with hexagonal symmetry. *Physical Review B* **2018**, *98* (7). DOI: 10.1103/PhysRevB.98.075106

(75) Zhang, X. X.; You, Y.; Zhao, S. Y.; et al. Experimental Evidence for Dark Excitons in Monolayer WSe_2. *Phys Rev Lett* **2015**, *115* (25), 257403. DOI: 10.1103/PhysRevLett.115.257403

(76) Tang, Y.; Mak, K. F.; Shan, J. Long valley lifetime of dark excitons in single-layer WSe_2. *Nat Commun* **2019**, *10* (1), 4047. DOI: 10.1038/s41467-019-12129-1

(77) Madeo, J.; Man, M. K. L.; Sahoo, C.; et al. Directly visualizing the momentum-forbidden dark excitons and their dynamics in atomically thin semiconductors. *Science* **2020**, *370* (6521), 1199-1204. DOI: 10.1126/science.aba1029

(78) Funk, V.; Wagner, K.; Wietek, E.; et al. Spectral asymmetry of phonon sideband luminescence in monolayer and bilayer
WSe_2. *Physical Review Research* **2021**, *3* (4). DOI: 10.1103/PhysRevResearch.3.L042019

(79) Li, Z.; Wang, T.; Jin, C.; et al. Emerging photoluminescence from the dark-exciton phonon replica in monolayer WSe_2. *Nat Commun* **2019**, *10* (1), 2469. DOI: 10.1038/s41467-019-10477-6

(80) Zhang, X. X.; Cao, T.; Lu, Z.; et al. Magnetic brightening and control of dark excitons in monolayer WSe_2. *Nat Nanotechnol* **2017**, *12* (9), 883-888. DOI: 10.1038/nnano.2017.105

(81) Park, K. D.; Jiang, T.; Clark, G.; et al. Radiative control of dark excitons at room temperature by nano-optical antenna-tip Purcell effect. *Nat Nanotechnol* **2018**, *13* (1), 59-64. DOI: 10.1038/s41565-017-0003-0

(82) Mueller, N. S.; Arul, R.; Kang, G.; et al. Photoluminescence upconversion in monolayer WSe_2 activated by plasmonic cavities through resonant excitation of dark excitons. *Nat Commun* **2023**, *14* (1), 5726. DOI: 10.1038/s41467-023-41401-8

(83) Luo, Y.; Shepard, G. D.; Ardelean, J. V.; et al. Deterministic coupling of site-controlled quantum emitters in monolayer WSe_2 to plasmonic nanocavities. *Nat Nanotechnol* **2018**, *13* (12), 1137-1142. DOI: 10.1038/s41565-018-0275-z

(84) Kern, J.; Niehues, I.; Tonndorf, P.; et al. Nanoscale Positioning of Single-Photon Emitters in Atomically Thin WSe_2. *Adv Mater* **2016**, *28* (33), 7101-7105. DOI: 10.1002/adma.201600560

(85) Hasz, K.; Hu, Z.; Park, K. D.; et al. Tip-Enhanced Dark Exciton Nanoimaging and Local Strain Control in Monolayer WSe_2. *Nano Lett* **2023**, *23* (1), 198-204. DOI: 10.1021/acs.nanolett.2c03959

(86) Schmidt, R.; Niehues, I.; Schneider, R.; et al. Reversible uniaxial strain tuning in atomically thin WSe_2. *2D Materials* **2016**, *3* (2). DOI: 10.1088/2053-1583/3/2/021011

(87) Hsu, W. T.; Lu, L. S.; Wang, D.; et al. Evidence of indirect gap in monolayer WSe_2. *Nat Commun* **2017**, *8* (1), 929. DOI: 10.1038/s41467-017-01012-6

(88) Kim, J. M.; Jeong, K. Y.; Kwon, S.; et al. Strained two-dimensional tungsten diselenide for mechanically tunable exciton transport. *Nat Commun* **2024**, *15* (1), 10847. DOI: 10.1038/s41467-024-55135-8

(89) Xiao, L.; Liu, Y.; Mohajerani, S. S.; et al. Quantum Light Funneling in Tailored Triangular Plasmonic Nanocavities. *ACS Nano* **2026**. DOI: 10.1021/acsnano.5c16988

(90) Branny, A.; Kumar, S.; Proux, R.; et al. Deterministic strain-induced arrays of quantum emitters in a two-dimensional semiconductor. *Nat Commun* **2017**, *8* (1), 15053. DOI: 10.1038/ncomms15053

(91) Peyskens, F.; Chakraborty, C.; Muneeb, M.; et al. Integration of single photon emitters in 2D layered materials with a silicon nitride photonic chip. *Nat Commun* **2019**, *10* (1), 4435. DOI: 10.1038/s41467-019-12421-0

(92) Errando-Herranz, C.; Scholl, E.; Picard, R.; et al. Resonance Fluorescence from Waveguide-Coupled, Strain-Localized, Two-Dimensional Quantum Emitters. *ACS Photonics* **2021**, *8* (4), 1069-1076. DOI: 10.1021/acsphotonics.0c01653

(93) Iff, O.; Buchinger, Q.; Moczala-Dusanowska, M.; et al. Purcell-Enhanced Single Photon Source Based on a Deterministically Placed WSe_2 Monolayer Quantum Dot in a Circular Bragg Grating Cavity. *Nano Lett* **2021**, *21* (11), 4715-4720. DOI: 10.1021/acs.nanolett.1c00978

(94) Frisenda, R.; Drüppel, M.; Schmidt, R.; et al. Biaxial strain tuning of the optical properties of single-layer transition metal dichalcogenides. *npj 2D Materials and Applications* **2017**, *1* (1). DOI: 10.1038/s41699-017-0013-7

(95) Aslan, B.; Deng, M.; Heinz, T. F. Strain tuning of excitons in monolayer WSe_2. *Physical Review B* **2018**, *98* (11). DOI: 10.1103/PhysRevB.98.115308

(96) Yuan, Z.; Kardynal, B. E.; Stevenson, R. M.; et al. Electrically driven single-photon source. *Science* **2002**, *295* (5552), 102-105. DOI: 10.1126/science.1066790

(97) Santori, C.; Fattal, D.; Vuckovic, J.; et al. Indistinguishable photons from a single-photon device. *Nature* **2002**, *419* (6907), 594-597. DOI: 10.1038/nature01086

(98) Michler, P.; Kiraz, A.; Becher, C.; et al. A quantum dot single-photon turnstile device. *Science* **2000**, *290* (5500), 2282-2285. DOI: 10.1126/science.290.5500.2282

(99) Strauf, S.; Michler, P.; Klude, M.; et al. Quantum optical studies on individual acceptor bound excitons in a semiconductor. *Phys Rev Lett* **2002**, *89* (17), 177403. DOI: 10.1103/PhysRevLett.89.177403

(100) Hsiao, T. K.; Rubino, A.; Chung, Y.; et al. Single-photon emission from single-electron transport in a SAW-driven lateral light-emitting diode. *Nat Commun* **2020**, *11* (1), 917. DOI: 10.1038/s41467-020-14560-1

(101) Rezus, Y. L.; Walt, S. G.; Lettow, R.; et al. Single-photon spectroscopy of a single molecule. *Phys Rev Lett* **2012**, *108* (9), 093601. DOI: 10.1103/PhysRevLett.108.093601

(102) Zhang, L.; Yu, Y. J.; Chen, L. G.; et al. Electrically driven single-photon emission from an isolated single molecule. *Nat Commun* **2017**, *8* (1), 580. DOI: 10.1038/s41467-017-00681-7

(103) Lounis, B.; Moerner, W. E. Single photons on demand from a single molecule at room temperature. *Nature* **2000**, *407* (6803), 491-493. DOI: 10.1038/35035032

(104) Doherty, M. W.; Manson, N. B.; Delaney, P.; et al. The nitrogen-vacancy colour centre in diamond. *Physics Reports* **2013**, *528* (1), 1-45. DOI: 10.1016/j.physrep.2013.02.001

(105) Brouri, R.; Beveratos, A.; Poizat, J. P.; et al. Photon antibunching in the fluorescence of individual color centers in diamond. *Opt Lett* **2000**, *25* (17), 1294-1296. DOI: 10.1364/ol.25.001294

(106) Kurtsiefer, C.; Mayer, S.; Zarda, P.; et al. Stable solid-state source of single photons. *Phys Rev Lett* **2000**, *85* (2), 290-293. DOI: 10.1103/PhysRevLett.85.290

(107) Linhart, L.; Paur, M.; Smejkal, V.; et al. Localized Intervalley Defect Excitons as Single-Photon Emitters in WSe_2. *Phys Rev Lett* **2019**, *123* (14), 146401. DOI: 10.1103/PhysRevLett.123.146401

(108) Kim, H.; Moon, J. S.; Noh, G.; et al. Position and Frequency Control of Strain-Induced Quantum Emitters in WSe_2 Monolayers. *Nano Lett* **2019**, *19* (10), 7534-7539. DOI: 10.1021/acs.nanolett.9b03421

(109) Parto, K.; Azzam, S. I.; Banerjee, K.; et al. Defect and strain engineering of monolayer WSe_2 enables site-controlled single-photon emission up to 150 K. *Nat Commun* **2021**, *12* (1), 3585. DOI: 10.1038/s41467-021-23709-5

(110) Zheng, Y. J.; Chen, Y.; Huang, Y. L.; et al. Point Defects and Localized Excitons in 2D WSe_2. *ACS Nano* **2019**, *13* (5), 6050-6059. DOI: 10.1021/acsnano.9b02316

(111) Barja, S.; Refaely-Abramson, S.; Schuler, B.; et al. Identifying substitutional oxygen as a prolific point defect in monolayer transition metal dichalcogenides. *Nat Commun* **2019**, *10* (1), 3382. DOI: 10.1038/s41467-019-11342-2

(112) Dang, J.; Sun, S.; Xie, X.; et al. Identifying defect-related quantum emitters in monolayer WSe_2. *npj 2D Materials and Applications* **2020**, *4* (2). DOI: 10.1038/s41699-020-0136-0

(113) Luo, Y.; Liu, N.; Kim, B.; et al. Exciton Dipole Orientation of Strain-Induced Quantum Emitters in WSe_2. *Nano Lett* **2020**, *20* (7), 5119-5126. DOI: 10.1021/acs.nanolett.0c01358

(114) Serati de Brito, C.; Rosa, B. L. T.; Chaves, A.; et al. Probing the Nature of Single-Photon Emitters in a WSe_2 Monolayer by Magneto-Photoluminescence Spectroscopy. *Nano Lett* **2024**, *24* (42), 13300-13306. DOI: 10.1021/acs.nanolett.4c03686

(115) Yang, L.; Yuan, Y.; Fu, B.; et al. Revealing broken valley symmetry of quantum emitters in WSe_2 with chiral nanocavities. *Nat Commun* **2023**, *14* (1), 4265. DOI: 10.1038/s41467-023-39972-7

(116) Paralikis, A.; Wyborski, P.; Metuh, P.; et al. Tunable and Low-Noise WSe_2 Quantum Emitters for Quantum Photonics. *PRX Quantum* **2025**, *6* (4). DOI: 10.1103/cynh-ql3j

(117) Loudon, R. *The Quantum Theory of Light*; Oxford University Press, 2000.

(118) Glauber, R. J. The Quantum Theory of Optical Coherence. *Physical Review* **1963**, *130* (6), 2529-2539. DOI: 10.1103/PhysRev.130.2529

(119) Planck, M. Über das Gesetz der Energieverteilung im Normalspektrum. *Annalen der Physik* **1901**, *4*, 553-563.

(120) Planck, M. Zur Theorie des Gesetzes der Energieverteilung im Normalspektrum. *Annalen der Physik* **1900**, *4*, 553-563.

(121) Ye, Y.; Dou, X.; Ding, K.; et al. Single photon emission from deep-level defects in monolayer WSe_2. *Physical Review B* **2017**, *95* (24). DOI: 10.1103/PhysRevB.95.245313

(122) Rosenberger, M. R.; Dass, C. K.; Chuang, H. J.; et al. Quantum Calligraphy: Writing Single-Photon Emitters in a Two-Dimensional Materials Platform. *ACS Nano* **2019**, *13* (1), 904-912. DOI: 10.1021/acsnano.8b08730

(123) Xu, D. D.; Vong, A. F.; Lebedev, D.; et al. Conversion of Classical Light Emission from a Nanoparticle-Strained WSe_2 Monolayer into Quantum Light Emission via Electron Beam Irradiation. *Adv Mater* **2023**, *35* (5), e2208066. DOI: 10.1002/adma.202208066

(124) Lan, H. Y.; Lin, C. P.; Liu, L.; et al. Uncovering the doping mechanism of nitric oxide in high-performance P-type WSe_2 transistors. *Nat Commun* **2025**, *16* (1), 4160. DOI: 10.1038/s41467-025-59423-9

(125) Zhao, Y.; Tripathi, M.; Cernevics, K.; et al. Electrical spectroscopy of defect states and their hybridization in monolayer MoS_2. *Nat Commun* **2023**, *14* (1), 44. DOI: 10.1038/s41467-022-35651-1

(126) Edelberg, D.; Rhodes, D.; Kerelsky, A.; et al. Approaching the Intrinsic Limit in Transition Metal Diselenides via Point Defect Control. *Nano Lett* **2019**, *19* (7), 4371-4379. DOI: 10.1021/acs.nanolett.9b00985

(127) Liu, S.; Liu, Y.; Holtzman, L.; et al. Two-Step Flux Synthesis of Ultrapure Transition-Metal Dichalcogenides. *ACS Nano* **2023**, *17* (17), 16587-16596. DOI: 10.1021/acsnano.3c02511

(128) Holbrook, M.; Holtzman, L. N.; Hou, B.; et al. Revealing Substitutional Oxygen as the Dominant Defect in Flux-Grown Transition Metal Diselenides. *Nano Lett* **2025**, *25* (37), 13795-13801. DOI: 10.1021/acs.nanolett.5c03126

(129) Luo, Y.; Liu, N.; Li, X.; et al. Single photon emission in WSe_2 up to 160 K by quantum yield control. *2D Materials* **2019**, *6* (3). DOI: 10.1088/2053-1583/ab15fe

(130) Utama, M. I. B.; Zeng, H.; Sadhukhan, T.; et al. Chemomechanical modification of quantum emission in monolayer WSe_2. *Nat Commun* **2023**, *14* (1), 2193. DOI: 10.1038/s41467-023-37892-0

(131) Zhao, Y.; Gali, S. M.; Wang, C.; et al. Molecular Functionalization of Chemically Active Defects in WSe_2 for Enhanced Opto-Electronics. *Advanced Functional Materials* **2020**, *30* (45). DOI: 10.1002/adfm.202005045

(132) Ananth, R.; Utama, M. I. B.; Xu, D. D.; et al. Enhanced spectral purity of WSe_2 quantum emitters via conformal organic adlayers. *Sci Adv* **2025**, *11* (40), eady7557. DOI: 10.1126/sciadv.ady7557

(133) Guo, S.; Germanis, S.; Taniguchi, T.; et al. Electrically Driven Site-Controlled Single Photon Source. *ACS Photonics* **2023**, *10* (8), 2549-2555. DOI: 10.1021/acsphotonics.3c00097

(134) So, J. P.; Kim, H. R.; Baek, H.; et al. Electrically driven strain-induced deterministic single-photon emitters in a van der Waals heterostructure. *Sci Adv* **2021**, *7* (43), eabj3176. DOI: 10.1126/sciadv.abj3176

(135) Shepard, G. D.; Ajayi, O. A.; Li, X.; et al. Nanobubble induced formation of quantum emitters in monolayer semiconductors. *2D Materials* **2017**, *4* (2). DOI: 10.1088/2053-1583/aa629d

(136) Stevens, C. E.; Chuang, H. J.; Rosenberger, M. R.; et al. Enhancing the Purity of Deterministically Placed Quantum Emitters in Monolayer WSe_2. *ACS Nano* **2022**, *16* (12), 20956-20963. DOI: 10.1021/acsnano.2c08553

(137) Abramov, A. N.; Chestnov, I. Y.; Alimova, E. S.; et al. Photoluminescence imaging of single photon emitters within nanoscale strain profiles in monolayer WSe_2. *Nat Commun* **2023**, *14* (1), 5737. DOI: 10.1038/s41467-023-41292-9

(138) Chang, S.; Yan, Y.; Geng, Y. Local Nanostrain Engineering of Monolayer MoS_2 Using Atomic Force Microscopy-Based Thermomechanical Nanoindentation. *Nano Lett* **2023**, *23* (20), 9219-9226. DOI: 10.1021/acs.nanolett.3c01809

(139) Li, X.; Jones, A. C.; Choi, J.; et al. Proximity-induced chiral quantum light generation in strain-engineered $WSe_2/NiPS_3$ heterostructures. *Nat Mater* **2023**, *22* (11), 1311-1316. DOI: 10.1038/s41563-023-01645-7

(140) Cunningham, P. D.; Proscia, N. V.; LaGasse, S. W.; et al. Site-Specific Exciton–Plasmon Coupling in Nanoindented WSe_2. *ACS Photonics* **2024**, *11* (8), 3250-3258. DOI: 10.1021/acsphotonics.4c00644

(141) Yücel, O.; Yagodkin, D.; Kirchhof, J. N.; et al. Strain activation of localized states in WSe_2. *2D Materials* **2025**, *12* (3). DOI: 10.1088/2053-1583/add414

(142) Peng, L.; Chan, H.; Choo, P.; et al. Creation of Single-Photon Emitters in WSe_2 Monolayers Using Nanometer-Sized Gold Tips. *Nano Lett* **2020**, *20* (8), 5866-5872. DOI: 10.1021/acs.nanolett.0c01789

(143) Qian, Q.; Peng, L.; Perea-Lopez, N.; et al. Defect creation in WSe_2 with a microsecond photoluminescence lifetime by focused ion beam irradiation. *Nanoscale* **2020**, *12* (3), 2047-2056. DOI: 10.1039/c9nr08390a

(144) Klein, J.; Lorke, M.; Florian, M.; et al. Site-selectively generated photon emitters in monolayer MoS_2 via local helium ion irradiation. *Nat Commun* **2019**, *10* (1), 2755. DOI: 10.1038/s41467-019-10632-z

(145) Hecht, L. N. a. B. *Principles of Nano-Optics*; Cambridge University Press, 2012.

(146) Azzam, S. I.; Parto, K.; Moody, G. Purcell enhancement and polarization control of single-photon emitters in monolayer WSe_2 using dielectric nanoantennas. *Nanophotonics* **2023**, *12* (3), 477-484. DOI: 10.1515/nanoph-2022-0628

(147) Sortino, L.; Zotev, P. G.; Phillips, C. L.; et al. Bright single photon emitters with enhanced quantum efficiency in a two-dimensional semiconductor coupled with dielectric nano-antennas. *Nat Commun* **2021**, *12* (1), 6063. DOI: 10.1038/s41467-021-26262-3

(148) So, J. P.; Jeong, K. Y.; Lee, J. M.; et al. Polarization Control of Deterministic Single-Photon Emitters in Monolayer WSe_2. *Nano Lett* **2021**, *21* (3), 1546-1554. DOI: 10.1021/acs.nanolett.1c00078

(149) Noori, Y. J.; Cao, Y.; Roberts, J.; et al. Photonic Crystals for Enhanced Light Extraction from 2D Materials. *ACS Photonics* **2016**, *3* (12), 2515-2520. DOI: 10.1021/acsphotonics.6b00779

(150) Duong, N. M. H.; Xu, Z.-Q.; Kianinia, M.; et al. Enhanced Emission from WSe_2 Monolayers Coupled to Circular Bragg Gratings. *ACS Photonics* **2018**, *5* (10), 3950-3955. DOI: 10.1021/acsphotonics.8b00865

(151) Iff, O.; Davanco, M.; Betzold, S.; et al. Hyperspectral study of the coupling between trions in WSe_2 monolayers to a circular Bragg grating cavity. *C R Phys* **2021**, *22* (Suppl 4). DOI: 10.5802/crphys.76

(152) Hekmati, R.; Hadden, J. P.; Mathew, A.; et al. Bullseye dielectric cavities for photon collection from a surface-mounted quantum-light-emitter. *Sci Rep* **2023**, *13* (1), 5316. DOI: 10.1038/s41598-023-32359-0

(153) Strasbourg, M. C.; Yanev, E. S.; Darlington, T. P.; et al. Characterization of quantum dot-like emitters in programmable arrays of nanowrinkles of 1L-WSe_2. *Journal of Applied Physics* **2024**, *136* (4). DOI: 10.1063/5.0214410

(154) Bennett, C. H.; Brassard, G. Quantum cryptography: Public key distribution and coin tossing. *Theoretical Computer Science* **2014**, *560*, 7-11. DOI: 10.1016/j.tcs.2014.05.025

(1) Novoselov, K. S.; Geim, A. K.; Morozov, S. V.; et al. Electric field effect in atomically thin carbon films. *Science* **2004**, *306* (5696), 666-669. DOI: 10.1126/science.1102896

(2) Kumar, S.; Kaczmarczyk, A.; Gerardot, B. D. Strain-Induced Spatial and Spectral Isolation of Quantum Emitters in Mono- and Bilayer WSe_2. *Nano Lett* **2015**, *15* (11), 7567-7573. DOI: 10.1021/acs.nanolett.5b03312

(3) Chakraborty, C.; Kinnischtzke, L.; Goodfellow, K. M.; et al. Voltage-controlled quantum light from an atomically thin semiconductor. *Nat Nanotechnol* **2015**, *10* (6), 507-511. DOI: 10.1038/nnano.2015.79

(4) He, Y. M.; Clark, G.; Schaibley, J. R.; et al. Single quantum emitters in monolayer semiconductors. *Nat Nanotechnol* **2015**, *10* (6), 497-502. DOI: 10.1038/nnano.2015.75

(5) Koperski, M.; Nogajewski, K.; Arora, A.; et al. Single photon emitters in exfoliated WSe_2 structures. *Nat Nanotechnol* **2015**, *10* (6), 503-506. DOI: 10.1038/nnano.2015.67

(6) Srivastava, A.; Sidler, M.; Allain, A. V.; et al. Optically active quantum dots in monolayer WSe_2. *Nat Nanotechnol* **2015**, *10* (6), 491-496. DOI: 10.1038/nnano.2015.60

(7) Tonndorf, P.; Schmidt, R.; Schneider, R.; et al. Single-photon emission from localized excitons in an atomically thin semiconductor. *Optica* **2015**, *2* (4). DOI: 10.1364/optica.2.000347

(8) Raja, A.; Waldecker, L.; Zipfel, J.; et al. Dielectric disorder in two-dimensional materials. *Nat Nanotechnol* **2019**, *14* (9), 832-837. DOI: 10.1038/s41565-019-0520-0

(9) Dass, C. K.; Khan, M. A.; Clark, G.; et al. Ultra-Long Lifetimes of Single Quantum Emitters in Monolayer WSe_2/hBN Heterostructures. *Advanced Quantum Technologies* **2019**, *2* (5-6). DOI: 10.1002/qute.201900022

(10) Chhaperwal, M.; Tongale, H. M.; Hays, P.; et al. Simultaneously Enhancing Brightness and Purity of WSe_2 Single Photon Emitter Using High-Aspect-Ratio Nanopillar Array on Metal. *Nano Lett* **2024**, *24* (40), 12461-12468. DOI: 10.1021/acs.nanolett.4c03168

(11) Yanev, E. S.; Darlington, T. P.; Ladyzhets, S. A.; et al. Programmable nanowrinkle-induced room-temperature exciton localization in monolayer WSe_2. *Nat Commun* **2024**, *15* (1), 1543. DOI: 10.1038/s41467-024-45936-2

(12) Novoselov, K. S.; Mishchenko, A.; Carvalho, A.; et al. 2D materials and van der Waals heterostructures. *Science* **2016**, *353* (6298), aac9439. DOI: 10.1126/science.aac9439

(13) Campi, D.; Mounet, N.; Gibertini, M.; et al. Expansion of the Materials Cloud 2D Database. *ACS Nano* **2023**, *17* (12), 11268-11278. DOI: 10.1021/acsnano.2c11510

(14) Xiao, Y.; Liu, J.; Fu, L. Moiré is More: Access to New Properties of Two-Dimensional Layered Materials. *Matter* **2020**, *3* (4), 1142-1161. DOI: 10.1016/j.matt.2020.07.001

(15) Carr, S.; Massatt, D.; Fang, S.; et al. Twistronics: Manipulating the electronic properties of two-dimensional layered structures through their twist angle. *Physical Review B* **2017**, *95* (7). DOI: 10.1103/PhysRevB.95.075420

(16) Li, C.; Fröch, J. E.; Nonahal, M.; et al. Integration of hBN Quantum Emitters in Monolithically Fabricated Waveguides. *ACS Photonics* **2021**, *8* (10), 2966-2972. DOI: 10.1021/acsphotonics.1c00890

(17) Dutta, S.; Cai, T.; Buyukkaya, M. A.; et al. Coupling quantum emitters in WSe_2 monolayers to a metal-insulator-metal waveguide. *Applied Physics Letters* **2018**, *113* (19). DOI: 10.1063/1.5045727

(18) Ling, H.; Li, R.; Davoyan, A. R. All van der Waals Integrated Nanophotonics with Bulk Transition Metal Dichalcogenides. *ACS Photonics* **2021**, *8* (3), 721-730. DOI: 10.1021/acsphotonics.0c01964

(19) Parto, K.; Azzam, S. I.; Lewis, N.; et al. Cavity-Enhanced 2D Material Quantum Emitters Deterministically Integrated with Silicon Nitride Microresonators. *Nano Lett* **2022**, *22* (23), 9748-9756. DOI: 10.1021/acs.nanolett.2c03151

(20) Ren, T.; Granados Del Aguila, A.; Chen, Z.; et al. Van der Waals photonic integrated circuit with coherent light generation. *Nat Commun* **2025**, *16* (1), 5931. DOI: 10.1038/s41467-025-60778-2

(21) Al-Juboori, A.; Zeng, H. Z. J.; Nguyen, M. A. P.; et al. Quantum Key Distribution Using a Quantum Emitter in Hexagonal Boron Nitride. *Advanced Quantum Technologies* **2023**, *6* (9). DOI: 10.1002/qute.202300038

(22) Samaner, Ç.; Paçal, S.; Mutlu, G.; et al. Free-Space Quantum Key Distribution with Single Photons from Defects in Hexagonal Boron Nitride. *Advanced Quantum Technologies* **2022**, *5* (9). DOI: 10.1002/qute.202200059

(23) Zeng, H. Z. J.; Ngyuen, M. A. P.; Ai, X.; et al. Integrated room temperature single-photon source for quantum key distribution. *Opt Lett* **2022**, *47* (7), 1673-1676. DOI: 10.1364/OL.454450

(24) Gao, T.; von Helversen, M.; Antón-Solanas, C.; et al. Atomically-thin single-photon sources for quantum communication. *npj 2D Materials and Applications* **2023**, *7* (1). DOI: 10.1038/s41699-023-00366-4

(25) Rizzato, R.; Schalk, M.; Mohr, S.; et al. Extending the coherence of spin defects in hBN enables advanced qubit control and quantum sensing. *Nat Commun* **2023**, *14* (1), 5089. DOI: 10.1038/s41467-023-40473-w

(26) Ramsay, A. J.; Hekmati, R.; Patrickson, C. J.; et al. Coherence protection of spin qubits in hexagonal boron nitride. *Nat Commun* **2023**, *14* (1), 461. DOI: 10.1038/s41467-023-36196-7

(27) Haykal, A.; Tanos, R.; Minotto, N.; et al. Decoherence of VB- spin defects in monoisotopic hexagonal boron nitride. *Nat Commun* **2022**, *13* (1), 4347. DOI: 10.1038/s41467-022-31743-0

(28) Eich, M.; Herman, F.; Pisoni, R.; et al. Spin and Valley States in Gate-Defined Bilayer Graphene Quantum Dots. *Physical Review X* **2018**, *8* (3). DOI: 10.1103/PhysRevX.8.031023

(29) Banszerus, L.; Hecker, K.; Moller, S.; et al. Spin relaxation in a single-electron graphene quantum dot. *Nat Commun* **2022**, *13* (1), 3637. DOI: 10.1038/s41467-022-31231-5

(30) Garreis, R.; Tong, C.; Terle, J.; et al. Long-lived valley states in bilayer graphene quantum dots. *Nature Physics* **2024**, *20* (3), 428-434. DOI: 10.1038/s41567-023-02334-7

(31) Kormányos, A.; Zólyomi, V.; Drummond, N. D.; et al. Spin-Orbit Coupling, Quantum Dots, and Qubits in Monolayer Transition Metal Dichalcogenides. *Physical Review X* **2014**, *4* (1). DOI: 10.1103/PhysRevX.4.011034

(32) Zhang, Z. Z.; Song, X. X.; Luo, G.; et al. Electrotunable artificial molecules based on van der Waals heterostructures. *Sci Adv* **2017**, *3* (10), e1701699. DOI: 10.1126/sciadv.1701699

(33) Lu, X.; Chen, X.; Dubey, S.; et al. Optical initialization of a single spin-valley in charged WSe_2 quantum dots. *Nat Nanotechnol* **2019**, *14* (5), 426-431. DOI: 10.1038/s41565-019-0394-1

(34) Colmiais, I.; Silva, V.; Borme, J.; et al. Towards RF graphene devices: A review. *FlatChem* **2022**, *35*. DOI: 10.1016/j.flatc.2022.100409

(35) Han, S. J.; Garcia, A. V.; Oida, S.; et al. Graphene radio frequency receiver integrated circuit. *Nat Commun* **2014**, *5*, 3086. DOI: 10.1038/ncomms4086

(36) Ju, L.; Geng, B.; Horng, J.; et al. Graphene plasmonics for tunable terahertz metamaterials. *Nat Nanotechnol* **2011**, *6* (10), 630-634. DOI: 10.1038/nnano.2011.146

(37) Li, J.; Chen, J.; Yan, D.; et al. A Review: Active Tunable Terahertz Metamaterials. *Advanced Photonics Research* **2024**, *5* (7). DOI: 10.1002/adpr.202300351

(38) Zhang, X.; Ren, W.; Bell, E.; et al. Gate-tunable Veselago interference in a bipolar graphene microcavity. *Nat Commun* **2022**, *13* (1), 6711. DOI: 10.1038/s41467-022-34347-w

(39) Levesque, P. L.; Sabri, S. S.; Aguirre, C. M.; et al. Probing charge transfer at surfaces using graphene transistors. *Nano Lett* **2011**, *11* (1), 132-137. DOI: 10.1021/nl103015w

(40) Asenbauer, J.; Eisenmann, T.; Kuenzel, M.; et al. The success story of graphite as a lithium-ion anode material – fundamentals, remaining challenges, and recent developments including silicon (oxide) composites. *Sustainable Energy & Fuels* **2020**, *4* (11), 5387-5416. DOI: 10.1039/d0se00175a

(41) Chuang, H. J.; Stevens, C. E.; Rosenberger, M. R.; et al. Enhancing Single Photon Emission Purity via Design of van der Waals Heterostructures. *Nano Lett* **2024**, *24* (18), 5529-5535. DOI: 10.1021/acs.nanolett.4c00683

(42) Yu, Y.; Seo, I. C.; Luo, M.; et al. Tunable single-photon emitters in 2D materials. *Nanophotonics* **2024**, *13* (19), 3615-3629. DOI: 10.1515/nanoph-2024-0050

(43) Ai, R.; Cui, X.; Li, Y.; et al. Local Strain Engineering of Two-Dimensional Transition Metal Dichalcogenides Towards Quantum Emitters. *Nanomicro Lett* **2025**, *17* (1), 104. DOI: 10.1007/s40820-024-01611-1

(44) Reina, A.; Jia, X.; Ho, J.; et al. Large area, few-layer graphene films on arbitrary substrates by chemical vapor deposition. *Nano Lett* **2009**, *9* (1), 30-35. DOI: 10.1021/nl801827v

(45) Bae, S.; Kim, H.; Lee, Y.; et al. Roll-to-roll production of 30-inch graphene films for transparent electrodes. *Nat Nanotechnol* **2010**, *5* (8), 574-578. DOI: 10.1038/nnano.2010.132

(46) Kim, K. S.; Zhao, Y.; Jang, H.; et al. Large-scale pattern growth of graphene films for stretchable transparent electrodes. *Nature* **2009**, *457* (7230), 706-710. DOI: 10.1038/nature07719

(47) Li, X.; Cai, W.; An, J.; et al. Large-area synthesis of high-quality and uniform graphene films on copper foils. *Science* **2009**, *324* (5932), 1312-1314. DOI: 10.1126/science.1171245

(48) Dean, C. R.; Young, A. F.; Meric, I.; et al. Boron nitride substrates for high-quality graphene electronics. *Nat Nanotechnol* **2010**, *5* (10), 722-726. DOI: 10.1038/nnano.2010.172

(49) Wang, L.; Meric, I.; Huang, P. Y.; et al. One-dimensional electrical contact to a two-dimensional material. *Science* **2013**, *342* (6158), 614-617. DOI: 10.1126/science.1244358

(50) Tran, T. T.; Bray, K.; Ford, M. J.; et al. Quantum emission from hexagonal boron nitride monolayers. *Nat Nanotechnol* **2016**, *11* (1), 37-41. DOI: 10.1038/nnano.2015.242

(51) Sajid, A.; Ford, M. J.; Reimers, J. R. Single-photon emitters in hexagonal boron nitride: a review of progress. *Rep Prog Phys* **2020**, *83* (4), 044501. DOI: 10.1088/1361-6633/ab6310

(52) Dean, C. R.; Wang, L.; Maher, P.; et al. Hofstadter's butterfly and the fractal quantum Hall effect in moire superlattices. *Nature* **2013**, *497* (7451), 598-602. DOI: 10.1038/nature12186

(53) Ponomarenko, L. A.; Gorbachev, R. V.; Yu, G. L.; et al. Cloning of Dirac fermions in graphene superlattices. *Nature* **2013**, *497* (7451), 594-597. DOI: 10.1038/nature12187

(54) Cao, Y.; Fatemi, V.; Fang, S.; et al. Unconventional superconductivity in magic-angle graphene superlattices. *Nature* **2018**, *556* (7699), 43-50. DOI: 10.1038/nature26160

(55) Cao, Y.; Fatemi, V.; Demir, A.; et al. Correlated insulator behaviour at half-filling in magic-angle graphene superlattices. *Nature* **2018**, *556* (7699), 80-84. DOI: 10.1038/nature26154

(56) Tran, K.; Moody, G.; Wu, F.; et al. Evidence for moire excitons in van der Waals heterostructures. *Nature* **2019**, *567* (7746), 71-75. DOI: 10.1038/s41586-019-0975-z

(57) Mak, K. F.; Lee, C.; Hone, J.; et al. Atomically thin MoS_2: a new direct-gap semiconductor. *Phys Rev Lett* **2010**, *105* (13), 136805. DOI: 10.1103/PhysRevLett.105.136805

(58) Splendiani, A.; Sun, L.; Zhang, Y.; et al. Emerging photoluminescence in monolayer MoS_2. *Nano Lett* **2010**, *10* (4), 1271-1275. DOI: 10.1021/nl903868w

(59) He, K.; Kumar, N.; Zhao, L.; et al. Tightly bound excitons in monolayer WSe_2. *Phys Rev Lett* **2014**, *113* (2), 026803. DOI: 10.1103/PhysRevLett.113.026803

(60) Arora, A.; Koperski, M.; Nogajewski, K.; et al. Excitonic resonances in thin films of WSe_2: from monolayer to bulk material. *Nanoscale* **2015**, *7* (23), 10421-10429. DOI: 10.1039/c5nr01536g

(61) Yu, H.; Liao, M.; Zhao, W.; et al. Wafer-Scale Growth and Transfer of Highly-Oriented Monolayer MoS_2 Continuous Films. *ACS Nano* **2017**, *11* (12), 12001-12007. DOI: 10.1021/acsnano.7b03819

(62) Lan, C.; Zhou, Z.; Zhou, Z.; et al. Wafer-scale synthesis of monolayer WS_2 for high-performance flexible photodetectors by enhanced chemical vapor deposition. *Nano Research* **2018**, *11* (6), 3371-3384. DOI: 10.1007/s12274-017-1941-4

(63) Hu, J.; Zhou, F.; Wang, J.; et al. Chemical Vapor Deposition Syntheses of Wafer-Scale 2D Transition Metal Dichalcogenide Films toward Next-Generation Integrated Circuits Related Applications. *Advanced Functional Materials* **2023**, *33* (40). DOI: 10.1002/adfm.202303520

(64) Chou, S. A.; Chang, C.; Wu, B. H.; et al. Large-scale alkali-assisted growth of monolayer and bilayer WSe_2 with a low defect density. *Nat Commun* **2025**, *16* (1), 2777. DOI: 10.1038/s41467-025-57986-1

(65) Velicky, M.; Donnelly, G. E.; Hendren, W. R.; et al. Mechanism of Gold-Assisted Exfoliation of Centimeter-Sized Transition-Metal Dichalcogenide Monolayers. *ACS Nano* **2018**, *12* (10), 10463-10472. DOI: 10.1021/acsnano.8b06101

(66) Chen, S.; Li, B.; Dai, C.; et al. Controlling Gold-Assisted Exfoliation of Large-Area MoS_2 Monolayers with External Pressure. *Nanomaterials (Basel)* **2024**, *14* (17). DOI: 10.3390/nano14171418

(67) Panasci, S. E.; Schiliro, E.; Greco, G.; et al. Strain, Doping, and Electronic Transport of Large Area Monolayer MoS_2 Exfoliated on Gold and Transferred to an Insulating Substrate. *ACS Appl Mater Interfaces* **2021**, *13* (26), 31248-31259. DOI: 10.1021/acsami.1c05185

(68) Panasci, S. E.; Schilirò, E.; Migliore, F.; et al. Substrate impact on the thickness dependence of vibrational and optical properties of large area MoS_2 produced by gold-assisted exfoliation. *Applied Physics Letters* **2021**, *119* (9). DOI: 10.1063/5.0062106

(69) Zhang, L.; Chen, Z.; Zhang, R.; et al. Direct Observation of Charge Injection of Graphene in the Graphene/WSe_2 Heterostructure by Optical-Pump Terahertz-Probe Spectroscopy. *ACS Appl Mater Interfaces* **2019**, *11* (50), 47501-47506. DOI: 10.1021/acsami.9b13996

(70) Pan, Y.; Rahaman, M.; He, L.; et al. Exciton tuning in monolayer WSe_2 via substrate induced electron doping. *Nanoscale Adv* **2022**, *4* (23), 5102-5108. DOI: 10.1039/d2na00495j

(71) Carvalho, A.; Ribeiro, R. M.; Castro Neto, A. H. Band nesting and the optical response of two-dimensional semiconducting transition metal dichalcogenides. *Physical Review B* **2013**, *88* (11). DOI: 10.1103/PhysRevB.88.115205

(72) Mørch Nielsen, C. E.; Fischer, F.; Bester, G. Beyond the K-valley: exploring unique trion states in indirect band gap monolayer WSe_2. *npj 2D Materials and Applications* **2025**, *9* (1). DOI: 10.1038/s41699-025-00532-w

(73) Shih, Y.-C.; Nilsson, F. A.; Guo, G.-Y. Electron energy loss spectra and exciton band structure of WSe_2 monolayers studied by ab initio Bethe-Salpeter equation calculations. *Physical Review B* **2024**, *110* (20). DOI: 10.1103/PhysRevB.110.205417

(74) Fang, S.; Carr, S.; Cazalilla, M. A.; et al. Electronic structure theory of strained two-dimensional materials with hexagonal symmetry. *Physical Review B* **2018**, *98* (7). DOI: 10.1103/PhysRevB.98.075106

(75) Zhang, X. X.; You, Y.; Zhao, S. Y.; et al. Experimental Evidence for Dark Excitons in Monolayer WSe_2. *Phys Rev Lett* **2015**, *115* (25), 257403. DOI: 10.1103/PhysRevLett.115.257403

(76) Tang, Y.; Mak, K. F.; Shan, J. Long valley lifetime of dark excitons in single-layer WSe_2. *Nat Commun* **2019**, *10* (1), 4047. DOI: 10.1038/s41467-019-12129-1

(77) Madeo, J.; Man, M. K. L.; Sahoo, C.; et al. Directly visualizing the momentum-forbidden dark excitons and their dynamics in atomically thin semiconductors. *Science* **2020**, *370* (6521), 1199-1204. DOI: 10.1126/science.aba1029

(78) Funk, V.; Wagner, K.; Wietek, E.; et al. Spectral asymmetry of phonon sideband luminescence in monolayer and bilayer WSe_2. *Physical Review Research* **2021**, *3* (4). DOI: 10.1103/PhysRevResearch.3.L042019

(79) Li, Z.; Wang, T.; Jin, C.; et al. Emerging photoluminescence from the dark-exciton phonon replica in monolayer WSe_2. *Nat Commun* **2019**, *10* (1), 2469. DOI: 10.1038/s41467-019-10477-6

(80) Zhang, X. X.; Cao, T.; Lu, Z.; et al. Magnetic brightening and control of dark excitons in monolayer WSe_2. *Nat Nanotechnol* **2017**, *12* (9), 883-888. DOI: 10.1038/nnano.2017.105

(81) Park, K. D.; Jiang, T.; Clark, G.; et al. Radiative control of dark excitons at room temperature by nano-optical antenna-tip Purcell effect. *Nat Nanotechnol* **2018**, *13* (1), 59-64. DOI: 10.1038/s41565-017-0003-0

(82) Mueller, N. S.; Arul, R.; Kang, G.; et al. Photoluminescence upconversion in monolayer WSe_2 activated by plasmonic cavities through resonant excitation of dark excitons. *Nat Commun* **2023**, *14* (1), 5726. DOI: 10.1038/s41467-023-41401-8

(83) Luo, Y.; Shepard, G. D.; Ardelean, J. V.; et al. Deterministic coupling of site-controlled quantum emitters in monolayer WSe_2 to plasmonic nanocavities. *Nat Nanotechnol* **2018**, *13* (12), 1137-1142. DOI: 10.1038/s41565-018-0275-z

(84) Kern, J.; Niehues, I.; Tonndorf, P.; et al. Nanoscale Positioning of Single-Photon Emitters in Atomically Thin WSe_2. *Adv Mater* **2016**, *28* (33), 7101-7105. DOI: 10.1002/adma.201600560

(85) Hasz, K.; Hu, Z.; Park, K. D.; et al. Tip-Enhanced Dark Exciton Nanoimaging and Local Strain Control in Monolayer WSe_2. *Nano Lett* **2023**, *23* (1), 198-204. DOI: 10.1021/acs.nanolett.2c03959

(86) Schmidt, R.; Niehues, I.; Schneider, R.; et al. Reversible uniaxial strain tuning in atomically thin WSe_2. *2D Materials* **2016**, *3* (2). DOI: 10.1088/2053-1583/3/2/021011

(87) Hsu, W. T.; Lu, L. S.; Wang, D.; et al. Evidence of indirect gap in monolayer WSe_2. *Nat Commun* **2017**, *8* (1), 929. DOI: 10.1038/s41467-017-01012-6

(88) Kim, J. M.; Jeong, K. Y.; Kwon, S.; et al. Strained two-dimensional tungsten diselenide for mechanically tunable exciton transport. *Nat Commun* **2024**, *15* (1), 10847. DOI: 10.1038/s41467-024-55135-8

(89) Xiao, L.; Liu, Y.; Mohajerani, S. S.; et al. Quantum Light Funneling in Tailored Triangular Plasmonic Nanocavities. *ACS Nano* **2026**. DOI: 10.1021/acsnano.5c16988

(90) Branny, A.; Kumar, S.; Proux, R.; et al. Deterministic strain-induced arrays of quantum emitters in a two-dimensional semiconductor. *Nat Commun* **2017**, *8* (1), 15053. DOI: 10.1038/ncomms15053

(91) Peyskens, F.; Chakraborty, C.; Muneeb, M.; et al. Integration of single photon emitters in 2D layered materials with a silicon nitride photonic chip. *Nat Commun* **2019**, *10* (1), 4435. DOI: 10.1038/s41467-019-12421-0

(92) Errando-Herranz, C.; Scholl, E.; Picard, R.; et al. Resonance Fluorescence from Waveguide-Coupled, Strain-Localized, Two-Dimensional Quantum Emitters. *ACS Photonics* **2021**, *8* (4), 1069-1076. DOI: 10.1021/acsphotonics.0c01653

(93) Iff, O.; Buchinger, Q.; Moczala-Dusanowska, M.; et al. Purcell-Enhanced Single Photon Source Based on a Deterministically Placed WSe_2 Monolayer Quantum Dot in a Circular Bragg Grating Cavity. *Nano Lett* **2021**, *21* (11), 4715-4720. DOI: 10.1021/acs.nanolett.1c00978

(94) Frisenda, R.; Drüppel, M.; Schmidt, R.; et al. Biaxial strain tuning of the optical properties of single-layer transition metal dichalcogenides. *npj 2D Materials and Applications* **2017**, *1* (1). DOI: 10.1038/s41699-017-0013-7

(95) Aslan, B.; Deng, M.; Heinz, T. F. Strain tuning of excitons in monolayer WSe_2. *Physical Review B* **2018**, *98* (11). DOI: 10.1103/PhysRevB.98.115308

(96) Yuan, Z.; Kardynal, B. E.; Stevenson, R. M.; et al. Electrically driven single-photon source. *Science* **2002**, *295* (5552), 102-105. DOI: 10.1126/science.1066790

(97) Santori, C.; Fattal, D.; Vuckovic, J.; et al. Indistinguishable photons from a single-photon device. *Nature* **2002**, *419* (6907), 594-597. DOI: 10.1038/nature01086

(98) Michler, P.; Kiraz, A.; Becher, C.; et al. A quantum dot single-photon turnstile device. *Science* **2000**, *290* (5500), 2282-2285. DOI: 10.1126/science.290.5500.2282

(99) Strauf, S.; Michler, P.; Klude, M.; et al. Quantum optical studies on individual acceptor bound excitons in a semiconductor. *Phys Rev Lett* **2002**, *89* (17), 177403. DOI: 10.1103/PhysRevLett.89.177403

(100) Hsiao, T. K.; Rubino, A.; Chung, Y.; et al. Single-photon emission from single-electron transport in a SAW-driven lateral light-emitting diode. *Nat Commun* **2020**, *11* (1), 917. DOI: 10.1038/s41467-020-14560-1

(101) Rezus, Y. L.; Walt, S. G.; Lettow, R.; et al. Single-photon spectroscopy of a single molecule. *Phys Rev Lett* **2012**, *108* (9), 093601. DOI: 10.1103/PhysRevLett.108.093601

(102) Zhang, L.; Yu, Y. J.; Chen, L. G.; et al. Electrically driven single-photon emission from an isolated single molecule. *Nat Commun* **2017**, *8* (1), 580. DOI: 10.1038/s41467-017-00681-7

(103) Lounis, B.; Moerner, W. E. Single photons on demand from a single molecule at room temperature. *Nature* **2000**, *407* (6803), 491-493. DOI: 10.1038/35035032

(104) Doherty, M. W.; Manson, N. B.; Delaney, P.; et al. The nitrogen-vacancy colour centre in diamond. *Physics Reports* **2013**, *528* (1), 1-45. DOI: 10.1016/j.physrep.2013.02.001

(105) Brouri, R.; Beveratos, A.; Poizat, J. P.; et al. Photon antibunching in the fluorescence of individual color centers in diamond. *Opt Lett* **2000**, *25* (17), 1294-1296. DOI: 10.1364/ol.25.001294

(106) Kurtsiefer, C.; Mayer, S.; Zarda, P.; et al. Stable solid-state source of single photons. *Phys Rev Lett* **2000**, *85* (2), 290-293. DOI: 10.1103/PhysRevLett.85.290

(107) Linhart, L.; Paur, M.; Smejkal, V.; et al. Localized Intervalley Defect Excitons as Single-Photon Emitters in WSe_2. *Phys Rev Lett* **2019**, *123* (14), 146401. DOI: 10.1103/PhysRevLett.123.146401

(108) Kim, H.; Moon, J. S.; Noh, G.; et al. Position and Frequency Control of Strain-Induced Quantum Emitters in WSe_2 Monolayers. *Nano Lett* **2019**, *19* (10), 7534-7539. DOI: 10.1021/acs.nanolett.9b03421

(109) Parto, K.; Azzam, S. I.; Banerjee, K.; et al. Defect and strain engineering of monolayer WSe_2 enables site-controlled single-photon emission up to 150 K. *Nat Commun* **2021**, *12* (1), 3585. DOI: 10.1038/s41467-021-23709-5

(110) Zheng, Y. J.; Chen, Y.; Huang, Y. L.; et al. Point Defects and Localized Excitons in 2D WSe_2. *ACS Nano* **2019**, *13* (5), 6050-6059. DOI: 10.1021/acsnano.9b02316

(111) Barja, S.; Refaely-Abramson, S.; Schuler, B.; et al. Identifying substitutional oxygen as a prolific point defect in monolayer transition metal dichalcogenides. *Nat Commun* **2019**, *10* (1), 3382. DOI: 10.1038/s41467-019-11342-2

(112) Dang, J.; Sun, S.; Xie, X.; et al. Identifying defect-related quantum emitters in monolayer WSe_2. *npj 2D Materials and Applications* **2020**, *4* (2). DOI: 10.1038/s41699-020-0136-0

(113) Luo, Y.; Liu, N.; Kim, B.; et al. Exciton Dipole Orientation of Strain-Induced Quantum Emitters in WSe_2. *Nano Lett* **2020**, *20* (7), 5119-5126. DOI: 10.1021/acs.nanolett.0c01358

(114) Serati de Brito, C.; Rosa, B. L. T.; Chaves, A.; et al. Probing the Nature of Single-Photon Emitters in a WSe_2 Monolayer by Magneto-Photoluminescence Spectroscopy. *Nano Lett* **2024**, *24* (42), 13300-13306. DOI: 10.1021/acs.nanolett.4c03686

(115) Yang, L.; Yuan, Y.; Fu, B.; et al. Revealing broken valley symmetry of quantum emitters in WSe_2 with chiral nanocavities. *Nat Commun* **2023**, *14* (1), 4265. DOI: 10.1038/s41467-023-39972-7

(116) Paralikis, A.; Wyborski, P.; Metuh, P.; et al. Tunable and Low-Noise WSe_2 Quantum Emitters for Quantum Photonics. *PRX Quantum* **2025**, *6* (4). DOI: 10.1103/cynh-ql3j

(117) Loudon, R. *The Quantum Theory of Light*; Oxford University Press, 2000.

(118) Glauber, R. J. The Quantum Theory of Optical Coherence. *Physical Review* **1963**, *130* (6), 2529-2539. DOI: 10.1103/PhysRev.130.2529

(119) Planck, M. Über das Gesetz der Energieverteilung im Normalspektrum. *Annalen der Physik* **1901**, *4*, 553-563.

(120) Planck, M. Zur Theorie des Gesetzes der Energieverteilung im Normalspektrum. *Annalen der Physik* **1900**, *4*, 553-563.

(121) Ye, Y.; Dou, X.; Ding, K.; et al. Single photon emission from deep-level defects in monolayer WSe_2. *Physical Review B* **2017**, *95* (24). DOI: 10.1103/PhysRevB.95.245313

(122) Rosenberger, M. R.; Dass, C. K.; Chuang, H. J.; et al. Quantum Calligraphy: Writing Single-Photon Emitters in a Two-Dimensional Materials Platform. *ACS Nano* **2019**, *13* (1), 904-912. DOI: 10.1021/acsnano.8b08730

(123) Xu, D. D.; Vong, A. F.; Lebedev, D.; et al. Conversion of Classical Light Emission from a Nanoparticle-Strained WSe_2 Monolayer into Quantum Light Emission via Electron Beam Irradiation. *Adv Mater* **2023**, *35* (5), e2208066. DOI: 10.1002/adma.202208066

(124) Lan, H. Y.; Lin, C. P.; Liu, L.; et al. Uncovering the doping mechanism of nitric oxide in high-performance P-type WSe_2 transistors. *Nat Commun* **2025**, *16* (1), 4160. DOI: 10.1038/s41467-025-59423-9

(125) Zhao, Y.; Tripathi, M.; Cernevics, K.; et al. Electrical spectroscopy of defect states and their hybridization in monolayer MoS_2. *Nat Commun* **2023**, *14* (1), 44. DOI: 10.1038/s41467-022-35651-1

(126) Edelberg, D.; Rhodes, D.; Kerelsky, A.; et al. Approaching the Intrinsic Limit in Transition Metal Diselenides via Point Defect Control. *Nano Lett* **2019**, *19* (7), 4371-4379. DOI: 10.1021/acs.nanolett.9b00985

(127) Liu, S.; Liu, Y.; Holtzman, L.; et al. Two-Step Flux Synthesis of Ultrapure Transition-Metal Dichalcogenides. *ACS Nano* **2023**, *17* (17), 16587-16596. DOI: 10.1021/acsnano.3c02511

(128) Holbrook, M.; Holtzman, L. N.; Hou, B.; et al. Revealing Substitutional Oxygen as the Dominant Defect in Flux-Grown Transition Metal Diselenides. *Nano Lett* **2025**, *25* (37), 13795-13801. DOI: 10.1021/acs.nanolett.5c03126

(129) Luo, Y.; Liu, N.; Li, X.; et al. Single photon emission in WSe_2 up to 160 K by quantum yield control. *2D Materials* **2019**, *6* (3). DOI: 10.1088/2053-1583/ab15fe

(130) Utama, M. I. B.; Zeng, H.; Sadhukhan, T.; et al. Chemomechanical modification of quantum emission in monolayer WSe_2. *Nat Commun* **2023**, *14* (1), 2193. DOI: 10.1038/s41467-023-37892-0

(131) Zhao, Y.; Gali, S. M.; Wang, C.; et al. Molecular Functionalization of Chemically Active Defects in WSe_2 for Enhanced Opto-Electronics. *Advanced Functional Materials* **2020**, *30* (45). DOI: 10.1002/adfm.202005045

(132) Ananth, R.; Utama, M. I. B.; Xu, D. D.; et al. Enhanced spectral purity of WSe_2 quantum emitters via conformal organic adlayers. *Sci Adv* **2025**, *11* (40), eady7557. DOI: 10.1126/sciadv.ady7557

(133) Guo, S.; Germanis, S.; Taniguchi, T.; et al. Electrically Driven Site-Controlled Single Photon Source. *ACS Photonics* **2023**, *10* (8), 2549-2555. DOI: 10.1021/acsphotonics.3c00097

(134) So, J. P.; Kim, H. R.; Baek, H.; et al. Electrically driven strain-induced deterministic single-photon emitters in a van der Waals heterostructure. *Sci Adv* **2021**, *7* (43), eabj3176. DOI: 10.1126/sciadv.abj3176

(135) Shepard, G. D.; Ajayi, O. A.; Li, X.; et al. Nanobubble induced formation of quantum emitters in monolayer semiconductors. *2D Materials* **2017**, *4* (2). DOI: 10.1088/2053-1583/aa629d

(136) Stevens, C. E.; Chuang, H. J.; Rosenberger, M. R.; et al. Enhancing the Purity of Deterministically Placed Quantum Emitters in Monolayer WSe_2. *ACS Nano* **2022**, *16* (12), 20956-20963. DOI: 10.1021/acsnano.2c08553

(137) Abramov, A. N.; Chestnov, I. Y.; Alimova, E. S.; et al. Photoluminescence imaging of single photon emitters within nanoscale strain profiles in monolayer WSe_2. *Nat Commun* **2023**, *14* (1), 5737. DOI: 10.1038/s41467-023-41292-9

(138) Chang, S.; Yan, Y.; Geng, Y. Local Nanostrain Engineering of Monolayer MoS_2 Using Atomic Force Microscopy-Based Thermomechanical Nanoindentation. *Nano Lett* **2023**, *23* (20), 9219-9226. DOI: 10.1021/acs.nanolett.3c01809

(139) Li, X.; Jones, A. C.; Choi, J.; et al. Proximity-induced chiral quantum light generation in strain-engineered $WSe_2/NiPS_3$ heterostructures. *Nat Mater* **2023**, *22* (11), 1311-1316. DOI: 10.1038/s41563-023-01645-7

(140) Cunningham, P. D.; Proscia, N. V.; LaGasse, S. W.; et al. Site-Specific Exciton–Plasmon Coupling in Nanoindented WSe_2. *ACS Photonics* **2024**, *11* (8), 3250-3258. DOI: 10.1021/acsphotonics.4c00644

(141) Yücel, O.; Yagodkin, D.; Kirchhof, J. N.; et al. Strain activation of localized states in WSe_2. *2D Materials* **2025**, *12* (3). DOI: 10.1088/2053-1583/add414

(142) Peng, L.; Chan, H.; Choo, P.; et al. Creation of Single-Photon Emitters in WSe_2 Monolayers Using Nanometer-Sized Gold Tips. *Nano Lett* **2020**, *20* (8), 5866-5872. DOI: 10.1021/acs.nanolett.0c01789

(143) Qian, Q.; Peng, L.; Perea-Lopez, N.; et al. Defect creation in WSe_2 with a microsecond photoluminescence lifetime by focused ion beam irradiation. *Nanoscale* **2020**, *12* (3), 2047-2056. DOI: 10.1039/c9nr08390a

(144) Klein, J.; Lorke, M.; Florian, M.; et al. Site-selectively generated photon emitters in monolayer MoS_2 via local helium ion irradiation. *Nat Commun* **2019**, *10* (1), 2755. DOI: 10.1038/s41467-019-10632-z

(145) Hecht, L. N. a. B. *Principles of Nano-Optics*; Cambridge University Press, 2012.

(146) Azzam, S. I.; Parto, K.; Moody, G. Purcell enhancement and polarization control of single-photon emitters in monolayer WSe_2 using dielectric nanoantennas. *Nanophotonics* **2023**, *12* (3), 477-484. DOI: 10.1515/nanoph-2022-0628

(147) Sortino, L.; Zotev, P. G.; Phillips, C. L.; et al. Bright single photon emitters with enhanced quantum efficiency in a two-dimensional semiconductor coupled with dielectric nano-antennas. *Nat Commun* **2021**, *12* (1), 6063. DOI: 10.1038/s41467-021-26262-3

(148) So, J. P.; Jeong, K. Y.; Lee, J. M.; et al. Polarization Control of Deterministic Single-Photon Emitters in Monolayer WSe_2. *Nano Lett* **2021**, *21* (3), 1546-1554. DOI: 10.1021/acs.nanolett.1c00078

(149) Noori, Y. J.; Cao, Y.; Roberts, J.; et al. Photonic Crystals for Enhanced Light Extraction from 2D Materials. *ACS Photonics* **2016**, *3* (12), 2515-2520. DOI: 10.1021/acsphotonics.6b00779

(150) Duong, N. M. H.; Xu, Z.-Q.; Kianinia, M.; et al. Enhanced Emission from WSe_2 Monolayers Coupled to Circular Bragg Gratings. *ACS Photonics* **2018**, *5* (10), 3950-3955. DOI: 10.1021/acsphotonics.8b00865

(151) Iff, O.; Davanco, M.; Betzold, S.; et al. Hyperspectral study of the coupling between trions in WSe_2 monolayers to a circular Bragg grating cavity. *C R Phys* **2021**, *22* (Suppl 4). DOI: 10.5802/crphys.76

(152) Hekmati, R.; Hadden, J. P.; Mathew, A.; et al. Bullseye dielectric cavities for photon collection from a surface-mounted quantum-light-emitter. *Sci Rep* **2023**, *13* (1), 5316. DOI: 10.1038/s41598-023-32359-0

(153) Strasbourg, M. C.; Yanev, E. S.; Darlington, T. P.; et al. Characterization of quantum dot-like emitters in programmable arrays of nanowrinkles of 1L-WSe_2. *Journal of Applied Physics* **2024**, *136* (4). DOI: 10.1063/5.0214410

(154) Bennett, C. H.; Brassard, G. Quantum cryptography: Public key distribution and coin tossing. *Theoretical Computer Science* **2014**, *560*, 7-11. DOI: 10.1016/j.tcs.2014.05.025

CHAPTER 2

METHODS

For the research done in this dissertation, nanophotonic structures are lithographically fabricated and modeled, monolayer 2D materials are exfoliated and transferred, and the light-matter interactions of the hybrid systems are studied using various spectroscopic techniques. Here, the methods and techniques used throughout this dissertation are described with detailed discussion, in-process images, and various figures to aid in the understanding and replication of results. Each section of this chapter also contains a short motivation/historical summary of the technique to add context alongside references to the specific research chapter in which the technique was used.

2.1 Exfoliation Techniques

Van der Waals (vdW) materials are a unique subset of layered materials held together by strong in-plane chemical bonds and weak out-of-plane vdW forces. These weak vdW forces allow for facile exfoliation of the layered materials using Scotch tape, first conducted in 2004 by Novoselov *et al.*[1-4]. This initial finding helped develop the field of 2D materials research and inspired future scientists to expand on the technique by using surface treatments, Au, and polymers. In this dissertation, every sample fabricated required the exfoliation of 2D materials.

2.1.1 Scotch Tape Exfoliation

The most used technique for exfoliation is Scotch tape exfoliation[5-8]. Scotch tape exfoliation is facilitated through the fabrication of a master tape (Figure 2.1.1). A master tape is a piece of Scotch tape that has a large amount of bulk crystal attached to it, which has been thinned

out to spread across a larger area of the tape. To make a master tape, a thin line of bulk material is attached to a long piece of tape. Then, by sticking the tape together and pulling it apart, that line is propagated along the tape. By progressively moving the line of bulk material along the tape, a uniform layer is generated.

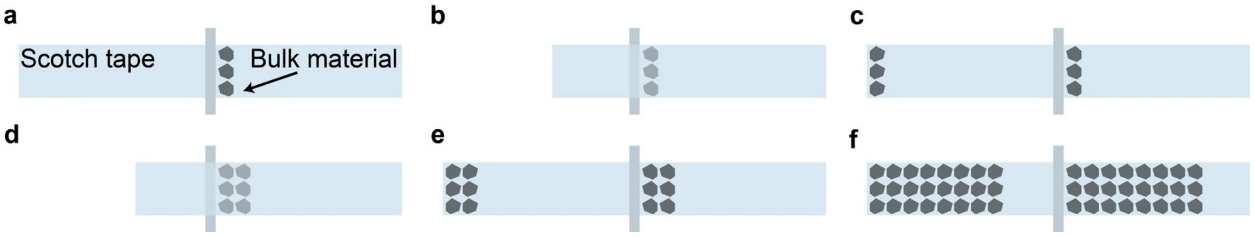


Figure 2.1.1: Generation of a master tape for exfoliation. (a) A long piece of Scotch tape is attached to a flat surface, adhesive side up, and a thin line of bulk 2D material is pressed onto the tape. (b) The other side of the Scotch tape is pressed onto the bulk 2D material. (c) The two sides of the tape are separated, and the line of 2D material is thinned and propagated to the other side. (d) The line of 2D material is spread across the tape, effectively doubling the covered area. (e) The tape is separated, and the 2D material is further thinned. (f) Steps (b) - (e) are repeated to create a large area of exposed and thinned 2D material for exfoliation.

Once the master tape is made, copy tapes are pulled from the master for individual exfoliation runs. The process of Scotch tape exfoliation is schematically detailed in Figure 2.1.2. First, SiO_2 chips are progressively sonicated in acetone, IPA, and deionized water (DIW) for 5 minutes each to remove debris and are thoroughly dried with a stream of N_2. Next, the chips are treated in an ~10 min O_2 plasma. This plasma treatment does two important things to the SiO_2 surface: it increases the surface energy of the SiO_2 by increasing the presence of hydroxyl groups[9, 10], and eliminates organic surface contaminants. The hydroxyl groups readily adhere to 2D materials and increase the yield of monolayer exfoliation[4]. Quickly after the chips are removed from the plasma treatment, the copy tape is pressed onto the SiO_2 surface. Uniform contact is made between the crystallites on the copy tape and the SiO_2 surface using light pressure, applied by a

large Q-Tip. Systematic studies on the outcome of exfoliation have shown that at this stage, small air/water bubbles are trapped between the SiO_2 surface and 2D crystallites[4]. To alleviate this issue, the SiO_2 substrates with the copy tape attached are placed on a 100 °C hotplate for ~2 minutes and then cooled to room temperature (to reduce tape residue) before slowly removing the copy tape.

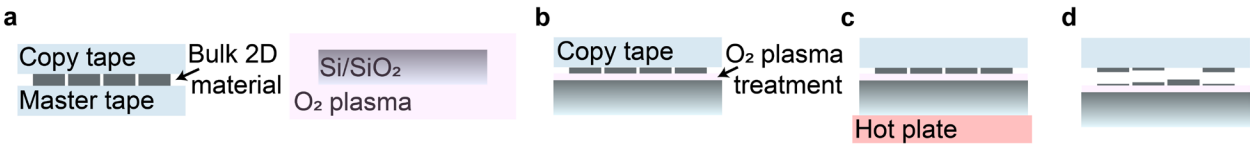


Figure 2.1.2: Scotch tape exfoliation. (a) A copy tape is attached to a pre-made master tape while cleaned Si/SiO_2 substrates are in an O_2 plasma for ~10 mins. (b) Once the Si/SiO_2 substrates have been treated in O_2 plasma, the copy tape is removed from the master tape and adhered to the O_2 plasma-treated SiO_2 surface. (c) The substrate and copy tape were placed onto a 100 °C hotplate for ~ 90 s to increase the contact area. (d) After cooling for another ~ 90 s, the copy tape is slowly removed, leaving behind exfoliated 2D material on the SiO_2 surface.

The outcome of Scotch tape exfoliation is probabilistic. Since the adhesion between the SiO_2 and 2D material surface is comparable to the interlayer adhesion of the 2D material at ~0.48 Jm^{-2}, there is an equal likelihood of obtaining any random flake number as there are monolayer flakes[11, 12]. Figure 2.1.3 represents this probabilistic nature by showing a wide-area optical micrograph of a WSe_2 sample made using Scotch tape exfoliation. With these camera settings, white flakes are thick ($t > 100$ nm), blue flakes are of intermediate thickness (3 nm $< t < 100$ nm), and brown flakes are thin ($t < 3$ nm). Also present in these images is tape residue. Tape residue manifests in various colors and shapes, but generally has a perimeter that appears amorphous, and different colors within the tape residue will follow soft contours rather than rigid lines.

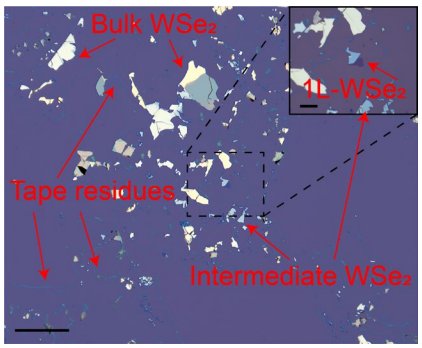


Figure 2.1.3: Optical micrograph of exfoliated WSe_2 on a SiO_2 surface. Optical micrograph of WSe_2 exfoliated on a SiO_2 surface with labels highlighting relative flake thickness (bulk, intermediate, and monolayer) and tape residues (scale bar = 100 μm). The inset is a higher resolution image of the indicated region containing a monolayer WSe_2 crystallite (scale bar = 20 μm).

2.1.2 Gel-Assisted Exfoliation

Gel-assisted exfoliation is another exfoliation technique that is used for 2D material exfoliation on non-rigid substrates such as polydimethylsiloxane (PDMS), polymethyl acrylate (PMMA), and other polymers. In this dissertation, gel-assisted exfoliation is used in Chapter 4 to produce 2D material flakes directly on PDMS that can be transferred onto different substrates deterministically, as discussed in the 2D material transferring subsection of this Chapter, and is also used to further exfoliate from PDMS onto PMMA in Chapters 3 and 5. Traditional Scotch tape exfoliation onto polymer surfaces leaves large amounts of tape residue and can create defects in the polymer surface. To avoid these pitfalls, Nitto tape is used as a copy tape rather than Scotch tape. Nitto tape is a pressure-sensitive tape commonly used in micro- and nanofabrication facilities for wafer processing. Nitto tape has lower adhesion than Scotch tape and does not leave behind much residue, making it an ideal candidate for gel-assisted exfoliation.

Exfoliation of 2D materials onto PDMS closely resembles that of Scotch tape exfoliation (Figure 2.1.4). First, a master tape is made following Figure 2.1.1, on Scotch tape, and then a copy

tape is made using Nitto tape. Afterwards, the PDMS surface is prepared using a light UV ozone treatment (~2 mins) to create dangling siloxane groups on the surface of the PDMS. These dangling bonds serve the same purpose as the hydroxyl groups made on the SiO_2 surface from O_2 plasma treatment, but PDMS is more delicate, and an O_2 plasma will crack and degrade the surface. Once the PDMS is removed from the UV ozone, the copy tape is adhered to the surface, and uniform contact is made through the gentle pressure of a Q-tip. Afterwards, the copy tape is removed, and 2D material flakes are left behind on the PDMS.

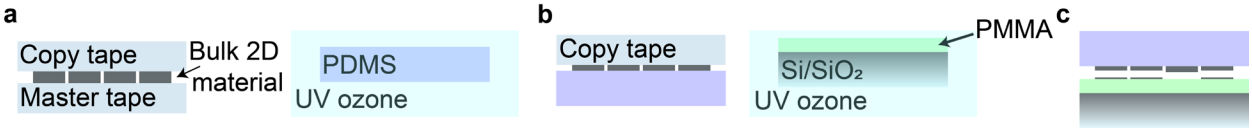


Figure 2.1.4: Gel-assisted exfoliation. (a) A Nitto copy tape is attached to a pre-made master tape while a PDMS substrate is in UV ozone for ~2 mins. (b) The Nitto copy tape is attached to the UV ozone-treated PDMS, while a PMMA substrate is in UV ozone for ~ 2 mins. (c) The PDMS copy tape is attached to the UV ozone-treated PMMA and slowly removed to exfoliate 2D flakes.

For Chapter 4 of this dissertation, 2D material flakes on PDMS were the goal for transferring deterministically onto nanostructures, and in that case, the exfoliation procedure stops here, but for 2D materials on PMMA, the PDMS is now used as a copy tape for further exfoliation. PMMA substrates are made by spin coating A4 PMMA onto cleaned SiO_2 chips at 1500 rpm for 2 minutes. Afterwards, the PMMA is hard baked to remove most of the solvent in the polymer matrix, on an 80 °C hotplate for 40 minutes, adding rigidity to the ~400 nm thick PMMA layer. Next, the PMMA is treated in UV ozone for 2 minutes, and the PDMS copy tape is adhered with light pressure and then removed. Now, 2D materials are deposited onto the PMMA surface and are ready for their application. In the case of Chapters 3 and 5, these flakes are used for nanoindentation. One observation made over many trials of Scotch tape and gel-assisted

exfoliation is that gel-assisted exfoliation yields an overall lower quantity of flakes, but the relative proportion of flakes that are monolayer is significantly higher[13].

2.1.3 Gold-Assisted Exfoliation

As the field of 2D materials developed and the need for wafer-scale fabrication efforts became desired, research efforts were put into large-area exfoliation. Wafer-scale growth of monolayer TMDs using chemical vapor deposition (CVD) quickly emerged[14-17], however, CVD-grown crystallites have significant downsides, including being multi-crystalline, intrinsically doped, and containing high chalcogen defect densities, leading to less desirable electronic and optical properties. To address these shortcomings, gold-assisted exfoliation techniques were developed in 2018[18-20]. Gold-assisted exfoliation enables the use of chemical vapor transport (CVT) or flux-grown TMDs for large-scale applications, resolving the defect density issue with CVD-grown TMDs. By generating crystal-sized monolayer flakes (~ 1cm^2) with comparable properties to Scotch tape exfoliated monolayers, Au-assisted exfoliation became the leading technique for high-quality, large-scale monolayer exfoliation. For this reason, Au-assisted exfoliation was used in the work of this dissertation for prototyping samples, where the marginal decrease in material quality was not important in comparison to the decrease in time required to obtain monolayers.

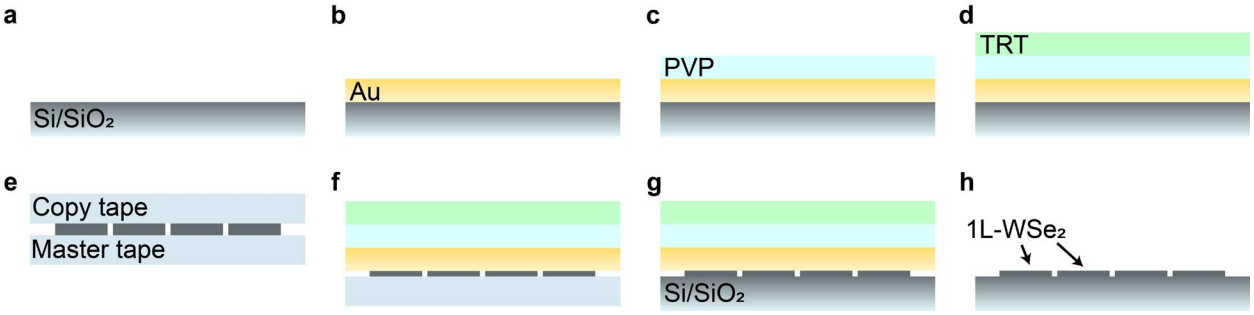


Figure 2.1.5: Gold-assisted exfoliation. (a) A Si/SiO_2 substrate is thoroughly cleaned. (b) A ~50 nm thick Au layer is deposited using electron beam evaporation at 2A/s. (c) 7 wt% PVP is spun onto the Au surface at 2000 rpm for 7 mins to evaporate most of the DIW in solution. (d) TRT is attached to the PVP surface. (e) A Nitto copy tape is prepared. (f) Moving quickly to avoid Carbon contamination of the Au surface, the TRT/PVP/Au membrane is removed, and the copy tape is adhered. (g) The copy tape is removed from the TRT/PVP/Au/WSe_2 membrane and adhered to a clean Si/SiO_2 substrate. (h) The sample is heated to 140 °C to delaminate the TRT, soaked in DIW for ~ 5 minutes to remove the PVP, and etched in KI/I_2 for ~ 60 s to remove excess Au. Afterwards, the sample is rinsed in DIW and dried with a N_2 gun, leaving behind mostly 1L-WSe_2.

Within the field, there are two general types of Au-assisted exfoliation. One technique, which will not be discussed in detail, involves using the Au layer as a substrate for the TMD, generating nanoscale bubbles that act as background-free quantum light sources[21-24]. The more robust technique generates large monolayer areas on SiO_2 that can be manipulated and transferred like flakes exfoliated using the Scotch tape method. Most commercial sellers of TMD material now sell special bulk crystals made for Au-assisted exfoliation due to their flat crystal faces[25, 26]. Using one of these specialized crystals increases the yield of Au-assisted monolayers. The outline for this method of Au-assisted exfoliation is shown in Figure 2.1.5. First, a master tape consisting of Nitto tape and a piece of bulk TMD material is made. Afterwards, another piece of Nitto tape (copy tape) is then placed over the master tape, but not removed until later to avoid excessive contamination of the cleaved 2D material that will contact the Au. To prepare the Au, a thin (~50 nm) layer is deposited onto a clean and polished SiO_2 surface. Without deposition of an adhesion

layer, the adhesion between the Au and SiO_2 is weak, permitting the Au to be easily removed; however, a 50 nm thick Au layer needs added rigidity to be handled. By spin coating a layer of 7 wt% polyvinylpyrrolidone (PVP) in DIW onto the Au surface for 7 minutes at 2000 rpm and attaching a piece of thermal release tape (TRT) to the polymer surface, the Au layer is given a surface to adhere to after it is removed from the SiO_2. Acting quickly to avoid carbon contamination of the Au layer[27], the Au is removed from the SiO_2 using upwards pressure on the TRT, and the TMD copy tape is removed from the master and placed into contact with the Au surface. Light pressure is applied to the copy tape to ensure uniform contact, and then the copy tape is removed.

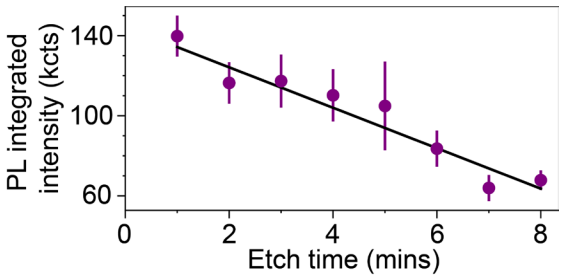


Figure 2.1.6: PL intensity degradation with extended KI/I_2 etch times. Plot showing the integrated PL intensity of gold-assisted monolayers, generated using the same master tape, as a function of KI/I_2 etch time. Data points represent an average intensity acquired from hyperspectral imaging of monolayer flakes.

With the copy tape removed, Au remains on the PVP / TRT stack where the TMD material was present on the copy tape. If there appears to be a large amount of bulk TMD material remaining on the PVP / TRT, the Au surface was likely too rough, or the copy tape and Au were not brought into contact quickly enough. These are common problems with Au-assisted exfoliation. Decreasing surface roughness is one way to address failed monolayer isolation. This is because the large 2D material face has a reduced contact area with the Au when the surface is rougher, bringing the

exfoliation back into a more probabilistic regime rather than deterministic. Addressing surface roughness by cleaning the SiO_2 or preparing a smoother Au layer using electron beam evaporation or magnetron / ion-beam sputtering can be beneficial. Research has found that the ideal Au film roughness for exfoliation of monolayers is sub-nanometer[19, 20].

If the TMDC / Au / PVP / TRT stack looks correct (as detailed above), it is brought into contact with a cleaned SiO_2 chip. To remove the extra layers, the sample is heated on a hotplate to 140 °C to remove the TRT, soaked in DIW (~5 mins) to remove the PVP, and etched in KI/I_2 (~60 s) to remove the Au. Over-etching of the sample in KI/I_2 leads to degradation of the optical properties of TMDs, as seen in Figure 2.1.6. After a thorough rinse in DIW, large monolayer crystallites are left behind on the SiO_2 surface. Figure 2.1.7 shows an optical microscopy image of different 1L-WSe_2 flakes obtained using Au-assisted exfoliation. Tears and fractures are common in Au-assisted flakes due to non-uniform contact between the TMD and Au layer, but flakes generated using this technique on average are ~ 1000x larger in area than those found using Scotch tape exfoliation.

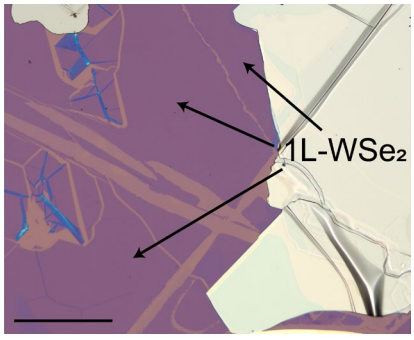


Figure 2.1.7: Optical micrograph of 1L-WSe_2 obtained using gold-assisted exfoliation. Optical micrograph showing the large-area exfoliation of 1L-WSe_2 generated using gold-assisted exfoliation (scale bar = 100 μm).

2.2 Lithography Techniques for Nanophotonic Stressor Fabrication

Tensile strain plays a critical role in the development of single-photon emitters (SPEs) in monolayer WSe_2 (1L-WSe_2), making the engineering and fabrication of stressors an important step in producing quantum light sources. In Chapters 3 and 5 of this dissertation, SPEs are deterministically patterned into 1L-WSe_2 using nanoindentation, an imprint lithography conjugate. While in Chapter 4, an emergent lithography technique, thermal scanning probe lithography (TSPL), is used to fabricate arrays of Au nanoantennas embedded into SiO_2 cavities that strain 1L-WSe_2 when draped over their tips, while also enhancing the quantum yield of the single photon states through the nanoantennas' localized surface plasmon resonance. Here, the different fabrication protocols for these two different types of nanophotonic stressors are discussed, and optical lithography (lift-off) is reviewed for added context.

The simplest lithography technique, optical lithography, was originally developed for use in printing presses, engravings, and early circuits. Lithography, as a general term, was adopted from printers by treating areas of a surface to repel ink, leaving behind a deterministic pattern. In 1959, optical lithography was conceived using UV light and a photosensitive polymer resist for use in Si transistors. Nearly a decade later, in the late 1960's, a different polymer layer, PMMA, was found to act as a lithographic masking material under electron bombardment, advancing lithography beyond the diffraction limit. With the newly found versatility of lithographic fabrication techniques, more niche lithography methods such as imprint lithography, scanning probe lithography, and colloidal lithography gained traction. In the context of quantum light sources in TMDs, lithography is widely used to fabricate pillars[28-31], photonic resonators[32-35],

plasmonic colloidal dispersions[36-39], and surface acoustic wave devices[40, 41] to generate, enhance, or study single photon states.

2.2.1 Optical Lithography

Optical lithography is a top-down approach to nanofabrication based on spin coating a photosensitive polymer resist onto a substrate while using a mask to control the areas of the resist that are exposed to UV light. Masks for optical lithography are pre-determined quartz, soda-lime, or Mylar plates that have transparent windows to permit exposure of the resist. The properties of a resist polymer are traditionally defined as either positive or negative, depending on whether the resist degrades (positive) or polymerizes (negative) under UV exposure.

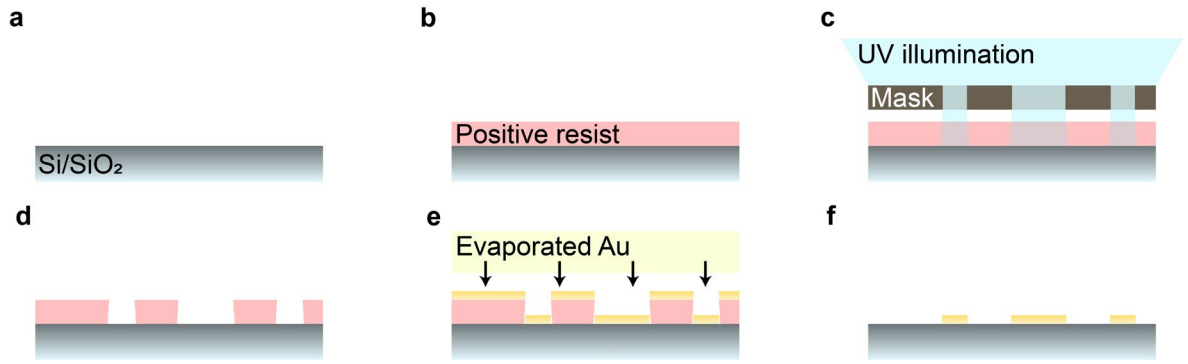


Figure 2.2.1: Optical lithography (lift-off). (a) A Si/SiO_2 substrate is cleaned. (b) Positive photoresist is spun onto the Si/SiO_2 substrate. (c) A mask is brought near the resist surface and is illuminated by UV light. Transparent regions of the mask permit exposure in regions of the resist. (d) Development removes regions of the resist that were exposed in (c). (e) Cr or Ti/Au is evaporated onto the sample surface using an electron beam evaporator. (f) The resist layer and excess Cr or Ti/Au are removed by dissolving the resist in Acetone.

The fabrication procedure for optical lithography and lift-off using a positive resist is shown in Figure 2.2.1. Lift-off is a common adaptation to lithographic fabrication where a layer of material is deposited onto the resist surface after patterning the resist using UV light and

chemical development. Once the material is deposited, it adheres to the substrate where the resist layer was washed away, and the excess resist and material are “lifted off” of the substrate using solvents (acetone, AZ Kwik Strip).

2.2.2 Thermal Scanning Probe Lithography

Thermal scanning probe lithography (TSPL) is a nanoscale lithography technique based on using an atomic force microscopy (AFM) tip with a small Ohmic circuit to induce Joule heating, elevating the tip temperature to up to 1400 °C. With this hot tip, patterns are written into polymer layers at length scales commensurate with the radius of curvature of the tip apex (~10 nm). TSPL has been shown to have a wide variety of applications, including making molds for nanoimprint lithography, masks for deep ion etching, cutting and patterning 2D materials, surface cleaning, and 3D substrate patterning[42, 43].

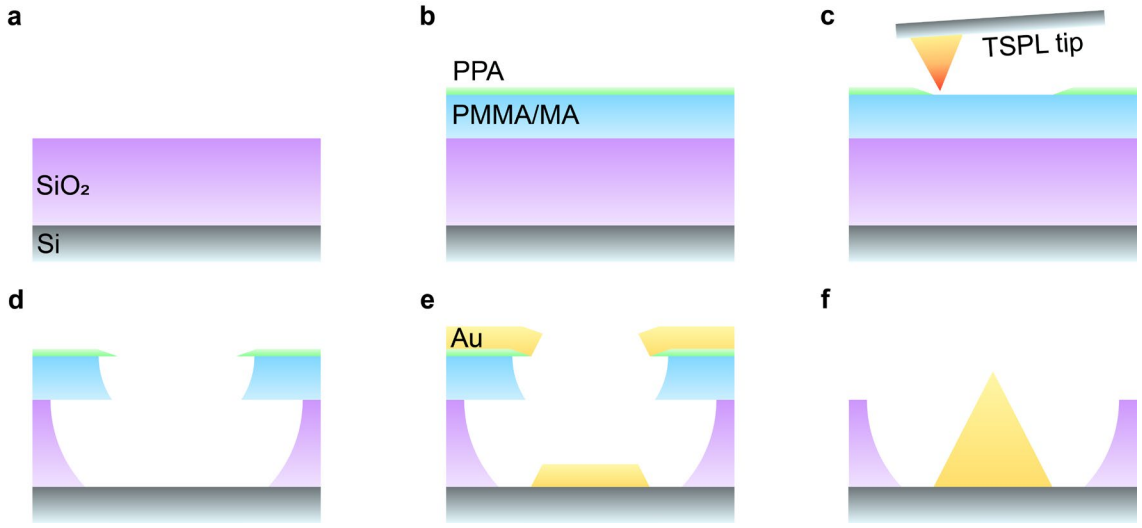


Figure 2.2.2: Fabrication of embedded nanoantennas using TSPL. (a) A Si/SiO_2 substrate is cleaned. (b) A Bilayer polymer resist is spun onto the surface of the SiO_2. (c) TSPL is done on the PPA to generate a mask. (d) The underlying PMMA/MA and SiO_2 are etched in sonicated IPA/DIW and 6:1 BOE, respectively. (e) Cr/Au is deposited onto the PPA surface with a normal angle of incidence. Normal deposition begins to form a leading edge of convergence. (f) Once the nanoantenna is fully formed from the converging leading edge, the resists and excess Cr/Au are removed in Acetone.

2.2.3 Fabrication of Embedded Plasmonic Nanoantennas Using TSPL

TSPL was used in this dissertation to fabricate the embedded plasmonic nanoantennas found in Chapter 4. Figure 2.2.2 shows the fabrication procedure for embedded plasmonic nanoantennas. To prepare the SiO_2 surface for TSPL, the chips are sonicated in acetone, IPA, and DIW for 5 minutes each to remove surface contamination. Afterwards, chips are dried using a stream of N_2 gas and baked at 150 °C on a hotplate for ~60 s to dehydrate the surface. A polymer bilayer is then spun onto the cleaned SiO_2 surface. The first layer of the bilayer is polymethyl methacrylate-co-methacrylic acid (PMMA/MA) (3% volume ratio in propylene glycol monomethyl ether (PGME)) and is spun onto the surface at 6000 rpm for 60 s, followed by an immediate bake on a 180 °C hotplate for 90 s. Next, a polyphthalamide (PPA) (2% volume ratio

in anisole) was spun on top of the PMMA/MA at 6000 rpm for 120 s, followed by a bake on a 110 °C hotplate for 120 s.

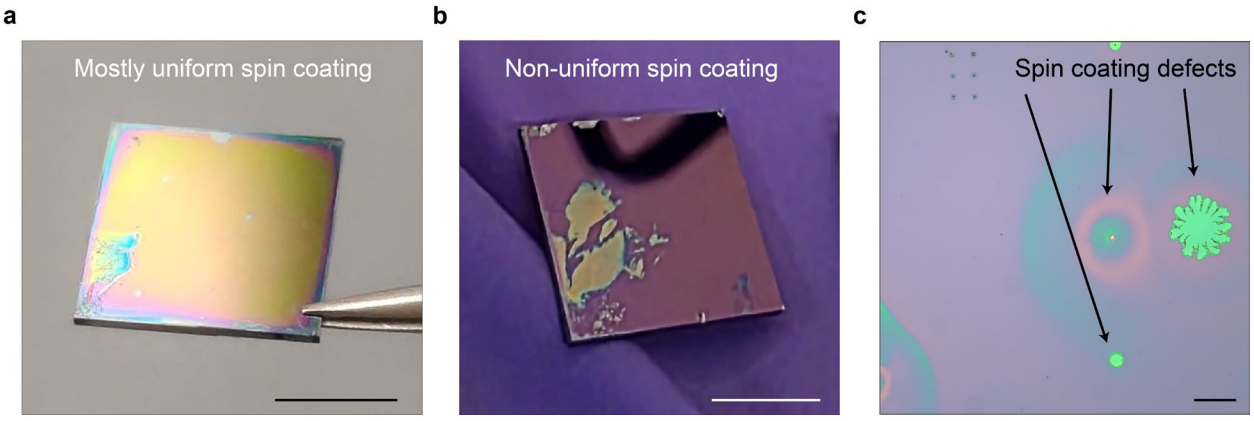


Figure 2.2.3: Polymer uniformity after spin coating. (a) Image showing a mostly uniform bilayer spin coat. Uniformity is visually validated as a consistent color gradient from the center to the edge of the sample. At the edge of the sample, polymer that was not ejected during spin coating accumulates, forming a thicker edge, hence the larger color gradient. The defect in the bottom left of the chip is a tweezer mark. (b) Image of a non-uniform spin coat. Here, the substrate surface was not properly cleaned and dehydrated. This resulted in a low surface energy that repelled much of the polymer during spin coating, leaving only a small area of the chip with polymer coverage of an unknown thickness. (c) Microscope image of a uniform polymer spin coat highlighting microscopic defects. Despite the uniform appearance of (a), since this spin coating is not done in a cleanroom, dust particles still accumulate on the surface between cleaning and spin coating, leaving behind defects (comets) in the polymer surface. Scale bars in (a-b) are 500 mm, and in (c) are 200 μm.

After each polymer layer was spun on, the condition of the film was checked for uniformity, meaning that there should be a smooth gradient of color from the center of the chip to the edges as seen in Figure 2.2.3a. Because of thin-film interference, the color may change across the sample, but a smooth transition indicates a near-uniform spin coat. As seen in Figure 2.2.3c, sometimes small dust particles can cause comets in the spin of a polymer layer, but as long as these make up only a small fraction of the sample, TSPL can be conducted away from the comets. What is more concerning is a fully non-uniform spin, as seen in Figure 2.2.3b. When this occurs, the overall

polymer thickness varies greatly from the measured spin curves, making wet etching times unreliable and the sample unusable.

TSPL was then conducted on the PPA surface with a write temperature set between 950 – 1000 °C with a write depth of 60 nm. Here, the heated tip ablates through the PPA surface, directly writing a mask for further development steps. The PMMA/MA layer acts as a buffer for the tip. Since PMMA/MA is more robust and does not ablate at the operation temperatures of the tip, it protects the tip apex when the write depth is deeper than the PPA thickness. 60 nm was chosen as the write depth to ensure that the tip apex would write all the way through the ~45 nm thick PPA layer. To obtain high-resolution writing, the pixel size of each bitmap used was set to 10 nm, commensurate with the expected radius of curvature of the TSPL tip. For hole arrays, the tip is required to dip in and out of contact with the polymer surface quickly and frequently. This can cause elongation of the pattern due to the tips' comparatively slow vertical motion. To rectify this issue, the tip cantilever parameters were optimized to a pretension voltage of 1.5 V, pretension time of 5 μs, and tip-sample height of 200-225 nm. These settings bring the apex of the tip closer to the surface during TSPL, allowing for a faster response of the tip.

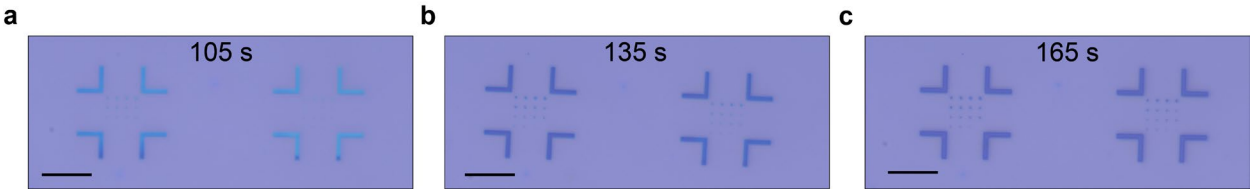


Figure 2.2.4: Polymer development after TSPL. (a) Microscope image showing two TSPL patterns after 105 s of development. The color of the patterns at this time is inconsistent, reflecting that development has not fully etched down to the substrate. (b) Microscope image of the same patterns in (a), but now after 135 s. The color is now closer to fully uniform in the border regions. However, the effective etch rate of the border regions is higher than that of the nanoscale holes in the center of the patterns because the developing solution can circulate and eject polymer-rich solution more easily. (c) Microscope image of the same patterns now after 165 s. Now the border region is uniform in color, but also wider than in (a-b), indicating that those regions are over etched. Slight over etching of the border region signifies that the nanoscale holes are likely perfectly etched due to the slower effective etch rate. Scale bars in (a-c) are 10 μm.

With TSPL writing complete, the PMMA/MA was developed in a stirred solution of a 20% volume ratio mixture of DIW in IPA stored at ~0 °C for 120 s. This cosolvent mixture has been shown to support larger proportions of polymer in solution, decreasing development times and adding consistency[44]. Occasionally, further development time was needed for chips that were optically identified as not fully developed. Examples of the different stages of development can be seen in Figure 2.2.4a-c, showing that the color of the write regions has not yet matched the expected substrate color after 120 s. Once development had been optically confirmed as complete, the sample was rinsed in IPA and dried in a stream of N_2 gas.

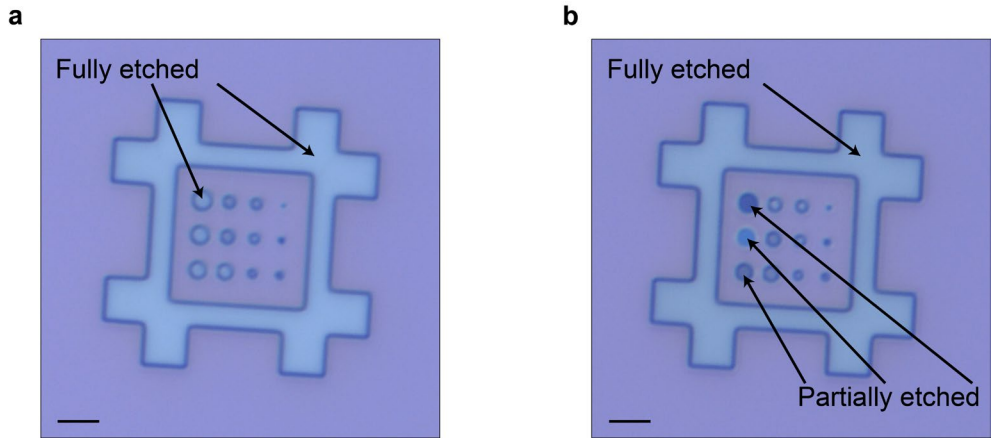


Figure 2.2.5: Effect of sonication during BOE etching. (a) Microscope image of a fully etched TSPL pattern conducted in sonicated 6:1 buffered oxide. (b) Microscope image of a non-uniform etch. Here, sonication was not used, resulting in air bubbles that caused inconsistent etching of the nanoscale holes. In comparison, the buffer region is fully etched in both (a) and (b) because air bubbles are easily circulated/popped in these large channels. Scale bars in (a-b) are 3 μm.

Next, the SiO_2 cavities are formed using a sonicated 6:1 buffered oxide etch (BOE) at ~90 nm/min with a ~15% over etch. Sonication is used for the development and BOE etching because the nanoscale cavities from TSPL trap air bubbles that block etchants from accessing the PMMA/MA and SiO_2, respectively[45]. Once the BOE etch is complete, the chips are thoroughly rinsed in DIW and dried using N_2. The consistency of the etch is then checked in an optical microscope. Figure 2.2.5a-b shows optical images of a BOE etch conducted without and with sonication to highlight the added consistency from sonication. In the etch done without sonication, some of the SiO_2 cavities have not been etched fully, as represented by the color in the center of the cavity not matching the buffer region. Since the buffer regions are significantly wider and larger than the cavities, they do not trap air bubbles in the same way and are always etched regardless of sonication, making them ideal for quick etch depth comparisons.

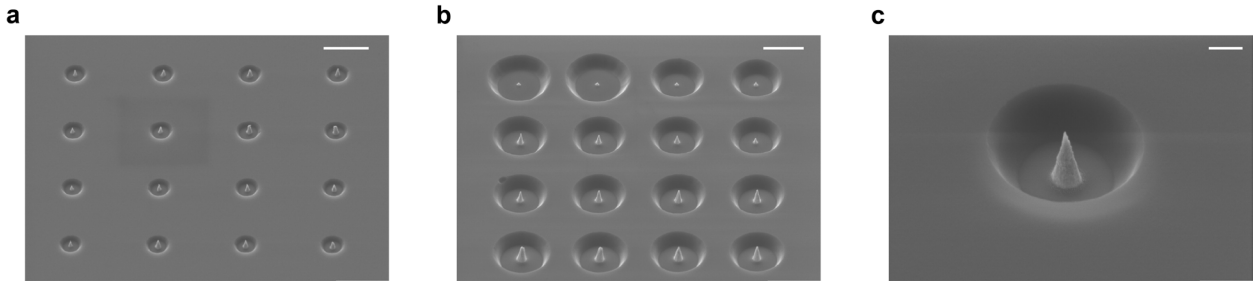


Figure 2.2.6: SEM imaging of embedded nanoantennas. (a) SEM image of embedded nanoantennas made in a 90 nm thick SiO_2 layer. (b) SEM image of embedded nanoantennas made in a 285 nm thick SiO_2 layer. (c) High-resolution SEM image of an embedded nanoantenna (scale bars = 1 μm for (a-b), and 200 nm for (c)).

Lastly, the nanoantennas are formed through the normal angle electron beam evaporation of Cr/Au. Once deposition begins, metal builds up on the periphery of the cavities and converges towards the center, closing the diameter of the window to the bottom of the SiO_2 cavity. This leading-edge convergence forms the profile of the nanoantenna and was used initially for fabricating field ionization arrays and non-embedded nanocones[46-48]. Then, the samples were placed in stirred acetone overnight to lift-off the polymer bilayer and residual Cr/Au. One thing to note is that if Cr/Au is lifted off but a polymer layer seems to persist on the SiO_2 surface, likely the polymers were exposed to charged ions and electrons in the electron beam evaporator during the ramp and soak cycles, before metal was deposited. PMMA/MA specifically is a negative electron-sensitive resist, meaning that it will polymerize under high-intensity exposure. We addressed this issue by increasing the sample-to-crucible distance in the evaporator, but certain compact evaporators may introduce shields and magnets to divert charged particles from contacting the polymer surface before deposition[49]. Figure 2.2.6 shows SEM images of the resulting embedded nanoantennas, highlighting their small (~10 nm) radii of curvature at the apex and consistent half-cone angle of ~24°. Further discussion on the fabrication of embedded

plasmonic nanoantennas, considerations on the SiO_2 thickness and cavity diameter, and convergence behavior can be found in Chapter 4 of this dissertation.

2.2.4 Imprint Lithography

In Chapter 3, a new lithography technique based on imprint lithography is developed for investigating the condition of nanoindented 2D materials. Imprint lithography in a traditional sense uses a stamp pressed into an impressionable polymer layer to form copies or masks for further processing[50-52]. Here, imprint lithography is extended to two different techniques, nanoindentation and nanoinversion. In nanoindentation, an AFM tip is pressed into a 2D material crystallite on top of a PMMA/SiO_2/Si substrate, causing plastic deformation of the PMMA[53]. During indentation, there are two parameters of interest: indentation force and contact angle. Indentation force is a measure of the force on the AFM tip during indentation, and contact angle is an imposed in-plane motion of the substrate during indentation required to maintain the contact point of the tip on the PMMA surface. A more in-depth discussion of these parameters can be found in Chapter 3 of this dissertation and in the dissertation of Dr. J. Pierce Fix[54]. Figure 2.2.7a schematically shows the process of nanoindentation and AFM imaging of nanoindented 1L-WSe_2. After the tip is retracted, the permanent deformation of the 2D material and PMMA acts as a strain center for investigating quantum states of light; however, an ongoing question is whether the 2D material tears or fractures during the indentation process.

To address the concern of tearing, we developed a nanoinversion process that converts nanoindents into protruding pillars so they can be analyzed with scanning probe and electron microscopy. Nanoinversion is schematically outlined in Figure 2.2.7b, and is conducted by evaporating Au (or other materials) normal to the PMMA surface, effectively filling the indent.

Once the indent is filled with Au, another Si/SiO_2 substrate is epoxied onto the exposed Au surface. After ~24 hours, by cleaving at the PMMA surface with a razor blade, the Si/SiO_2/Au/2D material/PMMA surface is separated, and excess PMMA is rinsed off using acetone. This leaves behind a gold inversion of the nanoindents and permits direct observations on the condition of the indented 2D material. Figures 2.2.7b-c show AFM and SEM images of inverted nanoindents. Further details on the identification of tearing and the importance of angle of incidence, indentation force, and contact angle on the geometry of nano-indents/inversions can be found in the methods section and SI of Chapter 3.

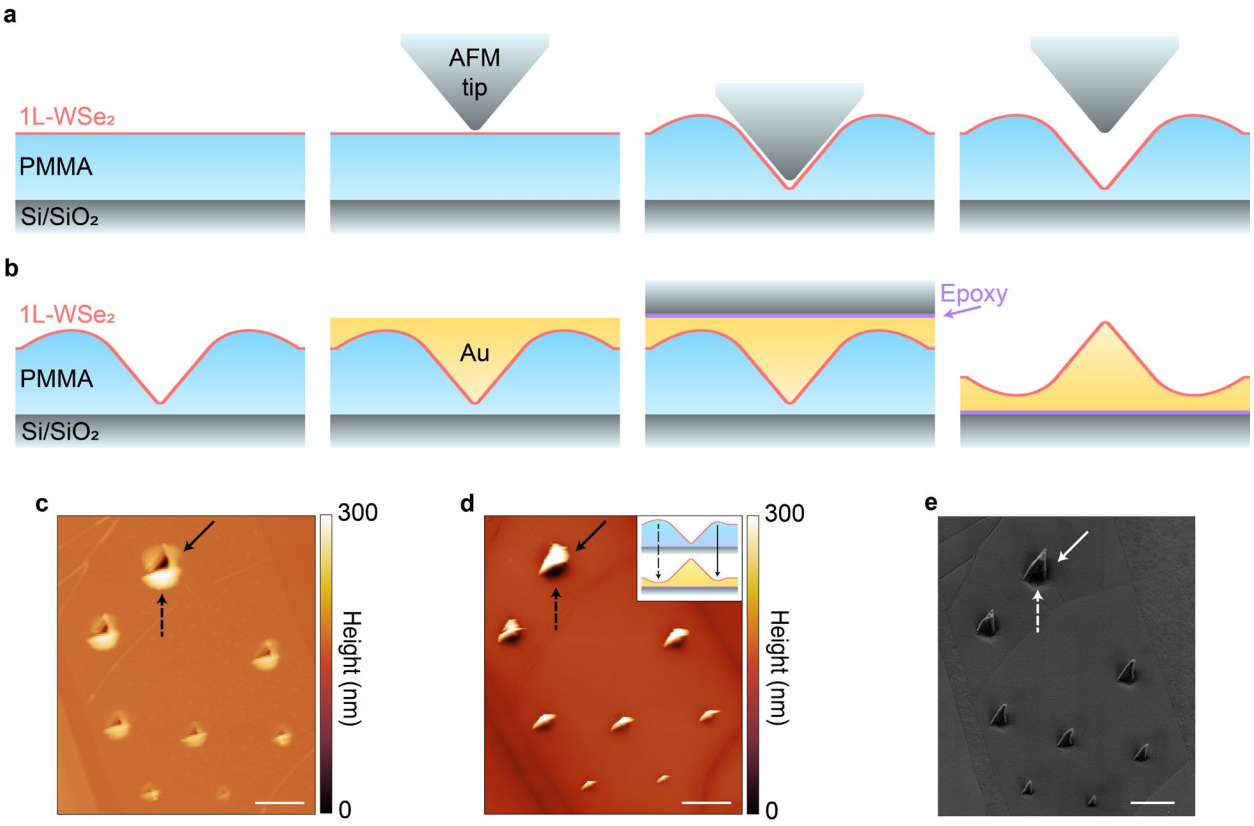


Figure 2.2.7: Nanoindentation and nanoinversion. (a) Schematic illustration of nanoindentation. An AFM tip is brought into near contact with 1L-WSe_2 on a PMMA surface. By raising the substrate into the AFM tip, the PMMA is plastically deformed, forming a nanoindent. (b) Schematic illustration of nanoinversion. Depositing Au with a normal angle of incidence uniformly fills the nanoindents made in (a). Then, by attaching a second Si/SiO_2 substrate using epoxy, the Au inversion and 1L-WSe_2 are separated from the PMMA. (c) AFM image of nanoindents in 1L-WSe_2. (d) AFM image of the inverted indents seen in (c). The inset represents the structural asymmetry of the buildup region, with the dashed and solid arrows in (c-e) highlighting the asymmetry in the data. (e) SEM image of the inverted indents in (c) (scale bars = 1 μm).

2.3 Finite Element Modeling in COMSOL

To understand the expected plasmonic behavior of a nanophotonic structure and theoretically motivate an optical measurement, modeling techniques can elucidate the ideal case. Finite element analysis (FEA) using the software packages of COMSOL Multiphysics has proven itself to be a leading simulation tool for studying complex scientific problems in physics[55-59]. In

this dissertation, the Wave Optics module of COMSOL Multiphysics was used to predict electromagnetic wave propagation and resonance effects in nanophotonic structures and plasmonic materials. FEA is a robust way to solve differential equations in complex geometries. By subdividing a geometry into many domains, local solutions are found in each domain based on initial values and boundary conditions, which are then stitched together to form a general numerical solution.

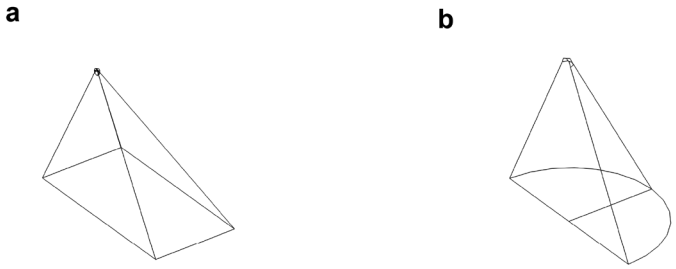


Figure 2.3.1: COMSOL Geometries. (a) COMSOL geometry of a nanopyramid. (b) COMSOL geometry of a nanocone.

Building a successful and accurate simulation of nanoscale effects starts by defining a geometry in which Maxwell's equations will be solved. Figure 2.3.1 highlights two different geometries, nanopyramids (Figure 2.3.1a) and nanocones (Figure 2.3.1b). Once a geometry is established, materials are defined using custom properties input by the user or the extensive materials library based on peer-reviewed articles hosted within COMSOL. Since optical effects are generally wavelength dependent, it is important to ensure the material properties used are valid across the wavelength range of interest. Next is defining the study type of the model (stationary, time dependent, eigenfrequency, or frequency domain). The model study type determines the

solvers, and hence the type of solution, that COMSOL makes available. For the models seen in Chapter 4, the study type is frequency dependent to solve for plasmonic resonances.

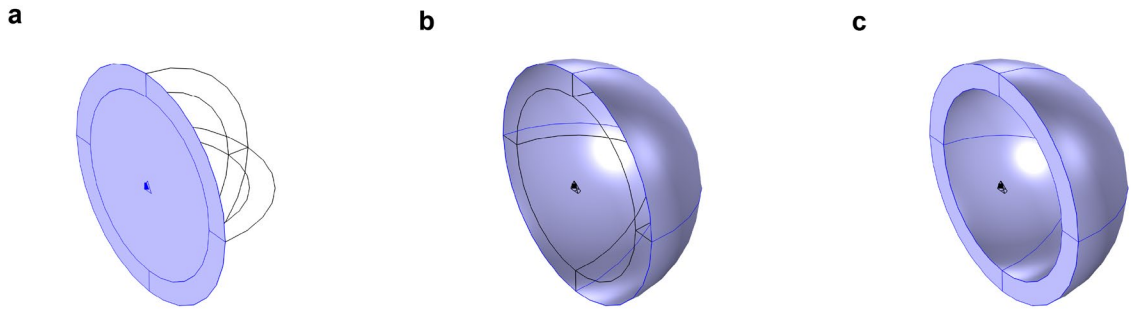


Figure 2.3.2: Boundaries and domains for wave optics COMSOL models. (a) Locations of the PMC boundary conditions. When the geometry is split to simplify the model, a PMC boundary is set on the split geometry to mimic a method of images problem. (b) Location of the PEC boundary on the exterior of the PML domain. (c) Location of the PML domain. By defining the PML as a concentric layer on the exterior of the modeling region with a PEC boundary, reflected waves from the nanostructure are efficiently terminated.

To obtain accurate simulations, boundary conditions must be established. The boundary conditions used in these electromagnetic simulations are perfect electric conductor (PEC), perfect magnetic conductor (PMC), and perfectly matched layer (PML), the locations of which are highlighted in Figure 2.3.2. PMC boundaries are established to lower the computation time of each model. By splitting the 3D geometry into two hemispheres and defining the symmetry plane as a PMC, the problem is made into a simplified method of images problem with the same solution as the general case. A PEC boundary is set at the exterior of the model interface to mitigate reflected fields when coupled with a PML domain. Finally, the exterior of the modeling region is defined as a PML domain to perfectly absorb scattered waves without reflections. PML domains are paramount to obtaining accurate simulation results, but to define them properly, the exterior region must be meshed radially to the center of the model.

Meshing is the way COMSOL subdivides a geometry into domain elements, and an example mesh for a nanocone model is shown in Figure 2.3.3a. Outside of exterior mesh elements for the PML domain (Figure 2.3.3c), special care is also taken for areas of the model with features $\ll \lambda$, such as the nanocone apex (Figure 2.3.3b). In such regions, the average domain size, x, is set to $\lambda/1000 < x < \lambda/10$ to ensure accurate model results.

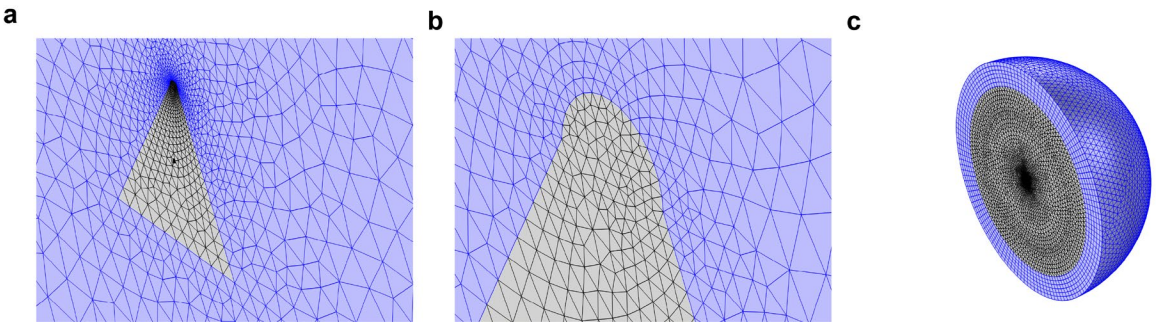


Figure 2.3.3: Mesh example in COMSOL. (a) Mesh for a nanocone model. The non-highlighted regions in (a) and (b) are the nanocone. (b) Zoomed-in mesh of a nanocone showing the smaller domains near the apex of the nanocone. (c) Radial mesh of the PML domain.

With the modeling geometry, boundary conditions, and study type established, the last thing to consider is the excitation field. For the model result seen in Figure 2.3.4a on a Au nanocone, the excitation wave is a plane wave polarized along the long axis of the resonator. This model highlights the local field enhancement that occurs at the apex of such plasmonic resonators due to a localized surface plasmon resonance (LSPR) along the long axis of the nanocone. In COMSOL, the user defines a specific polarization state and time dependence. In the case of a frequency-dependent study, time dependence is not permitted; however, pulsed excitation schemes and other exotic time-dependent studies are possible. In models with ~300,000,000 domains, solving for one excitation frequency/polarization state takes ~ 3.5 minutes with 32 GB of DDR4 RAM and a modest 2.7 GHz 8-core processor. To avoid having to manually start a model to build

up large datasets, solving many models back-to-back can save significant time. COMSOL has established a parametric sweep function that allows users to define variables and value ranges to sweep through when solving to address the need for multiple consecutive model solutions. Meaning that with one solution run, ~150 excitation frequencies or polarization states are solved and have their solutions stored in ~8 hours. One downside of parametric sweeps is that the solutions are stored in the system's RAM as successive solving iterations are processed, which can limit the extent of the parametric sweep.

In Figure 2.3.4b, the plasmonic enhancement spectrum (PES) of the Au nanocone seen in Figure 2.3.4a is plotted. PES are obtained using the parametric sweep function. By extracting the maximal field enhancement at the apex of the nanocone and plotting the data as a function of excitation wavelength, the PES gives insight into the resonance of the LSPR mode.

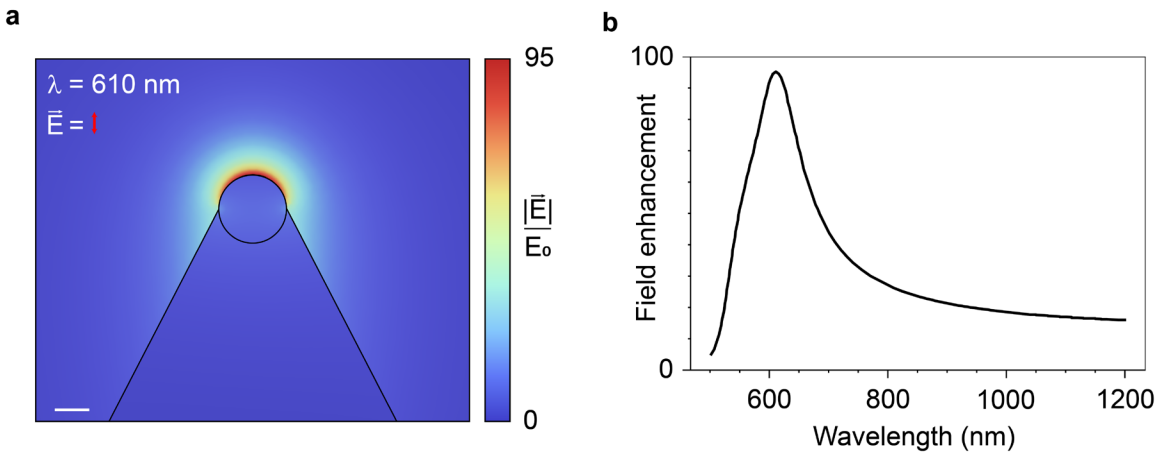


Figure 2.3.4: Model results for a nanocone. (a) COMSOL model results for a gold nanocone showing local field enhancement at the apex from a localized surface plasmon mode. (b) Plasmonic enhancement spectra of the nanocone seen in (a) by running a parametric sweep over excitation wavelength and extracting the max field enhancement above the apex. Scale bar = 5 nm

2.4 2D Material Transferring

The main instrument used for 2D material transfer in this body of work is the transfer microscope. Figure 2.4.1 shows an image of the transfer microscope with its key items labeled. The transfer microscope is a home-built, 9-degree-of-freedom tool with independent control over two stages (sample and stamp) while a long working distance objective observes alignment from above. Fixing the substrate and stamp to their respective stages is done using a vacuum line and stamp clamp. To compensate for small misalignments during transfer, the stamp stage is outfitted with slip and stick piezo actuators rather than typical micrometer screws. These piezo actuators can be driven one step at a time, which translates to motion of ~3 nm/step. Delamination of 2D flakes from either the substrate or stamp is caused by thermally induced adhesion changes of the underlying materials[60]. To impose a thermal load on the sample stage, a small heater is attached to a copper block capable of reaching temperatures ~275 °C. Some transfers, such as moiré heterostructures, require alignment of the crystal axis of two or more different flakes, so rotation of the substrate stage is also incorporated.

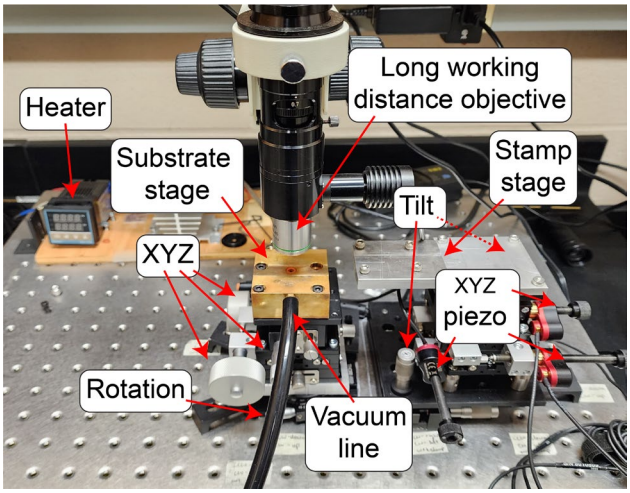


Figure 2.4.1: Transfer microscope components. An image highlighting the core components of the transfer microscope used for 2D material transferring.

Integrating a monolayer 2D material into a hybrid 2D material-nanophotonic device requires the use of different transfer techniques based on the system architecture. For example, in Chapters 3 and 5, dry transfer of 1L-WSe_2 using polydimethylsiloxane (PDMS) is ideal for integration onto PMMA because no solvent wash is required, preserving the PMMA substrate. However, integrating graphite of a specific thickness to the same PMMA substrate is done in Chapters 3 and 5 using wet transfer rather than dry transfer. This difference in technique is because PDMS transfer can only put flakes down, and atomic force microscopy (to check the graphite flake thickness) is experimentally difficult with PDMS as the substrate due to the sticking of the tip. Another common issue during transfer, requiring technique adjustment, is the fracturing of the 2D crystallite. Considering that a typical 2D material has a thickness of 1-10Å, the amount of strain (stress) these thin sheets can withstand before fracture is surprisingly high at 5-10% (5-10 GPa)[61], but the contact area between a 2D flake and the sharp edge of a nanostructure is generally small, creating immense localized pressures during transfer. To solve the issue of fracture in Chapter 4, when transferring 1L-WSe_2 over embedded nanoantennas, surface vibrations were minimized,

and/or an added polymer was used as an absorbing layer. All in all, integration of 2D material crystallites with nanophotonic structures has been a large challenge in the development of 2D materials-based devices because of scalability, nuanced technique modifications for each system, and fragility.

2.4.1 Dry Transfer Using PDMS

In cases where the target substrate for a 2D material flake is flat (surface roughness ~ 5 nm), such as the 1L-WSe_2 flakes on PMMA in Chapters 3 and 5, using PDMS as the transfer medium is the most straightforward approach. PDMS is a silicon-based elastomer commonly used in microfluidics due to its flexibility and transparency when cured. PDMS is commercially available in either fully cured sheets (Gel-Pak), generally used for gel-assisted exfoliation, or as a two-part kit with a base and curing agent (Sylgard 184), used for more custom applications.

For dry transfer using PDMS exclusively, direct formation of the transfer stamp by exfoliating onto Gel-Pak X4 sheets adhered to a glass slide is the easiest approach[62]. Figure 2.4.2 highlights the workflow for PDMS-based dry transfer. First, the target substrate and PDMS stamp are placed into their independent stages. Then, by using a long working distance objective, the focus of the transfer microscope can be set to either the target substrate or the stamp. Setting the focus on the substrate, the target area for transfer is located by translating the substrate stage. To obtain rough alignment of the flake to the target area, the focus is then set to the stamp, and the flake is found by translating the stamp stage. Next, to fix the substrate position, the heater is turned on to ~70 °C. Turning the heat on at this stage ensures that the thermal expansion of the copper block will not translate the alignment of the substrate and flake away from one another or introduce shear stress at the contacted interface. Heat is required for the transfer of 2D materials from a

PDMS film. At room temperature, the dominant adhesive stress is between the 2D material and the PDMS rather than the substrate (SiO_2); however, at temperatures > 65 °C, adhesion to the substrate becomes dominant, making transfer of 2D flakes from the PDMS surface favorable.



Figure 2.4.2: PDMS-based dry transfer. (a) A PDMS-based stamp with 1L-TMDC. (b) The stamp is brought into contact with a Si/SiO_2 substrate heated to ~70 °C to increase the substrate adhesion. (c) The stamp is retracted from the substrate, leaving behind the 1L-TMDC.

Once the substrate has reached the desired temperature, the stamp is slowly brought down towards the substrate. The alignment of the flake with respect to the target area on the substrate is periodically observed (~1 mm of vertical travel) since the stamp surface rarely moves normal to the substrate surface. Eventually, both the substrate and flake (stamp) will be within the focal volume of the objective, allowing for precise alignment using the piezo-controlled stamp stage. After the two items are aligned, the stamp stage is brought into contact with the substrate, forming a contact front. The contact front in this context is the area of contact between the PDMS stamp and substrate. The direction in which the contact front moves with added vertical motion of the stamp towards the substrate is very important for precise alignment. Figure 2.4.3 gives a schematic representation of how the direction of the contact front will affect the final location of the flake with respect to the substrate once contact is made. In short, the flake will translate away from the target location in the direction of the contact front. It is advantageous to track the position of a nearby flake or residue, closer to the contact front, as the front rolls over. Then, by adjusting the position of the flake of interest towards the contact front by a similar amount as the nearby flake

was moved, a more accurate spatial alignment can be obtained. Now with an accurate alignment, after 5-10 minutes of contact at 70 °C, the stamp is slowly brought up while monitoring the retraction of the contact front. Once the contact front approaches the flake, vertical motion of the stamp stage is greatly reduced to slow the motion of the front to mitigate tearing, wrinkling, and bubbling. After the contact front has fully moved past the flake, the stamp is quickly brought out of contact.

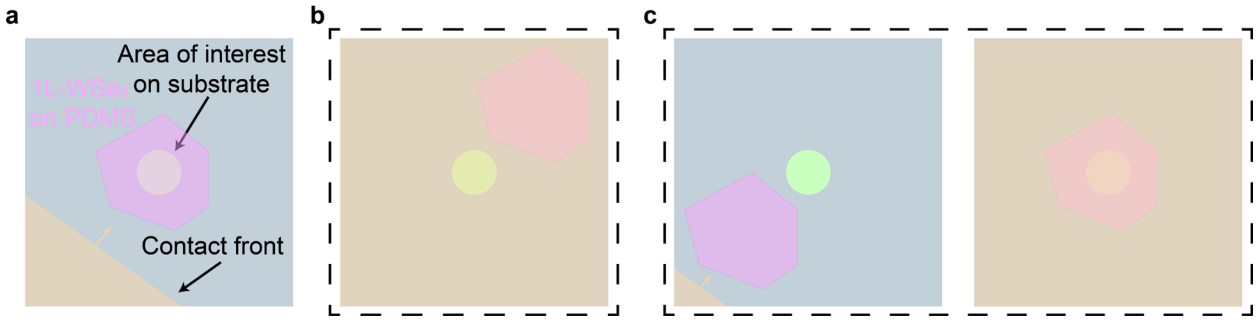


Figure 2.4.3: Contact front drift. (a) A schematic showing a 1L-WSe_2 flake on a PDMS stamp positioned in near contact above an area of interest. The contact front between the PDMS stamp and substrate is in the bottom left and moving towards the top right. (b) As the stamp is brought into full contact, the flake is moved away from the area of interest in the direction of the contact front's motion. (c) Left: Ideal positioning of 1L-WSe_2 to accommodate flake drift from the contact front. Right: After contact is made, the 1L-WSe_2 is positioned over the area of interest.

In this dissertation, the quality of a transfer was largely determined using atomic force microscopy (AFM). Figure 2.4.4 shows the result of a 1L-WSe_2 flake transferred onto SiO_2. Small nodules of PDMS residue cover the top surface of 2D material flakes transferred using this technique, and many nanoscale bubbles are formed by trapped surface contaminants. These nanobubbles are normally seen as a negative consequence of PDMS-based dry transfer. Another pitfall of PDMS transfer is that PDMS is incapable of picking up 2D materials; it can only be used for the final layer placement. To accommodate more complex 2D material heterostructures, a

second polymer layer is introduced to the stamp surface that can pick up and put down 2D materials.

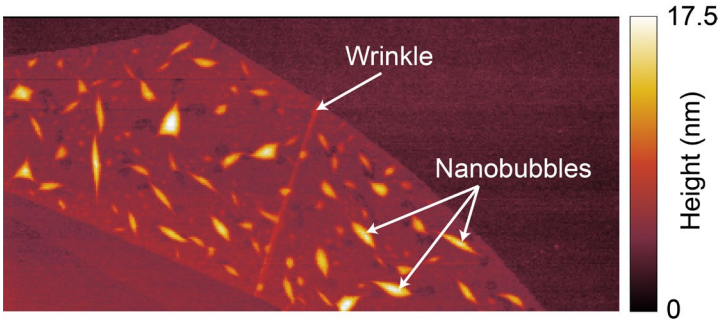


Figure 2.4.4: AFM of 1L-WSe_2 after PDMS transfer. An AFM image of a 1L-WSe_2 flake on SiO_2 after PDMS-based transfer. Arrows drawn towards wrinkles and nanobubbles that emerge because of using PDMS solely.

2.4.2 Dry Transfer Using Polymer Layers (PPC, PCL, PC)

Polymer layer dry transfer is a more advanced technique used in fabricating multilayer heterostructures, pick and place transfer, or when a cleaner interface is desired[63-65]. In this dissertation, polymer layer transfer was used to fabricate some of the 1L-WSe_2 on embedded nanoantenna samples in Chapter 4. Added polymer layers; polypropylene carbonate (PPC), polycaprolactone (PCL), and polycarbonate (PC) have relatively low glass transition temperatures of 60 – 150 °C. By heating the polymer to its respective glass transition temperature, the adhesion and flexibility are greatly enhanced, allowing it to tightly adhere to 2D material flakes for pickup from commonly used substrates such as SiO_2, mica, and Al_2O_3. To accommodate the added layer into a PDMS-based stamp, thin layers of polymer are made.

In Figure 2.4.5, the fabrication procedure used in this dissertation for thin polymer layers is shown. First, the polymer is spun onto a glass coverslip at 4000 rpm for 120 s. The extended duration in the spin coating time is to ensure most of the liquid solvent has evaporated from the

polymer matrix. Once the polymer film is spun, the polymer side of the coverslip is outlined with a low-adhesion Scotch tape on the perimeter to support the polymer film. Finally, the coverslip is intentionally broken from the non-polymer side while making sure not to puncture the polymer film. Then the glass is removed, and the result is a stand-alone polymer layer suspended in a Scotch tape frame.

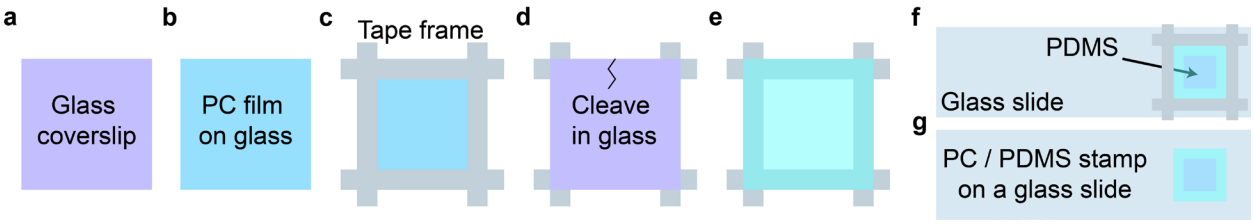


Figure 2.4.5: Fabrication of thin polymer films. (a) A glass coverslip is cleaned. (b) PC polymer is spun onto the glass coverslip at 4000 rpm for 120 s. (c) A tape frame is made of Scotch tape, and the polymer side is adhered. (d) The coverslip is flipped over, and the glass is intentionally fractured. (e) The broken glass is removed from the PC surface. (f) The thin polymer film is attached to a PDMS stamp. (g) Excess PC / tape is removed, and the PC polymer is reflowed over the PDMS at 190 °C.

In PDMS-based transfer, the stamp was simply the PDMS used for 2D material exfoliation, adhered to a glass slide with double-sided tape. However, for polymer layer transfer, a PDMS supporting layer is still used, but it is covered with the layer of polymer. The role of the PDMS supporting layer is to bring the transfer surface away from the glass slide, allowing for angular misalignment to not render contact impossible. To elaborate, if the transfer stamp was only composed of 2D material flakes on a glass slide surface, when the stamp is brought near contact with the substrate, the two surfaces would need to be perfectly smooth and parallel with one another for contact to be made. Since PDMS is an elastomer, it conforms and compresses to surfaces when pressure is applied, so rather than requiring perfectly smooth and parallel surfaces, the PDMS can compensate for imperfections.



Figure 2.4.6: Different stamp types. (a) PDMS-based stamp. (b) Polymer layer stamp on flat PDMS. (c) Double dome PDMS, polymer layer stamp.

When the underlying PDMS is planar, accurate alignment of the 2D material flake to the region of interest is tedious (as seen in Figure 2.4.3). To address this issue, we developed a new geometry of a stamp called the double dome. For most polymer layer transfers, the double dome is seen as a large advantage due to its deterministic contact front. Instead of having to anticipate the direction and magnitude of the contact front propagation to achieve precise placement of a 2D material flake onto the substrate, the flake is positioned exactly where it is intended. Percise placement is achieved because the first point of contact with the double dome is the predictable tip, where all the 2D material flakes are.

The fabrication procedure to make double dome PDMS/polymer stamps is shown in Figure 2.4.7. By mixing Sylgard 184 PDMS at a 10:1 (base/curing agent) ratio, a liquid, but curable, version of PDMS can be used to form the double dome. First, a small amount of liquid PDMS is dropped onto a square of double-sided tape adhered to a glass slide. The double-sided tape promotes the PDMS to hold itself into a dome because of surface tension. Then the stamp is placed into a 100 °C oven for ~20 minutes to cure. Afterwards, another (smaller) drop of PDMS is placed at the apex of the first dome. Curing the stamp again in the same conditions results in a double dome PDMS stamp. Integration of the thin polymer is done by plasma treating the double dome for ~60 s in an oxygen plasma to create dangling siloxane bonds on the surface of the PDMS. Then, by placing the polymer layer onto the PDMS surface and cutting the surrounding tape frame

off, the polymer attaches to the PDMS. To fully conform the polymer to the PDMS double dome, the stamp is placed onto a hotplate at 60 °C, 90 °C, or 190 °C for PCL, PPC, and PC, respectively, to reflow the polymer.

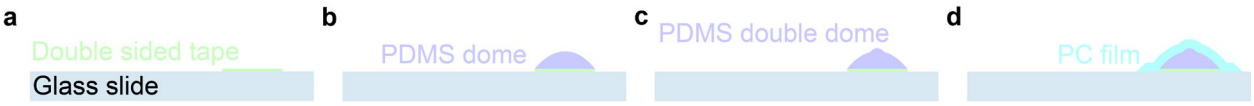


Figure 2.4.7: Double dome stamp fabrication. (a) A piece of double-sided tape is attached to a bare glass slide. (b) A PDMS dome is made on double-sided tape by drop casting liquid Sylgard 184 PDMS. The PDMS dome is then cured in a 100 °C oven. (c) A second dome is made on top of the first in the same manner as (b). (d) The double dome PDMS is treated in an O_2 plasma for ~ 60 s, and the thin polymer film is quickly adhered and reflowed.

Using a polymer layer double dome stamp to transfer differs substantially from PDMS-based transfer. Polymer layer transfer first requires the pickup of 2D flakes from their native substrate. The first step is finding the center of the double dome, i.e., the first contact point. To find the first contact point, the stamp is lowered onto the substrate surface at room temperature, and the direction of the contact front with respect to the center of the field of view is observed. For example, if the contact front emerges from the right, then the stamp should be retracted and brought to the left. By repeatedly lowering the stamp, observing the contact front direction, retracting, and moving the stamp, the first point of contact will eventually be in the center of the field of view. Once the stamp is centered, when the apex of the double dome is brought into contact, there is a circular contact front. An example of the circular contact front can be seen in Figure 2.4.8.

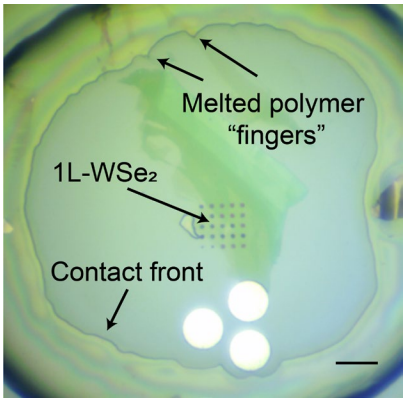


Figure 2.4.8: Circular contact front. Optical image of the circular contact front made by a double dome PDMS stamp. Melted polymer, "fingers", indicate that the thin polymer layer has melted.

With the center of the stamp now in the center of the field of view, picking up flakes is done by heating the substrate to 70 °C or 150 °C (PPC and PCL / PC) and bringing the stamp into light contact. In the case of the PPC and PCL, 70 °C melts the polymer and causes the flake to depress into the polymer layer. After cooling to room temperature, retracting the stamp away from the substrate brings all 2D flakes with the stamp. PC behaves differently; by heating to 150 °C, the glass transition temperature is reached. This transition changes the PC layer from a glass-like polymer into an adhesive rubber-like polymer. Then, without needing to cool to room temperature, retracting the PC stamp removes all 2D flakes from the substrate. This process can then be repeated to pick up subsequent layers forming 2D material heterostructures.

To place down 2D layers with a polymer layer stamp, the polymer must be detached from the underlying PDMS. The most consistent way to achieve delamination is by melting the polymer off the PDMS using heat (70 °C for PPC and PCL, 275 °C for PC). This entire process is very similar to that of bare PDMS. First, the substrate is heated to the target temperature, and then the stamp is brought closer to the substrate while periodically checking the alignment to the region of interest. Once contact is made, the stamp is held down for ~5-10 minutes to increase the contact

area between the flakes and substrate, and then slowly retracted. Now, since the polymer layer is melted, the retracted contact front will appear as a more fluid interface. Fingers of polymer (Figure 2.4.8) will emerge from the edge of the contact front, indicating that a layer is melting off the stamp. This layer of melted polymer will pin the flakes to the substrate. Once the stamp is fully retracted, the substrate is then washed in either acetone (PPC and PCL) or chloroform (PC) for ~ 8 hours to remove the excess polymer.

The resulting transfer will have less surface residue than the bare PDMS transfer because PPC, PCL, and PC are soluble in their respective solvents, while PDMS will absorb most solvents into the polymer rather than dissolve. However, this solvent rinse also comes as a downside to polymer layer transfer. Some substrates, such as PMMA, commonly used for nanoindentation, will dissolve in a quick acetone rinse. Using a bare PDMS stamp solves the requirement for an acetone rinse, but if AFM confirmation of the flake thickness is required before transfer, PDMS will not work either due to AFM tips interacting strongly with the PDMS layer, leading to sticking and inaccurate AFM step heights. In these cases, a wet transfer technique is used to remove 2D flakes from SiO_2. Wet techniques permit preliminary AFM analysis and the use of a PDMS layer for solvent-free transfer onto PMMA, as done in Chapters 3 and 5.

2.4.3 Wet Transfer Using PDMS

The first transfer techniques developed for 2D materials were wet transfers used to remove CVD-grown graphene from a SiO_2 substrate using chemical etching[66-71]. CVD-grown 2D materials such as graphene adhere strongly to the SiO_2 surface due to added surface defects and covalent bonding between carbon atoms and dangling oxygen atoms in the SiO_2. Etching of the SiO_2 surface is generally done in $FeCl_3$, NaOH, KOH, NaClO, and NH_4OH. Solutions made with these

chemicals slowly roughen the surface of the SiO_2 substrate and promote interfacial delamination of the flakes. To support the flakes, a thin polymer layer of PMMA or PDMS is spun over the flakes before etching.

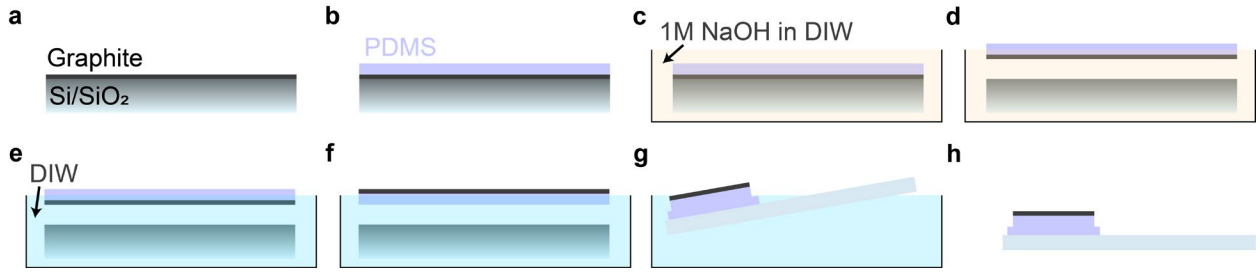


Figure 2.4.9: Wet transfer. (a) An ~8 nm graphite flake is identified on a Si/SiO_2 substrate using AFM. (b) PDMS is spun onto the substrate to act as the stamp media. The PDMS is then cured at 100 °C. (c) The sample is placed into a 1M NaOH in DIW solution heated to 90 °C. (d) After ~10 minutes, the PDMS and graphite detach from the Si/SiO_2 substrate. (e) The PDMS layer is transferred to a DIW bath to rinse excess NaOH off the graphite flakes. (f) The PDMS layer is flipped so the flakes are facing out. (g) The PDMS layer is scooped out of the DIW using a PDMS stamp. (h) The resulting PDMS stamp with graphite flakes.

Wet transfer was used in Chapters 3 and 5 for transferring graphite flakes of a desired thickness (~8 nm) onto a 1L-WSe_2 flake on a PMMA substrate. PDMS and polymer layer transfer are insufficient for such a transfer due to the requirement of AFM to validate the graphite thickness and the sensitivity of PMMA to solvents, respectively. Once a graphene flake was located and the AFM step height was confirmed, a thin layer of Sylgard 184 PDMS was spun onto the SiO_2 surface (Figure 2.4.9). After curing in a 100 °C oven for ~20 minutes, the edges of the PDMS layer are cut off to allow the etching solution access to the 2D material/SiO_2 interface. Next, the sample is placed into a 1M solution of NaOH in DIW at 90 °C for ~10 minutes or until bubbles begin to form on the perimeter of the PDMS film. Bubbles indicate that the SiO_2 surface has started to etch. Between 5 and 10 minutes after bubbles are present, the PDMS film will either delaminate by itself

or the PDMS will need gentle agitation from a pair of tweezers. After delamination, the film (and all the flakes) will float on the surface of the NaOH/DIW solution. Removing excess NaOH from the film is done in a bath of DIW for ~ 12 hours. After rinsing, the film is flipped over and scooped up by a bare PDMS stamp. The result is then a PDMS stamp with the desired ~8 nm thick graphite flake. Transfer of the graphite off the PDMS stamp follows the PDMS transfer technique outlined earlier in this section. Figure 2.4.10 shows how minimal folding, tearing, and wrinkling of the graphite flake occur during the various steps of wet transfer.

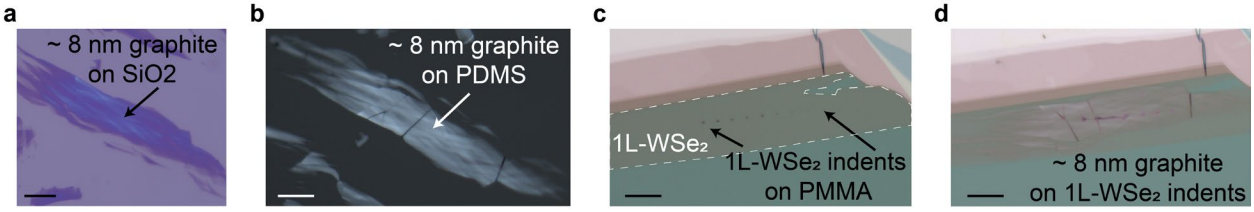


Figure 2.4.10: Flake condition during wet transfer. (a) Optical image of a ~8 nm graphite flake on a SiO_2 substrate. (b) Optical image of the same graphite flake in (a) on PDMS. (c) Optical image of the 1L-WSe_2 indents of interest. (d) Optical image of the graphite flake transferred over 1L-WSe_2 indents.

2.5 Photoluminescence (PL) and Raman Spectroscopy

1L-TMD materials are often studied using spectroscopy due to their direct band gap and large exciton binding energies, permitting stable room temperature exciton populations[2, 72, 73]. At cryogenic temperatures, the TMD material of interest for the work in this dissertation, WSe_2, isolated into its monolayer form, commonly hosts SPE states at areas of tensile strain[74-79]. These SPE states can be modulated by their environment. By positioning the SPE state within an optical cavity or near a plasmonic resonator, the excited state lifetime can be reduced through the Purcell effect, increasing the SPE state's brightness. Also, by coupling 1L-WSe_2 to electrodes to make

electrically addressable devices, the carrier concentration and SPE states can be further controlled[29, 80-83]. Here, spectroscopy is conducted on hybrid 1L-WSe_2/nanophotonic systems to study SPE states and better understand the light-matter interactions in such systems.

The room temperature and cryogenic spectroscopy found in this dissertation were taken using the Quantum Optical Microscope (QOM), a homebuilt confocal microscope designed by Dr. Matthew Strasbourg. Details on the setup, design considerations, optimizations, and full suite of capabilities can be found in the dissertation of Dr. Matthew Strasbourg[84]. In short, samples were either measured on a room temperature 3-axis stage or cooled to 4 K in a s50 Montana Instruments closed-cycle cryostat. On the QOM, for steady-state PL and Raman spectroscopy, a 532 nm CW diode laser was used, and in time-resolved or excitation wavelength-dependent measurements, a NKT supercontinuum laser with an acousto-optical tunable filter (AOTF) was used. The QOM uses a Nikon infinity corrected S Plan Fluor 40X (0.6 NA) objective for exciting and collecting PL. With this objective and proper alignment, the QOM has a diffraction-limited resolution at room temperature with the 532 nm diode laser, corresponding to a laser spot full width at half maximum (FWHM) of ~445 nm. In comparison, when taking spectroscopy at 4 K, the resolution is coarser (FWHM ~750 nm); a thin glass window above the sample requires the objective correction collar to be properly tuned to compensate for the window's thickness and index of refraction. Another factor that limits the resolution at 4 K is the cryostat compressor. The compressor cycles at ~2 Hz and couples subtle vibrations into the microscope despite isolation efforts to mitigate the effect.

2.5.1 Measuring the Laser Spot Size

To achieve the highest resolution spectroscopy data, the resolution of the QOM must first be accounted for. To measure the FWHM of the laser spot, two different methods are used and

cross-checked with each other for the spectroscopy done in this dissertation. The first method uses a Gaussian fit to the intensity profile of the spot, acquired using an Amscope camera fixed into the QOM. After fitting to the intensity profile, the FWHM and standard error are extracted. There are three primary sources of error in this technique. The first error source comes from the location of the line-cut intensity profile used for the fit. Since the line-cut is positioned by eye, getting the exact center point of the laser spot is unlikely. In conjunction with this error source, at 4 K, the helium compressor vibrations cause the spot to spatially oscillate at ~2 Hz, broadening the intensity line-cut. The last source of error is the integration time of the image. When the integration time is too long, the central pixels become saturated, leading to a poor fit and generally enlarged FWHM, and when the integration time is too short, pixels on the periphery are near the noise floor, making the FWHM artificially smaller. With that considered, when obtaining the intensity profile, the integration time of the camera is set to fix the central intensity to be ~80% of the maximum. To show an example of this method, simulated data of a Gaussian function with shot noise and Gaussian readout noise is plotted in Figure 2.5.1a and fit with a Gaussian function.

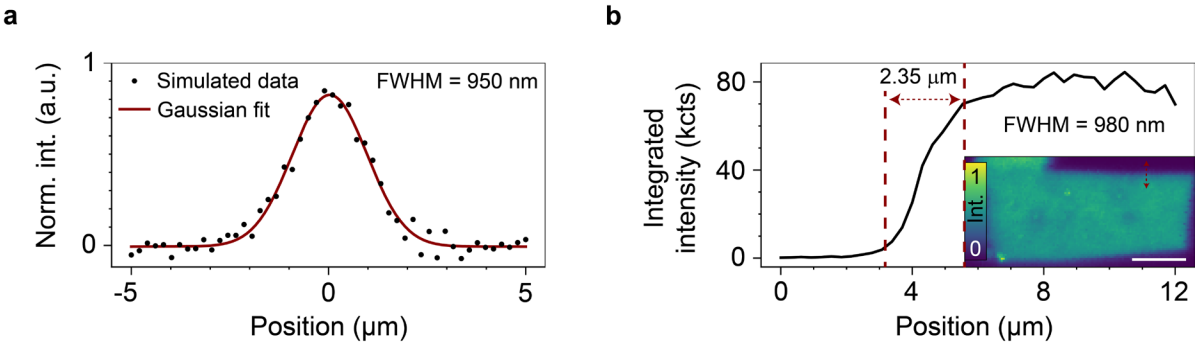


Figure 2.5.1: Measuring the laser spot FWHM. (a) Simulated data showing a line cut across the center of the laser spot as seen by the QOM camera fit by a Gaussian function to approximate the FWHM. (b) PL intensity linecut taken along the red line seen in the inset scan. By measuring the distance between no emission (off the flake) and the steady state emission of the 1L-WSe_2, and dividing by 2.4, the FWHM is approximated. Inset scale bar = 10 μm

The second technique for measuring the resolution of the QOM is done by taking a PL intensity map of a 1L-WSe_2 flake using an avalanche photodiode (APD), measuring the distance between the substrate (near 0 intensity) and the constant PL intensity of the flake, and dividing that distance by 2.4. The value 2.4 comes from the relationship between the FWHM and the width of the transition region, acquired by taking the convolution of a step function with a Gaussian. The inset in Figure 2.5.1b shows a PL intensity map of a 1L-WSe_2 flake on a PMMA substrate. The main figure is the intensity profile from the red dashed line showing the spatial extent of the convoluted step function. The distance between the red dashed lines is the value that is divided by 2.4 to estimate the FWHM. Error in this technique also comes from compressor vibrations at 4 K, broadening the effective excitation spot size. A source of error unique to this technique is the pixel size of the PL intensity map. Since the PL intensity map does not have perfect resolution, for the most accurate measurement, the pixel size should be as small as possible, but greater than or equal to the Nyquist frequency. This ensures that the measured spatial extent is as close to the theoretical case as possible.

2.5.2 Laser Power-Induced Damage on 2D Materials

When taking spectroscopy on 2D materials, the excitation power is a crucial parameter to minimize to avoid laser-induced damage. When taking PL, excitonic states generally saturate with higher excitation powers, 200 - 1000 nW. These excitation powers at 532 nm do not cause noticeable damage to a 1L-WSe_2 flake; however, Raman scattering, a third-order susceptibility process, requires higher excitation powers to acquire sufficient signal to form a spectrum. Typical powers for Raman spectroscopy are ~1 mW. Figure 2.5.2 highlights the consequences of using high excitation powers. Figure 2.5.2a-b shows a PL hyperspectral scan of a 1L-WSe_2 flake, both before and after Raman spectra were taken at the circled locations. Within the circled regions, the average PL intensity was reduced by ~80%, indicating a significant degradation of the optical properties of the material. For this reason, all Raman spectroscopy taken in this dissertation uses excitation powers of ~200 μW with longer exposure times to avoid damaging the material system.

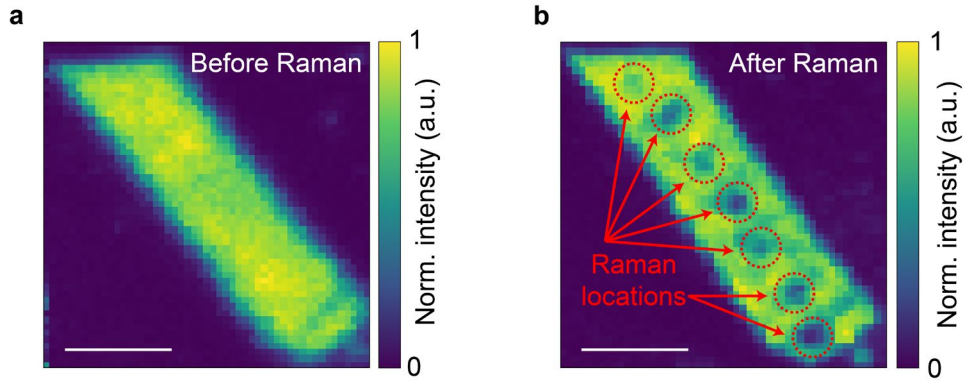


Figure 2.5.2: Laser-induced damage of 1L-WSe_2 (a) PL intensity scan of a 1L-WSe_2 flake on SiO_2 showing a nominally homogenous intensity across the flake. (b) PL intensity scan of the same 1L-WSe_2 flake as in (a), but after Raman spectra were taken. The high-intensity laser caused reductions in the PL intensity in the locations where Raman spectroscopy was taken. Scale bars = 5 μm

2.6 Optimization of an HBT Interferometer for Low Fluence SPE Measurements

Hanbury Brown Twiss (HBT) interferometry is an optical technique first conceived in 1977 for its use in measuring sub-Poissonian distributions of photons in time from microscopic light sources such as single molecules[85-87], NV centers[88-90], quantum dots[91-93], and excitonic quantum states[74-78, 80, 94-96]. A standard two-channel HBT interferometer consists of a 50/50 beam splitter to split the incident photon stream, and two single-photon avalanche photodiodes (Excelitas SPCM-AQRH-14-TR APDs) connected to a time tagging module (PicoQuant Hydra Harp 400). By monitoring the detection of single photons on each APD as a function of time with ps resolution, a correlation histogram is generated between the two APDs. In the case of a light source that is emitting single photons, correlations at zero-time delay between APDs should be 0 since photons are emitted one at a time. These types of anti-bunched light sources behave as an isolated two-level system cycling between an excited and ground state with a given excited state lifetime, τ, greater than the timing resolution of the APDs and time tagging module. For this dissertation, HBT

interferometry was used to validate the presence of SPE states in hybrid 1L-WSe_2/nanophotonic systems in Chapters 3 and 4.

2.6.1 Spectral Filters to Isolate SPE States

In theory, single-photon antibunching measurements are straightforward, similar to PL spectroscopy; however, in real laboratory settings with solid-state samples, many complications arise. Quantum light sources, such as the excitonic states studied in this dissertation, are known to vary in intensity and wavelength in time (spectral blinking and spectral wandering, respectively)[75, 77, 97, 98]. Figure 2.6.1a shows the variable nature of SPEs in 1L-WSe_2. To obtain a high-quality antibunching measurement, only photons related to the single-photon state should be made incident onto the APD channels to avoid unwanted correlations from stray light.

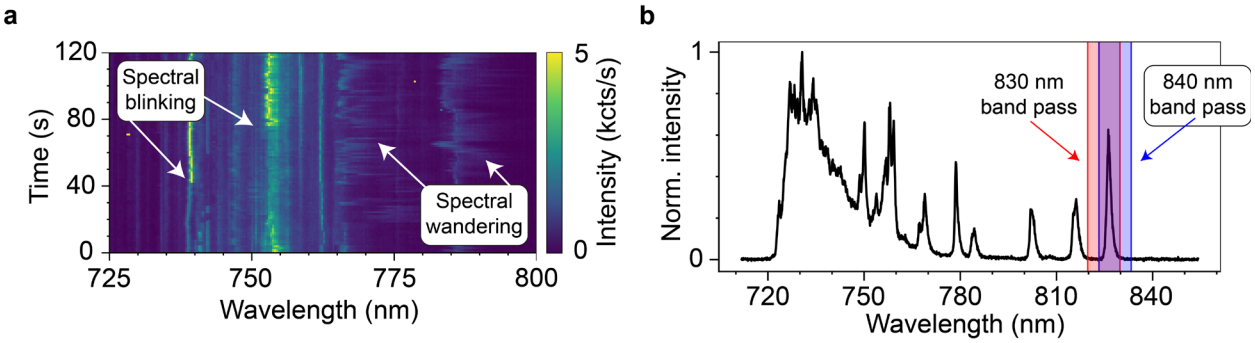


Figure 2.6.1: Isolating a SPE in 1L-WSe_2. (a) 4 K PL time series of SPE states in 1L-WSe_2 showing spectral blinking and wandering occurring on second time scales. (b) 4 K PL spectra of SPE states. A single SPE state is isolated using two 10 nm FWHM spectral band pass filters rotated to clip the low and high wavelength tails of the SPE.

Originally, isolation of the SPE state PL was done by setting the center position of the spectrometer grating to the SPE wavelength and using a monochromator exit slit as a spatial spectral filter. This technique imposed the grating efficiency of the spectrometer into the output intensity of the photon stream. Also, the grating imposed abnormal diffusion to the photon stream

leading into the HBT interferometer, making the collection efficiency low due to clipping. To address this issue, the HBT interferometer was moved before the spectrometer, and spectral filters would be used to isolate the SPE state rather than a grating, as seen in Figure 2.6.1b. The original set-up (bottom right) and all implemented changes (upper center) are reflected in an optical block diagram, Figure 2.6.2a. The spectral position of SPEs in intrinsic 1L-WSe_2 has been found to most commonly lie within 720 – 810 nm, Figure 2.6.3, so by using a pair of band pass filters with a 10 nm FWHM pass band and rotating them to align with the SPE state, maximal photon fluence is sent to the HBT interferometer.

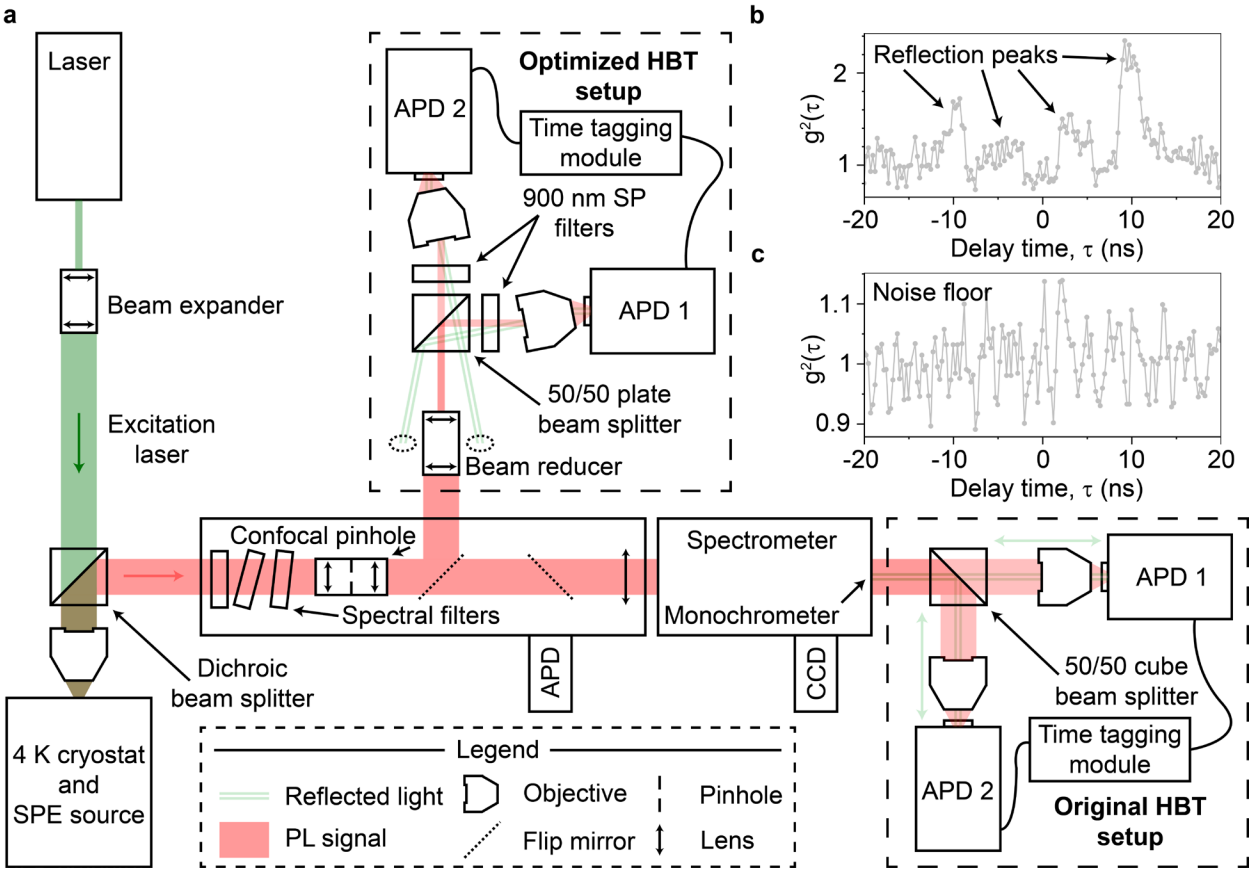


Figure 2.6.2: Optimized HBT setup and consequential $g^2(\tau)$ baseline. (a) HBT optical setup. In the bottom right is the original HBT setup, where reflected light off a 50/50 cube beam splitter causes reflection peaks in a $g^2(\tau)$ baseline measurement. In the upper center is the optimized HBT setup. Here, a beam reducer is implemented to increase photon counts on each APD channel. To resolve the problem of reflection peaks, the objectives are rotated by ~11°. Due to the rotation, reflected PL is collimated off-axis from the incident optical path, causing it to decouple from the HBT interferometer. (b) Antibunching calibration showing a series of peaks emerging due to reflections in the HBT interferometer. (c) Antibunching calibration with no reflections leads to a featureless noise floor.

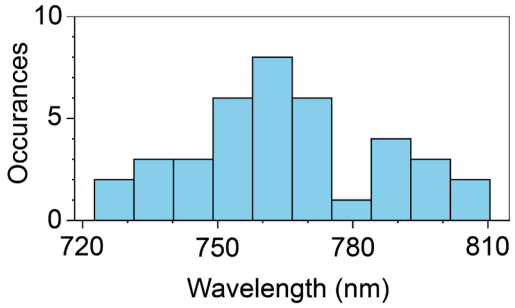


Figure 2.6.3: Histogram of SPE wavelengths in literature. Histogram of SPE wavelengths reported in studies of single photon emission in 1L-WSe_2.

2.6.2 Elimination of Reflections Using Rotated Optics and a Plate Beam Splitter

Though changing the location of the HBT interferometer in the optical system increased the total APD intensity signal by approximately an order of magnitude, it now permitted SPE photons and Si afterglow to back reflect through the optics and create echoes in the coincidence count signal. These echoes manifest in the antibunching curve as peaks in the signal, seen in Figure 2.6.2b. The back reflected signal comes from planar optics along the optical path. The first step in correcting this is to change the 50/50 beam splitter cube to a 50/50 plate beam splitter. Since the beam splitter was in proximity to the APDs, changing to a plate eliminated the echoes seen near 3 ns in time delay. Next, there are the spectral filters used to eliminate back-reflected laser light and isolate the SPE photons from the broad PL signal. Since the laser clean-up filter cannot be easily changed, and the spectral filters have variable rotation angles depending on the SPE state, changing these directly will not eliminate reflections off these surfaces. Instead, by rotating the objectives that focus light onto the APD sensors, the back-reflected light will be outcoupled at an angle offset from the incident optical path. So, to avoid this new optical path returning to the APDs, the angular offset needs to be large enough so that the other planar optics are missed. In the case of the optimized optical setup in Figure 2.6.2a, this was an ~11-degree rotation. After implementing the

rotated objectives and realigning the HBT interferometer, all reflection echoes in the coincidence count signal were eliminated as seen in Figure 2.6.2c.

2.6.3 Enhanced Collection Efficiency Using a Beam Reducer

After rotating the collection objectives to remove back-reflected echoes in the coincidence count signal, the effective area of the back aperture able to focus light was reduced. This spatial reduction led to a drop in SPE intensity on the APDs, so to fix this final issue, a beam reducer was introduced into the optical path. Due to limitations in table space, a Galilean beam reducer was built using a 25 mm and -125 mm focal length lens. This beam reducer recollimated and shrunk the beam waste by ~5x, allowing more SPE photons to pass through the collection objectives. With all the changes implemented into the HBT interferometer, the system saw a ~20x increase in collection efficiency and aided in the antibunching measurements of low fluence SPE states seen in Chapter 4.

2.6.4 Time Correlated Single-Photon Counting (TCSPC)

Since an HBT interferometer is set up for precise measurement of single photons with respect to time, by removing the beam splitter and using a single APD connected to a time tagging module with a pulsed excitation source, the fluorescence lifetime of a state can be measured. Using an NKT Photonic Supercontinuum laser with a ~14 ns pulse separation, the excited state is thermalized and begins radiative recombination before the next pulse arrives at the sample. Since the sync signal of the pulsed laser is input into the time tagging module, a lifetime curve of PL intensity vs time is generated by considering photons incident on the APD after each pulse. An example lifetime curve is shown in Figure 2.6.4a. Assuming that there is only one two-level system

contributing to the PL signal, by fitting a monoexponential function to the normalized lifetime curve, the decay constant is the lifetime of the state. In some lifetime measurements, there is more than one state contributing to the signal; in these cases, a monoexponential function does not fit well to the data, so the lifetime is obtained by calculating the $1/e$ time. The $1/e$ time is shown in Figure 2.6.4b as the separation in time between the point of maximal PL intensity and the point where the normalized PL intensity reached $1/e$.

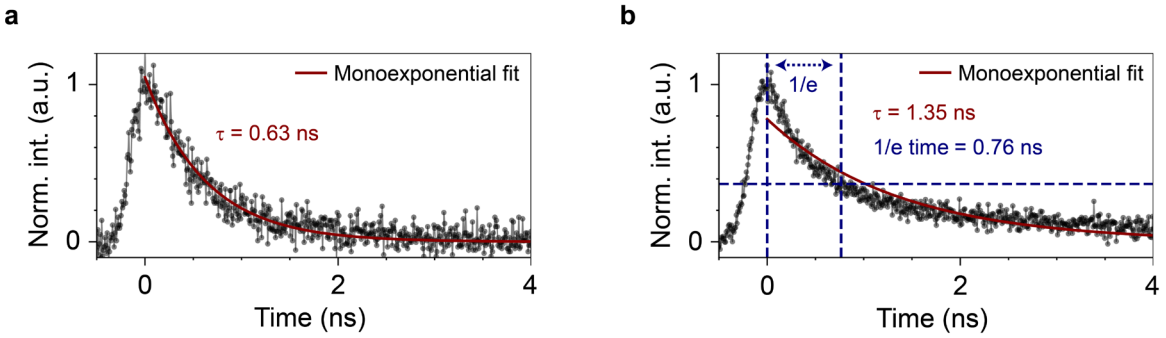


Figure 2.5.4: Extracting the excited state lifetime. (a) Lifetime curve of a 1L-WSe_2 SPE state. This state exhibits time-dependent emission that fits well with a monoexponential function, indicating a pure two-level system. (b) Lifetime curve of a 1L-WSe_2 SPE state. This state is not well fit by a monoexponential function, indicating multiple states/recombination pathways. To extract the lifetime of this curve, the $1/e$ time is used rather than the τ value from the monoexponential fit.

In Chapter 5, the dynamics of SPE states in graphene-covered 1L-WSe_2 were carefully characterized using TCSPC. For these measurements, wavelength-dependent dynamics were taken using the monochrometer exit slit in the original HBT setup and location, seen in Figure 2.6.2a. To get wavelength dependence, the monochrometer exit slit was opened to 0.5 mm to pass a band of ~4 nm to an APD. Then the grating center position is swept in 5 nm steps every 30 seconds, collecting a new lifetime curve every step. Then, by calculating the 1/e time of each step,

wavelength-dependent lifetimes are found. Results and discussion on these wavelength-dependent dynamics measurements are found in Chapter 5.

2.7 Photoluminescence Excitation Spectroscopy (PLE)

PLE is a spectroscopic technique used to probe the absorption spectra of a material system. The measurement is done by using a tunable laser source to collect excitation wavelength-dependent PL data. As long as both the relaxation and radiative recombination rates are practically constant throughout the excitation wavelength range, then by normalizing the photon flux to a constant value, the collected PL intensity is proportional to the absorption spectra. An example of this similarity can be seen in Figure 2.7.1, where all of the excitonic states (A, B, and C) are matched in both the absorption and PLE spectra of 1L-WSe_2. In this dissertation, PLE was used to identify plasmonically enhanced absorption in the SPE states of 1L-WSe_2 positioned within the plasmonic hotspot of Au nanoantennas.

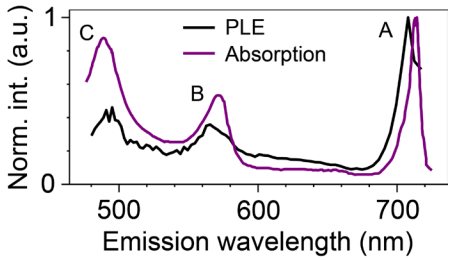


Figure 2.7.1: PLE spectra maps absorption. Example PLE and absorption spectra taken on 1L-WSe_2 showing the A, B, and C exciton resonances. The absorption spectra are adapted from Lee, Jeong, et al., Optics Express, 2018, 26, 18, 23061 – 23068[99].

To normalize the incident photon flux in a PLE measurement, correction factors are calculated and applied afterwards. To calculate the correction factors, chromatic aberrations in the optical microscope must be accounted for by measuring the excitation laser FWHM at 10 different

wavelengths across the excitation range. Then, by interpolating between these measurements, measuring the excitation powers at each wavelength, and assuming that the material system is in a linear excitation regime, excitation intensities at each excitation power are found. Correction factors are then calculated by fixing the excitation intensity to a constant value. Examples of the calibration measurements are shown in Figure 2.7.2. By multiplying the correction factors by the integrated PL intensity at each excitation wavelength, the PLE curve is obtained, as shown in Figure 2.7.3. One important consideration in this approach to PLE is that the material system must have a near-constant quantum yield at the powers and excitation wavelengths used. In the case of 1L-WSe_2, excitonic states reach a saturation regime at high excitation powers (>200 nW), so if some excitation wavelengths use higher powers that saturate the state in question, those PLE data points will be artificially lowered, skewing the dataset. To avoid this, excitation powers are minimized.

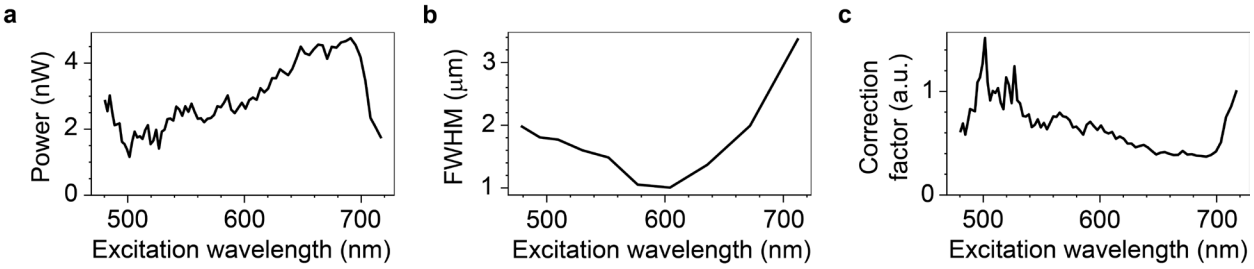


Figure 2.7.2: PLE spectroscopy calibration measurements. (a) Measured excitation powers, converted to power on sample, at each wavelength during a PLE measurement. (b) Interpolated curve showing the FWHM of the excitation laser spot. (c) Calculated correction factors at each excitation wavelength.

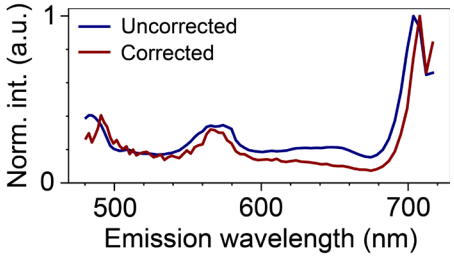


Figure 2.7.3: Effect of correction factors on a PLE spectrum. PLE curves with and without correction factors applied. Without the correction factors, the spectral position, linewidth, and noise floor are not accurately shown.

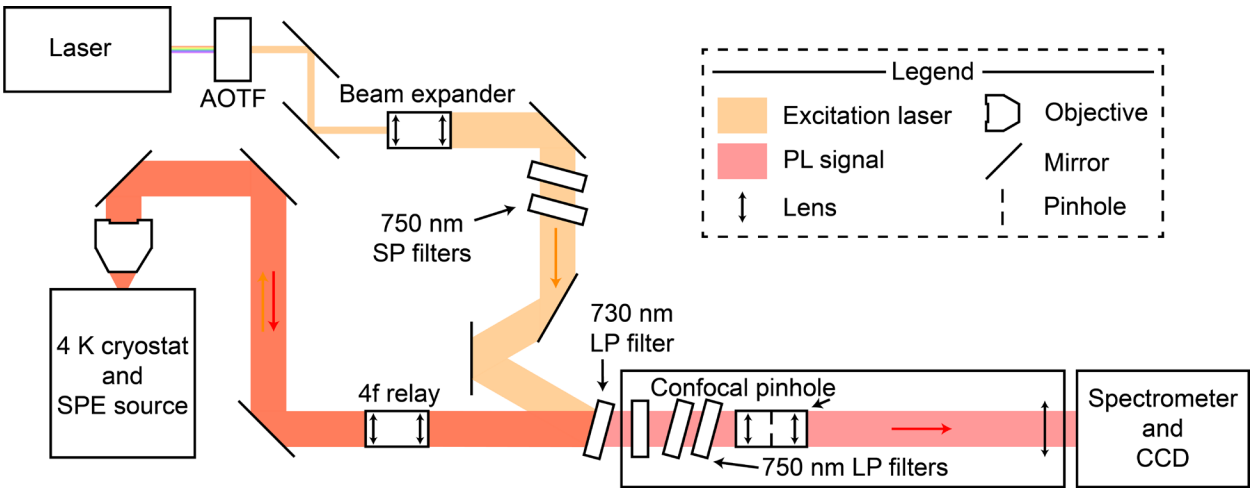


Figure 2.7.4: Optical setup for PLE spectroscopy. Schematic showing the optical setup used to collect PLE data. Due to the need for various excitation wavelengths, a white light laser coupled to an AOTF is used to isolate narrow excitation bands. Instead of a dichroic mirror, a 730 nm spectral LP filter is used to reflect the excitation laser while transmitting the PL signal.

Figure 2.7.4 shows the optical setup used to collect PLE data. An NKT Photonic Supercontinuum laser was passed into a Gooch and Housego acusto-optic tunable filter (AOTF) acting as a tunable laser system. These types of setups are known to couple other diffraction peaks and stray light into the optical path. To block these photons, 750 nm short pass filters are rotated into 720 nm short pass filters. For 1L-WSe_2 at 4 K, the A exciton lies around ~720 nm, so by

exciting as close to the A exciton resonance as possible, observations into the strain of each SPE state are also made.

The easiest way to guide a wide variety of excitation wavelengths (480 – 715 nm) to the sample is by using a dichroic beam splitter. Due to the low availability of dichroic mirrors with narrow transmission step edges and custom wavelengths, a high-quality 730 nm spectral long pass filter is used to guide photons to the sample and isolate back-reflected laser light from the PL signal. PL spectra are then acquired using a Horiba iHR320 spectrometer and an Andor idus 416 CCD camera. Although all the optical elements used are achromatic between 400 – 700 nm, chromatic aberrations and field curvature led to substantial changes in the focus of the microscope as the wavelength is swept. To best account for this, the 4f relay is optimized for a central wavelength (595 nm). This optimization is apparent when observing that the FWHM measured near 595 nm is the minimum value in Figure 2.7.2b. By implementing automated optical elements and active feedback to the microscope, these calibrations and chromatic aberrations can be minimized from the measurement, but doing so adds multiple layers of complexity. For an in-depth analysis of adding automated systems to a PLE measurement, please see the dissertation of Dr. Matthew Strasbourg[84].

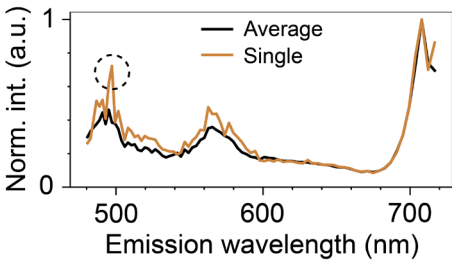


Figure 2.7.5: Averaging multiple PLE spectra eliminates noise. Average and single measurement PLE spectra showing how anomalous quantum behavior is reduced. The spike seen in the single PLE spectra, shown in the black dashed circle, is resolved using the average of 7 independent PLE measurements.

2.7.1 PLE Data on Nanophotonic Systems with Quantum Light Sources

In Chapter 4, PLE spectra are taken on 1L-WSe_2 flakes draped over embedded plasmonic nanoantennas at 4 K. PLE is used to identify anomalous enhancements in the absorption of SPEs positioned above the apex of the nanoantenna. The enhanced absorption observed comes from localized surface plasmon resonances in the nanoantenna. Taking PLE spectroscopy on quantum light sources adds a layer of difficulty because these states are known to spectrally blink and drift in time (as shown in Figure 2.6.1a), so for a ~120-second PLE measurement, the state could change significantly. To accommodate this, multiple (5-10) PLE spectra are taken consecutively at the same location. These added iterations reduce the overall noise in the measurement, as seen in Figure 2.7.5. Averaging the PLE spectra into one dataset (Figure 2.7.6a) and integrating about each specific quantum state results in emitter-resolved PLE curves, such as in Figure 2.7.6b. Also seen in this PLE curve is the plasmonic enhancement spectra of the nanoantenna, calculated using finite element analysis and seen in Figure 2.3.4b, meaning that the 803 nm emitter studied is positioned within the plasmonic hot spot of the nanoantenna. More details on the analysis of this PLE data set can be found in Chapter 4.

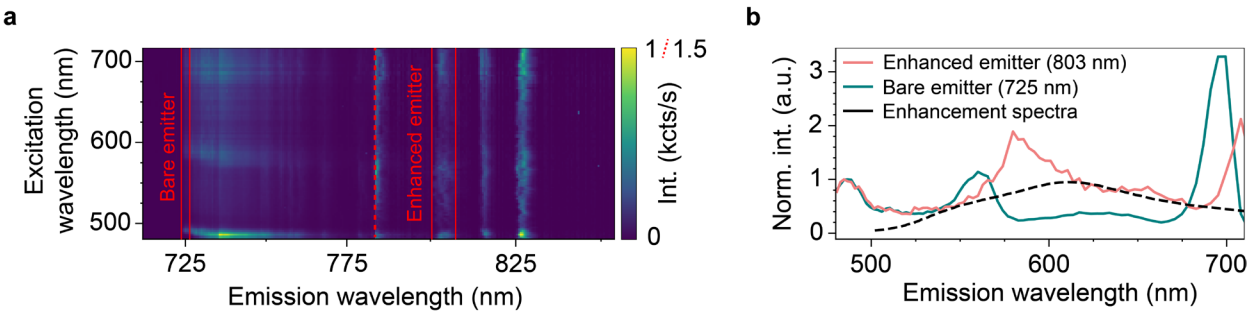


Figure 2.7.6: Emitter integrated PLE spectra. (a) PLE data before integration. The red dashed line represents different intensity scaling for the short and long wavelength regions. Labeled in red solid lines are the integration regions for the emitters in (b). (b) Emitter integrated PLE spectra. The enhanced emitter at 803 nm lies within the plasmonic hotspot of the underlying Au nanoantenna, represented by the enhancement spectra matching the PLE data.

2.8 Near-Field Optical Spectroscopy

Scanning near-field optical microscopy (SNOM) is a technique for spectroscopic measurements beneath the diffraction limit. The SNOM measurements conducted in Chapter 4 are done using an AFM outfitted with a side objective to excite an Au-coated AFM tip and collect fluorescence from the sample. These SNOM measurements were paramount to determining the quality of the plasmonic resonance of Au nanoantennas. The operating principle in SNOM varies based on the type of tip used, but generally relies on localized evanescent fields at the apex of a tip to generate an enhanced signal when the tip is in contact with the sample.

For this work, the tips used are apertureless Au-coated AFM tips. The evanescent fields used to excite regions of the sample beneath the diffraction limit are created by the localized surface plasmon resonance in the Au coating of the tips. Localized surface plasmons are collective excitations of electrons in plasmonic nanostructures that, when resonantly excited, host areas of electric field enhancement. By exciting the Au tip with laser light polarized along the long axis of the tip, fields are enhanced at the apex as seen in the finite element model of Figure 2.3.4a. One of

many complications with this SNOM modality is that by exciting the tip from the side, an area of the sample larger than the tip's evanescent field is also excited. Subtracting the far-field contribution from the data is done by considering the near-field contrast rather than the gross signal.

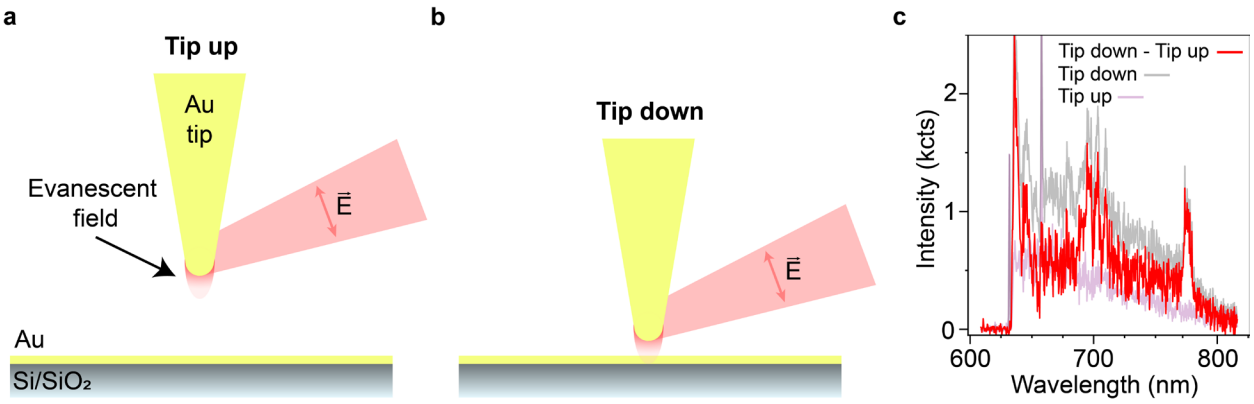


Figure 2.8.1: Tip up vs Tip down in SNOM. (a) Simplified schematic showing that the evanescent field, generated from an LSPR in the Au tip, is not interacting with the underlying Au surface because the tip is retracted from the surface. (b) A similar schematic to (a), but now with the tip near the Au surface. This proximity permits the evanescent field to enhance electron excitations in the Au film. (c) Example Au luminescence spectra taken with the Au tip up and down. By subtracting the tip-up spectra from the tip-down spectra, the enhanced luminescence and Raman lines from material within the gap are shown.

2.8.1 Near-Field Contrast

Since SNOM is conducted using an AFM as the platform, simultaneous topological measurements are conducted alongside spectroscopic data collection. This allows the tool to take two separate hyperspectral maps during a near-field measurement. One with the tip retracted away from the surface by ~100 nm (tip-up Figure 2.8.1a) and another with the tip on the surface (tip-down Figure 2.8.1b). Then, by subtracting the tip-up spectra from the tip-down spectra, the contribution of the evanescent field is isolated from the far-field. An example of these different spectra is seen in Figure 2.8.1c. Here, Au luminescence and a series of Raman lines near 680 – 720

nm and ~775 nm show enhancement. This indicates that a plasmonic gap mode is being excited between the Au tip and the Au layer on the substrate, creating enhanced emission from the Au surfaces within the gap.

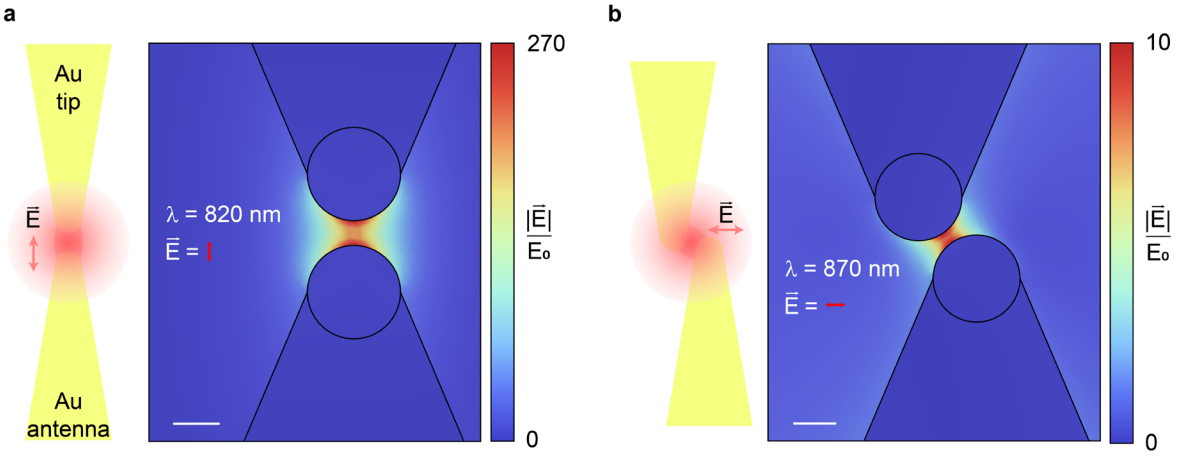


Figure 2.8.2: Polarization-dependent gap plasmons between two Au tips. (a) An example excitation scheme and COMSOL model for a p-polarized gap plasmon between the Au-coated AFM tip and an underlying Au nanoantenna with the same dimensions. (b) An example excitation scheme and COMSOL model for an s-polarized gap plasmon between the Au-coated AFM tip and an underlying Au nanoantenna. Scale bars = 5 nm

Another form of near-field contrast comes from tuning the polarization state of the laser used to excite the Au AFM tip. For the Au luminescence measurements taken in Chapter 4, to test the plasmonic nature of a sample of Au nanoantennas, exciting with different polarization states should permit gap plasmon modes for both p (long axis) and s (radial axis) polarized incident waves. Figure 2.8.2a-b shows the excitation scheme and a finite element model of the resulting gap plasmon for p and s-wave excitation, respectively. For p-wave excitation, the gap plasmon is most intense when the tips are in line with one another, so the spatial pattern shown in Figure 2.8.3a is circular and centered about the Au antenna. However, for s-wave excitation, either the Au tip or Au antenna will block the excitation when aligned with the optical axis, generating two side

lobes of enhancement as seen in Figure 2.8.3b. To change the polarization state of the laser for this measurement, we rotate a λ/2 waveplate in the excitation path by 45°.

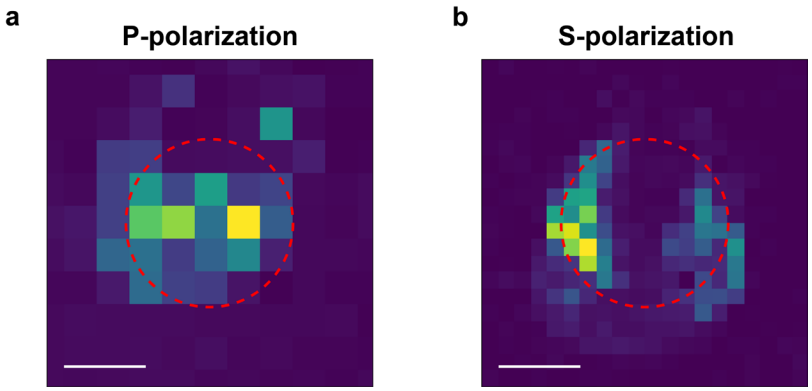


Figure 2.8.3: Polarization-dependent near-field maps. (a) Near-field map of Au luminescence from an underlying Au nanoantenna taken with p-polarization. Highlighted with a red dashed circle in both (a) and (b) is the estimated base diameter of the Au nanoantenna. (b) A similar map to (b), but now taken with a s-polarized incident laser. Now, instead of a circular spatial dependence, two lobes appear, representing the gap plasmon between the two tips when they are side by side.

Chapter 2 References

(1) Novoselov, K. S.; Geim, A. K.; Morozov, S. V.; et al. Electric field effect in atomically thin carbon films. *Science* **2004**, *306* (5696), 666-669. DOI: 10.1126/science.1102896

(2) Mak, K. F.; Lee, C.; Hone, J.; et al. Atomically thin MoS_2: a new direct-gap semiconductor. *Phys Rev Lett* **2010**, *105* (13), 136805. DOI: 10.1103/PhysRevLett.105.136805

(3) Splendiani, A.; Sun, L.; Zhang, Y.; et al. Emerging photoluminescence in monolayer MoS_2. *Nano Lett* **2010**, *10* (4), 1271-1275. DOI: 10.1021/nl903868w

(4) Huang, Y.; Sutter, E.; Shi, N. N.; et al. Reliable Exfoliation of Large-Area High-Quality Flakes of Graphene and Other Two-Dimensional Materials. *ACS Nano* **2015**, *9* (11), 10612-10620. DOI: 10.1021/acsnano.5b04258

(5) Giza, M.; Mukhopadhyay, K.; Ravichandran, H.; et al. Exploring the Application of Gold-Assisted Exfoliation in Large-scale Integration of n-Type and p-Type 2D-FETs. *Small Methods* **2026**, *10* (3), e2500559. DOI: 10.1002/smtd.202500559

(6) Huang, G.; Chen, R.; Chen, M.; et al. Transfer and beyond: emerging strategies and trends in two-dimensional material device fabrication. *Chem Soc Rev* **2026**. DOI: 10.1039/d5cs00531k

(7) Heyl, M.; List-Kratochvil, E. J. W. Only gold can pull this off: mechanical exfoliations of transition metal dichalcogenides beyond scotch tape. *Applied Physics A* **2022**, *129* (1). DOI: 10.1007/s00339-022-06297-z

(8) Islam, M. A.; Serles, P.; Kumral, B.; et al. Exfoliation mechanisms of 2D materials and their applications. *Applied Physics Reviews* **2022**, *9* (4). DOI: 10.1063/5.0090717

(9) Chen, C.; Zhang, N.; Li, W.; et al. Water Contact Angle Dependence with Hydroxyl Functional Groups on Silica Surfaces under CO_2 Sequestration Conditions. *Environ Sci Technol* **2015**, *49* (24), 14680-14687. DOI: 10.1021/acs.est.5b03646

(10) Godin, K.; Kang, K.; Fu, S.; et al. Increased monolayer domain size and patterned growth of tungsten disulfide through controlling surface energy of substrates. *Journal of Physics D: Applied Physics* **2016**, *49* (32). DOI: 10.1088/0022-3727/49/32/325304

(11) Rokni, H.; Lu, W. Direct measurements of interfacial adhesion in 2D materials and van der Waals heterostructures in ambient air. *Nat Commun* **2020**, *11* (1), 5607. DOI: 10.1038/s41467-020-19411-7

(12) Torres, J.; Zhu, Y.; Liu, P.; et al. Adhesion Energies of 2D Graphene and MoS_2 to Silicon and Metal Substrates. *physica status solidi (a)* **2017**, *215* (1). DOI: 10.1002/pssa.201700512

(13) Budania, P.; Baine, P. T.; Montgomery, J. H.; et al. Comparison between Scotch tape and gel-assisted mechanical exfoliation techniques for preparation of 2D transition metal dichalcogenide flakes. *Micro & Nano Letters* **2017**, *12* (12), 970-973. DOI: 10.1049/mnl.2017.0280

(14) Yu, H.; Liao, M.; Zhao, W.; et al. Wafer-Scale Growth and Transfer of Highly-Oriented Monolayer MoS_2 Continuous Films. *ACS Nano* **2017**, *11* (12), 12001-12007. DOI: 10.1021/acsnano.7b03819

(15) Lan, C.; Zhou, Z.; Zhou, Z.; et al. Wafer-scale synthesis of monolayer WS_2 for high-performance flexible photodetectors by enhanced chemical vapor deposition. *Nano Research* **2018**, *11* (6), 3371-3384. DOI: 10.1007/s12274-017-1941-4

(16) Hu, J.; Zhou, F.; Wang, J.; et al. Chemical Vapor Deposition Syntheses of Wafer-Scale 2D Transition Metal Dichalcogenide Films toward Next-Generation Integrated Circuits Related Applications. *Advanced Functional Materials* **2023**, *33* (40). DOI: 10.1002/adfm.202303520

(17) Chou, S. A.; Chang, C.; Wu, B. H.; et al. Large-scale alkali-assisted growth of monolayer and bilayer WSe_2 with a low defect density. *Nat Commun* **2025**, *16* (1), 2777. DOI: 10.1038/s41467-025-57986-1

(18) Velicky, M.; Donnelly, G. E.; Hendren, W. R.; et al. Mechanism of Gold-Assisted Exfoliation of Centimeter-Sized Transition-Metal Dichalcogenide Monolayers. *ACS Nano* **2018**, *12* (10), 10463-10472. DOI: 10.1021/acsnano.8b06101

(19) Panasci, S. E.; Schiliro, E.; Greco, G.; et al. Strain, Doping, and Electronic Transport of Large Area Monolayer MoS_2 Exfoliated on Gold and Transferred to an Insulating Substrate. *ACS Appl Mater Interfaces* **2021**, *13* (26), 31248-31259. DOI: 10.1021/acsami.1c05185

(20) Chen, S.; Li, B.; Dai, C.; et al. Controlling Gold-Assisted Exfoliation of Large-Area MoS_2 Monolayers with External Pressure. *Nanomaterials (Basel)* **2024**, *14* (17). DOI: 10.3390/nano14171418

(21) Shepard, G. D.; Ajayi, O. A.; Li, X.; et al. Nanobubble induced formation of quantum emitters in monolayer semiconductors. *2D Materials* **2017**, *4* (2). DOI: 10.1088/2053-1583/aa629d

(22) Darlington, T. P.; Carmesin, C.; Florian, M.; et al. Imaging strain-localized excitons in nanoscale bubbles of monolayer WSe_2 at room temperature. *Nat Nanotechnol* **2020**, *15* (10), 854-860. DOI: 10.1038/s41565-020-0730-5

(23) Blundo, E.; Surrente, A.; Spirito, D.; et al. Vibrational Properties in Highly Strained Hexagonal Boron Nitride Bubbles. *Nano Lett* **2022**, *22* (4), 1525-1533. DOI: 10.1021/acs.nanolett.1c04197

(24) Shabani, S.; Darlington, T. P.; Gordon, C.; et al. Ultralocalized Optoelectronic Properties of Nanobubbles in 2D Semiconductors. *Nano Lett* **2022**, *22* (18), 7401-7407. DOI: 10.1021/acs.nanolett.2c02265

(25) 2D Semiconductors. *2D Semiconductors all products*. 2026. https://2dsemiconductors.com/all-products/ (accessed March 5, 2026).

(26) HQ Graphene. *HQ Graphene all semiconductors*. 2026. https://www.hqgraphene.com/All-Semiconductors.php (accessed March 5, 2026).

(27) Smith, T. The hydrophilic nature of a clean gold surface. *Journal of Colloid and Interface Science* **1980**, *75* (1), 51-55. DOI: 10.1016/0021-9797(80)90348-3

(28) Cai, T.; Kim, J.-H.; Yang, Z.; et al. Radiative Enhancement of Single Quantum Emitters in WSe2 Monolayers Using Site-Controlled Metallic Nanopillars. *ACS Photonics* **2018**, *5* (9), 3466-3471. DOI: 10.1021/acsphotonics.8b00580

(29) Guo, S.; Germanis, S.; Taniguchi, T.; et al. Electrically Driven Site-Controlled Single Photon Source. *ACS Photonics* **2023**, *10* (8), 2549-2555. DOI: 10.1021/acsphotonics.3c00097

(30) Chhaperwal, M.; Tongale, H. M.; Hays, P.; et al. Simultaneously Enhancing Brightness and Purity of WSe_2 Single Photon Emitter Using High-Aspect-Ratio Nanopillar Array on Metal. *Nano Lett* **2024**, *24* (40), 12461-12468. DOI: 10.1021/acs.nanolett.4c03168

(31) Branny, A.; Kumar, S.; Proux, R.; et al. Deterministic strain-induced arrays of quantum emitters in a two-dimensional semiconductor. *Nat Commun* **2017**, *8* (1), 15053. DOI: 10.1038/ncomms15053

(32) Duong, N. M. H.; Xu, Z.-Q.; Kianinia, M.; et al. Enhanced Emission from WSe_2 Monolayers Coupled to Circular Bragg Gratings. *ACS Photonics* **2018**, *5* (10), 3950-3955. DOI: 10.1021/acsphotonics.8b00865

(33) Iff, O.; Davanco, M.; Betzold, S.; et al. Hyperspectral study of the coupling between trions in WSe_2 monolayers to a circular Bragg grating cavity. *C R Phys* **2021**, *22* (Suppl 4). DOI: 10.5802/crphys.76

(34) Iff, O.; Buchinger, Q.; Moczala-Dusanowska, M.; et al. Purcell-Enhanced Single Photon Source Based on a Deterministically Placed WSe_2 Monolayer Quantum Dot in a Circular Bragg Grating Cavity. *Nano Lett* **2021**, *21* (11), 4715-4720. DOI: 10.1021/acs.nanolett.1c00978

(35) Hekmati, R.; Hadden, J. P.; Mathew, A.; et al. Bullseye dielectric cavities for photon collection from a surface-mounted quantum-light-emitter. *Sci Rep* **2023**, *13* (1), 5316. DOI: 10.1038/s41598-023-32359-0

(36) Luo, Y.; Liu, N.; Li, X.; et al. Single photon emission in WSe_2 up to 160 K by quantum yield control. *2D Materials* **2019**, *6* (3). DOI: 10.1088/2053-1583/ab15fe

(37) Li, C.; Luo, H.; Hou, L.; et al. Giant Photoluminescence Enhancement of Monolayer WSe_2 Using a Plasmonic Nanocavity with On-Demand Resonance. *Nano Lett* **2024**, *24* (19), 5879-5885. DOI: 10.1021/acs.nanolett.4c01260

(38) Peng, L.; Chan, H.; Choo, P.; et al. Creation of Single-Photon Emitters in WSe_2 Monolayers Using Nanometer-Sized Gold Tips. *Nano Lett* **2020**, *20* (8), 5866-5872. DOI: 10.1021/acs.nanolett.0c01789

(39) Luo, Y.; Shepard, G. D.; Ardelean, J. V.; et al. Deterministic coupling of site-controlled quantum emitters in monolayer WSe_2 to plasmonic nanocavities. *Nat Nanotechnol* **2018**, *13* (12), 1137-1142. DOI: 10.1038/s41565-018-0275-z

(40) Drawer, J. C.; Mitryakhin, V. N.; Shan, H.; et al. Monolayer-Based Single-Photon Source in a Liquid-Helium-Free Open Cavity Featuring 65% Brightness and Quantum Coherence. *Nano Lett* **2023**, *23* (18), 8683-8689. DOI: 10.1021/acs.nanolett.3c02584

(41) Mohajerani, S. S.; Noual, A.; Ma, Y.; et al. Acoustic Manipulation of Deterministic Quantum Emitters in WSe_2. *ACS Nano* **2025**, *19* (28), 25851-25859. DOI: 10.1021/acsnano.5c04710

(42) Erbas, B.; Conde-Rubio, A.; Liu, X.; et al. Combining thermal scanning probe lithography and dry etching for grayscale nanopattern amplification. *Microsyst Nanoeng* **2024**, *10*, 28. DOI: 10.1038/s41378-024-00655-y

(43) Howell, S. T.; Grushina, A.; Holzner, F.; et al. Thermal scanning probe lithography-a review. *Microsyst Nanoeng* **2020**, *6*, 21. DOI: 10.1038/s41378-019-0124-8

(44) Ocola, L. E.; Costales, M.; Gosztola, D. J. Development characteristics of polymethyl methacrylate in alcohol/water mixtures: a lithography and Raman spectroscopy study. *Nanotechnology* **2016**, *27* (3), 035302. DOI: 10.1088/0957-4484/27/3/035302

(45) Yasin, S.; Hasko, D. G.; Ahmed, H. Fabrication of <5 nm width lines in poly(methylmethacrylate) resist using a water:isopropyl alcohol developer and ultrasonically-assisted development. *Applied Physics Letters* **2001**, *78* (18), 2760-2762. DOI: 10.1063/1.1369615

(46) Spindt, C. A. Microfabricated field-emission and field-ionization sources. *Surface Science* **1992**, *266* (1-3), 145-154. DOI: 10.1016/0039-6028(92)91012-z

(47) Huang, J.; Huang, Y.; Zeng, M.; et al. Fabrication of Spindt-Type Nanometer-Sized Chromium Tips for Application as Field-Electron Emitters by Releasing the Stress of the Deposited Thin Film. *ACS Applied Nano Materials* **2022**, *6* (1), 351-357. DOI: 10.1021/acsanm.2c04457

(48) Eschimese, D.; Vaurette, F.; Melin, T.; et al. Precise tailoring of evaporated gold nanocones using electron beam lithography and lift-off. *Nanotechnology* **2020**, *31* (22), 225302. DOI: 10.1088/1361-6528/ab746e

(49) Sun, B.; Grap, T.; Frahm, T.; et al. Role of electron and ion irradiation in a reliable lift-off process with electron beam evaporation and a bilayer PMMA resist system. *Journal of Vacuum Science & Technology B, Nanotechnology and Microelectronics: Materials, Processing, Measurement, and Phenomena* **2021**, *39* (5). DOI: 10.1116/6.0001161

(50) Chou, S. Y.; Krauss, P. R.; Renstrom, P. J. Imprint of sub-25 nm vias and trenches in polymers. *Applied Physics Letters* **1995**, *67* (21), 3114-3116. DOI: 10.1063/1.114851

(51) Guo, L. J. Nanoimprint Lithography: Methods and Material Requirements. *Advanced Materials* **2007**, *19* (4), 495-513. DOI: 10.1002/adma.200600882

(52) Schift, H. Nanoimprint lithography: An old story in modern times? A review. *Journal of Vacuum Science & Technology B: Microelectronics and Nanometer Structures Processing, Measurement, and Phenomena* **2008**, *26* (2), 458-480. DOI: 10.1116/1.2890972

(53) Rosenberger, M. R.; Dass, C. K.; Chuang, H. J.; et al. Quantum Calligraphy: Writing Single-Photon Emitters in a Two-Dimensional Materials Platform. *ACS Nano* **2019**, *13* (1), 904-912. DOI: 10.1021/acsnano.8b08730

(54) Fix, J. P. Bandgap Engineering of 2D Semiconductors for Quantum and Optoelectronic Technologies. Montana State University, 2025.

(55) Yao, J.; Lai, F.; Fan, Y.; et al. Nonlocal meta-lens with Huygens' bound states in the continuum. *Nat Commun* **2024**, *15* (1), 6543. DOI: 10.1038/s41467-024-50965-y

(56) Rosiek, C. A.; Arregui, G.; Vladimirova, A.; et al. Observation of strong backscattering in valley-Hall photonic topological interface modes. *Nature Photonics* **2023**, *17* (5), 386-392. DOI: 10.1038/s41566-023-01189-x

(57) Rose, A.; Hoang, T. B.; McGuire, F.; et al. Control of radiative processes using tunable plasmonic nanopatch antennas. *Nano Lett* **2014**, *14* (8), 4797-4802. DOI: 10.1021/nl501976f

(58) Camacho, M.; Edwards, B.; Engheta, N. A single inverse-designed photonic structure that performs parallel computing. *Nat Commun* **2021**, *12* (1), 1466. DOI: 10.1038/s41467-021-21664-9

(59) Liu, Y.; Zentgraf, T.; Bartal, G.; et al. Transformational plasmon optics. *Nano Lett* **2010**, *10* (6), 1991-1997. DOI: 10.1021/nl1008019

(60) Barreau, V.; Yu, D.; Hensel, R.; et al. Elevated temperature adhesion of bioinspired polymeric micropatterns to glass. *J Mech Behav Biomed Mater* **2017**, *76*, 110-118. DOI: 10.1016/j.jmbbm.2017.04.007

(61) Liu, K.; Yan, Q.; Chen, M.; et al. Elastic properties of chemical-vapor-deposited monolayer MoS_2, WS_2, and their bilayer heterostructures. *Nano Lett* **2014**, *14* (9), 5097-5103. DOI: 10.1021/nl501793a

(62) Castellanos-Gomez, A.; Buscema, M.; Molenaar, R.; et al. Deterministic transfer of two-dimensional materials by all-dry viscoelastic stamping. *2D Materials* **2014**, *1* (1). DOI: 10.1088/2053-1583/1/1/011002

(63) Xie, L.; Du, L.; Lu, X.; et al. A facile and efficient dry transfer technique for two-dimensional Van der Waals heterostructure. *Chinese Physics B* **2017**, *26* (8). DOI: 10.1088/1674-1056/26/8/087306

(64) Son, S.; Shin, Y. J.; Zhang, K.; et al. Strongly adhesive dry transfer technique for van der Waals heterostructure. *2D Materials* **2020**, *7* (4). DOI: 10.1088/2053-1583/abad0b

(65) Wang, W.; Clark, N.; Hamer, M.; et al. Clean assembly of van der Waals heterostructures using silicon nitride membranes. *Nature Electronics* **2023**, *6* (12), 981-990. DOI: 10.1038/s41928-023-01075-y

(66) Reina, A.; Jia, X.; Ho, J.; et al. Large area, few-layer graphene films on arbitrary substrates by chemical vapor deposition. *Nano Lett* **2009**, *9* (1), 30-35. DOI: 10.1021/nl801827v

(67) Lee, Y.; Bae, S.; Jang, H.; et al. Wafer-scale synthesis and transfer of graphene films. *Nano Lett* **2010**, *10* (2), 490-493. DOI: 10.1021/nl903272n

(68) Li, B.; He, Y.; Lei, S.; et al. Scalable Transfer of Suspended Two-Dimensional Single Crystals. *Nano Lett* **2015**, *15* (8), 5089-5097. DOI: 10.1021/acs.nanolett.5b01210

(69) Ma, X.; Liu, Q.; Xu, D.; et al. Capillary-Force-Assisted Clean-Stamp Transfer of Two-Dimensional Materials. *Nano Lett* **2017**, *17* (11), 6961-6967. DOI: 10.1021/acs.nanolett.7b03449

(70) Hempel, M.; Lu, A. Y.; Hui, F.; et al. Repeated roll-to-roll transfer of two-dimensional materials by electrochemical delamination. *Nanoscale* **2018**, *10* (12), 5522-5531. DOI: 10.1039/c7nr07369k

(71) Chen, S.; Chen, G.; Zhao, Y.; et al. Tunable Adhesion for All-Dry Transfer of 2D Materials Enabled by the Freezing of Transfer Medium. *Adv Mater* **2024**, *36* (15), e2308950. DOI: 10.1002/adma.202308950

(72) Chernikov, A.; Berkelbach, T. C.; Hill, H. M.; et al. Exciton binding energy and nonhydrogenic Rydberg series in monolayer WS_2. *Phys Rev Lett* **2014**, *113* (7), 076802. DOI: 10.1103/PhysRevLett.113.076802

(73) He, K.; Kumar, N.; Zhao, L.; et al. Tightly bound excitons in monolayer WSe_2. *Phys Rev Lett* **2014**, *113* (2), 026803. DOI: 10.1103/PhysRevLett.113.026803

(74) He, Y. M.; Clark, G.; Schaibley, J. R.; et al. Single quantum emitters in monolayer semiconductors. *Nat Nanotechnol* **2015**, *10* (6), 497-502. DOI: 10.1038/nnano.2015.75

(75) Koperski, M.; Nogajewski, K.; Arora, A.; et al. Single photon emitters in exfoliated WSe_2 structures. *Nat Nanotechnol* **2015**, *10* (6), 503-506. DOI: 10.1038/nnano.2015.67

(76) Kumar, S.; Kaczmarczyk, A.; Gerardot, B. D. Strain-Induced Spatial and Spectral Isolation of Quantum Emitters in Mono- and Bilayer WSe_2. *Nano Lett* **2015**, *15* (11), 7567-7573. DOI: 10.1021/acs.nanolett.5b03312

(77) Srivastava, A.; Sidler, M.; Allain, A. V.; et al. Optically active quantum dots in monolayer WSe_2. *Nat Nanotechnol* **2015**, *10* (6), 491-496. DOI: 10.1038/nnano.2015.60

(78) Tonndorf, P.; Schmidt, R.; Schneider, R.; et al. Single-photon emission from localized excitons in an atomically thin semiconductor. *Optica* **2015**, *2* (4). DOI: 10.1364/optica.2.000347

(79) Linhart, L.; Paur, M.; Smejkal, V.; et al. Localized Intervalley Defect Excitons as Single-Photon Emitters in WSe_2. *Phys Rev Lett* **2019**, *123* (14), 146401. DOI: 10.1103/PhysRevLett.123.146401

(80) Chakraborty, C.; Kinnischtzke, L.; Goodfellow, K. M.; et al. Voltage-controlled quantum light from an atomically thin semiconductor. *Nat Nanotechnol* **2015**, *10* (6), 507-511. DOI: 10.1038/nnano.2015.79

(81) Palacios-Berraquero, C.; Barbone, M.; Kara, D. M.; et al. Atomically thin quantum light-emitting diodes. *Nat Commun* **2016**, *7* (1), 12978. DOI: 10.1038/ncomms12978

(82) Schwarz, S.; Kozikov, A.; Withers, F.; et al. Electrically pumped single-defect light emitters in WSe_2. *2D Materials* **2016**, *3* (2). DOI: 10.1088/2053-1583/3/2/025038

(83) So, J. P.; Kim, H. R.; Baek, H.; et al. Electrically driven strain-induced deterministic single-photon emitters in a van der Waals heterostructure. *Sci Adv* **2021**, *7* (43), eabj3176. DOI: 10.1126/sciadv.abj3176

(84) Strasbourg, M. Thermalization and Exciton Localization in 2D Semiconductors. Montana State University, 2023.

(85) Zhang, L.; Yu, Y. J.; Chen, L. G.; et al. Electrically driven single-photon emission from an isolated single molecule. *Nat Commun* **2017**, *8* (1), 580. DOI: 10.1038/s41467-017-00681-7

(86) Rezus, Y. L.; Walt, S. G.; Lettow, R.; et al. Single-photon spectroscopy of a single molecule. *Phys Rev Lett* **2012**, *108* (9), 093601. DOI: 10.1103/PhysRevLett.108.093601

(87) Lounis, B.; Moerner, W. E. Single photons on demand from a single molecule at room temperature. *Nature* **2000**, *407* (6803), 491-493. DOI: 10.1038/35035032

(88) Doherty, M. W.; Manson, N. B.; Delaney, P.; et al. The nitrogen-vacancy colour centre in diamond. *Physics Reports* **2013**, *528* (1), 1-45. DOI: 10.1016/j.physrep.2013.02.001

(89) Kurtsiefer, C.; Mayer, S.; Zarda, P.; et al. Stable solid-state source of single photons. *Phys Rev Lett* **2000**, *85* (2), 290-293. DOI: 10.1103/PhysRevLett.85.290

(90) Brouri, R.; Beveratos, A.; Poizat, J. P.; et al. Photon antibunching in the fluorescence of individual color centers in diamond. *Opt Lett* **2000**, *25* (17), 1294-1296. DOI: 10.1364/ol.25.001294

(91) Yuan, Z.; Kardynal, B. E.; Stevenson, R. M.; et al. Electrically driven single-photon source. *Science* **2002**, *295* (5552), 102-105. DOI: 10.1126/science.1066790

(92) Santori, C.; Fattal, D.; Vuckovic, J.; et al. Indistinguishable photons from a single-photon device. *Nature* **2002**, *419* (6907), 594-597. DOI: 10.1038/nature01086

(93) Michler, P.; Kiraz, A.; Becher, C.; et al. A quantum dot single-photon turnstile device. *Science* **2000**, *290* (5500), 2282-2285. DOI: 10.1126/science.290.5500.2282

(94) Tran, T. T.; Bray, K.; Ford, M. J.; et al. Quantum emission from hexagonal boron nitride monolayers. *Nat Nanotechnol* **2016**, *11* (1), 37-41. DOI: 10.1038/nnano.2015.242

(95) Sajid, A.; Ford, M. J.; Reimers, J. R. Single-photon emitters in hexagonal boron nitride: a review of progress. *Rep Prog Phys* **2020**, *83* (4), 044501. DOI: 10.1088/1361-6633/ab6310

(96) Li, C.; Fröch, J. E.; Nonahal, M.; et al. Integration of hBN Quantum Emitters in Monolithically Fabricated Waveguides. *ACS Photonics* **2021**, *8* (10), 2966-2972. DOI: 10.1021/acsphotonics.1c00890

(97) Serati de Brito, C.; Rosa, B. L. T.; Chaves, A.; et al. Probing the Nature of Single-Photon Emitters in a WSe_2 Monolayer by Magneto-Photoluminescence Spectroscopy. *Nano Lett* **2024**, *24* (42), 13300-13306. DOI: 10.1021/acs.nanolett.4c03686

(98) Strasbourg, M. C.; Yanev, E. S.; Darlington, T. P.; et al. Characterization of quantum dot-like emitters in programmable arrays of nanowrinkles of 1L-WSe_2. *Journal of Applied Physics* **2024**, *136* (4). DOI: 10.1063/5.0214410

(99) Lee, S. Y.; Jeong, T. Y.; Kim, J. H.; et al. Self-consistent dielectric constant determination for monolayer WSe_2. *Opt Express* **2018**, *26* (18), 23061-23068. DOI: 10.1364/OE.26.023061

(1) Novoselov, K. S.; Geim, A. K.; Morozov, S. V.; et al. Electric field effect in atomically thin carbon films. *Science* **2004**, *306* (5696), 666-669. DOI: 10.1126/science.1102896

(2) Mak, K. F.; Lee, C.; Hone, J.; et al. Atomically thin MoS_2: a new direct-gap semiconductor. *Phys Rev Lett* **2010**, *105* (13), 136805. DOI: 10.1103/PhysRevLett.105.136805

(3) Splendiani, A.; Sun, L.; Zhang, Y.; et al. Emerging photoluminescence in monolayer MoS_2. *Nano Lett* **2010**, *10* (4), 1271-1275. DOI: 10.1021/nl903868w

(4) Huang, Y.; Sutter, E.; Shi, N. N.; et al. Reliable Exfoliation of Large-Area High-Quality Flakes of Graphene and Other Two-Dimensional Materials. *ACS Nano* **2015**, *9* (11), 10612-10620. DOI: 10.1021/acsnano.5b04258

(5) Giza, M.; Mukhopadhyay, K.; Ravichandran, H.; et al. Exploring the Application of Gold-Assisted Exfoliation in Large-scale Integration of n-Type and p-Type 2D-FETs. *Small Methods* **2026**, *10* (3), e2500559. DOI: 10.1002/smtd.202500559

(6) Huang, G.; Chen, R.; Chen, M.; et al. Transfer and beyond: emerging strategies and trends in two-dimensional material device fabrication. *Chem Soc Rev* **2026**. DOI: 10.1039/d5cs00531k

(7) Heyl, M.; List-Kratochvil, E. J. W. Only gold can pull this off: mechanical exfoliations of transition metal dichalcogenides beyond scotch tape. *Applied Physics A* **2022**, *129* (1). DOI: 10.1007/s00339-022-06297-z

(8) Islam, M. A.; Serles, P.; Kumral, B.; et al. Exfoliation mechanisms of 2D materials and their applications. *Applied Physics Reviews* **2022**, *9* (4). DOI: 10.1063/5.0090717

(9) Chen, C.; Zhang, N.; Li, W.; et al. Water Contact Angle Dependence with Hydroxyl Functional Groups on Silica Surfaces under CO_2 Sequestration Conditions. *Environ Sci Technol* **2015**, *49* (24), 14680-14687. DOI: 10.1021/acs.est.5b03646

(10) Godin, K.; Kang, K.; Fu, S.; et al. Increased monolayer domain size and patterned growth of tungsten disulfide through controlling surface energy of substrates. *Journal of Physics D: Applied Physics* **2016**, *49* (32). DOI: 10.1088/0022-3727/49/32/325304

(11) Rokni, H.; Lu, W. Direct measurements of interfacial adhesion in 2D materials and van der Waals heterostructures in ambient air. *Nat Commun* **2020**, *11* (1), 5607. DOI: 10.1038/s41467-020-19411-7

(12) Torres, J.; Zhu, Y.; Liu, P.; et al. Adhesion Energies of 2D Graphene and MoS_2 to Silicon and Metal Substrates. *physica status solidi (a)* **2017**, *215* (1). DOI: 10.1002/pssa.201700512

(13) Budania, P.; Baine, P. T.; Montgomery, J. H.; et al. Comparison between Scotch tape and gel-assisted mechanical exfoliation techniques for preparation of 2D transition metal dichalcogenide flakes. *Micro & Nano Letters* **2017**, *12* (12), 970-973. DOI: 10.1049/mnl.2017.0280

(14) Yu, H.; Liao, M.; Zhao, W.; et al. Wafer-Scale Growth and Transfer of Highly-Oriented Monolayer MoS_2 Continuous Films. *ACS Nano* **2017**, *11* (12), 12001-12007. DOI: 10.1021/acsnano.7b03819

(15) Lan, C.; Zhou, Z.; Zhou, Z.; et al. Wafer-scale synthesis of monolayer WS_2 for high-performance flexible photodetectors by enhanced chemical vapor deposition. *Nano Research* **2018**, *11* (6), 3371-3384. DOI: 10.1007/s12274-017-1941-4

(16) Hu, J.; Zhou, F.; Wang, J.; et al. Chemical Vapor Deposition Syntheses of Wafer-Scale 2D Transition Metal Dichalcogenide Films toward Next-Generation Integrated Circuits Related Applications. *Advanced Functional Materials* **2023**, *33* (40). DOI: 10.1002/adfm.202303520

(17) Chou, S. A.; Chang, C.; Wu, B. H.; et al. Large-scale alkali-assisted growth of monolayer and bilayer WSe_2 with a low defect density. *Nat Commun* **2025**, *16* (1), 2777. DOI: 10.1038/s41467-025-57986-1

(18) Velicky, M.; Donnelly, G. E.; Hendren, W. R.; et al. Mechanism of Gold-Assisted Exfoliation of Centimeter-Sized Transition-Metal Dichalcogenide Monolayers. *ACS Nano* **2018**, *12* (10), 10463-10472. DOI: 10.1021/acsnano.8b06101

(19) Panasci, S. E.; Schiliro, E.; Greco, G.; et al. Strain, Doping, and Electronic Transport of Large Area Monolayer MoS_2 Exfoliated on Gold and Transferred to an Insulating Substrate. *ACS Appl Mater Interfaces* **2021**, *13* (26), 31248-31259. DOI: 10.1021/acsami.1c05185

(20) Chen, S.; Li, B.; Dai, C.; et al. Controlling Gold-Assisted Exfoliation of Large-Area MoS_2 Monolayers with External Pressure. *Nanomaterials (Basel)* **2024**, *14* (17). DOI: 10.3390/nano14171418

(21) Shepard, G. D.; Ajayi, O. A.; Li, X.; et al. Nanobubble induced formation of quantum emitters in monolayer semiconductors. *2D Materials* **2017**, *4* (2). DOI: 10.1088/2053-1583/aa629d

(22) Darlington, T. P.; Carmesin, C.; Florian, M.; et al. Imaging strain-localized excitons in nanoscale bubbles of monolayer WSe_2 at room temperature. *Nat Nanotechnol* **2020**, *15* (10), 854-860. DOI: 10.1038/s41565-020-0730-5

(23) Blundo, E.; Surrente, A.; Spirito, D.; et al. Vibrational Properties in Highly Strained Hexagonal Boron Nitride Bubbles. *Nano Lett* **2022**, *22* (4), 1525-1533. DOI: 10.1021/acs.nanolett.1c04197

(24) Shabani, S.; Darlington, T. P.; Gordon, C.; et al. Ultralocalized Optoelectronic Properties of Nanobubbles in 2D Semiconductors. *Nano Lett* **2022**, *22* (18), 7401-7407. DOI: 10.1021/acs.nanolett.2c02265

(25) 2D Semiconductors. *2D Semiconductors all products*. 2026. https://2dsemiconductors.com/all-products/ (accessed March 5, 2026).

(26) HQ Graphene. *HQ Graphene all semiconductors*. 2026. https://www.hqgraphene.com/All-Semiconductors.php (accessed March 5, 2026).

(27) Smith, T. The hydrophilic nature of a clean gold surface. *Journal of Colloid and Interface Science* **1980**, *75* (1), 51-55. DOI: 10.1016/0021-9797(80)90348-3

(28) Cai, T.; Kim, J.-H.; Yang, Z.; et al. Radiative Enhancement of Single Quantum Emitters in WSe2 Monolayers Using Site-Controlled Metallic Nanopillars. *ACS Photonics* **2018**, *5* (9), 3466-3471. DOI: 10.1021/acsphotonics.8b00580

(29) Guo, S.; Germanis, S.; Taniguchi, T.; et al. Electrically Driven Site-Controlled Single Photon Source. *ACS Photonics* **2023**, *10* (8), 2549-2555. DOI: 10.1021/acsphotonics.3c00097

(30) Chhaperwal, M.; Tongale, H. M.; Hays, P.; et al. Simultaneously Enhancing Brightness and Purity of WSe_2 Single Photon Emitter Using High-Aspect-Ratio Nanopillar Array on Metal. *Nano Lett* **2024**, *24* (40), 12461-12468. DOI: 10.1021/acs.nanolett.4c03168

(31) Branny, A.; Kumar, S.; Proux, R.; et al. Deterministic strain-induced arrays of quantum emitters in a two-dimensional semiconductor. *Nat Commun* **2017**, *8* (1), 15053. DOI: 10.1038/ncomms15053

(32) Duong, N. M. H.; Xu, Z.-Q.; Kianinia, M.; et al. Enhanced Emission from WSe_2 Monolayers Coupled to Circular Bragg Gratings. *ACS Photonics* **2018**, *5* (10), 3950-3955. DOI: 10.1021/acsphotonics.8b00865

(33) Iff, O.; Davanco, M.; Betzold, S.; et al. Hyperspectral study of the coupling between trions in WSe_2 monolayers to a circular Bragg grating cavity. *C R Phys* **2021**, *22* (Suppl 4). DOI: 10.5802/crphys.76

(34) Iff, O.; Buchinger, Q.; Moczala-Dusanowska, M.; et al. Purcell-Enhanced Single Photon Source Based on a Deterministically Placed WSe_2 Monolayer Quantum Dot in a Circular Bragg Grating Cavity. *Nano Lett* **2021**, *21* (11), 4715-4720. DOI: 10.1021/acs.nanolett.1c00978

(35) Hekmati, R.; Hadden, J. P.; Mathew, A.; et al. Bullseye dielectric cavities for photon collection from a surface-mounted quantum-light-emitter. *Sci Rep* **2023**, *13* (1), 5316. DOI: 10.1038/s41598-023-32359-0

(36) Luo, Y.; Liu, N.; Li, X.; et al. Single photon emission in WSe_2 up to 160 K by quantum yield control. *2D Materials* **2019**, *6* (3). DOI: 10.1088/2053-1583/ab15fe

(37) Li, C.; Luo, H.; Hou, L.; et al. Giant Photoluminescence Enhancement of Monolayer WSe_2 Using a Plasmonic Nanocavity with On-Demand Resonance. *Nano Lett* **2024**, *24* (19), 5879-5885. DOI: 10.1021/acs.nanolett.4c01260

(38) Peng, L.; Chan, H.; Choo, P.; et al. Creation of Single-Photon Emitters in WSe_2 Monolayers Using Nanometer-Sized Gold Tips. *Nano Lett* **2020**, *20* (8), 5866-5872. DOI: 10.1021/acs.nanolett.0c01789

(39) Luo, Y.; Shepard, G. D.; Ardelean, J. V.; et al. Deterministic coupling of site-controlled quantum emitters in monolayer WSe_2 to plasmonic nanocavities. *Nat Nanotechnol* **2018**, *13* (12), 1137-1142. DOI: 10.1038/s41565-018-0275-z

(40) Drawer, J. C.; Mitryakhin, V. N.; Shan, H.; et al. Monolayer-Based Single-Photon Source in a Liquid-Helium-Free Open Cavity Featuring 65% Brightness and Quantum Coherence. *Nano Lett* **2023**, *23* (18), 8683-8689. DOI: 10.1021/acs.nanolett.3c02584

(41) Mohajerani, S. S.; Noual, A.; Ma, Y.; et al. Acoustic Manipulation of Deterministic Quantum Emitters in WSe_2. *ACS Nano* **2025**, *19* (28), 25851-25859. DOI: 10.1021/acsnano.5c04710

(42) Erbas, B.; Conde-Rubio, A.; Liu, X.; et al. Combining thermal scanning probe lithography and dry etching for grayscale nanopattern amplification. *Microsyst Nanoeng* **2024**, *10*, 28. DOI: 10.1038/s41378-024-00655-y

(43) Howell, S. T.; Grushina, A.; Holzner, F.; et al. Thermal scanning probe lithography-a review. *Microsyst Nanoeng* **2020**, *6*, 21. DOI: 10.1038/s41378-019-0124-8

(44) Ocola, L. E.; Costales, M.; Gosztola, D. J. Development characteristics of polymethyl methacrylate in alcohol/water mixtures: a lithography and Raman spectroscopy study. *Nanotechnology* **2016**, *27* (3), 035302. DOI: 10.1088/0957-4484/27/3/035302

(45) Yasin, S.; Hasko, D. G.; Ahmed, H. Fabrication of <5 nm width lines in poly(methylmethacrylate) resist using a water:isopropyl alcohol developer and ultrasonically-assisted development. *Applied Physics Letters* **2001**, *78* (18), 2760-2762. DOI: 10.1063/1.1369615

(46) Spindt, C. A. Microfabricated field-emission and field-ionization sources. *Surface Science* **1992**, *266* (1-3), 145-154. DOI: 10.1016/0039-6028(92)91012-z

(47) Huang, J.; Huang, Y.; Zeng, M.; et al. Fabrication of Spindt-Type Nanometer-Sized Chromium Tips for Application as Field-Electron Emitters by Releasing the Stress of the Deposited Thin Film. *ACS Applied Nano Materials* **2022**, *6* (1), 351-357. DOI: 10.1021/acsanm.2c04457

(48) Eschimese, D.; Vaurette, F.; Melin, T.; et al. Precise tailoring of evaporated gold nanocones using electron beam lithography and lift-off. *Nanotechnology* **2020**, *31* (22), 225302. DOI: 10.1088/1361-6528/ab746e

(49) Sun, B.; Grap, T.; Frahm, T.; et al. Role of electron and ion irradiation in a reliable lift-off process with electron beam evaporation and a bilayer PMMA resist system. *Journal of Vacuum Science & Technology B, Nanotechnology and Microelectronics: Materials, Processing, Measurement, and Phenomena* **2021**, *39* (5). DOI: 10.1116/6.0001161

(50) Chou, S. Y.; Krauss, P. R.; Renstrom, P. J. Imprint of sub-25 nm vias and trenches in polymers. *Applied Physics Letters* **1995**, *67* (21), 3114-3116. DOI: 10.1063/1.114851

(51) Guo, L. J. Nanoimprint Lithography: Methods and Material Requirements. *Advanced Materials* **2007**, *19* (4), 495-513. DOI: 10.1002/adma.200600882

(52) Schift, H. Nanoimprint lithography: An old story in modern times? A review. *Journal of Vacuum Science & Technology B: Microelectronics and Nanometer Structures Processing, Measurement, and Phenomena* **2008**, *26* (2), 458-480. DOI: 10.1116/1.2890972

(53) Rosenberger, M. R.; Dass, C. K.; Chuang, H. J.; et al. Quantum Calligraphy: Writing Single-Photon Emitters in a Two-Dimensional Materials Platform. *ACS Nano* **2019**, *13* (1), 904-912. DOI: 10.1021/acsnano.8b08730

(54) Fix, J. P. Bandgap Engineering of 2D Semiconductors for Quantum and Optoelectronic Technologies. Montana State University, 2025.

(55) Yao, J.; Lai, F.; Fan, Y.; et al. Nonlocal meta-lens with Huygens' bound states in the continuum. *Nat Commun* **2024**, *15* (1), 6543. DOI: 10.1038/s41467-024-50965-y

(56) Rosiek, C. A.; Arregui, G.; Vladimirova, A.; et al. Observation of strong backscattering in valley-Hall photonic topological interface modes. *Nature Photonics* **2023**, *17* (5), 386-392. DOI: 10.1038/s41566-023-01189-x

(57) Rose, A.; Hoang, T. B.; McGuire, F.; et al. Control of radiative processes using tunable plasmonic nanopatch antennas. *Nano Lett* **2014**, *14* (8), 4797-4802. DOI: 10.1021/nl501976f

(58) Camacho, M.; Edwards, B.; Engheta, N. A single inverse-designed photonic structure that performs parallel computing. *Nat Commun* **2021**, *12* (1), 1466. DOI: 10.1038/s41467-021-21664-9

(59) Liu, Y.; Zentgraf, T.; Bartal, G.; et al. Transformational plasmon optics. *Nano Lett* **2010**, *10* (6), 1991-1997. DOI: 10.1021/nl1008019

(60) Barreau, V.; Yu, D.; Hensel, R.; et al. Elevated temperature adhesion of bioinspired polymeric micropatterns to glass. *J Mech Behav Biomed Mater* **2017**, *76*, 110-118. DOI: 10.1016/j.jmbbm.2017.04.007

(61) Liu, K.; Yan, Q.; Chen, M.; et al. Elastic properties of chemical-vapor-deposited monolayer MoS_2, WS_2, and their bilayer heterostructures. *Nano Lett* **2014**, *14* (9), 5097-5103. DOI: 10.1021/nl501793a

(62) Castellanos-Gomez, A.; Buscema, M.; Molenaar, R.; et al. Deterministic transfer of two-dimensional materials by all-dry viscoelastic stamping. *2D Materials* **2014**, *1* (1). DOI: 10.1088/2053-1583/1/1/011002

(63) Xie, L.; Du, L.; Lu, X.; et al. A facile and efficient dry transfer technique for two-dimensional Van der Waals heterostructure. *Chinese Physics B* **2017**, *26* (8). DOI: 10.1088/1674-1056/26/8/087306

(64) Son, S.; Shin, Y. J.; Zhang, K.; et al. Strongly adhesive dry transfer technique for van der Waals heterostructure. *2D Materials* **2020**, *7* (4). DOI: 10.1088/2053-1583/abad0b

(65) Wang, W.; Clark, N.; Hamer, M.; et al. Clean assembly of van der Waals heterostructures using silicon nitride membranes. *Nature Electronics* **2023**, *6* (12), 981-990. DOI: 10.1038/s41928-023-01075-y

(66) Reina, A.; Jia, X.; Ho, J.; et al. Large area, few-layer graphene films on arbitrary substrates by chemical vapor deposition. *Nano Lett* **2009**, *9* (1), 30-35. DOI: 10.1021/nl801827v

(67) Lee, Y.; Bae, S.; Jang, H.; et al. Wafer-scale synthesis and transfer of graphene films. *Nano Lett* **2010**, *10* (2), 490-493. DOI: 10.1021/nl903272n

(68) Li, B.; He, Y.; Lei, S.; et al. Scalable Transfer of Suspended Two-Dimensional Single Crystals. *Nano Lett* **2015**, *15* (8), 5089-5097. DOI: 10.1021/acs.nanolett.5b01210

(69) Ma, X.; Liu, Q.; Xu, D.; et al. Capillary-Force-Assisted Clean-Stamp Transfer of Two-Dimensional Materials. *Nano Lett* **2017**, *17* (11), 6961-6967. DOI: 10.1021/acs.nanolett.7b03449

(70) Hempel, M.; Lu, A. Y.; Hui, F.; et al. Repeated roll-to-roll transfer of two-dimensional materials by electrochemical delamination. *Nanoscale* **2018**, *10* (12), 5522-5531. DOI: 10.1039/c7nr07369k

(71) Chen, S.; Chen, G.; Zhao, Y.; et al. Tunable Adhesion for All-Dry Transfer of 2D Materials Enabled by the Freezing of Transfer Medium. *Adv Mater* **2024**, *36* (15), e2308950. DOI: 10.1002/adma.202308950

(72) Chernikov, A.; Berkelbach, T. C.; Hill, H. M.; et al. Exciton binding energy and nonhydrogenic Rydberg series in monolayer WS_2. *Phys Rev Lett* **2014**, *113* (7), 076802. DOI: 10.1103/PhysRevLett.113.076802

(73) He, K.; Kumar, N.; Zhao, L.; et al. Tightly bound excitons in monolayer WSe_2. *Phys Rev Lett* **2014**, *113* (2), 026803. DOI: 10.1103/PhysRevLett.113.026803

(74) He, Y. M.; Clark, G.; Schaibley, J. R.; et al. Single quantum emitters in monolayer semiconductors. *Nat Nanotechnol* **2015**, *10* (6), 497-502. DOI: 10.1038/nnano.2015.75

(75) Koperski, M.; Nogajewski, K.; Arora, A.; et al. Single photon emitters in exfoliated WSe_2 structures. *Nat Nanotechnol* **2015**, *10* (6), 503-506. DOI: 10.1038/nnano.2015.67

(76) Kumar, S.; Kaczmarczyk, A.; Gerardot, B. D. Strain-Induced Spatial and Spectral Isolation of Quantum Emitters in Mono- and Bilayer WSe_2. *Nano Lett* **2015**, *15* (11), 7567-7573. DOI: 10.1021/acs.nanolett.5b03312

(77) Srivastava, A.; Sidler, M.; Allain, A. V.; et al. Optically active quantum dots in monolayer WSe_2. *Nat Nanotechnol* **2015**, *10* (6), 491-496. DOI: 10.1038/nnano.2015.60

(78) Tonndorf, P.; Schmidt, R.; Schneider, R.; et al. Single-photon emission from localized excitons in an atomically thin semiconductor. *Optica* **2015**, *2* (4). DOI: 10.1364/optica.2.000347

(79) Linhart, L.; Paur, M.; Smejkal, V.; et al. Localized Intervalley Defect Excitons as Single-Photon Emitters in WSe_2. *Phys Rev Lett* **2019**, *123* (14), 146401. DOI: 10.1103/PhysRevLett.123.146401

(80) Chakraborty, C.; Kinnischtzke, L.; Goodfellow, K. M.; et al. Voltage-controlled quantum light from an atomically thin semiconductor. *Nat Nanotechnol* **2015**, *10* (6), 507-511. DOI: 10.1038/nnano.2015.79

(81) Palacios-Berraquero, C.; Barbone, M.; Kara, D. M.; et al. Atomically thin quantum light-emitting diodes. *Nat Commun* **2016**, *7* (1), 12978. DOI: 10.1038/ncomms12978

(82) Schwarz, S.; Kozikov, A.; Withers, F.; et al. Electrically pumped single-defect light emitters in WSe_2. *2D Materials* **2016**, *3* (2). DOI: 10.1088/2053-1583/3/2/025038

(83) So, J. P.; Kim, H. R.; Baek, H.; et al. Electrically driven strain-induced deterministic single-photon emitters in a van der Waals heterostructure. *Sci Adv* **2021**, *7* (43), eabj3176. DOI: 10.1126/sciadv.abj3176

(84) Strasbourg, M. Thermalization and Exciton Localization in 2D Semiconductors. Montana State University, 2023.

(85) Zhang, L.; Yu, Y. J.; Chen, L. G.; et al. Electrically driven single-photon emission from an isolated single molecule. *Nat Commun* **2017**, *8* (1), 580. DOI: 10.1038/s41467-017-00681-7

(86) Rezus, Y. L.; Walt, S. G.; Lettow, R.; et al. Single-photon spectroscopy of a single molecule. *Phys Rev Lett* **2012**, *108* (9), 093601. DOI: 10.1103/PhysRevLett.108.093601

(87) Lounis, B.; Moerner, W. E. Single photons on demand from a single molecule at room temperature. *Nature* **2000**, *407* (6803), 491-493. DOI: 10.1038/35035032

(88) Doherty, M. W.; Manson, N. B.; Delaney, P.; et al. The nitrogen-vacancy colour centre in diamond. *Physics Reports* **2013**, *528* (1), 1-45. DOI: 10.1016/j.physrep.2013.02.001

(89) Kurtsiefer, C.; Mayer, S.; Zarda, P.; et al. Stable solid-state source of single photons. *Phys Rev Lett* **2000**, *85* (2), 290-293. DOI: 10.1103/PhysRevLett.85.290

(90) Brouri, R.; Beveratos, A.; Poizat, J. P.; et al. Photon antibunching in the fluorescence of individual color centers in diamond. *Opt Lett* **2000**, *25* (17), 1294-1296. DOI: 10.1364/ol.25.001294

(91) Yuan, Z.; Kardynal, B. E.; Stevenson, R. M.; et al. Electrically driven single-photon source. *Science* **2002**, *295* (5552), 102-105. DOI: 10.1126/science.1066790

(92) Santori, C.; Fattal, D.; Vuckovic, J.; et al. Indistinguishable photons from a single-photon device. *Nature* **2002**, *419* (6907), 594-597. DOI: 10.1038/nature01086

(93) Michler, P.; Kiraz, A.; Becher, C.; et al. A quantum dot single-photon turnstile device. *Science* **2000**, *290* (5500), 2282-2285. DOI: 10.1126/science.290.5500.2282

(94) Tran, T. T.; Bray, K.; Ford, M. J.; et al. Quantum emission from hexagonal boron nitride monolayers. *Nat Nanotechnol* **2016**, *11* (1), 37-41. DOI: 10.1038/nnano.2015.242

(95) Sajid, A.; Ford, M. J.; Reimers, J. R. Single-photon emitters in hexagonal boron nitride: a review of progress. *Rep Prog Phys* **2020**, *83* (4), 044501. DOI: 10.1088/1361-6633/ab6310

(96) Li, C.; Fröch, J. E.; Nonahal, M.; et al. Integration of hBN Quantum Emitters in Monolithically Fabricated Waveguides. *ACS Photonics* **2021**, *8* (10), 2966-2972. DOI: 10.1021/acsphotonics.1c00890

(97) Serati de Brito, C.; Rosa, B. L. T.; Chaves, A.; et al. Probing the Nature of Single-Photon Emitters in a WSe_2 Monolayer by Magneto-Photoluminescence Spectroscopy. *Nano Lett* **2024**, *24* (42), 13300-13306. DOI: 10.1021/acs.nanolett.4c03686

(98) Strasbourg, M. C.; Yanev, E. S.; Darlington, T. P.; et al. Characterization of quantum dot-like emitters in programmable arrays of nanowrinkles of 1L-WSe_2. *Journal of Applied Physics* **2024**, *136* (4). DOI: 10.1063/5.0214410

(99) Lee, S. Y.; Jeong, T. Y.; Kim, J. H.; et al. Self-consistent dielectric constant determination for monolayer WSe_2. *Opt Express* **2018**, *26* (18), 23061-23068. DOI: 10.1364/OE.26.023061

CHAPTER 3

DETERMINATION OF THE ROLES OF STRAIN AND TEARING IN SINGLE PHOTON EMISSION FROM NANOINDENTED WSe_2

Contributions of Authors and Co-Authors

Manuscript in Chapter 3

Author: Joseph Stage

Contributions: Conceived this work, prepared the samples, developed the nanoinversion process, conducted atomic force microscopy imaging, conducted scanning electron microscopy imaging, conducted cryogenic photoluminescence, conducted single-photon antibunching measurements, developed the emitter counting protocol, and wrote the manuscript

Author: J. Pierce Fix

Contributions: Conceived this work, prepared the samples, established and conducted nanoindentation, developed the nanoinversion process, conducted atomic force microscopy, performed room temperature photoluminescence, and wrote the manuscript

Co-Author: Matthew C. Strasbourg

Contributions: Established the cryogenic optical microscope

Co-Author: Amir Darabi

Contributions: Conducted nanoindentation, aided in developing the nanoinversion process, and wrote the manuscript

Co-Author: Torrey McLoughlin

Contributions: Aided in developing the nanoinversion process

Co-Author: Sheikh Parvez

Contributions: Prepared the samples

Co-Author: Elijah Stuvland

Contributions: Aided in developing the nanoinversion process

Co-Author: Andrew Lingley

Contributions: Aided in developing the nanoinversion process

Co-Author: Nicholas J. Borys

Contributions: Conceived this work and wrote the manuscript

Manuscript Information

Joseph Stage, J. Pierce Fix, Matthew C. Strasbourg, Amir Darabi, Torrey McLoughlin, Sheikh Parvez, Elijah Stuvland, Andrew Lingley, and Nicholas Borys

Status of Manuscript:
☐Prepared for submission to a peer-reviewed journal
☒Officially submitted to a peer-reviewed journal
☐Accepted by a peer-reviewed journal
☐ Published in a peer-reviewed journal

Abstract

Single photon emission in two-dimensional single-layer WSe_2 is an attractive solid-state phenomenon for the on-demand generation of quantum states of light. The electronic states that are responsible for single photon generation preferentially form in regions of localized tensile strain, making them uniquely able to be deterministically positioned and strain-engineered. Nanoindentation of single-layer WSe_2 and other 2D semiconductors on a pliable substrate is a promising approach to take advantage of these opportunities. However, it is hindered by key questions on the structural integrity of the indented 2D material, the resulting strain generated, and the location of the emitters. In this work, we report a detailed study of the structure of indented 1L-WSe_2 that is enabled by a fabrication process that inverts the indents into protruding pillars that can be probed using electron microscopy. We explicitly identify strain relaxation of the indented 1L-WSe_2 due to tearing in a subset of indents and confirm that the formation of single photon-emitting states still occurs in these systems, likely at the extremities of the tear. For indents that are confirmed to be intact (i.e., not torn), we assess the ability to strain engineer the single photon emitters. While strain does not strongly affect the emission energy or the brightness, we find that increased strain in the indent reduces the spatial density of emitter states. This trend indicates that an optimal amount of strain is needed for emitter formation and/or the emitters preferentially form on the periphery of the indent. Our investigation provides critical insight into the most relevant structure-property relationships for using nanoindentation to reliably and systematically engineer quantum light sources in single-layer WSe_2 and other 2D semiconductors.

Introduction

From new developments to improvements in performance, many aspects of quantum technologies stand to benefit from a system that produces tailorable quantum states of light on demand. Solid-state single photon emitters (SPEs) that are based on localized electronic states in semiconducting and insulating materials have the potential to address this need, and further, have several advantageous physical properties for technological development[1-5]. One appealing opportunity for this class of SPEs is their ultimate development into an electrically triggerable device with a micron or sub-micron footprint that is compatible with photonic integrated circuits. Solid-state SPE systems that are ideal for such device integration, however, need to meet stringent requirements. Not only do they need to be able to produce single photons at sufficient purity and indistinguishability, but they also need to be amenable to advanced manufacturing and nanofabrication. In particular, they need to possess the versatility to be deterministically positioned and heterogeneously integrated with photonic and nanophotonic systems such as waveguides and cavities.

Several aspects of the localized states responsible for single photon emission in single-layer WSe_2 (1L-WSe_2)—a prototypical 2D semiconductor—make them appealing for solid-state SPE devices. Since their initial discovery in 1L-WSe_2[6-13], prototype electrically triggerable SPE devices have been demonstrated[13-17], strain-engineering has been explored[10, 18-21], and non-classical emission has been reported at temperatures up to 160 K[22, 23]. Additionally, it is well established that the SPE-active state preferentially forms in regions of localized tensile strain[4, 10, 19, 24, 25], a property that can be leveraged to achieve deterministic placement of the SPE state[14, 26-

[34]. Nanoindentation, where a nanoscale atomic force microscopy (AFM) probe is used to plastically indent 1L-WSe_2 on top of a deformable polymer, is an elegant method to deterministically position regions of localized tensile strain as well as tailor the amount of strain with the indentation force. Following the first report of creating SPE states with nanoindentation[32], the technique has been leveraged to demonstrate how graphite can improve photon purity[28], as well as deterministically place an SPE state in an electrically triggered device[14] and near a plasmonic structure[35]. Despite these initial successes, several questions about the nanoindentation procedure and the extent to which SPEs can be strain-engineered persist. Specifically, the roles, whether deleterious or advantageous, of micro- and nanoscale tearing are unknown, and the properties of the SPEs appear to only weakly depend on the amount of strain in the indent. Further, it is unclear where within the indented structure the SPE states exist[26]. These unresolved issues are critical impediments to achieving reproducible manufacturing of SPE states in 2D semiconductors using nanoindentation.

Here, we report a detailed study of the structure of nanoindented 1L-WSe_2 that resolves the presence of tearing. Using photoluminescence spectroscopy and imaging, we confirm that tearing can occur and result in a significant amount of strain relaxation across the entire indented structure. Remarkably, despite the strain relaxation, we confirm that SPEs form in the indents where tearing occurs, which strongly suggests that in these cases, the SPE states are localized to the tear. Further, we use our ability to discern tearing to assess the ability to strain-engineer the SPE states in indents that remain intact and preserve the localized strain. By explicitly eliminating the instances where tearing occurs, we find that increasing the amount of strain with the indentation force does not significantly alter the physical properties of the generated SPE states themselves. However, we do

find that as the indentation force increases, the spatial density of the SPE states decreases, which suggests that either an optimal range of tensile strain exists for the formation of SPE states or that the SPE states preferentially localize to the periphery of the indent, as was concluded from super-resolution imaging measurements[26]. Our results substantially improve the understanding of the SPE formation process in indented 1L-WSe_2 and, as a result, also improve the ability to leverage nanoindentation as a highly controllable process to position and strain-engineer SPEs in all 2D systems.

Results and Discussion

Figure 1a illustrates the process of generating the localized strain in the 1L-WSe_2 using nanoindentation[14, 26-34, 36]. The samples are comprised of 1L-WSe_2 that is directly exfoliated onto ~350 nm thick PMMA films. To indent the 1L-WSe_2, an atomic force microscope (AFM) probe is brought into initial contact at a fixed location on the 1L-WSe_2/PMMA layer. The contact force can then be increased by further raising the sample into the AFM probe, where, at sufficiently large forces, the PMMA is plastically deformed into an indent. Because of strong adhesion, the 1L-WSe_2 is suspected to be conformally stretched along the profile of the indent, resulting in a region of localized strain where the amount of strain is dependent upon the size (e.g., depth) of the indent. The geometry/structure of the indent, and thus the generated strain, depends on the nano- and microscale structure of the AFM probe combined with the displacement of the PMMA, resulting in a peripheral buildup region around the indent. Further, the depth, width, and size of the buildup region for a given indent depend on the force constant of the AFM cantilever used during indentation and the additional z-displacement of the sample beyond the initial contact point.

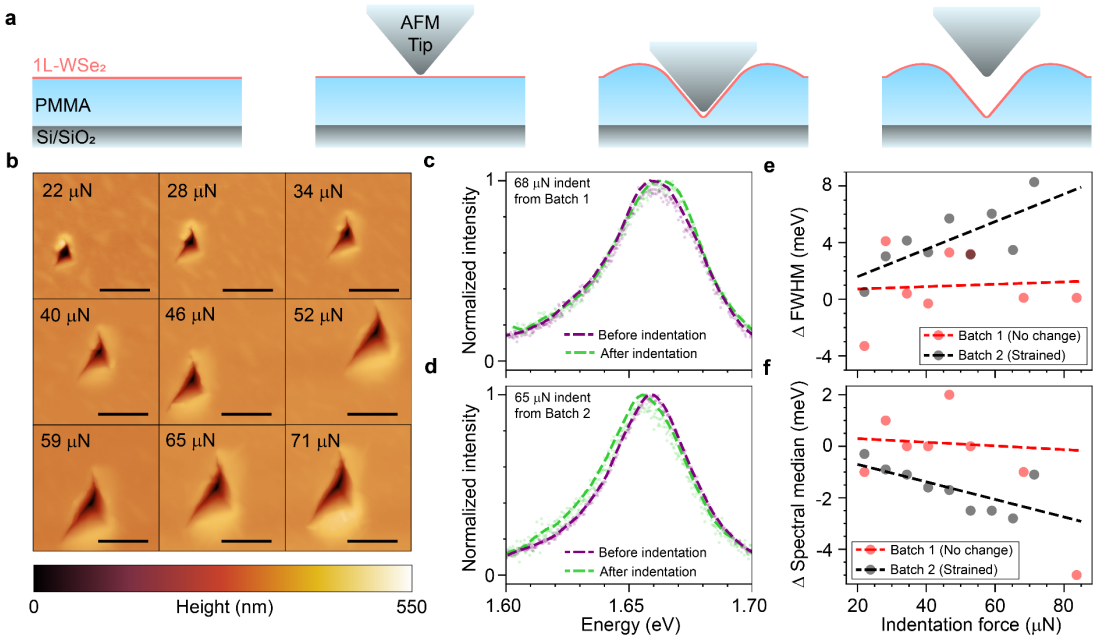


Figure 1 – The nanoindentation process and room temperature PL characterization: (a) A schematic of the indentation process. An AFM tip is positioned over a 1L-WSe_2 flake on a PMMA/SiO_2 substrate. The substrate is moved into the tip, where the WSe_2 and PMMA are deformed into the shape of the tip. When the substrate is retracted, an indent in the shape of the tip is left. AFM scale bars are 400 nm. (b) High-resolution AFM scans of nine indents made with indentation forces ranging from 22 to 71 μN. (c, d) The average PL spectra of before and after indenting from Batch 1 and Batch 2, respectively. (e) The difference in the full-width half maximum (FWHM) of the PL spectra between after and before indentation. A positive difference corresponds to an increase in FWHM after indentation. (f) The difference in PL emission energy is calculated by taking the difference between before and after indenting. Negative values correspond to a redshift or decrease in emission energy after indenting. Scale bars in (c) are 400 nm.

Prior studies of localized strain in 2D semiconductors generated by nanoindentation used blunted probes and *z*-displacements ranging from 200-2000 nm[32]. Using the cantilever force constant, the applied forces in these studies spanned 1-80 μN. In comparison, we use as-supplied commercial Tap300Al-G probes (Supplementary Figure 1) and *z*-displacements of 1000-3000 nm corresponding to forces from 22-84 μN (see methods and Supplementary Figure 2). Figure 1b shows the topography of a representative set of indents from our process, demonstrating how the structure of the buildup regions, as well as the size and depths of the indents, depend on the

indentation force. To probe the strain generated, the average PL spectrum from a 900×900 nm^2 region at each indentation site was recorded both before and after indentation. The before-and-after comparison of the PL spectra reveals two distinct behaviors. In the first case (Figure 1c), the PL of the indented region is unaffected by the indentation process: both the peak energy and spectral width of the PL are the same before and after the indentation process. The lack of observable change in the PL indicates that the nanoindentation process did not impart a significant amount of strain to the region. In the second case (Figure 1d), the indentation process shifts the PL spectrum to lower energies and increases the spectral linewidth. Such lower energy and broader PL are expected from a region with localized, inhomogeneous tensile strain[8, 19, 22, 37-40], indicating that the indentation process generated a measurable amount of strain.

For a given "batch" of indents (i.e., a set of nanoindents created with the same AFM probe and identical tip-sample-cantilever geometry), the before-and-after behavior is uniform up to a critical indentation force: either all indents exhibit signatures of localized strain or not. Figures 1e and 1f report how the nanoindentation-induced changes in the energy and width of the PL of 1L-WSe_2 depend on the indentation force for both types of batches. Neither the energy nor the linewidth of the PL substantially changes for the set of indents labeled "Batch 1". For this batch, signatures of strain are only observed at the highest indentation force of 84 μN (z-displacement of 3000 nm), resulting in an abrupt redshift of ~5 meV. We suspect that this shift at the greatest force is due to a significant structural perturbation beyond indentation and has been observed in prior studies of indents with lateral dimensions on the length scale of 4 μm[27]. In contrast, for the indents of Batch 2, greater indentation forces generate both larger redshifts and increases in linewidth, indicating force-induced increases of strain and structural inhomogeneity. In particular, the shifts

in emission energy are consistent with observations made for similar strain profiles of prior studies[14]. These approximately linear relationships indicate that with the right processing conditions (e.g., AFM probe and tip-sample-cantilever geometry), the indentation force provides a degree of tunability of the localized strain. The different behaviors between the two batches of indents suggest that the indentation-induced strain in the indents of Batch 1 has relaxed, likely due to the tearing of the 1L-WSe_2[41], whereas in Batch 2, the 1L-WSe_2 remains intact, preserving the indentation-induced strain.

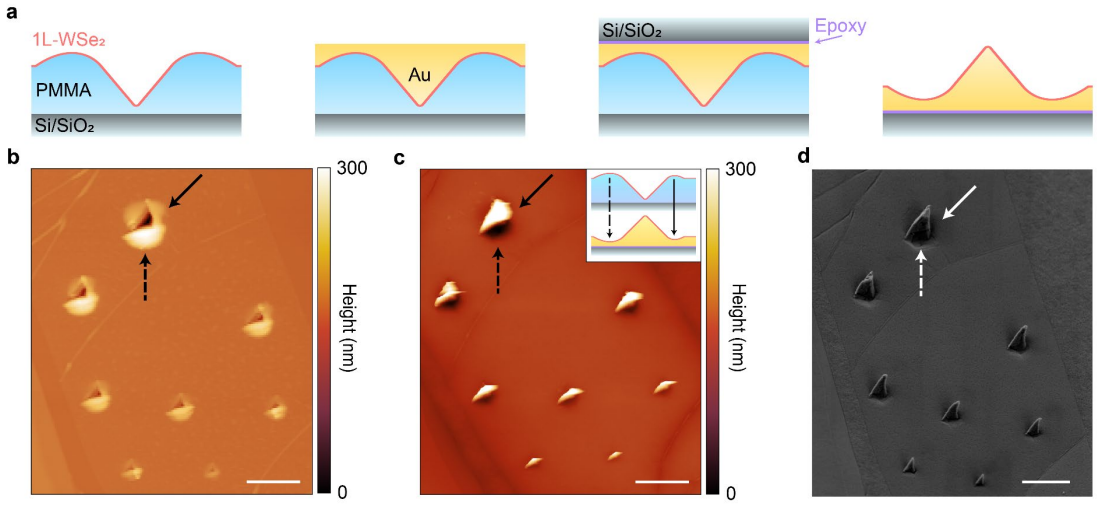


Figure 2 – Inverting the nanoindents: (a) A schematic demonstrating the inversion process. Starting with an indented 1L-WSe_2/ PMMA/SiO_2/Si sample, a ~550 nm thick layer of gold is deposited on the sample, filling the indent with gold, and leaving a gold surface on which a second SiO_2/Si substrate is epoxied. The PMMA holding the initial SiO_2/Si substrate is dissolved, leaving an inverted indent (b, c). AFM topography maps of Batch 1 indents and the corresponding inverted structure, respectively. The inset in (c) is a schematic demonstrating that the asymmetric PMMA buildup in the indents becomes valleys when inverted. The black (white) dashed and solid lines mark how the larger and smaller buildup regions around the indent correspond to the larger and smaller valleys when inverted. (d) SEM of the inverted indents in panel c. The scale bars are 1 µm.

To more directly probe the presence of tearing within the indented material, we developed a process to invert the indents into protruding pillars so that the structure of the 1L-WSe_2 within

the indent can be assessed using scanning electron microscopy (SEM). For inversion, we follow a template stripping process that is summarized in Figure 2a. In short, a 550 nm-thick gold film is deposited on top of the indented 1L-WSe_2/PMMA stack. Care is taken to ensure the evaporated gold is incident parallel to the normal surface to minimize shadow masking and ensure the indents are uniformly filled (see methods and Supplementary Figure 3). After deposition, a second Si/SiO_2 substrate is epoxied to the exposed surface of the gold film. Once cured, the Si/SiO_2/epoxy/Au/1L-WSe_2/PMMA is stripped from the original substrate, and the residual PMMA is removed by rinsing the substrate with solvent. This inversion process has a high success rate of ~90%, which we suspect is aided by chalcogen vacancies in the TMDs binding with the gold layer[42-45]. With that said, the inversion process also works for other 2D materials (WS_2, h-BN) and filling layers (PDMS, SiO_2, Ti).

The inverted structure is a coarse replication of the AFM probe that was used for the indentation (see Supplementary Figure 4). However, the radius of curvature of the apex of the inverted structure is ~2-5× larger than that of the indenting AFM probe. This enlargement is likely caused by both the slipping of the AFM probe during indentation and the difference in elastic modulus between PMMA and 1L-WSe_2 (see Supplementary Figure 5)[46, 47]. Like prior nanoindentation studies[14, 26-34], a bulge is present around the periphery of the indent/inversion (black/white solid and dashed arrows in Figures 2b-d). This bulge arises from the buildup of PMMA as it is pushed away from the indented region, but is not uniformly distributed around the indent. Most likely, the tilt of the indenting AFM probe concentrates PMMA on one side of the indent (Supplementary Figure 6). High-resolution AFM micrographs of the indents and inversions confirm the asymmetric bulge. The bulge in the indentation appears as a depression in the inverted

structures, demonstrating how the inversion process preserves the structure of the original indents (cf. Figure 2c, inset). Figure 2d shows a SEM micrograph of the inverted structures at a 45° tilt. Within these images, the structure of the 1L-WSe_2 is resolvable, confirming that the 1L-WSe_2 is preserved during the inversion process.

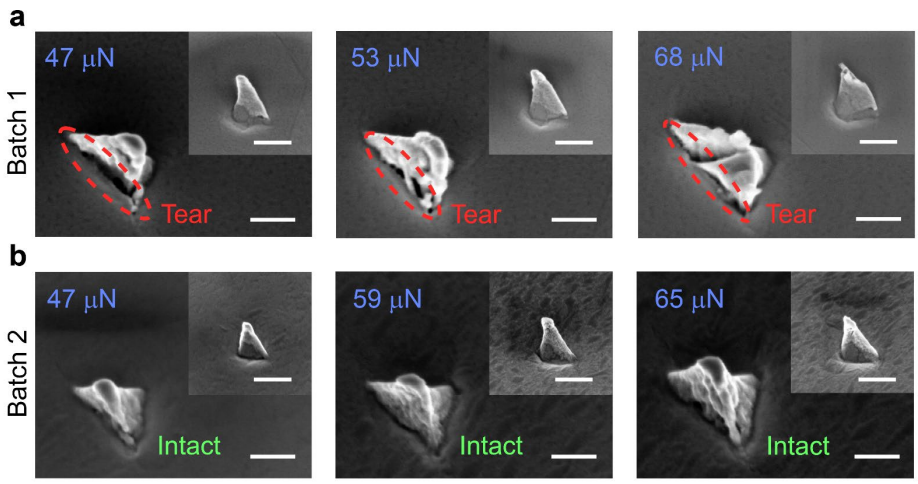


Figure 3 – SEM of Batch 1 and 2 inverted indents: (a) SEM images of inverted indents from Batch 1. The red dash ovals mark tears in the 1L-WSe_2. This tearing is in sharp contrast to Batch 2, where no tearing is observed in (b). The insets are of the same inverted indents but rotated 180° to show the other side. The blue values in each panel are the indentation forces used to make the indent. Main figure scale bars are 200 nm (insets are 400 nm).

The tearing of the 1L-WSe_2 can be assessed with more detailed SEM imaging (again at a 45° tilt). Figure 3 shows higher-resolution imaging of individual indentations from Batch 1 (Figures 3a) and Batch 2 (Figures 3b) from both sides of the indent. The indents from Batch 1, where the room-temperature spectroscopy indicated the occurrence of strain relaxation, have dark voids that are spanned by filaments of 1L-WSe_2 at the depressions that occur at the base of the inverted indents. These features signify tearing of the 1L-WSe_2 and generally are only observed on one side of the inverted structure. Further, they occur on the same side for a given batch of

indents. Additional examples of torn inversions and their dependence on indentation force, contact angle, and the condition of the AFM probe can be found in Supplementary Figure 7. In contrast, the indents from Batch 2, where the spectroscopy at room temperature showed indentation force-dependent strain, are devoid of analogous signatures of tearing. We note that the indents of Batch 1 and Batch 2 were made using nearly the same process. The only variations were the specific AFM probe used and unavoidable slight differences in the specific geometry of how it was mounted in the AFM. From these observations, we suspect three potential origins of the tears. First, and most importantly, is the use of a dulled AFM probe during indentation, creating a larger and less uniform contact surface. Second is a misalignment in the contact angle used, causing the tip to slide on the WSe_2 surface from an insufficient/excessive in-plane motion of the stage. Lastly is the yaw tilt of the probe within the AFM tip mount, causing spatially inhomogeneous strain generation during the indent. Future studies that systematically characterize and control for these factors are needed to determine their relative contributions to the tearing effect.

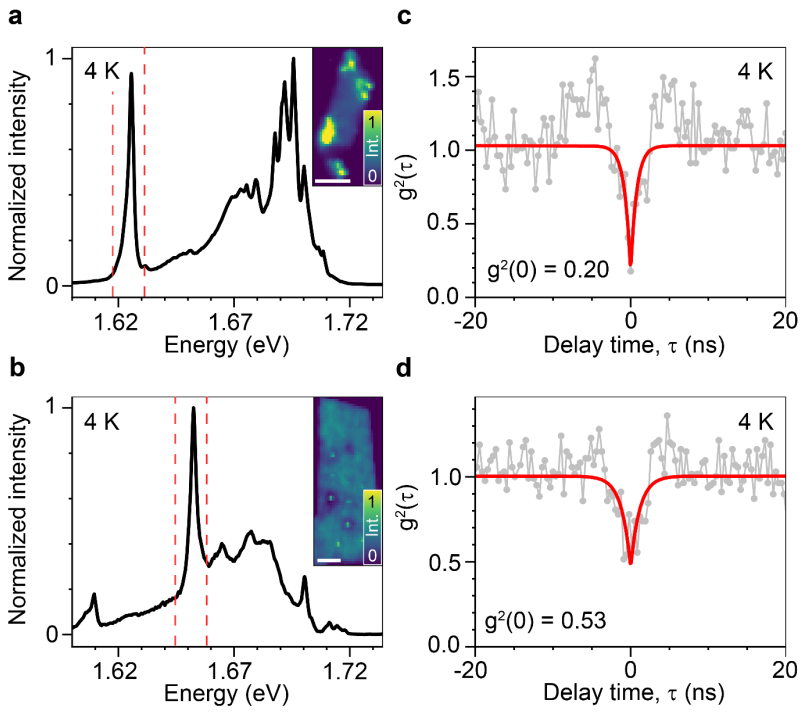


Figure 4 – Confirmation of single-photon emitters in Batch 1 and 2: (a, b) Average PL spectra at 4 K of an indent from Batch 1 and Batch 2, respectively. The inset in (a) is the integrated intensity map of Batch 1 integrated over the range 1.52 – 1.84 eV. The inset in (b) is the integrated intensity map of Batch 2 integrated over the range 1.51 – 1.83 eV. The scale bars of the insets are 5 μm. (c, d) Second-order correlation function ($g^2(\tau)$) of the emitters marked by red dashed lines in (a) and (b), respectively. Both emitters measured show antibunching behavior with $g^2(0)$ below or near 0.5.

The nanoindentation procedure semi-deterministically positions quantum emitters in 1L-WSe_2[14, 26-34]. However, the role of the observed tearing in both the formation and strain-engineering of the quantum emitters has not been established. Addressing this question, Figure 4 shows that quantum light sources emerge in both batches of indents. Localized emission in narrow wavelength bands is observed at the indentation sites for the torn indents of Batch 1 (Figure 4a and inset). However, as contrasted in Figure 4b, the PL of the intact indents is much more uniformly localized to the indentation sites. Detailed imaging of the indents over different emission bands is provided in Supplementary Figures 8-9. The spectra of the localized PL at cryogenic temperatures

from a representative torn indent in Batch 1 (where the strain has relaxed) and an intact indent in Batch 2 (where the strain is preserved) are shown in the main panels of Figures 4a and 4b, respectively. Despite the disparity in strain relaxation, narrowband emission from localized states is observed from both types of indentation sites. The quantum nature of the emission from both indentation sites is confirmed with antibunching measurements presented in Figures 4c and 4d. For the torn indentation (Figure 4c), a high single photon purity of 80% is observed, whereas the brightest emitter from the intact indent (Figure 4d) overlaps with a broadband background, reducing the single photon purity to 47%. It is well known that localized tensile strain is a critical precursor to the formation of quantum light sources in 1L-WSe_2[4, 6, 48, 49], so the emergence of these states in the torn, strain-relaxed indents is not immediately anticipated. Although the strain is relaxed, we suspect that localized strain exists in the immediate vicinity of the tear, providing a secondary route for the formation of the quantum emitters[6]. For such torn indents, the emitter properties at an indentation site (i.e., number of emitters, emitter energy, brightness, etc.) are not expected to depend on the indentation force (beyond achieving mechanical failure) since the strain beyond the tear is relaxed. Several prior studies have reported a similar weak or nonexistent dependence of emitter properties on indentation force[32, 34], indicating that tear-induced formation of quantum emitters could be surprisingly prevalent in these systems.

Finally, for both the intact and torn indents, we measured the strain-tunability of the emitter populations and their properties for indentation forces ranging from 22-71 μN (1000-2600 nm z-displacement). As shown in the Supplementary Figure 10, even after verifying the presence of strain in the indents (c.f. Figure 1), clear relationships between the indentation force, emitter energies, and brightnesses were not observed, indicating that the ability to use the indentation force

alone to imbue emitters with specific characteristics is limited. However, as shown in Figure 5, the indentation force affects the number and spatial density of emitters that form at an indent. To measure the emitter populations meaningfully, however, two major challenges exist for obtaining accurate counts. First, a broadband background emission obscures weaker narrowband emitters (Figure 5a). So, first, we counted emitters in the presence of this pronounced background. Then, to suppress this background, we overlaid a batch of intact indents in 1L-WSe_2 with a thin layer of graphite (~8 nm). The addition of a top layer of graphite was previously shown to quench the background and improve the spectral isolation of the localized emitter states[28]. The enhanced PL emission of the localized states over the background is shown in the lower panel of Figure 5a. In addition to a strong suppression of the background, the addition of the graphite activated a larger number of additional emitters that were not resolvable in the original indent. The second challenge that we addressed in the counting process is the fluctuations of the emitters as exemplified in the temporal evolution of the PL spectrum of a single indentation site (inset, Figure 5a). To reduce the effects of these fluctuations, we identified emissive states in the time-averaged spectra shown in Figures 5a and then confirmed that each line displayed independent fluctuations (i.e., spectral diffusion/wandering) using PL time series such as the inset in Figure 5a[50]. For instance, the emission peaks encircled in the black-dashed line in Figure 5a are examples of single states that are fluctuating between two dominant energies. Individual PL spectra used for emitter counting can be found in Supplementary Figures 11-13.

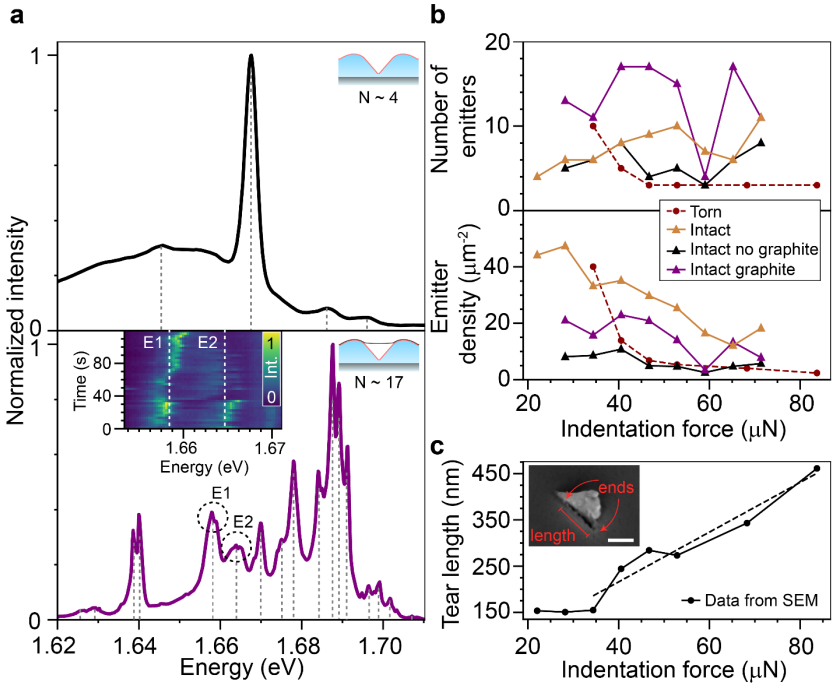


Figure 5 – Emitter density and emitter count dependence on indentation force: (a) Average 4 K PL spectra from an intact indent without graphite (top) and an intact indent with graphite (bottom). N is the number of emitters counted from the average spectra. The schematics in (a) represent the indents with or without graphite. The inset in (a, bottom) is the time series of the emitters circled in black and marked E1 and E2. The corresponding emitters in the time series are marked with white dashed lines. (b) Emitter number and emitter density with respect to indent area as a function of indentation force. In (b), the red circles correspond to Batch 1 (torn), and the yellow triangles correspond to Batch 2 (intact). The Batch 3 indents without graphite are marked by the black triangles, and the indents with graphite are represented by the purple triangles. (c) The tear length of each indent in Batch 1 as a function of indentation force. The tear lengths were measured from SEM images. The dashed black line is a guide to the eye. An example of how the tear was measured is shown in the SEM inset. The SEM image scale bar is 200 nm.

Following the above counting protocol, Figure 5b shows how the number of emitters depends on the indentation force for torn indents, intact indents, and intact indents overlaid with graphene. The probed indentation forces range from 22-84 μN (1000-3000 nm z-displacement). For Batches 1 (torn) and 3 (intact without graphite and intact with graphite), the smallest forces used did not generate localized emitters, and we excluded those points from the plot. For all cases

where the indents are intact, the absolute number of emitters weakly depends on the indentation force for the smallest forces, which is most evident in the intact indents of Batch 2 (intact). Beyond 41 μN (~1600 nm z-displacement), the number of emitters appears to be independent of the indentation force. This general behavior was observed in two independent batches of indents. We note the indent made with 59 μN (2200 nm z-displacement) in Batch 3 is a significant outlier. The overall PL intensity at this site was also vastly reduced, indicating that an issue likely occurred during the indentation process for this site. The trend for the torn indents is dramatically different: as the indentation force increases, the number of emitters *decreases* with a rate that drastically slows beyond ~50 μN. While the number of emitters reveals a clear discrepancy between intact and torn indents, a strong dependence on the force is not observed for the intact indents. In contrast, Figure 5b shows that the *areal density* of the localized emitters has a stronger dependence on the indentation force. The surface area, which includes the indented and buildup regions, is determined with high-resolution AFM imaging. For intact indents, the emitter density decreases linearly with increasing force, indicating that either quantum emitter formation favors a specific range of tensile strains and/or the emitters are localized to a specific feature of the indent, such as its apex or surrounding buildup region. For instance, recent studies have shown the importance of nanoscale wrinkles in the formation of quantum emitter states in 1L-WSe_2[18, 51, 52]. A potential hypothesis is that such wrinkles are suppressed within the indent and confined to the surrounding buildup regions. Such localization to the buildup region agrees with prior super-resolution measurements[26]. Empirically, the area of the buildup regions increases linearly with indentation force (see Supplementary Figure 14). In contrast, the surface area of the indent increases quadratically. Thus,

localization of the emitters to the buildup region would lead to the observed decrease in emitter density.

The more dramatic decrease in both the absolute number of emitters as well as the emitter density for the torn indents corroborates our hypothesis that the emitters are localized to the tear. As shown in Figure 5c, the length of the tear is constant up to 34 μN and then increases linearly with indentation force (see Supplementary Figure 15 for SEM images). At 34 μN, an abrupt increase in the number of emitters occurs, which then rapidly decreases with greater forces until a constant number of three emitters. We believe that this behavior indicates that the emitters are localized to specific regions of the tear. If this is not the case and the emitters are uniformly distributed along the length of the tear, we would expect a linearly decreasing trend as seen in the intact indents. We suspect that the 34 μN threshold marks a critical threshold for strain relaxation in the 1L-WSe_2. Along these lines, we interpret the rapid decrease of the number of emitters between 34-48 μN to increasing relaxation of the strain by the tear until maximum relaxation beyond 48 μN. At the point of maximum relaxation, we only observe three emitters per site, regardless of the force used.

For the intact indents, whether the localized emitters are predominantly in the indent itself or in the peripheral buildup region around the indent remains unresolved. While, as noted above, the decrease in the emitter density could be explained by localization to the buildup region, a similar trend may be observed if emitter formation requires tensile strains in a closed range of values (i.e., requires a strain between a minimum and maximum value). Further, we note that the strong suppression of the number of emitters in the torn indents and the isolation of the tearing to a single side of the indent indicate that the emitters are predominantly located within the indent

itself for the intact indents. Our rationale is that it is unlikely that the tearing on a single side would substantially relax the strain in the buildup region on the other sides. Our hypothesis is further supported by the fact that overlaying the indents with graphite enhances the formation of the SPE states. Any emitters in the buildup region should be preferentially quenched due to their proximity to the graphite. Further exploration of this issue motivates future studies that, for instance, could leverage a dielectric material for the inversion process so that emitters are not quenched and can be localized using nano-optical or super-resolution microscopy techniques[18, 25, 52-55]. More quantitative structural models of the strain in both the torn and intact indents would shed additional light on this open question.

Conclusion

In conclusion, our study provides a detailed characterization of the structure of indented 1L-WSe_2 for deterministically creating SPE states. Using a process to invert the indents, we are able to assess the physical structure of the indented 1L-WSe_2 and confidently differentiate between indents where the 2D semiconductor is torn from those where it remains intact. For the intact indents, clear signatures of strain are identified in room-temperature PL characterization: the indentation process results in a localized red-shift and broadening of the PL. The magnitudes of the red shift and broadening increase with increasing indentation force, indicating that larger indentation forces generate greater amounts of localized strain. In contrast, in the idents where the 2D semiconductor is torn, the tear sufficiently relaxes the localized strain such that neither a shift nor broadening of the PL spectrum can be resolved. Remarkably, when focusing on the intact indents, the indentation force does not systematically alter the emitter energies nor the emitter intensities. However, we find that the larger localized strains from the greater indentation forces

reduce the density of the localized emitters within an indent, providing strong evidence that the emitters are localized to a limited region within the indent, possibly because they only form over a limited range of tensile strain. For the indents where tearing occurs, the dependence of the number of emitters on the indentation force is dramatically different, indicating that the localized emitters are isolated to specific regions of the indent. These measurements provide critical insight into the mechanisms of deterministic strain localization and engineering of SPEs in 2D semiconductors, both of which are critical for their development as light sources for quantum technologies. Improved quantitative understanding of these processes will enable refined approaches that further improve the reliability of localizing high-quality, background-free emitters to specific positions for quantum photonic applications.

Methods

Sample Fabrication

Exfoliating WSe_2 onto PMMA Polymethyl methacrylate (PMMA) layers on Si/SiO_2 were made by spinning 950K A4 PMMA at 1500 RPM, followed by an 80 ºC bake for 45 mins. WSe_2 flakes were then exfoliated onto PMMA using an adapted Scotch tape method[56]. First, WSe_2 was exfoliated onto X4 polydimethylsiloxane (PDMS) that was treated in a light UV ozone for 2 mins, and then the WSe_2/PDMS was used to exfoliate onto PMMA that was treated in the same UV ozone. Here, PDMS was used to exfoliate onto PMMA rather than typical tapes due to the reduced residue we observed.

Generation of Nanoindents To generate nanoindents in 1L-WSe_2, we followed the initial protocol set by Rosenburger *et al.*[32]. We used an AIST-NT SmartSPM HE002 AFM from HORIBA Scientific. In the AFM software, we used the nanoindentation application in the software in "Zsweep" mode, which allows for control of the Z-axis piezo motor of the AFM sample stage. When the location of an indent was defined, the desired indentation force was set by inputting the z-displacement, which is the distance the AFM stage moved into the AFM tip. The z-displacement ranged from 1000-3000 nm, corresponding to 22-84 μN in indentation force. At these indentation forces, the AFM tip slips, meaning the tip does not stay in the defined location throughout the indentation process. To minimize the slipping, we introduced a lateral movement of the sample stage along the y-axis to keep the tip in the same initial position during the indentation process (see Supplementary Figure 5).

Inversion of Nanoindents To invert a batch of nanoindented 2D materials on PMMA, samples are placed in an electron-beam evaporator directly above the crucible to ensure normal incidence during evaporation. For Au inversion, a layer of Au 150 – 200 nm thicker than the deepest indent depth of a given batch was deposited at 2 Å/s (550 nm in total). Due to the PMMA surface, certain compact evaporators may have issues of polymerized PMMA or substantial film stress caused by excessive electron and charged ion irradiation. This issue can be solved with added magnets and shields[57]. After evaporation, a thin layer of epoxy is spun onto the exposed Au surface at 6000 RPM, and a second Si/SiO_2 substrate is attached. Once cured, a razor blade stuck into the corners of the sample stack was used to separate the two substrates. The 2D material/Au/epoxy/SiO_2/Si

was then quickly rinsed in acetone to remove residual PMMA residue, subsequently cleaned with IPA, and dried with N_2.

Wet Transfer of Thin Graphite To transfer graphite layers onto WSe_2 indents, graphite was first exfoliated onto a Si/SiO_2 substrate using the Scotch tape method[56]. Afterwards, flakes with thicknesses ranging from 6-10 nm were identified using AFM, and a thin layer of 10:1 Sylgard 184 PDMS was spun on at 4000 RPM. After curing in a 100 ºC oven for ~60 mins, the chip was submerged in a 1M solution of NaOH in DIW heated to 90 ºC to lightly etch the SiO_2 surface and encourage liftoff of the graphite/PDMS stamp[58, 59]. Once bubbles formed on the perimeter of the chip (~15 mins), the film was separated from the Si/SiO_2, sometimes requiring manual assistance using a pair of tweezers. To remove excess NaOH residue, the film was left in a DIW bath for ~12 hours. Afterwards, the film was retrieved from the DIW, dried with Nitrogen, and transferred over the WSe_2 indents using the viscoelastic stamping method[60, 61].

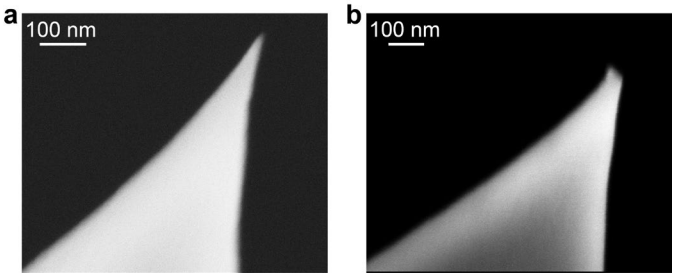
Optical Measurements

Room Temperature Photoluminescence (PL) The room temperature PL measurements were conducted in ambient atmosphere using a commercially built microscope (HORIBA Scientific TRIOS system). We coupled a 532 nm CW diode laser in the microscope and focused the laser onto the sample using a Nikon LU Plan Fluor 100X (0.9 NA) objective. In this system, the sample is scanned using an XY piezo motor, and this scanning confocal microscope has a spatial resolution of ~630 nm. The room temperature PL spectra were recorded using a grating spectrometer (Andor Kymera) and a CCD camera (Andor iXon Ultra 888 EMCCD).

Cryogenic PL Cryogenic PL measurements were taken inside a liquid helium-cooled Montana Instruments s50 Cryostation (4 K) equipped with optical access. 532 nm CW laser light was focused on the sample with a Nikon infinity corrected S Plan Fluor 40X (0.6 NA) objective equipped with a correction collar to compensate for a thin glass window above the sample. This home-built scanning confocal microscope has a spatial resolution of ~1 μm. PL spectra were then recorded using a grating spectrometer (Horiba iHR320) and a CCD camera (Andor idus 416). Single-photon antibunching measurements were conducted by isolating a narrow band of quantum emission using the exit slit of the spectrometer as a monochromator. The narrowband emission was sent into a free-space Hanbury-Brown and Twiss (HBT) interferometer. The single-photon avalanche photodiodes that make up the arms of the HBT were connected to a PicoQuant HydraHarp 400 that acted as our time tagging module.

Supplementary Information

Details on Nanoindentation and Indentation Force Calculation

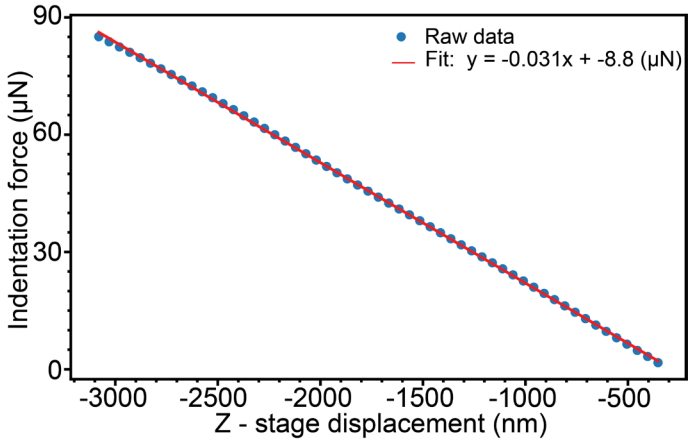


Supplementary Figure 1: Comparing new and dulled AFM tips via SEM. (a) SEM images of a new Tap300Al-G AFM, k= 40 N/m probe before dulling. (b) SEM of the same AFM probe after dulling.

To indent the 1L-WSe2, we used Tap300Al-G AFM probes with a spring constant (k) of 40 N/m and a tip radius of 10 nm. During the nanoindentation process, the location of each indent and the movement of the sample stage into the probe (z-displacement) were set. This allows for control of the location and indentation force of each indent. At z-displacements over 1000 nm, a lateral displacement in the y-direction is introduced to keep the AFM tip in the same initial location throughout the indentation process. In the software, the y-displacement is set by inputting an angle. We can convert the z-displacement to indentation force by creating a calibration equation based on the indentation force (μN) that the software calculates as a function of z-displacement (see Supplementary Figure 2). After 3050 nm of z-displacement, the reflected laser from the cantilever reaches the edge of the photodiode, and the indentation force calculation provided by the software becomes inaccurate. Motivating the need for a calibration equation to calculate indentation force from the z-displacement. Note that the software reports the z-displacement as

negative values. The resulting equation from the linear fit is shown below.

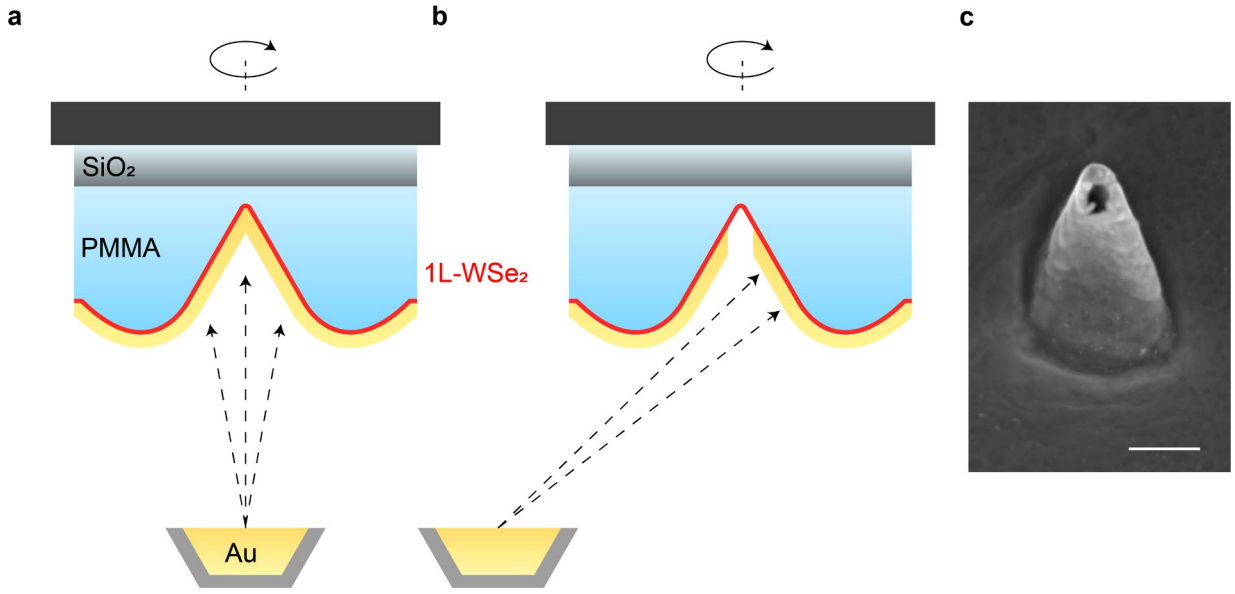
$$\text{Indentation force } (\mu\text{N}) = -0.031\ (\frac{\mu\text{N}}{\text{nm}}) * \text{z} + (-8.8\ \mu\text{N})$$



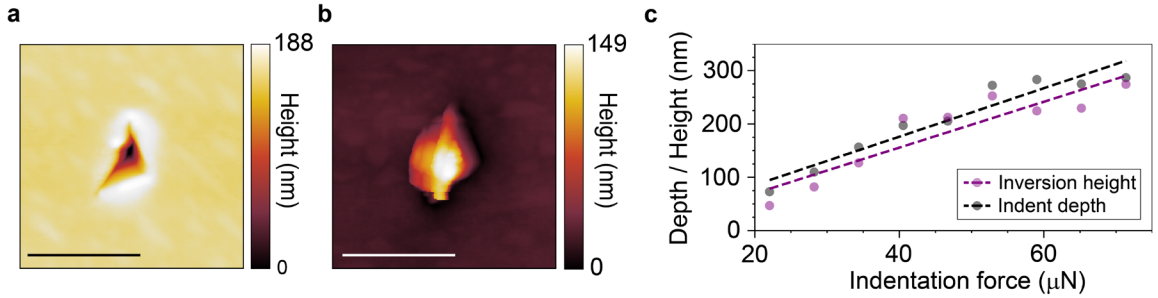
Supplementary Figure 2: Indentation force calibration. Calculating an equation to convert z-displacement into indentation force in μN. The y-axis is the raw signal of the indentation force.

Development of Inversions with Non-normal Incidence Au Evaporation

During the inversion process, having the evaporated Au incident normal to the substrate ensures uniform filling of the indent as shown in Supplementary Figure 3a. On the other hand, Supplementary Figure 3b shows how non-normal evaporation can lead to shadow masking near the apex. SEM imaging of an inversion made with non-normal incidence evaporation can be seen in Supplementary Figure 3c, where the apex is nominally void.



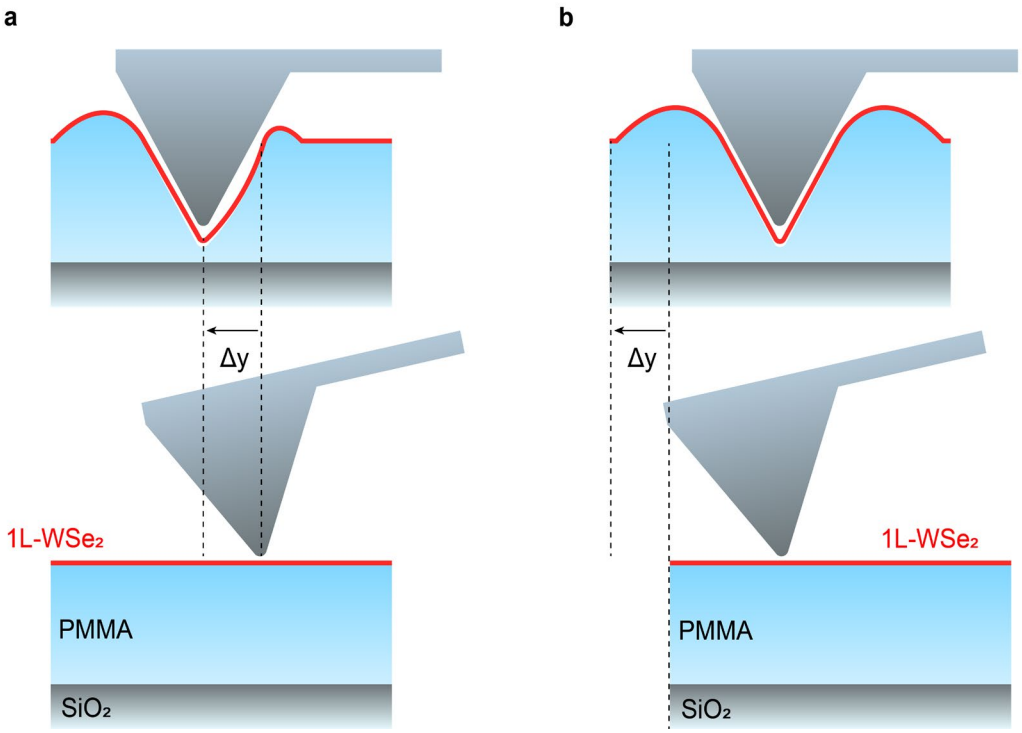
Supplementary Figure 3: Effect of non-normal incidence during inversion. (a) Schematic showing perfect filling of an indent when a normal angle of incidence is used. (b) Schematic of a non-normal incidence evaporation leading to shadow masking at the apex of the indent/inversion. (c) SEM image of an inversion generated with non-normal incidence evaporation (scale bar = 200 nm).



Supplementary Figure 4: Inversions are near replications of nanoindents. (a, b) High-resolution AFM images of a 34 μN indent and inversion, respectively. (c) The depth of indents made using indentation forces ranging from 22 – 71 μN, and the heights of the corresponding inversions (scale bars = 500 nm).

Sliding of the AFM Tip from a Misaligned Contact Angle

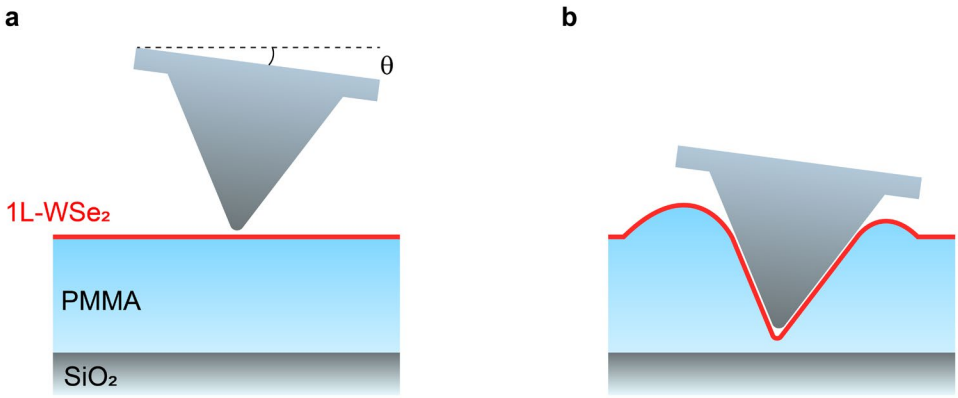
Due to the declination angle of the AFM cantilever with respect to the PMMA surface, a y-translation of the AFM stage is incorporated during indentation to maintain the location of the tip apex. The amount of y-translation required to maintain the tip position is prescribed in the Horiba AIST software through the "contact angle", and the optimal value is a function of cantilever stiffness, declination angle, and substrate elastic modulus. Supplementary Figure 5a schematically shows an example indentation with a contact angle of 0° (no y-translation of the AFM stage). As the AFM stage is brought up into the tip, sliding occurs due to cantilever deflection, leading to an enlarged side and an increased radius of curvature. We suspect another contributing factor to the enlarged apex radius of curvature of nanoinversions in comparison to the indenting AFM tip is the ~100x difference in elastic modulus between PMMA and 1L-WSe_2[46, 47]. Therefore, the strain applied at the apex results in much higher stress in the 1L-WSe_2 compared to PMMA, overcoming the adhesion at the interface, and softening the apex. Supplementary Figure 5b represents an indent made with a perfectly aligned contact angle. Here, the stage moves laterally the same distance that the apex would be translated from the cantilever deflection. The indent generated is then a more accurate replication of the AFM tip geometry.



Supplementary Figure 5: Sliding of the AFM tip from a misaligned contact angle. (a) Schematic representing an indent made with a contact angle of 0° (no y-translation of the AFM stage). (b) Schematic representing an indent made with a perfectly aligned contact angle.

Yaw Tilt of the AFM Cantilever Generating an Asymmetric Buildup Region

Yaw tilt is described as a rotation of the cantilever with respect to the PMMA surface when looking at the cantilever head-on. This can occur from small misalignments in the mounting of the AFM tip (dust under the Si, AFM tip fabrication issues) or from the substrate surface being tilted. During indentation, yaw tilt leads to an asymmetry in the build region. The side that the tip is rotated into will generate a larger buildup region since PMMA is displaced in that direction (seen in Supplementary Figure 6).

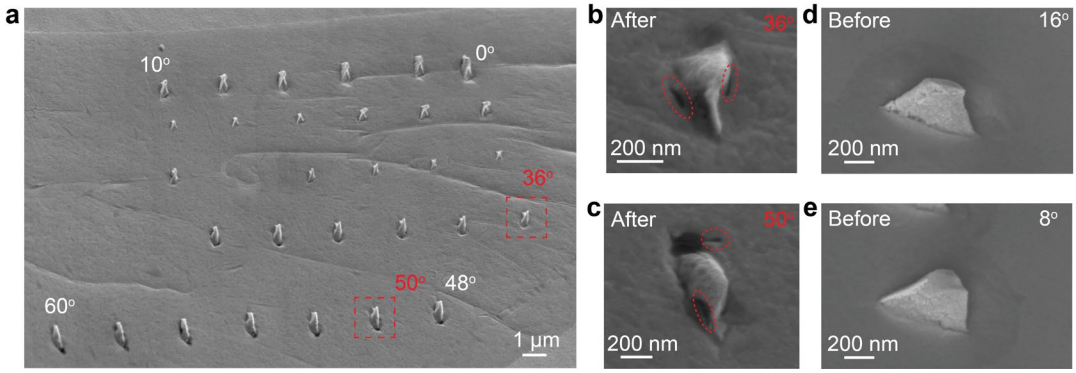


Supplementary Figure 6: Yaw tilt generating an asymmetric buildup region. (a) Schematic of an AFM tip with yaw tilt (θ) positioned above the PMMA surface before indentation. (b) Schematic of indentation where the AFM cantilever has a yaw tilt leading to an asymmetric buildup region.

Tearing in Indented Materials from Dulled AFM Tips with Different Y-Displacements

To see the effect of the y-displacement on the indents, defined by the contact angle setting in the AFM software, we made two inverted indent arrays with a constant indentation force of 53 μN, shown in Supplementary Figure 7. The array shown in Supplementary Figure 7a was made with a dulled Tap300Al-G AFM, k = 40 N/m probe. As the y-displacement increases and limits the effect of the AFM tip slipping forward during the indentation process, the base of the inverted indent gets smaller, which means the AFM tip stays in the initial location of the tip (see Supplementary Figure 7a). This is the behavior seen from 0° to 24°. In contrast, from 26° to 60°, the y-displacement causes the natural tip slipping to increase, resulting in the inverted indent base to elongate and appear stretched. High-resolution SEM images are taken of the inverted indents, and two examples are shown in Supplementary Figure 7b-c. In Supplementary Figures 7b-c, tears are observed in the 1L-WSe2. Tears like the ones seen in Supplementary Figure 7b-c are observed in all the other inverted indents in Supplementary Figure 7a. In contrast, the inverted indents in

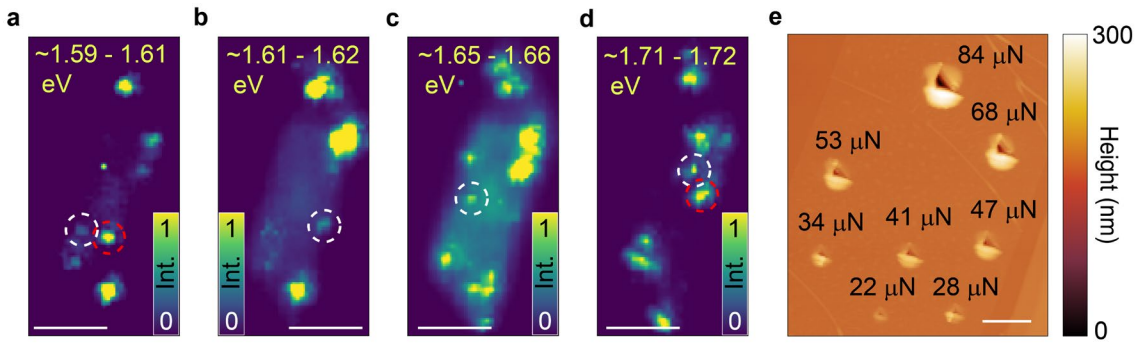
Supplementary Figure 7d-e are made with the same probe before dulling, but they do not show tearing.



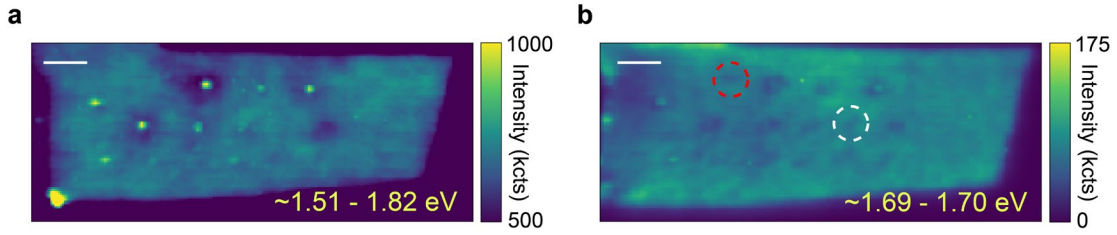
Supplementary Figure 7: Two inverted 1L-WSe_2 indent arrays made with the same AFM probe before and after dulling. The same indentation force was used, and the angle was changed from 0 to 60° in steps of 2° for both arrays of indents. (a) SEM image of an array of inverted indents made with a dulled Tap300Al-G, k = 40 N/m AFM probe. The angles set the y-displacement of the sample stage. The Indentation force for all the indents in panels (a – e) was 53 µN. (b, c) SEM of two indents outlined by red squares in (a), made with angles of 36° and 50°, respectively. The red ovals mark tears in the 1L-WSe_2. (d, e) SEM of inverted indents made with a fresh AFM probe, meaning the probe was not dulled. The indents were made with 16° (d) and 8° (e) and do not show signs of tearing as seen in (b) and (c).

Properties of the Emitter Ensemble at Each Site in Batch 3

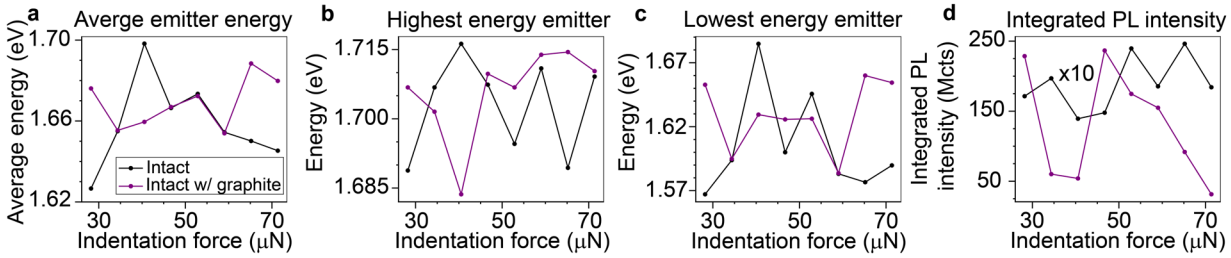
4 K photoluminescence (PL) taken at each indentation site of Batch 3 was used to investigate if properties of the emitter ensemble had a dependence on indentation force. Similar to previous reports, in Supplementary Figure 10a-d, we note no trend of integrated PL intensity, average emitter energy, highest emitter energy, or lowest emitter energy to indentation force (strain)[32, 34]. These metrics were extracted using an average PL spectra from a 120 s PL time series, both before and after, graphite was added to quench excessive background emission[33]. Determination of average, highest, and lowest emitter energy was done using the emitters identified from the counting protocol.



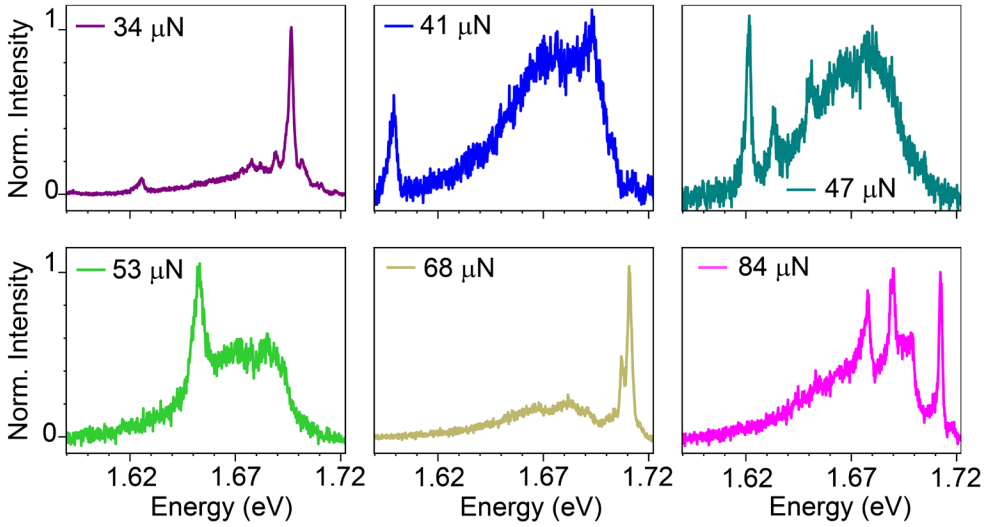
Supplementary Figure 8: Locating indentation sites in Batch 1. (a) Hyperspectral image integrated from ~1.59 – 1.61 eV used to identify the 34 and 41 μN indents in white and red, respectively. (b) Hyperspectral image integrated from ~1.61 – 1.62 eV used to identify the 47 μN indent. (c) Hyperspectral image integrated from ~1.65 – 1.66 eV used to identify the 53 μN indent. (d) Hyperspectral image integrated from ~1.71 – 1.72 eV used to identify the 68 and 84 μN indents in red and white, respectively (scale bars = 5 μm). (e) AFM image of the indents in Batch 1, ranging in indentation force from 22 – 84 μN (scale bars = 1 μm).



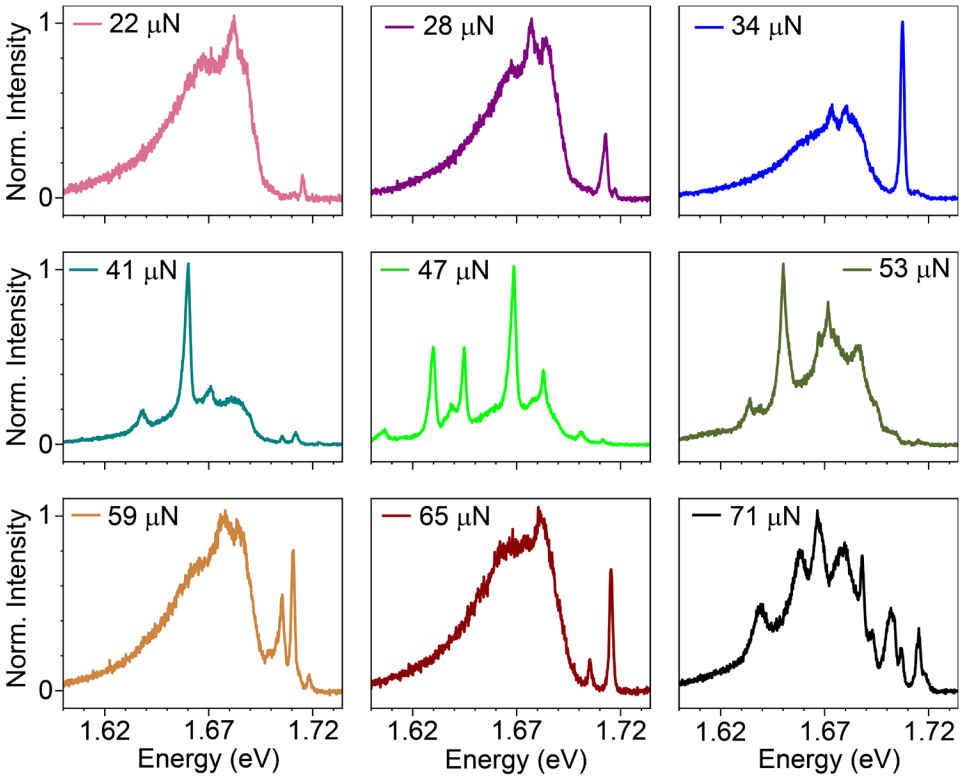
Supplementary Figure 9: Locating indentation sites in Batch 2. (a) Hyperspectral image integrated from 1.51 – 1.82 eV. (b) Hyperspectral image integrated from 1.69 – 1.70 eV used to identify the 28 and 65 μN indents in white and red, respectively (scale bars = 10 μm).



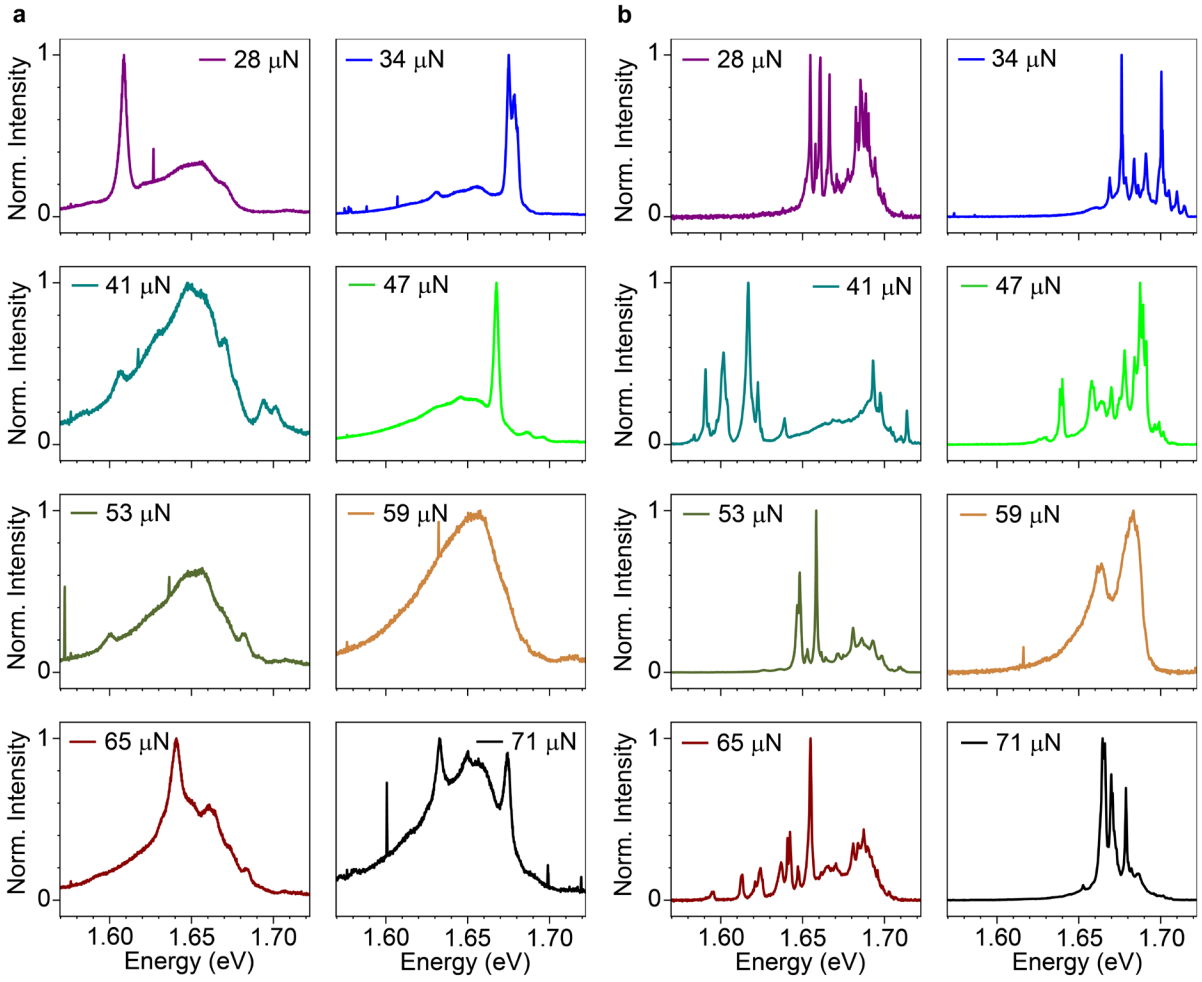
Supplementary Figure 10: Emitter ensemble properties of each site in Batch 3. (a) Average energy of the emitter ensemble at each indentation site. (b, c) The lowest and highest energy emitter of the ensemble at each site, respectively. (d) Integrated PL intensity (1.575 – 1.725 eV) at each indentation site.



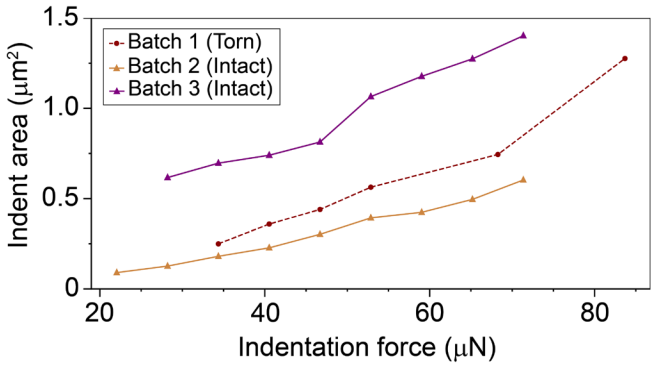
Supplementary Figure 11: PL spectra of each site in Batch 1. PL spectra of indentation sites made with indentation forces ranging from 34 to 84 μN.



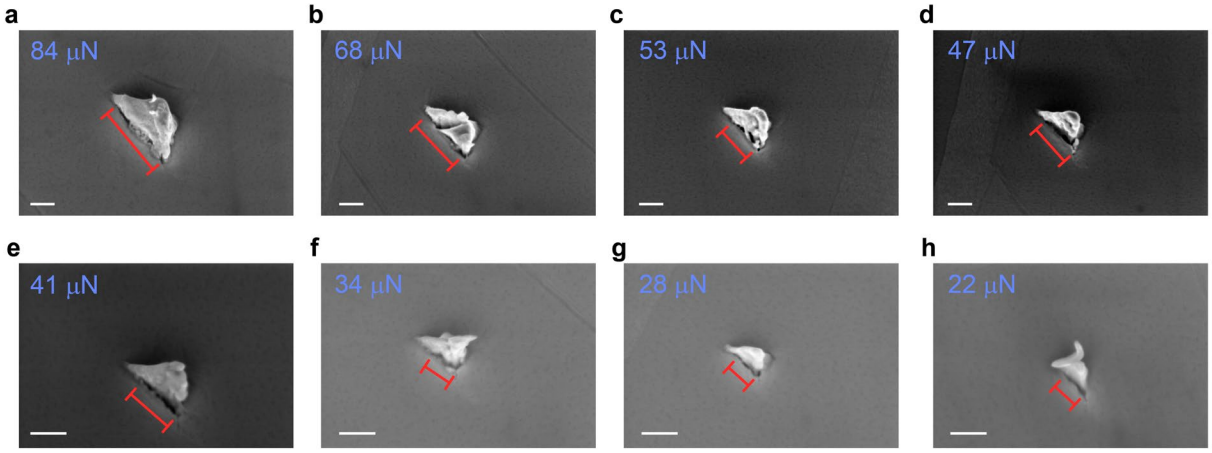
Supplementary Figure 12: PL spectra of each site in Batch 2. PL spectra of indentation sites made with indentation forces ranging from 22 – 71 μN.



Supplementary Figure 13: Average PL spectra of each site in Batch 3. Average PL spectra of indentation sites made with indentation forces ranging from 28 – 71 μN. (a) Average PL spectra from a 120 s PL time-series without graphite. (b) Average PL spectra from a 120 s PL time-series with graphite.



Supplementary Figure 14: Total indent area of each site. Indent areas, including the indent and buildup region of each site, were acquired from high-resolution AFM imaging.



Supplementary Figure 15: Tear length of Batch 1 indents using SEM imaging. (a-h) SEM images of Batch 1 inversions. Torn regions are highlighted using a red line, and the indentation force used to generate each indent is listed in blue (scale bars = 200 nm).

Chapter 3 References

(1) Montblanch, A. R.; Barbone, M.; Aharonovich, I.; et al. Layered materials as a platform for quantum technologies. *Nat Nanotechnol* **2023**, *18* (6), 555-571. DOI: 10.1038/s41565-023-01354-x

(2) Yu, Y.; Seo, I. C.; Luo, M.; et al. Tunable single-photon emitters in 2D materials. *Nanophotonics* **2024**, *13* (19), 3615-3629. DOI: 10.1515/nanoph-2024-0050

(3) Sortino, L.; Zotev, P. G.; Phillips, C. L.; et al. Bright single photon emitters with enhanced quantum efficiency in a two-dimensional semiconductor coupled with dielectric nano-antennas. *Nat Commun* **2021**, *12* (1), 6063. DOI: 10.1038/s41467-021-26262-3

(4) Luo, Y.; Shepard, G. D.; Ardelean, J. V.; et al. Deterministic coupling of site-controlled quantum emitters in monolayer WSe_2 to plasmonic nanocavities. *Nat Nanotechnol* **2018**, *13* (12), 1137-1142. DOI: 10.1038/s41565-018-0275-z

(5) Gao, T.; von Helversen, M.; Antón-Solanas, C.; et al. Atomically-thin single-photon sources for quantum communication. *npj 2D Materials and Applications* **2023**, *7* (4). DOI: 10.1038/s41699-023-00366-4

(6) Tonndorf, P.; Schmidt, R.; Schneider, R.; et al. Single-photon emission from localized excitons in an atomically thin semiconductor. *Optica* **2015**, *2* (4). DOI: 10.1364/optica.2.000347

(7) Srivastava, A.; Sidler, M.; Allain, A. V.; et al. Optically active quantum dots in monolayer WSe_2. *Nat Nanotechnol* **2015**, *10* (6), 491-496. DOI: 10.1038/nnano.2015.60

(8) Li, H.; Contryman, A. W.; Qian, X.; et al. Optoelectronic crystal of artificial atoms in strain-textured molybdenum disulphide. *Nat Commun* **2015**, *6* (1), 7381. DOI: 10.1038/ncomms8381

(9) Koperski, M.; Nogajewski, K.; Arora, A.; et al. Single photon emitters in exfoliated WSe_2 structures. *Nat Nanotechnol* **2015**, *10* (6), 503-506. DOI: 10.1038/nnano.2015.67

(10) Kumar, S.; Kaczmarczyk, A.; Gerardot, B. D. Strain-Induced Spatial and Spectral Isolation of Quantum Emitters in Mono- and Bilayer WSe_2. *Nano Lett* **2015**, *15* (11), 7567-7573. DOI: 10.1021/acs.nanolett.5b03312

(11) Moody, G.; Kavir Dass, C.; Hao, K.; et al. Intrinsic homogeneous linewidth and broadening mechanisms of excitons in monolayer transition metal dichalcogenides. *Nat Commun* **2015**, *6* (1), 8315. DOI: 10.1038/ncomms9315

(12) He, Y. M.; Clark, G.; Schaibley, J. R.; et al. Single quantum emitters in monolayer semiconductors. *Nat Nanotechnol* **2015**, *10* (6), 497-502. DOI: 10.1038/nnano.2015.75

(13) Chakraborty, C.; Kinnischtzke, L.; Goodfellow, K. M.; et al. Voltage-controlled quantum light from an atomically thin semiconductor. *Nat Nanotechnol* **2015**, *10* (6), 507-511. DOI: 10.1038/nnano.2015.79

(14) So, J. P.; Kim, H. R.; Baek, H.; et al. Electrically driven strain-induced deterministic single-photon emitters in a van der Waals heterostructure. *Sci Adv* **2021**, *7* (43), eabj3176. DOI: 10.1126/sciadv.abj3176

(15) Palacios-Berraquero, C.; Barbone, M.; Kara, D. M.; et al. Atomically thin quantum light-emitting diodes. *Nat Commun* **2016**, *7* (1), 12978. DOI: 10.1038/ncomms12978

(16) Schwarz, S.; Kozikov, A.; Withers, F.; et al. Electrically pumped single-defect light emitters in WSe_2. *2D Materials* **2016**, *3* (2). DOI: 10.1088/2053-1583/3/2/025038

(17) Guo, S.; Germanis, S.; Taniguchi, T.; et al. Electrically Driven Site-Controlled Single Photon Source. *ACS Photonics* **2023**, *10* (8), 2549-2555. DOI: 10.1021/acsphotonics.3c00097

(18) Yanev, E. S.; Darlington, T. P.; Ladyzhets, S. A.; et al. Programmable nanowrinkle-induced room-temperature exciton localization in monolayer WSe_2. *Nat Commun* **2024**, *15* (1), 1543. DOI: 10.1038/s41467-024-45936-2

(19) Branny, A.; Kumar, S.; Proux, R.; et al. Deterministic strain-induced arrays of quantum emitters in a two-dimensional semiconductor. *Nat Commun* **2017**, *8* (1), 15053. DOI: 10.1038/ncomms15053

(20) Azzam, S. I.; Parto, K.; Moody, G. Purcell enhancement and polarization control of single-photon emitters in monolayer WSe_2 using dielectric nanoantennas. *Nanophotonics* **2023**, *12* (3), 477-484. DOI: 10.1515/nanoph-2022-0628

(21) Kim, H.; Moon, J. S.; Noh, G.; et al. Position and Frequency Control of Strain-Induced Quantum Emitters in WSe_2 Monolayers. *Nano Lett* **2019**, *19* (10), 7534-7539. DOI: 10.1021/acs.nanolett.9b03421

(22) Parto, K.; Azzam, S. I.; Banerjee, K.; et al. Defect and strain engineering of monolayer WSe_2 enables site-controlled single-photon emission up to 150 K. *Nat Commun* **2021**, *12* (1), 3585. DOI: 10.1038/s41467-021-23709-5

(23) Luo, Y.; Liu, N.; Li, X.; et al. Single photon emission in WSe_2 up to 160 K by quantum yield control. *2D Materials* **2019**, *6* (3). DOI: 10.1088/2053-1583/ab15fe

(24) Shepard, G. D.; Ajayi, O. A.; Li, X.; et al. Nanobubble induced formation of quantum emitters in monolayer semiconductors. *2D Materials* **2017**, *4* (2). DOI: 10.1088/2053-1583/aa629d

(25) Darlington, T. P.; Carmesin, C.; Florian, M.; et al. Imaging strain-localized excitons in nanoscale bubbles of monolayer WSe_2 at room temperature. *Nat Nanotechnol* **2020**, *15* (10), 854-860. DOI: 10.1038/s41565-020-0730-5

(26) Abramov, A. N.; Chestnov, I. Y.; Alimova, E. S.; et al. Photoluminescence imaging of single photon emitters within nanoscale strain profiles in monolayer WSe_2. *Nat Commun* **2023**, *14* (1), 5737. DOI: 10.1038/s41467-023-41292-9

(27) Chang, S.; Yan, Y.; Geng, Y. Local Nanostrain Engineering of Monolayer MoS_2 Using Atomic Force Microscopy-Based Thermomechanical Nanoindentation. *Nano Lett* **2023**, *23* (20), 9219-9226. DOI: 10.1021/acs.nanolett.3c01809

(28) Chuang, H. J.; Stevens, C. E.; Rosenberger, M. R.; et al. Enhancing Single Photon Emission Purity via Design of van der Waals Heterostructures. *Nano Lett* **2024**, *24* (18), 5529-5535. DOI: 10.1021/acs.nanolett.4c00683

(29) Cunningham, P. D.; Proscia, N. V.; LaGasse, S. W.; et al. Site-Specific Exciton–Plasmon Coupling in Nanoindented WSe_2. *ACS Photonics* **2024**, *11* (8), 3250-3258. DOI: 10.1021/acsphotonics.4c00644

(30) Lee, S.-J.; Chuang, H.-J.; Yeats, A. L.; et al. Ferroelectric Modulation of Quantum Emitters in Monolayer WS_2. *ACS Nano* **2024**, *18* (36), 25349-25358. DOI: 10.1021/acsnano.4c10528

(31) Li, X.; Jones, A. C.; Choi, J.; et al. Proximity-induced chiral quantum light generation in strain-engineered $WSe_2/NiPS_3$ heterostructures. *Nat Mater* **2023**, *22* (11), 1311-1316. DOI: 10.1038/s41563-023-01645-7

(32) Rosenberger, M. R.; Dass, C. K.; Chuang, H. J.; et al. Quantum Calligraphy: Writing Single-Photon Emitters in a Two-Dimensional Materials Platform. *ACS Nano* **2019**, *13* (1), 904-912. DOI: 10.1021/acsnano.8b08730

(33) Stevens, C. E.; Chuang, H. J.; Rosenberger, M. R.; et al. Enhancing the Purity of Deterministically Placed Quantum Emitters in Monolayer WSe_2. *ACS Nano* **2022**, *16* (12), 20956-20963. DOI: 10.1021/acsnano.2c08553

(34) Yücel, O.; Yagodkin, D.; Kirchhof, J. N.; et al. Strain activation of localized states in WSe_2. *2D Materials* **2025**, *12* (3). DOI: 10.1088/2053-1583/add414

(35) Peng, L.; Chan, H.; Choo, P.; et al. Creation of Single-Photon Emitters in WSe_2 Monolayers Using Nanometer-Sized Gold Tips. *Nano Lett* **2020**, *20* (8), 5866-5872. DOI: 10.1021/acs.nanolett.0c01789

(36) Lee, S. J.; Chuang, H. J.; McCreary, K. M.; et al. Voltage-Induced Degradation for Enhanced Purity and Reproducibility of Quantum Emission in Monolayer 2D Materials. *ACS Nano* **2025**, *19* (38), 33981-33990. DOI: 10.1021/acsnano.5c09799

(37) Aslan, B.; Deng, M.; Heinz, T. F. Strain tuning of excitons in monolayer WSe_2. *Physical Review B* **2018**, *98* (11). DOI: 10.1103/PhysRevB.98.115308

(38) Conley, H. J.; Wang, B.; Ziegler, J. I.; et al. Bandgap engineering of strained monolayer and bilayer MoS_2. *Nano Lett* **2013**, *13* (8), 3626-3630. DOI: 10.1021/nl4014748

(39) Desai, S. B.; Seol, G.; Kang, J. S.; et al. Strain-induced indirect to direct bandgap transition in multilayer WSe_2. *Nano Lett* **2014**, *14* (8), 4592-4597. DOI: 10.1021/nl501638a

(40) Hsu, W. T.; Lu, L. S.; Wang, D.; et al. Evidence of indirect gap in monolayer WSe_2. *Nat Commun* **2017**, *8* (1), 929. DOI: 10.1038/s41467-017-01012-6

(41) Taghinejad, H.; Eftekhar, A. A.; Campbell, P. M.; et al. Strain relaxation via formation of cracks in compositionally modulated two-dimensional semiconductor alloys. *npj 2D Materials and Applications* **2018**, *2* (10). DOI: 10.1038/s41699-018-0056-4

(42) Panasci, S. E.; Schiliro, E.; Greco, G.; et al. Strain, Doping, and Electronic Transport of Large Area Monolayer MoS_2 Exfoliated on Gold and Transferred to an Insulating Substrate. *ACS Appl Mater Interfaces* **2021**, *13* (26), 31248-31259. DOI: 10.1021/acsami.1c05185

(43) Chen, S.; Li, B.; Dai, C.; et al. Controlling Gold-Assisted Exfoliation of Large-Area MoS_2 Monolayers with External Pressure. *Nanomaterials (Basel)* **2024**, *14* (17). DOI: 10.3390/nano14171418

(44) Smith, T. The hydrophilic nature of a clean gold surface. *Journal of Colloid and Interface Science* **1980**, *75* (1), 51-55. DOI: 10.1016/0021-9797(80)90348-3

(45) Velicky, M.; Donnelly, G. E.; Hendren, W. R.; et al. Mechanism of Gold-Assisted Exfoliation of Centimeter-Sized Transition-Metal Dichalcogenide Monolayers. *ACS Nano* **2018**, *12* (10), 10463-10472. DOI: 10.1021/acsnano.8b06101

(46) Stafford, C. M.; Harrison, C.; Beers, K. L.; et al. A buckling-based metrology for measuring the elastic moduli of polymeric thin films. *Nat Mater* **2004**, *3* (8), 545-550. DOI: 10.1038/nmat1175

(47) Falin, A.; Holwill, M.; Lv, H.; et al. Mechanical Properties of Atomically Thin Tungsten Dichalcogenides: WS_2, WSe_2, and WTe_2. *ACS Nano* **2021**, *15* (2), 2600-2610. DOI: 10.1021/acsnano.0c07430

(48) Dang, J.; Sun, S.; Xie, X.; et al. Identifying defect-related quantum emitters in monolayer WSe_2. *npj 2D Materials and Applications* **2020**, *4* (2). DOI: 10.1038/s41699-020-0136-0

(49) Linhart, L.; Paur, M.; Smejkal, V.; et al. Localized Intervalley Defect Excitons as Single-Photon Emitters in WSe_2. *Phys Rev Lett* **2019**, *123* (14), 146401. DOI: 10.1103/PhysRevLett.123.146401

(50) Schneider, L. M.; Lippert, S.; Kuhnert, J.; et al. The influence of the environment on monolayer tungsten diselenide photoluminescence. *Nano-Structures & Nano-Objects* **2018**, *15*, 84-97. DOI: 10.1016/j.nanoso.2017.08.009

(51) Daveau, R. S.; Vandekerckhove, T.; Mukherjee, A.; et al. Spectral and spatial isolation of single tungsten diselenide quantum emitters using hexagonal boron nitride wrinkles. *APL Photonics* **2020**, *5* (9). DOI: 10.1063/5.0013825

(52) Strasbourg, M. C.; Yanev, E. S.; Darlington, T. P.; et al. Characterization of quantum dot-like emitters in programmable arrays of nanowrinkles of 1L-WSe_2. *Journal of Applied Physics* **2024**, *136* (4). DOI: 10.1063/5.0214410

(53) Yao, K.; Zhang, S.; Yanev, E.; et al. Nanoscale Optical Imaging of 2D Semiconductor Stacking Orders by Exciton-Enhanced Second Harmonic Generation. *Advanced Optical Materials* **2022**, *10* (12). DOI: 10.1002/adom.202200085

(54) Shabani, S.; Darlington, T. P.; Gordon, C.; et al. Ultralocalized Optoelectronic Properties of Nanobubbles in 2D Semiconductors. *Nano Lett* **2022**, *22* (18), 7401-7407. DOI: 10.1021/acs.nanolett.2c02265

(55) Jo, K.; Marino, E.; Lynch, J.; et al. Direct nano-imaging of light-matter interactions in nanoscale excitonic emitters. *Nat Commun* **2023**, *14* (1), 2649. DOI: 10.1038/s41467-023-38189-y

(56) Novoselov, K. S.; Geim, A. K.; Morozov, S. V.; et al. Electric field effect in atomically thin carbon films. *Science* **2004**, *306* (5696), 666-669. DOI: 10.1126/science.1102896

(57) Sun, B.; Grap, T.; Frahm, T.; et al. Role of electron and ion irradiation in a reliable lift-off process with electron beam evaporation and a bilayer PMMA resist system. *Journal of Vacuum Science & Technology B, Nanotechnology and Microelectronics: Materials, Processing, Measurement, and Phenomena* **2021**, *39* (5). DOI: 10.1116/6.0001161

(58) Reina, A.; Jia, X.; Ho, J.; et al. Large area, few-layer graphene films on arbitrary substrates by chemical vapor deposition. *Nano Lett* **2009**, *9* (1), 30-35. DOI: 10.1021/nl801827v

(59) Lee, Y.; Bae, S.; Jang, H.; et al. Wafer-scale synthesis and transfer of graphene films. *Nano Lett* **2010**, *10* (2), 490-493. DOI: 10.1021/nl903272n

(60) Castellanos-Gomez, A.; Buscema, M.; Molenaar, R.; et al. Deterministic transfer of two-dimensional materials by all-dry viscoelastic stamping. *2D Materials* **2014**, *1* (1). DOI: 10.1088/2053-1583/1/1/011002

(61) Son, S.; Shin, Y. J.; Zhang, K.; et al. Strongly adhesive dry transfer technique for van der Waals heterostructure. *2D Materials* **2020**, *7* (4). DOI: 10.1088/2053-1583/abad0b

(1) Montblanch, A. R.; Barbone, M.; Aharonovich, I.; et al. Layered materials as a platform for quantum technologies. *Nat Nanotechnol* **2023**, *18* (6), 555-571. DOI: 10.1038/s41565-023-01354-x

(2) Yu, Y.; Seo, I. C.; Luo, M.; et al. Tunable single-photon emitters in 2D materials. *Nanophotonics* **2024**, *13* (19), 3615-3629. DOI: 10.1515/nanoph-2024-0050

(3) Sortino, L.; Zotev, P. G.; Phillips, C. L.; et al. Bright single photon emitters with enhanced quantum efficiency in a two-dimensional semiconductor coupled with dielectric nano-antennas. *Nat Commun* **2021**, *12* (1), 6063. DOI: 10.1038/s41467-021-26262-3

(4) Luo, Y.; Shepard, G. D.; Ardelean, J. V.; et al. Deterministic coupling of site-controlled quantum emitters in monolayer WSe_2 to plasmonic nanocavities. *Nat Nanotechnol* **2018**, *13* (12), 1137-1142. DOI: 10.1038/s41565-018-0275-z

(5) Gao, T.; von Helversen, M.; Antón-Solanas, C.; et al. Atomically-thin single-photon sources for quantum communication. *npj 2D Materials and Applications* **2023**, *7* (4). DOI: 10.1038/s41699-023-00366-4

(6) Tonndorf, P.; Schmidt, R.; Schneider, R.; et al. Single-photon emission from localized excitons in an atomically thin semiconductor. *Optica* **2015**, *2* (4). DOI: 10.1364/optica.2.000347

(7) Srivastava, A.; Sidler, M.; Allain, A. V.; et al. Optically active quantum dots in monolayer WSe_2. *Nat Nanotechnol* **2015**, *10* (6), 491-496. DOI: 10.1038/nnano.2015.60

(8) Li, H.; Contryman, A. W.; Qian, X.; et al. Optoelectronic crystal of artificial atoms in strain-textured molybdenum disulphide. *Nat Commun* **2015**, *6* (1), 7381. DOI: 10.1038/ncomms8381

(9) Koperski, M.; Nogajewski, K.; Arora, A.; et al. Single photon emitters in exfoliated WSe_2 structures. *Nat Nanotechnol* **2015**, *10* (6), 503-506. DOI: 10.1038/nnano.2015.67

(10) Kumar, S.; Kaczmarczyk, A.; Gerardot, B. D. Strain-Induced Spatial and Spectral Isolation of Quantum Emitters in Mono- and Bilayer WSe_2. *Nano Lett* **2015**, *15* (11), 7567-7573. DOI: 10.1021/acs.nanolett.5b03312

(11) Moody, G.; Kavir Dass, C.; Hao, K.; et al. Intrinsic homogeneous linewidth and broadening mechanisms of excitons in monolayer transition metal dichalcogenides. *Nat Commun* **2015**, *6* (1), 8315. DOI: 10.1038/ncomms9315

(12) He, Y. M.; Clark, G.; Schaibley, J. R.; et al. Single quantum emitters in monolayer semiconductors. *Nat Nanotechnol* **2015**, *10* (6), 497-502. DOI: 10.1038/nnano.2015.75

(13) Chakraborty, C.; Kinnischtzke, L.; Goodfellow, K. M.; et al. Voltage-controlled quantum light from an atomically thin semiconductor. *Nat Nanotechnol* **2015**, *10* (6), 507-511. DOI: 10.1038/nnano.2015.79

(14) So, J. P.; Kim, H. R.; Baek, H.; et al. Electrically driven strain-induced deterministic single-photon emitters in a van der Waals heterostructure. *Sci Adv* **2021**, *7* (43), eabj3176. DOI: 10.1126/sciadv.abj3176

(15) Palacios-Berraquero, C.; Barbone, M.; Kara, D. M.; et al. Atomically thin quantum light-emitting diodes. *Nat Commun* **2016**, *7* (1), 12978. DOI: 10.1038/ncomms12978

(16) Schwarz, S.; Kozikov, A.; Withers, F.; et al. Electrically pumped single-defect light emitters in WSe_2. *2D Materials* **2016**, *3* (2). DOI: 10.1088/2053-1583/3/2/025038

(17) Guo, S.; Germanis, S.; Taniguchi, T.; et al. Electrically Driven Site-Controlled Single Photon Source. *ACS Photonics* **2023**, *10* (8), 2549-2555. DOI: 10.1021/acsphotonics.3c00097

(18) Yanev, E. S.; Darlington, T. P.; Ladyzhets, S. A.; et al. Programmable nanowrinkle-induced room-temperature exciton localization in monolayer WSe_2. *Nat Commun* **2024**, *15* (1), 1543. DOI: 10.1038/s41467-024-45936-2

(19) Branny, A.; Kumar, S.; Proux, R.; et al. Deterministic strain-induced arrays of quantum emitters in a two-dimensional semiconductor. *Nat Commun* **2017**, *8* (1), 15053. DOI: 10.1038/ncomms15053

(20) Azzam, S. I.; Parto, K.; Moody, G. Purcell enhancement and polarization control of single-photon emitters in monolayer WSe_2 using dielectric nanoantennas. *Nanophotonics* **2023**, *12* (3), 477-484. DOI: 10.1515/nanoph-2022-0628

(21) Kim, H.; Moon, J. S.; Noh, G.; et al. Position and Frequency Control of Strain-Induced Quantum Emitters in WSe_2 Monolayers. *Nano Lett* **2019**, *19* (10), 7534-7539. DOI: 10.1021/acs.nanolett.9b03421

(22) Parto, K.; Azzam, S. I.; Banerjee, K.; et al. Defect and strain engineering of monolayer WSe_2 enables site-controlled single-photon emission up to 150 K. *Nat Commun* **2021**, *12* (1), 3585. DOI: 10.1038/s41467-021-23709-5

(23) Luo, Y.; Liu, N.; Li, X.; et al. Single photon emission in WSe_2 up to 160 K by quantum yield control. *2D Materials* **2019**, *6* (3). DOI: 10.1088/2053-1583/ab15fe

(24) Shepard, G. D.; Ajayi, O. A.; Li, X.; et al. Nanobubble induced formation of quantum emitters in monolayer semiconductors. *2D Materials* **2017**, *4* (2). DOI: 10.1088/2053-1583/aa629d

(25) Darlington, T. P.; Carmesin, C.; Florian, M.; et al. Imaging strain-localized excitons in nanoscale bubbles of monolayer WSe_2 at room temperature. *Nat Nanotechnol* **2020**, *15* (10), 854-860. DOI: 10.1038/s41565-020-0730-5

(26) Abramov, A. N.; Chestnov, I. Y.; Alimova, E. S.; et al. Photoluminescence imaging of single photon emitters within nanoscale strain profiles in monolayer WSe_2. *Nat Commun* **2023**, *14* (1), 5737. DOI: 10.1038/s41467-023-41292-9

(27) Chang, S.; Yan, Y.; Geng, Y. Local Nanostrain Engineering of Monolayer MoS_2 Using Atomic Force Microscopy-Based Thermomechanical Nanoindentation. *Nano Lett* **2023**, *23* (20), 9219-9226. DOI: 10.1021/acs.nanolett.3c01809

(28) Chuang, H. J.; Stevens, C. E.; Rosenberger, M. R.; et al. Enhancing Single Photon Emission Purity via Design of van der Waals Heterostructures. *Nano Lett* **2024**, *24* (18), 5529-5535. DOI: 10.1021/acs.nanolett.4c00683

(29) Cunningham, P. D.; Proscia, N. V.; LaGasse, S. W.; et al. Site-Specific Exciton–Plasmon Coupling in Nanoindented WSe_2. *ACS Photonics* **2024**, *11* (8), 3250-3258. DOI: 10.1021/acsphotonics.4c00644

(30) Lee, S.-J.; Chuang, H.-J.; Yeats, A. L.; et al. Ferroelectric Modulation of Quantum Emitters in Monolayer WS_2. *ACS Nano* **2024**, *18* (36), 25349-25358. DOI: 10.1021/acsnano.4c10528

(31) Li, X.; Jones, A. C.; Choi, J.; et al. Proximity-induced chiral quantum light generation in strain-engineered $WSe_2/NiPS_3$ heterostructures. *Nat Mater* **2023**, *22* (11), 1311-1316. DOI: 10.1038/s41563-023-01645-7

(32) Rosenberger, M. R.; Dass, C. K.; Chuang, H. J.; et al. Quantum Calligraphy: Writing Single-Photon Emitters in a Two-Dimensional Materials Platform. *ACS Nano* **2019**, *13* (1), 904-912. DOI: 10.1021/acsnano.8b08730

(33) Stevens, C. E.; Chuang, H. J.; Rosenberger, M. R.; et al. Enhancing the Purity of Deterministically Placed Quantum Emitters in Monolayer WSe_2. *ACS Nano* **2022**, *16* (12), 20956-20963. DOI: 10.1021/acsnano.2c08553

(34) Yücel, O.; Yagodkin, D.; Kirchhof, J. N.; et al. Strain activation of localized states in WSe_2. *2D Materials* **2025**, *12* (3). DOI: 10.1088/2053-1583/add414

(35) Peng, L.; Chan, H.; Choo, P.; et al. Creation of Single-Photon Emitters in WSe_2 Monolayers Using Nanometer-Sized Gold Tips. *Nano Lett* **2020**, *20* (8), 5866-5872. DOI: 10.1021/acs.nanolett.0c01789

(36) Lee, S. J.; Chuang, H. J.; McCreary, K. M.; et al. Voltage-Induced Degradation for Enhanced Purity and Reproducibility of Quantum Emission in Monolayer 2D Materials. *ACS Nano* **2025**, *19* (38), 33981-33990. DOI: 10.1021/acsnano.5c09799

(37) Aslan, B.; Deng, M.; Heinz, T. F. Strain tuning of excitons in monolayer WSe_2. *Physical Review B* **2018**, *98* (11). DOI: 10.1103/PhysRevB.98.115308

(38) Conley, H. J.; Wang, B.; Ziegler, J. I.; et al. Bandgap engineering of strained monolayer and bilayer MoS_2. *Nano Lett* **2013**, *13* (8), 3626-3630. DOI: 10.1021/nl4014748

(39) Desai, S. B.; Seol, G.; Kang, J. S.; et al. Strain-induced indirect to direct bandgap transition in multilayer WSe_2. *Nano Lett* **2014**, *14* (8), 4592-4597. DOI: 10.1021/nl501638a

(40) Hsu, W. T.; Lu, L. S.; Wang, D.; et al. Evidence of indirect gap in monolayer WSe_2. *Nat Commun* **2017**, *8* (1), 929. DOI: 10.1038/s41467-017-01012-6

(41) Taghinejad, H.; Eftekhar, A. A.; Campbell, P. M.; et al. Strain relaxation via formation of cracks in compositionally modulated two-dimensional semiconductor alloys. *npj 2D Materials and Applications* **2018**, *2* (10). DOI: 10.1038/s41699-018-0056-4

(42) Panasci, S. E.; Schiliro, E.; Greco, G.; et al. Strain, Doping, and Electronic Transport of Large Area Monolayer MoS_2 Exfoliated on Gold and Transferred to an Insulating Substrate. *ACS Appl Mater Interfaces* **2021**, *13* (26), 31248-31259. DOI: 10.1021/acsami.1c05185

(43) Chen, S.; Li, B.; Dai, C.; et al. Controlling Gold-Assisted Exfoliation of Large-Area MoS_2 Monolayers with External Pressure. *Nanomaterials (Basel)* **2024**, *14* (17). DOI: 10.3390/nano14171418

(44) Smith, T. The hydrophilic nature of a clean gold surface. *Journal of Colloid and Interface Science* **1980**, *75* (1), 51-55. DOI: 10.1016/0021-9797(80)90348-3

(45) Velicky, M.; Donnelly, G. E.; Hendren, W. R.; et al. Mechanism of Gold-Assisted Exfoliation of Centimeter-Sized Transition-Metal Dichalcogenide Monolayers. *ACS Nano* **2018**, *12* (10), 10463-10472. DOI: 10.1021/acsnano.8b06101

(46) Stafford, C. M.; Harrison, C.; Beers, K. L.; et al. A buckling-based metrology for measuring the elastic moduli of polymeric thin films. *Nat Mater* **2004**, *3* (8), 545-550. DOI: 10.1038/nmat1175

(47) Falin, A.; Holwill, M.; Lv, H.; et al. Mechanical Properties of Atomically Thin Tungsten Dichalcogenides: WS_2, WSe_2, and WTe_2. *ACS Nano* **2021**, *15* (2), 2600-2610. DOI: 10.1021/acsnano.0c07430

(48) Dang, J.; Sun, S.; Xie, X.; et al. Identifying defect-related quantum emitters in monolayer WSe_2. *npj 2D Materials and Applications* **2020**, *4* (2). DOI: 10.1038/s41699-020-0136-0

(49) Linhart, L.; Paur, M.; Smejkal, V.; et al. Localized Intervalley Defect Excitons as Single-Photon Emitters in WSe_2. *Phys Rev Lett* **2019**, *123* (14), 146401. DOI: 10.1103/PhysRevLett.123.146401

(50) Schneider, L. M.; Lippert, S.; Kuhnert, J.; et al. The influence of the environment on monolayer tungsten diselenide photoluminescence. *Nano-Structures & Nano-Objects* **2018**, *15*, 84-97. DOI: 10.1016/j.nanoso.2017.08.009

(51) Daveau, R. S.; Vandekerckhove, T.; Mukherjee, A.; et al. Spectral and spatial isolation of single tungsten diselenide quantum emitters using hexagonal boron nitride wrinkles. *APL Photonics* **2020**, *5* (9). DOI: 10.1063/5.0013825

(52) Strasbourg, M. C.; Yanev, E. S.; Darlington, T. P.; et al. Characterization of quantum dot-like emitters in programmable arrays of nanowrinkles of 1L-WSe_2. *Journal of Applied Physics* **2024**, *136* (4). DOI: 10.1063/5.0214410

(53) Yao, K.; Zhang, S.; Yanev, E.; et al. Nanoscale Optical Imaging of 2D Semiconductor Stacking Orders by Exciton-Enhanced Second Harmonic Generation. *Advanced Optical Materials* **2022**, *10* (12). DOI: 10.1002/adom.202200085

(54) Shabani, S.; Darlington, T. P.; Gordon, C.; et al. Ultralocalized Optoelectronic Properties of Nanobubbles in 2D Semiconductors. *Nano Lett* **2022**, *22* (18), 7401-7407. DOI: 10.1021/acs.nanolett.2c02265

(55) Jo, K.; Marino, E.; Lynch, J.; et al. Direct nano-imaging of light-matter interactions in nanoscale excitonic emitters. *Nat Commun* **2023**, *14* (1), 2649. DOI: 10.1038/s41467-023-38189-y

(56) Novoselov, K. S.; Geim, A. K.; Morozov, S. V.; et al. Electric field effect in atomically thin carbon films. *Science* **2004**, *306* (5696), 666-669. DOI: 10.1126/science.1102896

(57) Sun, B.; Grap, T.; Frahm, T.; et al. Role of electron and ion irradiation in a reliable lift-off process with electron beam evaporation and a bilayer PMMA resist system. *Journal of Vacuum Science & Technology B, Nanotechnology and Microelectronics: Materials, Processing, Measurement, and Phenomena* **2021**, *39* (5). DOI: 10.1116/6.0001161

(58) Reina, A.; Jia, X.; Ho, J.; et al. Large area, few-layer graphene films on arbitrary substrates by chemical vapor deposition. *Nano Lett* **2009**, *9* (1), 30-35. DOI: 10.1021/nl801827v

(59) Lee, Y.; Bae, S.; Jang, H.; et al. Wafer-scale synthesis and transfer of graphene films. *Nano Lett* **2010**, *10* (2), 490-493. DOI: 10.1021/nl903272n

(60) Castellanos-Gomez, A.; Buscema, M.; Molenaar, R.; et al. Deterministic transfer of two-dimensional materials by all-dry viscoelastic stamping. *2D Materials* **2014**, *1* (1). DOI: 10.1088/2053-1583/1/1/011002

(61) Son, S.; Shin, Y. J.; Zhang, K.; et al. Strongly adhesive dry transfer technique for van der Waals heterostructure. *2D Materials* **2020**, *7* (4). DOI: 10.1088/2053-1583/abad0b

CHAPTER FOUR

A PLATFORM FOR NANO-OPTICAL ENGINEERING OF LIGHT-MATTER INTERACTIONS IN 2D MATERIALS WITH INDEPENDENTLY TAILORED STRAIN

Contributions of Authors and Co-Authors

Manuscript in Chapter 4

Author: Joseph Stage

Contributions: Conceived this work, developed the fabrication of embedded nanoantennas, conducted scanning electron microscopy imaging, conducted atomic force microscopy imaging, modeled the plasmonic response in COMSOL, conducted near-field optical microscopy, performed room temperature and cryogenic photoluminescence spectroscopy, performed photoluminescence excitation spectroscopy, conducted single photon antibunching, performed localization spectroscopy, data analysis, and wrote the manuscript

Co-Author: Elijah Stuvland

Contributions: Developed the fabrication of embedded nanoantennas, wrote the manuscript

Co-Author: Matthew Strasbourg

Contributions: Conducted near-field optical microscopy

Co-Author: Mohammad Soroush

Contributions: Data analysis

Co-Author: Luke Holtzman

Contributions: Grew two-step flux-synthesized WSe_2 bulk crystals

Co-Author: Amirhossein Hasani

Contributions: Established thermal scanning probe lithography

Co-Author: Katayun Barmak

Contributions: Grew two-step flux-synthesized WSe_2 bulk crystals

Co-Author: James Hone

Contributions: Grew two-step flux-synthesized WSe_2 bulk crystals

Co-Author: Andrew Lingley

Contributions: Aided in the development of the fabrication of embedded nanoantennas

Co-Author: P. James Schuck

Contributions: Conceived this work

Co-Author: Nicholas J. Borys

Contributions: Conceived this work, wrote the manuscript

Preamble to the Status of This Work

This work investigates the localization of single photon emitters in 1L-WSe_2 to the apex of an underlying embedded gold nanoantenna. Here, we have reported the fabrication procedure, metrological characterization, and optical characterization of this system. The relief tunable tips that we fabricate position the 1L-WSe_2 sheet at various heights above a reflective Si surface. Room temperature and cryogenic photoluminescence of such structures would suggest a shift of the optical bandgap to lower energies with increasing strain, but we observe nearly no strain-dependent shift, and in some cases a shift to higher energies. We suspect this to be due to a photonic interference effect caused by reflections from the underlying Si surface.

When developing the model that photonic interference is canceling out the strain-dependent shift of the optical bandgap (Figures 3c and 4e), we realized that one way to directly probe the presence of strain in this system is through Raman spectroscopy and numerical strain modeling. Because of this realization, some discussion that we intend to include for the final submission, mostly around Figure 3, is missing from this manuscript. We have currently identified a sample that is ideal for Raman spectroscopy; however have yet to perform these measurements. We expect over the next two weeks to have this data included and the discussion added to this manuscript. Similarly, strain modeling by solving the von Kármán plate equations is also intended. Our close collaborator, Tom Darlington, has been sent the AFM data required for these calculations; however, we await the results.

Manuscript Information

Joseph Stage, Elijah Stuvland, Matthew Strasbourg, Mohammad Soroush, Luke Holtzman, Amirhossein Hasani, Katayun Barmak, James Hone, Andrew Lingley, P. James Schuck, and Nicholas J. Borys

Status of Manuscript:
☒Prepared for submission to a peer-reviewed journal
☐Officially submitted to a peer-reviewed journal
☐Accepted by a peer-reviewed journal
☐ Published in a peer-reviewed journal

Abstract

Single photon emitters in monolayer WSe_2 are promising states of light for future applications in integrated quantum technologies. Activation of these states has been shown to occur at cryogenic temperatures in areas of tensile strain, where dark excitons in the WSe_2 can hybridize with defect levels to form an efficient radiative decay channel, making deterministic strain generation appealing. However, one open question is the role of defects in the single photon emitter formation process. Observations of a single photon emission from individual defect sites have been notoriously difficult due to the high defect densities (1×10^{13} defects/cm^2) present in WSe_2 and the inability to isolate emission from a small enough area. One such method for addressing ~20×20 nm^2 areas is near field-optical spectroscopy, but cryogenic near-field studies have proven difficult to achieve. In this work, we present strain-tunable embedded plasmonic nanoantennas, capable of locally enhancing single photon states in low defect density (~1×10^{11}), flux-synthesized WSe_2, eliminating the requirement for external near-field studies at cryogenic temperatures. By integrating the near-field resonator into the substrate, we are able to identify enhanced single photon states using photoluminescence excitation spectroscopy and localize these states to a nanoscale region above the apex of a nanoantenna. This platform also enables independent control over the imposed strain in the WSe_2 and underlying localized surface plasmon resonance by tuning the relief of the apex with respect to the dielectric surface. Our study provides insight into the localization of single photon emission in WSe_2 and can act as a platform for the correlation of cryogenic defect localized emitters and room temperature defect emission using gap mode near field optical spectroscopy when another Au tip is positioned above the apex, which is yet to be realized.

Introduction

Two-dimensional (2D) semiconductors such as single-layer (1L) MoS_2, $MoSe_2$, WS_2, and WSe_2 are promising material platforms where light-matter interactions, strain- and defect-engineering of optoelectronic properties, nano-optics, and photonic and electronic device engineering can be synergized for numerous technological applications and explorations of new physical phenomena. For instance, in single-layer (1L) WSe_2, localized tensile strain[1-3] is empirically known to activate highly localized electronic states that behave as solid-state single-photon emitters (SPEs) at cryogenic temperatures[4-9]. The formation of these states is commonly attributed to the strain-induced hybridization of excitons with localized defects[10], such as Se vacancies[11-13]. The requisite localized tensile strain enables deterministic positioning of the SPEs with sub-micron precision[12, 14-17] with physical properties that depend on the precise nanoscale structure of the strain field[7, 18, 19]. SPEs in 1L-WSe_2 have been used in quantum key distribution systems[20], coupled to integrated photonic elements[15, 21-25], and electrically addressed in 2D heterostructure devices[26, 27]. Further, they have been coupled to nano-optical systems[3, 28, 29] where the plasmonic response of the nanoantenna yields a combination of excitation and Purcell enhancement of the emitter. This combination of localized strain and such nano-optical enhancement was observed to activate emission from highly localized states in the 1L-WSe_2 at room temperature[30].

The versatility and breadth of simultaneously engineering strain and nanoscale light-matter interactions in 2D semiconductors typically requires prioritization of one design target at the cost of the others. For example, the majority of platforms to deterministically strain 2D materials rely on draping a 2D material over a nanoscale stressor (e.g., a dielectric pillar or nanoscale cone) that

lies on the surface of a flat substrate[13, 14, 19, 24, 28, 31-34]. The amount of tensile strain generated in the 2D material depends on the aspect ratio of the stressor, where, in general, a larger aspect ratio is assumed to generate greater strain[13, 31, 35]. As a result, the geometry of the stressor is tightly constrained by the amount of desired strain (or vice versa). For nanoplasmonic systems, this constraint limits the ability to independently tailor both the localized plasmonic resonance and the amount of strain in the 2D material, because both depend on the geometry of the stressor. In this work, we present a nano-plasmonic antenna architecture that substantially expands the ability to independently tailor the localized strain and plasmonic resonance of a nanoplasmonic antenna. We show that the system can generate tensile strain with significantly fewer constraints on the plasmonics resonance, which can be tuned from the visible to the near infrared. Nearfield optical microscopy demonstrates the versatility of the antenna for enhancing light-matter interactions, especially for nano-optical exploration of strong light-matter interactions in a plasmonic nanogap[36-41]. Finally, by integrating 1L-WSe_2, we confirm the emergence of high-quality SPEs at 4 K that benefit from plasmonic excitation enhancement and persist up to temperatures of 180 K. The nano-optical antenna architecture presented here opens new possibilities for simultaneous nano-optical and strain-engineering of light-matter interactions for a large library of 2D materials, as well as future measurements that could unambiguously identify the defect states responsible for the formation of SPEs in 1L-WSe_2.

Results and Discussion

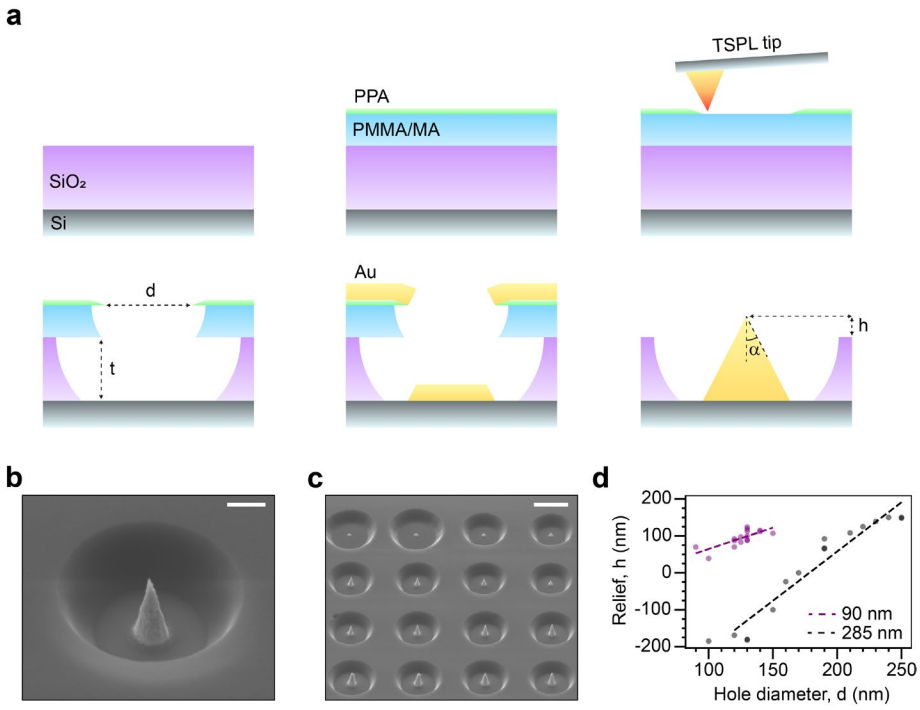


Figure 1 – Fabrication and characterization of relief tunable embedded gold nanoantennas: (a) Schematic representation of the fabrication procedure. TSPL is used to create openings in the PPA layer, permitting development and BOE etching down to the Si surface. Afterwards, Au deposition normal to the surface creates a leading edge that converges towards the center, forming the embedded antennas. (b-c) SEM images of a single and an array of embedded nanoantennas, respectively. (d) Plot comparing the measured relief of nanoantennas made in two different oxide thicknesses for a variety of hole diameters, d. Scale bars in the SEM images are 200 nm (b) and 1 μm (c).

Figure 1 summarizes our embedded Au nanocone architecture that greatly increases the freedom to independently tailor strain and nano-optical enhancement. In brief, thermal scanning probe lithography with two sacrificial resist layers is used to etch nanoscale holes into SiO_2 with a prescribed diameter (d) and depth (t) (Figure 1a). Metallization of the cavity structure simultaneously deposits metal within the etched hole and at the edges of the top of the hole. As the metallization progresses, the deposited metal at the top surface forms a progressively shrinking

aperture that increasingly restricts the amount of metal deposited in the hole. Once the aperture closes off, metal deposition within the hole terminates. As discussed in detail in the SI, the diameter, depth, and thickness of the sacrificial layers can be tuned such that the deposition within the hole terminates beneath, at, or above the SiO_2 surface, providing nanoscale control of the relief (h) of the gold nanostructure, as represented in Figure 1a. Figure 1b-c shows scanning electron microscopy (SEM) micrographs of a single and a collage of embedded gold nanoscones spanning reliefs from -182 – 150 nm. Although the relief is tunable, we note that the angle of the cone is fixed by the ratio of the normal deposition rate to that of the lateral growth of the metal at the hole aperture. In our system, every nanoantenna has a similar half-cone angle of ~24° (c.f., Figure 1a).

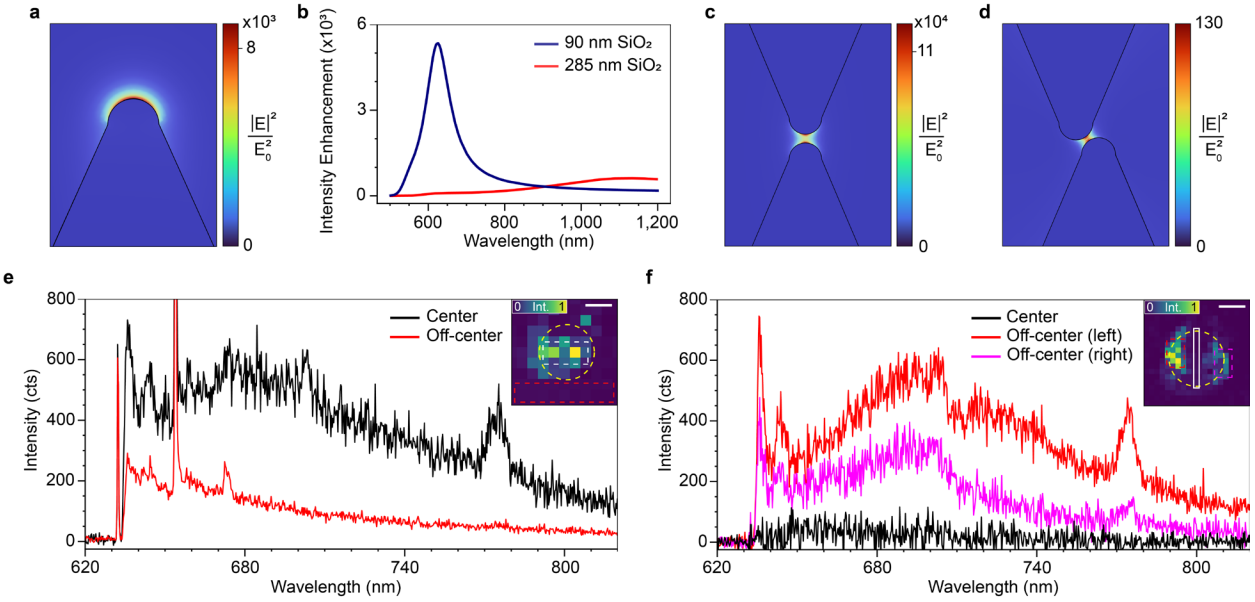


Figure 2 – Near-field enhancement from gold nanoantennas: (a) Finite element model of a gold nanocone with base diameter of 130 nm, height of 135 nm, and radius of curvature of 7.5 nm under 625 nm excitation polarized along the long axis of the nanocone. (b) Plasmonic enhancement spectra (PES) of a typical nanocone made in 90 nm oxide, (a), and 285 nm oxide. The PES is generated by extracting the maximum field intensity 1 nm above the surface of the nanocone at a variety of excitation wavelengths. (c) Finite element model of a gap plasmon between a gold nanocone and a similar near-field probe under polarized excitation along the long axis of the resonators. (d) Finite element model of the offset gap plasmon between a gold nanocone and a similar near-field probe under polarized excitation perpendicular to (c). (e) Near-field spectra of Au luminescence under the excitation condition shown in (c). Near-field intensity is clearly enhanced when the two tips are above one another. The inset shows a near-field map where the yellow circle is the approximate diameter of the cavity, and the white and red bounding boxes are the integration regions for the black and red spectra, respectively. (f) Near-field spectra of Au luminescence under the excitation condition shown in (d). As opposed to (e), near-field enhancement is maximized when the offset gap plasmon is excited. The inset shows a near-field map where the yellow circle is the approximate diameter of the cavity, and the red, magenta, and white bounding boxes represent the integration regions for the red, magenta, and black spectra, respectively. Scale bars for the insets in (e-f) are 100 nm.

Figure 2 demonstrates that the gold nanocone structures have a strong, tunable plasmonic response, making them very versatile nano-optical antennas for enhancing light-matter interactions. From the SEM characterization, we estimate that the radius of curvature of the embedded Au nanocones is 5-10 nm. As shown by the finite element model in Figure 2a, enhanced

local electrical fields are expected to form at the apex of the tip when the system is illuminated with optical radiation polarized along the long-axis of the antenna. Figure 2b quantifies how the resonant enhancement depends on the geometry of the cone: as the size of the antenna is increased, the resonance exhibits an expected shift to longer wavelengths. For a single embedded Au nanocone, the numerical simulations predict that the field enhancement can be as large as 10,000×.

The breadth of nanophotonic capabilities of the embedded Au nanocone is greatly expanded with the inclusion of a second gold nanocone, as shown in Figure 2c. Such a second antenna can be introduced, for instance, in a scattering-type nano-optical system[30, 42-44]. When the second Au nanocone is directly above the embedded Au nanocone, intense field enhancement occurs within the gap when the optical fields are resonant with the combined system. By displacing the top Au nanocone with respect to the apex of the bottom embedded Au nanocone, a modified offset gap can be realized by rotating the polarization of the optical field (Figure 2d). In such an offset gap configuration, the polarization within the gap (e.g., with respect to the transition dipoles in an overlaid 2D material) can be precisely controlled. Figures 2e and 2f experimentally demonstrate enhanced optical excitation processes in both these direct and offset gap configurations, respectively. In both cases, a nano-optical probe (i.e., a metalized AFM probe) is raster scanned over a bare embedded Au nanocone while being illuminated from the side with continuous wave optical excitation ($\lambda = 633$ nm). Complete experimental details are provided in the Methods. When the optical excitation is p-polarized such that its polarization maximally aligns with the long axes of the embedded Au nanocone and nano-optical probe, enhanced luminescence from the gold structures is observed when the nano-optical probe is directly over the apex of the embedded Au nanocone (Figure 2e). In contrast, when the optical excitation is s-polarized, the

enhancement shifts to the periphery around the apex of the embedded Au nanocone, as expected for the offset gap mode (Figure 2f).

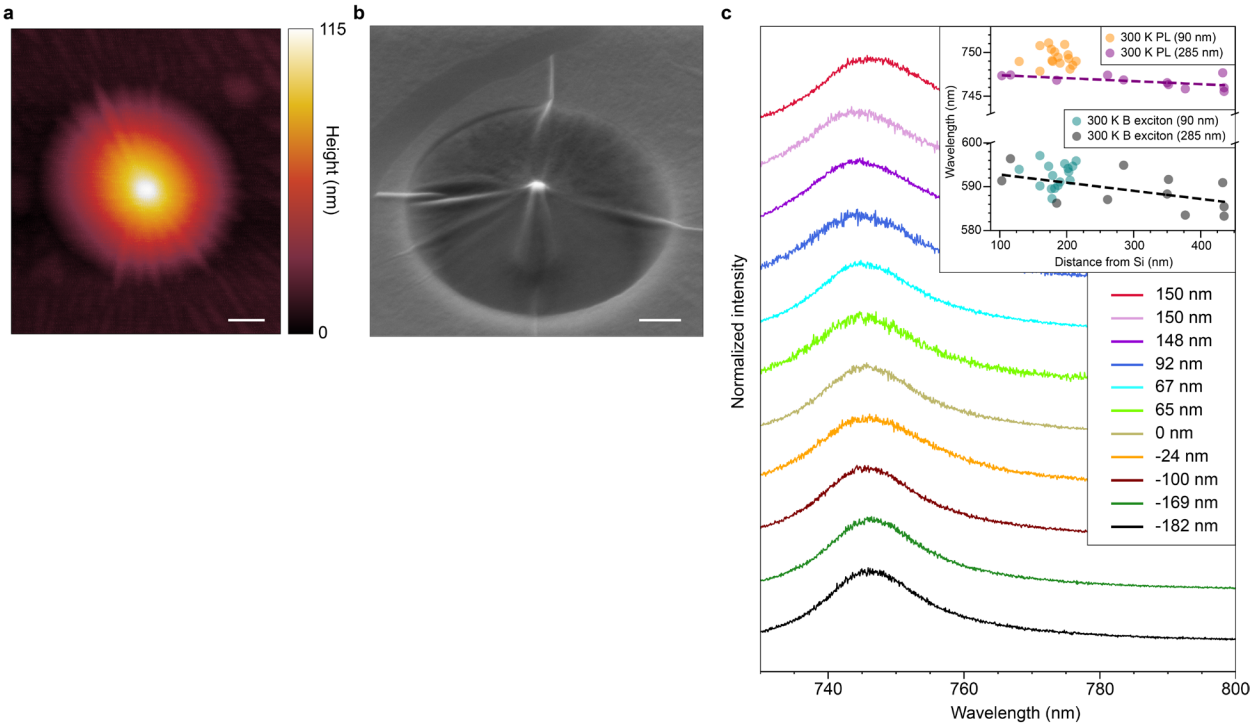


Figure 3 – Strain and photonic effects on room temperature PL: (a) AFM image of an embedded nanocone with 103 nm of positive relief covered by 1L-WSe_2. (b) SEM image of an embedded nanocone with 139 nm of positive relief covered by 1L-WSe_2. In both the AFM and SEM, hyperfine nanowrinkles radiating outward from the apex are observed. The radius of curvature seen in (b) is increased from nano-optical probing of the antenna. (c) Room temperature PL of nanoantennas with reliefs ranging from -182 to 150 nm made in 285 nm thick oxide. Inset is the spectral median and B exciton resonance of this range of nanoantennas. Scale bars are 200 nm.

In addition to nano-optical enhancement, the embedded Au nanocones can also serve as nanoscale stressors that generate localized tensile strain in 2D materials. Figure 3a-b shows AFM and SEM micrographs of 1L-WSe_2 draped over embedded Au nanocones with positive reliefs of 103 nm and 139 nm, respectively. The 1L-WSe_2 was dry transferred onto the embedded Au nanocones using a modified dry-transfer process (see Methods for details)[45, 46]. Both the SEM and

AFM reveal that the 1L-WSe_2 is fully intact and suspended over the SiO_2 cavity, supported by the apex of the embedded Au nanocone. Hyperfine nanowrinkles radiate outward from the central apex, leading to a robust strain architecture for investigating quantum states of light within 1L-WSe_2[18, 19]. In arrays of nanocones on a flat SiO_2 surface, such wrinkled 1L-WSe_2 has been shown to host single photon emitters (SPEs) at temperatures <50 K[19, 47] with improved distributions of excited state dynamics[18].

In our system, signatures of strain are absent in the far-field photoluminescence (PL) emission and excitation (PLE) spectra of the 1L-WSe_2 that is suspended over the embedded Au nanocones. Figure 3c shows the room-temperature photoluminescence collected from the suspended 1L-WSe_2/embedded Au nanocone system for reliefs from -182-150 nm. Across this range of reliefs, the emission energy is nearly constant. Further, the absorption resonance of the B exciton in the 1L-WSe_2/embedded Au nanocone system, as probed with PLE spectroscopy (Figure 3c), shows a slight blueshift of ~5 nm over the range of positive reliefs (0-150 nm), which would suggest increasing compressive strain with increasing relief. As summarized in Figure 3c and discussed in detail in the SI, we hypothesize that the strain-induced reduction of the band-gap that is expected for strained 1L-WSe_2[48-50] is counteracted by photonic effects, where increased elevation of the 1L-WSe_2 above the partially reflective Si layer reduces the out and in coupling of shorter wavelengths for the dimensions of our system. Such effects have been observed in the PLE spectroscopy of 2D materials[51, 52], Purcell enhancement in $MoSe_2$[53], and for quantum emitters in h-BN[54, 55]. Our calculations in the SI show that the convolution of the wavelength-dependent external quantum yield can substantially affect the optical spectra when the 2D material is substantially ($\sim\lambda/5$) above the reflective surface. Additionally, we note that dark-exciton

antifunneling[56-58] could also mask strong signatures of tensile strain in the observed excitonic photoluminescence due to the finite extent of our strained regions.

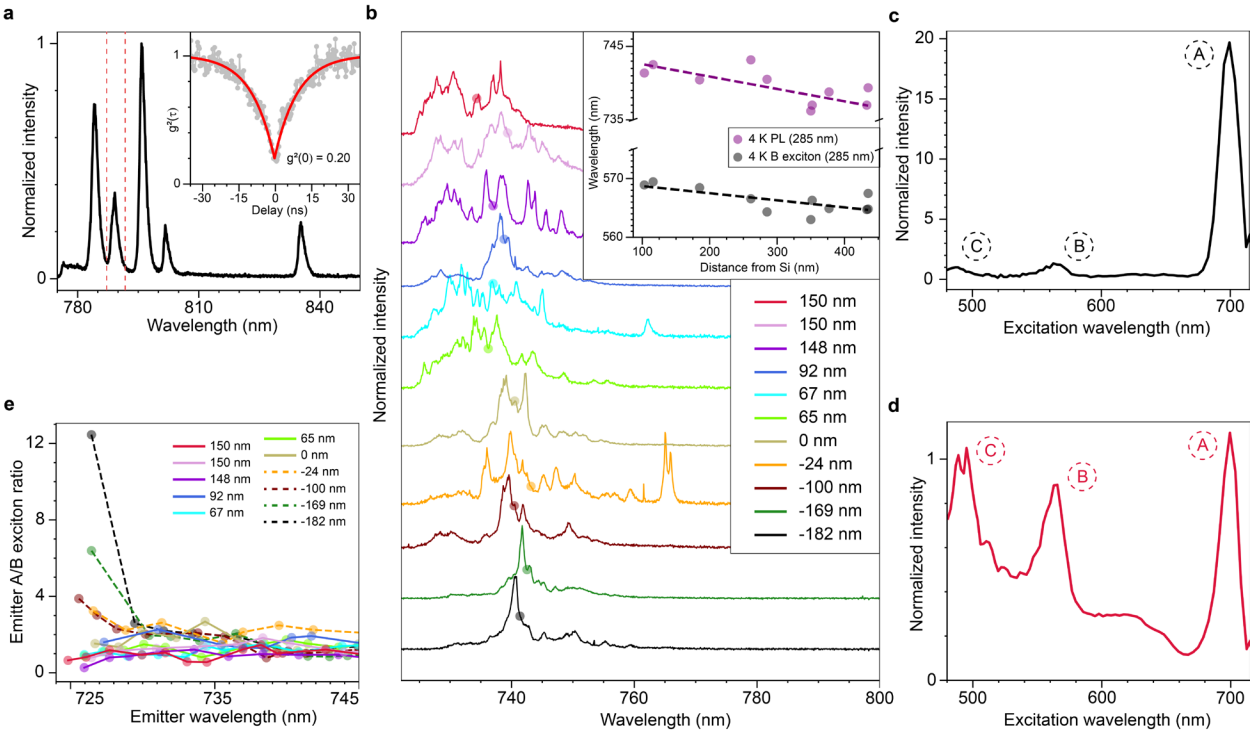


Figure 4 – Single photon emission and spectral dependence on the excitation process: (a) Cryogenic (4 K) PL spectra of 5 single photon emitters present from a 65 nm positive relief nanoantenna made in 90 nm oxide. Inset is the result of a single photon antibunching for the bound emitter. (b) Cryogenic PL of the same nanoantenna sites seen in Figure 3c. Now, a more notable blueshift of the spectral median and B exciton resonance is present (inset). The colored dots on each PL spectra are the respective calculated spectral medians. (c) Emitter resolved PLE spectra of a ~724 nm emitter from a -182 nm relief nanoantenna site. Note the reduced intensity of the B exciton resonance. (d) Emitte resolved PLE spectra of a ~724 nm emitter from a +150 nm relief nanoantenna site. Now the intensity ratio between the A and B excitons is closer to 1. PLE spectra are normalized to the C exciton. (e) Summary of the A/B exciton ratios for various emitters at nanoantenna sites with reliefs ranging from -182 to 150 nm. The A/B exciton ratio for low wavelength emitters in negative relief sites is substantially increased.

When cooled to 4 K, the PL emission from the suspended 1L-WSe_2 is dominated by narrowband defect-bound excitons, as shown in a representative PL spectrum shown in Figure 4a. As shown in the inset of Figure 4a, these narrowband emitters show strong signatures of photon

antibunching (see SI for details). Based on prior studies of 1L-WSe_2 draped over nanocone arrays [18, 19, 59], we strongly suspect that these emitters originate at the wrinkles that are formed in the suspended system, where the strain is sufficiently large to hybridize with the dark excitons in the system[10]. The comparison of emitter populations in the suspended 1L-WSe_2 for the entire range of reliefs in Figure 4b does not reveal a strong dependence on the relief, corroborating that the emitters are localized to the wrinkles. However, as shown in the inset, both the spectral median of the emitter populations, which characterizes the average wavelength of the emission, and the energy of the excitation resonance due to the B exciton shift to lower wavelengths with increasing relief, most likely due to the photonic effects described above.

Careful inspection of the PLE spectra of individual narrowband emitters at 4 K reveals that the relief of the embedded Au nanoantenna systematically alters the relaxation pathways for the highest-energy species. Two example PLE spectra for emitters at ~725 nm in suspended 1L-WSe_2 at different reliefs of -182 nm and 150 nm are shown in Figures 4c and 4d, respectively. For the emitters in the system with negative relief, the excitation resonance corresponding to the B exciton is strongly suppressed. As shown in Figure 4e, the suppression is strongest for the most negative relief and diminishes as the relief of the antenna approaches 0 nm. At 0 nm and above, the ratio of the intensities of the A and B exciton resonances in the PLE spectrum is ~1.5, as expected for 1L-WSe_2[60, 61]. This effect, which warrants additional future study, demonstrates how the relief-tunable structural properties imparted to the 2D material systematically alter the dynamics of the narrowband emitters in the system. Similar systematic alteration of the dynamics of quantum emitters in 1L-WSe_2 was shown in programmable wrinkles of 1L-WSe_2[18].

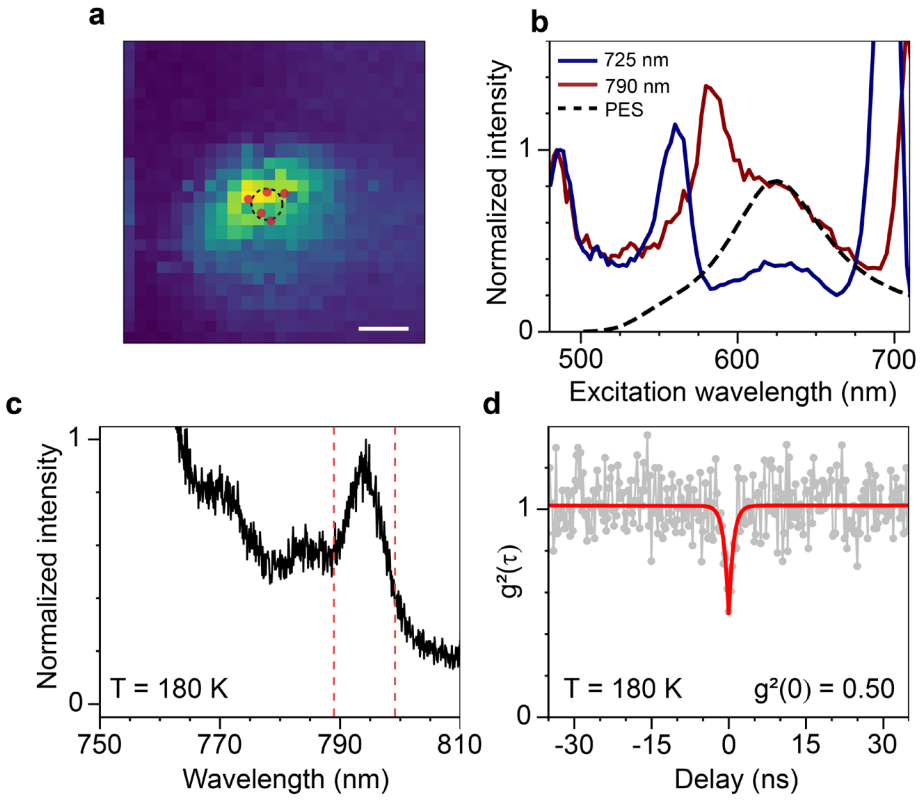


Figure 5 – Localization and plasmonic enhancement of SPEs: (a) Localization spectroscopy of the 5 emitters shown in Figure 4a to a ~500 x 500 nm^2 region about the center of a 65 nm positive relief nanoantenna site made in 90 nm oxide (black circle). (b) Emitter resolved PLE for a ~790 and ~725 nm emitter from the site shown in (a). The ~790 nm emitter shows anomalous enhancement in between the B and A excitons that directly correlates with the plasmonic enhancement spectra (PES) calculated for this nanoantenna site. (c) 180 K PL of a localized emitter. (d) 180 K Single photon antibunching of the emitter shown in (c). Scale bar is 800 nm.

In Figure 5, localization microscopy[62] of the emitters reveals that they are spatially dispersed in the suspended 1L-WSe_2 around the apex of the supporting embedded Au nanocone. Figure 5a shows the localization centers of 5 emitters in 1L-WSe_2 draped over an antenna with a positive relief of 65 nm. The centroid positions of the emitters are localized within a ~500×500 nm^2 region of one another. In future measurements, this localization microscopy, combined with high-resolution AFM and nano-optical characterization of the suspended membranes, may enable unambiguous assignment of specific emitters to wrinkles (or other features in the 1L-WSe_2). Such

an experiment was attempted on these systems, but was hindered by mechanical failure of the suspended membrane when measured with the AFM (see SI for details). Nevertheless, the variation in emitter position implies that a sub-ensemble of emitters may be sufficiently close to the plasmonic antenna to achieve nearfield enhancement of optical excitation and/or emission. Such plasmonic enhancement of emission has been observed in Au nanotips[63, 64], nanocubes[2, 3, 65, 66], and other nanophotonic device[28, 34]. In contrast, the resonant response of our nanoantennas here lies at higher-energies commensurate with the optical excitation process. Figure 5b contrasts the PLE spectra of two emitters in the 1L-WSe_2 suspended by an embedded Au nanocone with 65 nm of positive relief. For the emitter at 724.8 nm, the PLE spectrum exhibits strong excitation resonances for the A and B excitons. Between these two resonances, only weak, off-resonant excitation of the emitter occurs. In contrast, for the emitter at 802.6 nm, strong enhancement of the excitation between the A and B resonances is observed. This enhanced excitation band occurs in the same wavelength band as the resonant response of the nanocone, as shown in the overlaid enhancement spectra. This increase in excitation appears to preferentially occur only in the longest wavelength emitters (>780 nm) (see SI for all emitter PLE curves), which could be due to band bending and local doping in close-proximity to the gold[67].

The enhanced excitation provides strong evidence that a sub-ensemble of the emitters in the 1L-WSe_2 can be positioned within the nearfield region of the plasmonic antenna without suffering complete quenching effects due to being in proximity to the gold. As shown in Figure 5c-d, these emitters in the nearfield region of the Au nanocone can exhibit antibunching up to temperatures of 180 K. While further studies are needed to unravel the interplay of plasmonic enhancement, defect states, strain, and effects due to the close-proximity of a 1L-WSe_2/Au point

contact, the results suggest an empirical architecture for high-temperature quantum light sources in 1L-WSe_2[30]. Along these lines, the defect density may be an important architectural element: the $O(1)$ number of emitters near the nanocone apex that are enhanced (i.e., within a radius of ~20 nm of the apex) is commensurate with the anticipated defect density in the flux-grown 1L-WSe_2, which is expected to be ~$10^{11}/cm^2$ [68, 69]. At such a density, we expect 1-10 defects to exist within this region.

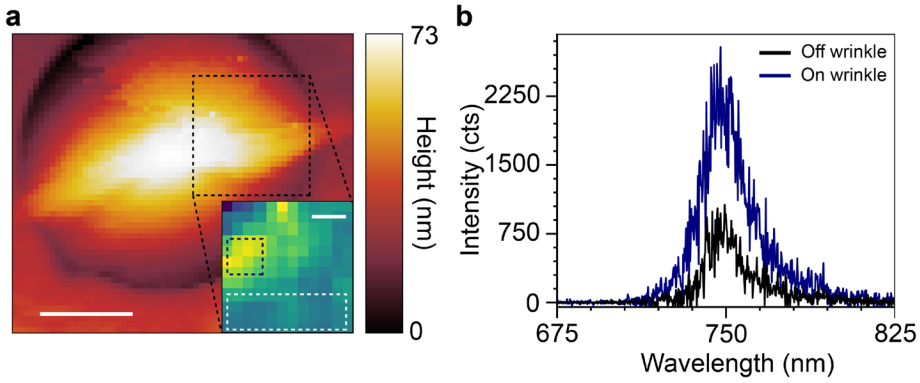


Figure 6 – Near-field optical spectroscopy of a nanoantenna site with 1L-WSe_2: (a) AFM image of a 38 nm positive relief nanoantenna site. The inset shows a near-field map of the bounded region adjacent to the apex of the nanoantenna. Increased enhancement is present from the wrinkle of the 1L-WSe_2. (b) Near-field spectra integrated from the bounding boxes seen in the inset of (a). On the wrinkle, there is an added low-energy shoulder, indicating defect emission in the 1L-WSe_2. Scale bars are 400 nm and 125 nm for the AFM and near-field map, respectively.

To provide a preliminary demonstration of the gap-mode enhancement, Figure 6 shows tip-enhanced photoluminescence from a single wrinkle of 1L-WSe_2 suspended by an embedded Au nanocone with a 38 nm relief at 300 K. The wrinkle crosses over the apex of the nanoantenna and promotes the funneling of excitons into defects along the wrinkle due to the spatial modulation of the optical bandgap in 1L-WSe_2 with increasing tensile strain [70, 71]. The nanoscale map of the tip-enhanced PL is inset in the AFM topography of the wrinkle shown in Figure 6a. With p-polarized

optical excitation, a clear enhancement of the PL occurs along the wrinkle near the apex of the antenna. The spectrum of the tip-enhanced PL (Figure 6b) shows that the emission is dominated by the bright exciton and includes a weaker, but clearly enhanced, low-energy shoulder indicative of defect emission in 1L-WSe_2[30]. By combining such nearfield optical studies with unambiguous identification of plasmonically enhanced emitters at 4 K (as demonstrated above), the embedded plasmonic antenna structures have the potential to enable correlated nano-optical and cryogenic spectroscopy of defect states in 1L-WSe_2 in future studies.

Conclusion

In conclusion, we have developed a nano-optical platform for independent tailoring of imposed tensile strain and underlying plasmonic resonance to be used in conjunction with 2D materials. We report the relief tunability of nanoantennas, ranging from deeply embedded to protruding tips 150 nm above the surrounding SiO_2. With near-field optical spectroscopy, we were able to validate the plasmonic performance of these nanoantennas by observing both gap mode and offset gap mode Au luminescence enhancement. Then, by overlaying a monolayer of low defect density, flux-synthesized WSe_2, we identified an ensemble of long-wavelength emitters with plasmonically enhanced absorption commensurate with the plasmonic enhancement spectra of the nanoantenna using PLE. We conclude that the enhanced emitters are single-photon emitters, and one such emitter even persisted in the WSe_2 to temperatures as high as 180 K. By analyzing the room temperature and cryogenic photoluminescence and PLE of a variety of different nanoantenna reliefs, we signify both photonic interference and a modified excitation process that affects the far field PL signatures of excitons in such systems. We foresee this platform having a wide range of

possible applications, including sensing, cavity quantum electrodynamics, and as a deterministic strain platform for single photon emission.

Methods

Sample Fabrication

Fabrication of Embedded Plasmonic Nanoantennas Sample preparation for thermal scanning probe lithography (TSPL) was done by cleaning a Si/SiO_2 chip in sonicated acetone, isopropyl alcohol (IPA), and deionized water (DIW) to remove debris from the surface and spin coating layers of polymethyl methacrylate-co-methacrylic acid (PMMA/MA) and polyphthalamide (PPA) at 6000 rpm that were progressively baked at 180 °C for 90 s and 110 °C for 120 s, respectively. TSPL was done using a Heidelberg Instruments NanoFrazor Scholar thermal scanning probe lithography (TSPL) system with a tip temperature of 1000 °C and a write depth of 60 nm. The tip efficiently ablates the PPA layer while the PMMA/MA layer acts as a buffer for the apex. Development of the PMMA/MA was done in a sonicated 20% volume ratio solution of DIW in IPA stored at ~0 °C for ~120 s. This cosolvent mixture has been shown to support larger proportions of polymer in solution, decreasing development times and adding consistency[72]. Cavities in the SiO_2 were formed using a sonicated 6:1 buffered oxide etch. Sonication of both the development and buffered oxide etch was used to expel trapped air bubbles from the nanoscale cavities of the future nanoantennas. Sonication during etch steps has also been shown to result in steeper sidewalls because of the increased etch rate[73]. Metallization was then achieved using an electron beam evaporator to deposit Cr/Au at 2Å/s. Lift-off of the excess polymer and metal was done over the course of ~12 hours in acetone. We note that the polymers used for TSPL are highly sensitive to excess electrons and charged ions within electron beam evaporators, and certain

compact evaporators may benefit from added shields and or magnets to divert these charged particles[74].

Dry Transfer of 1L-WSe_2 Dry transfer of 1L-WSe_2 onto the embedded was conducted using a modified viscoelastic stamping method[45]. The modification to the traditional method was made by ensuring complete vibration and air current isolation of the stamping system. We experienced that the super fine tips of the embedded nanoantennas would apply large amounts of pressure to the 1L-WSe_2, greatly increasing the likelihood of fracture. After isolating the system, the success rate of dry transfer onto nanoantennas without fracture increased significantly.

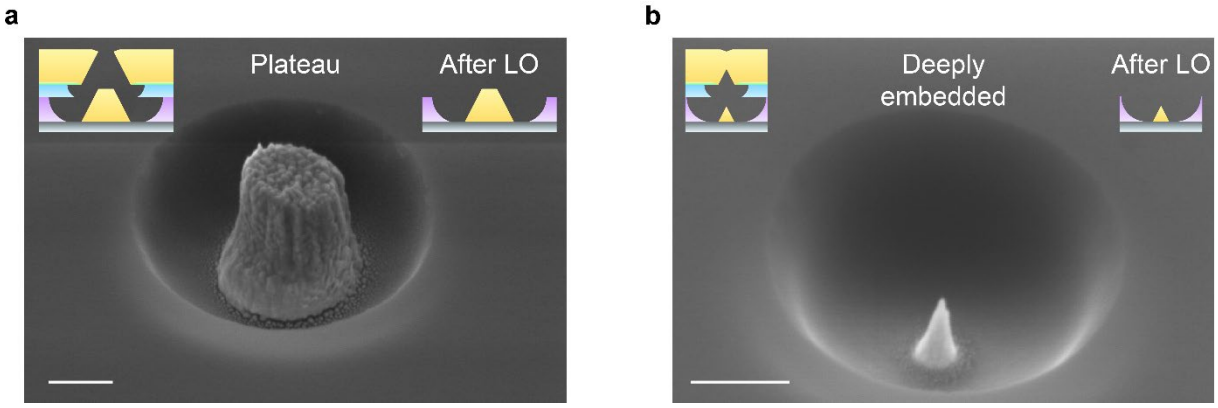
Optical Measurements

Cryogenic optical spectroscopy Cryogenic spectroscopy was performed using a closed-cycle Montana Instruments s50 Cryostation. Samples were illuminated with either a 532 nm continuous wave (CW) laser (Cobalt Samba) or a NKT Photonics SuperK EXTREME laser filtered with a Gooch and Housego acoustic-optical tunable filter, focused through a Nikon infinity corrected S Plan Flour 40X (0.6 NA) objective. Spectra were then recorded using a HORIBA iHR320 grating spectrometer and an Andor idus 416 CCD camera. Single photon antibunching measurements were done using the 532 nm CW laser source and a free-space Hanbury-Brown and Twiss (HBT) interferometer. The HBT interferometer consisted of 2 Excelitas AQRH-14-TR single-photon avalanche photo-diodes connected to a PicoQuant HydraHarp 400 time tagging module. Localization spectroscopy was conducted using 532 nm CW laser light, and emitters were isolated using combinations of different spectral bandpass filters (10 nm FWHM) rotated to shift their step edges for complete isolation from other emitters.

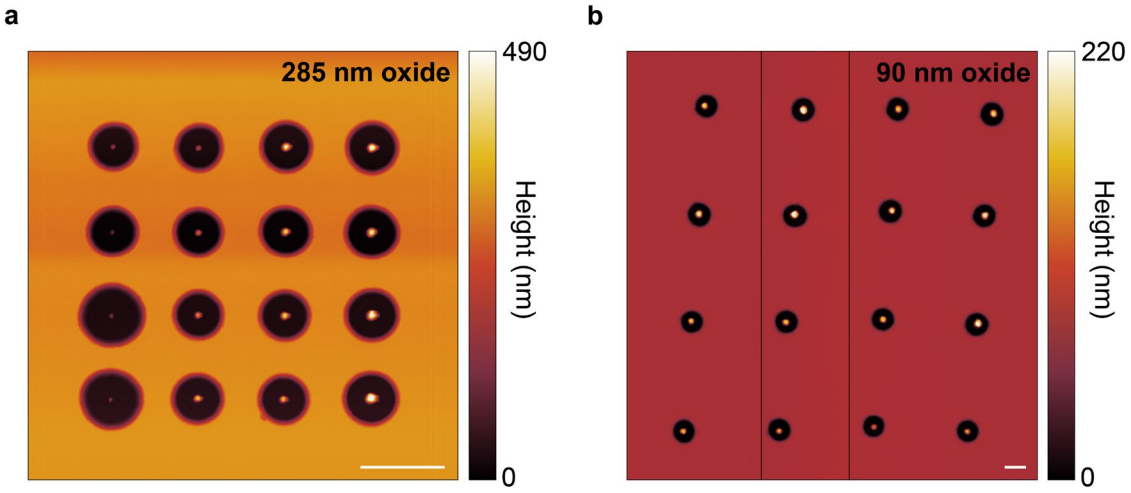
Near-Field Optical Spectroscopy Simultaneous near-field optical spectroscopy and AFM topography was conducted using a HORIBA OmegaScope AFM with an AppNano Omni TERS-SNC-Au tip (150 kHz). For near-field spectroscopy, the tip was excited using a HeNe laser (632.8 nm) provided by a HORIBA LabRam with an integrated spectrometer and cooled EMCCD detector. To rotate the polarization for the polarization-dependent near-field mapping, we placed a $\lambda/2$ waveplate in the excitation path.

Photoluminescence excitation spectroscopy (PLE) To perform PLE, we used an NKT Photonics SuperK EXTREME laser filtered with a Gooch and Housego acoustic-optical tunable filter (AOTF), focused through a Nikon infinity corrected S Plan Flour 40X (0.6 NA) objective with samples either on an ambient room temperature stage or within a Montana Instruments s50 Cryostation. Pairs of 750 short-pass and 750 long-pass spectral filters were used to isolate unwanted diffraction peaks from the AOTF and laser light from the optical path, respectively. To mitigate chromatic aberrations, we align the system with 595 nm light (the central wavelength of our PLE measurements). Correcting for a constant photon flux incident onto the sample is done after the measurement by measuring the excitation powers and the approximate laser spot size at every excitation wavelength.

Supplementary Information



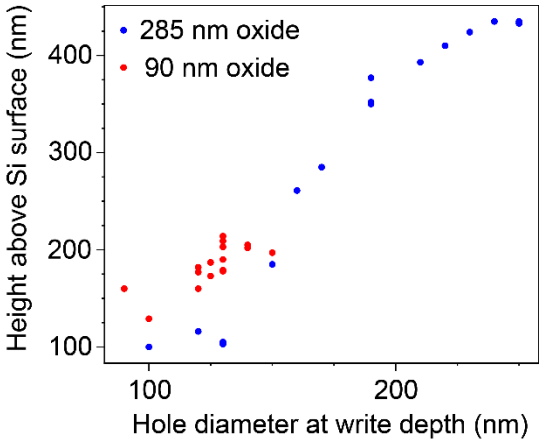
Supplementary Figure 1: Cavity diameter to SiO_2 thickness ratio determines convergence location. (a) An SEM image of a plateau structure formed within a wide SiO_2 cavity, such that convergence did not occur after 550 nm of Au deposition. (b) An SEM image of a deeply embedded nanoantenna within a narrow SiO_2 cavity. Here, the leading edge converged early during the deposition, setting the relief of this site to be negative. Inset in (a-b) are diagrams indicating how these structures emerge during Au evaporation. Scale bars = 200 nm



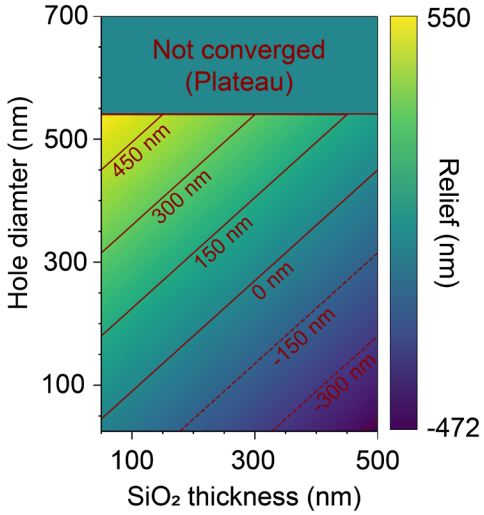
Supplementary Figure 2: High-resolution AFM of nanoantenna sites. (a) AFM taken of nanoantenna sites made in a 285 nm thick SiO_2. (b) AFM collage of nanoantenna sites made in a 90 nm thick SiO_2. Vertical black lines indicate the stitch locations of the collage. Scale bars are 2 μm and 400 nm for (a) and (b), respectively.

Tuning the Convergence of Embedded Nanoantennas

Determination of the convergence for embedded nanoantennas is highly dependent on the SiO_2 thickness and cavity diameter. For a given SiO_2 thickness, by changing the hole diameter, the leading edge convergence during electron beam evaporation can be pushed into either an early convergence, resulting in deeply embedded antennas, or no convergence, resulting in nanoplateaus. Supplementary Figure 1 highlights these two different resulting structures with SEM images and inset schematics showing how each scenario manifests from a cross-section. By doing an initial sweep of hole diameters for each SiO_2 thickness and electron beam evaporator, and measuring the relief of each cavity size using AFM, desirable ranges of reliefs can be prescribed and used for future fabrication runs.



Supplementary Figure 3: Mask hole diameter and nanoantenna height relationship. Plot showing the hole diameter at write depth (mask diameter) against the overall height of each nanoantenna. This plot differs from the plot in Figure 1 of the main manuscript as relief is swapped for overall height. The near-linear relationship here, even across different SiO_2 thicknesses, indicates that the convergence mechanism is consistent across the same electron beam evaporator.



Supplementary Figure 4: Relief model. Model showing the expected relief of a nanoantenna site considering the site's hole diameter and the sample's SiO_2 thickness. Contours represent lines of equal relief, labeled in the model. The overall deposition thickness in this model is 600 nm, limiting the region of convergence. Sites with diameters above ~545 nm will not converge and instead form plateaus.

Modeling Expected Reliefs Using Electron Beam Evaporation Rates

To demonstrate the wide range of reliefs for embedded nanoantennas available using the fabrication protocol explained in Figure 1, we have developed a model to predict the apex relief of an antenna at a given cavity site using the SiO_2 thickness, hole diameter, and electron beam evaporation rates. This model is shown in Supplementary Figure 4 and covers SiO_2 thickness and hole diameters ranging from 50 – 500 nm and 25 – 1000 nm, respectively. To calculate the apex relief at a cavity site, we first determine the vertical and horizontal electron beam evaporation rates. The vertical evaporation rate is commonly reported by the evaporator as simply the evaporation rate (valid only with normal incidence and a well-tuned tooling factor). To approximate the horizontal evaporation rate, we first write a wide variety of hole diameters and process the sample as done in Figure 1. Afterwards, by taking high-resolution AFM, we locate a

site that is converged but also has a relief matching the total metal thickness that was deposited. So if 300 nm of Au was deposited with a 10 nm Cr adhesion layer, we are looking for a converged site that has an apex 310 nm above the Si surface. Then, by extracting that site's hole radius from the NanoFrazor write file and dividing the radius by the deposition time, the horizontal evaporation rate is estimated.

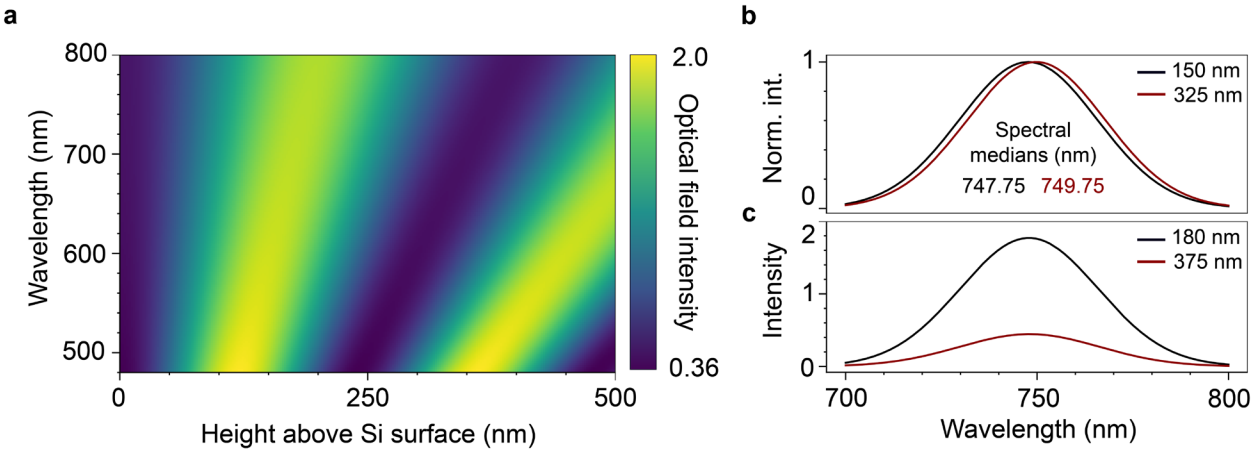
For the electron beam evaporator used in this work, we used a vertical deposition rate, r_{vert}, of 2 Å/s and found a horizontal rate, r_{horiz}, of ~0.9 Å/s. Using these deposition rates and assuming a total deposition thickness of 600 nm, the total convergence times, t_{conv}, for a given hole diameter, d_{hole}, are:

$$t_{conv}(s) = \frac{d_{hole}\ (nm)\ 10\left(\frac{\text{Å}}{nm}\right)}{2\ r_{horiz}\left(\frac{\text{Å}}{s}\right)} \quad (1)$$

Then the relief is obtained using the vertical deposition rate, convergence time, and SiO_2 thickness, t_{SiO_2}, as:

$$relief\ (nm) = \frac{t_{conv}(s)\ r_{vert}\ \left(\frac{\text{Å}}{s}\right)}{10\ \left(\frac{\text{Å}}{nm}\right)} - t_{SiO_2}(nm) \quad (2)$$

In the model shown in Supplementary Figure 4, cavity sites that would not converge for 600 nm of total deposition thickness are listed as plateaus.



Supplementary Figure 5: Reflectance model. (a) Simulated reflectance model of optical field intensities generated by assuming reflections off a Si surface at various wavelengths and distances from the Si. (b) Simulated effect of photonic reflections on the spectral position of a Gaussian peak. These results came from applying the optical field intensities seen in (a) to a Gaussian centered at 748 nm. (c) Simulated effect of photonic reflections on the intensity of a Gaussian peak.

Modeling the Optical Field Intensities from Reflections

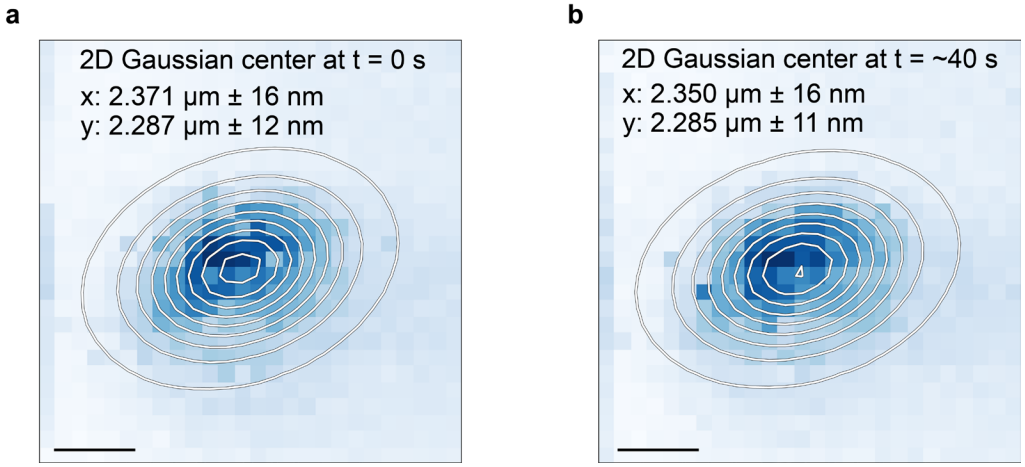
To model the photonic interference effect seen in Figure 2 of the main manuscript, we first assume that a radiating dipole, representing an exciton, is positioned above a Si mirror and radiates a plane wave. This wave then reaches the Si mirror, where, depending on the wavelength of the dipole, λ, a fraction is reflected (depending on the reflectivity of the Si, $R_{Si}(\lambda)$) with a pi phase shift that propagates back toward the dipole. Then we obtain the relative phase shift, $\varphi_{diff}(h_{Si})$, between the original and back-reflected waves for each height above the Si surface, h_{Si} , and calculate the optical field intensity, $OFI(\lambda, h_{Si})$, as:

$$OFI(\lambda, h_{Si}) = \left(E_0\, R_{Si}(\lambda)\right)^2 + (E_0)^2 + 2\, E_0^2\, R_{Si}(\lambda)\, cos\left(\varphi_{diff}(h_{Si})\right)$$

For the case of the model seen in Supplementary Figure 5a, $E_0 = 1$.

It is clear to see that depending on the distance away from the Si surface and dipole wavelength, the resulting optical field intensities can vary greatly. To highlight how these reflections can change

a 4 K photoluminescence (PL) spectrum, we use a broad Gaussian to represent the broad emission spectrum of SPE states at 4 K and multiply the calculated OFIs at different distances away from the Si surface. In Supplementary Figure 5b, we show how, for two different emitter distances away from the Si surface, the spectral median of this peak is shifted by a few nanometers, similar to what we experimentally observed in Figure 2 of the main manuscript. Then, in Supplementary Figure 5c, we take two other distances away from the Si surface and show how the reflections modulate the overall intensity of the peak.

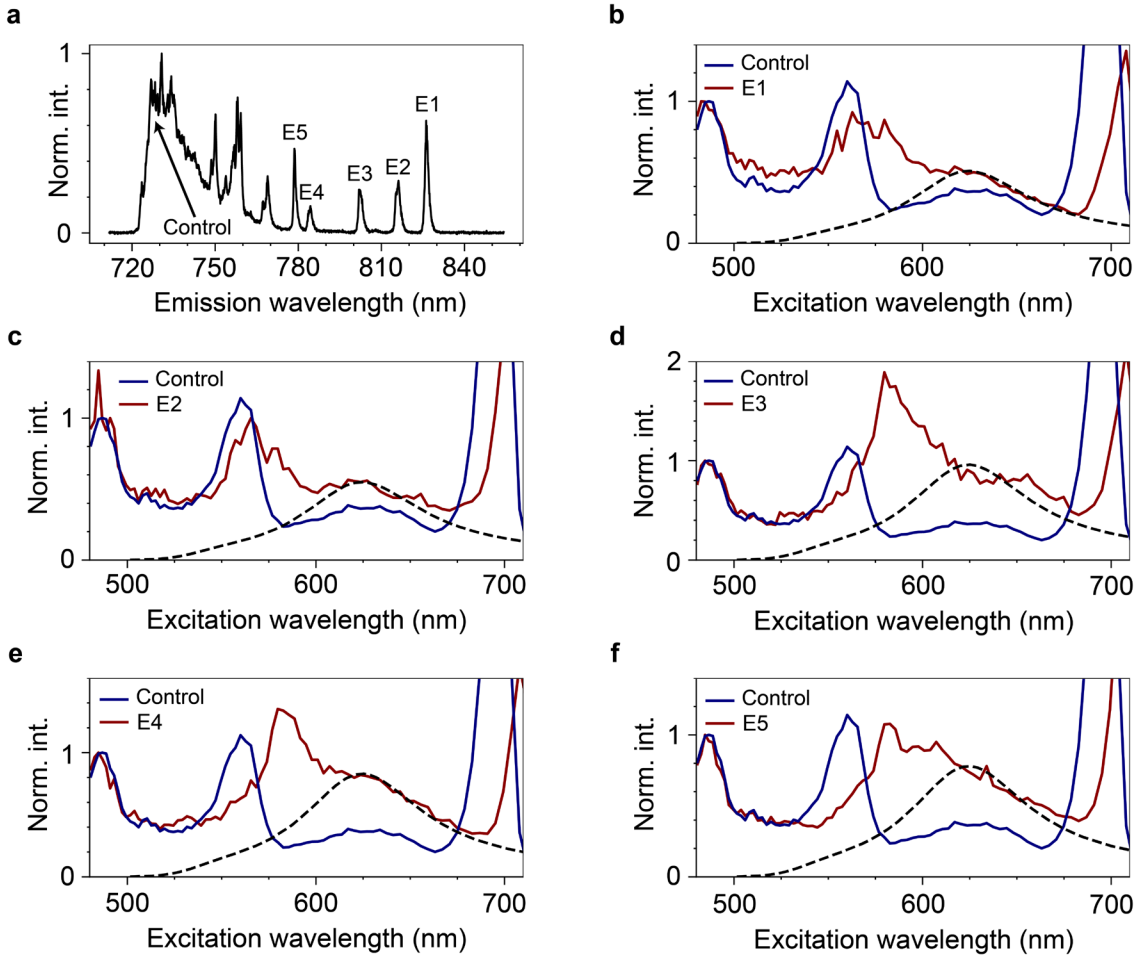


Supplementary Figure 6: Drift calibration measurement. (a) PL intensity scan of the ensemble of long wavelength emitters seen in the main manuscript Figure 4. Overlaid are the contours of a 2D Gaussian fit, with the center position listed in the figure. (b) PL intensity scan of the same ensemble of emitter, but 40 s later. 40 s represents the average time between scans for the localization measurement conducted in the main manuscript, Figure 5. Scale bars are 1 µm.

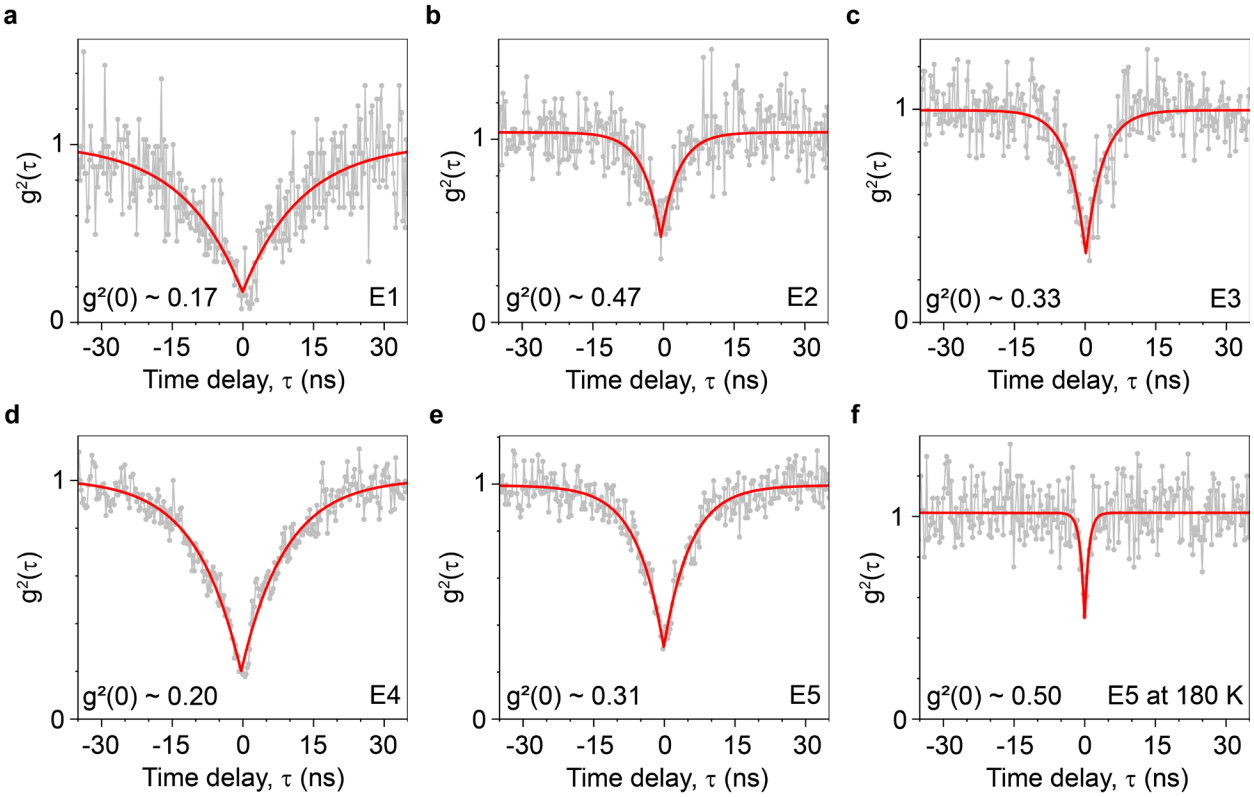
Calibrating for Drift During a PL Intensity Localization Measurement

During cryogenic spectroscopy, samples will commonly drift due to thermal fluctuations in the environment. For the localization measurements taken in Figure 5 of the main manuscript, drift could lead to a misinterpretation of the spatial location of each emitter with respect to the

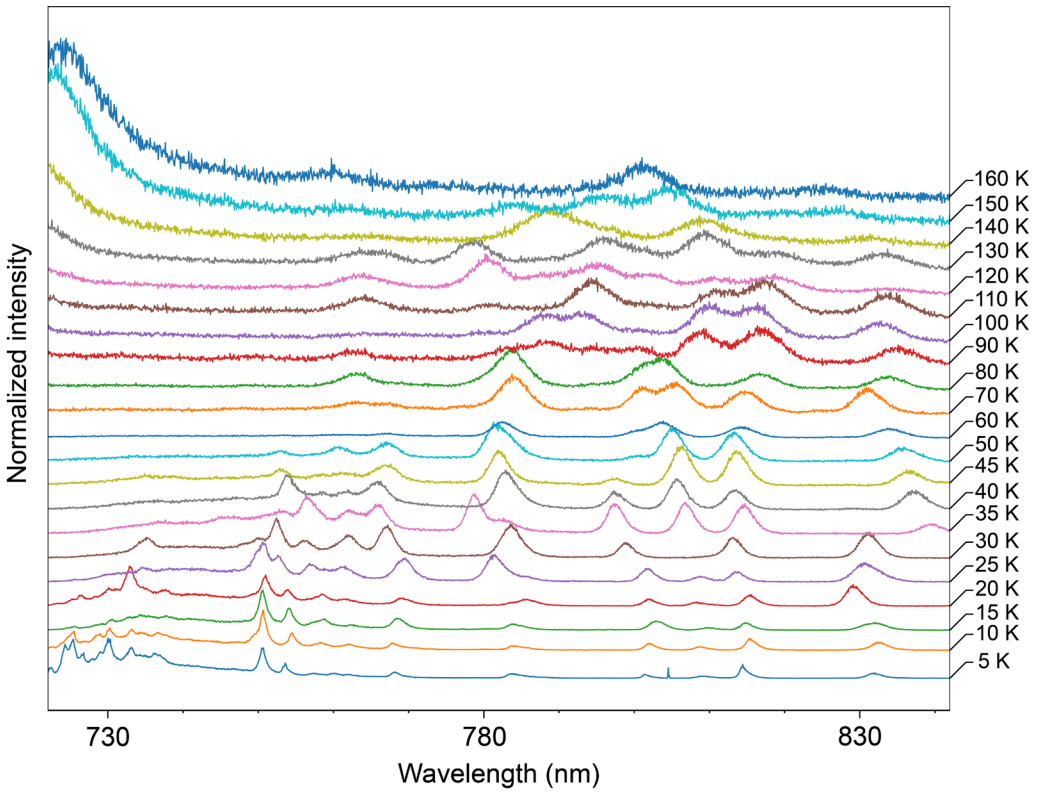
nanoantenna apex. To understand the amount of drift that should be expected between two PL intensity scans, we take sets of calibration measurements and observe how the center points of emission for a scan taken at $t = 0\ s$, and another scan at $t \cong 40\ s$ shift. The center points of emission are obtained through least squares fitting of a 2D Gaussian to the PL intensity maps. An example of two scans of the same feature with 40 s timing separation can be seen in Supplementary Figure 6. We note that the calculated center positions of these scans shift slightly but are within the standard errors of each other, indicating that drift on the time scale of 40 s is likely not important to the analysis of Figure 5. We chose 40 s as the timing window of interest because this was the average amount of time between the scans in Figure 5.



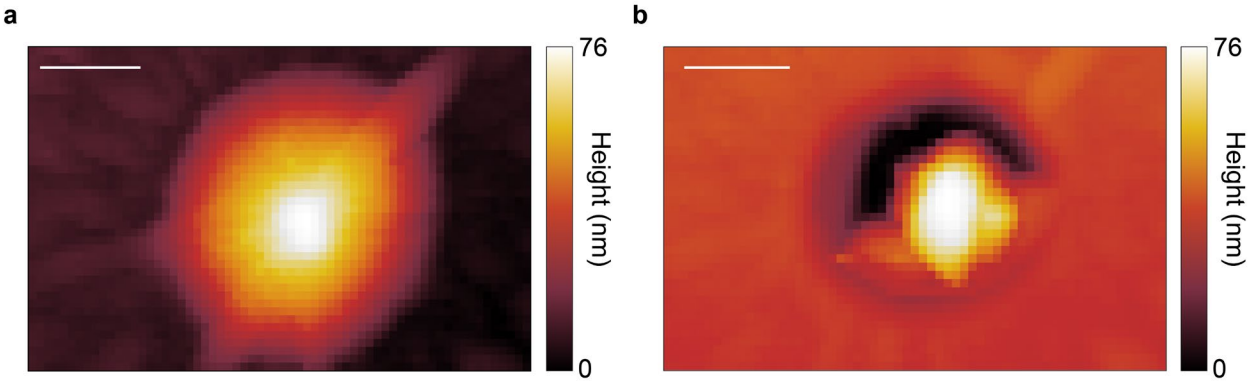
Supplementary Figure 7: Emitter PLE curves. (a) Cryogenic PL spectra of the long wavelength ensemble of emitters labeled E1-E5, and the control emitter. (b-f) Emitter PLE spectra compared against the control emitter. Certain emitters, such as E3, E4, and E5, show strong enhancement with respect to the PES, while E1 and E2 show weaker enhancement. We believe this to be caused by the proximity of the emitter to the apex of the nanoantenna.



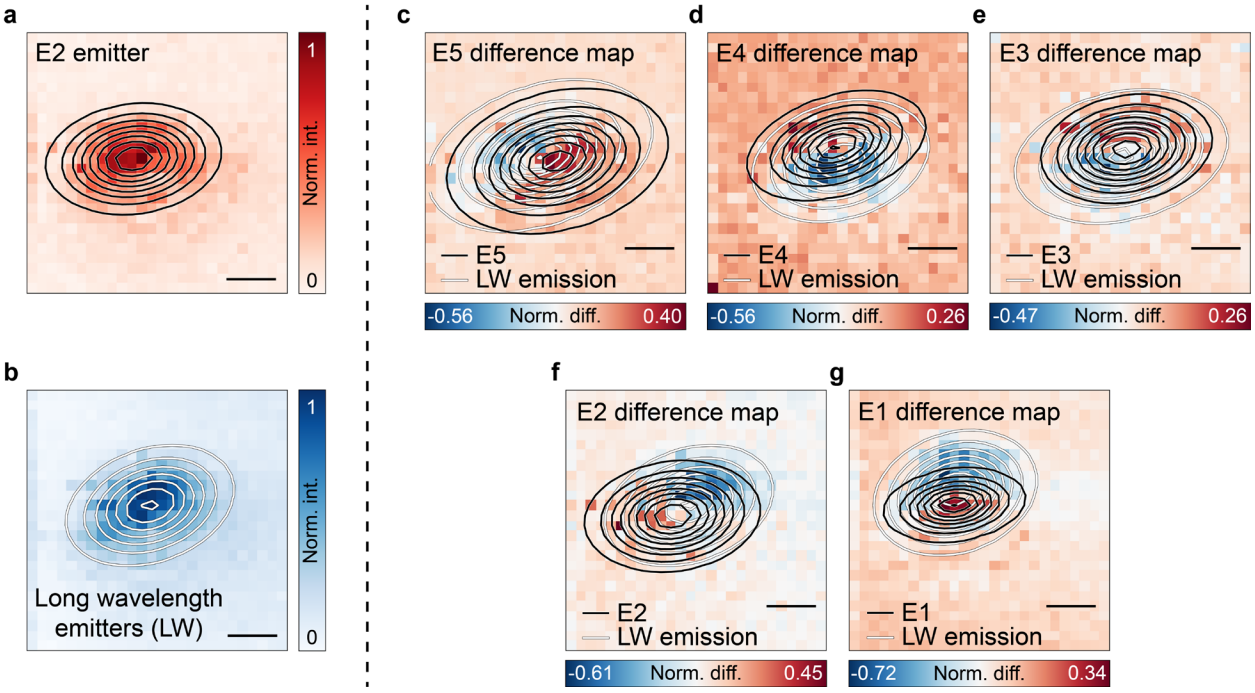
Supplementary Figure 8: Single photon antibunching of plasmonically enhanced emitters. (a-e) Antibunching curves of emitters E1 – E5 with their respective $g^2(0)$ values. (f) Antibunching curve of what we suspect is E5, now at 180 K.



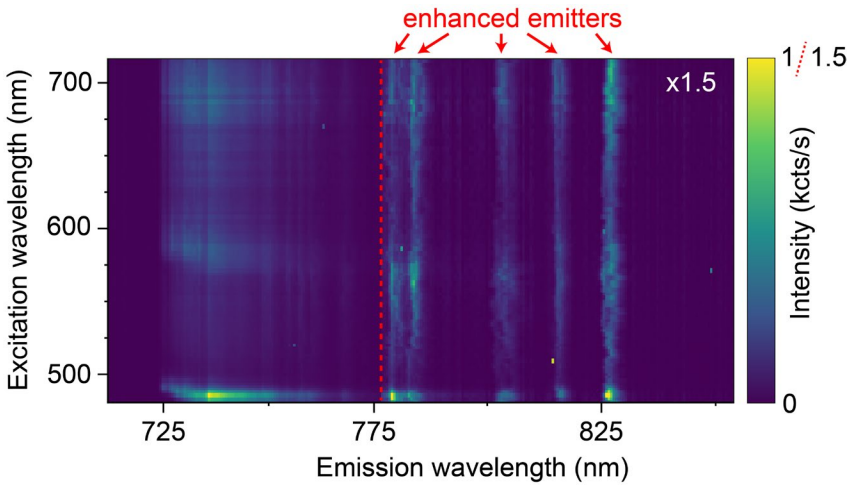
Supplementary Figure 9: Temperature-dependent PL spectroscopy. (a) Temperature-dependent PL spectroscopy of a 65 nm positive relief nanoantenna in 90 nm oxide. The long-wavelength emitters present are E1 – E5. Notably, the spectral fluctuations of these emitters make tracking a specific emitter throughout the temperature series difficult, especially considering the expected Varshni shift behavior.



Supplementary Figure 10: Rupture of the 1L-WSe_2. (a-b) AFM images of a nanoantenna site before and after near-field optical spectroscopy. During near-field measurements, rupture was a common outcome caused by excessive forces on the delicate 1L-WSe_2 by the near-field probe. Scale bars are 200 nm.



Supplementary Figure 11: Localization spectroscopy. (a-b) PL intensity maps for E2 and the ensemble of long-wavelength emitters, respectively. Overlaid are 2D Gaussian fits to the intensity spatial distributions. (c-g) Normalized PL difference maps to visualize the localization of each emitter with respect to the emitter ensemble. Overlaid are the respective 2D Gaussian fits for each emitter scan and long wavelength emitter scan. For example, (f) shows (a)-(b) and the fits from both (a) and (b). The difference in center positions of these fits is what is used for the localization of the emitters with respect to the apex of the nanoantenna. Scale bars are 1 μm.



Supplementary Figure 12: Long wavelength emitter PLE dataset. The raw PLE data before integration for the long wavelength emitters that show plasmonic enhancement. The red dashed line in the center represents a change in the color scale from a maximum of 1 kcts/s to 1.5 kcts/s

Chapter 4 References

(1) Xiao, L.; Liu, Y.; Mohajerani, S. S.; et al. Quantum Light Funneling in Tailored Triangular Plasmonic Nanocavities. *ACS Nano* **2026**. DOI: 10.1021/acsnano.5c16988

(2) Luo, Y.; Liu, N.; Li, X.; et al. Single photon emission in WSe_2 up to 160 K by quantum yield control. *2D Materials* **2019**, *6* (3). DOI: 10.1088/2053-1583/ab15fe

(3) Luo, Y.; Shepard, G. D.; Ardelean, J. V.; et al. Deterministic coupling of site-controlled quantum emitters in monolayer WSe_2 to plasmonic nanocavities. *Nat Nanotechnol* **2018**, *13* (12), 1137-1142. DOI: 10.1038/s41565-018-0275-z

(4) Chakraborty, C.; Kinnischtzke, L.; Goodfellow, K. M.; et al. Voltage-controlled quantum light from an atomically thin semiconductor. *Nat Nanotechnol* **2015**, *10* (6), 507-511. DOI: 10.1038/nnano.2015.79

(5) He, Y. M.; Clark, G.; Schaibley, J. R.; et al. Single quantum emitters in monolayer semiconductors. *Nat Nanotechnol* **2015**, *10* (6), 497-502. DOI: 10.1038/nnano.2015.75

(6) Koperski, M.; Nogajewski, K.; Arora, A.; et al. Single photon emitters in exfoliated WSe_2 structures. *Nat Nanotechnol* **2015**, *10* (6), 503-506. DOI: 10.1038/nnano.2015.67

(7) Kumar, S.; Kaczmarczyk, A.; Gerardot, B. D. Strain-Induced Spatial and Spectral Isolation of Quantum Emitters in Mono- and Bilayer WSe_2. *Nano Lett* **2015**, *15* (11), 7567-7573. DOI: 10.1021/acs.nanolett.5b03312

(8) Srivastava, A.; Sidler, M.; Allain, A. V.; et al. Optically active quantum dots in monolayer WSe_2. *Nat Nanotechnol* **2015**, *10* (6), 491-496. DOI: 10.1038/nnano.2015.60

(9) Tonndorf, P.; Schmidt, R.; Schneider, R.; et al. Single-photon emission from localized excitons in an atomically thin semiconductor. *Optica* **2015**, *2* (4). DOI: 10.1364/optica.2.000347

(10) Linhart, L.; Paur, M.; Smejkal, V.; et al. Localized Intervalley Defect Excitons as Single-Photon Emitters in WSe_2. *Phys Rev Lett* **2019**, *123* (14), 146401. DOI: 10.1103/PhysRevLett.123.146401

(11) Barja, S.; Refaely-Abramson, S.; Schuler, B.; et al. Identifying substitutional oxygen as a prolific point defect in monolayer transition metal dichalcogenides. *Nat Commun* **2019**, *10* (1), 3382. DOI: 10.1038/s41467-019-11342-2

(12) Rosenberger, M. R.; Dass, C. K.; Chuang, H. J.; et al. Quantum Calligraphy: Writing Single-Photon Emitters in a Two-Dimensional Materials Platform. *ACS Nano* **2019**, *13* (1), 904-912. DOI: 10.1021/acsnano.8b08730

(13) Parto, K.; Azzam, S. I.; Banerjee, K.; et al. Defect and strain engineering of monolayer WSe_2 enables site-controlled single-photon emission up to 150 K. *Nat Commun* **2021**, *12* (1), 3585. DOI: 10.1038/s41467-021-23709-5

(14) Branny, A.; Kumar, S.; Proux, R.; et al. Deterministic strain-induced arrays of quantum emitters in a two-dimensional semiconductor. *Nat Commun* **2017**, *8* (1), 15053. DOI: 10.1038/ncomms15053

(15) Iff, O.; Buchinger, Q.; Moczala-Dusanowska, M.; et al. Purcell-Enhanced Single Photon Source Based on a Deterministically Placed WSe_2 Monolayer Quantum Dot in a Circular Bragg Grating Cavity. *Nano Lett* **2021**, *21* (11), 4715-4720. DOI: 10.1021/acs.nanolett.1c00978

(16) So, J. P.; Jeong, K. Y.; Lee, J. M.; et al. Polarization Control of Deterministic Single-Photon Emitters in Monolayer WSe_2. *Nano Lett* **2021**, *21* (3), 1546-1554. DOI: 10.1021/acs.nanolett.1c00078

(17) Mohajerani, S. S.; Noual, A.; Ma, Y.; et al. Acoustic Manipulation of Deterministic Quantum Emitters in WSe_2. *ACS Nano* **2025**, *19* (28), 25851-25859. DOI: 10.1021/acsnano.5c04710

(18) Strasbourg, M. C.; Yanev, E. S.; Parvez, S.; et al. Structure-Dependent Dynamics of Quantum Emitters in Single-Layer WSe_2. *Nano Lett* **2025**, *25* (25), 10254-10261. DOI: 10.1021/acs.nanolett.5c02620

(19) Yanev, E. S.; Darlington, T. P.; Ladyzhets, S. A.; et al. Programmable nanowrinkle-induced room-temperature exciton localization in monolayer WSe_2. *Nat Commun* **2024**, *15* (1), 1543. DOI: 10.1038/s41467-024-45936-2

(20) Gao, T.; von Helversen, M.; Antón-Solanas, C.; et al. Atomically-thin single-photon sources for quantum communication. *npj 2D Materials and Applications* **2023**, *7* (1). DOI: 10.1038/s41699-023-00366-4

(21) Duong, N. M. H.; Xu, Z.-Q.; Kianinia, M.; et al. Enhanced Emission from WSe_2 Monolayers Coupled to Circular Bragg Gratings. *ACS Photonics* **2018**, *5* (10), 3950-3955. DOI: 10.1021/acsphotonics.8b00865

(22) Noori, Y. J.; Cao, Y.; Roberts, J.; et al. Photonic Crystals for Enhanced Light Extraction from 2D Materials. *ACS Photonics* **2016**, *3* (12), 2515-2520. DOI: 10.1021/acsphotonics.6b00779

(23) Peyskens, F.; Chakraborty, C.; Muneeb, M.; et al. Integration of single photon emitters in 2D layered materials with a silicon nitride photonic chip. *Nat Commun* **2019**, *10* (1), 4435. DOI: 10.1038/s41467-019-12421-0

(24) Parto, K.; Azzam, S. I.; Lewis, N.; et al. Cavity-Enhanced 2D Material Quantum Emitters Deterministically Integrated with Silicon Nitride Microresonators. *Nano Lett* **2022**, *22* (23), 9748-9756. DOI: 10.1021/acs.nanolett.2c03151

(25) Ren, T.; Granados Del Aguila, A.; Chen, Z.; et al. Van der Waals photonic integrated circuit with coherent light generation. *Nat Commun* **2025**, *16* (1), 5931. DOI: 10.1038/s41467-025-60778-2

(26) Schwarz, S.; Kozikov, A.; Withers, F.; et al. Electrically pumped single-defect light emitters in WSe_2. *2D Materials* **2016**, *3* (2). DOI: 10.1088/2053-1583/3/2/025038

(27) Guo, S.; Germanis, S.; Taniguchi, T.; et al. Electrically Driven Site-Controlled Single Photon Source. *ACS Photonics* **2023**, *10* (8), 2549-2555. DOI: 10.1021/acsphotonics.3c00097

(28) Cai, T.; Kim, J.-H.; Yang, Z.; et al. Radiative Enhancement of Single Quantum Emitters in WSe2 Monolayers Using Site-Controlled Metallic Nanopillars. *ACS Photonics* **2018**, *5* (9), 3466-3471. DOI: 10.1021/acsphotonics.8b00580

(29) Tripathi, L. N.; Iff, O.; Betzold, S.; et al. Spontaneous Emission Enhancement in Strain-Induced WSe_2 Monolayer-Based Quantum Light Sources on Metallic Surfaces. *ACS Photonics* **2018**, *5* (5), 1919-1926. DOI: 10.1021/acsphotonics.7b01053

(30) Darlington, T. P.; Carmesin, C.; Florian, M.; et al. Imaging strain-localized excitons in nanoscale bubbles of monolayer WSe_2 at room temperature. *Nat Nanotechnol* **2020**, *15* (10), 854-860. DOI: 10.1038/s41565-020-0730-5

(31) Palacios-Berraquero, C.; Kara, D. M.; Montblanch, A. R.; et al. Large-scale quantum-emitter arrays in atomically thin semiconductors. *Nat Commun* **2017**, *8*, 15093. DOI: 10.1038/ncomms15093

(32) Sortino, L.; Zotev, P. G.; Phillips, C. L.; et al. Bright single photon emitters with enhanced quantum efficiency in a two-dimensional semiconductor coupled with dielectric nano-antennas. *Nat Commun* **2021**, *12* (1), 6063. DOI: 10.1038/s41467-021-26262-3

(33) Chhaperwal, M.; Tongale, H. M.; Hays, P.; et al. Simultaneously Enhancing Brightness and Purity of WSe_2 Single Photon Emitter Using High-Aspect-Ratio Nanopillar Array on Metal. *Nano Lett* **2024**, *24* (40), 12461-12468. DOI: 10.1021/acs.nanolett.4c03168

(34) Azzam, S. I.; Parto, K.; Moody, G. Purcell enhancement and polarization control of single-photon emitters in monolayer WSe_2 using dielectric nanoantennas. *Nanophotonics* **2023**, *12* (3), 477-484. DOI: 10.1515/nanoph-2022-0628

(35) Khestanova, E.; Guinea, F.; Fumagalli, L.; et al. Universal shape and pressure inside bubbles appearing in van der Waals heterostructures. *Nat Commun* **2016**, *7*, 12587. DOI: 10.1038/ncomms12587

(36) Park, K. D.; Khatib, O.; Kravtsov, V.; et al. Hybrid Tip-Enhanced Nanospectroscopy and Nanoimaging of Monolayer WSe_2 with Local Strain Control. *Nano Lett* **2016**, *16* (4), 2621-2627. DOI: 10.1021/acs.nanolett.6b00238

(37) Zhou, Y.; Scuri, G.; Wild, D. S.; et al. Probing dark excitons in atomically thin semiconductors via near-field coupling to surface plasmon polaritons. *Nat Nanotechnol* **2017**, *12* (9), 856-860. DOI: 10.1038/nnano.2017.106

(38) Gelly, R. J.; Renaud, D.; Liao, X.; et al. Probing dark exciton navigation through a local strain landscape in a WSe_2 monolayer. *Nat Commun* **2022**, *13* (1), 232. DOI: 10.1038/s41467-021-27877-2

(39) Zhang, S.; Li, B.; Chen, X.; et al. Nano-spectroscopy of excitons in atomically thin transition metal dichalcogenides. *Nat Commun* **2022**, *13* (1), 542. DOI: 10.1038/s41467-022-28117-x

(40) Casses, L. N.; Zhou, B.; Lin, Q.; et al. Full Quantitative Near-Field Characterization of Strongly Coupled Exciton–Plasmon Polaritons in Thin-Layered WSe_2 on a Monocrystalline Gold Platelet. *ACS Photonics* **2024**, *11* (9), 3593-3601. DOI: 10.1021/acsphotonics.4c00580

(41) Zhou, J.; Goncalves, P. A. D.; Riminucci, F.; et al. Probing plexciton emission from 2D materials on gold nanotrenches. *Nat Commun* **2024**, *15* (1), 9583. DOI: 10.1038/s41467-024-53669-5

(42) Garg, S.; Fix, J. P.; Krayev, A. V.; et al. Nanoscale Raman Characterization of a 2D Semiconductor Lateral Heterostructure Interface. *ACS Nano* **2022**, *16* (1), 340-350. DOI: 10.1021/acsnano.1c06595

(43) Bao, W.; Borys, N. J.; Ko, C.; et al. Visualizing nanoscale excitonic relaxation properties of disordered edges and grain boundaries in monolayer molybdenum disulfide. *Nat Commun* **2015**, *6*, 7993. DOI: 10.1038/ncomms8993

(44) Jo, K.; Marino, E.; Lynch, J.; et al. Direct nano-imaging of light-matter interactions in nanoscale excitonic emitters. *Nat Commun* **2023**, *14* (1), 2649. DOI: 10.1038/s41467-023-38189-y

(45) Castellanos-Gomez, A.; Buscema, M.; Molenaar, R.; et al. Deterministic transfer of two-dimensional materials by all-dry viscoelastic stamping. *2D Materials* **2014**, *1* (1). DOI: 10.1088/2053-1583/1/1/011002

(46) Son, S.; Shin, Y. J.; Zhang, K.; et al. Strongly adhesive dry transfer technique for van der Waals heterostructure. *2D Materials* **2020**, *7* (4). DOI: 10.1088/2053-1583/abad0b

(47) Strasbourg, M. C.; Yanev, E. S.; Darlington, T. P.; et al. Characterization of quantum dot-like emitters in programmable arrays of nanowrinkles of 1L-WSe_2. *Journal of Applied Physics* **2024**, *136* (4). DOI: 10.1063/5.0214410

(48) Aslan, B.; Deng, M.; Heinz, T. F. Strain tuning of excitons in monolayer WSe_2. *Physical Review B* **2018**, *98* (11). DOI: 10.1103/PhysRevB.98.115308

(49) Schmidt, R.; Niehues, I.; Schneider, R.; et al. Reversible uniaxial strain tuning in atomically thin WSe_2. *2D Materials* **2016**, *3* (2). DOI: 10.1088/2053-1583/3/2/021011

(50) Desai, S. B.; Seol, G.; Kang, J. S.; et al. Strain-induced indirect to direct bandgap transition in multilayer WSe_2. *Nano Lett* **2014**, *14* (8), 4592-4597. DOI: 10.1021/nl501638a

(51) Borys, N. J.; Barnard, E. S.; Gao, S.; et al. Anomalous Above-Gap Photoexcitations and Optical Signatures of Localized Charge Puddles in Monolayer Molybdenum Disulfide. *ACS Nano* **2017**, *11* (2), 2115-2123. DOI: 10.1021/acsnano.6b08278

(52) Strasbourg, M. C.; Yanev, E. S.; Parvez, S.; et al. Increased Formation of Trions and Charged Biexcitons by Above-Gap Excitation in Single-layer WSe_2. *ACS Nano* **2024**, *18* (47), 32973-32983. DOI: 10.1021/acsnano.4c13208

(53) Fang, H. H.; Han, B.; Robert, C.; et al. Control of the Exciton Radiative Lifetime in van der Waals Heterostructures. *Phys Rev Lett* **2019**, *123* (6), 067401. DOI: 10.1103/PhysRevLett.123.067401

(54) Sakib, M. A.; Triplett, B.; Harris, W.; et al. Purcell-Induced Bright Single Photon Emitters in Hexagonal Boron Nitride. *Nano Lett* **2024**, *24* (40), 12390-12397. DOI: 10.1021/acs.nanolett.4c02581

(55) Gérard, D.; Pierret, A.; Fartas, H.; et al. Quantum Efficiency and Vertical Position of Quantum Emitters in hBN Determined by Purcell Effect in Hybrid Metal-Dielectric Planar Photonic Structures. *ACS Photonics* **2024**, *11* (12), 5188-5194. DOI: 10.1021/acsphotonics.4c01416

(56) Rosati, R.; Schmidt, R.; Brem, S.; et al. Dark exciton anti-funneling in atomically thin semiconductors. *Nat Commun* **2021**, *12* (1), 7221. DOI: 10.1038/s41467-021-27425-y

(57) Su, H.; Xu, D.; Cheng, S. W.; et al. Dark-Exciton Driven Energy Funneling into Dielectric Inhomogeneities in Two-Dimensional Semiconductors. *Nano Lett* **2022**, *22* (7), 2843-2850. DOI: 10.1021/acs.nanolett.1c04997

(58) Kim, J. M.; Jeong, K. Y.; Kwon, S.; et al. Strained two-dimensional tungsten diselenide for mechanically tunable exciton transport. *Nat Commun* **2024**, *15* (1), 10847. DOI: 10.1038/s41467-024-55135-8

(59) Li, X.; Wyss, S.; Yanev, E.; et al. Width-dependent continuous growth of atomically thin quantum nanoribbons from nanoalloy seeds in chalcogen vapor. *Nat Commun* **2024**, *15* (1), 10080. DOI: 10.1038/s41467-024-54413-9

(60) He, K.; Kumar, N.; Zhao, L.; et al. Tightly bound excitons in monolayer WSe_2. *Phys Rev Lett* **2014**, *113* (2), 026803. DOI: 10.1103/PhysRevLett.113.026803

(61) Li, Y.; Chernikov, A.; Zhang, X.; et al. Measurement of the optical dielectric function of monolayer transition-metal dichalcogenides: MoS_2, $MoSe_2$, WS_2, and WSe_2. *Physical Review B* **2014**, *90* (20). DOI: 10.1103/PhysRevB.90.205422

(62) Thompson, R. E.; Larson, D. R.; Webb, W. W. Precise nanometer localization analysis for individual fluorescent probes. *Biophys J* **2002**, *82* (5), 2775-2783. DOI: 10.1016/S0006-3495(02)75618-X

(63) Park, K. D.; Jiang, T.; Clark, G.; et al. Radiative control of dark excitons at room temperature by nano-optical antenna-tip Purcell effect. *Nat Nanotechnol* **2018**, *13* (1), 59-64. DOI: 10.1038/s41565-017-0003-0

(64) Peng, L.; Chan, H.; Choo, P.; et al. Creation of Single-Photon Emitters in WSe_2 Monolayers Using Nanometer-Sized Gold Tips. *Nano Lett* **2020**, *20* (8), 5866-5872. DOI: 10.1021/acs.nanolett.0c01789

(65) Wang, Z.; Dong, Z.; Gu, Y.; et al. Giant photoluminescence enhancement in tungsten-diselenide-gold plasmonic hybrid structures. *Nat Commun* **2016**, *7*, 11283. DOI: 10.1038/ncomms11283

(66) Li, C.; Luo, H.; Hou, L.; et al. Giant Photoluminescence Enhancement of Monolayer WSe_2 Using a Plasmonic Nanocavity with On-Demand Resonance. *Nano Lett* **2024**, *24* (19), 5879-5885. DOI: 10.1021/acs.nanolett.4c01260

(67) Jariwala, D.; Krayev, A.; Wong, J.; et al. Nanoscale doping heterogeneity in few-layer WSe_2 exfoliated onto noble metals revealed by correlated SPM and TERS imaging. *2D Materials* **2018**, *5* (3). DOI: 10.1088/2053-1583/aab7bc

(68) Holbrook, M.; Holtzman, L. N.; Hou, B.; et al. Revealing Substitutional Oxygen as the Dominant Defect in Flux-Grown Transition Metal Diselenides. *Nano Lett* **2025**, *25* (37), 13795-13801. DOI: 10.1021/acs.nanolett.5c03126

(69) Liu, S.; Liu, Y.; Holtzman, L.; et al. Two-Step Flux Synthesis of Ultrapure Transition-Metal Dichalcogenides. *ACS Nano* **2023**, *17* (17), 16587-16596. DOI: 10.1021/acsnano.3c02511

(70) Li, H.; Contryman, A. W.; Qian, X.; et al. Optoelectronic crystal of artificial atoms in strain-textured molybdenum disulphide. *Nat Commun* **2015**, *6* (1), 7381. DOI: 10.1038/ncomms8381

(71) Conley, H. J.; Wang, B.; Ziegler, J. I.; et al. Bandgap engineering of strained monolayer and bilayer MoS_2. *Nano Lett* **2013**, *13* (8), 3626-3630. DOI: 10.1021/nl4014748

(72) Ocola, L. E.; Costales, M.; Gosztola, D. J. Development characteristics of polymethyl methacrylate in alcohol/water mixtures: a lithography and Raman spectroscopy study. *Nanotechnology* **2016**, *27* (3), 035302. DOI: 10.1088/0957-4484/27/3/035302

(73) Yasin, S.; Hasko, D. G.; Ahmed, H. Fabrication of <5 nm width lines in poly(methylmethacrylate) resist using a water:isopropyl alcohol developer and ultrasonically-assisted development. *Applied Physics Letters* **2001**, *78* (18), 2760-2762. DOI: 10.1063/1.1369615

(74) Sun, B.; Grap, T.; Frahm, T.; et al. Role of electron and ion irradiation in a reliable lift-off process with electron beam evaporation and a bilayer PMMA resist system. *Journal of Vacuum Science & Technology B, Nanotechnology and Microelectronics: Materials, Processing, Measurement, and Phenomena* **2021**, *39* (5). DOI: 10.1116/6.0001161

(1) Xiao, L.; Liu, Y.; Mohajerani, S. S.; et al. Quantum Light Funneling in Tailored Triangular Plasmonic Nanocavities. *ACS Nano* **2026**. DOI: 10.1021/acsnano.5c16988

(2) Luo, Y.; Liu, N.; Li, X.; et al. Single photon emission in WSe_2 up to 160 K by quantum yield control. *2D Materials* **2019**, *6* (3). DOI: 10.1088/2053-1583/ab15fe

(3) Luo, Y.; Shepard, G. D.; Ardelean, J. V.; et al. Deterministic coupling of site-controlled quantum emitters in monolayer WSe_2 to plasmonic nanocavities. *Nat Nanotechnol* **2018**, *13* (12), 1137-1142. DOI: 10.1038/s41565-018-0275-z

(4) Chakraborty, C.; Kinnischtzke, L.; Goodfellow, K. M.; et al. Voltage-controlled quantum light from an atomically thin semiconductor. *Nat Nanotechnol* **2015**, *10* (6), 507-511. DOI: 10.1038/nnano.2015.79

(5) He, Y. M.; Clark, G.; Schaibley, J. R.; et al. Single quantum emitters in monolayer semiconductors. *Nat Nanotechnol* **2015**, *10* (6), 497-502. DOI: 10.1038/nnano.2015.75

(6) Koperski, M.; Nogajewski, K.; Arora, A.; et al. Single photon emitters in exfoliated WSe_2 structures. *Nat Nanotechnol* **2015**, *10* (6), 503-506. DOI: 10.1038/nnano.2015.67

(7) Kumar, S.; Kaczmarczyk, A.; Gerardot, B. D. Strain-Induced Spatial and Spectral Isolation of Quantum Emitters in Mono- and Bilayer WSe_2. *Nano Lett* **2015**, *15* (11), 7567-7573. DOI: 10.1021/acs.nanolett.5b03312

(8) Srivastava, A.; Sidler, M.; Allain, A. V.; et al. Optically active quantum dots in monolayer WSe_2. *Nat Nanotechnol* **2015**, *10* (6), 491-496. DOI: 10.1038/nnano.2015.60

(9) Tonndorf, P.; Schmidt, R.; Schneider, R.; et al. Single-photon emission from localized excitons in an atomically thin semiconductor. *Optica* **2015**, *2* (4). DOI: 10.1364/optica.2.000347

(10) Linhart, L.; Paur, M.; Smejkal, V.; et al. Localized Intervalley Defect Excitons as Single-Photon Emitters in WSe_2. *Phys Rev Lett* **2019**, *123* (14), 146401. DOI: 10.1103/PhysRevLett.123.146401

(11) Barja, S.; Refaely-Abramson, S.; Schuler, B.; et al. Identifying substitutional oxygen as a prolific point defect in monolayer transition metal dichalcogenides. *Nat Commun* **2019**, *10* (1), 3382. DOI: 10.1038/s41467-019-11342-2

(12) Rosenberger, M. R.; Dass, C. K.; Chuang, H. J.; et al. Quantum Calligraphy: Writing Single-Photon Emitters in a Two-Dimensional Materials Platform. *ACS Nano* **2019**, *13* (1), 904-912. DOI: 10.1021/acsnano.8b08730

(13) Parto, K.; Azzam, S. I.; Banerjee, K.; et al. Defect and strain engineering of monolayer WSe_2 enables site-controlled single-photon emission up to 150 K. *Nat Commun* **2021**, *12* (1), 3585. DOI: 10.1038/s41467-021-23709-5

(14) Branny, A.; Kumar, S.; Proux, R.; et al. Deterministic strain-induced arrays of quantum emitters in a two-dimensional semiconductor. *Nat Commun* **2017**, *8* (1), 15053. DOI: 10.1038/ncomms15053

(15) Iff, O.; Buchinger, Q.; Moczala-Dusanowska, M.; et al. Purcell-Enhanced Single Photon Source Based on a Deterministically Placed WSe_2 Monolayer Quantum Dot in a Circular Bragg Grating Cavity. *Nano Lett* **2021**, *21* (11), 4715-4720. DOI: 10.1021/acs.nanolett.1c00978

(16) So, J. P.; Jeong, K. Y.; Lee, J. M.; et al. Polarization Control of Deterministic Single-Photon Emitters in Monolayer WSe_2. *Nano Lett* **2021**, *21* (3), 1546-1554. DOI: 10.1021/acs.nanolett.1c00078

(17) Mohajerani, S. S.; Noual, A.; Ma, Y.; et al. Acoustic Manipulation of Deterministic Quantum Emitters in WSe_2. *ACS Nano* **2025**, *19* (28), 25851-25859. DOI: 10.1021/acsnano.5c04710

(18) Strasbourg, M. C.; Yanev, E. S.; Parvez, S.; et al. Structure-Dependent Dynamics of Quantum Emitters in Single-Layer WSe_2. *Nano Lett* **2025**, *25* (25), 10254-10261. DOI: 10.1021/acs.nanolett.5c02620

(19) Yanev, E. S.; Darlington, T. P.; Ladyzhets, S. A.; et al. Programmable nanowrinkle-induced room-temperature exciton localization in monolayer WSe_2. *Nat Commun* **2024**, *15* (1), 1543. DOI: 10.1038/s41467-024-45936-2

(20) Gao, T.; von Helversen, M.; Antón-Solanas, C.; et al. Atomically-thin single-photon sources for quantum communication. *npj 2D Materials and Applications* **2023**, *7* (1). DOI: 10.1038/s41699-023-00366-4

(21) Duong, N. M. H.; Xu, Z.-Q.; Kianinia, M.; et al. Enhanced Emission from WSe_2 Monolayers Coupled to Circular Bragg Gratings. *ACS Photonics* **2018**, *5* (10), 3950-3955. DOI: 10.1021/acsphotonics.8b00865

(22) Noori, Y. J.; Cao, Y.; Roberts, J.; et al. Photonic Crystals for Enhanced Light Extraction from 2D Materials. *ACS Photonics* **2016**, *3* (12), 2515-2520. DOI: 10.1021/acsphotonics.6b00779

(23) Peyskens, F.; Chakraborty, C.; Muneeb, M.; et al. Integration of single photon emitters in 2D layered materials with a silicon nitride photonic chip. *Nat Commun* **2019**, *10* (1), 4435. DOI: 10.1038/s41467-019-12421-0

(24) Parto, K.; Azzam, S. I.; Lewis, N.; et al. Cavity-Enhanced 2D Material Quantum Emitters Deterministically Integrated with Silicon Nitride Microresonators. *Nano Lett* **2022**, *22* (23), 9748-9756. DOI: 10.1021/acs.nanolett.2c03151

(25) Ren, T.; Granados Del Aguila, A.; Chen, Z.; et al. Van der Waals photonic integrated circuit with coherent light generation. *Nat Commun* **2025**, *16* (1), 5931. DOI: 10.1038/s41467-025-60778-2

(26) Schwarz, S.; Kozikov, A.; Withers, F.; et al. Electrically pumped single-defect light emitters in WSe_2. *2D Materials* **2016**, *3* (2). DOI: 10.1088/2053-1583/3/2/025038

(27) Guo, S.; Germanis, S.; Taniguchi, T.; et al. Electrically Driven Site-Controlled Single Photon Source. *ACS Photonics* **2023**, *10* (8), 2549-2555. DOI: 10.1021/acsphotonics.3c00097

(28) Cai, T.; Kim, J.-H.; Yang, Z.; et al. Radiative Enhancement of Single Quantum Emitters in WSe2 Monolayers Using Site-Controlled Metallic Nanopillars. *ACS Photonics* **2018**, *5* (9), 3466-3471. DOI: 10.1021/acsphotonics.8b00580

(29) Tripathi, L. N.; Iff, O.; Betzold, S.; et al. Spontaneous Emission Enhancement in Strain-Induced WSe_2 Monolayer-Based Quantum Light Sources on Metallic Surfaces. *ACS Photonics* **2018**, *5* (5), 1919-1926. DOI: 10.1021/acsphotonics.7b01053

(30) Darlington, T. P.; Carmesin, C.; Florian, M.; et al. Imaging strain-localized excitons in nanoscale bubbles of monolayer WSe_2 at room temperature. *Nat Nanotechnol* **2020**, *15* (10), 854-860. DOI: 10.1038/s41565-020-0730-5

(31) Palacios-Berraquero, C.; Kara, D. M.; Montblanch, A. R.; et al. Large-scale quantum-emitter arrays in atomically thin semiconductors. *Nat Commun* **2017**, *8*, 15093. DOI: 10.1038/ncomms15093

(32) Sortino, L.; Zotev, P. G.; Phillips, C. L.; et al. Bright single photon emitters with enhanced quantum efficiency in a two-dimensional semiconductor coupled with dielectric nano-antennas. *Nat Commun* **2021**, *12* (1), 6063. DOI: 10.1038/s41467-021-26262-3

(33) Chhaperwal, M.; Tongale, H. M.; Hays, P.; et al. Simultaneously Enhancing Brightness and Purity of WSe_2 Single Photon Emitter Using High-Aspect-Ratio Nanopillar Array on Metal. *Nano Lett* **2024**, *24* (40), 12461-12468. DOI: 10.1021/acs.nanolett.4c03168

(34) Azzam, S. I.; Parto, K.; Moody, G. Purcell enhancement and polarization control of single-photon emitters in monolayer WSe_2 using dielectric nanoantennas. *Nanophotonics* **2023**, *12* (3), 477-484. DOI: 10.1515/nanoph-2022-0628

(35) Khestanova, E.; Guinea, F.; Fumagalli, L.; et al. Universal shape and pressure inside bubbles appearing in van der Waals heterostructures. *Nat Commun* **2016**, *7*, 12587. DOI: 10.1038/ncomms12587

(36) Park, K. D.; Khatib, O.; Kravtsov, V.; et al. Hybrid Tip-Enhanced Nanospectroscopy and Nanoimaging of Monolayer WSe_2 with Local Strain Control. *Nano Lett* **2016**, *16* (4), 2621-2627. DOI: 10.1021/acs.nanolett.6b00238

(37) Zhou, Y.; Scuri, G.; Wild, D. S.; et al. Probing dark excitons in atomically thin semiconductors via near-field coupling to surface plasmon polaritons. *Nat Nanotechnol* **2017**, *12* (9), 856-860. DOI: 10.1038/nnano.2017.106

(38) Gelly, R. J.; Renaud, D.; Liao, X.; et al. Probing dark exciton navigation through a local strain landscape in a WSe_2 monolayer. *Nat Commun* **2022**, *13* (1), 232. DOI: 10.1038/s41467-021-27877-2

(39) Zhang, S.; Li, B.; Chen, X.; et al. Nano-spectroscopy of excitons in atomically thin transition metal dichalcogenides. *Nat Commun* **2022**, *13* (1), 542. DOI: 10.1038/s41467-022-28117-x

(40) Casses, L. N.; Zhou, B.; Lin, Q.; et al. Full Quantitative Near-Field Characterization of Strongly Coupled Exciton–Plasmon Polaritons in Thin-Layered WSe_2 on a Monocrystalline Gold Platelet. *ACS Photonics* **2024**, *11* (9), 3593-3601. DOI: 10.1021/acsphotonics.4c00580

(41) Zhou, J.; Goncalves, P. A. D.; Riminucci, F.; et al. Probing plexciton emission from 2D materials on gold nanotrenches. *Nat Commun* **2024**, *15* (1), 9583. DOI: 10.1038/s41467-024-53669-5

(42) Garg, S.; Fix, J. P.; Krayev, A. V.; et al. Nanoscale Raman Characterization of a 2D Semiconductor Lateral Heterostructure Interface. *ACS Nano* **2022**, *16* (1), 340-350. DOI: 10.1021/acsnano.1c06595

(43) Bao, W.; Borys, N. J.; Ko, C.; et al. Visualizing nanoscale excitonic relaxation properties of disordered edges and grain boundaries in monolayer molybdenum disulfide. *Nat Commun* **2015**, *6*, 7993. DOI: 10.1038/ncomms8993

(44) Jo, K.; Marino, E.; Lynch, J.; et al. Direct nano-imaging of light-matter interactions in nanoscale excitonic emitters. *Nat Commun* **2023**, *14* (1), 2649. DOI: 10.1038/s41467-023-38189-y

(45) Castellanos-Gomez, A.; Buscema, M.; Molenaar, R.; et al. Deterministic transfer of two-dimensional materials by all-dry viscoelastic stamping. *2D Materials* **2014**, *1* (1). DOI: 10.1088/2053-1583/1/1/011002

(46) Son, S.; Shin, Y. J.; Zhang, K.; et al. Strongly adhesive dry transfer technique for van der Waals heterostructure. *2D Materials* **2020**, *7* (4). DOI: 10.1088/2053-1583/abad0b

(47) Strasbourg, M. C.; Yanev, E. S.; Darlington, T. P.; et al. Characterization of quantum dot-like emitters in programmable arrays of nanowrinkles of 1L-WSe_2. *Journal of Applied Physics* **2024**, *136* (4). DOI: 10.1063/5.0214410

(48) Aslan, B.; Deng, M.; Heinz, T. F. Strain tuning of excitons in monolayer WSe_2. *Physical Review B* **2018**, *98* (11). DOI: 10.1103/PhysRevB.98.115308

(49) Schmidt, R.; Niehues, I.; Schneider, R.; et al. Reversible uniaxial strain tuning in atomically thin WSe_2. *2D Materials* **2016**, *3* (2). DOI: 10.1088/2053-1583/3/2/021011

(50) Desai, S. B.; Seol, G.; Kang, J. S.; et al. Strain-induced indirect to direct bandgap transition in multilayer WSe_2. *Nano Lett* **2014**, *14* (8), 4592-4597. DOI: 10.1021/nl501638a

(51) Borys, N. J.; Barnard, E. S.; Gao, S.; et al. Anomalous Above-Gap Photoexcitations and Optical Signatures of Localized Charge Puddles in Monolayer Molybdenum Disulfide. *ACS Nano* **2017**, *11* (2), 2115-2123. DOI: 10.1021/acsnano.6b08278

(52) Strasbourg, M. C.; Yanev, E. S.; Parvez, S.; et al. Increased Formation of Trions and Charged Biexcitons by Above-Gap Excitation in Single-layer WSe_2. *ACS Nano* **2024**, *18* (47), 32973-32983. DOI: 10.1021/acsnano.4c13208

(53) Fang, H. H.; Han, B.; Robert, C.; et al. Control of the Exciton Radiative Lifetime in van der Waals Heterostructures. *Phys Rev Lett* **2019**, *123* (6), 067401. DOI: 10.1103/PhysRevLett.123.067401

(54) Sakib, M. A.; Triplett, B.; Harris, W.; et al. Purcell-Induced Bright Single Photon Emitters in Hexagonal Boron Nitride. *Nano Lett* **2024**, *24* (40), 12390-12397. DOI: 10.1021/acs.nanolett.4c02581

(55) Gérard, D.; Pierret, A.; Fartas, H.; et al. Quantum Efficiency and Vertical Position of Quantum Emitters in hBN Determined by Purcell Effect in Hybrid Metal-Dielectric Planar Photonic Structures. *ACS Photonics* **2024**, *11* (12), 5188-5194. DOI: 10.1021/acsphotonics.4c01416

(56) Rosati, R.; Schmidt, R.; Brem, S.; et al. Dark exciton anti-funneling in atomically thin semiconductors. *Nat Commun* **2021**, *12* (1), 7221. DOI: 10.1038/s41467-021-27425-y

(57) Su, H.; Xu, D.; Cheng, S. W.; et al. Dark-Exciton Driven Energy Funneling into Dielectric Inhomogeneities in Two-Dimensional Semiconductors. *Nano Lett* **2022**, *22* (7), 2843-2850. DOI: 10.1021/acs.nanolett.1c04997

(58) Kim, J. M.; Jeong, K. Y.; Kwon, S.; et al. Strained two-dimensional tungsten diselenide for mechanically tunable exciton transport. *Nat Commun* **2024**, *15* (1), 10847. DOI: 10.1038/s41467-024-55135-8

(59) Li, X.; Wyss, S.; Yanev, E.; et al. Width-dependent continuous growth of atomically thin quantum nanoribbons from nanoalloy seeds in chalcogen vapor. *Nat Commun* **2024**, *15* (1), 10080. DOI: 10.1038/s41467-024-54413-9

(60) He, K.; Kumar, N.; Zhao, L.; et al. Tightly bound excitons in monolayer WSe_2. *Phys Rev Lett* **2014**, *113* (2), 026803. DOI: 10.1103/PhysRevLett.113.026803

(61) Li, Y.; Chernikov, A.; Zhang, X.; et al. Measurement of the optical dielectric function of monolayer transition-metal dichalcogenides: MoS_2, $MoSe_2$, WS_2, and WSe_2. *Physical Review B* **2014**, *90* (20). DOI: 10.1103/PhysRevB.90.205422

(62) Thompson, R. E.; Larson, D. R.; Webb, W. W. Precise nanometer localization analysis for individual fluorescent probes. *Biophys J* **2002**, *82* (5), 2775-2783. DOI: 10.1016/S0006-3495(02)75618-X

(63) Park, K. D.; Jiang, T.; Clark, G.; et al. Radiative control of dark excitons at room temperature by nano-optical antenna-tip Purcell effect. *Nat Nanotechnol* **2018**, *13* (1), 59-64. DOI: 10.1038/s41565-017-0003-0

(64) Peng, L.; Chan, H.; Choo, P.; et al. Creation of Single-Photon Emitters in WSe_2 Monolayers Using Nanometer-Sized Gold Tips. *Nano Lett* **2020**, *20* (8), 5866-5872. DOI: 10.1021/acs.nanolett.0c01789

(65) Wang, Z.; Dong, Z.; Gu, Y.; et al. Giant photoluminescence enhancement in tungsten-diselenide-gold plasmonic hybrid structures. *Nat Commun* **2016**, *7*, 11283. DOI: 10.1038/ncomms11283

(66) Li, C.; Luo, H.; Hou, L.; et al. Giant Photoluminescence Enhancement of Monolayer WSe_2 Using a Plasmonic Nanocavity with On-Demand Resonance. *Nano Lett* **2024**, *24* (19), 5879-5885. DOI: 10.1021/acs.nanolett.4c01260

(67) Jariwala, D.; Krayev, A.; Wong, J.; et al. Nanoscale doping heterogeneity in few-layer WSe_2 exfoliated onto noble metals revealed by correlated SPM and TERS imaging. *2D Materials* **2018**, *5* (3). DOI: 10.1088/2053-1583/aab7bc

(68) Holbrook, M.; Holtzman, L. N.; Hou, B.; et al. Revealing Substitutional Oxygen as the Dominant Defect in Flux-Grown Transition Metal Diselenides. *Nano Lett* **2025**, *25* (37), 13795-13801. DOI: 10.1021/acs.nanolett.5c03126

(69) Liu, S.; Liu, Y.; Holtzman, L.; et al. Two-Step Flux Synthesis of Ultrapure Transition-Metal Dichalcogenides. *ACS Nano* **2023**, *17* (17), 16587-16596. DOI: 10.1021/acsnano.3c02511

(70) Li, H.; Contryman, A. W.; Qian, X.; et al. Optoelectronic crystal of artificial atoms in strain-textured molybdenum disulphide. *Nat Commun* **2015**, *6* (1), 7381. DOI: 10.1038/ncomms8381

(71) Conley, H. J.; Wang, B.; Ziegler, J. I.; et al. Bandgap engineering of strained monolayer and bilayer MoS_2. *Nano Lett* **2013**, *13* (8), 3626-3630. DOI: 10.1021/nl4014748

(72) Ocola, L. E.; Costales, M.; Gosztola, D. J. Development characteristics of polymethyl methacrylate in alcohol/water mixtures: a lithography and Raman spectroscopy study. *Nanotechnology* **2016**, *27* (3), 035302. DOI: 10.1088/0957-4484/27/3/035302

(73) Yasin, S.; Hasko, D. G.; Ahmed, H. Fabrication of <5 nm width lines in poly(methylmethacrylate) resist using a water:isopropyl alcohol developer and ultrasonically-assisted development. *Applied Physics Letters* **2001**, *78* (18), 2760-2762. DOI: 10.1063/1.1369615

(74) Sun, B.; Grap, T.; Frahm, T.; et al. Role of electron and ion irradiation in a reliable lift-off process with electron beam evaporation and a bilayer PMMA resist system. *Journal of Vacuum Science & Technology B, Nanotechnology and Microelectronics: Materials, Processing, Measurement, and Phenomena* **2021**, *39* (5). DOI: 10.1116/6.0001161

CHAPTER FIVE

GRAPHITE-INDUCED PHOTOLUMINESCENT BRIGHTENING OF QUANTUM LIGHT IN MONOLAYER WSe_2 NANOINDENTS

Contributions of Authors and Co-Authors

Author: Joseph Stage

Contributions: Conceived this work, sample preparation, conducted cryogenic photoluminescence spectroscopy, conducted room temperature photoluminescence spectroscopy, performed spectrally resolved lifetime measurements, data analysis, and wrote the manuscript

Co-Author: J. Pierce Fix

Contributions: Performed nanoindentation, conducted room temperature photoluminescence spectroscopy, and wrote the manuscript

Co-Author: Tim Faltermeier

Contributions: Conducted room temperature photoluminescence spectroscopy and wrote the manuscript

Co-Author: Nicholas J. Borys

Contributions: Conceived this work and wrote the manuscript

Manuscript Information

Joseph Stage, J. Pierce Fix, Tim Faltermeier, and Nicholas J. Borys

Status of Manuscript:
☒Prepared for submission to a peer-reviewed journal
☐Officially submitted to a peer-reviewed journal
☐Accepted by a peer-reviewed journal
☐ Published in a peer-reviewed journal

Abstract

Nanoindentation of 2D materials, such as monolayer WSe_2, is an ideal platform for the deterministic placement of single photon emitters that strays away from the formation of stochastically generated bubbles, wrinkles, and fractures common in out-of-plane strain generators. During nanoindentation, a sharp atomic force microscopy tip is driven into a polymer surface to form the indent via plastic deformation of the polymer, but a natural consequence of this technique is a peripheral region of buildup. The dynamics of excitons within the buildup region impose a large amount of defect-mediated background emission observed using cryogenic photoluminescence of the WSe_2 at indent locations. A previous study has shown that the addition of a graphite layer on top of an array of indents creates a fast ($\sim 1 ps^{-1}$) non-radiative decay channel that greatly suppresses the background emission through the dissociation of long-lived defect excitons. This study showed a significant increase in the single-photon emitter purity, but did not quantify the emission intensity and relaxation dynamics of the emitters they observed. Here, we study the effects of an additional graphite layer on single photon emitters in nanoindented WSe_2. We identify a substantial change in the spectral position, emission intensity, and excited state lifetimes of single photon emitters after the addition of graphite. Notably, the change in spectral position could reflect new emissive states being activated after the graphite quenched emitters localized to the buildup region. We suspect that graphite also significantly dopes the WSe_2, as supported by room temperature photoluminescence spectroscopy, and affects the charge carriers in the WSe_2 after photoexcitation, resulting in a near 100× increase in emitter brightness and 2× increase in excited state lifetimes. Lastly, we show that this effect is independent of emitter energy and tensile strain using spectrally and time-resolved photoluminescence, providing clear insight into how excited state quenching can tailor single photon emitters in WSe_2.

Introduction

In 2015, single-layer (1L) WSe_2, a two-dimensional (2D) transition metal dichalcogenide semiconductor, was shown to host single photon emitters (SPEs) in the presence of localized tensile strain at cryogenic temperatures[1-6]. The single photons generated by these solid-state emitters are suitable for possible applications in quantum photonic technologies, as demonstrated with Hong-Ou-Mandel photon indistinguishability measurements[7] and assessment as sources for quantum key distribution using the BB84 protocol[8]. However, strong variability of the wavelength of the emitters, as well as the need to further improve the precision at which they can be deterministically positioned, has held back further development of 1L-WSe_2 quantum photonic devices. Spatial localization has been addressed previously by taking advantage of exciton funneling[9-11] towards regions of tensile strain and the deterministic generation of strain sites[4, 12, 13] using nanostructures such as pillars, cones, and holes, among many other geometries. Most commonly, the deterministic localized strain sites in 2D materials devices are generated with out-of-plane stressors. When the stressor also has a nano-optical response, these stressors have the added benefit of tailoring the photonic outcoupling of emission[14-16], Purcell enhancement of the optical transition[17-22], and plasmonic enhancement of the excitation process[18, 19]. However, a major drawback of these stressors is that unwanted wrinkles, fractures, and nanobubbles in 2D material that are stochastically created by the dry transfer procedure have so far proven to be incredibly difficult to eliminate. The added inhomogeneity of the nanoscale strain around the stressor leads to spectral crowding, unwanted emitters, positioning inaccuracy, and excessive background emission that hinders SPE performance[23-25].

Nanoindentation of 1L-WSe_2 on a pliable plastic surface is a strain generation technique that can potentially alleviate such reproducibility challenges[24, 26-35]. First reported in 2019, nanoindentation creates nanoscale impressions of 2D materials into a poly(methyl methacrylate) (PMMA) substrate through plastic deformation induced by an atomic force microscopy (AFM) tip[26]. Since its inception, nanoindentation has been used to electrically address single photon emission[28], study strong coupling between excitons and plasmons[32], and probe how strain-relaxation through tearing affects SPE formation, as discussed in Chapter 3 of this dissertation. Despite these successes, there are several unresolved challenges and questions regarding nanoindentation-induced SPEs in 1L-WSe_2. Although deformations created with nanoindentation are substantially more consistent than draping material over stressors, ambiguity of whether the emitter is located around the periphery or in the indent itself remains[24]. Further, emission from the SPE states often overlaps with a broadband background of defect-mediated emission, which can significantly diminish photon purity. To mitigate these issues, a thin layer of graphite can be stacked onto the nanoindented 1L-WSe_2. The graphite both quenches emission from regions where it was well-coupled to the 1L-WSe_2, better isolating SPEs to the indent site, as well as suppresses the broadband background emission[31]. As a result, the purity of the SPEs at the nanoindentation sites was improved from nominal values of 60% to 92%[31, 36].

Here, we use time-resolved photoluminescence (PL) spectroscopy to better elucidate how graphite alters the excited states of the 1L-WSe_2 and the nanoindentation-induced SPEs. The prior studies that first reported the effect focused on steady-state PL, and by probing the dynamics, we find that the mechanism is more complex than just excited-state quenching by the graphite. By probing the same nanoindentation site before and after the addition of graphite, we find that the

populations of SPE states, their intensities, and dynamics are dramatically altered by the introduction of graphite. Under nearly identical excitation conditions, the intensity of the SPE emission increases by over 100×, and the average excited state lifetime of the emitters increases by ~2×. From our observations, it appears that charge transfer from the graphite into the 1L-WSe_2, as supported by room temperature PL spectroscopy, both quenches the excited state emission from the non-indented material as well as reduces the carrier density in the 1L-WSe_2 within the indent, which both enhances exciton localization to defects and the PL quantum yield of the SPEs. Importantly, we observe that the change in SPE dynamics and brightness induced by the graphite is independent of the imposed strain in the nanoindents as well as the energy of individual emitters. These findings deepen our understanding of how 2D heterostructure engineering of excited state quenching can tailor the formation and performance of SPEs in nanoindented 1L-WSe_2.

Results and Discussion

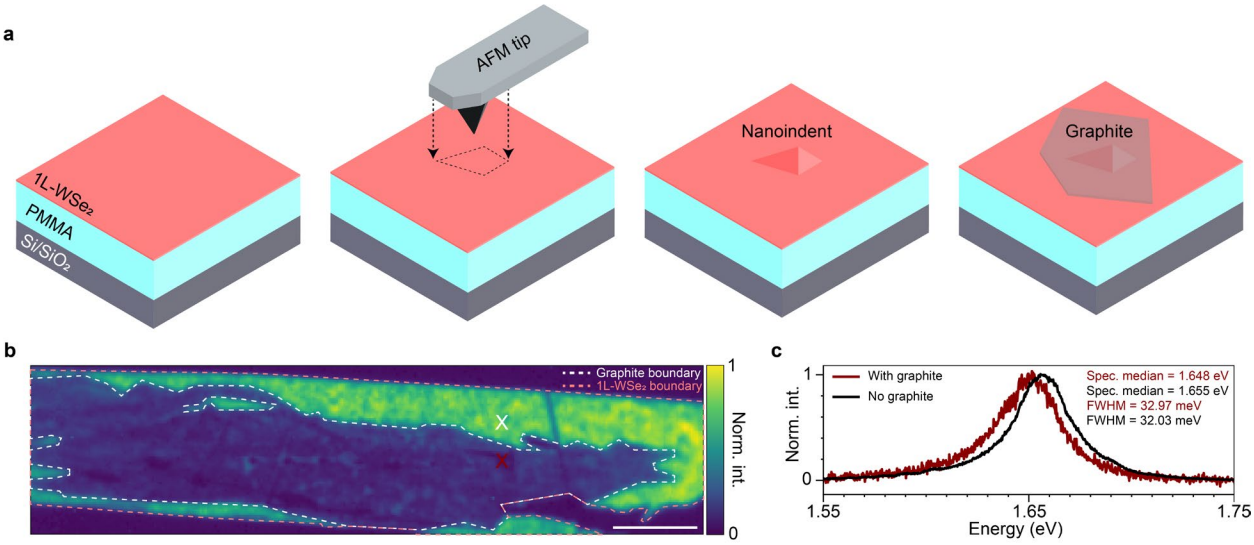


Figure 1 – Generation of graphite-covered indents and room temperature PL: (a) Schematic representation of nanoindentation and the hybrid dry/wet transfer of graphite. (b) Room temperature PL map of a graphite/1L-WSe_2 heterostructure. The red and white X's relate to the locations where the point spectra in (c) were taken. (c) Point spectra PL comparison showing a redshift, slight linewidth broadening, and reduction in intensity in regions of interlayer coupling between graphite and 1L-WSe_2. Scale bar is 10 μm.

Figure 1a illustrates the process for fabricating graphite-covered nanoindents of 1L-WSe_2. In short, 1L-WSe_2 is directly exfoliated onto a PMMA substrate using an adapted gel-assisted exfoliation technique[37], and nanoindents are subsequently formed in the 1L-WSe_2 by pressing an atomic force microscopy (AFM) probe to a specified indentation force that ranges from 28.81-71.35 μN (see Methods for details). After indentation, thin graphite is transferred onto the indented 1L-WSe_2 using a hybrid wet and dry transfer method. This transfer approach enables AFM characterization of the graphite flakes before the final transfer onto PMMA (see Methods for details). The effect of the graphite layer is seen by comparing the room temperature PL of the 1L-WSe_2 with and without the top layer of graphite. As seen in the spatial PL map shown in Figure

1b, the graphite quenches the excitonic emission from the 1L-WSe_2 by ~12×, which is comparable to previous studies[38]. The quenching occurs over the extent of the graphite/1L-WSe_2 heterostructure, indicating that strong interlayer coupling occurs relatively uniformly across the heterostructure. Sample PL spectra from indent-free regions of 1L-WSe_2 with and without the top layer of graphite are shown in Figure 1c. In addition to a reduction in intensity, PL for the graphite-covered 1L-WSe_2 is redshifted by ~7 meV. Further, we observe that the graphite also subtly increases the full width at half maximum (FWHM) of the spectrum by ~1 meV. These graphite-induced changes are consistent with prior reports of steady-state charge transfer/doping of the 1L-WSe_2 by the graphite[38, 39].

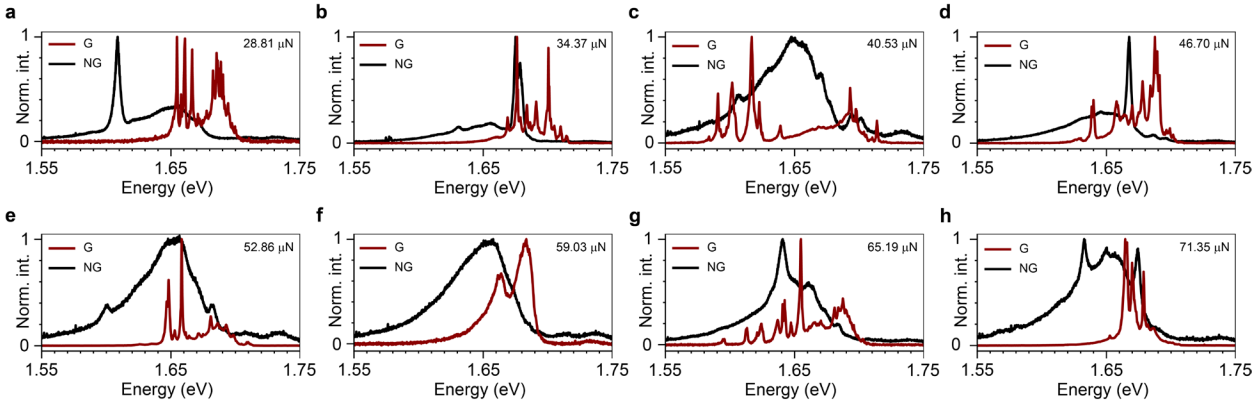


Figure 2 – 4 K PL spectra of nanoindents before and after graphite transfer: (a-h) A range of 4 K PL spectra taken at nanoindent sites made with indentation forces from 28.81 – 71.35 μN.

Figure 2 shows the effect of the graphite layer on the SPE states on nanoindentation-induced SPEs for the full range of indentation forces at 4 K. In general, the localized strain as well as the depth of the apex of the indent increases with indentation force[27, 40], so Figures 2a-h probe how the effect depends on these physical properties. Before the graphite layer was added, all of the nanoindentations exhibited intense broadband background PL emission ranging from ~1.57–

1.67 eV. This background dominates the PL emission, obscuring emission from any narrowband states associated with SPEs. After graphite is added, the background emission is efficiently quenched, which has been previously attributed to fast (~1 ps^{-1}) non-radiative decay that dissociates defect excitons that contribute to a much longer-lived background of emission (~600 ns^{-1})[31, 41, 42]. Additionally, the spectral position of the ensemble of SPEs shifts to higher energies, indicating that different SPE states may be activated or selectively brightened by the graphite. In particular, we note that for several indents (28.81, 34.37, and 46.70 μN) in Figures 2a, 2b, and 2d, respectively, intense SPEs emerge at energies where minimal broadband defect PL was observed in the uncovered 1L-WSe_2 nanoindents. Such dramatic changes in the defect emission could be due to the quenching of buildup region localized SPE states, where the graphite is in direct contact with the 1L-WSe_2, where prior reports have observed the presence of emitters localized to the buildup region[24].

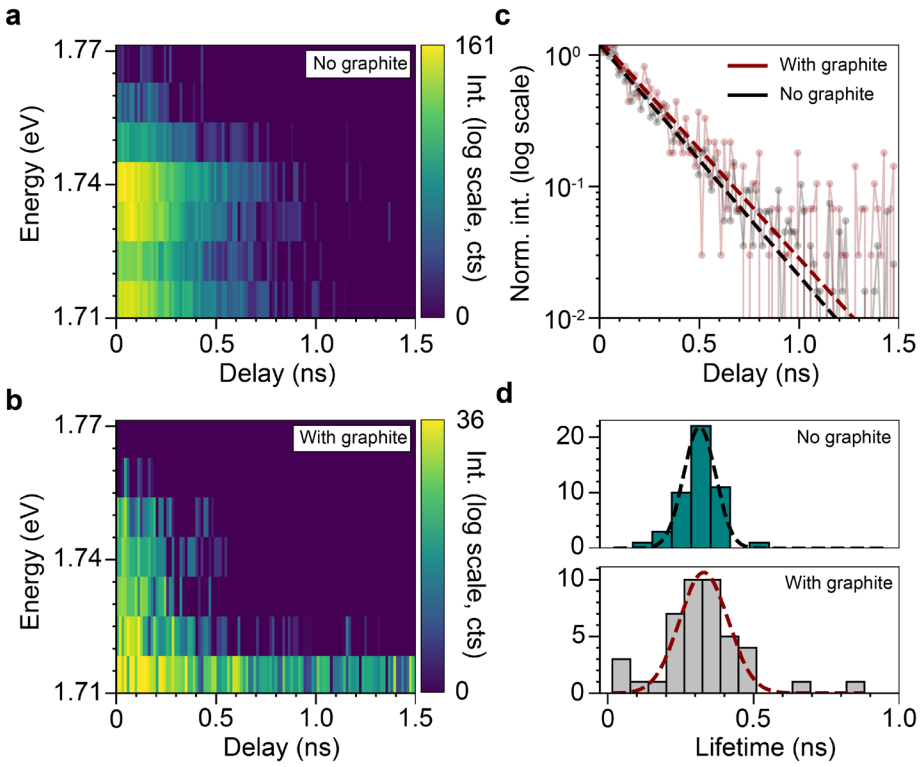


Figure 3 – Spectrally and time resolved PL of A-exciton-like emission: (a-b) Maps of the spectrally and time resolved PL of a 40.53 μN nanoindent before and after graphite transfer, respectively, limited to A-excitonic-like emission. (c) Example PL transience from A-exciton-like emission with and without graphite. (d) Histograms of the lifetimes of A-exciton-like emission with and without graphite.

Previous studies on graphite-covered indents concluded that the primary effect of the graphite was to quench the background PL emission[31] and did not address how it alters the formation of SPEs at the indent site. By directly comparing the defect PL at the indents before and after, we find that the graphite substantially changes the PL at the indent site on top of the strong quenching of the broadband background. Chapter 3 of this dissertation probed how tearing during the nanoindentation process affects the formation of SPEs, offering additional insight into this change in SPE states. This study found that 1L-WSe_2 nanoindents that have torn and where the strain has relaxed still host SPE states, likely localized to the torn region along the indent wall

rather than the buildup region. Such states could potentially be electronically isolated from the graphite, substantially reducing any excited-state quenching processes. In contrast, any strain-localized SPEs in the periphery of the nanoindent, such as the buildup region of displaced PMMA, would be in direct contact with the graphite and quenched. The substantially modified distribution of emitters after the addition of the graphite may indicate that the broadband background emission originates from the areas surrounding the indent. Additionally, the dramatic increase in the intensity of the PL after the addition of the graphite further indicates that the graphite results in more than just an efficient excited-state quenching pathway. Considering these observations, this prior study[31] may have been working with torn nanoindents, where the untorn indents used in this work see exciton funneling into previously unoccupied indent site SPEs.

To probe the graphite-induced changes on the dynamics of the various excited states in the 1L-WSe_2, we also compared the spectrally and time-resolved PL of the 1L-WSe_2 before and after the addition of the graphite layer (see Methods) over emission energies from 1.77 to 1.57 eV. The PL transients spanning the energy range of the A exciton from 1.71-1.77 eV for the indentation site created with a 40.53 μN indentation force before and after the graphite was added are shown in Figures 3a and 3b, respectively. The addition of the graphite does not lead to a dramatic acceleration of the relaxation of the A exciton. Such before-and-after spectrally- and time-resolved measurements were performed at each indentation site in Figure 2. Single-exponential decays were fitted to each spectral bin ($\Delta E \approx 10\ meV$) to extract an excited state lifetime. Example transients are shown in Figure 3c, and the distributions of extracted excited state lifetimes are shown in Figure 3d. For A-exciton-like emission, the distributions are very similar. The mean lifetime for the A exciton with bare 1L-WSe_2 is 290 ps, whereas it is 330 ps for the 1L-WSe_2 with the graphite.

We note that the distribution of lifetimes for the 1L-WSe_2 with the graphite is slightly broadened, especially towards lower lifetimes, which could signify a non-radiative decay channel into the graphite for a relatively small area around the indent, as was previously reported in such heterostructures[39]. Nevertheless, we do not observe a dramatic change in the excited state dynamics of the A exciton at indentation sites.

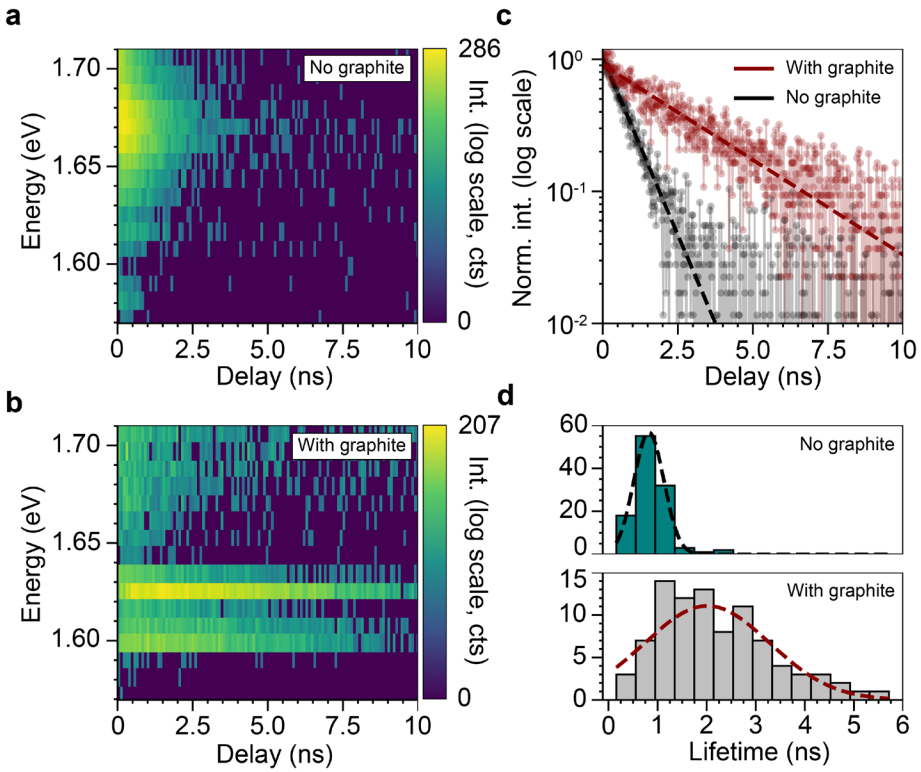


Figure 4 - Spectrally and time resolved PL of quantum emission: (a-b) Maps of the spectrally and time resolved PL of a 40.53 μN nanoindent before and after graphite transfer, respectively, limited to quantum emission. (c) Example PL transience from quantum emission with and without graphite. (d) Histograms of the lifetimes of quantum emission with and without graphite.

Figure 4 shows that, in contrast to the A exciton, the addition of the graphite has a much more pronounced effect on the excited state lifetimes of the defect-localized excitons and quantum emitters in the system. Figures 4a and 4b show the excited state dynamics in the lower-energy

range that is associated with quantum light emission and SPEs without and with graphite, respectively, for the same indent as Figures 3a and 3b. The states that are activated by the addition of the graphite have dramatically longer lifetimes than the defect emission in the bare 1L-WSe_2. Example transients are shown in Figure 4c, and the distributions of extracted lifetimes over this energy range for all indentation sites are shown in Figure 4d. Now, the distribution for the 1L-WSe_2 with graphite is significantly broadened and shifted to longer lifetimes compared to the bare 1L-WSe_2. Surprisingly, not only does the graphite quench the background emission and activate new emitter states, but the lifetimes of the emitters it activates are significantly increased.

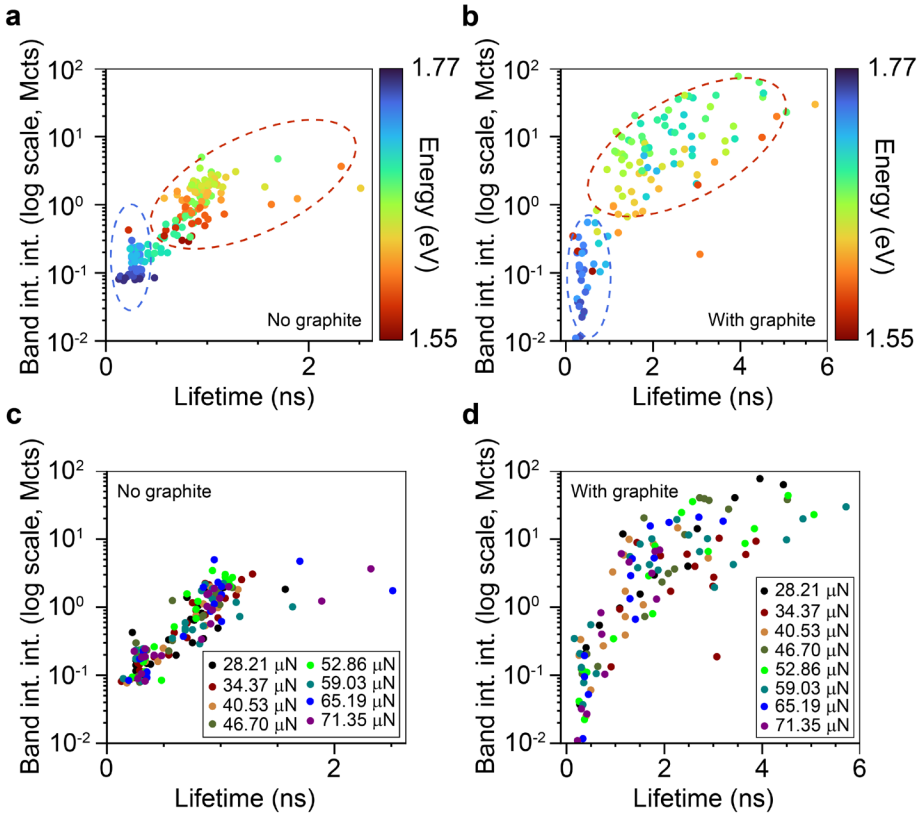


Figure 5 – Energy and strain dependence on PL lifetimes: (a-b) Energy-dependent scatter plots of PL lifetimes vs band integrated intensities for 1L-WSe_2 nanoindents without and with a graphite adlayer, respectively. (c-d) Scatter plots of indentation force-dependent PL lifetimes vs band integrated intensities for 1L-WSe_2 nanoindents without and with graphite, respectively.

Strain and wavelength dependence on the relaxation dynamics are investigated in Figure 5, which shows the correlation plots between the measured excited state lifetime and intensity in the emission band probed in Figures 3 and 4. The integrated intensities for each band were calculated by calibrating the bandwidth of emission that was passed to the avalanche photo-diode (APD) used to collect each decay trace (see Methods for details) and integrating the intensity of each band, while the energy of emission is simply the center position of each band. Figures 5a and 5b color-code the individual points based on the energy of the band and show that the lifetime of A-exciton-like emission (1.71 - 1.77 eV) for the indents without and with graphite are nearly

constant, and a reduction in average intensity of the A exciton is present after graphite is added. In stark contrast, the low-energy bands, which include the background emission and SPEs (1.55 – 1.71 eV), exhibit a large increase in the integrated intensity as well as a large increase in excited state lifetimes after graphite is added. In these plots, a strong correlation exists between lifetime and emission brightness in both systems, indicating that the brighter emitters likely have reduced non-radiative decay rates and higher PL quantum yields[15]. Noticeable dependences of the increases in lifetime and emission intensity on emission energy are not observed, demonstrating that the effect of the graphite is indiscriminate and not selective to a specific spectral region or sub-ensemble of SPE/defect states. Figures 5c and 5d report the same correlation plots as Figures 5a and 5b, but now the data points are colored according to the indentation force used to generate each indent as a proxy of tensile strain generated in the indent. As observed in prior studies of the strain-dependent SPE formation in nanoindents[26], neither the intensity nor the lifetime of the emission is strongly affected by the indentation force used.

For the SPE states in the nanoindented 1L-WSe_2, our steady-state and time-resolved before-and-after measurements reveal that the graphite activates new emitters that are not resolvable in the bare indented 1L-WSe_2 that are significantly brighter and have longer excited state lifetimes than the broadband defect emission in the bare indented 1L-WSe_2. These observations indicate that the effect of the graphite is greater than just an additional non-radiative rate that quenches the background. Many possible effects could contribute to the increase in the average lifetime of quantum emission in graphite-covered indents, such as suppression of the non-radiative decay, charge state stabilization, and a changing dielectric environment. One previously published study showed a SPE lifetime increase of ~2× in nanoindented 1L-WSe_2, where the

material surrounding the indent was partially oxidized using voltage-induced degradation[34]. There is a high likelihood that our systems' increase of ~2× in lifetime with the introduction of graphite is in part due to suppression of competing emission channels in the surrounding 1L-WSe_2, analogous to voltage-induced degradation; however, to fully understand the mechanism for increased decay time requires further studies into the possible effects listed above.

Increases in SPE intensity have been reported previously by gating the indented 1L-WSe_2 at positive bias voltages that correspond to hole doping[28], establishing that the steady-state carrier density in the 1L-WSe_2 strongly affects SPE brightness. In contrast, the graphite is suspected to transfer electrons into the 1L-WSe_2[36, 38]. It is possible that both hole and electron-doping improve the brightness of the emitters, depending on the initial state of the 1L-WSe_2, which, in our system, we suspect is p-doped by the supporting PMMA layer[43, 44]. Photoinduced doping could also be occurring, and helicity-resolved spectroscopy suggests carrier injection from 1L-WSe_2 into graphite on ultrafast time scales[45]. If the 1L-WSe_2 was strongly p-doped, graphite may alter the photoexcited carrier population in the 1L-WSe_2 through interlayer charge transfer, providing a possible photoinduced doping mechanism for the observed increase in SPE brightness.

We hypothesize that the modification of the free carrier density induced by the graphite layer is a major contributing factor to the effects observed. SPEs in 1L-WSe_2 have been theorized to originate from the hybridization of dark excitons with defect states in regions of tensile strain[46] to form defect-localized excitons that are responsible for the SPE emission. In bulk semiconductors, such localization is unstable if the defect state is charged (as would be the case for donor/acceptor defects near the band edges)[47]. The induced changes in carrier density by the graphite may change the charge states of the defects, such that a much smaller number of

localization sites exist in the indent. Such a reduction in competing localized states would concentrate the bath of excitons within the nanoindent into a smaller share of possible SPEs, effectively increasing the excitation rate of each state. The remaining SPE states may also have a more resonant band alignment of dark excitons and defect levels due to the difference in tensile strain within a nanoindent, leading to larger oscillator strengths and improved brightness. Strain modeling of nanoindents has been performed previously[24, 29], but did not investigate the spatial extent of the nanoindent. If the tensile strain across a nanoindent is continuously modulated, then there could exist an optimized strain value along a peripheral ring in the indent where dark exciton hybridization is maximized.

Conclusion

In conclusion, we have demonstrated the PL brightening and increase of the excited state lifetime of SPEs in 1L-WSe_2 nanoindents after the introduction of a thin graphite capping layer. We observed room temperature signatures of graphite-induced doping in the graphite/1L-WSe_2 heterostructure, consistent with prior studies of devices with interlayer coupling. As reported previously, graphite coupling introduces a fast non-radiative decay channel that efficiently dissociates excitons, eliminating broadband background emission from the cryogenic PL spectra. Using time and spectrally resolved PL, we measure SPE brightness and excited state lifetime increases of 100× and 2×, respectively. By categorizing our dataset to account for the SPE energy and tensile strain, we note that these effects are nominally independent of spectral position and indentation force used to generate the nanoindent. We suspect that these effects are caused by three competing mechanisms: the deactivation of buildup region SPEs redistributing the excitation bath to a smaller quantity of indent localized SPEs, photoinduced doping of the 1L-WSe_2 from the

graphite, and the suppression of non-radiative decay via charge localization, which each requires further study to fully understand. This study should aid in the understanding of how steady state and photoinduced charges move at a graphite/1L-WSe_2 interface and how doping affects SPE states.

Methods

Sample Fabrication

Gel-Assisted Exfoliation onto PMMA Substrates To generate 1L-WSe_2 flakes on a PMMA surface, we used a gel-assisted exfoliation technique rather than traditional Scotch Tape exfoliation to lower the adhesion of the contacting "tape" and better preserve the PMMA surface. We first made a 1L-WSe_2 mother tape on Scotch Magic Tape, and pulled a copy tape from it using Nitto tape. Here, Nitto tape was chosen for the copy tape because of its lower polymer residue. We then adhered the Nitto tape onto a UV ozone-treated (2 mins) piece of X4 Gel-Pak polydimethylsiloxane (PDMS) and heated the stack on a 95 °C hotplate for 90 s. After another 90 s of cooling, the Nitto tape is removed, leaving behind WSe_2 on the PDMS surface. PMMA substrates were then fabricated by spin coating 950K A4 PMMA onto a cleaned SiO_2 chip at 1500 rpm, followed by a 40 min hard bake on an 80 °C hotplate. Exfoliation on the PMMA is then done by treating the PMMA surface in a UV ozone environment for 2 mins, and adhering the PDMS "tape" onto the PMMA surface. We then followed the same heating and cooling procedure as before and removed the PDMS "tape". Left behind on the PMMA is a lower quantity of 2D material crystallites, but a higher yield of monolayers with, on average, larger areas[37].

Nanoindentation of 1L-WSe_2 To generate nanoindents in the 1L-WSe_2, we followed the initial protocol set by Rosenburger *et al*. We used an AIST-NT SmartSPM HE002 AFM from HORIBA Scientific. In the AFM software, we used the nanoindentation application in "Zsweep" mode, which allows for control of the z-axis piezo motor of the sample stage. When the location of an indent was defined, the indentation force was set by inputting the z-displacement, which is defined by the distance the AFM stage moved into the AFM tip. The z-displacement ranged from 1200-2600 nm, corresponding to 28.81–71.35 μN in indentation force. The indentation forces were calculated from the calibration equation shown below. Where z is the desired z-displacement.

$$Indentation\ force\ (\mu N) = -0.031\left(\frac{\mu N}{nm}\right) \times z + (-8.8\ \mu N)$$

At these indentation forces, the AFM tip slips, meaning the tip does not stay in the defined location throughout the indentation process. To minimize the tip slipping, we introduced a lateral movement of the sample stage along the y-axis, through the AFM software, to keep the tip in the same initial position during the indentation process.

Hybrid Wet and Dry Transfer of Graphite The hybrid wet and dry transfer technique used to transfer graphite flakes onto 1L-WSe_2 nanoindents was chosen to permit AFM analysis of the graphite flakes on a rigid SiO_2 substrate before transfer. First, we exfoliated graphite onto a cleaned and O_2 plasma-treated SiO_2 substrate using traditional Scotch Magic Tape exfoliation[48, 49]. Then, we would spin coat a layer of Sylgard 184 PDMS at a 10:1 base to curing agent ratio at 4000 rpm and bake the sample at 100 °C for 60 minutes to cure the PDMS layer. Once cured, the sample was placed into a 90 °C 1M solution of NaOH in deionized water (DIW) to lightly etch the SiO_2 surface and promote liftoff of the graphite/PDMS stamp. After 15 mins, bubbles would begin to form on the perimeter of the chip, indicating release was imminent. If the graphite/PDMS stamp did not

release on its own after ~30 mins, gentle assistance from a pair of tweezers was used. The stamp was then moved to a room temperature bath of DIW to rinse excess NaOH from the flakes for ~12 hours, and the stamp was flipped over so the flakes faced away from the DIW. The PDMS/graphite stamp was then scooped by a glass slide with X4 Gel-Pak PDMS attached to it, forming the complete stamp used for the dry transfer. Finally, the graphite flake of interest was transferred onto the 1L-WSe_2 indents using the viscoelastic stamping method[50].

Optical Measurements

Room Temperature Photoluminescence Room temperature PL measurements were performed on a Horiba TRIOS system with a 532 nm continuous wave laser (Cobalt Samba) and 100x (NA 0.8) objective. The PL signal was separated from the back-reflected laser using a 532 nm long-pass filter (Semrock). The isolated PL signal was then detected by an air-cooled EMCCD (Andor iXon Ultra 888) attached to a spectrometer (Andor Kymera 328i). The sample was excited with a spot size of ~450 nm and an excitation power of ~500 nW.

Cryogenic Photoluminescence Cryogenic PL was taken inside a closed-cycle liquid helium-cooled Montana Instruments s50 Cryostation equipped with an optical access port. Samples were illuminated under 532 nm pulsed excitation from a NKT Photonics SuperK EXTREME laser filtered with a Gooch and Housego acoustic-optical tunable filter and focused through a Nikon infinity corrected S Plan Fluor 40X (0.6 NA) objective equipped with a correction collar to compensate for the cryostat window. The samples were excited with ~50 nW of power across a ~750 nm FWHM laser spot, both before and after graphite was added, and spectra were then recorded using a Horiba iHR320 grating spectrometer and an Andor idus 416 CCD camera.

Spectral and Time Resolved Photoluminescence Spectral and time-resolved PL maps were made by stepping a passband of $\sim 10\, meV$ to an Excelitas SPCM-AQRH-14-TR single-photon avalanche photo-diode connected to a PicoQuant HydraHarp 400 TCSPC module. The passband was created using the monochromator exit slit of our Horiba iHR320 grating spectrometer and tuned by moving the center position of the grating.

Chapter 5 References

(1) Chakraborty, C.; Kinnischtzke, L.; Goodfellow, K. M.; et al. Voltage-controlled quantum light from an atomically thin semiconductor. *Nat Nanotechnol* **2015**, *10* (6), 507-511. DOI: 10.1038/nnano.2015.79

(2) He, Y. M.; Clark, G.; Schaibley, J. R.; et al. Single quantum emitters in monolayer semiconductors. *Nat Nanotechnol* **2015**, *10* (6), 497-502. DOI: 10.1038/nnano.2015.75

(3) Koperski, M.; Nogajewski, K.; Arora, A.; et al. Single photon emitters in exfoliated WSe_2 structures. *Nat Nanotechnol* **2015**, *10* (6), 503-506. DOI: 10.1038/nnano.2015.67

(4) Kumar, S.; Kaczmarczyk, A.; Gerardot, B. D. Strain-Induced Spatial and Spectral Isolation of Quantum Emitters in Mono- and Bilayer WSe_2. *Nano Lett* **2015**, *15* (11), 7567-7573. DOI: 10.1021/acs.nanolett.5b03312

(5) Srivastava, A.; Sidler, M.; Allain, A. V.; et al. Optically active quantum dots in monolayer WSe_2. *Nat Nanotechnol* **2015**, *10* (6), 491-496. DOI: 10.1038/nnano.2015.60

(6) Tonndorf, P.; Schmidt, R.; Schneider, R.; et al. Single-photon emission from localized excitons in an atomically thin semiconductor. *Optica* **2015**, *2* (4). DOI: 10.1364/optica.2.000347

(7) Drawer, J. C.; Mitryakhin, V. N.; Shan, H.; et al. Monolayer-Based Single-Photon Source in a Liquid-Helium-Free Open Cavity Featuring 65% Brightness and Quantum Coherence. *Nano Lett* **2023**, *23* (18), 8683-8689. DOI: 10.1021/acs.nanolett.3c02584

(8) Gao, T.; von Helversen, M.; Antón-Solanas, C.; et al. Atomically-thin single-photon sources for quantum communication. *npj 2D Materials and Applications* **2023**, *7* (1). DOI: 10.1038/s41699-023-00366-4

(9) Branny, A.; Kumar, S.; Proux, R.; et al. Deterministic strain-induced arrays of quantum emitters in a two-dimensional semiconductor. *Nat Commun* **2017**, *8* (1), 15053. DOI: 10.1038/ncomms15053

(10) Rosati, R.; Schmidt, R.; Brem, S.; et al. Dark exciton anti-funneling in atomically thin semiconductors. *Nat Commun* **2021**, *12* (1), 7221. DOI: 10.1038/s41467-021-27425-y

(11) Kim, J. M.; Jeong, K. Y.; Kwon, S.; et al. Strained two-dimensional tungsten diselenide for mechanically tunable exciton transport. *Nat Commun* **2024**, *15* (1), 10847. DOI: 10.1038/s41467-024-55135-8

(12) Parto, K.; Azzam, S. I.; Banerjee, K.; et al. Defect and strain engineering of monolayer WSe_2 enables site-controlled single-photon emission up to 150 K. *Nat Commun* **2021**, *12* (1), 3585. DOI: 10.1038/s41467-021-23709-5

(13) Yanev, E. S.; Darlington, T. P.; Ladyzhets, S. A.; et al. Programmable nanowrinkle-induced room-temperature exciton localization in monolayer WSe_2. *Nat Commun* **2024**, *15* (1), 1543. DOI: 10.1038/s41467-024-45936-2

(14) Iff, O.; Buchinger, Q.; Moczala-Dusanowska, M.; et al. Purcell-Enhanced Single Photon Source Based on a Deterministically Placed WSe_2 Monolayer Quantum Dot in a Circular Bragg Grating Cavity. *Nano Lett* **2021**, *21* (11), 4715-4720. DOI: 10.1021/acs.nanolett.1c00978

(15) Sortino, L.; Zotev, P. G.; Phillips, C. L.; et al. Bright single photon emitters with enhanced quantum efficiency in a two-dimensional semiconductor coupled with dielectric nano-antennas. *Nat Commun* **2021**, *12* (1), 6063. DOI: 10.1038/s41467-021-26262-3

(16) Paralikis, A.; Piccinini, C.; Madigawa, A. A.; et al. Tailoring polarization in WSe_2 quantum emitters through deterministic strain engineering. *NPJ 2D Mater Appl* **2024**, *8* (1), 59. DOI: 10.1038/s41699-024-00497-2

(17) Azzam, S. I.; Parto, K.; Moody, G. Purcell enhancement and polarization control of single-photon emitters in monolayer WSe_2 using dielectric nanoantennas. *Nanophotonics* **2023**, *12* (3), 477-484. DOI: 10.1515/nanoph-2022-0628

(18) Luo, Y.; Shepard, G. D.; Ardelean, J. V.; et al. Deterministic coupling of site-controlled quantum emitters in monolayer WSe_2 to plasmonic nanocavities. *Nat Nanotechnol* **2018**, *13* (12), 1137-1142. DOI: 10.1038/s41565-018-0275-z

(19) Luo, Y.; Liu, N.; Li, X.; et al. Single photon emission in WSe_2 up to 160 K by quantum yield control. *2D Materials* **2019**, *6* (3). DOI: 10.1088/2053-1583/ab15fe

(20) Luo, Y.; Liu, N.; Kim, B.; et al. Exciton Dipole Orientation of Strain-Induced Quantum Emitters in WSe_2. *Nano Lett* **2020**, *20* (7), 5119-5126. DOI: 10.1021/acs.nanolett.0c01358

(21) Park, K. D.; Khatib, O.; Kravtsov, V.; et al. Hybrid Tip-Enhanced Nanospectroscopy and Nanoimaging of Monolayer WSe_2 with Local Strain Control. *Nano Lett* **2016**, *16* (4), 2621-2627. DOI: 10.1021/acs.nanolett.6b00238

(22) Park, K. D.; Jiang, T.; Clark, G.; et al. Radiative control of dark excitons at room temperature by nano-optical antenna-tip Purcell effect. *Nat Nanotechnol* **2018**, *13* (1), 59-64. DOI: 10.1038/s41565-017-0003-0

(23) Xu, D. D.; Vong, A. F.; Utama, M. I. B.; et al. Sub-Diffraction Correlation of Quantum Emitters and Local Strain Fields in Strain-Engineered WSe_2 Monolayers. *Adv Mater* **2024**, *36* (25), e2314242. DOI: 10.1002/adma.202314242

(24) Abramov, A. N.; Chestnov, I. Y.; Alimova, E. S.; et al. Photoluminescence imaging of single photon emitters within nanoscale strain profiles in monolayer WSe_2. *Nat Commun* **2023**, *14* (1), 5737. DOI: 10.1038/s41467-023-41292-9

(25) Daveau, R. S.; Vandekerckhove, T.; Mukherjee, A.; et al. Spectral and spatial isolation of single tungsten diselenide quantum emitters using hexagonal boron nitride wrinkles. *APL Photonics* **2020**, *5* (9). DOI: 10.1063/5.0013825

(26) Rosenberger, M. R.; Dass, C. K.; Chuang, H. J.; et al. Quantum Calligraphy: Writing Single-Photon Emitters in a Two-Dimensional Materials Platform. *ACS Nano* **2019**, *13* (1), 904-912. DOI: 10.1021/acsnano.8b08730

(27) So, J. P.; Kim, H. R.; Baek, H.; et al. Electrically driven strain-induced deterministic single-photon emitters in a van der Waals heterostructure. *Sci Adv* **2021**, *7* (43), eabj3176. DOI: 10.1126/sciadv.abj3176

(28) Stevens, C. E.; Chuang, H. J.; Rosenberger, M. R.; et al. Enhancing the Purity of Deterministically Placed Quantum Emitters in Monolayer WSe_2. *ACS Nano* **2022**, *16* (12), 20956-20963. DOI: 10.1021/acsnano.2c08553

(29) Chang, S.; Yan, Y.; Geng, Y. Local Nanostrain Engineering of Monolayer MoS_2 Using Atomic Force Microscopy-Based Thermomechanical Nanoindentation. *Nano Lett* **2023**, *23* (20), 9219-9226. DOI: 10.1021/acs.nanolett.3c01809

(30) Li, X.; Jones, A. C.; Choi, J.; et al. Proximity-induced chiral quantum light generation in strain-engineered $WSe_2/NiPS_3$ heterostructures. *Nat Mater* **2023**, *22* (11), 1311-1316. DOI: 10.1038/s41563-023-01645-7

(31) Chuang, H. J.; Stevens, C. E.; Rosenberger, M. R.; et al. Enhancing Single Photon Emission Purity via Design of van der Waals Heterostructures. *Nano Lett* **2024**, *24* (18), 5529-5535. DOI: 10.1021/acs.nanolett.4c00683

(32) Cunningham, P. D.; Proscia, N. V.; LaGasse, S. W.; et al. Site-Specific Exciton–Plasmon Coupling in Nanoindented WSe_2. *ACS Photonics* **2024**, *11* (8), 3250-3258. DOI: 10.1021/acsphotonics.4c00644

(33) Gavin, S. C.; Chuang, H. J.; Dasgupta, A.; et al. High-Temperature Single-Photon Emission From Covalently Functionalized van der Waals Heterostructures. *Adv Sci (Weinh)* **2025**, *12* (48), e11319. DOI: 10.1002/advs.202511319

(34) Lee, S. J.; Chuang, H. J.; McCreary, K. M.; et al. Voltage-Induced Degradation for Enhanced Purity and Reproducibility of Quantum Emission in Monolayer 2D Materials. *ACS Nano* **2025**, *19* (38), 33981-33990. DOI: 10.1021/acsnano.5c09799

(35) Yücel, O.; Yagodkin, D.; Kirchhof, J. N.; et al. Strain activation of localized states in WSe_2. *2D Materials* **2025**, *12* (3). DOI: 10.1088/2053-1583/add414

(36) Dong, S.; Beaulieu, S.; Selig, M.; et al. Observation of ultrafast interfacial Meitner-Auger energy transfer in a Van der Waals heterostructure. *Nat Commun* **2023**, *14* (1), 5057. DOI: 10.1038/s41467-023-40815-8

(37) Budania, P.; Baine, P. T.; Montgomery, J. H.; et al. Comparison between Scotch tape and gel-assisted mechanical exfoliation techniques for preparation of 2D transition metal dichalcogenide flakes. *Micro & Nano Letters* **2017**, *12* (12), 970-973. DOI: 10.1049/mnl.2017.0280

(38) Pan, Y.; Rahaman, M.; He, L.; et al. Exciton tuning in monolayer WSe_2 via substrate induced electron doping. *Nanoscale Adv* **2022**, *4* (23), 5102-5108. DOI: 10.1039/d2na00495j

(39) Xing, X.; Zhao, L.; Zhang, W.; et al. Influence of a substrate on ultrafast interfacial charge transfer and dynamical interlayer excitons in monolayer WSe_2/graphene heterostructures. *Nanoscale* **2020**, *12* (4), 2498-2506. DOI: 10.1039/c9nr09309e

(40) Yang, K.; Yang, Y.; Rhodes, D. A.; et al. Local strain-engineering of exciton energy in 2D materials with nanoindentation. *Nanoscale* **2026**, *18* (10), 5575-5587. DOI: 10.1039/d6nr00112b

(41) He, J.; Kumar, N.; Bellus, M. Z.; et al. Electron transfer and coupling in graphene-tungsten disulfide van der Waals heterostructures. *Nat Commun* **2014**, *5*, 5622. DOI: 10.1038/ncomms6622

(42) Hill, H. M.; Rigosi, A. F.; Raja, A.; et al. Exciton broadening in WS_2/graphene heterostructures. *Physical Review B* **2017**, *96* (20). DOI: 10.1103/PhysRevB.96.205401

(43) Liang, J.; Xu, K.; Toncini, B.; et al. Impact of Post-Lithography Polymer Residue on the Electrical Characteristics of MoS_2 and WSe_2 Field Effect Transistors. *Advanced Materials Interfaces* **2018**, *6* (3). DOI: 10.1002/admi.201801321

(44) Urban, F.; Martucciello, N.; Peters, L.; et al. Environmental Effects on the Electrical Characteristics of Back-Gated WSe_2 Field-Effect Transistors. *Nanomaterials (Basel)* **2018**, *8* (11). DOI: 10.3390/nano8110901

(45) Zhou, H.; Chen, Y.; Zhu, H. Deciphering asymmetric charge transfer at transition metal dichalcogenide-graphene interface by helicity-resolved ultrafast spectroscopy. *Sci Adv* **2021**, *7* (34). DOI: 10.1126/sciadv.abg2999

(46) Linhart, L.; Paur, M.; Smejkal, V.; et al. Localized Intervalley Defect Excitons as Single-Photon Emitters in WSe_2. *Phys Rev Lett* **2019**, *123* (14), 146401. DOI: 10.1103/PhysRevLett.123.146401

(47) Klingshirn, C. *Semiconductor Optics*; 2007. DOI: 10.1007/978-3-540-38347-5.

(48) Novoselov, K. S.; Geim, A. K.; Morozov, S. V.; et al. Electric field effect in atomically thin carbon films. *Science* **2004**, *306* (5696), 666-669. DOI: 10.1126/science.1102896

(49) Huang, Y.; Sutter, E.; Shi, N. N.; et al. Reliable Exfoliation of Large-Area High-Quality Flakes of Graphene and Other Two-Dimensional Materials. *ACS Nano* **2015**, *9* (11), 10612-10620. DOI: 10.1021/acsnano.5b04258

(50) Castellanos-Gomez, A.; Buscema, M.; Molenaar, R.; et al. Deterministic transfer of two-dimensional materials by all-dry viscoelastic stamping. *2D Materials* **2014**, *1* (1). DOI: 10.1088/2053-1583/1/1/011002

(1) Chakraborty, C.; Kinnischtzke, L.; Goodfellow, K. M.; et al. Voltage-controlled quantum light from an atomically thin semiconductor. *Nat Nanotechnol* **2015**, *10* (6), 507-511. DOI: 10.1038/nnano.2015.79

(2) He, Y. M.; Clark, G.; Schaibley, J. R.; et al. Single quantum emitters in monolayer semiconductors. *Nat Nanotechnol* **2015**, *10* (6), 497-502. DOI: 10.1038/nnano.2015.75

(3) Koperski, M.; Nogajewski, K.; Arora, A.; et al. Single photon emitters in exfoliated WSe_2 structures. *Nat Nanotechnol* **2015**, *10* (6), 503-506. DOI: 10.1038/nnano.2015.67

(4) Kumar, S.; Kaczmarczyk, A.; Gerardot, B. D. Strain-Induced Spatial and Spectral Isolation of Quantum Emitters in Mono- and Bilayer WSe_2. *Nano Lett* **2015**, *15* (11), 7567-7573. DOI: 10.1021/acs.nanolett.5b03312

(5) Srivastava, A.; Sidler, M.; Allain, A. V.; et al. Optically active quantum dots in monolayer WSe_2. *Nat Nanotechnol* **2015**, *10* (6), 491-496. DOI: 10.1038/nnano.2015.60

(6) Tonndorf, P.; Schmidt, R.; Schneider, R.; et al. Single-photon emission from localized excitons in an atomically thin semiconductor. *Optica* **2015**, *2* (4). DOI: 10.1364/optica.2.000347

(7) Drawer, J. C.; Mitryakhin, V. N.; Shan, H.; et al. Monolayer-Based Single-Photon Source in a Liquid-Helium-Free Open Cavity Featuring 65% Brightness and Quantum Coherence. *Nano Lett* **2023**, *23* (18), 8683-8689. DOI: 10.1021/acs.nanolett.3c02584

(8) Gao, T.; von Helversen, M.; Antón-Solanas, C.; et al. Atomically-thin single-photon sources for quantum communication. *npj 2D Materials and Applications* **2023**, *7* (1). DOI: 10.1038/s41699-023-00366-4

(9) Branny, A.; Kumar, S.; Proux, R.; et al. Deterministic strain-induced arrays of quantum emitters in a two-dimensional semiconductor. *Nat Commun* **2017**, *8* (1), 15053. DOI: 10.1038/ncomms15053

(10) Rosati, R.; Schmidt, R.; Brem, S.; et al. Dark exciton anti-funneling in atomically thin semiconductors. *Nat Commun* **2021**, *12* (1), 7221. DOI: 10.1038/s41467-021-27425-y

(11) Kim, J. M.; Jeong, K. Y.; Kwon, S.; et al. Strained two-dimensional tungsten diselenide for mechanically tunable exciton transport. *Nat Commun* **2024**, *15* (1), 10847. DOI: 10.1038/s41467-024-55135-8

(12) Parto, K.; Azzam, S. I.; Banerjee, K.; et al. Defect and strain engineering of monolayer WSe_2 enables site-controlled single-photon emission up to 150 K. *Nat Commun* **2021**, *12* (1), 3585. DOI: 10.1038/s41467-021-23709-5

(13) Yanev, E. S.; Darlington, T. P.; Ladyzhets, S. A.; et al. Programmable nanowrinkle-induced room-temperature exciton localization in monolayer WSe_2. *Nat Commun* **2024**, *15* (1), 1543. DOI: 10.1038/s41467-024-45936-2

(14) Iff, O.; Buchinger, Q.; Moczala-Dusanowska, M.; et al. Purcell-Enhanced Single Photon Source Based on a Deterministically Placed WSe_2 Monolayer Quantum Dot in a Circular Bragg Grating Cavity. *Nano Lett* **2021**, *21* (11), 4715-4720. DOI: 10.1021/acs.nanolett.1c00978

(15) Sortino, L.; Zotev, P. G.; Phillips, C. L.; et al. Bright single photon emitters with enhanced quantum efficiency in a two-dimensional semiconductor coupled with dielectric nano-antennas. *Nat Commun* **2021**, *12* (1), 6063. DOI: 10.1038/s41467-021-26262-3

(16) Paralikis, A.; Piccinini, C.; Madigawa, A. A.; et al. Tailoring polarization in WSe_2 quantum emitters through deterministic strain engineering. *NPJ 2D Mater Appl* **2024**, *8* (1), 59. DOI: 10.1038/s41699-024-00497-2

(17) Azzam, S. I.; Parto, K.; Moody, G. Purcell enhancement and polarization control of single-photon emitters in monolayer WSe_2 using dielectric nanoantennas. *Nanophotonics* **2023**, *12* (3), 477-484. DOI: 10.1515/nanoph-2022-0628

(18) Luo, Y.; Shepard, G. D.; Ardelean, J. V.; et al. Deterministic coupling of site-controlled quantum emitters in monolayer WSe_2 to plasmonic nanocavities. *Nat Nanotechnol* **2018**, *13* (12), 1137-1142. DOI: 10.1038/s41565-018-0275-z

(19) Luo, Y.; Liu, N.; Li, X.; et al. Single photon emission in WSe_2 up to 160 K by quantum yield control. *2D Materials* **2019**, *6* (3). DOI: 10.1088/2053-1583/ab15fe

(20) Luo, Y.; Liu, N.; Kim, B.; et al. Exciton Dipole Orientation of Strain-Induced Quantum Emitters in WSe_2. *Nano Lett* **2020**, *20* (7), 5119-5126. DOI: 10.1021/acs.nanolett.0c01358

(21) Park, K. D.; Khatib, O.; Kravtsov, V.; et al. Hybrid Tip-Enhanced Nanospectroscopy and Nanoimaging of Monolayer WSe_2 with Local Strain Control. *Nano Lett* **2016**, *16* (4), 2621-2627. DOI: 10.1021/acs.nanolett.6b00238

(22) Park, K. D.; Jiang, T.; Clark, G.; et al. Radiative control of dark excitons at room temperature by nano-optical antenna-tip Purcell effect. *Nat Nanotechnol* **2018**, *13* (1), 59-64. DOI: 10.1038/s41565-017-0003-0

(23) Xu, D. D.; Vong, A. F.; Utama, M. I. B.; et al. Sub-Diffraction Correlation of Quantum Emitters and Local Strain Fields in Strain-Engineered WSe_2 Monolayers. *Adv Mater* **2024**, *36* (25), e2314242. DOI: 10.1002/adma.202314242

(24) Abramov, A. N.; Chestnov, I. Y.; Alimova, E. S.; et al. Photoluminescence imaging of single photon emitters within nanoscale strain profiles in monolayer WSe_2. *Nat Commun* **2023**, *14* (1), 5737. DOI: 10.1038/s41467-023-41292-9

(25) Daveau, R. S.; Vandekerckhove, T.; Mukherjee, A.; et al. Spectral and spatial isolation of single tungsten diselenide quantum emitters using hexagonal boron nitride wrinkles. *APL Photonics* **2020**, *5* (9). DOI: 10.1063/5.0013825

(26) Rosenberger, M. R.; Dass, C. K.; Chuang, H. J.; et al. Quantum Calligraphy: Writing Single-Photon Emitters in a Two-Dimensional Materials Platform. *ACS Nano* **2019**, *13* (1), 904-912. DOI: 10.1021/acsnano.8b08730

(27) So, J. P.; Kim, H. R.; Baek, H.; et al. Electrically driven strain-induced deterministic single-photon emitters in a van der Waals heterostructure. *Sci Adv* **2021**, *7* (43), eabj3176. DOI: 10.1126/sciadv.abj3176

(28) Stevens, C. E.; Chuang, H. J.; Rosenberger, M. R.; et al. Enhancing the Purity of Deterministically Placed Quantum Emitters in Monolayer WSe_2. *ACS Nano* **2022**, *16* (12), 20956-20963. DOI: 10.1021/acsnano.2c08553

(29) Chang, S.; Yan, Y.; Geng, Y. Local Nanostrain Engineering of Monolayer MoS_2 Using Atomic Force Microscopy-Based Thermomechanical Nanoindentation. *Nano Lett* **2023**, *23* (20), 9219-9226. DOI: 10.1021/acs.nanolett.3c01809

(30) Li, X.; Jones, A. C.; Choi, J.; et al. Proximity-induced chiral quantum light generation in strain-engineered $WSe_2/NiPS_3$ heterostructures. *Nat Mater* **2023**, *22* (11), 1311-1316. DOI: 10.1038/s41563-023-01645-7

(31) Chuang, H. J.; Stevens, C. E.; Rosenberger, M. R.; et al. Enhancing Single Photon Emission Purity via Design of van der Waals Heterostructures. *Nano Lett* **2024**, *24* (18), 5529-5535. DOI: 10.1021/acs.nanolett.4c00683

(32) Cunningham, P. D.; Proscia, N. V.; LaGasse, S. W.; et al. Site-Specific Exciton–Plasmon Coupling in Nanoindented WSe_2. *ACS Photonics* **2024**, *11* (8), 3250-3258. DOI: 10.1021/acsphotonics.4c00644

(33) Gavin, S. C.; Chuang, H. J.; Dasgupta, A.; et al. High-Temperature Single-Photon Emission From Covalently Functionalized van der Waals Heterostructures. *Adv Sci (Weinh)* **2025**, *12* (48), e11319. DOI: 10.1002/advs.202511319

(34) Lee, S. J.; Chuang, H. J.; McCreary, K. M.; et al. Voltage-Induced Degradation for Enhanced Purity and Reproducibility of Quantum Emission in Monolayer 2D Materials. *ACS Nano* **2025**, *19* (38), 33981-33990. DOI: 10.1021/acsnano.5c09799

(35) Yücel, O.; Yagodkin, D.; Kirchhof, J. N.; et al. Strain activation of localized states in WSe_2. *2D Materials* **2025**, *12* (3). DOI: 10.1088/2053-1583/add414

(36) Dong, S.; Beaulieu, S.; Selig, M.; et al. Observation of ultrafast interfacial Meitner-Auger energy transfer in a Van der Waals heterostructure. *Nat Commun* **2023**, *14* (1), 5057. DOI: 10.1038/s41467-023-40815-8

(37) Budania, P.; Baine, P. T.; Montgomery, J. H.; et al. Comparison between Scotch tape and gel-assisted mechanical exfoliation techniques for preparation of 2D transition metal dichalcogenide flakes. *Micro & Nano Letters* **2017**, *12* (12), 970-973. DOI: 10.1049/mnl.2017.0280

(38) Pan, Y.; Rahaman, M.; He, L.; et al. Exciton tuning in monolayer WSe_2 via substrate induced electron doping. *Nanoscale Adv* **2022**, *4* (23), 5102-5108. DOI: 10.1039/d2na00495j

(39) Xing, X.; Zhao, L.; Zhang, W.; et al. Influence of a substrate on ultrafast interfacial charge transfer and dynamical interlayer excitons in monolayer WSe_2/graphene heterostructures. *Nanoscale* **2020**, *12* (4), 2498-2506. DOI: 10.1039/c9nr09309e

(40) Yang, K.; Yang, Y.; Rhodes, D. A.; et al. Local strain-engineering of exciton energy in 2D materials with nanoindentation. *Nanoscale* **2026**, *18* (10), 5575-5587. DOI: 10.1039/d6nr00112b

(41) He, J.; Kumar, N.; Bellus, M. Z.; et al. Electron transfer and coupling in graphene-tungsten disulfide van der Waals heterostructures. *Nat Commun* **2014**, *5*, 5622. DOI: 10.1038/ncomms6622

(42) Hill, H. M.; Rigosi, A. F.; Raja, A.; et al. Exciton broadening in WS_2/graphene heterostructures. *Physical Review B* **2017**, *96* (20). DOI: 10.1103/PhysRevB.96.205401

(43) Liang, J.; Xu, K.; Toncini, B.; et al. Impact of Post-Lithography Polymer Residue on the Electrical Characteristics of MoS_2 and WSe_2 Field Effect Transistors. *Advanced Materials Interfaces* **2018**, *6* (3). DOI: 10.1002/admi.201801321

(44) Urban, F.; Martucciello, N.; Peters, L.; et al. Environmental Effects on the Electrical Characteristics of Back-Gated WSe_2 Field-Effect Transistors. *Nanomaterials (Basel)* **2018**, *8* (11). DOI: 10.3390/nano8110901

(45) Zhou, H.; Chen, Y.; Zhu, H. Deciphering asymmetric charge transfer at transition metal dichalcogenide-graphene interface by helicity-resolved ultrafast spectroscopy. *Sci Adv* **2021**, *7* (34). DOI: 10.1126/sciadv.abg2999

(46) Linhart, L.; Paur, M.; Smejkal, V.; et al. Localized Intervalley Defect Excitons as Single-Photon Emitters in WSe_2. *Phys Rev Lett* **2019**, *123* (14), 146401. DOI: 10.1103/PhysRevLett.123.146401

(47) Klingshirn, C. *Semiconductor Optics*; 2007. DOI: 10.1007/978-3-540-38347-5.

(48) Novoselov, K. S.; Geim, A. K.; Morozov, S. V.; et al. Electric field effect in atomically thin carbon films. *Science* **2004**, *306* (5696), 666-669. DOI: 10.1126/science.1102896

(49) Huang, Y.; Sutter, E.; Shi, N. N.; et al. Reliable Exfoliation of Large-Area High-Quality Flakes of Graphene and Other Two-Dimensional Materials. *ACS Nano* **2015**, *9* (11), 10612-10620. DOI: 10.1021/acsnano.5b04258

(50) Castellanos-Gomez, A.; Buscema, M.; Molenaar, R.; et al. Deterministic transfer of two-dimensional materials by all-dry viscoelastic stamping. *2D Materials* **2014**, *1* (1). DOI: 10.1088/2053-1583/1/1/011002

CHAPTER SIX

CONCLUSION

6.1 Summary and Outlook

In summary, the work conducted in this dissertation studied single photon emitters (SPEs) in single-layer WSe_2 (1L-WSe_2) when integrated with nanophotonic devices such as embedded plasmonic nanoantennas, gold nano-inversions/indentations, and graphite-covered nanoindentations. This work contributes to a large body of knowledge on the study of SPEs to better understand their origin, formation mechanisms, and excited state dynamics. The impact of the embedded plasmonic nanoantennas seen in Chapter 4 is especially important to me. This platform could pave the way for the direct correlation between room temperature defect emission and cryogenic SPE states, theorized to originate from individual point defects in the 1L-WSe_2. This correlation measurement was the intended goal of the structure after we were successful in fabrication. However, the sensitivity of highly strained 1L-WSe_2 over a sharp nanoantenna and the arduousness of near-field optical spectroscopy made the realization of this correlation exceedingly difficult, and all of the samples fabricated here were unfortunately destroyed. Nevertheless, the fabrication procedures, optical spectroscopy techniques, and data analysis conducted will be passed on to the next generation of 2D materials scientists to contribute to the future of solid-state quantum light sources.

6.2 Ongoing Studies and Future Directions

Embedded Micropillar Arrays

In Chapter 4, we report the fabrication procedure for embedded plasmonic nanoantennas based on thermal scanning probe lithography, buffered oxide etching, and lift-off. This fabrication process was originally developed for embedded micropillar arrays over the first 4 years of my Ph.D. The fabrication techniques, cryogenic photoluminescence (PL), and 2D materials transferring conducted for the micropillar project built a platform for the rest of the research done in this dissertation, so quickly after getting results, other higher-impact projects began to move quickly and garner most of my focus. However, during the micropillar project, we discovered a process for deterministic strain generation and arrays of SPE sites using only optical lithography, and to what we are aware, this is yet to be done in the literature. Nearly all stressors for SPE generation with 2D materials are either done using electron beam lithography or in-situ photolithography, not wide-scale optical lithography. The benefit of optical lithography is that you can expose and create an entire wafer of micropillar sites all at once, as opposed to requiring individual writing for each specific site. Assuming micropillar site center-to-center spacings of ~10 μm, this results in nearly 79 million sites per 4-inch wafer!

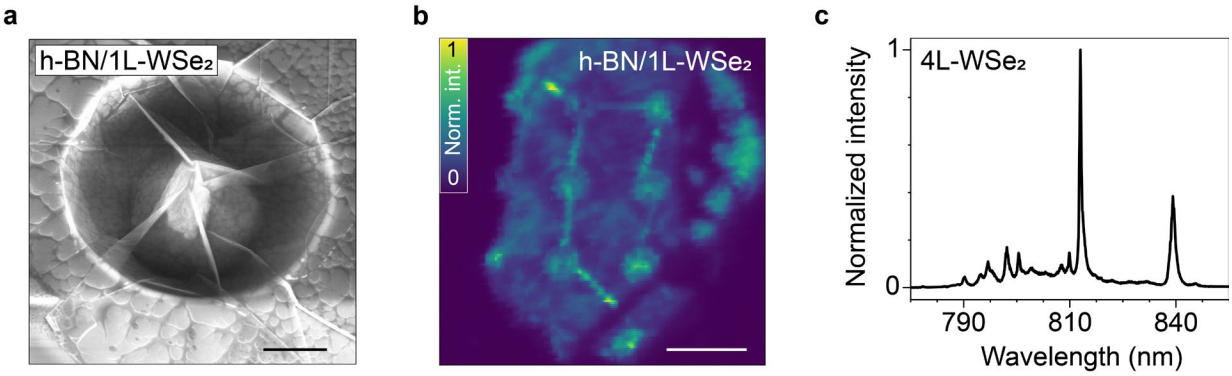


Figure 6.2.1: Embedded aluminum micropillars. (a) An SEM image of a h-BN/1L-WSe_2 heterostructure transferred onto an embedded micropillar site. (b) 4 K hyperspectral PL intensity map of an array of embedded micropillar sites covered by a h-BN/1L-WSe_2 heterostructure. (c) 4 K PL spectra of 4L-WSe_2 on top of an embedded micropillar. Scale bars are 1 μm and 10 μm for (a) and (b), respectively.

Using micropillars, we were able to realize quantum light generation in h-BN, 1L-WSe_2, h-BN/1L-WSe_2 heterostructures, and most interestingly, 4L-WSe_2, which is yet to be reported in the literature. Shown in Figure 6.2.1a is an SEM image of an embedded aluminum micropillar with a h-BN/1L-WSe_2 heterostructure transferred over it. As is evident, wrinkles radiate from the apex, as is also seen in the nanoscale conjugates in Chapter 4. Taking 4 K PL of these sites results in a rich suite of structure property relationships between the generated wrinkles and micropillar sites, localizing excitons to the highly strained regions (Figure 6.2.1b). Lastly, when studying few-layer WSe_2 on these sites, we noticed narrow emission lines coming from 3L and 4L-WSe_2 under large amounts (~250 μW) of 532 nm excitation (Figure 6.2.1c). Single photon antibunching was never conducted on this sample, but the appearance of these states is incredibly similar to the SPEs seen in 1L and 2L-WSe_2 and is deserving of future analysis.

Selective Excitation of SPEs Using Narrow Beams

This project originated from a finite element analysis of Au nanocones, similar to those of Chapter 4, where instead of maintaining the polarization state of the excitation beam to be aligned with the long axis of the nanocone, we rotated the polarization by changing the angle of incidence. We noted that the near-field enhancement spot generated by the localized surface plasmon resonance (LSPR) rotated commensurate with the excitation polarization for certain nanocone geometries. Seen in Figure 6.2.2a for a 45° angle of incidence, the hotspot is shifted away from the center. By running finite element models over all non-equivalent angles of incidence, we see this hotspot move nearly continuously around the spherical particle that makes up the nanocone apex (Figure 6.2.2b).

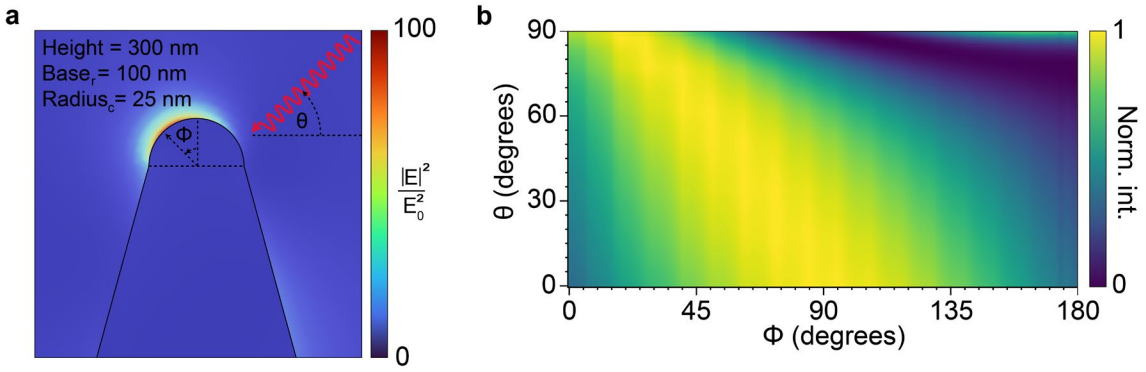


Figure 6.2.2: Selective near-field excitation. (a) Finite element model showing the near-field hotspot of a gold nanocone offset by ~45° due to a rotated angle of incidence of the excitation beam. Here, Φ is the angle away from the nanocone long axis that shows maximum field intensity. (b) A summary of finite element models similar to (a), where the maximum field intensity is extracted for a variety of different angles of incidence. At an angle of incidence of 0°, the maximum intensity is directly above the long axis of the nanocone, but as the angle of incidence is rotated, this maximum also rotates, indicated by the maximum intensity in (b) going to the left.

Giving it more direct thought, this rotation of the LSPR mode for a spherical particle is quite intuitive but has not been taken advantage of in the literature. Our intentions with this effect

were to use low defect density flux-synthesized 1L-WSe_2, and the embedded plasmonic nanoantennas in Chapter 4 of this dissertation were to selectively excite a specific SPE state by tuning the angle of incidence of the excitation beam. By reducing the beam waist of the excitation laser to a fraction of the size of the back aperture of our objective and sending it into different regions, we could vary the angle of incidence. This type of measurement would make SPE sites individually addressable and could have a future purpose in 1L-WSe_2-based quantum technologies.

Enhancing the Outcoupling of SPEs in Graphite Covered 1L-WSe_2 Nanoindents Using Polymer Microlenses

After measuring the increased PL intensity of SPE states in graphite-covered 1L-WSe_2 nanoindents in Chapter 5, the thought of fabricating microlenses on top of a specific indent site to increase the collection efficiency from the nanoindent became a nagging thought. Inspired by a study conducted in 2022 on h-BN single photon sources[1], we aimed to replicate their design for microlens arrays but with SPEs in 1L-WSe_2. Graphite-covered indents were a promising platform for this application because the SPEs from these nanoindents were already some of the brightest ever recorded, so by collecting even a factor of two more photons that are normally not collected because of inaccessible photon k vectors to the NA of our microscope objective, we may be in contention for the record of brightest SPEs in 1L-WSe_2. Also, since graphite quenched excitonic emission from everywhere but the nanoindents, the micron-sized scale of the microlenses would not collect light from anywhere but the nanoindent, avoiding the issue of thousands of SPEs crowding the same 4 K PL spectra.

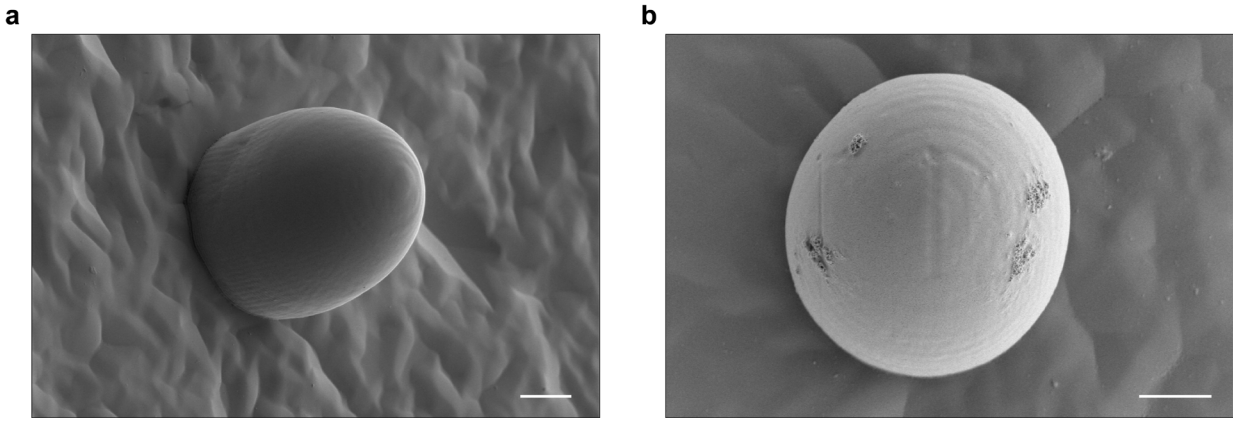


Figure 6.2.3: SEM images of polymer microlenses. (a-b) SEM images of Au-coated polymer microlenses fabricated on a SiO_2 surface taken at 45° and 0° angle of incidence, respectively. Scale bars are 4μm.

To fabricate these structures, seen in Figures 6.2.3a-b, we collaborated with Spectrum Lab, which has access to a two-photon lithography system. Two-photon lithography is a technique where a tightly focused femtosecond laser polymerizes a photosensitive resin in a small volume called a voxel. We had preliminary success with this project and even succeeded in fabricating microlenses on top of graphite flakes on poly(methyl methacrylate)(PMMA) substrates. Near our first attempt at fabricating a microlens on top of an actual graphite-covered indent, the two-photon lithography system was being moved from one lab to another across the building, which put the system out of commission for a couple of months, abruptly ending the project. However, if this project were to be fully realized, this hybrid photonic lens and 2D material heterostructure may act as the source for the brightest SPEs in 1L-WSe_2.

Using Dielectric Layers for the Nanoinversion Process

The nanoinversion process developed in Chapter 3 played a critical role in determining the role of tearing in 1L-WSe_2 nanoindents, but also simultaneously quenched all excitonic emission from the 1L-WSe_2. The simplicity, relatively low tool cost, and speed of the nanoinversion process

positioned it as an ideal entry-level fabrication procedure for nanoscale strain generation of 1L-WSe_2, permitting that a dielectric material could be used rather than Au. We attempted to use dielectric materials a handful of different times and did not have consistent results. From intuition, it seemed that deposition of SiO_2 as opposed to Au, or even a thin layer of Al_2O_3 before the Au, should also successfully invert the nanoindents, but it was held back by adhesion issues. The 1L-WSe_2 was inconsistently left behind in the PMMA layer rather than staying attached to the new dielectric. This difference could be attributed to the strong adhesion between WSe_2 and clean Au layers that is used for Au-assisted exfoliation[2-5], but for Au-assisted exfoliation, the success is highly dependent on a smooth, uniform, and clean Au film, and direct evaporation of Au into a cavity does not seem conducive to this.

One assumption is that the inconsistent inversion was caused by the nonuniformity of the dielectric depositions, resulting in a reduced contact area between the dielectric and the 1L-WSe_2. The electron beam evaporator used to deposit SiO_2 has a crucible offset from the sample holding platform, so to achieve normal incidence into the nanoindent, the sample stage had to be rotated to face the crucible. Around 6 months after attempting this process, we discovered that the rotation angle used by the microfabrication facility was off by ~10°. This difference could have led to shadow masking in the apex of the nanoindent (Chapter 3, Supplementary Figure 3) and a reduced likelihood of successful inversion. We also attempted Al_2O_3 deposition using atomic layer deposition (ALD) before Au evaporation, but the ALD tool was always finicky, and we never fully trusted or deeply investigated the consistency of the Al_2O_3 layers.

The Role of Au Nanostructures on SPE Emission in 1L-WSe_2 Nanoribbons

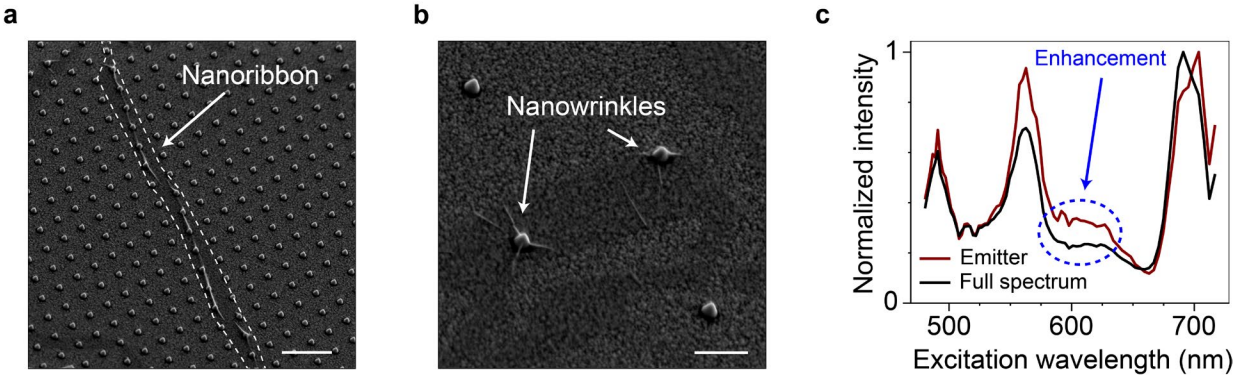


Figure 6.2.4: Plasmonic enhancement in 1L-WSe_2 nanoribbons on Au nanostressors. (a-b) SEM images of 1L-WSe_2 nanoribbons transferred onto Au nanocones. (c) PLE spectra of an enhanced emitter state, and the full 4 K PLE spectrum.

Through our close collaboration with Columbia University and the Honda Research Institute, we gained access to studying 1L-WSe_2 nanoribbons transferred onto Au nanocone and nanopyramids (Figure 6.2.4a-b). These nanoribbons range in width from ~50 nm to a couple μms and, when coupled with the Au nanostressors, have been shown to host SPE states that persist to temperatures as high as 120 K. Interestingly, when the same nanoribbons are isolated from the Au nanostressors, their SPE states are greatly diminished in purity and quantum efficiency. In this highly collaborative project, my role was to study the purpose of the underlying Au resonators using photoluminescence excitation spectroscopy (PLE). Similar to the PLE conducted in Chapter 4 for the embedded plasmonic nanoantennas, we have identified signatures of plasmonic enhancement in specific SPE states that we believe to be localized to nanowrinkles near the apex of the nanostressor.

6.3 Future Directions

SPEs in 1L-WSe_2 provide promise as a platform for nanoscale quantum light generation due to their optical accessibility, origins from an atomically thin sheet, mechanical flexibility, and integration into 2D materials heterostructures. Unlike other solid-state SPE sources, such as NV centers in diamond and quantum dots, 1L-WSe_2 can be easily transferred and positioned onto photonic chips, dielectric and metallic resonators, and electrical structures that permits engineering of the local optical density of states and tailored emission. However, realizing practical devices based on 1L-WSe_2 SPEs has proven challenging and requires more precise control over emitter formation, spectral uniformity and consistency, brightness, and coupling to optical modes.

A central future direction is to establish the formation mechanism of 1L-WSe_2 SPEs and their relationship with localized tensile strain, point defects, and dark excitons. As discussed in Chapters 1 and 4 of this dissertation, some aspects of the Linhart theory have been extensively studied and verified to result in SPE formation, but a correlation measurement of cryogenic SPE emission to localized defect emission at room temperature using near-field techniques is yet to be achieved. This measurement would provide the necessary data to further advance the nanoscale strain and defect engineering required for high-quality SPE sources in 1L-WSe_2. The nano-optical platform shown in Chapter 4 could illustrate the hybridization picture of dark excitons with defect levels in the 1L-WSe_2 electronic band structure by prescribing a variety of different tensile strain values in 1L-WSe_2 while using the same underlying plasmonic resonator fixed to the average SPE wavelength. The current understanding is that tensile strain is required for SPE formation, but if SPE formation occurs because of hybridization, an optimal value of tensile strain should also exist where dark excitons are fully degenerate with the defect levels. We tried to experimentally discover

an optimal value of tensile strain in Chapter 3 of this dissertation using nanoindentation, but came ot the conclusion that nanoindentation results in a non-uniform strain profile that made emitter brightness strain tunability hard to visualize. Nevertheless, figuring out this optimal value would completely change the current approach for fabricating bright SPE states in 1L-WSe_2. Instead of simply generating tensile strain, now locally enhancing SPEs using nanophotonics and ensuring the tensile strain in the near-field enhancement region is commensurate with the optimal tensile strain value would produce the brightness emission.

Another future direction is controlling the dielectric/charge environment of excitons in 1L-WSe_2 using 2D material adlayers and gating. As discussed in detail in Chapter 1, the 2D materials community has established that h-BN encapsulation increases the stability of SPEs in 1L-WSe_2 by generating a more consistent dielectric environment. In Chapter 5, we study the effects of a graphite adlayer on nanoindented 1L-WSe_2 in the context of SPE enhancement. We found that the addition of graphite likely reduces the non-radiative recombination rate of quantum emitters and may lead to charge state stabilization of localized defect sites that act as exciton traps for SPE formation. This type of tailoring of the dielectric/charge environment not only results in SPEs that are more stable and recombine more radiatively, but also can increase the purity and brightness while reducing the linewidth of the states.

With all of the above optimizations considered, the long-term application of 1L-WSe_2 SPEs likely comes from their compatibility with on-chip photonic integrated circuits (PICs). In a PIC, single photons can be generated, routed, filtered, interfered, and coupled off-chip using optical components such as waveguides, cavities, resonators, beamsplitters, and grating couplers. Some of these optical components have been individually studied with 1L-WSe_2 already, but future

devices will need multiple components integrated and controllable SPE states. The nanoantenna structures studied in Chapter 4 of this dissertation do not form a complete PIC, but they do demonstrate several design principles relevant to future PICs, such as pre-patterning, optical environment design, and plasmonic/strain tuning. Extending these principles to a more complex system is required for future studies to see SPEs in 1L-WSe_2 to be harnessed to their full potential.

Chapter 6 References

(1) Preuss, J. A.; Gehring, H.; Schmidt, R.; et al. Low-Divergence hBN Single-Photon Source with a 3D-Printed Low-Fluorescence Elliptical Polymer Microlens. *Nano Lett* **2023**, *23* (2), 407-413. DOI: 10.1021/acs.nanolett.2c03001

(2) Chen, S.; Li, B.; Dai, C.; et al. Controlling Gold-Assisted Exfoliation of Large-Area MoS_2 Monolayers with External Pressure. *Nanomaterials (Basel)* **2024**, *14* (17). DOI: 10.3390/nano14171418

(3) Panasci, S. E.; Schilirò, E.; Migliore, F.; et al. Substrate impact on the thickness dependence of vibrational and optical properties of large area MoS_2 produced by gold-assisted exfoliation. *Applied Physics Letters* **2021**, *119* (9). DOI: 10.1063/5.0062106

(4) Panasci, S. E.; Schiliro, E.; Greco, G.; et al. Strain, Doping, and Electronic Transport of Large Area Monolayer MoS_2 Exfoliated on Gold and Transferred to an Insulating Substrate. *ACS Appl Mater Interfaces* **2021**, *13* (26), 31248-31259. DOI: 10.1021/acsami.1c05185

(5) Velicky, M.; Donnelly, G. E.; Hendren, W. R.; et al. Mechanism of Gold-Assisted Exfoliation of Centimeter-Sized Transition-Metal Dichalcogenide Monolayers. *ACS Nano* **2018**, *12* (10), 10463-10472. DOI: 10.1021/acsnano.8b06101

(1) Preuss, J. A.; Gehring, H.; Schmidt, R.; et al. Low-Divergence hBN Single-Photon Source with a 3D-Printed Low-Fluorescence Elliptical Polymer Microlens. *Nano Lett* **2023**, *23* (2), 407-413. DOI: 10.1021/acs.nanolett.2c03001

(2) Chen, S.; Li, B.; Dai, C.; et al. Controlling Gold-Assisted Exfoliation of Large-Area MoS_2 Monolayers with External Pressure. *Nanomaterials (Basel)* **2024**, *14* (17). DOI: 10.3390/nano14171418

(3) Panasci, S. E.; Schilirò, E.; Migliore, F.; et al. Substrate impact on the thickness dependence of vibrational and optical properties of large area MoS_2 produced by gold-assisted exfoliation. *Applied Physics Letters* **2021**, *119* (9). DOI: 10.1063/5.0062106

(4) Panasci, S. E.; Schiliro, E.; Greco, G.; et al. Strain, Doping, and Electronic Transport of Large Area Monolayer MoS_2 Exfoliated on Gold and Transferred to an Insulating Substrate. *ACS Appl Mater Interfaces* **2021**, *13* (26), 31248-31259. DOI: 10.1021/acsami.1c05185

(5) Velicky, M.; Donnelly, G. E.; Hendren, W. R.; et al. Mechanism of Gold-Assisted Exfoliation of Centimeter-Sized Transition-Metal Dichalcogenide Monolayers. *ACS Nano* **2018**, *12* (10), 10463-10472. DOI: 10.1021/acsnano.8b06101

CUMULATIVE REFERENCES CITED

(1) Yang, K.; Yang, Y.; Rhodes, D. A.; et al. Local strain-engineering of exciton energy in 2D materials with nanoindentation. *Nanoscale* **2026**, *18* (10), 5575-5587. DOI: 10.1039/d6nr00112b

(2) Xiao, L.; Liu, Y.; Mohajerani, S. S.; et al. Quantum Light Funneling in Tailored Triangular Plasmonic Nanocavities. *ACS Nano* **2026**. DOI: 10.1021/acsnano.5c16988

(3) Huang, G.; Chen, R.; Chen, M.; et al. Transfer and beyond: emerging strategies and trends in two-dimensional material device fabrication. *Chem Soc Rev* **2026**. DOI: 10.1039/d5cs00531k

(4) HQ Graphene. *HQ Graphene all semiconductors*. 2026. https://www.hqgraphene.com/All-Semiconductors.php (accessed March 5, 2026).

(5) Giza, M.; Mukhopadhyay, K.; Ravichandran, H.; et al. Exploring the Application of Gold-Assisted Exfoliation in Large-scale Integration of n-Type and p-Type 2D-FETs. *Small Methods* **2026**, *10* (3), e2500559. DOI: 10.1002/smtd.202500559

(6) 2D Semiconductors. *2D Semiconductors all products*. 2026. https://2dsemiconductors.com/all-products/ (accessed March 5, 2026).

(7) Yücel, O.; Yagodkin, D.; Kirchhof, J. N.; et al. Strain activation of localized states in WSe_2. *2D Materials* **2025**, *12* (3). DOI: 10.1088/2053-1583/add414

(8) Strasbourg, M. C.; Yanev, E. S.; Parvez, S.; et al. Structure-Dependent Dynamics of Quantum Emitters in Single-Layer WSe_2. *Nano Lett* **2025**, *25* (25), 10254-10261. DOI: 10.1021/acs.nanolett.5c02620

(9) Ren, T.; Granados Del Aguila, A.; Chen, Z.; et al. Van der Waals photonic integrated circuit with coherent light generation. *Nat Commun* **2025**, *16* (1), 5931. DOI: 10.1038/s41467-025-60778-2

(10) Paralikis, A.; Wyborski, P.; Metuh, P.; et al. Tunable and Low-Noise WSe_2 Quantum Emitters for Quantum Photonics. *PRX Quantum* **2025**, *6* (4). DOI: 10.1103/cynh-ql3j

(11) Mørch Nielsen, C. E.; Fischer, F.; Bester, G. Beyond the K-valley: exploring unique trion states in indirect band gap monolayer WSe_2. *npj 2D Materials and Applications* **2025**, *9* (1). DOI: 10.1038/s41699-025-00532-w

(12) Mohajerani, S. S.; Noual, A.; Ma, Y.; et al. Acoustic Manipulation of Deterministic Quantum Emitters in WSe_2. *ACS Nano* **2025**, *19* (28), 25851-25859. DOI: 10.1021/acsnano.5c04710

(13) Lee, S. J.; Chuang, H. J.; McCreary, K. M.; et al. Voltage-Induced Degradation for Enhanced Purity and Reproducibility of Quantum Emission in Monolayer 2D Materials. *ACS Nano* **2025**, *19* (38), 33981-33990. DOI: 10.1021/acsnano.5c09799

(14) Lan, H. Y.; Lin, C. P.; Liu, L.; et al. Uncovering the doping mechanism of nitric oxide in high-performance P-type WSe_2 transistors. *Nat Commun* **2025**, *16* (1), 4160. DOI: 10.1038/s41467-025-59423-9

(15) Holbrook, M.; Holtzman, L. N.; Hou, B.; et al. Revealing Substitutional Oxygen as the Dominant Defect in Flux-Grown Transition Metal Diselenides. *Nano Lett* **2025**, *25* (37), 13795-13801. DOI: 10.1021/acs.nanolett.5c03126

(16) Gavin, S. C.; Chuang, H. J.; Dasgupta, A.; et al. High-Temperature Single-Photon Emission From Covalently Functionalized van der Waals Heterostructures. *Adv Sci (Weinh)* **2025**, *12* (48), e11319. DOI: 10.1002/advs.202511319

(17) Fix, J. P. Bandgap Engineering of 2D Semiconductors for Quantum and Optoelectronic Technologies. Montana State University, 2025.

(18) Chou, S. A.; Chang, C.; Wu, B. H.; et al. Large-scale alkali-assisted growth of monolayer and bilayer WSe_2 with a low defect density. *Nat Commun* **2025**, *16* (1), 2777. DOI: 10.1038/s41467-025-57986-1

(19) Ananth, R.; Utama, M. I. B.; Xu, D. D.; et al. Enhanced spectral purity of WSe_2 quantum emitters via conformal organic adlayers. *Sci Adv* **2025**, *11* (40), eady7557. DOI: 10.1126/sciadv.ady7557

(20) Ai, R.; Cui, X.; Li, Y.; et al. Local Strain Engineering of Two-Dimensional Transition Metal Dichalcogenides Towards Quantum Emitters. *Nanomicro Lett* **2025**, *17* (1), 104. DOI: 10.1007/s40820-024-01611-1

(21) Zhou, J.; Goncalves, P. A. D.; Riminucci, F.; et al. Probing plexciton emission from 2D materials on gold nanotrenches. *Nat Commun* **2024**, *15* (1), 9583. DOI: 10.1038/s41467-024-53669-5

(22) Yu, Y.; Seo, I. C.; Luo, M.; et al. Tunable single-photon emitters in 2D materials. *Nanophotonics* **2024**, *13* (19), 3615-3629. DOI: 10.1515/nanoph-2024-0050

(23) Yao, J.; Lai, F.; Fan, Y.; et al. Nonlocal meta-lens with Huygens' bound states in the continuum. *Nat Commun* **2024**, *15* (1), 6543. DOI: 10.1038/s41467-024-50965-y

(24) Yanev, E. S.; Darlington, T. P.; Ladyzhets, S. A.; et al. Programmable nanowrinkle-induced room-temperature exciton localization in monolayer WSe_2. *Nat Commun* **2024**, *15* (1), 1543. DOI: 10.1038/s41467-024-45936-2

(25) Xu, D. D.; Vong, A. F.; Utama, M. I. B.; et al. Sub-Diffraction Correlation of Quantum Emitters and Local Strain Fields in Strain-Engineered WSe_2 Monolayers. *Adv Mater* **2024**, *36* (25), e2314242. DOI: 10.1002/adma.202314242

(26) Strasbourg, M. C.; Yanev, E. S.; Parvez, S.; et al. Increased Formation of Trions and Charged Biexcitons by Above-Gap Excitation in Single-layer WSe_2. *ACS Nano* **2024**, *18* (47), 32973-32983. DOI: 10.1021/acsnano.4c13208

(27) Strasbourg, M. C.; Yanev, E. S.; Darlington, T. P.; et al. Characterization of quantum dot-like emitters in programmable arrays of nanowrinkles of 1L-WSe_2. *Journal of Applied Physics* **2024**, *136* (4). DOI: 10.1063/5.0214410

(28) Shih, Y.-C.; Nilsson, F. A.; Guo, G.-Y. Electron energy loss spectra and exciton band structure of WSe_2 monolayers studied by ab initio Bethe-Salpeter equation calculations. *Physical Review B* **2024**, *110* (20). DOI: 10.1103/PhysRevB.110.205417

(29) Serati de Brito, C.; Rosa, B. L. T.; Chaves, A.; et al. Probing the Nature of Single-Photon Emitters in a WSe_2 Monolayer by Magneto-Photoluminescence Spectroscopy. *Nano Lett* **2024**, *24* (42), 13300-13306. DOI: 10.1021/acs.nanolett.4c03686

(30) Sakib, M. A.; Triplett, B.; Harris, W.; et al. Purcell-Induced Bright Single Photon Emitters in Hexagonal Boron Nitride. *Nano Lett* **2024**, *24* (40), 12390-12397. DOI: 10.1021/acs.nanolett.4c02581

(31) Paralikis, A.; Piccinini, C.; Madigawa, A. A.; et al. Tailoring polarization in WSe_2 quantum emitters through deterministic strain engineering. *NPJ 2D Mater Appl* **2024**, *8* (1), 59. DOI: 10.1038/s41699-024-00497-2

(32) Li, X.; Wyss, S.; Yanev, E.; et al. Width-dependent continuous growth of atomically thin quantum nanoribbons from nanoalloy seeds in chalcogen vapor. *Nat Commun* **2024**, *15* (1), 10080. DOI: 10.1038/s41467-024-54413-9

(33) Li, J.; Chen, J.; Yan, D.; et al. A Review: Active Tunable Terahertz Metamaterials. *Advanced Photonics Research* **2024**, *5* (7). DOI: 10.1002/adpr.202300351

(34) Li, C.; Luo, H.; Hou, L.; et al. Giant Photoluminescence Enhancement of Monolayer WSe_2 Using a Plasmonic Nanocavity with On-Demand Resonance. *Nano Lett* **2024**, *24* (19), 5879-5885. DOI: 10.1021/acs.nanolett.4c01260

(35) Kim, J. M.; Jeong, K. Y.; Kwon, S.; et al. Strained two-dimensional tungsten diselenide for mechanically tunable exciton transport. *Nat Commun* **2024**, *15* (1), 10847. DOI: 10.1038/s41467-024-55135-8

(36) Gérard, D.; Pierret, A.; Fartas, H.; et al. Quantum Efficiency and Vertical Position of Quantum Emitters in hBN Determined by Purcell Effect in Hybrid Metal-Dielectric Planar Photonic Structures. *ACS Photonics* **2024**, *11* (12), 5188-5194. DOI: 10.1021/acsphotonics.4c01416

(37) Garreis, R.; Tong, C.; Terle, J.; et al. Long-lived valley states in bilayer graphene quantum dots. *Nature Physics* **2024**, *20* (3), 428-434. DOI: 10.1038/s41567-023-02334-7

(38) Erbas, B.; Conde-Rubio, A.; Liu, X.; et al. Combining thermal scanning probe lithography and dry etching for grayscale nanopattern amplification. *Microsyst Nanoeng* **2024**, *10*, 28. DOI: 10.1038/s41378-024-00655-y

(39) Cunningham, P. D.; Proscia, N. V.; LaGasse, S. W.; et al. Site-Specific Exciton–Plasmon Coupling in Nanoindented WSe_2. *ACS Photonics* **2024**, *11* (8), 3250-3258. DOI: 10.1021/acsphotonics.4c00644

(40) Chuang, H. J.; Stevens, C. E.; Rosenberger, M. R.; et al. Enhancing Single Photon Emission Purity via Design of van der Waals Heterostructures. *Nano Lett* **2024**, *24* (18), 5529-5535. DOI: 10.1021/acs.nanolett.4c00683

(41) Chhaperwal, M.; Tongale, H. M.; Hays, P.; et al. Simultaneously Enhancing Brightness and Purity of WSe_2 Single Photon Emitter Using High-Aspect-Ratio Nanopillar Array on Metal. *Nano Lett* **2024**, *24* (40), 12461-12468. DOI: 10.1021/acs.nanolett.4c03168

(42) Chen, S.; Li, B.; Dai, C.; et al. Controlling Gold-Assisted Exfoliation of Large-Area MoS_2 Monolayers with External Pressure. *Nanomaterials (Basel)* **2024**, *14* (17). DOI: 10.3390/nano14171418

(43) Chen, S.; Chen, G.; Zhao, Y.; et al. Tunable Adhesion for All-Dry Transfer of 2D Materials Enabled by the Freezing of Transfer Medium. *Adv Mater* **2024**, *36* (15), e2308950. DOI: 10.1002/adma.202308950

(44) Casses, L. N.; Zhou, B.; Lin, Q.; et al. Full Quantitative Near-Field Characterization of Strongly Coupled Exciton–Plasmon Polaritons in Thin-Layered WSe_2 on a Monocrystalline Gold Platelet. *ACS Photonics* **2024**, *11* (9), 3593-3601. DOI: 10.1021/acsphotonics.4c00580

(45) Zhao, Y.; Tripathi, M.; Cernevics, K.; et al. Electrical spectroscopy of defect states and their hybridization in monolayer MoS_2. *Nat Commun* **2023**, *14* (1), 44. DOI: 10.1038/s41467-022-35651-1

(46) Yang, L.; Yuan, Y.; Fu, B.; et al. Revealing broken valley symmetry of quantum emitters in WSe_2 with chiral nanocavities. *Nat Commun* **2023**, *14* (1), 4265. DOI: 10.1038/s41467-023-39972-7

(47) Xu, D. D.; Vong, A. F.; Lebedev, D.; et al. Conversion of Classical Light Emission from a Nanoparticle-Strained WSe_2 Monolayer into Quantum Light Emission via Electron Beam Irradiation. *Adv Mater* **2023**, *35* (5), e2208066. DOI: 10.1002/adma.202208066

(48) Wang, W.; Clark, N.; Hamer, M.; et al. Clean assembly of van der Waals heterostructures using silicon nitride membranes. *Nature Electronics* **2023**, *6* (12), 981-990. DOI: 10.1038/s41928-023-01075-y

(49) Utama, M. I. B.; Zeng, H.; Sadhukhan, T.; et al. Chemomechanical modification of quantum emission in monolayer WSe_2. *Nat Commun* **2023**, *14* (1), 2193. DOI: 10.1038/s41467-023-37892-0

(50) Strasbourg, M. Thermalization and Exciton Localization in 2D Semiconductors. Montana State University, 2023.

(51) Rosiek, C. A.; Arregui, G.; Vladimirova, A.; et al. Observation of strong backscattering in valley-Hall photonic topological interface modes. *Nature Photonics* **2023**, *17* (5), 386-392. DOI: 10.1038/s41566-023-01189-x

(52) Rizzato, R.; Schalk, M.; Mohr, S.; et al. Extending the coherence of spin defects in hBN enables advanced qubit control and quantum sensing. *Nat Commun* **2023**, *14* (1), 5089. DOI: 10.1038/s41467-023-40473-w

(53) Ramsay, A. J.; Hekmati, R.; Patrickson, C. J.; et al. Coherence protection of spin qubits in hexagonal boron nitride. *Nat Commun* **2023**, *14* (1), 461. DOI: 10.1038/s41467-023-36196-7

(54) Preuss, J. A.; Gehring, H.; Schmidt, R.; et al. Low-Divergence hBN Single-Photon Source with a 3D-Printed Low-Fluorescence Elliptical Polymer Microlens. *Nano Lett* **2023**, *23* (2), 407-413. DOI: 10.1021/acs.nanolett.2c03001

(55) Mueller, N. S.; Arul, R.; Kang, G.; et al. Photoluminescence upconversion in monolayer WSe_2 activated by plasmonic cavities through resonant excitation of dark excitons. *Nat Commun* **2023**, *14* (1), 5726. DOI: 10.1038/s41467-023-41401-8

(56) Montblanch, A. R.; Barbone, M.; Aharonovich, I.; et al. Layered materials as a platform for quantum technologies. *Nat Nanotechnol* **2023**, *18* (6), 555-571. DOI: 10.1038/s41565-023-01354-x

(57) Liu, S.; Liu, Y.; Holtzman, L.; et al. Two-Step Flux Synthesis of Ultrapure Transition-Metal Dichalcogenides. *ACS Nano* **2023**, *17* (17), 16587-16596. DOI: 10.1021/acsnano.3c02511

(58) Li, X.; Jones, A. C.; Choi, J.; et al. Proximity-induced chiral quantum light generation in strain-engineered $WSe_2/NiPS_3$ heterostructures. *Nat Mater* **2023**, *22* (11), 1311-1316. DOI: 10.1038/s41563-023-01645-7

(59) Jo, K.; Marino, E.; Lynch, J.; et al. Direct nano-imaging of light-matter interactions in nanoscale excitonic emitters. *Nat Commun* **2023**, *14* (1), 2649. DOI: 10.1038/s41467-023-38189-y

(60) Hu, J.; Zhou, F.; Wang, J.; et al. Chemical Vapor Deposition Syntheses of Wafer-Scale 2D Transition Metal Dichalcogenide Films toward Next-Generation Integrated Circuits Related Applications. *Advanced Functional Materials* **2023**, *33* (40). DOI: 10.1002/adfm.202303520

(61) Hekmati, R.; Hadden, J. P.; Mathew, A.; et al. Bullseye dielectric cavities for photon collection from a surface-mounted quantum-light-emitter. *Sci Rep* **2023**, *13* (1), 5316. DOI: 10.1038/s41598-023-32359-0

(62) Hasz, K.; Hu, Z.; Park, K. D.; et al. Tip-Enhanced Dark Exciton Nanoimaging and Local Strain Control in Monolayer WSe_2. *Nano Lett* **2023**, *23* (1), 198-204. DOI: 10.1021/acs.nanolett.2c03959

(63) Guo, S.; Germanis, S.; Taniguchi, T.; et al. Electrically Driven Site-Controlled Single Photon Source. *ACS Photonics* **2023**, *10* (8), 2549-2555. DOI: 10.1021/acsphotonics.3c00097

(64) Gao, T.; von Helversen, M.; Antón-Solanas, C.; et al. Atomically-thin single-photon sources for quantum communication. *npj 2D Materials and Applications* **2023**, *7* (1). DOI: 10.1038/s41699-023-00366-4

(65) Gao, T.; von Helversen, M.; Antón-Solanas, C.; et al. Atomically-thin single-photon sources for quantum communication. *npj 2D Materials and Applications* **2023**, *7* (4). DOI: 10.1038/s41699-023-00366-4

(66) Drawer, J. C.; Mitryakhin, V. N.; Shan, H.; et al. Monolayer-Based Single-Photon Source in a Liquid-Helium-Free Open Cavity Featuring 65% Brightness and Quantum Coherence. *Nano Lett* **2023**, *23* (18), 8683-8689. DOI: 10.1021/acs.nanolett.3c02584

(67) Dong, S.; Beaulieu, S.; Selig, M.; et al. Observation of ultrafast interfacial Meitner-Auger energy transfer in a Van der Waals heterostructure. *Nat Commun* **2023**, *14* (1), 5057. DOI: 10.1038/s41467-023-40815-8

(68) Chang, S.; Yan, Y.; Geng, Y. Local Nanostrain Engineering of Monolayer MoS_2 Using Atomic Force Microscopy-Based Thermomechanical Nanoindentation. *Nano Lett* **2023**, *23* (20), 9219-9226. DOI: 10.1021/acs.nanolett.3c01809

(69) Campi, D.; Mounet, N.; Gibertini, M.; et al. Expansion of the Materials Cloud 2D Database. *ACS Nano* **2023**, *17* (12), 11268-11278. DOI: 10.1021/acsnano.2c11510

(70) Azzam, S. I.; Parto, K.; Moody, G. Purcell enhancement and polarization control of single-photon emitters in monolayer WSe_2 using dielectric nanoantennas. *Nanophotonics* **2023**, *12* (3), 477-484. DOI: 10.1515/nanoph-2022-0628

(71) Al-Juboori, A.; Zeng, H. Z. J.; Nguyen, M. A. P.; et al. Quantum Key Distribution Using a Quantum Emitter in Hexagonal Boron Nitride. *Advanced Quantum Technologies* **2023**, *6* (9). DOI: 10.1002/qute.202300038

(72) Abramov, A. N.; Chestnov, I. Y.; Alimova, E. S.; et al. Photoluminescence imaging of single photon emitters within nanoscale strain profiles in monolayer WSe_2. *Nat Commun* **2023**, *14* (1), 5737. DOI: 10.1038/s41467-023-41292-9

(73) Zhang, X.; Ren, W.; Bell, E.; et al. Gate-tunable Veselago interference in a bipolar graphene microcavity. *Nat Commun* **2022**, *13* (1), 6711. DOI: 10.1038/s41467-022-34347-w

(74) Zhang, S.; Li, B.; Chen, X.; et al. Nano-spectroscopy of excitons in atomically thin transition metal dichalcogenides. *Nat Commun* **2022**, *13* (1), 542. DOI: 10.1038/s41467-022-28117-x

(75) Zeng, H. Z. J.; Ngyuen, M. A. P.; Ai, X.; et al. Integrated room temperature single-photon source for quantum key distribution. *Opt Lett* **2022**, *47* (7), 1673-1676. DOI: 10.1364/OL.454450

(76) Yao, K.; Zhang, S.; Yanev, E.; et al. Nanoscale Optical Imaging of 2D Semiconductor Stacking Orders by Exciton-Enhanced Second Harmonic Generation. *Advanced Optical Materials* **2022**, *10* (12). DOI: 10.1002/adom.202200085

(77) Su, H.; Xu, D.; Cheng, S. W.; et al. Dark-Exciton Driven Energy Funneling into Dielectric Inhomogeneities in Two-Dimensional Semiconductors. *Nano Lett* **2022**, *22* (7), 2843-2850. DOI: 10.1021/acs.nanolett.1c04997

(78) Stevens, C. E.; Chuang, H. J.; Rosenberger, M. R.; et al. Enhancing the Purity of Deterministically Placed Quantum Emitters in Monolayer WSe_2. *ACS Nano* **2022**, *16* (12), 20956-20963. DOI: 10.1021/acsnano.2c08553

(79) Shabani, S.; Darlington, T. P.; Gordon, C.; et al. Ultralocalized Optoelectronic Properties of Nanobubbles in 2D Semiconductors. *Nano Lett* **2022**, *22* (18), 7401-7407. DOI: 10.1021/acs.nanolett.2c02265

(80) Samaner, Ç.; Paçal, S.; Mutlu, G.; et al. Free-Space Quantum Key Distribution with Single Photons from Defects in Hexagonal Boron Nitride. *Advanced Quantum Technologies* **2022**, *5* (9). DOI: 10.1002/qute.202200059

(81) Parto, K.; Azzam, S. I.; Lewis, N.; et al. Cavity-Enhanced 2D Material Quantum Emitters Deterministically Integrated with Silicon Nitride Microresonators. *Nano Lett* **2022**, *22* (23), 9748-9756. DOI: 10.1021/acs.nanolett.2c03151

(82) Pan, Y.; Rahaman, M.; He, L.; et al. Exciton tuning in monolayer WSe_2 via substrate induced electron doping. *Nanoscale Adv* **2022**, *4* (23), 5102-5108. DOI: 10.1039/d2na00495j

(83) Islam, M. A.; Serles, P.; Kumral, B.; et al. Exfoliation mechanisms of 2D materials and their applications. *Applied Physics Reviews* **2022**, *9* (4). DOI: 10.1063/5.0090717

(84) Huang, J.; Huang, Y.; Zeng, M.; et al. Fabrication of Spindt-Type Nanometer-Sized Chromium Tips for Application as Field-Electron Emitters by Releasing the Stress of the Deposited Thin Film. *ACS Applied Nano Materials* **2022**, *6* (1), 351-357. DOI: 10.1021/acsanm.2c04457

(85) Heyl, M.; List-Kratochvil, E. J. W. Only gold can pull this off: mechanical exfoliations of transition metal dichalcogenides beyond scotch tape. *Applied Physics A* **2022**, *129* (1). DOI: 10.1007/s00339-022-06297-z

(86) Haykal, A.; Tanos, R.; Minotto, N.; et al. Decoherence of VB- spin defects in monoisotopic hexagonal boron nitride. *Nat Commun* **2022**, *13* (1), 4347. DOI: 10.1038/s41467-022-31743-0

(87) Gelly, R. J.; Renaud, D.; Liao, X.; et al. Probing dark exciton navigation through a local strain landscape in a WSe_2 monolayer. *Nat Commun* **2022**, *13* (1), 232. DOI: 10.1038/s41467-021-27877-2

(88) Garg, S.; Fix, J. P.; Krayev, A. V.; et al. Nanoscale Raman Characterization of a 2D Semiconductor Lateral Heterostructure Interface. *ACS Nano* **2022**, *16* (1), 340-350. DOI: 10.1021/acsnano.1c06595

(89) Colmiais, I.; Silva, V.; Borme, J.; et al. Towards RF graphene devices: A review. *FlatChem* **2022**, *35*. DOI: 10.1016/j.flatc.2022.100409

(90) Blundo, E.; Surrente, A.; Spirito, D.; et al. Vibrational Properties in Highly Strained Hexagonal Boron Nitride Bubbles. *Nano Lett* **2022**, *22* (4), 1525-1533. DOI: 10.1021/acs.nanolett.1c04197

(91) Banszerus, L.; Hecker, K.; Moller, S.; et al. Spin relaxation in a single-electron graphene quantum dot. *Nat Commun* **2022**, *13* (1), 3637. DOI: 10.1038/s41467-022-31231-5

(92) Zhou, H.; Chen, Y.; Zhu, H. Deciphering asymmetric charge transfer at transition metal dichalcogenide-graphene interface by helicity-resolved ultrafast spectroscopy. *Sci Adv* **2021**, *7* (34). DOI: 10.1126/sciadv.abg2999

(93) Sun, B.; Grap, T.; Frahm, T.; et al. Role of electron and ion irradiation in a reliable lift-off process with electron beam evaporation and a bilayer PMMA resist system. *Journal of Vacuum Science & Technology B, Nanotechnology and Microelectronics: Materials, Processing, Measurement, and Phenomena* **2021**, *39* (5). DOI: 10.1116/6.0001161

(94) Sortino, L.; Zotev, P. G.; Phillips, C. L.; et al. Bright single photon emitters with enhanced quantum efficiency in a two-dimensional semiconductor coupled with dielectric nano-antennas. *Nat Commun* **2021**, *12* (1), 6063. DOI: 10.1038/s41467-021-26262-3

(95) So, J. P.; Kim, H. R.; Baek, H.; et al. Electrically driven strain-induced deterministic single-photon emitters in a van der Waals heterostructure. *Sci Adv* **2021**, *7* (43), eabj3176. DOI: 10.1126/sciadv.abj3176

(96) So, J. P.; Jeong, K. Y.; Lee, J. M.; et al. Polarization Control of Deterministic Single-Photon Emitters in Monolayer WSe_2. *Nano Lett* **2021**, *21* (3), 1546-1554. DOI: 10.1021/acs.nanolett.1c00078

(97) Rosati, R.; Schmidt, R.; Brem, S.; et al. Dark exciton anti-funneling in atomically thin semiconductors. *Nat Commun* **2021**, *12* (1), 7221. DOI: 10.1038/s41467-021-27425-y

(98) Parto, K.; Azzam, S. I.; Banerjee, K.; et al. Defect and strain engineering of monolayer WSe_2 enables site-controlled single-photon emission up to 150 K. *Nat Commun* **2021**, *12* (1), 3585. DOI: 10.1038/s41467-021-23709-5

(99) Panasci, S. E.; Schilirò, E.; Migliore, F.; et al. Substrate impact on the thickness dependence of vibrational and optical properties of large area MoS_2 produced by gold-assisted exfoliation. *Applied Physics Letters* **2021**, *119* (9). DOI: 10.1063/5.0062106

(100) Panasci, S. E.; Schiliro, E.; Greco, G.; et al. Strain, Doping, and Electronic Transport of Large Area Monolayer MoS_2 Exfoliated on Gold and Transferred to an Insulating Substrate. *ACS Appl Mater Interfaces* **2021**, *13* (26), 31248-31259. DOI: 10.1021/acsami.1c05185

(101) Ling, H.; Li, R.; Davoyan, A. R. All van der Waals Integrated Nanophotonics with Bulk Transition Metal Dichalcogenides. *ACS Photonics* **2021**, *8* (3), 721-730. DOI: 10.1021/acsphotonics.0c01964

(102) Li, C.; Fröch, J. E.; Nonahal, M.; et al. Integration of hBN Quantum Emitters in Monolithically Fabricated Waveguides. *ACS Photonics* **2021**, *8* (10), 2966-2972. DOI: 10.1021/acsphotonics.1c00890

(103) Iff, O.; Davanco, M.; Betzold, S.; et al. Hyperspectral study of the coupling between trions in WSe_2 monolayers to a circular Bragg grating cavity. *C R Phys* **2021**, *22* (Suppl 4). DOI: 10.5802/crphys.76

(104) Iff, O.; Buchinger, Q.; Moczala-Dusanowska, M.; et al. Purcell-Enhanced Single Photon Source Based on a Deterministically Placed WSe_2 Monolayer Quantum Dot in a Circular Bragg Grating Cavity. *Nano Lett* **2021**, *21* (11), 4715-4720. DOI: 10.1021/acs.nanolett.1c00978

(105) Funk, V.; Wagner, K.; Wietek, E.; et al. Spectral asymmetry of phonon sideband luminescence in monolayer and bilayer
WSe_2. *Physical Review Research* **2021**, *3* (4). DOI: 10.1103/PhysRevResearch.3.L042019

(106) Falin, A.; Holwill, M.; Lv, H.; et al. Mechanical Properties of Atomically Thin Tungsten Dichalcogenides: WS_2, WSe_2, and WTe_2. *ACS Nano* **2021**, *15* (2), 2600-2610. DOI: 10.1021/acsnano.0c07430

(107) Errando-Herranz, C.; Scholl, E.; Picard, R.; et al. Resonance Fluorescence from Waveguide-Coupled, Strain-Localized, Two-Dimensional Quantum Emitters. *ACS Photonics* **2021**, *8* (4), 1069-1076. DOI: 10.1021/acsphotonics.0c01653

(108) Camacho, M.; Edwards, B.; Engheta, N. A single inverse-designed photonic structure that performs parallel computing. *Nat Commun* **2021**, *12* (1), 1466. DOI: 10.1038/s41467-021-21664-9

(109) Zhao, Y.; Gali, S. M.; Wang, C.; et al. Molecular Functionalization of Chemically Active Defects in WSe_2 for Enhanced Opto-Electronics. *Advanced Functional Materials* **2020**, *30* (45). DOI: 10.1002/adfm.202005045

(110) Xing, X.; Zhao, L.; Zhang, W.; et al. Influence of a substrate on ultrafast interfacial charge transfer and dynamical interlayer excitons in monolayer WSe_2/graphene heterostructures. *Nanoscale* **2020**, *12* (4), 2498-2506. DOI: 10.1039/c9nr09309e

(111) Xiao, Y.; Liu, J.; Fu, L. Moiré is More: Access to New Properties of Two-Dimensional Layered Materials. *Matter* **2020**, *3* (4), 1142-1161. DOI: 10.1016/j.matt.2020.07.001

(112) Son, S.; Shin, Y. J.; Zhang, K.; et al. Strongly adhesive dry transfer technique for van der Waals heterostructure. *2D Materials* **2020**, *7* (4). DOI: 10.1088/2053-1583/abad0b

(113) Sajid, A.; Ford, M. J.; Reimers, J. R. Single-photon emitters in hexagonal boron nitride: a review of progress. *Rep Prog Phys* **2020**, *83* (4), 044501. DOI: 10.1088/1361-6633/ab6310

(114) Rokni, H.; Lu, W. Direct measurements of interfacial adhesion in 2D materials and van der Waals heterostructures in ambient air. *Nat Commun* **2020**, *11* (1), 5607. DOI: 10.1038/s41467-020-19411-7

(115) Qian, Q.; Peng, L.; Perea-Lopez, N.; et al. Defect creation in WSe_2 with a microsecond photoluminescence lifetime by focused ion beam irradiation. *Nanoscale* **2020**, *12* (3), 2047-2056. DOI: 10.1039/c9nr08390a

(116) Peng, L.; Chan, H.; Choo, P.; et al. Creation of Single-Photon Emitters in WSe_2 Monolayers Using Nanometer-Sized Gold Tips. *Nano Lett* **2020**, *20* (8), 5866-5872. DOI: 10.1021/acs.nanolett.0c01789

(117) Madeo, J.; Man, M. K. L.; Sahoo, C.; et al. Directly visualizing the momentum-forbidden dark excitons and their dynamics in atomically thin semiconductors. *Science* **2020**, *370* (6521), 1199-1204. DOI: 10.1126/science.aba1029

(118) Luo, Y.; Liu, N.; Kim, B.; et al. Exciton Dipole Orientation of Strain-Induced Quantum Emitters in WSe_2. *Nano Lett* **2020**, *20* (7), 5119-5126. DOI: 10.1021/acs.nanolett.0c01358

(119) Hsiao, T. K.; Rubino, A.; Chung, Y.; et al. Single-photon emission from single-electron transport in a SAW-driven lateral light-emitting diode. *Nat Commun* **2020**, *11* (1), 917. DOI: 10.1038/s41467-020-14560-1

(120) Howell, S. T.; Grushina, A.; Holzner, F.; et al. Thermal scanning probe lithography-a review. *Microsyst Nanoeng* **2020**, *6*, 21. DOI: 10.1038/s41378-019-0124-8

(121) Eschimese, D.; Vaurette, F.; Melin, T.; et al. Precise tailoring of evaporated gold nanocones using electron beam lithography and lift-off. *Nanotechnology* **2020**, *31* (22), 225302. DOI: 10.1088/1361-6528/ab746e

(122) Daveau, R. S.; Vandekerckhove, T.; Mukherjee, A.; et al. Spectral and spatial isolation of single tungsten diselenide quantum emitters using hexagonal boron nitride wrinkles. *APL Photonics* **2020**, *5* (9). DOI: 10.1063/5.0013825

(123) Darlington, T. P.; Carmesin, C.; Florian, M.; et al. Imaging strain-localized excitons in nanoscale bubbles of monolayer WSe_2 at room temperature. *Nat Nanotechnol* **2020**, *15* (10), 854-860. DOI: 10.1038/s41565-020-0730-5

(124) Dang, J.; Sun, S.; Xie, X.; et al. Identifying defect-related quantum emitters in monolayer WSe_2. *npj 2D Materials and Applications* **2020**, *4* (2). DOI: 10.1038/s41699-020-0136-0

(125) Asenbauer, J.; Eisenmann, T.; Kuenzel, M.; et al. The success story of graphite as a lithium-ion anode material – fundamentals, remaining challenges, and recent developments including silicon (oxide) composites. *Sustainable Energy & Fuels* **2020**, *4* (11), 5387-5416. DOI: 10.1039/d0se00175a

(126) Zheng, Y. J.; Chen, Y.; Huang, Y. L.; et al. Point Defects and Localized Excitons in 2D WSe_2. *ACS Nano* **2019**, *13* (5), 6050-6059. DOI: 10.1021/acsnano.9b02316

(127) Zhang, L.; Chen, Z.; Zhang, R.; et al. Direct Observation of Charge Injection of Graphene in the Graphene/WSe_2 Heterostructure by Optical-Pump Terahertz-Probe Spectroscopy. *ACS Appl Mater Interfaces* **2019**, *11* (50), 47501-47506. DOI: 10.1021/acsami.9b13996

(128) Tran, K.; Moody, G.; Wu, F.; et al. Evidence for moire excitons in van der Waals heterostructures. *Nature* **2019**, *567* (7746), 71-75. DOI: 10.1038/s41586-019-0975-z

(129) Tang, Y.; Mak, K. F.; Shan, J. Long valley lifetime of dark excitons in single-layer WSe_2. *Nat Commun* **2019**, *10* (1), 4047. DOI: 10.1038/s41467-019-12129-1

(130) Rosenberger, M. R.; Dass, C. K.; Chuang, H. J.; et al. Quantum Calligraphy: Writing Single-Photon Emitters in a Two-Dimensional Materials Platform. *ACS Nano* **2019**, *13* (1), 904-912. DOI: 10.1021/acsnano.8b08730

(131) Raja, A.; Waldecker, L.; Zipfel, J.; et al. Dielectric disorder in two-dimensional materials. *Nat Nanotechnol* **2019**, *14* (9), 832-837. DOI: 10.1038/s41565-019-0520-0

(132) Peyskens, F.; Chakraborty, C.; Muneeb, M.; et al. Integration of single photon emitters in 2D layered materials with a silicon nitride photonic chip. *Nat Commun* **2019**, *10* (1), 4435. DOI: 10.1038/s41467-019-12421-0

(133) Luo, Y.; Liu, N.; Li, X.; et al. Single photon emission in WSe_2 up to 160 K by quantum yield control. *2D Materials* **2019**, *6* (3). DOI: 10.1088/2053-1583/ab15fe

(134) Lu, X.; Chen, X.; Dubey, S.; et al. Optical initialization of a single spin-valley in charged WSe_2 quantum dots. *Nat Nanotechnol* **2019**, *14* (5), 426-431. DOI: 10.1038/s41565-019-0394-1

(135) Linhart, L.; Paur, M.; Smejkal, V.; et al. Localized Intervalley Defect Excitons as Single-Photon Emitters in WSe_2. *Phys Rev Lett* **2019**, *123* (14), 146401. DOI: 10.1103/PhysRevLett.123.146401

(136) Li, Z.; Wang, T.; Jin, C.; et al. Emerging photoluminescence from the dark-exciton phonon replica in monolayer WSe_2. *Nat Commun* **2019**, *10* (1), 2469. DOI: 10.1038/s41467-019-10477-6

(137) Klein, J.; Lorke, M.; Florian, M.; et al. Site-selectively generated photon emitters in monolayer MoS_2 via local helium ion irradiation. *Nat Commun* **2019**, *10* (1), 2755. DOI: 10.1038/s41467-019-10632-z

(138) Kim, H.; Moon, J. S.; Noh, G.; et al. Position and Frequency Control of Strain-Induced Quantum Emitters in WSe_2 Monolayers. *Nano Lett* **2019**, *19* (10), 7534-7539. DOI: 10.1021/acs.nanolett.9b03421

(139) Fang, H. H.; Han, B.; Robert, C.; et al. Control of the Exciton Radiative Lifetime in van der Waals Heterostructures. *Phys Rev Lett* **2019**, *123* (6), 067401. DOI: 10.1103/PhysRevLett.123.067401

(140) Edelberg, D.; Rhodes, D.; Kerelsky, A.; et al. Approaching the Intrinsic Limit in Transition Metal Diselenides via Point Defect Control. *Nano Lett* **2019**, *19* (7), 4371-4379. DOI: 10.1021/acs.nanolett.9b00985

(141) Dass, C. K.; Khan, M. A.; Clark, G.; et al. Ultra-Long Lifetimes of Single Quantum Emitters in Monolayer WSe_2/hBN Heterostructures. *Advanced Quantum Technologies* **2019**, *2* (5-6). DOI: 10.1002/qute.201900022

(142) Barja, S.; Refaely-Abramson, S.; Schuler, B.; et al. Identifying substitutional oxygen as a prolific point defect in monolayer transition metal dichalcogenides. *Nat Commun* **2019**, *10* (1), 3382. DOI: 10.1038/s41467-019-11342-2

(143) Velicky, M.; Donnelly, G. E.; Hendren, W. R.; et al. Mechanism of Gold-Assisted Exfoliation of Centimeter-Sized Transition-Metal Dichalcogenide Monolayers. *ACS Nano* **2018**, *12* (10), 10463-10472. DOI: 10.1021/acsnano.8b06101

(144) Urban, F.; Martucciello, N.; Peters, L.; et al. Environmental Effects on the Electrical Characteristics of Back-Gated WSe_2 Field-Effect Transistors. *Nanomaterials (Basel)* **2018**, *8* (11). DOI: 10.3390/nano8110901

(145) Tripathi, L. N.; Iff, O.; Betzold, S.; et al. Spontaneous Emission Enhancement in Strain-Induced WSe_2 Monolayer-Based Quantum Light Sources on Metallic Surfaces. *ACS Photonics* **2018**, *5* (5), 1919-1926. DOI: 10.1021/acsphotonics.7b01053

(146) Taghinejad, H.; Eftekhar, A. A.; Campbell, P. M.; et al. Strain relaxation via formation of cracks in compositionally modulated two-dimensional semiconductor alloys. *npj 2D Materials and Applications* **2018**, *2* (10). DOI: 10.1038/s41699-018-0056-4

(147) Schneider, L. M.; Lippert, S.; Kuhnert, J.; et al. The influence of the environment on monolayer tungsten diselenide photoluminescence. *Nano-Structures & Nano-Objects* **2018**, *15*, 84-97. DOI: 10.1016/j.nanoso.2017.08.009

(148) Park, K. D.; Jiang, T.; Clark, G.; et al. Radiative control of dark excitons at room temperature by nano-optical antenna-tip Purcell effect. *Nat Nanotechnol* **2018**, *13* (1), 59-64. DOI: 10.1038/s41565-017-0003-0

(149) Luo, Y.; Shepard, G. D.; Ardelean, J. V.; et al. Deterministic coupling of site-controlled quantum emitters in monolayer WSe_2 to plasmonic nanocavities. *Nat Nanotechnol* **2018**, *13* (12), 1137-1142. DOI: 10.1038/s41565-018-0275-z

(150) Liang, J.; Xu, K.; Toncini, B.; et al. Impact of Post-Lithography Polymer Residue on the Electrical Characteristics of MoS_2 and WSe_2 Field Effect Transistors. *Advanced Materials Interfaces* **2018**, *6* (3). DOI: 10.1002/admi.201801321

(151) Lee, S. Y.; Jeong, T. Y.; Kim, J. H.; et al. Self-consistent dielectric constant determination for monolayer WSe_2. *Opt Express* **2018**, *26* (18), 23061-23068. DOI: 10.1364/OE.26.023061

(152) Lan, C.; Zhou, Z.; Zhou, Z.; et al. Wafer-scale synthesis of monolayer WS_2 for high-performance flexible photodetectors by enhanced chemical vapor deposition. *Nano Research* **2018**, *11* (6), 3371-3384. DOI: 10.1007/s12274-017-1941-4

(153) Jariwala, D.; Krayev, A.; Wong, J.; et al. Nanoscale doping heterogeneity in few-layer WSe_2 exfoliated onto noble metals revealed by correlated SPM and TERS imaging. *2D Materials* **2018**, *5* (3). DOI: 10.1088/2053-1583/aab7bc

(154) Hempel, M.; Lu, A. Y.; Hui, F.; et al. Repeated roll-to-roll transfer of two-dimensional materials by electrochemical delamination. *Nanoscale* **2018**, *10* (12), 5522-5531. DOI: 10.1039/c7nr07369k

(155) Fang, S.; Carr, S.; Cazalilla, M. A.; et al. Electronic structure theory of strained two-dimensional materials with hexagonal symmetry. *Physical Review B* **2018**, *98* (7). DOI: 10.1103/PhysRevB.98.075106

(156) Eich, M.; Herman, F.; Pisoni, R.; et al. Spin and Valley States in Gate-Defined Bilayer Graphene Quantum Dots. *Physical Review X* **2018**, *8* (3). DOI: 10.1103/PhysRevX.8.031023

(157) Dutta, S.; Cai, T.; Buyukkaya, M. A.; et al. Coupling quantum emitters in WSe_2 monolayers to a metal-insulator-metal waveguide. *Applied Physics Letters* **2018**, *113* (19). DOI: 10.1063/1.5045727

(158) Duong, N. M. H.; Xu, Z.-Q.; Kianinia, M.; et al. Enhanced Emission from WSe_2 Monolayers Coupled to Circular Bragg Gratings. *ACS Photonics* **2018**, *5* (10), 3950-3955. DOI: 10.1021/acsphotonics.8b00865

(159) Cao, Y.; Fatemi, V.; Fang, S.; et al. Unconventional superconductivity in magic-angle graphene superlattices. *Nature* **2018**, *556* (7699), 43-50. DOI: 10.1038/nature26160

(160) Cao, Y.; Fatemi, V.; Demir, A.; et al. Correlated insulator behaviour at half-filling in magic-angle graphene superlattices. *Nature* **2018**, *556* (7699), 80-84. DOI: 10.1038/nature26154

(161) Cai, T.; Kim, J.-H.; Yang, Z.; et al. Radiative Enhancement of Single Quantum Emitters in WSe2 Monolayers Using Site-Controlled Metallic Nanopillars. *ACS Photonics* **2018**, *5* (9), 3466-3471. DOI: 10.1021/acsphotonics.8b00580

(162) Aslan, B.; Deng, M.; Heinz, T. F. Strain tuning of excitons in monolayer WSe_2. *Physical Review B* **2018**, *98* (11). DOI: 10.1103/PhysRevB.98.115308

(163) Zhou, Y.; Scuri, G.; Wild, D. S.; et al. Probing dark excitons in atomically thin semiconductors via near-field coupling to surface plasmon polaritons. *Nat Nanotechnol* **2017**, *12* (9), 856-860. DOI: 10.1038/nnano.2017.106

(164) Zhang, Z. Z.; Song, X. X.; Luo, G.; et al. Electrotunable artificial molecules based on van der Waals heterostructures. *Sci Adv* **2017**, *3* (10), e1701699. DOI: 10.1126/sciadv.1701699

(165) Zhang, X. X.; Cao, T.; Lu, Z.; et al. Magnetic brightening and control of dark excitons in monolayer WSe_2. *Nat Nanotechnol* **2017**, *12* (9), 883-888. DOI: 10.1038/nnano.2017.105

(166) Zhang, L.; Yu, Y. J.; Chen, L. G.; et al. Electrically driven single-photon emission from an isolated single molecule. *Nat Commun* **2017**, *8* (1), 580. DOI: 10.1038/s41467-017-00681-7

(167) Yu, H.; Liao, M.; Zhao, W.; et al. Wafer-Scale Growth and Transfer of Highly-Oriented Monolayer MoS_2 Continuous Films. *ACS Nano* **2017**, *11* (12), 12001-12007. DOI: 10.1021/acsnano.7b03819

(168) Ye, Y.; Dou, X.; Ding, K.; et al. Single photon emission from deep-level defects in monolayer WSe_2. *Physical Review B* **2017**, *95* (24). DOI: 10.1103/PhysRevB.95.245313

(169) Xie, L.; Du, L.; Lu, X.; et al. A facile and efficient dry transfer technique for two-dimensional Van der Waals heterostructure. *Chinese Physics B* **2017**, *26* (8). DOI: 10.1088/1674-1056/26/8/087306

(170) Torres, J.; Zhu, Y.; Liu, P.; et al. Adhesion Energies of 2D Graphene and MoS_2 to Silicon and Metal Substrates. *physica status solidi (a)* **2017**, *215* (1). DOI: 10.1002/pssa.201700512

(171) Shepard, G. D.; Ajayi, O. A.; Li, X.; et al. Nanobubble induced formation of quantum emitters in monolayer semiconductors. *2D Materials* **2017**, *4* (2). DOI: 10.1088/2053-1583/aa629d

(172) Palacios-Berraquero, C.; Kara, D. M.; Montblanch, A. R.; et al. Large-scale quantum-emitter arrays in atomically thin semiconductors. *Nat Commun* **2017**, *8*, 15093. DOI: 10.1038/ncomms15093

(173) Ma, X.; Liu, Q.; Xu, D.; et al. Capillary-Force-Assisted Clean-Stamp Transfer of Two-Dimensional Materials. *Nano Lett* **2017**, *17* (11), 6961-6967. DOI: 10.1021/acs.nanolett.7b03449

(174) Hsu, W. T.; Lu, L. S.; Wang, D.; et al. Evidence of indirect gap in monolayer WSe_2. *Nat Commun* **2017**, *8* (1), 929. DOI: 10.1038/s41467-017-01012-6

(175) Hill, H. M.; Rigosi, A. F.; Raja, A.; et al. Exciton broadening in WS_2/graphene heterostructures. *Physical Review B* **2017**, *96* (20). DOI: 10.1103/PhysRevB.96.205401

(176) Frisenda, R.; Drüppel, M.; Schmidt, R.; et al. Biaxial strain tuning of the optical properties of single-layer transition metal dichalcogenides. *npj 2D Materials and Applications* **2017**, *1* (1). DOI: 10.1038/s41699-017-0013-7

(177) Carr, S.; Massatt, D.; Fang, S.; et al. Twistronics: Manipulating the electronic properties of two-dimensional layered structures through their twist angle. *Physical Review B* **2017**, *95* (7). DOI: 10.1103/PhysRevB.95.075420

(178) Budania, P.; Baine, P. T.; Montgomery, J. H.; et al. Comparison between Scotch tape and gel-assisted mechanical exfoliation techniques for preparation of 2D transition metal dichalcogenide flakes. *Micro & Nano Letters* **2017**, *12* (12), 970-973. DOI: 10.1049/mnl.2017.0280

(179) Branny, A.; Kumar, S.; Proux, R.; et al. Deterministic strain-induced arrays of quantum emitters in a two-dimensional semiconductor. *Nat Commun* **2017**, *8* (1), 15053. DOI: 10.1038/ncomms15053

(180) Borys, N. J.; Barnard, E. S.; Gao, S.; et al. Anomalous Above-Gap Photoexcitations and Optical Signatures of Localized Charge Puddles in Monolayer Molybdenum Disulfide. *ACS Nano* **2017**, *11* (2), 2115-2123. DOI: 10.1021/acsnano.6b08278

(181) Barreau, V.; Yu, D.; Hensel, R.; et al. Elevated temperature adhesion of bioinspired polymeric micropatterns to glass. *J Mech Behav Biomed Mater* **2017**, *76*, 110-118. DOI: 10.1016/j.jmbbm.2017.04.007

(182) Wang, Z.; Dong, Z.; Gu, Y.; et al. Giant photoluminescence enhancement in tungsten-diselenide-gold plasmonic hybrid structures. *Nat Commun* **2016**, *7*, 11283. DOI: 10.1038/ncomms11283

(183) Tran, T. T.; Bray, K.; Ford, M. J.; et al. Quantum emission from hexagonal boron nitride monolayers. *Nat Nanotechnol* **2016**, *11* (1), 37-41. DOI: 10.1038/nnano.2015.242

(184) Schwarz, S.; Kozikov, A.; Withers, F.; et al. Electrically pumped single-defect light emitters in WSe_2. *2D Materials* **2016**, *3* (2). DOI: 10.1088/2053-1583/3/2/025038

(185) Schmidt, R.; Niehues, I.; Schneider, R.; et al. Reversible uniaxial strain tuning in atomically thin WSe_2. *2D Materials* **2016**, *3* (2). DOI: 10.1088/2053-1583/3/2/021011

(186) Park, K. D.; Khatib, O.; Kravtsov, V.; et al. Hybrid Tip-Enhanced Nanospectroscopy and Nanoimaging of Monolayer WSe_2 with Local Strain Control. *Nano Lett* **2016**, *16* (4), 2621-2627. DOI: 10.1021/acs.nanolett.6b00238

(187) Palacios-Berraquero, C.; Barbone, M.; Kara, D. M.; et al. Atomically thin quantum light-emitting diodes. *Nat Commun* **2016**, *7* (1), 12978. DOI: 10.1038/ncomms12978

(188) Ocola, L. E.; Costales, M.; Gosztola, D. J. Development characteristics of polymethyl methacrylate in alcohol/water mixtures: a lithography and Raman spectroscopy study. *Nanotechnology* **2016**, *27* (3), 035302. DOI: 10.1088/0957-4484/27/3/035302

(189) Novoselov, K. S.; Mishchenko, A.; Carvalho, A.; et al. 2D materials and van der Waals heterostructures. *Science* **2016**, *353* (6298), aac9439. DOI: 10.1126/science.aac9439

(190) Noori, Y. J.; Cao, Y.; Roberts, J.; et al. Photonic Crystals for Enhanced Light Extraction from 2D Materials. *ACS Photonics* **2016**, *3* (12), 2515-2520. DOI: 10.1021/acsphotonics.6b00779

(191) Khestanova, E.; Guinea, F.; Fumagalli, L.; et al. Universal shape and pressure inside bubbles appearing in van der Waals heterostructures. *Nat Commun* **2016**, *7*, 12587. DOI: 10.1038/ncomms12587

(192) Kern, J.; Niehues, I.; Tonndorf, P.; et al. Nanoscale Positioning of Single-Photon Emitters in Atomically Thin WSe_2. *Adv Mater* **2016**, *28* (33), 7101-7105. DOI: 10.1002/adma.201600560

(193) Godin, K.; Kang, K.; Fu, S.; et al. Increased monolayer domain size and patterned growth of tungsten disulfide through controlling surface energy of substrates. *Journal of Physics D: Applied Physics* **2016**, *49* (32). DOI: 10.1088/0022-3727/49/32/325304

(194) Zhang, X. X.; You, Y.; Zhao, S. Y.; et al. Experimental Evidence for Dark Excitons in Monolayer WSe_2. *Phys Rev Lett* **2015**, *115* (25), 257403. DOI: 10.1103/PhysRevLett.115.257403

(195) Tonndorf, P.; Schmidt, R.; Schneider, R.; et al. Single-photon emission from localized excitons in an atomically thin semiconductor. *Optica* **2015**, *2* (4). DOI: 10.1364/optica.2.000347

(196) Srivastava, A.; Sidler, M.; Allain, A. V.; et al. Optically active quantum dots in monolayer WSe_2. *Nat Nanotechnol* **2015**, *10* (6), 491-496. DOI: 10.1038/nnano.2015.60

(197) Moody, G.; Kavir Dass, C.; Hao, K.; et al. Intrinsic homogeneous linewidth and broadening mechanisms of excitons in monolayer transition metal dichalcogenides. *Nat Commun* **2015**, *6* (1), 8315. DOI: 10.1038/ncomms9315

(198) Li, H.; Contryman, A. W.; Qian, X.; et al. Optoelectronic crystal of artificial atoms in strain-textured molybdenum disulphide. *Nat Commun* **2015**, *6* (1), 7381. DOI: 10.1038/ncomms8381

(199) Li, B.; He, Y.; Lei, S.; et al. Scalable Transfer of Suspended Two-Dimensional Single Crystals. *Nano Lett* **2015**, *15* (8), 5089-5097. DOI: 10.1021/acs.nanolett.5b01210

(200) Kumar, S.; Kaczmarczyk, A.; Gerardot, B. D. Strain-Induced Spatial and Spectral Isolation of Quantum Emitters in Mono- and Bilayer WSe_2. *Nano Lett* **2015**, *15* (11), 7567-7573. DOI: 10.1021/acs.nanolett.5b03312

(201) Koperski, M.; Nogajewski, K.; Arora, A.; et al. Single photon emitters in exfoliated WSe_2 structures. *Nat Nanotechnol* **2015**, *10* (6), 503-506. DOI: 10.1038/nnano.2015.67

(202) Huang, Y.; Sutter, E.; Shi, N. N.; et al. Reliable Exfoliation of Large-Area High-Quality Flakes of Graphene and Other Two-Dimensional Materials. *ACS Nano* **2015**, *9* (11), 10612-10620. DOI: 10.1021/acsnano.5b04258

(203) He, Y. M.; Clark, G.; Schaibley, J. R.; et al. Single quantum emitters in monolayer semiconductors. *Nat Nanotechnol* **2015**, *10* (6), 497-502. DOI: 10.1038/nnano.2015.75

(204) Chen, C.; Zhang, N.; Li, W.; et al. Water Contact Angle Dependence with Hydroxyl Functional Groups on Silica Surfaces under CO_2 Sequestration Conditions. *Environ Sci Technol* **2015**, *49* (24), 14680-14687. DOI: 10.1021/acs.est.5b03646

(205) Chakraborty, C.; Kinnischtzke, L.; Goodfellow, K. M.; et al. Voltage-controlled quantum light from an atomically thin semiconductor. *Nat Nanotechnol* **2015**, *10* (6), 507-511. DOI: 10.1038/nnano.2015.79

(206) Bao, W.; Borys, N. J.; Ko, C.; et al. Visualizing nanoscale excitonic relaxation properties of disordered edges and grain boundaries in monolayer molybdenum disulfide. *Nat Commun* **2015**, *6*, 7993. DOI: 10.1038/ncomms8993

(207) Arora, A.; Koperski, M.; Nogajewski, K.; et al. Excitonic resonances in thin films of WSe_2: from monolayer to bulk material. *Nanoscale* **2015**, *7* (23), 10421-10429. DOI: 10.1039/c5nr01536g

(208) Rose, A.; Hoang, T. B.; McGuire, F.; et al. Control of radiative processes using tunable plasmonic nanopatch antennas. *Nano Lett* **2014**, *14* (8), 4797-4802. DOI: 10.1021/nl501976f

(209) Liu, K.; Yan, Q.; Chen, M.; et al. Elastic properties of chemical-vapor-deposited monolayer MoS_2, WS_2, and their bilayer heterostructures. *Nano Lett* **2014**, *14* (9), 5097-5103. DOI: 10.1021/nl501793a

(210) Li, Y.; Chernikov, A.; Zhang, X.; et al. Measurement of the optical dielectric function of monolayer transition-metal dichalcogenides: MoS_2, $MoSe_2$, WS_2, and WSe_2. *Physical Review B* **2014**, *90* (20). DOI: 10.1103/PhysRevB.90.205422

(211) Kormányos, A.; Zólyomi, V.; Drummond, N. D.; et al. Spin-Orbit Coupling, Quantum Dots, and Qubits in Monolayer Transition Metal Dichalcogenides. *Physical Review X* **2014**, *4* (1). DOI: 10.1103/PhysRevX.4.011034

(212) He, K.; Kumar, N.; Zhao, L.; et al. Tightly bound excitons in monolayer WSe_2. *Phys Rev Lett* **2014**, *113* (2), 026803. DOI: 10.1103/PhysRevLett.113.026803

(213) He, J.; Kumar, N.; Bellus, M. Z.; et al. Electron transfer and coupling in graphene-tungsten disulfide van der Waals heterostructures. *Nat Commun* **2014**, *5*, 5622. DOI: 10.1038/ncomms6622

(214) Han, S. J.; Garcia, A. V.; Oida, S.; et al. Graphene radio frequency receiver integrated circuit. *Nat Commun* **2014**, *5*, 3086. DOI: 10.1038/ncomms4086

(215) Desai, S. B.; Seol, G.; Kang, J. S.; et al. Strain-induced indirect to direct bandgap transition in multilayer WSe_2. *Nano Lett* **2014**, *14* (8), 4592-4597. DOI: 10.1021/nl501638a

(216) Chernikov, A.; Berkelbach, T. C.; Hill, H. M.; et al. Exciton binding energy and nonhydrogenic Rydberg series in monolayer WS_2. *Phys Rev Lett* **2014**, *113* (7), 076802. DOI: 10.1103/PhysRevLett.113.076802

(217) Castellanos-Gomez, A.; Buscema, M.; Molenaar, R.; et al. Deterministic transfer of two-dimensional materials by all-dry viscoelastic stamping. *2D Materials* **2014**, *1* (1). DOI: 10.1088/2053-1583/1/1/011002

(218) Bennett, C. H.; Brassard, G. Quantum cryptography: Public key distribution and coin tossing. *Theoretical Computer Science* **2014**, *560*, 7-11. DOI: 10.1016/j.tcs.2014.05.025

(219) Wang, L.; Meric, I.; Huang, P. Y.; et al. One-dimensional electrical contact to a two-dimensional material. *Science* **2013**, *342* (6158), 614-617. DOI: 10.1126/science.1244358

(220) Ponomarenko, L. A.; Gorbachev, R. V.; Yu, G. L.; et al. Cloning of Dirac fermions in graphene superlattices. *Nature* **2013**, *497* (7451), 594-597. DOI: 10.1038/nature12187

(221) Doherty, M. W.; Manson, N. B.; Delaney, P.; et al. The nitrogen-vacancy colour centre in diamond. *Physics Reports* **2013**, *528* (1), 1-45. DOI: 10.1016/j.physrep.2013.02.001

(222) Dean, C. R.; Wang, L.; Maher, P.; et al. Hofstadter's butterfly and the fractal quantum Hall effect in moire superlattices. *Nature* **2013**, *497* (7451), 598-602. DOI: 10.1038/nature12186

(223) Conley, H. J.; Wang, B.; Ziegler, J. I.; et al. Bandgap engineering of strained monolayer and bilayer MoS_2. *Nano Lett* **2013**, *13* (8), 3626-3630. DOI: 10.1021/nl4014748

(224) Carvalho, A.; Ribeiro, R. M.; Castro Neto, A. H. Band nesting and the optical response of two-dimensional semiconducting transition metal dichalcogenides. *Physical Review B* **2013**, *88* (11). DOI: 10.1103/PhysRevB.88.115205

(225) Rezus, Y. L.; Walt, S. G.; Lettow, R.; et al. Single-photon spectroscopy of a single molecule. *Phys Rev Lett* **2012**, *108* (9), 093601. DOI: 10.1103/PhysRevLett.108.093601

(226) Hecht, L. N. a. B. *Principles of Nano-Optics*; Cambridge University Press, 2012.

(227) Levesque, P. L.; Sabri, S. S.; Aguirre, C. M.; et al. Probing charge transfer at surfaces using graphene transistors. *Nano Lett* **2011**, *11* (1), 132-137. DOI: 10.1021/nl103015w

(228) Ju, L.; Geng, B.; Horng, J.; et al. Graphene plasmonics for tunable terahertz metamaterials. *Nat Nanotechnol* **2011**, *6* (10), 630-634. DOI: 10.1038/nnano.2011.146

(229) Splendiani, A.; Sun, L.; Zhang, Y.; et al. Emerging photoluminescence in monolayer MoS_2. *Nano Lett* **2010**, *10* (4), 1271-1275. DOI: 10.1021/nl903868w

(230) Mak, K. F.; Lee, C.; Hone, J.; et al. Atomically thin MoS_2: a new direct-gap semiconductor. *Phys Rev Lett* **2010**, *105* (13), 136805. DOI: 10.1103/PhysRevLett.105.136805

(231) Liu, Y.; Zentgraf, T.; Bartal, G.; et al. Transformational plasmon optics. *Nano Lett* **2010**, *10* (6), 1991-1997. DOI: 10.1021/nl1008019

(232) Lee, Y.; Bae, S.; Jang, H.; et al. Wafer-scale synthesis and transfer of graphene films. *Nano Lett* **2010**, *10* (2), 490-493. DOI: 10.1021/nl903272n

(233) Dean, C. R.; Young, A. F.; Meric, I.; et al. Boron nitride substrates for high-quality graphene electronics. *Nat Nanotechnol* **2010**, *5* (10), 722-726. DOI: 10.1038/nnano.2010.172

(234) Bae, S.; Kim, H.; Lee, Y.; et al. Roll-to-roll production of 30-inch graphene films for transparent electrodes. *Nat Nanotechnol* **2010**, *5* (8), 574-578. DOI: 10.1038/nnano.2010.132

(235) Reina, A.; Jia, X.; Ho, J.; et al. Large area, few-layer graphene films on arbitrary substrates by chemical vapor deposition. *Nano Lett* **2009**, *9* (1), 30-35. DOI: 10.1021/nl801827v

(236) Li, X.; Cai, W.; An, J.; et al. Large-area synthesis of high-quality and uniform graphene films on copper foils. *Science* **2009**, *324* (5932), 1312-1314. DOI: 10.1126/science.1171245

(237) Kim, K. S.; Zhao, Y.; Jang, H.; et al. Large-scale pattern growth of graphene films for stretchable transparent electrodes. *Nature* **2009**, *457* (7230), 706-710. DOI: 10.1038/nature07719

(238) Schift, H. Nanoimprint lithography: An old story in modern times? A review. *Journal of Vacuum Science & Technology B: Microelectronics and Nanometer Structures Processing, Measurement, and Phenomena* **2008**, *26* (2), 458-480. DOI: 10.1116/1.2890972

(239) Klingshirn, C. *Semiconductor Optics*; 2007. DOI: 10.1007/978-3-540-38347-5.

(240) Guo, L. J. Nanoimprint Lithography: Methods and Material Requirements. *Advanced Materials* **2007**, *19* (4), 495-513. DOI: 10.1002/adma.200600882

(241) Stafford, C. M.; Harrison, C.; Beers, K. L.; et al. A buckling-based metrology for measuring the elastic moduli of polymeric thin films. *Nat Mater* **2004**, *3* (8), 545-550. DOI: 10.1038/nmat1175

(242) Novoselov, K. S.; Geim, A. K.; Morozov, S. V.; et al. Electric field effect in atomically thin carbon films. *Science* **2004**, *306* (5696), 666-669. DOI: 10.1126/science.1102896

(243) Yuan, Z.; Kardynal, B. E.; Stevenson, R. M.; et al. Electrically driven single-photon source. *Science* **2002**, *295* (5552), 102-105. DOI: 10.1126/science.1066790

(244) Thompson, R. E.; Larson, D. R.; Webb, W. W. Precise nanometer localization analysis for individual fluorescent probes. *Biophys J* **2002**, *82* (5), 2775-2783. DOI: 10.1016/S0006-3495(02)75618-X

(245) Strauf, S.; Michler, P.; Klude, M.; et al. Quantum optical studies on individual acceptor bound excitons in a semiconductor. *Phys Rev Lett* **2002**, *89* (17), 177403. DOI: 10.1103/PhysRevLett.89.177403

(246) Santori, C.; Fattal, D.; Vuckovic, J.; et al. Indistinguishable photons from a single-photon device. *Nature* **2002**, *419* (6907), 594-597. DOI: 10.1038/nature01086

(247) Yasin, S.; Hasko, D. G.; Ahmed, H. Fabrication of <5 nm width lines in poly(methylmethacrylate) resist using a water:isopropyl alcohol developer and ultrasonically-assisted development. *Applied Physics Letters* **2001**, *78* (18), 2760-2762. DOI: 10.1063/1.1369615

(248) Michler, P.; Kiraz, A.; Becher, C.; et al. A quantum dot single-photon turnstile device. *Science* **2000**, *290* (5500), 2282-2285. DOI: 10.1126/science.290.5500.2282

(249) Lounis, B.; Moerner, W. E. Single photons on demand from a single molecule at room temperature. *Nature* **2000**, *407* (6803), 491-493. DOI: 10.1038/35035032

(250) Loudon, R. *The Quantum Theory of Light*; Oxford University Press, 2000.

(251) Kurtsiefer, C.; Mayer, S.; Zarda, P.; et al. Stable solid-state source of single photons. *Phys Rev Lett* **2000**, *85* (2), 290-293. DOI: 10.1103/PhysRevLett.85.290

(252) Brouri, R.; Beveratos, A.; Poizat, J. P.; et al. Photon antibunching in the fluorescence of individual color centers in diamond. *Opt Lett* **2000**, *25* (17), 1294-1296. DOI: 10.1364/ol.25.001294

(253) Chou, S. Y.; Krauss, P. R.; Renstrom, P. J. Imprint of sub-25 nm vias and trenches in polymers. *Applied Physics Letters* **1995**, *67* (21), 3114-3116. DOI: 10.1063/1.114851

(254) Spindt, C. A. Microfabricated field-emission and field-ionization sources. *Surface Science* **1992**, *266* (1-3), 145-154. DOI: 10.1016/0039-6028(92)91012-z

(255) Smith, T. The hydrophilic nature of a clean gold surface. *Journal of Colloid and Interface Science* **1980**, *75* (1), 51-55. DOI: 10.1016/0021-9797(80)90348-3

(256) Glauber, R. J. The Quantum Theory of Optical Coherence. *Physical Review* **1963**, *130* (6), 2529-2539. DOI: 10.1103/PhysRev.130.2529

(257) Planck, M. Über das Gesetz der Energieverteilung im Normalspektrum. *Annalen der Physik* **1901**, *4*, 553-563.

(258) Planck, M. Zur Theorie des Gesetzes der Energieverteilung im Normalspektrum. *Annalen der Physik* **1900**, *4*, 553-563.

(1) Yang, K.; Yang, Y.; Rhodes, D. A.; et al. Local strain-engineering of exciton energy in 2D materials with nanoindentation. *Nanoscale* **2026**, *18* (10), 5575-5587. DOI: 10.1039/d6nr00112b

(2) Xiao, L.; Liu, Y.; Mohajerani, S. S.; et al. Quantum Light Funneling in Tailored Triangular Plasmonic Nanocavities. *ACS Nano* **2026**. DOI: 10.1021/acsnano.5c16988

(3) Huang, G.; Chen, R.; Chen, M.; et al. Transfer and beyond: emerging strategies and trends in two-dimensional material device fabrication. *Chem Soc Rev* **2026**. DOI: 10.1039/d5cs00531k

(4) HQ Graphene. *HQ Graphene all semiconductors*. 2026. https://www.hqgraphene.com/All-Semiconductors.php (accessed March 5, 2026).

(5) Giza, M.; Mukhopadhyay, K.; Ravichandran, H.; et al. Exploring the Application of Gold-Assisted Exfoliation in Large-scale Integration of n-Type and p-Type 2D-FETs. *Small Methods* **2026**, *10* (3), e2500559. DOI: 10.1002/smtd.202500559

(6) 2D Semiconductors. *2D Semiconductors all products*. 2026. https://2dsemiconductors.com/all-products/ (accessed March 5, 2026).

(7) Yücel, O.; Yagodkin, D.; Kirchhof, J. N.; et al. Strain activation of localized states in WSe_2. *2D Materials* **2025**, *12* (3). DOI: 10.1088/2053-1583/add414

(8) Strasbourg, M. C.; Yanev, E. S.; Parvez, S.; et al. Structure-Dependent Dynamics of Quantum Emitters in Single-Layer WSe_2. *Nano Lett* **2025**, *25* (25), 10254-10261. DOI: 10.1021/acs.nanolett.5c02620

(9) Ren, T.; Granados Del Aguila, A.; Chen, Z.; et al. Van der Waals photonic integrated circuit with coherent light generation. *Nat Commun* **2025**, *16* (1), 5931. DOI: 10.1038/s41467-025-60778-2

(10) Paralikis, A.; Wyborski, P.; Metuh, P.; et al. Tunable and Low-Noise WSe_2 Quantum Emitters for Quantum Photonics. *PRX Quantum* **2025**, *6* (4). DOI: 10.1103/cynh-ql3j

(11) Mørch Nielsen, C. E.; Fischer, F.; Bester, G. Beyond the K-valley: exploring unique trion states in indirect band gap monolayer WSe_2. *npj 2D Materials and Applications* **2025**, *9* (1). DOI: 10.1038/s41699-025-00532-w

(12) Mohajerani, S. S.; Noual, A.; Ma, Y.; et al. Acoustic Manipulation of Deterministic Quantum Emitters in WSe_2. *ACS Nano* **2025**, *19* (28), 25851-25859. DOI: 10.1021/acsnano.5c04710

(13) Lee, S. J.; Chuang, H. J.; McCreary, K. M.; et al. Voltage-Induced Degradation for Enhanced Purity and Reproducibility of Quantum Emission in Monolayer 2D Materials. *ACS Nano* **2025**, *19* (38), 33981-33990. DOI: 10.1021/acsnano.5c09799

(14) Lan, H. Y.; Lin, C. P.; Liu, L.; et al. Uncovering the doping mechanism of nitric oxide in high-performance P-type WSe_2 transistors. *Nat Commun* **2025**, *16* (1), 4160. DOI: 10.1038/s41467-025-59423-9

(15) Holbrook, M.; Holtzman, L. N.; Hou, B.; et al. Revealing Substitutional Oxygen as the Dominant Defect in Flux-Grown Transition Metal Diselenides. *Nano Lett* **2025**, *25* (37), 13795-13801. DOI: 10.1021/acs.nanolett.5c03126

(16) Gavin, S. C.; Chuang, H. J.; Dasgupta, A.; et al. High-Temperature Single-Photon Emission From Covalently Functionalized van der Waals Heterostructures. *Adv Sci (Weinh)* **2025**, *12* (48), e11319. DOI: 10.1002/advs.202511319

(17) Fix, J. P. Bandgap Engineering of 2D Semiconductors for Quantum and Optoelectronic Technologies. Montana State University, 2025.

(18) Chou, S. A.; Chang, C.; Wu, B. H.; et al. Large-scale alkali-assisted growth of monolayer and bilayer WSe_2 with a low defect density. *Nat Commun* **2025**, *16* (1), 2777. DOI: 10.1038/s41467-025-57986-1

(19) Ananth, R.; Utama, M. I. B.; Xu, D. D.; et al. Enhanced spectral purity of WSe_2 quantum emitters via conformal organic adlayers. *Sci Adv* **2025**, *11* (40), eady7557. DOI: 10.1126/sciadv.ady7557

(20) Ai, R.; Cui, X.; Li, Y.; et al. Local Strain Engineering of Two-Dimensional Transition Metal Dichalcogenides Towards Quantum Emitters. *Nanomicro Lett* **2025**, *17* (1), 104. DOI: 10.1007/s40820-024-01611-1

(21) Zhou, J.; Goncalves, P. A. D.; Riminucci, F.; et al. Probing plexciton emission from 2D materials on gold nanotrenches. *Nat Commun* **2024**, *15* (1), 9583. DOI: 10.1038/s41467-024-53669-5

(22) Yu, Y.; Seo, I. C.; Luo, M.; et al. Tunable single-photon emitters in 2D materials. *Nanophotonics* **2024**, *13* (19), 3615-3629. DOI: 10.1515/nanoph-2024-0050

(23) Yao, J.; Lai, F.; Fan, Y.; et al. Nonlocal meta-lens with Huygens' bound states in the continuum. *Nat Commun* **2024**, *15* (1), 6543. DOI: 10.1038/s41467-024-50965-y

(24) Yanev, E. S.; Darlington, T. P.; Ladyzhets, S. A.; et al. Programmable nanowrinkle-induced room-temperature exciton localization in monolayer WSe_2. *Nat Commun* **2024**, *15* (1), 1543. DOI: 10.1038/s41467-024-45936-2

(25) Xu, D. D.; Vong, A. F.; Utama, M. I. B.; et al. Sub-Diffraction Correlation of Quantum Emitters and Local Strain Fields in Strain-Engineered WSe_2 Monolayers. *Adv Mater* **2024**, *36* (25), e2314242. DOI: 10.1002/adma.202314242

(26) Strasbourg, M. C.; Yanev, E. S.; Parvez, S.; et al. Increased Formation of Trions and Charged Biexcitons by Above-Gap Excitation in Single-layer WSe_2. *ACS Nano* **2024**, *18* (47), 32973-32983. DOI: 10.1021/acsnano.4c13208

(27) Strasbourg, M. C.; Yanev, E. S.; Darlington, T. P.; et al. Characterization of quantum dot-like emitters in programmable arrays of nanowrinkles of 1L-WSe_2. *Journal of Applied Physics* **2024**, *136* (4). DOI: 10.1063/5.0214410

(28) Shih, Y.-C.; Nilsson, F. A.; Guo, G.-Y. Electron energy loss spectra and exciton band structure of WSe_2 monolayers studied by ab initio Bethe-Salpeter equation calculations. *Physical Review B* **2024**, *110* (20). DOI: 10.1103/PhysRevB.110.205417

(29) Serati de Brito, C.; Rosa, B. L. T.; Chaves, A.; et al. Probing the Nature of Single-Photon Emitters in a WSe_2 Monolayer by Magneto-Photoluminescence Spectroscopy. *Nano Lett* **2024**, *24* (42), 13300-13306. DOI: 10.1021/acs.nanolett.4c03686

(30) Sakib, M. A.; Triplett, B.; Harris, W.; et al. Purcell-Induced Bright Single Photon Emitters in Hexagonal Boron Nitride. *Nano Lett* **2024**, *24* (40), 12390-12397. DOI: 10.1021/acs.nanolett.4c02581

(31) Paralikis, A.; Piccinini, C.; Madigawa, A. A.; et al. Tailoring polarization in WSe_2 quantum emitters through deterministic strain engineering. *NPJ 2D Mater Appl* **2024**, *8* (1), 59. DOI: 10.1038/s41699-024-00497-2

(32) Li, X.; Wyss, S.; Yanev, E.; et al. Width-dependent continuous growth of atomically thin quantum nanoribbons from nanoalloy seeds in chalcogen vapor. *Nat Commun* **2024**, *15* (1), 10080. DOI: 10.1038/s41467-024-54413-9

(33) Li, J.; Chen, J.; Yan, D.; et al. A Review: Active Tunable Terahertz Metamaterials. *Advanced Photonics Research* **2024**, *5* (7). DOI: 10.1002/adpr.202300351

(34) Li, C.; Luo, H.; Hou, L.; et al. Giant Photoluminescence Enhancement of Monolayer WSe_2 Using a Plasmonic Nanocavity with On-Demand Resonance. *Nano Lett* **2024**, *24* (19), 5879-5885. DOI: 10.1021/acs.nanolett.4c01260

(35) Kim, J. M.; Jeong, K. Y.; Kwon, S.; et al. Strained two-dimensional tungsten diselenide for mechanically tunable exciton transport. *Nat Commun* **2024**, *15* (1), 10847. DOI: 10.1038/s41467-024-55135-8

(36) Gérard, D.; Pierret, A.; Fartas, H.; et al. Quantum Efficiency and Vertical Position of Quantum Emitters in hBN Determined by Purcell Effect in Hybrid Metal-Dielectric Planar Photonic Structures. *ACS Photonics* **2024**, *11* (12), 5188-5194. DOI: 10.1021/acsphotonics.4c01416

(37) Garreis, R.; Tong, C.; Terle, J.; et al. Long-lived valley states in bilayer graphene quantum dots. *Nature Physics* **2024**, *20* (3), 428-434. DOI: 10.1038/s41567-023-02334-7

(38) Erbas, B.; Conde-Rubio, A.; Liu, X.; et al. Combining thermal scanning probe lithography and dry etching for grayscale nanopattern amplification. *Microsyst Nanoeng* **2024**, *10*, 28. DOI: 10.1038/s41378-024-00655-y

(39) Cunningham, P. D.; Proscia, N. V.; LaGasse, S. W.; et al. Site-Specific Exciton–Plasmon Coupling in Nanoindented WSe_2. *ACS Photonics* **2024**, *11* (8), 3250-3258. DOI: 10.1021/acsphotonics.4c00644

(40) Chuang, H. J.; Stevens, C. E.; Rosenberger, M. R.; et al. Enhancing Single Photon Emission Purity via Design of van der Waals Heterostructures. *Nano Lett* **2024**, *24* (18), 5529-5535. DOI: 10.1021/acs.nanolett.4c00683

(41) Chhaperwal, M.; Tongale, H. M.; Hays, P.; et al. Simultaneously Enhancing Brightness and Purity of WSe_2 Single Photon Emitter Using High-Aspect-Ratio Nanopillar Array on Metal. *Nano Lett* **2024**, *24* (40), 12461-12468. DOI: 10.1021/acs.nanolett.4c03168

(42) Chen, S.; Li, B.; Dai, C.; et al. Controlling Gold-Assisted Exfoliation of Large-Area MoS_2 Monolayers with External Pressure. *Nanomaterials (Basel)* **2024**, *14* (17). DOI: 10.3390/nano14171418

(43) Chen, S.; Chen, G.; Zhao, Y.; et al. Tunable Adhesion for All-Dry Transfer of 2D Materials Enabled by the Freezing of Transfer Medium. *Adv Mater* **2024**, *36* (15), e2308950. DOI: 10.1002/adma.202308950

(44) Casses, L. N.; Zhou, B.; Lin, Q.; et al. Full Quantitative Near-Field Characterization of Strongly Coupled Exciton–Plasmon Polaritons in Thin-Layered WSe_2 on a Monocrystalline Gold Platelet. *ACS Photonics* **2024**, *11* (9), 3593-3601. DOI: 10.1021/acsphotonics.4c00580

(45) Zhao, Y.; Tripathi, M.; Cernevics, K.; et al. Electrical spectroscopy of defect states and their hybridization in monolayer MoS_2. *Nat Commun* **2023**, *14* (1), 44. DOI: 10.1038/s41467-022-35651-1

(46) Yang, L.; Yuan, Y.; Fu, B.; et al. Revealing broken valley symmetry of quantum emitters in WSe_2 with chiral nanocavities. *Nat Commun* **2023**, *14* (1), 4265. DOI: 10.1038/s41467-023-39972-7

(47) Xu, D. D.; Vong, A. F.; Lebedev, D.; et al. Conversion of Classical Light Emission from a Nanoparticle-Strained WSe_2 Monolayer into Quantum Light Emission via Electron Beam Irradiation. *Adv Mater* **2023**, *35* (5), e2208066. DOI: 10.1002/adma.202208066

(48) Wang, W.; Clark, N.; Hamer, M.; et al. Clean assembly of van der Waals heterostructures using silicon nitride membranes. *Nature Electronics* **2023**, *6* (12), 981-990. DOI: 10.1038/s41928-023-01075-y

(49) Utama, M. I. B.; Zeng, H.; Sadhukhan, T.; et al. Chemomechanical modification of quantum emission in monolayer WSe_2. *Nat Commun* **2023**, *14* (1), 2193. DOI: 10.1038/s41467-023-37892-0

(50) Strasbourg, M. Thermalization and Exciton Localization in 2D Semiconductors. Montana State University, 2023.

(51) Rosiek, C. A.; Arregui, G.; Vladimirova, A.; et al. Observation of strong backscattering in valley-Hall photonic topological interface modes. *Nature Photonics* **2023**, *17* (5), 386-392. DOI: 10.1038/s41566-023-01189-x

(52) Rizzato, R.; Schalk, M.; Mohr, S.; et al. Extending the coherence of spin defects in hBN enables advanced qubit control and quantum sensing. *Nat Commun* **2023**, *14* (1), 5089. DOI: 10.1038/s41467-023-40473-w

(53) Ramsay, A. J.; Hekmati, R.; Patrickson, C. J.; et al. Coherence protection of spin qubits in hexagonal boron nitride. *Nat Commun* **2023**, *14* (1), 461. DOI: 10.1038/s41467-023-36196-7

(54) Preuss, J. A.; Gehring, H.; Schmidt, R.; et al. Low-Divergence hBN Single-Photon Source with a 3D-Printed Low-Fluorescence Elliptical Polymer Microlens. *Nano Lett* **2023**, *23* (2), 407-413. DOI: 10.1021/acs.nanolett.2c03001

(55) Mueller, N. S.; Arul, R.; Kang, G.; et al. Photoluminescence upconversion in monolayer WSe_2 activated by plasmonic cavities through resonant excitation of dark excitons. *Nat Commun* **2023**, *14* (1), 5726. DOI: 10.1038/s41467-023-41401-8

(56) Montblanch, A. R.; Barbone, M.; Aharonovich, I.; et al. Layered materials as a platform for quantum technologies. *Nat Nanotechnol* **2023**, *18* (6), 555-571. DOI: 10.1038/s41565-023-01354-x

(57) Liu, S.; Liu, Y.; Holtzman, L.; et al. Two-Step Flux Synthesis of Ultrapure Transition-Metal Dichalcogenides. *ACS Nano* **2023**, *17* (17), 16587-16596. DOI: 10.1021/acsnano.3c02511

(58) Li, X.; Jones, A. C.; Choi, J.; et al. Proximity-induced chiral quantum light generation in strain-engineered $WSe_2/NiPS_3$ heterostructures. *Nat Mater* **2023**, *22* (11), 1311-1316. DOI: 10.1038/s41563-023-01645-7

(59) Jo, K.; Marino, E.; Lynch, J.; et al. Direct nano-imaging of light-matter interactions in nanoscale excitonic emitters. *Nat Commun* **2023**, *14* (1), 2649. DOI: 10.1038/s41467-023-38189-y

(60) Hu, J.; Zhou, F.; Wang, J.; et al. Chemical Vapor Deposition Syntheses of Wafer-Scale 2D Transition Metal Dichalcogenide Films toward Next-Generation Integrated Circuits Related Applications. *Advanced Functional Materials* **2023**, *33* (40). DOI: 10.1002/adfm.202303520

(61) Hekmati, R.; Hadden, J. P.; Mathew, A.; et al. Bullseye dielectric cavities for photon collection from a surface-mounted quantum-light-emitter. *Sci Rep* **2023**, *13* (1), 5316. DOI: 10.1038/s41598-023-32359-0

(62) Hasz, K.; Hu, Z.; Park, K. D.; et al. Tip-Enhanced Dark Exciton Nanoimaging and Local Strain Control in Monolayer WSe_2. *Nano Lett* **2023**, *23* (1), 198-204. DOI: 10.1021/acs.nanolett.2c03959

(63) Guo, S.; Germanis, S.; Taniguchi, T.; et al. Electrically Driven Site-Controlled Single Photon Source. *ACS Photonics* **2023**, *10* (8), 2549-2555. DOI: 10.1021/acsphotonics.3c00097

(64) Gao, T.; von Helversen, M.; Antón-Solanas, C.; et al. Atomically-thin single-photon sources for quantum communication. *npj 2D Materials and Applications* **2023**, *7* (1). DOI: 10.1038/s41699-023-00366-4

(65) Gao, T.; von Helversen, M.; Antón-Solanas, C.; et al. Atomically-thin single-photon sources for quantum communication. *npj 2D Materials and Applications* **2023**, *7* (4). DOI: 10.1038/s41699-023-00366-4

(66) Drawer, J. C.; Mitryakhin, V. N.; Shan, H.; et al. Monolayer-Based Single-Photon Source in a Liquid-Helium-Free Open Cavity Featuring 65% Brightness and Quantum Coherence. *Nano Lett* **2023**, *23* (18), 8683-8689. DOI: 10.1021/acs.nanolett.3c02584

(67) Dong, S.; Beaulieu, S.; Selig, M.; et al. Observation of ultrafast interfacial Meitner-Auger energy transfer in a Van der Waals heterostructure. *Nat Commun* **2023**, *14* (1), 5057. DOI: 10.1038/s41467-023-40815-8

(68) Chang, S.; Yan, Y.; Geng, Y. Local Nanostrain Engineering of Monolayer MoS_2 Using Atomic Force Microscopy-Based Thermomechanical Nanoindentation. *Nano Lett* **2023**, *23* (20), 9219-9226. DOI: 10.1021/acs.nanolett.3c01809

(69) Campi, D.; Mounet, N.; Gibertini, M.; et al. Expansion of the Materials Cloud 2D Database. *ACS Nano* **2023**, *17* (12), 11268-11278. DOI: 10.1021/acsnano.2c11510

(70) Azzam, S. I.; Parto, K.; Moody, G. Purcell enhancement and polarization control of single-photon emitters in monolayer WSe_2 using dielectric nanoantennas. *Nanophotonics* **2023**, *12* (3), 477-484. DOI: 10.1515/nanoph-2022-0628

(71) Al-Juboori, A.; Zeng, H. Z. J.; Nguyen, M. A. P.; et al. Quantum Key Distribution Using a Quantum Emitter in Hexagonal Boron Nitride. *Advanced Quantum Technologies* **2023**, *6* (9). DOI: 10.1002/qute.202300038

(72) Abramov, A. N.; Chestnov, I. Y.; Alimova, E. S.; et al. Photoluminescence imaging of single photon emitters within nanoscale strain profiles in monolayer WSe_2. *Nat Commun* **2023**, *14* (1), 5737. DOI: 10.1038/s41467-023-41292-9

(73) Zhang, X.; Ren, W.; Bell, E.; et al. Gate-tunable Veselago interference in a bipolar graphene microcavity. *Nat Commun* **2022**, *13* (1), 6711. DOI: 10.1038/s41467-022-34347-w

(74) Zhang, S.; Li, B.; Chen, X.; et al. Nano-spectroscopy of excitons in atomically thin transition metal dichalcogenides. *Nat Commun* **2022**, *13* (1), 542. DOI: 10.1038/s41467-022-28117-x

(75) Zeng, H. Z. J.; Ngyuen, M. A. P.; Ai, X.; et al. Integrated room temperature single-photon source for quantum key distribution. *Opt Lett* **2022**, *47* (7), 1673-1676. DOI: 10.1364/OL.454450

(76) Yao, K.; Zhang, S.; Yanev, E.; et al. Nanoscale Optical Imaging of 2D Semiconductor Stacking Orders by Exciton-Enhanced Second Harmonic Generation. *Advanced Optical Materials* **2022**, *10* (12). DOI: 10.1002/adom.202200085

(77) Su, H.; Xu, D.; Cheng, S. W.; et al. Dark-Exciton Driven Energy Funneling into Dielectric Inhomogeneities in Two-Dimensional Semiconductors. *Nano Lett* **2022**, *22* (7), 2843-2850. DOI: 10.1021/acs.nanolett.1c04997

(78) Stevens, C. E.; Chuang, H. J.; Rosenberger, M. R.; et al. Enhancing the Purity of Deterministically Placed Quantum Emitters in Monolayer WSe_2. *ACS Nano* **2022**, *16* (12), 20956-20963. DOI: 10.1021/acsnano.2c08553

(79) Shabani, S.; Darlington, T. P.; Gordon, C.; et al. Ultralocalized Optoelectronic Properties of Nanobubbles in 2D Semiconductors. *Nano Lett* **2022**, *22* (18), 7401-7407. DOI: 10.1021/acs.nanolett.2c02265

(80) Samaner, Ç.; Paçal, S.; Mutlu, G.; et al. Free-Space Quantum Key Distribution with Single Photons from Defects in Hexagonal Boron Nitride. *Advanced Quantum Technologies* **2022**, *5* (9). DOI: 10.1002/qute.202200059

(81) Parto, K.; Azzam, S. I.; Lewis, N.; et al. Cavity-Enhanced 2D Material Quantum Emitters Deterministically Integrated with Silicon Nitride Microresonators. *Nano Lett* **2022**, *22* (23), 9748-9756. DOI: 10.1021/acs.nanolett.2c03151

(82) Pan, Y.; Rahaman, M.; He, L.; et al. Exciton tuning in monolayer WSe_2 via substrate induced electron doping. *Nanoscale Adv* **2022**, *4* (23), 5102-5108. DOI: 10.1039/d2na00495j

(83) Islam, M. A.; Serles, P.; Kumral, B.; et al. Exfoliation mechanisms of 2D materials and their applications. *Applied Physics Reviews* **2022**, *9* (4). DOI: 10.1063/5.0090717

(84) Huang, J.; Huang, Y.; Zeng, M.; et al. Fabrication of Spindt-Type Nanometer-Sized Chromium Tips for Application as Field-Electron Emitters by Releasing the Stress of the Deposited Thin Film. *ACS Applied Nano Materials* **2022**, *6* (1), 351-357. DOI: 10.1021/acsanm.2c04457

(85) Heyl, M.; List-Kratochvil, E. J. W. Only gold can pull this off: mechanical exfoliations of transition metal dichalcogenides beyond scotch tape. *Applied Physics A* **2022**, *129* (1). DOI: 10.1007/s00339-022-06297-z

(86) Haykal, A.; Tanos, R.; Minotto, N.; et al. Decoherence of VB- spin defects in monoisotopic hexagonal boron nitride. *Nat Commun* **2022**, *13* (1), 4347. DOI: 10.1038/s41467-022-31743-0

(87) Gelly, R. J.; Renaud, D.; Liao, X.; et al. Probing dark exciton navigation through a local strain landscape in a WSe_2 monolayer. *Nat Commun* **2022**, *13* (1), 232. DOI: 10.1038/s41467-021-27877-2

(88) Garg, S.; Fix, J. P.; Krayev, A. V.; et al. Nanoscale Raman Characterization of a 2D Semiconductor Lateral Heterostructure Interface. *ACS Nano* **2022**, *16* (1), 340-350. DOI: 10.1021/acsnano.1c06595

(89) Colmiais, I.; Silva, V.; Borme, J.; et al. Towards RF graphene devices: A review. *FlatChem* **2022**, *35*. DOI: 10.1016/j.flatc.2022.100409

(90) Blundo, E.; Surrente, A.; Spirito, D.; et al. Vibrational Properties in Highly Strained Hexagonal Boron Nitride Bubbles. *Nano Lett* **2022**, *22* (4), 1525-1533. DOI: 10.1021/acs.nanolett.1c04197

(91) Banszerus, L.; Hecker, K.; Moller, S.; et al. Spin relaxation in a single-electron graphene quantum dot. *Nat Commun* **2022**, *13* (1), 3637. DOI: 10.1038/s41467-022-31231-5

(92) Zhou, H.; Chen, Y.; Zhu, H. Deciphering asymmetric charge transfer at transition metal dichalcogenide-graphene interface by helicity-resolved ultrafast spectroscopy. *Sci Adv* **2021**, *7* (34). DOI: 10.1126/sciadv.abg2999

(93) Sun, B.; Grap, T.; Frahm, T.; et al. Role of electron and ion irradiation in a reliable lift-off process with electron beam evaporation and a bilayer PMMA resist system. *Journal of Vacuum Science & Technology B, Nanotechnology and Microelectronics: Materials, Processing, Measurement, and Phenomena* **2021**, *39* (5). DOI: 10.1116/6.0001161

(94) Sortino, L.; Zotev, P. G.; Phillips, C. L.; et al. Bright single photon emitters with enhanced quantum efficiency in a two-dimensional semiconductor coupled with dielectric nano-antennas. *Nat Commun* **2021**, *12* (1), 6063. DOI: 10.1038/s41467-021-26262-3

(95) So, J. P.; Kim, H. R.; Baek, H.; et al. Electrically driven strain-induced deterministic single-photon emitters in a van der Waals heterostructure. *Sci Adv* **2021**, *7* (43), eabj3176. DOI: 10.1126/sciadv.abj3176

(96) So, J. P.; Jeong, K. Y.; Lee, J. M.; et al. Polarization Control of Deterministic Single-Photon Emitters in Monolayer WSe_2. *Nano Lett* **2021**, *21* (3), 1546-1554. DOI: 10.1021/acs.nanolett.1c00078

(97) Rosati, R.; Schmidt, R.; Brem, S.; et al. Dark exciton anti-funneling in atomically thin semiconductors. *Nat Commun* **2021**, *12* (1), 7221. DOI: 10.1038/s41467-021-27425-y

(98) Parto, K.; Azzam, S. I.; Banerjee, K.; et al. Defect and strain engineering of monolayer WSe_2 enables site-controlled single-photon emission up to 150 K. *Nat Commun* **2021**, *12* (1), 3585. DOI: 10.1038/s41467-021-23709-5

(99) Panasci, S. E.; Schilirò, E.; Migliore, F.; et al. Substrate impact on the thickness dependence of vibrational and optical properties of large area MoS_2 produced by gold-assisted exfoliation. *Applied Physics Letters* **2021**, *119* (9). DOI: 10.1063/5.0062106

(100) Panasci, S. E.; Schiliro, E.; Greco, G.; et al. Strain, Doping, and Electronic Transport of Large Area Monolayer MoS_2 Exfoliated on Gold and Transferred to an Insulating Substrate. *ACS Appl Mater Interfaces* **2021**, *13* (26), 31248-31259. DOI: 10.1021/acsami.1c05185

(101) Ling, H.; Li, R.; Davoyan, A. R. All van der Waals Integrated Nanophotonics with Bulk Transition Metal Dichalcogenides. *ACS Photonics* **2021**, *8* (3), 721-730. DOI: 10.1021/acsphotonics.0c01964

(102) Li, C.; Fröch, J. E.; Nonahal, M.; et al. Integration of hBN Quantum Emitters in Monolithically Fabricated Waveguides. *ACS Photonics* **2021**, *8* (10), 2966-2972. DOI: 10.1021/acsphotonics.1c00890

(103) Iff, O.; Davanco, M.; Betzold, S.; et al. Hyperspectral study of the coupling between trions in WSe_2 monolayers to a circular Bragg grating cavity. *C R Phys* **2021**, *22* (Suppl 4). DOI: 10.5802/crphys.76

(104) Iff, O.; Buchinger, Q.; Moczala-Dusanowska, M.; et al. Purcell-Enhanced Single Photon Source Based on a Deterministically Placed WSe_2 Monolayer Quantum Dot in a Circular Bragg Grating Cavity. *Nano Lett* **2021**, *21* (11), 4715-4720. DOI: 10.1021/acs.nanolett.1c00978

(105) Funk, V.; Wagner, K.; Wietek, E.; et al. Spectral asymmetry of phonon sideband luminescence in monolayer and bilayer WSe_2. *Physical Review Research* **2021**, *3* (4). DOI: 10.1103/PhysRevResearch.3.L042019

(106) Falin, A.; Holwill, M.; Lv, H.; et al. Mechanical Properties of Atomically Thin Tungsten Dichalcogenides: WS_2, WSe_2, and WTe_2. *ACS Nano* **2021**, *15* (2), 2600-2610. DOI: 10.1021/acsnano.0c07430

(107) Errando-Herranz, C.; Scholl, E.; Picard, R.; et al. Resonance Fluorescence from Waveguide-Coupled, Strain-Localized, Two-Dimensional Quantum Emitters. *ACS Photonics* **2021**, *8* (4), 1069-1076. DOI: 10.1021/acsphotonics.0c01653

(108) Camacho, M.; Edwards, B.; Engheta, N. A single inverse-designed photonic structure that performs parallel computing. *Nat Commun* **2021**, *12* (1), 1466. DOI: 10.1038/s41467-021-21664-9

(109) Zhao, Y.; Gali, S. M.; Wang, C.; et al. Molecular Functionalization of Chemically Active Defects in WSe_2 for Enhanced Opto-Electronics. *Advanced Functional Materials* **2020**, *30* (45). DOI: 10.1002/adfm.202005045

(110) Xing, X.; Zhao, L.; Zhang, W.; et al. Influence of a substrate on ultrafast interfacial charge transfer and dynamical interlayer excitons in monolayer WSe_2/graphene heterostructures. *Nanoscale* **2020**, *12* (4), 2498-2506. DOI: 10.1039/c9nr09309e

(111) Xiao, Y.; Liu, J.; Fu, L. Moiré is More: Access to New Properties of Two-Dimensional Layered Materials. *Matter* **2020**, *3* (4), 1142-1161. DOI: 10.1016/j.matt.2020.07.001

(112) Son, S.; Shin, Y. J.; Zhang, K.; et al. Strongly adhesive dry transfer technique for van der Waals heterostructure. *2D Materials* **2020**, *7* (4). DOI: 10.1088/2053-1583/abad0b

(113) Sajid, A.; Ford, M. J.; Reimers, J. R. Single-photon emitters in hexagonal boron nitride: a review of progress. *Rep Prog Phys* **2020**, *83* (4), 044501. DOI: 10.1088/1361-6633/ab6310

(114) Rokni, H.; Lu, W. Direct measurements of interfacial adhesion in 2D materials and van der Waals heterostructures in ambient air. *Nat Commun* **2020**, *11* (1), 5607. DOI: 10.1038/s41467-020-19411-7

(115) Qian, Q.; Peng, L.; Perea-Lopez, N.; et al. Defect creation in WSe_2 with a microsecond photoluminescence lifetime by focused ion beam irradiation. *Nanoscale* **2020**, *12* (3), 2047-2056. DOI: 10.1039/c9nr08390a

(116) Peng, L.; Chan, H.; Choo, P.; et al. Creation of Single-Photon Emitters in WSe_2 Monolayers Using Nanometer-Sized Gold Tips. *Nano Lett* **2020**, *20* (8), 5866-5872. DOI: 10.1021/acs.nanolett.0c01789

(117) Madeo, J.; Man, M. K. L.; Sahoo, C.; et al. Directly visualizing the momentum-forbidden dark excitons and their dynamics in atomically thin semiconductors. *Science* **2020**, *370* (6521), 1199-1204. DOI: 10.1126/science.aba1029

(118) Luo, Y.; Liu, N.; Kim, B.; et al. Exciton Dipole Orientation of Strain-Induced Quantum Emitters in WSe_2. *Nano Lett* **2020**, *20* (7), 5119-5126. DOI: 10.1021/acs.nanolett.0c01358

(119) Hsiao, T. K.; Rubino, A.; Chung, Y.; et al. Single-photon emission from single-electron transport in a SAW-driven lateral light-emitting diode. *Nat Commun* **2020**, *11* (1), 917. DOI: 10.1038/s41467-020-14560-1

(120) Howell, S. T.; Grushina, A.; Holzner, F.; et al. Thermal scanning probe lithography-a review. *Microsyst Nanoeng* **2020**, *6*, 21. DOI: 10.1038/s41378-019-0124-8

(121) Eschimese, D.; Vaurette, F.; Melin, T.; et al. Precise tailoring of evaporated gold nanocones using electron beam lithography and lift-off. *Nanotechnology* **2020**, *31* (22), 225302. DOI: 10.1088/1361-6528/ab746e

(122) Daveau, R. S.; Vandekerckhove, T.; Mukherjee, A.; et al. Spectral and spatial isolation of single tungsten diselenide quantum emitters using hexagonal boron nitride wrinkles. *APL Photonics* **2020**, *5* (9). DOI: 10.1063/5.0013825

(123) Darlington, T. P.; Carmesin, C.; Florian, M.; et al. Imaging strain-localized excitons in nanoscale bubbles of monolayer WSe_2 at room temperature. *Nat Nanotechnol* **2020**, *15* (10), 854-860. DOI: 10.1038/s41565-020-0730-5

(124) Dang, J.; Sun, S.; Xie, X.; et al. Identifying defect-related quantum emitters in monolayer WSe_2. *npj 2D Materials and Applications* **2020**, *4* (2). DOI: 10.1038/s41699-020-0136-0

(125) Asenbauer, J.; Eisenmann, T.; Kuenzel, M.; et al. The success story of graphite as a lithium-ion anode material – fundamentals, remaining challenges, and recent developments including silicon (oxide) composites. *Sustainable Energy & Fuels* **2020**, *4* (11), 5387-5416. DOI: 10.1039/d0se00175a

(126) Zheng, Y. J.; Chen, Y.; Huang, Y. L.; et al. Point Defects and Localized Excitons in 2D WSe_2. *ACS Nano* **2019**, *13* (5), 6050-6059. DOI: 10.1021/acsnano.9b02316

(127) Zhang, L.; Chen, Z.; Zhang, R.; et al. Direct Observation of Charge Injection of Graphene in the Graphene/WSe_2 Heterostructure by Optical-Pump Terahertz-Probe Spectroscopy. *ACS Appl Mater Interfaces* **2019**, *11* (50), 47501-47506. DOI: 10.1021/acsami.9b13996

(128) Tran, K.; Moody, G.; Wu, F.; et al. Evidence for moire excitons in van der Waals heterostructures. *Nature* **2019**, *567* (7746), 71-75. DOI: 10.1038/s41586-019-0975-z

(129) Tang, Y.; Mak, K. F.; Shan, J. Long valley lifetime of dark excitons in single-layer WSe_2. *Nat Commun* **2019**, *10* (1), 4047. DOI: 10.1038/s41467-019-12129-1

(130) Rosenberger, M. R.; Dass, C. K.; Chuang, H. J.; et al. Quantum Calligraphy: Writing Single-Photon Emitters in a Two-Dimensional Materials Platform. *ACS Nano* **2019**, *13* (1), 904-912. DOI: 10.1021/acsnano.8b08730

(131) Raja, A.; Waldecker, L.; Zipfel, J.; et al. Dielectric disorder in two-dimensional materials. *Nat Nanotechnol* **2019**, *14* (9), 832-837. DOI: 10.1038/s41565-019-0520-0

(132) Peyskens, F.; Chakraborty, C.; Muneeb, M.; et al. Integration of single photon emitters in 2D layered materials with a silicon nitride photonic chip. *Nat Commun* **2019**, *10* (1), 4435. DOI: 10.1038/s41467-019-12421-0

(133) Luo, Y.; Liu, N.; Li, X.; et al. Single photon emission in WSe_2 up to 160 K by quantum yield control. *2D Materials* **2019**, *6* (3). DOI: 10.1088/2053-1583/ab15fe

(134) Lu, X.; Chen, X.; Dubey, S.; et al. Optical initialization of a single spin-valley in charged WSe_2 quantum dots. *Nat Nanotechnol* **2019**, *14* (5), 426-431. DOI: 10.1038/s41565-019-0394-1

(135) Linhart, L.; Paur, M.; Smejkal, V.; et al. Localized Intervalley Defect Excitons as Single-Photon Emitters in WSe_2. *Phys Rev Lett* **2019**, *123* (14), 146401. DOI: 10.1103/PhysRevLett.123.146401

(136) Li, Z.; Wang, T.; Jin, C.; et al. Emerging photoluminescence from the dark-exciton phonon replica in monolayer WSe_2. *Nat Commun* **2019**, *10* (1), 2469. DOI: 10.1038/s41467-019-10477-6

(137) Klein, J.; Lorke, M.; Florian, M.; et al. Site-selectively generated photon emitters in monolayer MoS_2 via local helium ion irradiation. *Nat Commun* **2019**, *10* (1), 2755. DOI: 10.1038/s41467-019-10632-z

(138) Kim, H.; Moon, J. S.; Noh, G.; et al. Position and Frequency Control of Strain-Induced Quantum Emitters in WSe_2 Monolayers. *Nano Lett* **2019**, *19* (10), 7534-7539. DOI: 10.1021/acs.nanolett.9b03421

(139) Fang, H. H.; Han, B.; Robert, C.; et al. Control of the Exciton Radiative Lifetime in van der Waals Heterostructures. *Phys Rev Lett* **2019**, *123* (6), 067401. DOI: 10.1103/PhysRevLett.123.067401

(140) Edelberg, D.; Rhodes, D.; Kerelsky, A.; et al. Approaching the Intrinsic Limit in Transition Metal Diselenides via Point Defect Control. *Nano Lett* **2019**, *19* (7), 4371-4379. DOI: 10.1021/acs.nanolett.9b00985

(141) Dass, C. K.; Khan, M. A.; Clark, G.; et al. Ultra-Long Lifetimes of Single Quantum Emitters in Monolayer WSe_2/hBN Heterostructures. *Advanced Quantum Technologies* **2019**, *2* (5-6). DOI: 10.1002/qute.201900022

(142) Barja, S.; Refaely-Abramson, S.; Schuler, B.; et al. Identifying substitutional oxygen as a prolific point defect in monolayer transition metal dichalcogenides. *Nat Commun* **2019**, *10* (1), 3382. DOI: 10.1038/s41467-019-11342-2

(143) Velicky, M.; Donnelly, G. E.; Hendren, W. R.; et al. Mechanism of Gold-Assisted Exfoliation of Centimeter-Sized Transition-Metal Dichalcogenide Monolayers. *ACS Nano* **2018**, *12* (10), 10463-10472. DOI: 10.1021/acsnano.8b06101

(144) Urban, F.; Martucciello, N.; Peters, L.; et al. Environmental Effects on the Electrical Characteristics of Back-Gated WSe_2 Field-Effect Transistors. *Nanomaterials (Basel)* **2018**, *8* (11). DOI: 10.3390/nano8110901

(145) Tripathi, L. N.; Iff, O.; Betzold, S.; et al. Spontaneous Emission Enhancement in Strain-Induced WSe_2 Monolayer-Based Quantum Light Sources on Metallic Surfaces. *ACS Photonics* **2018**, *5* (5), 1919-1926. DOI: 10.1021/acsphotonics.7b01053

(146) Taghinejad, H.; Eftekhar, A. A.; Campbell, P. M.; et al. Strain relaxation via formation of cracks in compositionally modulated two-dimensional semiconductor alloys. *npj 2D Materials and Applications* **2018**, *2* (10). DOI: 10.1038/s41699-018-0056-4

(147) Schneider, L. M.; Lippert, S.; Kuhnert, J.; et al. The influence of the environment on monolayer tungsten diselenide photoluminescence. *Nano-Structures & Nano-Objects* **2018**, *15*, 84-97. DOI: 10.1016/j.nanoso.2017.08.009

(148) Park, K. D.; Jiang, T.; Clark, G.; et al. Radiative control of dark excitons at room temperature by nano-optical antenna-tip Purcell effect. *Nat Nanotechnol* **2018**, *13* (1), 59-64. DOI: 10.1038/s41565-017-0003-0

(149) Luo, Y.; Shepard, G. D.; Ardelean, J. V.; et al. Deterministic coupling of site-controlled quantum emitters in monolayer WSe_2 to plasmonic nanocavities. *Nat Nanotechnol* **2018**, *13* (12), 1137-1142. DOI: 10.1038/s41565-018-0275-z

(150) Liang, J.; Xu, K.; Toncini, B.; et al. Impact of Post-Lithography Polymer Residue on the Electrical Characteristics of MoS_2 and WSe_2 Field Effect Transistors. *Advanced Materials Interfaces* **2018**, *6* (3). DOI: 10.1002/admi.201801321

(151) Lee, S. Y.; Jeong, T. Y.; Kim, J. H.; et al. Self-consistent dielectric constant determination for monolayer WSe_2. *Opt Express* **2018**, *26* (18), 23061-23068. DOI: 10.1364/OE.26.023061

(152) Lan, C.; Zhou, Z.; Zhou, Z.; et al. Wafer-scale synthesis of monolayer WS_2 for high-performance flexible photodetectors by enhanced chemical vapor deposition. *Nano Research* **2018**, *11* (6), 3371-3384. DOI: 10.1007/s12274-017-1941-4

(153) Jariwala, D.; Krayev, A.; Wong, J.; et al. Nanoscale doping heterogeneity in few-layer WSe_2 exfoliated onto noble metals revealed by correlated SPM and TERS imaging. *2D Materials* **2018**, *5* (3). DOI: 10.1088/2053-1583/aab7bc

(154) Hempel, M.; Lu, A. Y.; Hui, F.; et al. Repeated roll-to-roll transfer of two-dimensional materials by electrochemical delamination. *Nanoscale* **2018**, *10* (12), 5522-5531. DOI: 10.1039/c7nr07369k

(155) Fang, S.; Carr, S.; Cazalilla, M. A.; et al. Electronic structure theory of strained two-dimensional materials with hexagonal symmetry. *Physical Review B* **2018**, *98* (7). DOI: 10.1103/PhysRevB.98.075106

(156) Eich, M.; Herman, F.; Pisoni, R.; et al. Spin and Valley States in Gate-Defined Bilayer Graphene Quantum Dots. *Physical Review X* **2018**, *8* (3). DOI: 10.1103/PhysRevX.8.031023

(157) Dutta, S.; Cai, T.; Buyukkaya, M. A.; et al. Coupling quantum emitters in WSe_2 monolayers to a metal-insulator-metal waveguide. *Applied Physics Letters* **2018**, *113* (19). DOI: 10.1063/1.5045727

(158) Duong, N. M. H.; Xu, Z.-Q.; Kianinia, M.; et al. Enhanced Emission from WSe_2 Monolayers Coupled to Circular Bragg Gratings. *ACS Photonics* **2018**, *5* (10), 3950-3955. DOI: 10.1021/acsphotonics.8b00865

(159) Cao, Y.; Fatemi, V.; Fang, S.; et al. Unconventional superconductivity in magic-angle graphene superlattices. *Nature* **2018**, *556* (7699), 43-50. DOI: 10.1038/nature26160

(160) Cao, Y.; Fatemi, V.; Demir, A.; et al. Correlated insulator behaviour at half-filling in magic-angle graphene superlattices. *Nature* **2018**, *556* (7699), 80-84. DOI: 10.1038/nature26154

(161) Cai, T.; Kim, J.-H.; Yang, Z.; et al. Radiative Enhancement of Single Quantum Emitters in WSe2 Monolayers Using Site-Controlled Metallic Nanopillars. *ACS Photonics* **2018**, *5* (9), 3466-3471. DOI: 10.1021/acsphotonics.8b00580

(162) Aslan, B.; Deng, M.; Heinz, T. F. Strain tuning of excitons in monolayer WSe_2. *Physical Review B* **2018**, *98* (11). DOI: 10.1103/PhysRevB.98.115308

(163) Zhou, Y.; Scuri, G.; Wild, D. S.; et al. Probing dark excitons in atomically thin semiconductors via near-field coupling to surface plasmon polaritons. *Nat Nanotechnol* **2017**, *12* (9), 856-860. DOI: 10.1038/nnano.2017.106

(164) Zhang, Z. Z.; Song, X. X.; Luo, G.; et al. Electrotunable artificial molecules based on van der Waals heterostructures. *Sci Adv* **2017**, *3* (10), e1701699. DOI: 10.1126/sciadv.1701699

(165) Zhang, X. X.; Cao, T.; Lu, Z.; et al. Magnetic brightening and control of dark excitons in monolayer WSe_2. *Nat Nanotechnol* **2017**, *12* (9), 883-888. DOI: 10.1038/nnano.2017.105

(166) Zhang, L.; Yu, Y. J.; Chen, L. G.; et al. Electrically driven single-photon emission from an isolated single molecule. *Nat Commun* **2017**, *8* (1), 580. DOI: 10.1038/s41467-017-00681-7

(167) Yu, H.; Liao, M.; Zhao, W.; et al. Wafer-Scale Growth and Transfer of Highly-Oriented Monolayer MoS_2 Continuous Films. *ACS Nano* **2017**, *11* (12), 12001-12007. DOI: 10.1021/acsnano.7b03819

(168) Ye, Y.; Dou, X.; Ding, K.; et al. Single photon emission from deep-level defects in monolayer WSe_2. *Physical Review B* **2017**, *95* (24). DOI: 10.1103/PhysRevB.95.245313

(169) Xie, L.; Du, L.; Lu, X.; et al. A facile and efficient dry transfer technique for two-dimensional Van der Waals heterostructure. *Chinese Physics B* **2017**, *26* (8). DOI: 10.1088/1674-1056/26/8/087306

(170) Torres, J.; Zhu, Y.; Liu, P.; et al. Adhesion Energies of 2D Graphene and MoS_2 to Silicon and Metal Substrates. *physica status solidi (a)* **2017**, *215* (1). DOI: 10.1002/pssa.201700512

(171) Shepard, G. D.; Ajayi, O. A.; Li, X.; et al. Nanobubble induced formation of quantum emitters in monolayer semiconductors. *2D Materials* **2017**, *4* (2). DOI: 10.1088/2053-1583/aa629d

(172) Palacios-Berraquero, C.; Kara, D. M.; Montblanch, A. R.; et al. Large-scale quantum-emitter arrays in atomically thin semiconductors. *Nat Commun* **2017**, *8*, 15093. DOI: 10.1038/ncomms15093

(173) Ma, X.; Liu, Q.; Xu, D.; et al. Capillary-Force-Assisted Clean-Stamp Transfer of Two-Dimensional Materials. *Nano Lett* **2017**, *17* (11), 6961-6967. DOI: 10.1021/acs.nanolett.7b03449

(174) Hsu, W. T.; Lu, L. S.; Wang, D.; et al. Evidence of indirect gap in monolayer WSe_2. *Nat Commun* **2017**, *8* (1), 929. DOI: 10.1038/s41467-017-01012-6

(175) Hill, H. M.; Rigosi, A. F.; Raja, A.; et al. Exciton broadening in WS_2/graphene heterostructures. *Physical Review B* **2017**, *96* (20). DOI: 10.1103/PhysRevB.96.205401

(176) Frisenda, R.; Drüppel, M.; Schmidt, R.; et al. Biaxial strain tuning of the optical properties of single-layer transition metal dichalcogenides. *npj 2D Materials and Applications* **2017**, *1* (1). DOI: 10.1038/s41699-017-0013-7

(177) Carr, S.; Massatt, D.; Fang, S.; et al. Twistronics: Manipulating the electronic properties of two-dimensional layered structures through their twist angle. *Physical Review B* **2017**, *95* (7). DOI: 10.1103/PhysRevB.95.075420

(178) Budania, P.; Baine, P. T.; Montgomery, J. H.; et al. Comparison between Scotch tape and gel-assisted mechanical exfoliation techniques for preparation of 2D transition metal dichalcogenide flakes. *Micro & Nano Letters* **2017**, *12* (12), 970-973. DOI: 10.1049/mnl.2017.0280

(179) Branny, A.; Kumar, S.; Proux, R.; et al. Deterministic strain-induced arrays of quantum emitters in a two-dimensional semiconductor. *Nat Commun* **2017**, *8* (1), 15053. DOI: 10.1038/ncomms15053

(180) Borys, N. J.; Barnard, E. S.; Gao, S.; et al. Anomalous Above-Gap Photoexcitations and Optical Signatures of Localized Charge Puddles in Monolayer Molybdenum Disulfide. *ACS Nano* **2017**, *11* (2), 2115-2123. DOI: 10.1021/acsnano.6b08278

(181) Barreau, V.; Yu, D.; Hensel, R.; et al. Elevated temperature adhesion of bioinspired polymeric micropatterns to glass. *J Mech Behav Biomed Mater* **2017**, *76*, 110-118. DOI: 10.1016/j.jmbbm.2017.04.007

(182) Wang, Z.; Dong, Z.; Gu, Y.; et al. Giant photoluminescence enhancement in tungsten-diselenide-gold plasmonic hybrid structures. *Nat Commun* **2016**, *7*, 11283. DOI: 10.1038/ncomms11283

(183) Tran, T. T.; Bray, K.; Ford, M. J.; et al. Quantum emission from hexagonal boron nitride monolayers. *Nat Nanotechnol* **2016**, *11* (1), 37-41. DOI: 10.1038/nnano.2015.242

(184) Schwarz, S.; Kozikov, A.; Withers, F.; et al. Electrically pumped single-defect light emitters in WSe_2. *2D Materials* **2016**, *3* (2). DOI: 10.1088/2053-1583/3/2/025038

(185) Schmidt, R.; Niehues, I.; Schneider, R.; et al. Reversible uniaxial strain tuning in atomically thin WSe_2. *2D Materials* **2016**, *3* (2). DOI: 10.1088/2053-1583/3/2/021011

(186) Park, K. D.; Khatib, O.; Kravtsov, V.; et al. Hybrid Tip-Enhanced Nanospectroscopy and Nanoimaging of Monolayer WSe_2 with Local Strain Control. *Nano Lett* **2016**, *16* (4), 2621-2627. DOI: 10.1021/acs.nanolett.6b00238

(187) Palacios-Berraquero, C.; Barbone, M.; Kara, D. M.; et al. Atomically thin quantum light-emitting diodes. *Nat Commun* **2016**, *7* (1), 12978. DOI: 10.1038/ncomms12978

(188) Ocola, L. E.; Costales, M.; Gosztola, D. J. Development characteristics of polymethyl methacrylate in alcohol/water mixtures: a lithography and Raman spectroscopy study. *Nanotechnology* **2016**, *27* (3), 035302. DOI: 10.1088/0957-4484/27/3/035302

(189) Novoselov, K. S.; Mishchenko, A.; Carvalho, A.; et al. 2D materials and van der Waals heterostructures. *Science* **2016**, *353* (6298), aac9439. DOI: 10.1126/science.aac9439

(190) Noori, Y. J.; Cao, Y.; Roberts, J.; et al. Photonic Crystals for Enhanced Light Extraction from 2D Materials. *ACS Photonics* **2016**, *3* (12), 2515-2520. DOI: 10.1021/acsphotonics.6b00779

(191) Khestanova, E.; Guinea, F.; Fumagalli, L.; et al. Universal shape and pressure inside bubbles appearing in van der Waals heterostructures. *Nat Commun* **2016**, *7*, 12587. DOI: 10.1038/ncomms12587

(192) Kern, J.; Niehues, I.; Tonndorf, P.; et al. Nanoscale Positioning of Single-Photon Emitters in Atomically Thin WSe_2. *Adv Mater* **2016**, *28* (33), 7101-7105. DOI: 10.1002/adma.201600560

(193) Godin, K.; Kang, K.; Fu, S.; et al. Increased monolayer domain size and patterned growth of tungsten disulfide through controlling surface energy of substrates. *Journal of Physics D: Applied Physics* **2016**, *49* (32). DOI: 10.1088/0022-3727/49/32/325304

(194) Zhang, X. X.; You, Y.; Zhao, S. Y.; et al. Experimental Evidence for Dark Excitons in Monolayer WSe_2. *Phys Rev Lett* **2015**, *115* (25), 257403. DOI: 10.1103/PhysRevLett.115.257403

(195) Tonndorf, P.; Schmidt, R.; Schneider, R.; et al. Single-photon emission from localized excitons in an atomically thin semiconductor. *Optica* **2015**, *2* (4). DOI: 10.1364/optica.2.000347

(196) Srivastava, A.; Sidler, M.; Allain, A. V.; et al. Optically active quantum dots in monolayer WSe_2. *Nat Nanotechnol* **2015**, *10* (6), 491-496. DOI: 10.1038/nnano.2015.60

(197) Moody, G.; Kavir Dass, C.; Hao, K.; et al. Intrinsic homogeneous linewidth and broadening mechanisms of excitons in monolayer transition metal dichalcogenides. *Nat Commun* **2015**, *6* (1), 8315. DOI: 10.1038/ncomms9315

(198) Li, H.; Contryman, A. W.; Qian, X.; et al. Optoelectronic crystal of artificial atoms in strain-textured molybdenum disulphide. *Nat Commun* **2015**, *6* (1), 7381. DOI: 10.1038/ncomms8381

(199) Li, B.; He, Y.; Lei, S.; et al. Scalable Transfer of Suspended Two-Dimensional Single Crystals. *Nano Lett* **2015**, *15* (8), 5089-5097. DOI: 10.1021/acs.nanolett.5b01210

(200) Kumar, S.; Kaczmarczyk, A.; Gerardot, B. D. Strain-Induced Spatial and Spectral Isolation of Quantum Emitters in Mono- and Bilayer WSe_2. *Nano Lett* **2015**, *15* (11), 7567-7573. DOI: 10.1021/acs.nanolett.5b03312

(201) Koperski, M.; Nogajewski, K.; Arora, A.; et al. Single photon emitters in exfoliated WSe_2 structures. *Nat Nanotechnol* **2015**, *10* (6), 503-506. DOI: 10.1038/nnano.2015.67

(202) Huang, Y.; Sutter, E.; Shi, N. N.; et al. Reliable Exfoliation of Large-Area High-Quality Flakes of Graphene and Other Two-Dimensional Materials. *ACS Nano* **2015**, *9* (11), 10612-10620. DOI: 10.1021/acsnano.5b04258

(203) He, Y. M.; Clark, G.; Schaibley, J. R.; et al. Single quantum emitters in monolayer semiconductors. *Nat Nanotechnol* **2015**, *10* (6), 497-502. DOI: 10.1038/nnano.2015.75

(204) Chen, C.; Zhang, N.; Li, W.; et al. Water Contact Angle Dependence with Hydroxyl Functional Groups on Silica Surfaces under CO_2 Sequestration Conditions. *Environ Sci Technol* **2015**, *49* (24), 14680-14687. DOI: 10.1021/acs.est.5b03646

(205) Chakraborty, C.; Kinnischtzke, L.; Goodfellow, K. M.; et al. Voltage-controlled quantum light from an atomically thin semiconductor. *Nat Nanotechnol* **2015**, *10* (6), 507-511. DOI: 10.1038/nnano.2015.79

(206) Bao, W.; Borys, N. J.; Ko, C.; et al. Visualizing nanoscale excitonic relaxation properties of disordered edges and grain boundaries in monolayer molybdenum disulfide. *Nat Commun* **2015**, *6*, 7993. DOI: 10.1038/ncomms8993

(207) Arora, A.; Koperski, M.; Nogajewski, K.; et al. Excitonic resonances in thin films of WSe_2: from monolayer to bulk material. *Nanoscale* **2015**, *7* (23), 10421-10429. DOI: 10.1039/c5nr01536g

(208) Rose, A.; Hoang, T. B.; McGuire, F.; et al. Control of radiative processes using tunable plasmonic nanopatch antennas. *Nano Lett* **2014**, *14* (8), 4797-4802. DOI: 10.1021/nl501976f

(209) Liu, K.; Yan, Q.; Chen, M.; et al. Elastic properties of chemical-vapor-deposited monolayer MoS_2, WS_2, and their bilayer heterostructures. *Nano Lett* **2014**, *14* (9), 5097-5103. DOI: 10.1021/nl501793a

(210) Li, Y.; Chernikov, A.; Zhang, X.; et al. Measurement of the optical dielectric function of monolayer transition-metal dichalcogenides: MoS_2, $MoSe_2$, WS_2, and WSe_2. *Physical Review B* **2014**, *90* (20). DOI: 10.1103/PhysRevB.90.205422

(211) Kormányos, A.; Zólyomi, V.; Drummond, N. D.; et al. Spin-Orbit Coupling, Quantum Dots, and Qubits in Monolayer Transition Metal Dichalcogenides. *Physical Review X* **2014**, *4* (1). DOI: 10.1103/PhysRevX.4.011034

(212) He, K.; Kumar, N.; Zhao, L.; et al. Tightly bound excitons in monolayer WSe_2. *Phys Rev Lett* **2014**, *113* (2), 026803. DOI: 10.1103/PhysRevLett.113.026803

(213) He, J.; Kumar, N.; Bellus, M. Z.; et al. Electron transfer and coupling in graphene-tungsten disulfide van der Waals heterostructures. *Nat Commun* **2014**, *5*, 5622. DOI: 10.1038/ncomms6622

(214) Han, S. J.; Garcia, A. V.; Oida, S.; et al. Graphene radio frequency receiver integrated circuit. *Nat Commun* **2014**, *5*, 3086. DOI: 10.1038/ncomms4086

(215) Desai, S. B.; Seol, G.; Kang, J. S.; et al. Strain-induced indirect to direct bandgap transition in multilayer WSe_2. *Nano Lett* **2014**, *14* (8), 4592-4597. DOI: 10.1021/nl501638a

(216) Chernikov, A.; Berkelbach, T. C.; Hill, H. M.; et al. Exciton binding energy and nonhydrogenic Rydberg series in monolayer WS_2. *Phys Rev Lett* **2014**, *113* (7), 076802. DOI: 10.1103/PhysRevLett.113.076802

(217) Castellanos-Gomez, A.; Buscema, M.; Molenaar, R.; et al. Deterministic transfer of two-dimensional materials by all-dry viscoelastic stamping. *2D Materials* **2014**, *1* (1). DOI: 10.1088/2053-1583/1/1/011002

(218) Bennett, C. H.; Brassard, G. Quantum cryptography: Public key distribution and coin tossing. *Theoretical Computer Science* **2014**, *560*, 7-11. DOI: 10.1016/j.tcs.2014.05.025

(219) Wang, L.; Meric, I.; Huang, P. Y.; et al. One-dimensional electrical contact to a two-dimensional material. *Science* **2013**, *342* (6158), 614-617. DOI: 10.1126/science.1244358

(220) Ponomarenko, L. A.; Gorbachev, R. V.; Yu, G. L.; et al. Cloning of Dirac fermions in graphene superlattices. *Nature* **2013**, *497* (7451), 594-597. DOI: 10.1038/nature12187

(221) Doherty, M. W.; Manson, N. B.; Delaney, P.; et al. The nitrogen-vacancy colour centre in diamond. *Physics Reports* **2013**, *528* (1), 1-45. DOI: 10.1016/j.physrep.2013.02.001

(222) Dean, C. R.; Wang, L.; Maher, P.; et al. Hofstadter's butterfly and the fractal quantum Hall effect in moire superlattices. *Nature* **2013**, *497* (7451), 598-602. DOI: 10.1038/nature12186

(223) Conley, H. J.; Wang, B.; Ziegler, J. I.; et al. Bandgap engineering of strained monolayer and bilayer MoS_2. *Nano Lett* **2013**, *13* (8), 3626-3630. DOI: 10.1021/nl4014748

(224) Carvalho, A.; Ribeiro, R. M.; Castro Neto, A. H. Band nesting and the optical response of two-dimensional semiconducting transition metal dichalcogenides. *Physical Review B* **2013**, *88* (11). DOI: 10.1103/PhysRevB.88.115205

(225) Rezus, Y. L.; Walt, S. G.; Lettow, R.; et al. Single-photon spectroscopy of a single molecule. *Phys Rev Lett* **2012**, *108* (9), 093601. DOI: 10.1103/PhysRevLett.108.093601

(226) Hecht, L. N. a. B. *Principles of Nano-Optics*; Cambridge University Press, 2012.

(227) Levesque, P. L.; Sabri, S. S.; Aguirre, C. M.; et al. Probing charge transfer at surfaces using graphene transistors. *Nano Lett* **2011**, *11* (1), 132-137. DOI: 10.1021/nl103015w

(228) Ju, L.; Geng, B.; Horng, J.; et al. Graphene plasmonics for tunable terahertz metamaterials. *Nat Nanotechnol* **2011**, *6* (10), 630-634. DOI: 10.1038/nnano.2011.146

(229) Splendiani, A.; Sun, L.; Zhang, Y.; et al. Emerging photoluminescence in monolayer MoS_2. *Nano Lett* **2010**, *10* (4), 1271-1275. DOI: 10.1021/nl903868w

(230) Mak, K. F.; Lee, C.; Hone, J.; et al. Atomically thin MoS_2: a new direct-gap semiconductor. *Phys Rev Lett* **2010**, *105* (13), 136805. DOI: 10.1103/PhysRevLett.105.136805

(231) Liu, Y.; Zentgraf, T.; Bartal, G.; et al. Transformational plasmon optics. *Nano Lett* **2010**, *10* (6), 1991-1997. DOI: 10.1021/nl1008019

(232) Lee, Y.; Bae, S.; Jang, H.; et al. Wafer-scale synthesis and transfer of graphene films. *Nano Lett* **2010**, *10* (2), 490-493. DOI: 10.1021/nl903272n

(233) Dean, C. R.; Young, A. F.; Meric, I.; et al. Boron nitride substrates for high-quality graphene electronics. *Nat Nanotechnol* **2010**, *5* (10), 722-726. DOI: 10.1038/nnano.2010.172

(234) Bae, S.; Kim, H.; Lee, Y.; et al. Roll-to-roll production of 30-inch graphene films for transparent electrodes. *Nat Nanotechnol* **2010**, *5* (8), 574-578. DOI: 10.1038/nnano.2010.132

(235) Reina, A.; Jia, X.; Ho, J.; et al. Large area, few-layer graphene films on arbitrary substrates by chemical vapor deposition. *Nano Lett* **2009**, *9* (1), 30-35. DOI: 10.1021/nl801827v

(236) Li, X.; Cai, W.; An, J.; et al. Large-area synthesis of high-quality and uniform graphene films on copper foils. *Science* **2009**, *324* (5932), 1312-1314. DOI: 10.1126/science.1171245

(237) Kim, K. S.; Zhao, Y.; Jang, H.; et al. Large-scale pattern growth of graphene films for stretchable transparent electrodes. *Nature* **2009**, *457* (7230), 706-710. DOI: 10.1038/nature07719

(238) Schift, H. Nanoimprint lithography: An old story in modern times? A review. *Journal of Vacuum Science & Technology B: Microelectronics and Nanometer Structures Processing, Measurement, and Phenomena* **2008**, *26* (2), 458-480. DOI: 10.1116/1.2890972

(239) Klingshirn, C. *Semiconductor Optics*; 2007. DOI: 10.1007/978-3-540-38347-5.

(240) Guo, L. J. Nanoimprint Lithography: Methods and Material Requirements. *Advanced Materials* **2007**, *19* (4), 495-513. DOI: 10.1002/adma.200600882

(241) Stafford, C. M.; Harrison, C.; Beers, K. L.; et al. A buckling-based metrology for measuring the elastic moduli of polymeric thin films. *Nat Mater* **2004**, *3* (8), 545-550. DOI: 10.1038/nmat1175

(242) Novoselov, K. S.; Geim, A. K.; Morozov, S. V.; et al. Electric field effect in atomically thin carbon films. *Science* **2004**, *306* (5696), 666-669. DOI: 10.1126/science.1102896

(243) Yuan, Z.; Kardynal, B. E.; Stevenson, R. M.; et al. Electrically driven single-photon source. *Science* **2002**, *295* (5552), 102-105. DOI: 10.1126/science.1066790

(244) Thompson, R. E.; Larson, D. R.; Webb, W. W. Precise nanometer localization analysis for individual fluorescent probes. *Biophys J* **2002**, *82* (5), 2775-2783. DOI: 10.1016/S0006-3495(02)75618-X

(245) Strauf, S.; Michler, P.; Klude, M.; et al. Quantum optical studies on individual acceptor bound excitons in a semiconductor. *Phys Rev Lett* **2002**, *89* (17), 177403. DOI: 10.1103/PhysRevLett.89.177403

(246) Santori, C.; Fattal, D.; Vuckovic, J.; et al. Indistinguishable photons from a single-photon device. *Nature* **2002**, *419* (6907), 594-597. DOI: 10.1038/nature01086

(247) Yasin, S.; Hasko, D. G.; Ahmed, H. Fabrication of <5 nm width lines in poly(methylmethacrylate) resist using a water:isopropyl alcohol developer and ultrasonically-assisted development. *Applied Physics Letters* **2001**, *78* (18), 2760-2762. DOI: 10.1063/1.1369615

(248) Michler, P.; Kiraz, A.; Becher, C.; et al. A quantum dot single-photon turnstile device. *Science* **2000**, *290* (5500), 2282-2285. DOI: 10.1126/science.290.5500.2282

(249) Lounis, B.; Moerner, W. E. Single photons on demand from a single molecule at room temperature. *Nature* **2000**, *407* (6803), 491-493. DOI: 10.1038/35035032

(250) Loudon, R. *The Quantum Theory of Light*; Oxford University Press, 2000.

(251) Kurtsiefer, C.; Mayer, S.; Zarda, P.; et al. Stable solid-state source of single photons. *Phys Rev Lett* **2000**, *85* (2), 290-293. DOI: 10.1103/PhysRevLett.85.290

(252) Brouri, R.; Beveratos, A.; Poizat, J. P.; et al. Photon antibunching in the fluorescence of individual color centers in diamond. *Opt Lett* **2000**, *25* (17), 1294-1296. DOI: 10.1364/ol.25.001294

(253) Chou, S. Y.; Krauss, P. R.; Renstrom, P. J. Imprint of sub-25 nm vias and trenches in polymers. *Applied Physics Letters* **1995**, *67* (21), 3114-3116. DOI: 10.1063/1.114851

(254) Spindt, C. A. Microfabricated field-emission and field-ionization sources. *Surface Science* **1992**, *266* (1-3), 145-154. DOI: 10.1016/0039-6028(92)91012-z

(255) Smith, T. The hydrophilic nature of a clean gold surface. *Journal of Colloid and Interface Science* **1980**, *75* (1), 51-55. DOI: 10.1016/0021-9797(80)90348-3

(256) Glauber, R. J. The Quantum Theory of Optical Coherence. *Physical Review* **1963**, *130* (6), 2529-2539. DOI: 10.1103/PhysRev.130.2529

(257) Planck, M. Über das Gesetz der Energieverteilung im Normalspektrum. *Annalen der Physik* **1901**, *4*, 553-563.

(258) Planck, M. Zur Theorie des Gesetzes der Energieverteilung im Normalspektrum. *Annalen der Physik* **1900**, *4*, 553-563.